



OPTIMIZATION OF METHODS BASED ON LASER ABLATION - ICP - MASS SPECTROMETRY (LA-ICP-MS) FOR 2-D AND 3-D ELEMENTAL MAPPING

Word count: 90132

Stijn Van Malderen

Student number: 00800478

Supervisor: Prof. Dr. Frank Vanhaecke

A dissertation submitted to Ghent University in partial fulfilment of the requirements for the degree of Doctor of Science: Chemistry

Academic year: 2016 - 2017

In pursuit of scientific knowledge

Table of Contents

Preface.....	1
Abstract.....	1
Structure of this work	4
Acknowledgements	5
Nomenclature.....	7
Physics notations.....	11
Terminology.....	14
Bibliography	16
Chapter 1 Introduction	17
1.1 LA-ICP-MS	17
1.1.1 Instrumentation	18
1.1.2 Interferences.....	25
1.1.3 Introduction systems	26
1.2 Complementary analytical techniques	39
1.2.1 X-ray fluorescence ¹⁴⁴⁻¹⁴⁸	39
1.2.2 EPMA	40
1.2.3 micro-CT	41
1.2.4 AFM	42
1.2.5 Fluorescence microscopy ¹⁴⁹	42
1.2.6 Matrix-assisted laser desorption/ionization (MALDI) mass spectrometry	43
1.2.7 Secondary ion mass spectrometry (SIMS)	43
1.3 Sample preparation approaches	44
1.3.1 Biological samples	44
1.3.2 Geological and archaeological samples	44

1.4	Bibliography	45
Chapter 2	Aerosol transport systems	53
2.1	Introduction	54
2.2	Rapid response ablation cells: the state-of-the-art.....	55
2.2.1	State-of-the-art figures of merit.....	55
2.2.2	Trends in instrumentation development	56
2.2.3	Fundamental considerations.....	65
2.3	Considerations for ablation cell design	70
2.4	Transport line-induced dispersion	75
2.5	Background of CFD	77
2.6	Development of new ablation cells	79
2.6.1	Triple-inlet cell.....	79
2.6.2	Tube cell.....	83
2.7	Development of a viable prototype.....	89
2.7.1	ARIS.....	89
2.7.2	ATS sample chamber	93
2.8	Cryogenic low-profile stage	97
2.9	Conclusions	103
2.10	Bibliography	104
Chapter 3	Image deconvolution.....	111
3.1	Introduction	111
3.2	Deconvolution of spatially overlapping positions in one dimension	113
3.2.1	Theoretical background.....	113
3.2.2	Experimental section	116
3.2.3	Results and discussion	118
3.3	Deconvolution of 2D and 3D images	125
3.3.1	Theoretical section.....	126
3.3.2	Experimental section	134
3.3.3	Results and discussion	135
3.3.4	2D mapping applications	140
3.4	Conclusion	142
3.5	Bibliography	143
Chapter 4	Software development.....	145
4.1	Introduction	145
4.2	Goals	146
4.3	Description of the architecture	147
4.3.1	Library structure.....	147
4.3.2	Dependencies	150
4.3.3	Documentation	151
4.4	Data import	153
4.5	Data processing.....	158
4.6	Workflow.....	159
4.6.1	Filtering and transformations.....	163
4.6.2	Image segmentation	165

4.6.3	Peaks recognition and characterization.....	166
4.7	Export / interoperability	166
4.8	GUI	166
4.8.1	Main interface.....	167
4.8.2	Defining datasets.....	171
4.8.3	Importing/exporting data	172
4.8.4	Pipeline.....	172
4.8.5	Segmentation.....	173
4.8.6	Registration.....	174
4.8.7	Calibration.....	175
4.8.8	Filtering.....	176
4.8.9	Rendering.....	176
4.9	Conclusions and outlook	178
4.10	Bibliography	179
Chapter 5	Microarray standards for single cell analysis and imaging	181
5.1	Introduction	182
5.2	Experimental section	185
5.2.1	Exposure.....	185
5.2.2	Sample preparation.....	185
5.2.3	Preparation microarray standards.....	185
5.2.4	Calibration and sampling strategy.....	187
5.2.5	Safety considerations.....	190
5.3	Results and discussion	190
5.3.1	Microarray gelatine standards.....	190
5.3.2	Cu exposure effects on the population.....	191
5.3.3	Microimaging.....	193
5.4	Conclusions	193
5.5	Supporting Information.....	194
5.5.1	Cell culture conditions.....	194
5.5.2	Microwell preparation.....	194
5.5.3	Surface hydrophobicity.....	199
5.5.4	Choice of the standard medium	199
5.6	Bibliography	201
Chapter 6	3D imaging	205
6.1	Introduction	205
6.1.1	LA-ICP-MS 3D imaging	205
6.1.2	3D trace metal and metalloid distribution in mature wheat and rye grains.....	206
6.2	Experimental section	208
6.2.1	Sample preparation for LA-ICP-MS.....	208
6.2.2	Sample preparation for PN-ICP-MS.....	209
6.2.3	LA-ICP-MS imaging	210
6.2.4	Supporting CT and XRF imaging.....	212
6.3	Results and discussion	212
6.3.1	3D imaging.....	212

6.3.2	Metal distribution in seeds.....	216
6.3.3	Bulk concentrations.....	218
6.3.4	Longitudinal section <i>via</i> XRF.....	219
6.3.5	Micro-CT	220
6.3.6	Contamination risks associated with a polishing approach	220
6.4	Conclusions	221
6.5	Supporting information.....	221
6.5.1	Discussion on macro- and micronutrients.....	221
6.5.2	Segmentation.....	223
6.6	Bibliography	227
Chapter 7	Multimodal registration.....	231
7.1	Introduction	231
7.2	Experimental section part 1 / Materials and Methods	233
7.2.1	Sample preparation	233
7.2.2	LA-ICP-MS	233
7.2.3	High-resolution X-Ray Computed Tomography.....	234
7.2.4	Synchrotron radiation based 3D confocal μ -XRF.....	235
7.2.5	Safety considerations.....	235
7.3	Experimental section part 2 / Data processing.....	235
7.3.1	Data pre-processing and reconstruction of the LA-ICP-MS dataset.....	235
7.3.2	Multi-isotope extraction (MIE) of mass spectra.....	237
7.4	Results and discussion	238
7.4.1	MIE.....	238
7.4.2	SSR vs. CSR.....	239
7.4.3	Combined synchrotron radiation based confocal μ -XRF and absorption μ -CT.	240
7.4.4	3D segmentation & quantification	241
7.5	Conclusions	243
7.6	Supporting information.....	244
7.6.1	Exposure conditions.....	244
7.6.2	Analytical standards and sample preparation	245
7.6.3	High-resolution dorsoventral section.....	245
7.6.4	Limits of detection (LOD).....	246
7.6.5	3D segmentation tabulated results	247
7.6.6	Cross-modality projection (CP) of CT info onto LA-ICP-MS data	248
7.6.7	Experimental parameters of the ICP-MS system during imaging	250
7.7	Bibliography	251
Chapter 8	Conclusions and outlook	255
8.1	Outlook.....	258
8.2	Bibliography	260
Chapter 9	Samenvatting.....	261
Chapter A	Appendix.....	265
A.1	Publications and Activities.....	265
A.1.1	Peer-reviewed A-1 type publications.....	265
A.1.2	A-1 type publications submitted to peer review.....	266

A.1.3	Conferences and meeting abstracts	266
A.1.4	Patents	267
A.1.5	Product on the commercial market.....	268
A.1.6	Products in development.....	268
A.1.7	Attended SR-XRF beamtimes	268
A.1.8	Research trips.....	268
A.1.9	Teaching activities.....	268
A.2	Technical drawings.....	269
A.2.1	List of CAD drawings.....	269
A.2.2	Cad Drawings.....	269

This page was intentionally left blank

Preface

Abstract

Laser ablation-inductively coupled plasma-mass spectrometry has been one of the most significant elemental mapping techniques in the past decade, on par with XRF, and SIMS. This work pursued to improve LA-ICP-MS mapping in all aspects: throughput, sensitivity, spatial resolution, and information depth. This work followed multiple approaches to achieve this goal: i) design, manufacturing and testing of new types of ablation cells and transport lines to lower the dispersion of the aerosol plume transported into the ICP, ii) development of pre- and post-acquisition sampling and data processing strategies to improve the lateral resolution, and iii) development of 3D imaging strategies and multimodal data fusion *via* complementary techniques.

The lateral resolution of LA-ICP-MS ($\sim 5 - > 50 \mu m$) falls short of that achievable in nano XRF¹ and nano SIMS², which boast resolutions in the order of 100 nm and below, whilst the limits of detection of high-end implementations of these techniques are comparable ($\mu g/g - ng/g$ range). A large number of established and new applications, *e.g.*, in the context of metallomics³, zircon geochronology^{4,5}, multiplexed diagnostic analysis of biological tissues⁶, and trace element migration pattern imaging⁷, could benefit from higher spatial resolution in LA-ICP-MS imaging, due to the relevance of the spatial distribution of nuclides at the (sub-) μm scale level, and considering the limited accessibility to competitive nm-scale techniques. The figures of merit of LA-ICP-MS, relating to sample throughput, sensitivity and spatial resolution, depend in a large part on the ability of the ablation setup to rapidly remove the aerosol from the ablation site to the ICP-MS instrument in a manner that minimizes the mass losses and the dispersion induced in the aerosol cloud. Compressing the aerosol cloud, introduced into the ICP and produced by a single laser shot, into a shorter time window, effectively translates into a shorter, higher response peak. In an ideal situation, *i.e.* in the absence of particle losses and

plasma (mass) load effects, the integral of the signal peak remains constant, regardless of the dispersion induced. The dispersion of the aerosol plume is produced by the fluid dynamics during aerosol entrainment and transport, which are partly governed by the design of the ablation cell, *i.e.* the device in which the aerosol is captured. A number of custom ablation cell designs were produced and evaluated for their merit. The cells were retrofitted on a commercially available LA-ICP-MS setup. Significant improvements in LA-ICP-MS sensitivity and throughput were produced, with gains of up to 2-3 orders of magnitude when compared to the metrics of conventional setups. In a first iteration, a low-dispersion ablation ‘tube’ cell was manufactured. The cell and the connecting tubing achieved a 99% washout of the aerosol in approximately 6 ms, enabling separated pulse responses at frequencies up to 200–300 Hz. The tube cell was integrated into a custom-designed LA cell, which allowed for the analysis of samples with dimensions up to $100 \times 100 \times 20 \text{ mm}^3$, cryogenic cooling, faster throughput, and nm-level positioning, and was designed specifically for imaging, at no loss in performance.

To further promote the performance of LA-ICP-MS, new approaches to sampling and signal processing were developed. A post-acquisition methodology was developed for the deconvolution of overlapping ablation positions in scanning mode based on an iterative Richardson–Lucy algorithm. This algorithm enabled correction of the distortion in the scan profile upon traversing layers, in layered structures, with dimensions below the physical size of the laser beam. By overlapping the ablation positions of a $1 \text{ }\mu\text{m}$ diameter laser beam, a lateral resolution in the order of $0.3 \text{ }\mu\text{m}$ was demonstrated for 1D scanning of μm -sized layers in high capacitance multi-layer ceramic capacitors. The pre- and post-acquisition procedures for enhancing the lateral resolution of LA-ICP-MS were expanded to two- and three-dimensional (2D, 3D) nuclide distribution mapping. 2D images were constructed by projecting a rectangular grid of discrete LA ablation positions, arranged with interspaces smaller than the dimensions of the laser beam waist, onto the sample surface, thus oversampling the region of interest, and producing a 2D image convolved in the spatial domain. A 3D stack of these 2D images was deconvolved, enabling sub- μm image fidelity in a 3D image, which was demonstrated in the 3D imaging of trace level features in a corroded glass piece. A point spread function (PSF) could be derived from topography maps of single pulse craters from atomic force microscopy. This experimental PSF allows the approach to take into account the laser crater shape, beam aberrations, and the laser-solid interaction, which in turn enhances the spatial resolution of the reconstructed volume. Deconvolution algorithms were also implemented to resolve the response to individual pulses in the transient mass analyzer response at frequencies higher than the frequency at which the single-pulse response is natively separated.

A new type of high-density microarray calibration standard was developed to overcome the limitations in precision, accuracy, and throughput of current calibration approaches available for the quantification of elemental concentrations on the cellular level using LA-ICP-MS. As a case study, the accumulation of Cu in the model organism *Scrippsiella trochoidea* resulting from transition metal exposure (ranging from 0.5 to $100 \text{ }\mu\text{g/L}$) was evaluated. After the Cu exposure, cells of this photosynthetic dinoflagellate were treated with a critical point drying protocol, transferred to a carbon stub, and sputter-coated with a Au layer for SEM analysis. In subsequent LA-ICP-MS analysis, approximately 100 cells of each population were individually ablated. This approach permitted the determination of the mean concentration of Cu in the cell population

across different exposure levels and also allowed the examination of the cellular distribution of Cu within the populations. In a cross-validation exercise, subcellular LA-ICP-MS imaging was demonstrated to corroborate SR-XRF micro-imaging of single cells investigated under *in vivo* conditions. The improvement in sensitivity as a result of the fundamental developments mentioned above was crucial in the success of these experiments.

The information depth provided by LA-ICP-MS can be enhanced by recording spatial information in 3 dimensions, and fusion of LA-ICP-MS data with data provided by complementary techniques. This work explored the synergy between or within multimodal multiplexed data acquired by LA-ICP-MS and micro-computed tomography (μ -CT), a morphological probe. This work merged the spatial and spectral information of both technologies to enhance and correct a 3D visualization of the elemental distribution in a small freshwater crustacean, *Ceriodaphnia dubia*. A specimen underwent fixation, staining and embedding protocols and was analyzed using μ -CT, followed by LA-ICP-MS mapping after serial sectioning. Fusion of the data necessitated spatial alignment of the data related to each modality. An approach to register LA-ICP-MS 2D slices relative to the corresponding slices of the 3D μ -CT reconstruction with sub-pixel accuracy was demonstrated and was shown to provide advantages in the accuracy of the reconstruction of the 3D elemental distribution relative to approaches reported in literature. Data were subsequently combined to (i) enhance the spatial resolution, *via* the predictive power of the morphological probe, and (ii) improve the robustness of the data, by extracting complementary information from the mass spectrum. The imaging approach was compared to confocal SR-XRF imaging data on a *C. dubia* specimen. Furthermore, in this work, a new approach to LA-ICP-MS 3D imaging of trace-level metals in solid samples which cannot be readily sectioned using conventional microtome approaches, was presented. The probe depth of LA-ICP-MS was increased beyond the maximum laser drilling depth by serial sectioning realized *via* a polishing strategy, followed by registration of individual slices to reconstruct the 3D volume. This approach was demonstrated in the analysis of wheat and rye grains and enabled access to 3D information on a depth scale which would otherwise be inaccessible by a laser probe.

The practical implementation of the signal processing (registration, deconvolution, data fusion) approaches warranted the development of software. A python library was developed for processing transient mass spectrometry signals and other imaging data, with a specific emphasis on LA-ICP-MS imaging. This python library was based around the HDF file-type for full metadata retention and consists largely of unsupervised methods. The library provided excellent support towards ParaView, an open-source data analysis and visualization application. The architecture was designed to have a high amount of flexibility and supports large datasets both in storage, processing and rendering through distributed and parallel computation. A graphical user interface was designed around the library, which implements many of its features.

Structure of this work

Chapter 1 of the dissertation introduces the reader to the scientific fields and analytical instrumentation relevant to this work, with a particular focus on LA-ICP-MS. Chapters 2-4 focus on instrumental and methodological developments for LA-ICP-MS, whilst chapters 5-7 encompass the practical implementations of the developments. In Chapter 2, the reader is introduced to theoretical and applied concepts related to aerosol transport systems. The chapter discusses a number of ablation cell geometries developed. Chapter 3 discusses the mathematical frameworks developed for signal processing; these include approaches to deconvolution of the signal and other signal modeling and filtering strategies. In Chapter 4, a software library for image processing is described. Chapter 5 explores the quantification of element concentrations within single cells – a potential application of the improved instrumentation -, based on a new type of standard. In Chapter 6, the application field is extended to 3D imaging, in which the data processing protocols and instrumentation developed in this work, are utilized extensively. In Chapter 7, 3D image reconstruction through multiple modalities is explored more in depth. The conclusions in this work are summarized and a perspective for future developments is provided in Chapter 8. Chapter 9 provides an abstract of this work in Dutch.

Acknowledgements

First and foremost, I would like to thank my supervisor, Frank Vanhaecke, for giving me the opportunity to conduct this project, his continued support, patience, confidence, enthusiasm and encouragement. It has been no less than a privilege to work with such an outstanding supervisor and leading scientist in his field. I am grateful to the FWO (Research Fund Flanders, Fonds wetenschappelijk onderzoek – Vlaanderen) for providing financial support for this fundamental research project. The FWO is rightly regarded as the motor for top research in Flanders. Furthermore, I would like to show my gratitude to my collaborators at Teledyne CETAC technologies/Photon machines, particularly John Roy and Damon Green for their insightful advice and support –both financial and logistic–, which has lifted this research from a fundamental explorative investigation to real-world applications. I want to acknowledge Martin Tanner and Olga Borovinskaya for giving me the opportunity to dabble with the icpTOF at TOFWERK AG. I have been fortunate to have had the opportunity to conduct research visits abroad at the Slovenian National Institute for Chemistry; I appreciate the strong support of Vid Šelih, Martin Šala, and Johannes ‘Hans’ T. Van Elteren (member of the examination board) during my exciting experiments in their lab. I very much appreciated the brainstorming coffee breaks.

I have been a part of the atomic and mass spectrometry (A&MS) group for nearly 5 years (I conducted my master project here as well). I have made many friends here over the years. I would like to thank (current and former) colleagues and supporting staff of this group for the good working atmosphere they created during these years. We shared many coffee breaks, laughs, and headaches together and I wish you well in all your journeys. A special recognition goes out to Thibaut, whom has been at my side for almost 2 years. He has been a trusted colleague and I owe him thanks for helping me accomplish my many goals. I have full confidence in him to continue the laser activities in our group for the foreseeable future. Another word of thanks goes out to Steven Goderis, Stef Vansteenberge, Niels de Winter and Stepan Chernonozhkin, whom have brought me, directly and indirectly, exciting samples for analysis.

I would also like to thank the collaborators from universities abroad I work(ed) with for their friendship, close collaboration and the inspiring conversations: Jefferson Santos de Gois, Winfried Nishkauer, Sarah Theiner and Tessa Buckle.

Davy Deduytsche (CoCooN research group, UGent) is thanked for his support in the measurements involving the optical profilometer. Charlotte Nys, Maarten De Rijcke, Colin Janssen and Karel De Schampheleere from the Department of Applied Ecology and Environmental Biology are thanked for supplying little cells and daphnia, and the interesting discussions we had. Riet de Rycke and Michiel De Bruyne, thank you for aiding me in sample preparation.

The XMI group members are thanked, especially Brecht Laforce, Björn de Samber and Laszlo Vincze (member of the examination board) for the deeply beneficial cross-fertilization between

this research and the X-ray spectroscopic techniques. Their contributions to my work are highly appreciated.

I would also like to thank the other members of the examination board: Karel Strijckmans, Jorge Pisonero and Luc van Hoorebeke. Their efforts in improving this dissertation and critically reviewing parts of it, have helped to eliminate errors in the text, and have raised some interesting questions regarding the future of the field.

The staff at the Faculty of Science workshop – especially Davy De Pauw – are thanked for their efforts in producing the excellent mechanical parts for this project. Without their help and expertise, I would not have been able to accomplish many aspects of this project.

Last, but certainly not least I want to thank my parents for their unwavering support during all these years. Words fall short to express my gratitude to them for letting me spread my wings and their unequivocal support.

Nomenclature

Table 1 List of abbreviations, in alphabetical order

Abbreviation	Extended
AAS	Atomic Absorption Spectroscopy
AC	Alternating current
ADC	Analog-to-digital converter
AFM	Atomic force microscopy
AP	Atmospheric pressure
ATS	Aerosol transport system
BSE	Back-scattered electrons
CAD	Computer aided design
CCD	Charge-coupled device
<i>C. dubia</i>	<i>Ceriodaphnia dubia</i>
CFD	Computational fluid dynamics
CMOS	Complementary Metal Oxide Semiconductor
CRL	Compound refractive lens
CRM	Certified reference material
CSR	Correlative slice registration
CT	Computed tomography
CyTOF	Flow cytometry time-of-flight mass spectrometry instrument
DAQ	Data acquisition unit
DC	Direct current
DCI	Dual concentric injector
DESI	Desorption electrospray ionization mass spectrometry
DM	Dichroic mirror
DNA	Deoxyribonucleic acid
DUV	Deep ultraviolet
EPMA	Electron probe microanalysis
ESA	Electrostatic analyzer
ESI	Electrospray Ionisation
ESRF	European Synchrotron Radiation Facility
EXAFS	Extended X-Ray Absorption Fine Structure
FET	Field-effect transistor
FI	Fractionation index
fMRI	Functional magnetic resonance imaging
FWHM	Full Width at Half Maximum
FW0.1M	Full Width at 10% of the peak maximum
FW0.01M	Full Width at 1% of the peak maximum

FPM	Fundamental parameter method
FPC	Multi-channel focal plane camera
FT	Fourier transform
FTIR	Fourier transform infrared spectroscopy
FTICR	Fourier transform ion cyclotron resonance mas spectrometry
FV	Finite volume
GC	Gas chromatography
HAZ	Heat-affected zone
HDD	Hard disk drive
HDF	Hierarchical data format
HEAD	High Efficiency Aerosol Dispersion
HPLC	High performance liquid chromatography
ICR	Ion cyclotron resonance
IB	Inverse Bremsstrahlung
ID	Internal diameter
IE	Ionization energy
IP	Ionization potential or Intellectual property
IR	Infrared
ITO	In-Sn oxide
KB	Kirkpatrick-Baez
KED	Kinetic energy discrimination
KL	Knudsen layer
LAESI	Laser ablation electrospray ionization
LA-ICP-MS	Laser ablation-inductively coupled plasma-mass spectrometry
LAMIS	Laser ablation molecular isotopic spectrometry
LDI-MS	Laser desorption ionization mass spectrometry
LED	Light emitting diode
LIBS	Laser-induced breakdown spectroscopy
LITD	Laser-induced thermal desorption
LFR	Laminar flow reactor
LN ₂	Liquid nitrogen
LOD	Limit of detection
LOQ	Limit of quantification
LTE	Local thermal equilibrium
MALDI	Matrix-assisted laser desorption ionization mass spectrometry
MCA	Multi-channel analyzer
MIP	Microwave induced plasma
MOSFET	Metal-oxide-semiconductor field-effect transistor
MRI	Magnetic resonance imaging

MTF	Modulation transfer function
NA	Numerical aperture
NAA	Neutron activation analysis
Nd:YAG	Neodymium-doped yttrium aluminum garnet
NIST	National Institute of Standards and Technology
NMB	New mixing bulb
OD	Outer diameter
OES	Optical emission spectroscopy
OPC	Optical particle counter
OT	Optical tweezers
PCB	Printed circuit board
PDF	Probability density function
PE	Photoelectric effect
PET	Positron emission tomography
PEEK	Polyether ether ketone
PI	Photoionization
PID	Proportional-integral-derivative
PIGE	Particle-induced gamma emission
PIXE	Particle-induced X-ray emission
PMMA	Polymethylmethacrylate (Perspex® (UK) or Plexiglas® (USA))
POM	Polyoxymethylene (Delrin®)
POP	Proof of principle
PSF	Point spread function
PTFE	Polytetrafluoroethylene (Teflon®)
RAM	Random Access Memory
RANS	Reynolds-averaged Navier-Stokes
RBS	Rutherford backscattering spectrometry
RF	Radiofrequency
RNA	Ribose nucleic acid
ROI	Region-of-interest
RSD	Relative standard deviation
SAXS	Small angle X-ray scattering
SDD	Silicon drift detector or source-detector distance
SE	Secondary electrons
SEM	Scanning electron microscopy
SF	Sector-field
SHRIMP	Sensitive high mass-resolution ion microprobe
SIMS	Secondary ion mass spectrometry
SLM	Spatial light modulator

SOD	Source-object distance
SPECT	Single photon emission computed tomography
SPR	Single pulse response
SR	Synchrotron radiation or super-resolution
SRM	Standard reference material
SSB	Standard-Sample Bracketing
SSR	Sequential slice registration
STF	Setup transfer function
<i>S. trochoidea</i>	<i>Scrippsiella trochoidea</i> microalgae
SW	Shockwave
TC	Tube cell
TEC	Thermoelectric cooling
TEM	Transverse electromagnetic mode
TIMS	Thermal ionization mass spectrometry
TNT	Trinitrotoluene
ToF	Time-of-flight
VOI	Volume-of-interest
VUV	Vacuum ultra-violet (<150 nm)
WD	Working distance
XANES	X-ray absorption near edge structure
XRD	X-ray diffraction
XRF	X-ray fluorescence (spectroscopy)

Physics notations

8.1.1.1 Latin characters

Symbol	Physical meaning	Unit symbol	Constant Value
A	Area	m^2	
B	Magnetic flux density	T	
C	Capacitance	F	
c	Speed of light in vacuum	$m\ s^{-1}$	2.99792×10^8
d_a	Atomic diameter	m	
\vec{E}	Electric field vector	$V\ m^{-1}$	
E	Energy	J	
E_i	Ionization energy	J	
E_k	Kinetic energy	J	
E_p	Potential energy	J	
e	Base of the natural algorithm		2.71828
e	Elementary charge	C	1.60218×10^{-19}
eV	Electronvolt unit	J	1.60218×10^{-19}
F	Force	N	
F_L	Lorentz force	N	
f	Frequency	Hz	
g_0	Statistical weight for the ground state		
g_i	Statistical weight for the ionic state		
H	Hamiltonian	J	
H	Enthalpy (total heat content)	J	
h	Planck's constant	$J \cdot s$	6.62607×10^{-34}
I	Intensity	W/m^2	
k_B	Boltzmann's constant	$J \cdot K^{-1}$	1.38065×10^{-23}
k	Wavenumber	m^{-1}	
l	Mean free path length	m	
m	Mass	g	
m_a	Atomic mass	u	
m_e	Electron rest mass		
N	Atomic number		
N_A	Avogadro's constant	mol^{-1}	6.02214×10^{23}
n_e	Free electron number density	cm^{-3}	
n_q	Ionic atom number density	cm^{-3}	
n_0	Neutral atom number density	cm^{-3}	

n	Refractive index		
P	Power	W	
p	Pressure	Pa	
p_{atm}	Standard atmospheric pressure	Pa	101325
p	probability a null hypothesis holds true		
Q	Electric charge	C	
Q^+	Ionic partition function (first excitation level)		
Q^0	Atomic partition function		
R	Gas constant	$JK^{-1}mol^{-1}$	8.31446
R	Resistance	Ω	
R_e	Reynold's number		
r	Radius	m	
s	Estimated standard deviation		
T	Thermodynamic temperature	K	
T_b	Boiling temperature	K	
T_e	Electron temperature	K	
T_i	Ionization temperature	K	
T_s	Surface temperature	K	
t	Time	s	
U	Potential	V	
U_i	Internal energy	J	
U_0	Acceleration potential	V	
u	Unified atomic mass unit	g	1.66054×10^{-24}
V	Volume	m^3	
v	Velocity	$m s^{-1}$	
Z	Atomic number		

8.1.1.3 Greek characters

Symbol	Physical meaning	Unit symbol	Constant Value
${}^4_2\alpha$	Alpha particle (He)		
β	Beta particle (high energy electron or positron)		
γ	Gamma radiation (high-energy photon emission)		
δ	Displacement or difference		
Δ	Difference		
ε	Permittivity	$F\ m^{-1}$	
η	Coefficient of viscosity	$Pa\ s$	
η	Characteristic impedance		
θ	Angular displacement	rad	
λ	Wavelength	m	
μ	Dynamic viscosity	$Pa\ s$	
ν	Kinematic viscosity	$m^2\ s^{-1}$	
π	Pi		3.14159
ρ	Mass density	$g\ mol^{-1}$	
ρ_b	Background gas density		
σ	True standard deviation		
τ_s	Shear stress	Pa	
τ	Detector dead time	s	
Φ	Field strength	$T\ or\ V\ m^{-1}$	
Φ	Volumetric flow rate	$m^3\ s^{-1}$	
ω	Angular frequency	$rad\ s^{-1}$	

Terminology

Below is a glossary of selected domain-specific terminology used in this dissertation in alphabetical order.

Abundance sensitivity [IUPAC Gold book definition] The ratio of the maximum ion current recorded at a mass to the ion current arising from the same species recorded at an adjacent mass.

Anthropogenic isotope fractionation Isotope enrichment can be performed in nuclear reactors, centrifuges, cyclotrons, etc. for the production of radioisotopes for medical and nuclear applications.

Elemental fractionation [In the context of LA-ICP-MS] All non-stoichiometric effects occurring during ablation, aerosol formation, transport, vaporization, atomization, and ionization.

H&E stain Hematoxylin and eosin stain used in histology to visualize tissue and cell structure. Hematoxylin stains basophilic substances, such as DNA and RNA in the nuclei of cells, blue, whilst eosin colors acidophilic structures in various shades of red, pink and orange.

Internal standards [IS] Addition of an element or multiple elements to standardize the response across multiple samples and standards and within a single sample. Examples are Iridium intercalators, iodination, deposition of Au layers, inkjet patterns on membranes, and Indium-containing inks for immunoimaging.^{3,8-10} Although Iodine is a good indicator of protein density, Iodine is not well-suited as IS due to its high natural background. For a single IS, the corrected response of another mass channel response E is calculated according to $E_{corrected} = E_{raw} IS_{avg} / IS_{pixel}$. Internal reference elements must be chosen with care; the nuclide selected must be free from spectral interferences and must have similar fraction behaviour (*cf.* fractionation indices). The IS must be homogeneously distributed and the concentration must be known (either based on stoichiometry or measured by a secondary technique with a precision and accuracy better than LA)

Mass Discrimination Instrumental mass discrimination against lighter mass ions (favoring heavier ions) occurs as a result of energy-selective ion transmission (space-charge effects), collisions between ions and neutral species, and mass-independent fractionation. Mass discrimination can also be potentially produced by isotope-specific oxide formation. The magnitude of mass discrimination is in the order of 10 – 20% per u for light nuclides, *e.g.*, ^7Li and ^{10}B , and as low as 1% per u for heavy nuclides, *e.g.*, ^{238}U .

Mass bias correction model Mathematical corrections can be applied to compensate for mass bias. The correction models include the power law, $R_{i/j} = r_{i/j} e^{f_e(m_i - m_j)}$, and exponential law, $R_{i/j} = r_{i/j} (1 + f_p)^{m_i - m_j}$, with $R_{i/j}$ the corrected ratio of isotopes with mass m_i and m_j , $r_{i/j}$ the measured isotope amount ratio. These laws are not to be mistaken with Russel's law.

Mass resolution Figure of merit reflecting the ability of a mass analyzer to separate ions of different m/z . The mass resolution can be calculated based on the experimentally observed ion current peak width ($R = m/\delta m$). The resolution required to resolve 2 m/q ratios is $R_{req} =$

$((m_1 + m_2)/2)/(m_2 - m_1)$. Two ion current peaks p_1, p_2 are considered to be resolved if the minimum of the valley in-between p_1 and p_2 is $< 0.1p_{1,max}$, and $< 0.1p_{2,max}$.

Natural abundance The variation that exists in binding energy per nucleon (7.6 to 8.8 MeV) produces profound effects in the isotopic composition of elements, especially for the light elements for which the variation in binding energy is larger. Nuclides with an even number of protons and neutrons produce more stable nuclei. The variation in binding energy per nucleon as a function of the atomic number for the heavier elements is limited, though the variation among isotopes of an element can vary substantially. The mixing process in the pre-solar nebula (>4.6 billion years ago) has resulted in almost invariant isotopic ratios across our planet, giving rise to a *quasi*-stable average relative abundance of nuclides.

Natural isotope fractionation Isotope fractionation processes occur in nature as a result of mass-dependent and mass-independent (related to volume of the nucleus or its magnetic properties) reaction kinetics or reaction thermodynamics or transport, fusion and fission processes (α – decay, β – decay, γ – radiation) for radiogenic nuclides and cosmic ray-induced spallation.

Relative abundance The relative abundance of one nuclide xE of element E is relative amount (number of atoms N or number of moles n) of nuclide xE divided by the total amount (number of atoms or number of moles) of the element E (all m isotopes): $\theta^{xE} = N^{xE} / \sum_{i=1}^{i=m} N^iE$

Reynolds number, Re Indicative numerical value for the likelihood of the occurrence of turbulence. Within a tube flow, $Re = v_{mean}D/\nu$, with v_{mean} the mean fluid velocity, D the hydraulic diameter of the tube, and ν the kinematic viscosity of the fluid. Laminar flow is achieved at $Re \lesssim 2100$.

Standard-sample-bracketing Mass fractionation correction based on bracketing the measurand with calibrators. The corrected isotope ratio R_{corr} can be calculated as follows: $R_{smp} = K r_{smp}$; $K = R_{cal}/r_{cal}$, where R and r indicate the correct and measured isotope ratio, respectively, of the sample and calibrator.

Taylor-Aris dispersion Gas flows follow a parabolic velocity profile in a (laminar) pipe flow. The velocity profile in a straight pipe of diameter D can be modelled as a function of the radial position: $v(r) = v_{max} (1 - r^2/D^2)$, with v_{max} the maximum velocity (in the center position). The discrepancy in the velocities between the inner and outer flow induce (Taylor-Aris) dispersion. In a sharp bend of the pipe, the outer radius maintains higher gas flow velocities compared to the inner radius giving rise to a shear force which can push the flow into a turbulent flow regime.

Atomic or molecular orbitals A wave function representing the likelihood distribution of the spatial location of an electron.

Bibliography

- (1) Laforce, B.; Schmitz, S.; Vekemans, B.; Rudloff, J.; Garrevoet, J.; Tucoulou, R.; Brenker, F. E.; Martinez-Criado, G.; Vincze, L. *Anal Chem* **2014**, *86*, 12369-12374.
- (2) Pisonero, J.; Fernández, B.; Günther, D. *J Anal Atom Spectrom* **2009**, *24*, 1145-1160.
- (3) Giesen, C.; Waentig, L.; Mairinger, T.; Drescher, D.; Kneipp, J.; Roos, P. H.; Panne, U.; Jakubowski, N. *J Anal Atom Spectrom* **2011**, *26*, 2160-2165.
- (4) Farley, K. A.; Shuster, D. L.; Ketcham, R. A. *Geochimica et Cosmochimica Acta* **2011**, *75*, 4515-4530.
- (5) McCarron, T.; Gaidies, F.; McFarlane, C. R. M.; Easton, R. M.; Jones, P. *Mineralogy and Petrology* **2014**, *108*, 741-758.
- (6) Managh, A. J.; Edwards, S. L.; Bushell, A.; Wood, K. J.; Geissler, E. K.; Hutchinson, J. A.; Hutchinson, R. W.; Reid, H. J.; Sharp, B. L. *Anal Chem* **2013**, *85*, 10627-10634.
- (7) van Elteren, J. T.; Izmer, A.; Šala, M.; Orsega, E. F.; Šelih, V. S.; Panighello, S.; Vanhaecke, F. *J Anal Atom Spectrom* **2013**, *28*, 994-1004.
- (8) Frick, D. A.; Giesen, C.; Hemmerle, T.; Bodenmiller, B.; Günther, D. *J. Anal. At. Spectrom.* **2015**, *30*, 254-259.
- (9) Bonta, M.; Lohninger, H.; Marchetti-Deschmann, M.; Limbeck, A. *Analyst* **2014**, *139*, 1521-1531.
- (10) Limbeck, A.; Galler, P.; Bonta, M.; Bauer, G.; Nischkauer, W.; Vanhaecke, F. *Analytical and bioanalytical chemistry* **2015**, *407*, 6593-6617.

Chapter 1 Introduction

This chapter is based on a review paper titled ‘Recent developments in the design of rapid response cells for Laser Ablation – Inductively Coupled Plasma – Mass Spectrometry and their impact on bioimaging applications’ authored by Stijn J. M. Van Malderen, Amy J. Managh, Barry L. Sharp and Frank Vanhaecke, and published after peer review.¹ Parts of the Master dissertation ‘Trace element fingerprinting of stained glass (St. Jacobs Church, Antwerp) via laser ablation – ICP – mass spectrometry, authored by Stijn J. M. Van Malderen, have also been adopted and were updated.² S.V.M. is the first and principal author of both works.

This chapter introduces a reader with some experience in the analytical field to contemporary analytical instrumentation relevant to this work. This type of instrumentation can provide micro- and macroscale spatially resolved, and in some cases quantitative, information on metal distribution levels or sample topography and morphology. In pursuance of a comprehensive understanding of metal chemistry, multiple analytical modalities including mass spectrometry imaging (SIMS, LA-ICP-MS, MALDI, FTICR) and radiation-detection based methods (μ XRF, XRD, SEM-EDX/WDX, μ PIXE, FTIR, fluorescence microscopy, etc.) were enlisted or discussed in this work.

1.1 LA-ICP-MS

Laser Ablation-Inductively Coupled Plasma-Mass Spectrometry (LA-ICP-MS) is a hyphenated elemental microprobe technique capable of producing spatially resolved data at the μ m scale. Its capability of direct compositional characterization under atmospheric pressures, conceptual simplicity and extensive flexibility towards matrix types and analyte levels have established the method as a routine *quasi* non-destructive generic analysis tool. The scope of applications for LA-ICP-MS was initially limited to the analysis of geological material.³⁻⁷ This scope was

gradually extended to include key applications in geochronology^{8,9} and elemental imaging.¹⁰⁻¹⁴ At a later stage, the technique was adopted by archaeometry¹⁵⁻¹⁷, forensic sciences¹⁸⁻²¹, biology, and medicine²²⁻²⁸. In the past years, studies in the fields of proteomics, metallomics and nanotechnology have expanded the range of applications for the technique to, *e.g.*, the visualization of the distribution of drugs and tagged markers in biological tissue sections and single cells^{24,25,29}, quantitative elemental and isotope ratio determinations in tissue^{26,30,31}, and the uptake of nanoparticles^{32,33}. Bioimaging and geo-imaging have now arguably become the most prolific applications of the technique.

1.1.1 Instrumentation

ICP-MS instruments can be conceptually broken up into 5 modules: (i) the sample introduction system, (ii) the ionization source: the inductively coupled plasma, (iii) the ion extraction system, (iv) the mass analyzer and (v) the ion detector.³⁴ In the LA-ICP-MS setup (Figure 1), first demonstrated by Gray *et al.* in 1985, the sample introduction system is a laser unit that can remove material in a controlled manner from the surface of a solid or liquid using high-power laser pulses of *ns* to *fs* pulse width, *i.e.* *ablation*.³⁵ Ablation of the surface produces a particle-dense aerosol, which is transported by a carrier gas to an Ar-based inductively coupled plasma source which will desolvate, atomize, and ionize the aerosol. The ions are extracted by the interface from the analytical zone in the central channel of the ICP operating at atmospheric pressure ($\approx 10^5$ Pa) into the high vacuum environment ($10^{-1} - 10^{-6}$ Pa) maintained within the MS. Subsequently, ion optics guide the ion beam into a mass analyzer and filter away photons. The mass analyzer will either spread the ions temporal-spatially according to their m/q , or filter ions with a specified m/q prior to ion detection.³⁴ The general theoretical concepts of each of the 5 modules are elaborated below. More detailed information can be found in specialized reference works.^{34,36-38}

As an analytical tool, ICP-MS boasts distinct advantages such as a wide linear dynamic range, low LODs, high sample throughput, fast read-out, and full elemental mass spectrum coverage (enabling the detection of individual isotopes), all of which combined make it an ideal partner for the LA introduction system. The limitations of the technique include: (i) low tolerance for high total dissolved solids content solutions, (ii) spectral interferences, (iii) matrix effects, and (iv) considerable purchase and operating costs. Although full-spectrum capabilities are more readily accessible in LA-ICP-OES (in terms of purchase cost), mass spectrometry is preferred due to significantly better LODs. Compared to TIMS and NAA, ICP-MS is characterized by superior ease-of-analysis; this is especially the case when an LA-system is used, as minimal sample preparation is required. The main application of ICP-MS today is the trace element and isotopic analysis of solutions in industry, the academia now represents only a minor fraction of the market.

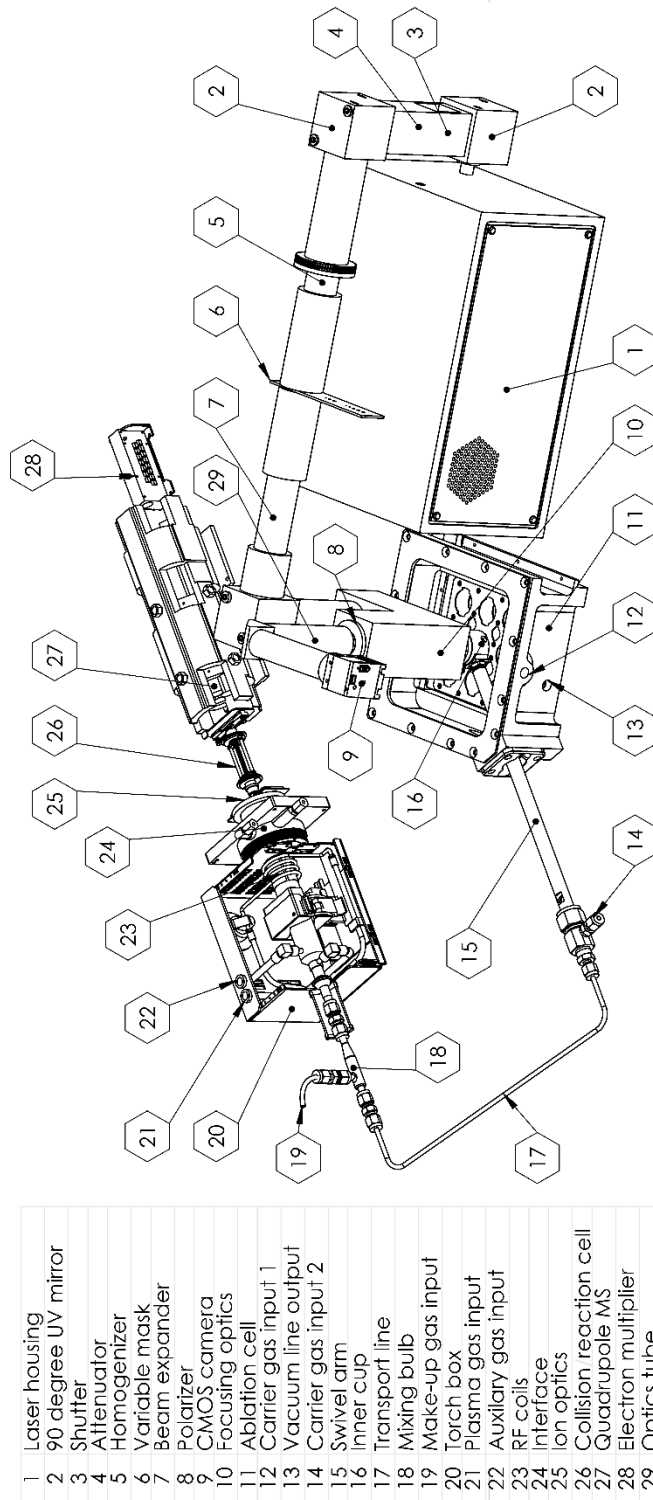


Figure 1 Annotated CAD 3D assembly drawing of a LA-ICP-MS system. This drawing is a fairly accurate representation of the instrumentation. The drawing pulls elements from the Agilent 7900 ICP-Q-MS unit (Agilent) and Analyte G2 ArF* lasing system (Teledyne Photon Machines, Bozeman, MT, USA).

1.1.1.1 Inductively coupled plasma

In 1980, the inductively coupled plasma (ICP), historically developed for OES, was coupled to a mass analyzer by Houk *et al.*³⁹. The elongated toroidal plasma of the ICP, a high-temperature gas mixture of neutral species, charged positive and negative particles, with an overall neutral electric charge, is sustained inside the torch (Figure 2) through energy transfer from a magnetic field *via* induction. The time-dependent magnetic field is created by sending an alternating RF current (*kW* range, 27.12 or 40.68 *MHz* in a free-running generator) through a water- or Ar-cooled load coil, forcing electrons to flow in a closed annular path. The plasma is initiated *via* ‘seed electrons’, generated by a high-voltage Tesla discharge spark, which produces the cascading electron generation process. Molecules are broken down in the plasma and the resulting atoms are ionized *via* electron impact and ionization, charge transfer from ionized Ar atoms (first E_i of 15.76 *eV*) or Penning ionization (ionization as a result of energy transfer from an excited neutral Ar atom with metastable states at 11.55 *eV* and 11.72 *eV*). Ionization efficiencies are high (> 80%) for many elements under typical conditions within the normal analytical zone (electron temperature of ~7000 – 8500 *K*, with electron number densities in the range of $1.6 - 7.0 \times 10^{15} \text{ cm}^{-3}$); an ionization degree of up to > 90% is attained for elements with a first $E_i \leq 10.5 \text{ eV}$.⁴⁰⁻⁴² Elements with high IPs (*e.g.*, diatomic non-metals and noble gases) and/or a light mass (as these are more prone to space charge losses) typically have lower sensitivities. The degree of (thermal) ionization can be estimated for a system in thermal equilibrium using the Saha equation (Equation 1).

$$\frac{n_q}{n_0} = \frac{(2\pi m_e k_B T)^{1.5}}{n_e h^3} \cdot \frac{2Q^+}{Q^0} e^{-\frac{E_i}{kT}} \quad \text{Equation 1}$$

The inductive heating process only penetrates ~0.1 *mm* into the plasma, as the plasma is shielded by an opposing magnetic field from the charge in the plasma. The ICP and load coil are decoupled by a grounded shield to avoid secondary electrical discharges. Particle ionization hence takes place in a zone which is heated by thermal transfer from the outer layers of the plasma. The Fassel torch consists of three concentric tubes, each providing a gas flow (in most cases Ar) into the plasma. Cool or plasma gas (10 – 15 *L min*⁻¹ Ar) sustains the plasma and acts as a sheath flow providing a protective thermal barrier for the quartz torch forward section. The auxiliary gas flow (0.5 – 1.2 *L min*⁻¹ Ar) can be fine-tuned to optimize the position of the plasma relative to the torch. The carrier fluid (0.5 – 1.2 *L min*⁻¹ Ar) flowing through the central tube transports the sample aerosol into the plasma on-axis with the sample cone opening. The composition of the carrier flow is altered depending on the plasma characteristics desired. The flow of the cool gas flow and auxiliary flow is not parallel. The flow connections are mounted off-axis, resulting in turbulent fluid flows with a rotational component, generating eddy currents around the plasma. Other, less common ionization sources include arc, spark, DC coupled and the cost-efficient microwave induced plasma (MIP), which can operate using N₂ as the plasma gas.

1.1.1.2 Ion extraction and lens system

Extraction of the ion beam is accomplished by the dual-stage interface assembly (Figure 2). The interface consists of two or three co-axially aligned water-cooled metal (Ni, Pt, Al) cones with

central apertures, approximately $0.4 - 1.2\text{ mm}$ in diameter. Sampler and skimmer cones are designed to establish a stepwise pressure gradient to a high vacuum environment pumped by rotary vacuum pumps, to reduce the frequency of collisions within the ion beam. The expanding plasma fluid reaches supersonic velocities in the low pressure environment ($100 - 500\text{ Pa}$) between the cones. The plasma fluid expansion is disturbed by local shock waves in the flow field, *e.g.*, a weak shock wave is formed at the skimmer tip and propagating towards the vacuum outlet.^{43,44} Due to the fast transition to a low-pressure, cold environment, most reactions that could alter the composition stop occurring, all but the exceptional ion-molecule or attachment process reaction. The ion beam is extracted from the interface assembly by the skimmer cone, accelerated and focused into the mass analyzer by electrostatic extraction, transfer and focusing optics (Figure 2). Due to the entrainment of the ions in the plasma fluid, all ions travel within a narrow velocity range through the interface, inducing a wide range of kinetic energies in the range of $\approx 0.3\text{ eV}$ for ^6Li and $\approx 12\text{ eV}$ for ^{238}U at 2200 m s^{-1} .⁴⁵ The mass analyser operates under a pressure of $10^{-2} - 10^{-5}\text{ Pa}$, at which the mean free path length of ions is in the order of $0.1 - 10\text{ m}$. Transfer optics are designed to minimize beam divergence (*cf.* space charge effects). Electrostatic lenses or photon beam stops separate ions from neutral species and photons, which otherwise give rise to background noise on the detector.^{34,36,46} The ions are collimated and accelerated through an entrance slit by an electrostatic lens assembly.

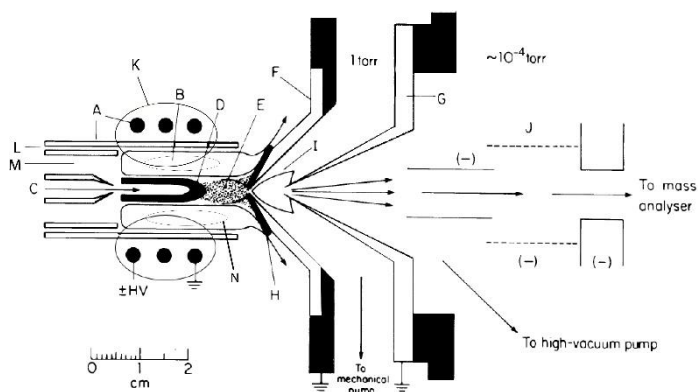


Figure 2 Schematic representation of an ICP sampling interface. Legend: A, load coil; B, induction region; C, aerosol carrier gas flow; D, initial radiation zone; E, normal analytical zone; F, sampler (cone); G, skimmer (cone); H, boundary layer of ICP gas deflected outside sampler; I, supersonic jet; J, ion lens; K, magnetic field; L, plasma gas flow; M, Auxiliary gas flow; N, high energy region. Adapted from Jarvis *et al.*⁴⁷

1.1.1.3 Mass spectrometers

The spatial or temporal separation of the ions in the ion beam based on the m/q can either be performed by static and variable (high-frequency) electric and magnetic fields in quadrupole, ion-trap, Fourier transform ion cyclotron resonance (*cf.* orbitraps⁴⁸), and sector field mass analyzers, or by pulsed ion packet injection followed by separation by velocity at *quasi*-constant

kinetic energy in Time-of-Flight⁴⁹ or Distance-of-flight mass analyzers⁵⁰. A list of historical mass spectrometers is provided by Burgoyne and Hieftje.⁵¹

1.1.1.3.1 Multipole mass analyzers

Quadrupole mass spectrometers are sequential, single detector mass spectrometers with settling times in the *ms* range, and large tolerances towards high pressures (10^2 Pa) and spread in K_e of incoming charged particles. They consist of four parallel cylindrical or hyperbolic electrically conducting rods, with diagonally opposite rods electrically connected. Electric fields are generated along the co-axial axis by superimposed DC [$-U_{DC}$, $+U_{DC}$] and phase-shifted RF AC [$U_{AC} \sin(\omega t)$, $U_{AC} \sin(\omega t + \pi)$] potential components on the electrode pairs. Charged particles with a m/q within a narrow, adjustable, low-pass/high-pass mass window ($0.3 - 3.0$ u) show trajectories with translational components $d^2x/dt^2 = 2e/mr_0^2[U_{DC} + U_{AC} \cos(\omega t)]x$ and $d^2y/dt^2 = -2e/mr_0^2[U_{DC} + U_{AC} \cos(\omega t)]y$, which permit them to pass through the quadrupole assembly whilst other particles have unstable paths and are rejected.

34,36,46,52-54

1.1.1.3.2 Sector field mass analyzers

Double focusing sector field mass spectrometers (SF-MS) are comprised of a momentum-dispersive magnetic sector, and an energy-dispersive electrostatic analyzer (ESA).^{46,55} Several configurations of the magnetic and electrostatic sector, each characterized by a different set of sector deflection angles and directions, have been developed. The most notable geometries are *Mattauch-Herzog* – in which all ions undergo directional and energy focusing on a focal plane directly behind the magnetic sector exit pole–, and (reversed/forward) *Nier-Johnson*. A charged particle of charge q and mass m translating with a velocity \vec{v} through an electro-magnetic field, with an electric field strength \vec{E} and magnetic flux density \vec{B} perpendicular to motion of travel of the particle, is subject to the Lorentz force $\vec{F}_L = q(\vec{E} + \vec{v} \times \vec{B})$.⁵⁵ In the magnetic sector, the magnetic component of the Lorentz force \vec{F}_B deflects charged particles accelerated over a potential U_0 (which determines their initial kinetic energy $E_k = 0.5mv^2$) into a curved trajectory of radius r_B (Equation 2).⁵⁵

$$r_B = \frac{mv}{qB} = \frac{1}{B} \left(\frac{2mU_0}{q} \right)^{0.5} \quad \text{Equation 2}$$

In the *Nier-Johnson* geometry, the ions are deflected by an ESA with an angle of $\Phi_E = \pi/2$, and by the magnetic sector with an angle of $\Phi_B = \pi/3$ (Figure 3). The selective transfer of a particle m/q range, is made possible by varying the position and width of the exit slit relative to the incoming resolved ion beam. Alternatively, the magnetic field strength (B-scan) and acceleration potential U_0 (E-scan) can be modulated to target the desired ions on a fixed exit slit position. In a double-focusing reversed *Nier-Johnson* geometry, an ESA – typically a cylindrical condenser – behind the magnetic sector performs kinetic energy and directional refocussing by compensating for the dispersion created within the magnetic sector, ensuring that a high ion transmission efficiency is maintained within the mass analyser. This geometry is preferred for single collector SF instruments, as the lower beam intensity after the first sector improves the

abundance sensitivity and the signal background. The radius of the charged particle trajectory in an electrostatic field with electric field strength \vec{E} can be predicted (Equation 3).

$$r_E = \frac{mv^2}{qE} = \frac{2U_0}{E} \quad \text{Equation 3}$$

By operating a sector field mass analyzer at high mass resolution using the collector slit (e.g., $R = 10000$), the beams of analyte ions and interfering ions can be resolved in the majority of cases (cf. mass resolution). SF mass spectrometers are well suited for isotopic analysis due to their stability, ion transmission efficiency and design which allows for simultaneous monitoring of a part of the mass spectrum. In this PhD research, a Thermo Fisher Scientific Element XR instrument of reverse *Nier-Johnson* geometry has been used.

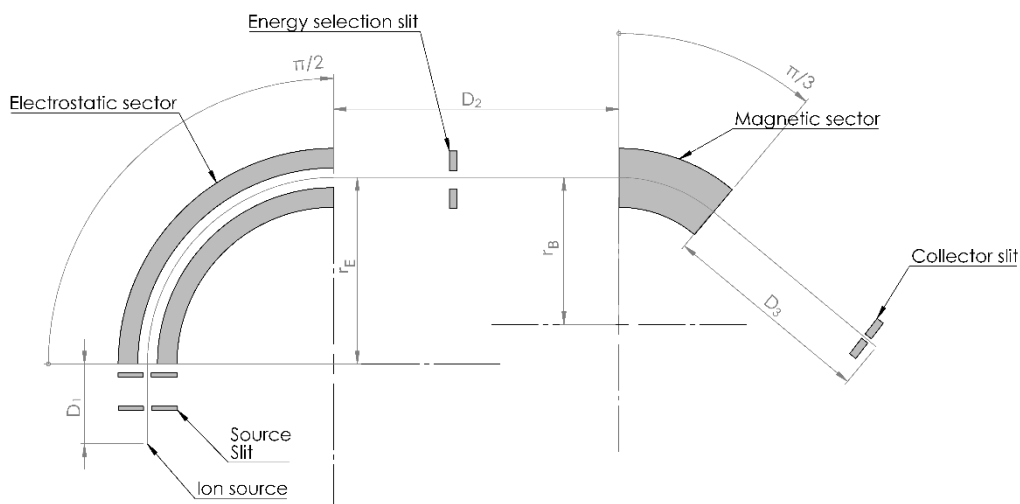


Figure 3 Schematic drawing of a sector field mass analyzer of forward *Nier-Johnson* geometry as found in multiple collectors (MC) SF instruments). Indicative dimensions of a reliable mass spectrometer configuration are: $r_E = 188.7 \text{ mm}$, $r_B = 152.4 \text{ mm}$, $D_1 = 66.1$, $D_2 = 413.8 \text{ mm}$ and $D_3 = 207.3 \text{ mm}$.

1.1.1.3.3 Time-of-flight mass analyzers

In a time-of-flight (ToF) mass analyzer, charged particles undergo an acceleration in an electric field, after which they drift through the flight tube, and are eventually detected using an electron multiplier (Figure 4). Within a field-free vacuum flight tube, ion packets accelerated to constant kinetic energy will be resolved according to their m/q in the temporal domain at the space focus plane.^{56,57}

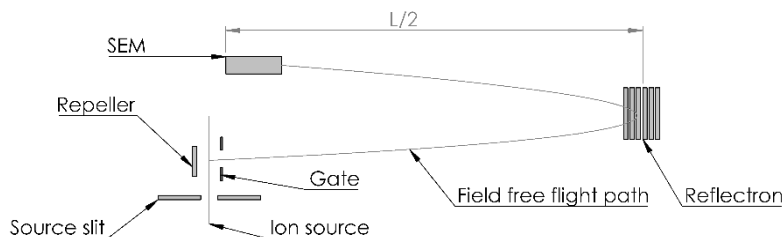


Figure 4 Schematic drawing of an orthogonal TOF mass analyzer.

Charged particles in a flight tube of length $L/2$ equipped with a dual-stage reflectron (an ion energy spread correction device) have a drift time $t_{drift} \cong L\sqrt{m/2qU_0}$, with U_0 the acceleration potential.

1.1.1.3.4 Mass cytometry

In 2009, Scott Tanner *et al.* have developed a new approach for labeling and detecting single cells. This approach is known as mass cytometry and enables single-cell identification. The technique derives its principles from flow cytometry, a technique where cells tagged with multiple types of fluorescently labeled antibodies are detected on a cell-by-cell basis in a flow cell. The simultaneous detection of fluorescence labels or – in the case of in mass cytometry – mass labels, permits the identification of cell types and other cell parameters by statistical analysis. Mono-isotopic lanthanide-tagged primary antibody labeling reagents (MAXPAR™ reagents) are used for mass cytometry due to spectral overlap, resulting in an increase in the number of potential antibody targets detected to > 50 . A time-of-flight ICP-MS system permits a throughput of $1000 \text{ cells s}^{-1}$. A notch filter is used to remove ions with a $m/z < 75$ as the reduction of space-charge effects improves the ion beam quality. Labelled cells are introduced to the ICP using a nebulizer, connected to a syringe pump, and a heated spray chamber. The technique has been commercialized by Fluidigm, under the name CyTOF.

1.1.1.4 Ion detectors

A positively charged particle impacting on the first dynode ($U \sim [-2 \text{ kV}, -3 \text{ kV}]$) of a discrete electron multiplier produces an electron avalanche driven by secondary emission between 10^5 's of successive dynodes at progressive potential, enabling the detection of charged discrete particles as signal pulses. The amplified signal pulses (current gain of up to 10^8) are registered within a DAQ ($\tau \sim [5 \text{ ns}, 100 \text{ ns}]$) as digital signals when the discriminator records a current peak maximum higher than a current threshold set above the detector noise. Corrections for the dead time τ : $I_{true} = I_{count}/(1 - (I_{count}\tau))$, are applied. Detectors are shielded from photoionization by the use of electrostatic lenses or by mounting the detector off-axis. The dynamic range of dual-stage dynode detectors [$0.01 - 2 \times 10^6 \text{ cps}$] can be extended by 2 – 3 orders of magnitude by monitoring the analogue current on an intermediate dynode, which has a dynamic range of [$5 \times 10^4 - 5 \times 10^9 \text{ cps}$]. Cross-calibration and corrections for pulse pile-up, dead time and quantum efficiency are required. Faraday detectors are analogue potentiometers with resistors up to $10^{13} \Omega$, which are characterized by higher signal stability, $10^3 - 10^4$ times less sensitivity and slower rise time. Other detectors include Daly detectors (which rely on photon multipliers) and array detectors, *e.g.*, multichannel focal plane cameras (FPC).^{50,55}

1.1.2 Interferences

Spectral and non-spectral interferences are considered to be the most important drawback of ICP-MS.

1.1.2.1 Spectral interference

Spectral interference is a result of spectral overlap between the signals of the analyte and interfering species. The types of interfering ions are: (i) polyatomic, (ii) isobaric, and (iii) doubly charged ions. General peak overlap of neighboring masses (*cf.* abundance sensitivity) can also be the origin of spectral overlap. Dry plasma conditions in LA-ICP-MS limit the influence of oxides and hydroxide ions, whilst argide and nitride ions remain prevalent. The presence of other polyatomic interfering species, such as carbides, depends on the sample matrix composition. Isobaric interferences can be circumvented in all cases, with the exception of Indium, by selecting an interference-free nuclide.³⁴

Spectral interferences can be overcome by: (i) offline and online target element isolation or separation, (ii) chemical resolution in collision/reaction cells, (iii) kinetic energy discrimination, (iv) spectral resolution, (v) mathematical correction, and in some cases, (vi) by operating the plasma in a different temperature regime.

1.1.2.1.1 Collision/reaction cell

A dynamic multipole collision/reaction cell (DRC), a multipole positioned between the ion optics and mass analyser, operating in 'RF mode' and pressurized with a reaction and sometimes an additional inert gas *e.g.*, CH₃F, NH₃, O₂, H₂, and He, can selectively convert analyte or interfering ions into reaction product ions, enabling interference-free measurement on the m/q of the analyte or its adduct. Chemical resolution is obtained as a result of differences in reaction enthalpy (only exothermic reactions can proceed) and/or reaction kinetics. However, despite the potential of this approach, particular care must be taken to avoid the formation of new spectral interferences, produced by reaction of the matrix component ions with the reaction gas. In a tandem quadrupole configuration (ICP-MS/MS), a quadrupole mass filter is placed before the collision/reaction cell to remove ions of other m/q *a priori*, *de facto* eliminating the risk of the formation of unexpected interferences. Alternatively, kinetic energy discrimination (KED) can suppress polyatomic species which, as a result of their larger collisional cross-section, will decelerate ($E_k \downarrow$) more when colliding with an inert gas, permitting their elimination *via* a potential barrier. Collision/reaction cells will however also suppress the response for other charged particles.⁵⁸

1.1.2.1.2 Mathematical corrections

For reasonably sized corrections, < 50% of the gross signal, mathematical corrections can be performed by monitoring uninterfered isotope(s) of the interfering nuclide/polyatomic species, whilst taking into account natural isotopic abundances and molecular formation ratios.

1.1.2.2 Non-spectral interferences

Non-spectral interferences, generally observed as signal suppression, are induced by matrix effects, *e.g.*, ambipolar diffusion and mass discrimination (*cf.* space charge and nozzle separation effects).⁵⁹

1.1.3 Introduction systems

1.1.3.1 *Pneumatic nebulization and spray chambers*

Pneumatic nebulizers, *e.g.*, (micro)concentric, crossflow and Burgener nebulizers, produce an aerosol with droplets $1 - 100 \mu\text{m}$ in size, as a result of the impact of an accelerated gas flow on the liquid surface of a sample solution introduced at $< 10 - 10^3 \mu\text{L min}^{-1}$. Some of these nebulizer designs produce gas flows generating a Venturi effect near the fluid outlet, permitting spontaneous nebulization, in the absence of a peristaltic pump. Spray chambers, *e.g.*, cyclonic, or Scott-type spray chambers, produce a finer, low-velocity, tertiary, less polydisperse aerosol, suitable for desolvation in the ICP, from the primary aerosol generated by a nebulizer, *via* gravitational settling, and inertial impact losses of droplets $> 10 \mu\text{m}$ in size.⁶⁰

1.1.3.2 *Laser ablation*

Light Amplification by Stimulated Emission of Radiation (LASER), theorized in 1917⁶¹, provides a quasi-monochromatic, coherent and highly directional photon beam of high flux capable of superficial, controlled material removal, permitting the direct, spatially resolved introduction of solid materials into ICP-MS.

1.1.3.2.1 *Laser operating principles*

According to Boltzmann's principle, as used by statistical mechanics, the fraction of compounds in a lower energy state exceeds the fraction of compounds in a higher, unstable, excited energy state (electrons are present in higher energy levels than their ground state) at thermodynamic equilibrium. This distribution of microstates can, however, be inverted in an active medium, *i.e.* population inversion, *via* continuous laser pumping by an external stimulus, *e.g.*, a flash lamp, secondary laser or electrical discharge. The lasing medium is positioned between a total reflection mirror and a partially reflective mirror (the output coupler). In an appropriate resonator configuration, undesirable off-axis photons are absorbed, whilst the reflected monochromatic beam will provoke, upon interaction with excited compounds, a cascading effect known as stimulated emission (photon-induced photoemission), as opposed to relaxation of the excited compounds by spontaneous emission or non-radiative processes. This cascade will result in a highly coherent emission of additional photons of the same wavelength and phase factor, originating from decaying compounds, in the direction of propagation of the primary photon.

The beam generated in the laser is sent through an optical attenuator with graduated transmission, which modulates the beam energy density, a set of 3-5 dichroic mirrors, and a homogenizer mounted before the focusing system which convolves the (semi-) Gaussian beam profile into a homogeneously distributed beam profile by recombining fractions of the incoming beam, which partially have inverted profiles. A beam expander may be present in the beamline to improve the beam quality or to expand the beam profile. Schwarzschild and refractive achromatic objectives allow for an adjustable condensed focus in an infinity-corrected system with a beam waist diameter of $0.7 - 2000 \mu\text{m}$. Beam splitters are present to introduce a co-axial illumination source into the beam path, and to project a sample image through a tube lens onto the CMOS or CCD camera chip, and to split of a fraction of the beam for online energy measurement.⁶²⁻⁶⁴ The beam is focused through a MgF_2 or fused silica window coated with an

anti-reflection coating which promotes UV transmission. The optical local plane is matched to the laser focal plane to allow for rapid, simultaneous, optical and laser focusing.

1.1.3.2.2 Laser types

A large array of pulsed laser types, including solid-state, dye, chemical, semiconductor, free-electron, metal-vapor and gas lasers, have been developed. Q-switched Nd:YAG lasers (1064 nm), solid-state four-level lasers with an active medium consisting of a single yttrium aluminum garnet (YAG) crystal doped with neodymium ions, are the most prevalent lasers in use for LA-ICP-MS. A frequency multiplier is employed to generate the 4th (266 nm) or 5th (212.8 nm) harmonic, as wavelengths > 300 nm are poorly absorbed by many crystalline and amorphous geological matrices. Higher harmonics are not commonly used as a result of the limitations in laser mirror damage thresholds and the cost of DUV and VUV optics. Excimer lasers operate *via* stimulated emission of an excited dimer or complex of a noble gas atom and a halogen atom, *e.g.*, ArF*, KrF*, XeCl*, pumped *via* high-powered electric discharges stored in a thyatron or solid-state switches. In ArF* lasers (193 nm), the process of electron impact ionization will ionize the F₂ dimer and Ar, enabling the formation of the unstable ArF* exciplex which undergoes relaxation and dissociation (lifetime 4 – 8 ns) followed by spontaneous and stimulated emission resulting in reformation of the stable F₂ dimer (Figure 5). Excimer lasers inherently work in ns pulsed mode (pulse-width 5 – 50 ns) due to their low amplification gain. The ArF* laser fundamental wavelength of 193 nm is considered a general purpose wavelength for LA. Furthermore, ArF* lasers are natively characterized by a less coherent, flat-top profile beam, allowing for a better optical homogenization and spatial resolution. Excimer lasers require periodical replenishment of the gas in the cavity after its degradation due to reactions of the highly reactive halogen atoms with the laser discharge tube, and the production of contaminants.^{15,65-71}

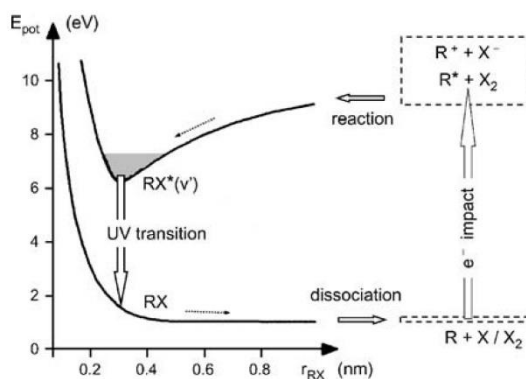


Figure 5 Simplified schematic energy level scheme for excimer lasers, the excimer potential energy and the laser transition are shown on the left and the electron impact generation processes for the excimer molecule are shown on the right. Reproduced from Telle *et al.*⁶⁵

1.1.3.2.3 Ablation-related processes

The laser-surface interaction process is very much dependent on the laser energy density, spot size, wavelength and pulse width (the pulse irradiance duration of the incident laser beam), and the sample-specific characteristics, *e.g.*, the ablation threshold, attenuation length, scattering properties, surface reflectivity/roughness, composition, compositional heterogeneity, boiling point, density, tensile toughness, thermal conductivity and morphology, *i.e.* the presence of porosities or fractures. Two modes of ablation can be identified: (i) thermal vaporization, and (ii) non-thermal ablation.

Upon irradiance, photons are absorbed by the surface layer, inducing photochemical electronic transitions on a $10^{-15} - 10^{-14}$ s time scale in valence and conduction electrons. These electron excitation processes (one- and multi-photon photolysis processes) can directly dissociate chemical bonds, *e.g.*, covalent and ionic bonds, solid lattice grids and crosslinks, as the combined energy of n 193 nm photons in n -photon processes, $n \times 6.42405$ eV or $n \times 619.827$ kJ mol⁻¹, exceeds the bond dissociation energies involved, *e.g.*, H-C 413 kJ mol⁻¹, H-O 366 kJ mol⁻¹, and C-C 348 kJ mol⁻¹. On a $10^{-14} - 10^{-11}$ s timescale, the energy contained in the excited species is transferred towards the lattice (electron-lattice heating) by electron-phonon coupling into the vibrational modes. A phonon represents a collective excitation in the vibrational modes of interacting particles in an elastic arrangement in condensed matter. A phonon can induce a vibration wave, which propagates through the lattice.

When the photon-induced phonon avalanche process occurs, the absorbed energy can either induce non-thermal vaporization (volatilization), when sufficient Helmholtz free energy is contained within the local volume, or undergo thermalization as observed as a sharp rise in the local temperature (> 1000 K in $< 10^{-8}$ s) and electron density at the surface down to several 100 nm below. *Quasi*-thermalization of the surface (the system actually never reaches LTE) is followed by an expulsion of electrons, and with a delay, ions, on a $10^{-12} - 10^{-9}$ s time scale.⁷² Generally, thermally driven material removal processes – including thermal vaporization, melting and evaporation at the target surface – occur when employing DUV lasers with laser pulse widths exceeding the electron-phonon relaxation time. Hence, the extent to which (non-)thermal ablation takes place depends on the thermal properties of the target, *e.g.*, geological materials are significantly affected by thermal phenomena when they are irradiated by ns-laser pulses in the IR regime, as their phonon relaxation rates are in the order of 10^{-12} s. Lasers with a pulse-width < 300 fs are capable of material removal largely based on non-thermal photochemistry in many materials. The expansion of the heat-affected zone is proportional to the square root of the pulse width. The peak energy density required for DUV lasers with pulse widths < 100 fs to achieve material removal at a detectable ablation yield, is typically higher ($10^{10} - 10^{15}$ W mm⁻²), compared to DUV lasers with a pulse width > 1 ps ($10^5 - 10^9$ W mm⁻²), but the total peak energy required is lower (10 μJ – 2 mJ vs. 3 – 10 mJ). Despite broad advantages of fs lasers, they are not readily adopted as the Ti-Sapphire lasers contain a significant level of system complexity: a seed laser, pump laser amplifier, and chirping unit are required, which also add significant purchase and maintenance cost.

When the energy density of the irradiance falls below the ablation threshold, excited electrons can still remove atoms and ions during ‘soft’ ablation. When operating in this regime, layers <100 nm thick can be ablated selectively.⁷³ When the energy density of the irradiance exceeds the ablation threshold, the rapid energy transfer can induce thermal vaporization by phase explosion, a laser desorption phase transition process, accompanied by the ejection of μm -sized particles and spallation of fragments, known as ‘strong’ ablation.⁷⁴ Explosive boiling and mechanical expansion are driven by spinodal breakdown, *i.e.* the decomposition of the irradiated volume, which resides within a superheated meta-stable phase, into a mixture of liquid and gas⁷⁵. Explosive boiling occurs when the irradiated volume is saturated homogeneously by nucleation bubbles. The time lag of nucleation depends on the nucleation rate and the dimensions of critical nuclei, which are larger for metallic matrices than for organic ones, as a result of heat delocalization (higher thermal conductivity).⁷²

The rapid volume expansion of the material gives rise to internal and external shockwaves (SW); a bow shock is produced which expands hemispherically and is forward offset by the laser-induced debris in a snowplough effect, though some high K_E particles can cut through it. In the proximity of the phase explosion, the local temperature is greatly increased on a 10^{-12} – 10^{-9} s time scale as a result of residual heat after heat transfer from the meta-stable phase, a phenomenon called zone heating, often accompanied by cracks as a result of thermal strains in the heating/cooling process, and material volatilization and evaporation in the melting region surrounding the crater. The ablation threshold is generally lower for biological samples than for metals and minerals. The laser-surface interaction can induce other morphological changes, *e.g.*, structural changes as a result of the laser SW propagating inside the solid, or microfoaming, *e.g.*, in gelatine targets.⁷⁶⁻⁷⁸ It should be noted that thermal processes play a more pronounced role in the ablation of biological matrices, relative to silicate, ceramic and polymer matrices, for these processes are a major source of fractionation.⁷⁹ In contrast to geochemical matrices, wavelengths <200 nm are not required to achieve efficient coupling to a biological matrix, however, thermal effects near the ablation zone become more pronounced at longer wavelengths. Biological samples are typically characterized by an optical penetration depth, *i.e.* the reciprocal of the absorption coefficient reduced by scattering effects, in the order of several μm ⁷⁴, whilst in metals it is limited to tens of nm⁷². The ablation depth and yield per shot (the ablation rate) is thus generally higher in biological samples than for metals. The ablation rate is NIST SRM 612 is approximately 150 nm / shot. Claverie *et al.*⁸⁰ identified that IR laser wavelengths induce evaporation-driven ablation, based on the presence of water in biological matrices, characterized by significant absorption at wavelengths > 1000 nm and < 200 nm, peaking around 2940 nm, and < 170 nm.^{81,82} IR wavelengths impose diffraction limits on the beam’s waist dimensions and generate more pronounced cracking and melting in targets depleted of water. It can be noted that at DUV wavelengths a higher efficiency of photoionization can be observed. In biological matrices, the relevant chromophores are the peptide bonds in proteins in the deep UV region (absorption peak centred around $\sim 190\text{ nm}$), and DNA (purine and pyrimidine bases), melanin, tryptophan, tyrosine, and phenylalanine at longer UV wavelengths.⁷⁴ The review by Vogel *et al.*⁷⁴ provides a detailed description of the effect of pulsed lasers on tissues.

The phase explosion ejects particles perpendicular to the surface $> 100 \text{ ps}$ after laser impact, with a shifted Maxwell-Boltzmann velocity distribution ranging between 10^{2-4} ms^{-1} and skewed towards velocities $> 10^3 \text{ m s}^{-1}$. The particle ejection velocities are critically dependent on the laser characteristics such as energy density, pulse length, spot size, and target properties.⁸³ As a result of the high density of volatilized material (for environments under atmospheric pressure), particle collision will rapidly transfer the K_E into heat. The particle cloud can be described to expand in 4 different regions along the orthogonal axis, each with its own dynamics, position relative to the surface, and lifetime: i) the surface-plasma region, ii) the Knudsen layer, iii) the coronal region, and iv) the charge separation/oscillation region. When sufficient electron density, local pressure and heat are present ($> 0.3 \times 10^8 \text{ W cm}^{-2}$), a laser plasma will be initiated in $< 1 \text{ ns}$ in the surface-plasma region, *i.e.* in close proximity to the surface ($\leq 0.5 \text{ mm}$). The initiation of the plasma occurs *via* a combination of single- and multi-photon ionization (PI), photoexcitation (PE), electron-neutral inverse bremsstrahlung (IB) by ejected species, and, to a lesser degree, electron-ion IB.^{84,85} This electron-dense plasma is maintained *via* electron-production by the photoelectric effect (PE), heating by three-body recombination, photoionization (PI), Mie scattering, and *via* inverse bremsstrahlung (IB), which, in combination with scattering effects, render the plasma opaque ($RI \approx 1$) to incident laser radiation, a phenomenon known as plasma shielding.⁸⁶ Plasma shielding optically attenuates the incident laser beam intensity reaching the sample surface in ns pulse length laser systems.^{86,87} The process is driven primarily by IB: photon absorption by free electrons at high electron densities during collisions with neutral or ionized atoms resulting in the excitation of the free electrons to a higher state in the continuum. Complete removal of particles from the cell volume between subsequent sampling events decreases the chances of unpredictable (for ns-lasers) particle-induced plasma breakdown, which can promote plume expansion horizontal to the sample surface, inducing depositional losses.^{88,89} Photon absorption in gas layers behind the SW and ensuing heat expansion can accelerate the SW (contact) front in the direction of the incoming laser pulse in a regime called laser-supported detonation, as part of the plasma shielding process.^{86,90} In a simplified model, the absorption coefficients for PI, electron-ion IB and electron-neutral IB can be expressed, respectively, as:^{85,91}

$$\alpha_{PI} = C \sum_{q=1}^2 \frac{\lambda^3 Q^2 n_e n_q}{\sqrt{T}} \overline{G_{fb}} \left[e^{\frac{hc}{\lambda k_B T}} - 1 \right] \quad \text{Equation 4}$$

$$\alpha_{IB,e-i} = C \sum_{q=1}^2 \frac{\lambda^3 Q^2 n_e n_q}{\sqrt{T}} \overline{G_{ff,e-i}} \quad \text{Equation 5}$$

$$\alpha_{IB,e-n} = C \frac{\lambda^3 n_e n_0}{\sqrt{T}} \overline{G_{ff,e-n}} \quad \text{Equation 6}$$

where n_e , n_q and n_0 are the electron, ionic (with charge Q) and neutral atoms number density, λ is the laser wavelength, T the plasma temperature, h and k_B are Planck's and Boltzmann's constant, respectively, c is the speed of light, C is a constant and $\overline{G_{fb}}$, $\overline{G_{ff,e-i}}$, $\overline{G_{ff,e-n}}$ are the free-bound and the free-free Gaunt factor in the cases of electron-ion and electron-neutral interaction, respectively. The experimental conditions will determine the relative strength of IB/PI processes, however, given the dependence on λ^3 , absorption mechanisms are more

efficient at IR wavelengths whilst PI is more prolific in the UV due to the exponential dependence on λ^{-1} and the occurrence of Mie absorption. The plasma can reach peak temperatures $> 10^4 K$ and pressures of $\sim 10^{7-8} Pa$, inducing supersonic expansion of the particle plume. The number density of excited species in the plasma can be calculated using the Boltzmann distribution of statistical thermodynamics:⁸⁴

$$n_i^Z = n_0^Z \frac{g_i^Z}{g_0^Z} e^{-\frac{E_i^Z - E_0^Z}{k_b T}} \quad \text{Equation 7}$$

where n_i and n_0 are the number density of ion and neutral atoms with charge Z , g_i and g_0 the statistical weight corresponding to the number of states with the given quantum number in a degenerated system for the ionic and atomic state, respectively, and E_i and E_0 the energy levels of the excited and ground state, respectively.

Bleiner *et al.*⁹² reported ion angular spreads to be dependent on the metal, and the bulk of fast ions to be ejected close to the normal.; the initial particle trajectories of most ions in the surface-plasma region are characterized by a forward thrust in a direction $\pm 15^\circ$ off-normal. In the Knudsen layer (KL), a transient non-equilibrium transition layer at the surface-plasma boundary, also known as the molecular beam expansion region, evaporated particles achieve translational equilibrium within a few mean free path lengths, by means of collisions. The particle plume undergoes adiabatic expansion over a larger off-axis angle on the ns time scale, which allows this region to establish a local thermal equilibrium (LTE) *via* thermalization. Surface evaporation is characterized by a clear phase boundary between the liquid-vapor phases and the KL. The Clausius-Clapeyron equations for heat conduction can be used to describe the binodal properties of the surface in a limited fluence regime, approximately $< 1 GW m^{-2}$.^{93,94} When the local temperature at the surface exceeds the melting temperature, vaporization becomes significant. Discontinuous phase transitions of a single constituent can be described by the Clausius-Clapeyron relation:

$$\frac{d \ln(p_{vap}/p_0)}{dT} = \frac{\Delta H_{lv}}{RT^2} \quad \text{Equation 8}$$

The vapor pressure (p_{vap}) is calculated from the surface temperature, by integrating the Clausius-Clapeyron equation:

$$p_{vap}(T_s) = p_0 e^{\frac{\Delta H_{lv}(T_s - T_b)}{RT_s T_b}} \quad \text{Equation 9}$$

Where T_s and T_b are the surface temperature and the normal boiling point at pressure $p_0 = 1 atm$, and ΔH_{lv} is the heat of vaporization. At higher laser intensities, the surface reaches temperatures near the critical temperature. In the $\mu s - ms$ timeframe, the particle cloud expands into the coronal region, which is characterized with a negligible rate of collision and three-body recombination as a result of the curtailment of energetic electrons. Heating through IB occurs at much lower rates in this spatial region. Under these conditions the LTE is absent. In the fourth region, faster electrons outrun the slower positive ions due to a lack of collisions, inducing a charge separation. Electrons are slowed down by this charge, whilst positive ions are accelerated forward, eventually inverting the charge distribution, producing an oscillation of

the charge in the particle cloud, a process described as double layer ion acceleration by ambipolar diffusion.⁹⁵⁻⁹⁷

Shadowgraphy is a camera technique which can be used to visualize the particle and shockwave front expansion through local differences in the ambient gas refractive index, involving a probe laser which fires through the plume at a variable delay relative to the ablation laser impact, regulated by a delay generator. A study by Bleiner *et al.* reported that based on shadowgraphy, the stopping power of Ar reaches $\sim 425 \text{ eV mm}^{-1}$ on the on-axis component in the initial expansion space of 2 mm.⁹⁸ The stopping power is progressive, *i.e.* stronger at higher KE, milder at lower KE, as the particle-background gas collision rate is a function of particle speed. Hence, the stronger background gas deceleration of the forward debris advancement front, flattens out the advancement of forward and slower fronts over time. In order to mitigate the erosive effects of the debris on the ablation cell window, the K_E of the high energy fraction of on-axis particles, *e.g.*, 1.1 keV, needs to be moderated below an erosive threshold value of 0.15 keV, which requires a 10^5 Pa Ar gas buffer thickness of $>10 \text{ mm}$ (or characteristic thermalization times of $1 \mu\text{s}$).⁹⁸ Conversely, Gurevich and Hergenröder⁹⁹ estimated the upper limits of the stopping distance of particle with sizes between $10 - 2000 \text{ nm}$, in He or Ar under atmospheric pressure, to be less than 2 mm , using a laser energy of 1 mJ . Experimental observations suggest that the observable fraction of the plume has a stopping distance $\leq 1 \text{ mm}$ (Figure 6).⁸⁶ The stopping power of a gas relates to its collisional cross-section, velocity, mass, and density.

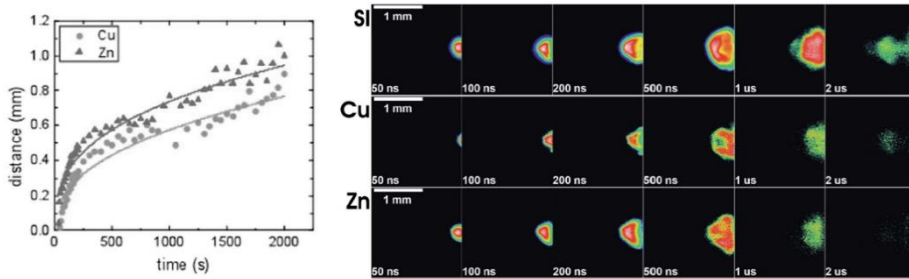


Figure 6 (left) Representative shadowgrams obtained with a fs pump pulse energy of 2 mJ and probe delays 125 ps to 1 ms. (right) Cu and Zn expansion in ICCD images plotted vs. time. Zn expands faster and to further distances than Cu. Reproduced from LaHaye *et al.*.¹⁰⁰

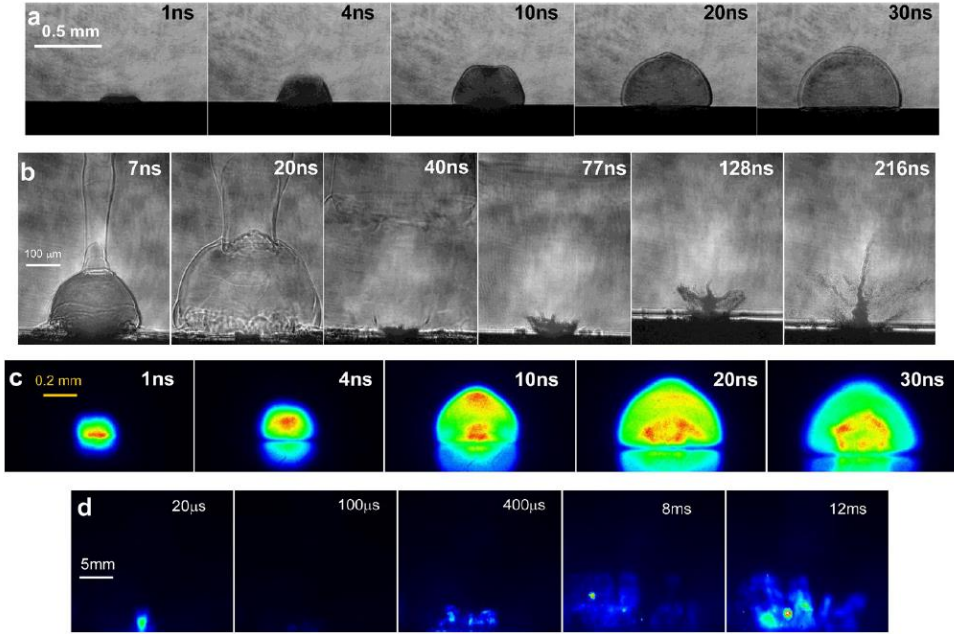


Figure 7 Time-resolved images of ablation processes: (a) shadowgraph images of shockwave and mass leaving the surface using a relatively low pulsed laser energy; (b) same as part a, except for a higher pulsed laser energy, inducing distortion of the shockwave and significant particle ejection; (c) false color images of Cu emission intensity; and (d) light scattering images showing initial particle ejection followed by particle condensation from vapour $>100 \mu\text{s}$ after the laser pulse. Reproduced from Russo *et al.*¹⁰¹

Multiple phases exist in the aerosol after plume expansion and cooling, including evaporates and condensates in the form of nanoparticles, melt expulsion in the form of micro-droplets, exfoliated fragments, and fibrinous agglomerates.⁷² The phase distribution will very much depend on the condensation, nucleation, evaporation, and agglomeration rates after the laser-solid interaction.^{102,103} Each of these phases has a different composition. The evaporation from a melted surface is described by the Hertz-Knudsen equation. Full development of the plume results in a mushroom-shaped particle cloud (Figure 6), as fluid mechanics guide the particles on eddy-currents in cooler and less dense space in the ms timeframe. The reflection of the bow shock may severely influence plume expansion and pressure in the plume; this effect is exploited for LIBS signal enhancement.¹⁰⁴⁻¹⁰⁶ Gradual SW expansion (Figure 7) reduces the pressure of the region behind the bow front, reducing its velocity below 320 m s^{-1} . The evolution of the hemi-spherical SW radius R can be approximated by a point strong explosion as described by the Taylor-Sedov model:⁸⁶

$$R(t) = \xi \left(\frac{E_0}{\rho_b} \right)^{1/\zeta+2} t^{2/\zeta+2} \quad \text{Equation 10}$$

Where ξ is a constant which depends on γ , the specific heat ratio of the background gas, E_0 , the energy deposited in the shock wave, and ρ_b , the density of the unperturbed background gas. The SW expansion decouples from the plume at an $R \simeq 1 \text{ mm}$. For a spherical SW expansion,

$\zeta = 3$, and for a cylindrical expansion, $\zeta = 2$.⁸⁶ The SW front pressure p_{sw} in the Sedov model can be expressed as:

$$p_{sw} = \frac{p_0(2\gamma M_a^2 - \gamma + 1)}{\gamma + 1} \quad \text{Equation 11}$$

Where M_a is the SW mach number ($M_a \sim 2$) and γ is the adiabatic coefficient ($\gamma \sim 1.4$ in air). The temperature inside the SW volume is higher than the temperature of the unperturbed background gas ($0.5 - 7 \times 10^3 \text{ K}$ vs. 300 K). As a result, the particle number density in the plume is substantially lower than in the background gas environment (Figure 8). The plume expansion can be considered a dynamic process, which is severely influenced by the surrounding gas medium and the phase distribution of the particles.¹⁰² Environments with gasses of high thermal conductivity, high first IP, and low density, *e.g.*, He under atmospheric pressure, will capture the thermal energy of particles at a relative fast rate, inducing agglomeration of particles in the Knudsen and Coronal region (condensation) with a narrow agglomerate/droplet size distribution.¹⁰⁷⁻¹⁰⁹ Conversely, gasses with a low thermal conductivity will produce a broader particle size distribution over a longer condensation period. Background gasses with a high mean free path length and low viscosity, *e.g.*, He, are well-suited for particle entrainment, resulting in substantially reduced particle deposition due to gravitational settling around the crater, and a 2-3 fold sensitivity enhancement.¹¹⁰ On the other hand, transport gasses with low mean free path lengths and high viscosity, *e.g.*, Ar, promote loss-less particle transport of the particles captured within, as settling and diffusion are reduced.

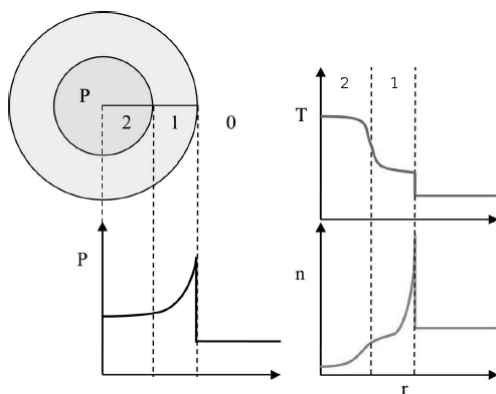


Figure 8 Qualitative sketch of the pressure, temperature and particles number density profiles as a function of the SW radius, according to the Sedov model predictions for the early phase of free-standing plume/SW expansion. Reproduced from Tognoni *et al.*⁸⁶

The plume formation in LITD and MALDI is similar to that described above for LA, though the ratio of atomic and ionic particles relative to molecular species is higher in LA as a result of the higher degree of photon-induced bond dissociation due to the higher beam energy density.

Radiative relaxation of excited species (ionized atoms and molecules) within the plasma produces photons, which interact with the particles in the plume and the target surface. These photons are captured by a wavelength-dispersive optical camera in Laser-Induced Breakdown

Spectroscopy (LIBS) or LAMIS, which enable the detection of lighter elements, offer stand-off capabilities and have heavy matrix tolerance, but are inferior in terms of absolute detection power compared to LA-ICP-MS. The optimum operation conditions for LIBS and LA-ICP-MS are mutually counteractive, resulting in compromise conditions when both techniques are used in tandem.^{101,111,112} Ions formed during ablation and plasma formation can also be directly introduced into a mass analyzer (LDI-MS), yet quantitative analysis is hampered by the unpredictable nature and poor reproducibility of the degree of ionization. Models of the ns laser-surface interactions focus on thermal processes described by the thermal heat conduction equation. Based on this equation the parameters of the macrostate during ablation, *e.g.*, the surface temperature profile on a macroscopic scale, can be estimated.^{113,114} Additionally, some of these models also try to describe the expansion of the evaporated material plume (sometimes described as a surface point explosion) by hydrodynamic models, *e.g.*, Euler equations, and Monte Carlo simulations.^{115,116}

1.1.3.2.4 Aerosol transport

Ablation cell types differ in volume and aerodynamic flow pattern. The design and characteristics of ablation cells and the transport tubing through which the aerosol is transported can have a severe impact on throughput, sensitivity, accuracy, and precision. This topic is discussed in depth in Chapter 2.

1.1.3.2.5 Elemental fractionation

Elemental fractionation is considered to be one of the main limiting factors for quantitative analysis in LA-ICP-MS. This effect refers to matrix-dependent and laser-, transport- or ICP-induced changes in the relative proportions of the chemical elements within the particle beam. In recent literature, a number of superpositioned processes have been identified to play a role in elemental fractionation.^{102,117,118}

- i. Thermalization of the phonon avalanche (zone heating) will produce an outward temperature gradient (the heat-affected zone) and melt target material in proximity to the ablation site, enabling non-congruent evaporation of volatile elements from the melt: the higher rate of evaporation of volatile over refractory elements in the melt created in the zone heating process induces cumulative compositional disparity between deposited and ablated material, leading to fractionation.¹¹⁹ Thermal diffusion processes are also expected to increase the mobility of analytes in the subliquidus phases of the heat-affected zone (HAZ) around each ablation crater. This mobility may cause elements to be redistributed away or towards the sample surface *via* diffusion, *e.g.*, based on differences in density or mobility (zone refinement).^{120,121} By lowering the sample bulk temperature by cryogenic cooling, thermal expansion of the HAZ and the volume under a metastable superheated state is slowed down, reducing the area affected by visible thermal degradation and vaporisation.^{74,122,123} Furthermore, the thermoelastic stress required to fracture the tissue decreases as a result of the cryogenic conditions on the tensile strength.

- ii. Fractional condensation of the cooling plume of the microplasma at the ablation site will precipitate refractory condensates onto the walls of the ablation pit, the sample surface, and ablation cell surfaces at the expense of the most volatile species.
- iii. The surface/volume ratio for a spherical particle is $3/r$: particles $\ll 1\ \mu\text{m}$ in diameter have a larger surface/volume ratio relative to particles $> 1\ \mu\text{m}$ in diameter. A low surface/volume ratio promotes the selective transfer of particles with a high vapour pressure into the vapour phase, through a competition process at the particle surface. Consequently, large particles are depleted in volatile elements and enriched in refractory elements.
- iv. The efficiency of particle transport is particle-size and mass-dependent as a result of gravitational settling of immobile particles $>500\ \text{nm}$, impact and condensation losses of particulates $<100\ \text{nm}$ on the ablation chamber and transport tubing walls, and diffusion of mobile particles with a high mean free path length into areas of the ablation chamber with a low gas velocity. Diffusion of mobile particles also occurs in the ICP.
- v. Kuhn *et al.*¹²⁴ demonstrated particles $\lesssim 90\ \text{nm}$ to be vaporized and ionized completely within the ICP, whilst element-dependent incomplete vaporisation and ionisation of aerosol particles $\gtrsim 150\ \text{nm}$, biasing signal responses in favour of more volatile elements, was observed.^{118,124-126}
- vi. Elements with low melting points, *e.g.*, Zn, Cd, and Pb, are heavily influenced by the mass load-enhanced matrix effect. An increase of mass load, *i.e.* the flux of material introduced in the plasma, by a factor 16, leads to a decrease of certain intensity ratios (*e.g.*, Cu/Ca) with up to 25%. In contrast, a decrease in plasma (mass) load by applying dilution leads to a stabilization of intensity ratios.¹²⁷ One hypothesis to explain this observation would be that the response factor increases for these low-abundant elements if the repression by main compounds decreases. The change in repression could, *e.g.*, take place inside the plasma as ionization efficiencies change as a function of the mass load of the ICP.¹²⁷ This effect illustrates the need for comparable mass loading (of the plasma) and plasma status, and as a consequence, the need for consistency in operating conditions (*e.g.*, spot size, fluence) and matrix matching between the sample and standards. Ideally, all analytes should be monitored during the same ablation run. Internal standardization based on a single element will correct for variations in the ablation yield, however, it will not adequately and accurately correct for the matrix-dependent processes that constitute the origin of elemental fractionation.¹²⁸ For bulk characterization, a precision of 3-5% can be obtained for homogeneous matrices with matrix-matched standards, however, for heterogeneous samples this precision may rise, depending on the sampling strategy, to $>10\%$, whilst the absence of matrix-matched standards may decrease accuracy further.

The overall effect of these processes is a suppression of refractory elements. The significance of ICP-induced matrix effects has been shown, for most elements, to exceed the contribution of laser-induced fractionation. The temporal changes of particle size distributions were

insufficient to explain the variation observed for in the element ratios.¹²⁷ The severity of the fractionation effect depends on the extent of thermal events, and particle size and phase distributions; narrow laser-generated particle-size distributions with the largest fraction between 10 – 150 nm in size reduce elemental fractionation, as these particles are vaporized and ionized efficiently (*vide supra*). Narrow, smaller particle-size distributions and mitigation of thermal fractionation events are achieved by:

- i. A laser output of a wavelength ≤ 200 nm, as a result of the higher absorptivity by, and energy coupling to, most minerals, particularly transparent ones.
- ii. A laser output with a pulse width below the electron-phonon relaxation time (*vide supra*).

The extent to which thermal events are minimized and a favorable particle size and phase distribution are produced is greater for the latter (pulse width) compared to the former (wavelength). The extent of thermal effects and the particle size and phase distributions generated are obviously also very much dependent on sample properties, such as thermal conductivity and electron-phonon relaxation times. A reduction in thermal energy dissipation to adjacent areas enables a better control of the ablation process, *i.e.* a superior delineation of the ablation crater when melting processes are reduced.^{15,129,130} An overall smaller particle size reduces gravitational settling, resulting in less particle deposition at the ablation site and signal enhancements of up to a factor 3.^{36,71} fs-pulse widths can, as opposed to ns-pulse widths, negate the initiation of the plasma shielding effect in a deterministic way, preventing a reheating process of condensed particles which can induce fractional evaporation of the volatile elements and droplet agglomeration.^{15,121,131} This observation is valid across the UV-VIS region, *e.g.*, the element fractionation was favorable for fs-LA, as compared to ps-LA, with both lasers operating at 785 nm.¹³² The higher peak power of fs-lasers also promotes multi-photon processes, reducing the ablation yield. Furthermore, time-dependent elemental fractionation is also reduced by the use of these types of fs-lasers as many matrices tend to absorb with similar efficiency.^{70,71,133}

The laser beam impact position can either be kept stationary in a 'drilling' mode or dynamic, by scanning the beam over the surface in a pattern of lines. Sample movement is made possible by the placement of the sample inside a gastight sample cell, which is mounted on a motorized computer-controlled XYZ translation stage. Spot/drilling mode restricts sample consumption to the minimum (ng to mg level) while maximizing the lateral spatial resolution (the spots can be overlapped). The large disadvantage of laser drilling is its depth- and time-dependent elemental fractionation effect as the ablation rate, mean particle size extracted from the crater, and particle transport efficiency decrease at deeper drilling levels.^{129,134} These changes are related to laser defocusing, reflection and scattering of the crater walls, and the *quasi*-stationary fluid dynamics inside the crater, which are unable to fully remove scattering particles inside the crater, produced by previous shots, in the between-pulse interval. A fractionation index (FI) is a comparative measure of the level of fractionation that occurs relative to Ca, and is defined as the ratio of normalized intensities (relative to the intensity of ⁴³Ca) during the first and second half of a measurement (Equation 12).¹³⁵

$$FI_E = \frac{(I_{sample,E}(t_2)/I_{sample,^{43}Ca}(t_2))}{(I_{sample,E}(t_1)/I_{sample,^{43}Ca}(t_1))} \quad \text{Equation 12}$$

FIs correlate strongly with condensation temperatures for non-metal matrices and remain stable for a wide range of matrices and operating conditions.^{62,136} Pb/U zircon dating is one of the most significant applications where fractionation effect can undermine the proxy. It is recognized that the crater aspect ratio should not exceed a ratio of (1:1) in fractionation effects.^{107,131,137} The effect of the crater size on the level of fractionation can be corrected for empirically to some extent.¹³⁸ Line profiling (rastering) modes increase the ablation area, thus providing a more representative sample of the bulk contents of inhomogeneous samples, and produces lower, steady-state fractionation, owing to the improved heat dissipation and stable particle yield, size distribution, and transport efficiency.^{15,129} In a study by Perkins *et al.*, rastering was demonstrated to induce additional elemental fractionation for certain elements, *e.g.*, Cd, Th, U, presumably as a result of a preferential loss of these relatively volatile large ions from the glass structure.¹³⁹

1.1.3.2.6 Balancing the operational parameters

Higher laser ablation pulse firing frequencies (given a constant peak power) produce a higher mass flux, which translates into a higher sensitivity, however, plasma shielding, matrix suppression, and zone heating can also increase. A clear trade-off is presented between lateral resolution, throughput, and sensitivity. Fluence (ratio of the time-integrated photon flux over the focal spot area) and intensity (ratio of the peak power, *i.e.* pulse energy per time unit, over the focal spot area) just above the ablation threshold, *i.e.* high enough to achieve an efficient ablation whilst low enough to keep thermal effects to an acceptable level, provides the best balance of sensitivity and accuracy.¹⁴⁰ Fluence can be regulated by a telescopic beam expander or an attenuator in the beam path.

For bulk analysis and isotope ratio measurements, the ICP-MS data acquisition parameters must be optimized for filtering out as many sources of noise affecting the signal as possible. In this regard, the preferences are short settling times, short dwell times, and short acquisition times for ensuring 'quasi-stable' signal conditions, combined with a sufficiently high amount of replicates to improve counting statistics. Whenever possible, sensitivity adjustments should be done by changing the crater spot size and laser repetition rate, rather than by changing the laser fluence or carrier flow rates. This reduces laser-induced problems such as elemental fractionation or heterogeneous particle size distributions. When sample concentration and sample damage requirements permit it, it is preferable to maximize the signal intensity such that the analog mode in the SEM or a faraday cup can be used for detection, avoiding the uncertainty related to dead time correction. The optimal conditions can only be met when the ICP parameters are tuned to the effective, and stoichiometric vaporization, atomization and ionization of the aerosol. The parameters tuned include most notably the extraction lens voltage, ion optics voltages, RF power, and gas flow rates. Ar is added to the gas stream behind the ablation cell to ensure stable plasma conditions and signal responses. The addition of dry Ar as a make-up gas flow into the transport tubing, as opposed to moist Ar, results in a decrease of polyatomic interferences (oxide formation) in the low mass region and an improvement in

detection limits, as plasma ionization efficiency improves.¹⁰⁹ The addition of N₂, H₂ or CH₄ can also lead to sensitivity enhancements for certain elements.^{141,142} Recommendations concerning the experimental parameters for LA-ICP-MS can be found in literature.^{36,54,143} The exact metrics monitored during tuning, and trade-offs made, are highly application-dependent; they are described separately for each application hereinafter.

1.2 Complementary analytical techniques

Structural and chemical characterization *prior* to destructive LA sampling is often of particular interest to reveal correlations and complementary information, or to support a correct reconstruction and interpretation of the data. Furthermore, the processes of LA are studied using other analytical techniques. In the subsections below, a select number of these techniques are briefly explained. These include Mass spectrometry imaging (MSI) techniques such as MALDI and SIMS, which visualize the spatial distribution of macromolecules, e.g., biomarkers, metabolites, peptides or proteins by their molecular masses in a multiplexed way. The information captured by MSI is highly complementary to element distribution information obtained via LA-ICP-MS; this information can be combined in future applications via data fusion. Complementary techniques not explained hereafter include SHRIMP, PIXE, and PIGE.

1.2.1 X-ray fluorescence¹⁴⁴⁻¹⁴⁸

High energy photons of a wavelength of 0.01-10 nm (energy range of *ca.* 100eV-100keV), which is in the range of interatomic distances, can transfer their energy to electrons of the inner atomic orbitals upon photon-matter interaction, exciting these inner shell electrons towards higher orbitals, or ejecting them with an $E_k = h\nu - E_{binding}$ (the photoelectric effect) and creating inner shell vacancies. Relaxation of the electron cloud to the ground state can provoke: i) the emission of fluorescence photons ($p_{emission} = \omega$) with energies equivalent to the energy differences of electron transitions of the electron cascade and wavenumber $\tilde{\nu} = k(Z - \sigma)^2$ with σ a screening constant, and ii) internal conversion (radiationless transitions) with energy dissipation towards vibrational modes, and iii) Auger electron emission. The atomic photoelectric absorption cross-section τ is $\sim Z^4/E_0^3$. Incoherent (Compton) scattering transfers part of the incident photon energy towards an ejected valence electron, resulting in an energy shift of the scattered photon:

$$E_{scat} = E_0 / (1 + (E_0 m_e^{-1} c^{-2}) / (1 - \cos \theta_{scat})) \quad \text{Equation 13}$$

where E_0 is the energy of the incoming photon, and m_e the mass of an electron. The cross-section for Compton scatter on free electrons over solid angle Ω is a function of the scattering angle θ , azimuthal angle ϕ , E_{scat} and Z , and is dominant for small Z . Coherent (Rayleigh) scattering of photons on inner shell electrons will scatter the photon without energy loss/gain (elastically) in a direction derived from the Rayleigh differential cross-section, which is a function of the scattering angle θ , azimuthal angle ϕ , E_0 and Z . Both scatter types are minimal for $\theta = 90^\circ$, $\phi = 0^\circ$ and a linearly polarized primary beam, though their ratio will depend on the mean Z . The total mass attenuation coefficient for photon-matter interaction:

$$\mu_p(Z, E_0) = \frac{n}{\rho} (\tau(Z, E_0) + \sigma_{coh}(Z, E_0) + \sigma_{incoh}(Z, E_0)) \quad \text{Equation 14}$$

where n is the number density, determines the X-ray transmission $I = I_0 e^{-\mu \rho T}$ for samples of thickness T . The X-ray tube lab-size sources (*e.g.*, a hot filament electron emitter in a high vacuum tube or field emission emitter) produce continuous polychromatic X-ray radiation through Bremsstrahlung, with sharp intensity peaks at the anode characteristic lines, *e.g.*, K_α line, as a result of impact ionization and subsequent X-ray emission. The maximum brilliance of these sources varies between $10^8 - 10^{10} \text{ photons s}^{-1} \text{ mm}^{-2} \text{ mrad}^{-2} 0.1\% \text{ BW}^{-1}$. Synchrotron radiation undulator sources produce a primary X-ray beam having a typical energy range of $1 - 100 \text{ keV}$ and a brilliance $> 10^{20} \text{ photons s}^{-1} \text{ mm}^{-2} \text{ mrad}^{-2} 0.1\% \text{ BW}^{-1}$, which is ultimately the result of energy losses of a relativistic electron or positron under the influence of an oscillatory acceleration over small deflection angles, induced by an alternating high frequency Lorentz force field, generated by a magnet array. X-ray optics, including monochromators, total reflection optics (KB mirrors, capillary optics), refractive optics (compound refraction lens) and diffractive optics (Fresnel zone plate, doubly curved crystal optics), produce a beam of the desired characteristics, and collimate the beam to the target on the sample. Outgoing photons are detected using energy-dispersive silicon drift detectors (SDD) or CCD (full-field) detectors. In SDD, a primary photoelectron generated upon X-ray-matter interaction can promote valence band electrons to the conduction band when they received an energy $> 1.12 \text{ eV}$, thereby generating electron-hole pairs in the reverse biased pn-diode chip. Secondary electrons, when sufficiently energetic, can produce an electron cascade. The electrons and holes migrate under the influence of an electric field towards electrodes, permitting their collection, pre-amplification of the signal by a field effect transistor (FET), pulse-shaping, and conversion of the signal using an analog-to-digital convertor (ADC). SDD are affected by dead times (typically used below $\leq 30\%$) and produce escape peaks 1.74 keV below the detected parent peaks, in case of incident X-ray energies above the Si K_α -edge.

Because the energy differences between quantum energy levels are unique to each electron cloud and nucleus configuration, deconvolution of the detected fluorescence spectrum permits to obtain element-specific from the materials under investigation. Combined with microbeam-based scanning techniques, spatially resolved characterization, *i.e.* elemental mapping, is achieved. The energy levels with principal quantum numbers 1, 2, 3 are termed K, L, and M under the Siegbahn notation; characteristic spectral lines of transitions $L \rightarrow K$, $M \rightarrow K$, and $M \rightarrow L$, are designated K_α , K_β , and L_α respectively. Furthermore, the X-ray radiation diffraction-limit is $< 10 \text{ nm}$, enabling resolutions that can range from $100 \mu\text{m}$ down to 10 nm , provided enough brilliance is produced by the source. XRF imaging hence probes almost identical modalities as LA-ICP-MS ($Z \geq 10$), in a *quasi*-non-destructive approach with, in the case of a synchrotron source, similar LOD ($10^{-1} - 10^2 \mu\text{g g}^{-1}$) for elements with $Z \lesssim 40$, establishing it as a highly valuable and complementary tool for elemental imaging. Other X-ray based imaging techniques such as XANES, EXAFS and S/WAXS, may provide more information on the chemical state of the elements and molecular structure.

1.2.2 EPMA

An electron beam ($10^{-1} - 10^2 \text{ keV}$), emitted from an electron gun and focused onto a sample surface, interacts with matter through:

- i. Inelastic scattering on inner and outer shell electrons, producing secondary electrons (SE, $< 50 \text{ eV}$), X-ray radiation (fluorescence, *vide supra*) and Auger electrons.
- ii. Elastic scattering, producing back-scattered electrons (BSE, $> 10^2 \text{ eV}$)

SE and BSE can be detected under vacuum conditions by a scintillator-photomultiplier or semiconductor detector. BSE provide contrast between areas with different average Z, whilst SE visualize topography; the SE output yield increases as the angle of incidence increases. In scanning electron microscopy, the electron beam is scanned over the surface using an XY deflector plate, permitting imaging with resolutions down to 0.5 nm (the wavelength of an electron is 12.2 pm in a 10 kV SEM). Non-conductive specimens are sputter-coated with heavy Z metals, *e.g.*, Au, to prevent charge build-up. SEMs are often combined with focused ion beam (FIB) systems for SE and secondary ion detection and for ion milling (depth analysis).

1.2.3 micro-CT

Laboratory-based high-resolution tomography techniques can produce X-ray absorption 3D images with a resolution better than $1 \mu\text{m}$ (micro-CT). The flux of transmitted X-ray photons, produced by a Coolidge tube with a cone beam geometry, is detected using a planar 2D CMOS or CCD detector array. The scanned object is placed within the field-of-view of the detector and X-ray beam. The resolution achievable using a conical beam R, depends on the magnification M (the ratio of source-detector (SDD) and source-object distance (SOD)), the focal spot size d_s and the pixel size d of the detector (Equation 15).

$$R = \frac{d}{M} + \left(1 - \frac{1}{M}\right) d_s \quad \text{Equation 15}$$

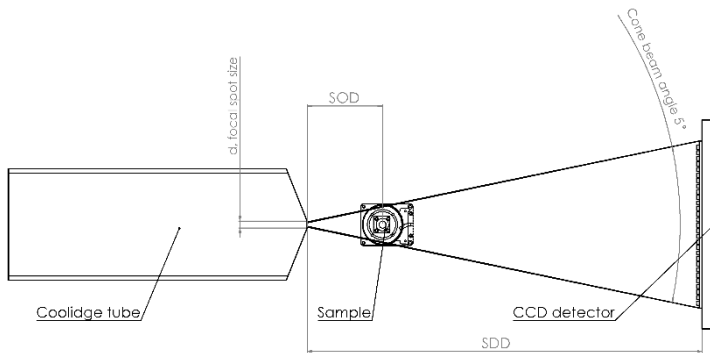


Figure 9 Schematic overview of a rotate-only CT instrument.

In the rotate-only CT mode, the sample object is rotated under many rotation angles during tomographic acquisition, whilst recording X-ray projection images (slices). In case of a 1D detector, the sample can be repositioned vertically by the distance of the slice width after each full rotation. Although slices can be acquired in seconds, the acquisition time can vary depending on the geometry of the particular scan, the material density of the object being scanned and the number of views acquired. The number of projections required is theoretically

defined as $\pi N/2$, with N number of detector row pixels. Ring artefacts may occur when one or more detector channels produce a stronger signal than the surrounding ones. The sinograms acquired can be manipulated in digital geometry processing software to reconstruct a 3D image of the object, in which each voxel conveys information on the linear attenuation coefficient at the corresponding position in space, through an analytical, statistical or algebraic reconstruction algorithm. For the reconstruction of cone beam tomography images, a 3D inverse Radon transformation can be applied.

1.2.4 AFM

When a spring-loaded Si cantilever with a probe tip radius of curvature of a few nm is brought in proximity to the sample surface, the tip is deflected by van der Waals forces, electrostatic forces, and chemical bonds, which reflect the topography and local chemistry of the sample. The deflection of the tip can be monitored by two photodiodes which detect the change in the angle of reflection of a laser focused on the cantilever (incident under an angle). In atomic force microscopy (AFM) the probe is scanned in a raster pattern, $\leq 100 \times 100 \mu m^2$ in size, over the sample surface, imaging the topography of a sample with a depth resolution $< 0.1 \text{ nm}$. In contact mode the probe is dragged across the surface, enabling a direct feedback of the topography, but potentially damaging the surface. In dynamic contact mode (also called *tapping* mode), the cantilever is oscillated near its resonance frequency using a piezo element; intermittent probe-surface contact modulates the amplitude of the oscillation, permitting detection of the surface height *via* a compensating amplitude-locked feedback servo loop on the Z-axis. In non-contact mode, the frequency modulation in the cantilever oscillation – which is free-running at resonant frequency – induced by long-range forces, is compensated using a frequency-locked feedback servo loop on the Z-axis. This permits height detection without direct contact with the sample.

1.2.5 Fluorescence microscopy¹⁴⁹

Fluorescence, photon-emission as a result of the relaxation of atoms/molecules in the excited singlet state, has been the key to the detection of intracellular modalities *via* confocal microscopy with pinhole excitation and super-resolution (SR) microscopy. SR microscopy comprises: structured illumination microscopy (SIM), stimulated emission depletion (STED), stochastic optical reconstruction microscopy (STORM), photoactivation localization microscopy (PALM), and many others.¹⁵⁰⁻¹⁵² Up to 7 exogenous fluorophores and molecular probes (using quantum dot probes with large Stoke shifts, applied *via* incubation), can be imaged with a resolution down to the sub-nm level (with deconvolution strategies). In flow cytometry, as many as 17 fluorophores can be acquired.¹⁵³ These probes, *e.g.*, genetically encoded fluorescent sensor probes (GFP, YFP), can target endogenous and exogenous metals with a specific coordination environment, antigens, proteins, RNA and DNA sequences and many other molecules. These fluorescence images present information on the distribution of the target. As the imaging procedure is non-destructive, and applicable to cells *in vivo*, the images can be acquired *prior* to LA, and combined with the LA-image in *post*-processing.

1.2.6 Matrix-assisted laser desorption/ionization (MALDI) mass spectrometry

MALDI is an atmospheric pressure soft ionization mass spectrometric technique for the quantitative determination of macromolecules such as biopolymers. Similar to desorption electrospray ionization (DESI) the soft ionization process overcomes the propensity of these kDa molecules to fragment when ionized. However, as MALDI produces less multiply charged ions, the mass range can be extended to MDa levels. Related techniques include electrospray laser desorption ionization, matrix-assisted laser desorption electrospray ionization, and laser ablation electrospray ionization. In MALDI, a matrix of crystallized molecules such as 3,5-dimethoxy-4-hydroxycinnamic acid is deposited onto the sample using an organic solvent such as acetonitrile or ethanol. Upon soft ablation by a Nd:YAG (266 nm or 355 nm) or nitrogen laser (337 nm), the matrix desorbs and is ionized through protonation; the matrix then ionizes the analyte through ion (proton) transfer processes. Although the lateral resolution of MALDI and DESI (50-10 μm) falls short of that of LA-ICP-MS, it is, like immunohistochemistry, a crucial source of complementary data in many projects, as these techniques can provide a better insight in the distribution of metal-containing compounds, *e.g.*, by differentiating a metal-containing (drug) macromolecule and its metabolites. MALDI and similar techniques like it can thus aid in the interpretation of the metal distribution as imaged by LA-ICP-MS.

1.2.7 Secondary ion mass spectrometry (SIMS)

SIMS is a highly sensitive (ng/g level) surface analysis technique based on sputtering the surface of the specimen using a focused primary ion beam from an ion gun, typically a liquid metal ion gun, collecting the secondary ions formed upon ion impact, and detecting these ions by (TOF-) MS. SIMS operates in a high-vacuum environment, which places restrictions on the types of samples that can be analyzed, and necessitates sample preparation steps to prevent sample outgassing. Static SIMS has a probe depth of 1-2 nm and images both the isotopic and molecular composition of the sample at a spatial resolution of <50 nm. Dynamic SIMS on the other hand has an ion beam density of $> 10^{12} \text{ ions/cm}^2$, and is more geared towards isotopic and trace element analysis, making it a direct competitor to LA-ICP-MS, in terms of capabilities. Although both techniques are competitive in terms of sensitivity (ppm-ppb range), SIMS boasts significantly better spatial resolution (depth resolution of 10's of nm and lateral resolution <100 nm). As ionic, atomic and molecular species are produced during sputtering at a matrix-dependent ratio, quantitative analysis requires complex corrections and matrix-matched conditions. Nevertheless, quantification can be achieved. It should be noted that the purchasing cost of SIMS instrumentation (\$2M-\$3M) lies significantly higher than that of high-end LA-ICP-MS instrumentation (\$500K-\$1M), and much higher than that of basic LA-ICP-MS setups (\$250K). Sensitive high mass-resolution ion microprobe (SHRIMP) is a double-focusing sector SIMS instrument dedicated to stable isotope analysis for geochronology purposes. SHRIMP can achieve a typical precision of $<0.3\text{‰}$ (1 s, $\delta^{36}\text{S}$) at a mass resolution of > 10000 for a primary ion beam diameter of $<1\text{-}25 \mu\text{m}$. This level of precision can easily be achieved for trace elements in (multi-collector) ICP-MS, whilst aspirating a solution by pneumatic nebulization, but is not straightforward to achieve for direct solid sample introduction via laser ablation operating at spot sizes $<10 \mu\text{m}$ in diameter.

1.3 Sample preparation approaches

In the context of LA-ICP-MS, sample preparation is a process to i) preserve the native chemical environment and external and internal sample morphology after sampling (by preventing autolysis and putrefaction) and during exposure to the environment of the analytical apparatus, and ii), to present the sample in a suitable and accessible format for analysis.

1.3.1 Biological samples

Cryogenic methods based on flash-freezing the hydrated sample with LN₂ (77 K) with or without cryoprotectants, relying on amorphous (*i.e.* non-crystalline) ice formation at temperatures < 136 K, are generally perceived as the most reliable (apart from *in vivo* experiments) for biological samples, though there is a risk of structural deformation and damage when the sample is not handled correctly. Sometimes, cryogenic methods are not available or applicable to the sample, in which case chemical fixation agents, including OsO₄, paraformaldehyde, glutaraldehyde, and ethanol, are often applied to preserve the structure of the sample through cross-linking, denaturation and oxidation of proteins. *Prior* to fixation, biological samples are often dehydrated in an EtOH series. Individual cells attached to microscope slides and filters can often be analyzed directly. Drying, freezing or fixation is required to prevent leakage of cytoplasm and cellular material (mitochondria, lysosomes, etc.) from its lipid bilayer membrane container. Tissues are however sectioned with a(n) (ultra-) microtome, often equipped with a cryostat, to a thickness of 2 – 20 μm . Thin, fragile sections often require an embedding medium, *e.g.*, paraffin, gelatin, or Spurr's resin. Aside from *post-mortem* natural breakdown, sample fixation and embedding can have profound, relevant effects, which can interfere with the elemental distribution, confounding the relationship between the acquired data and the *in vivo* distribution. Light elements (Na, K, Cl) of high mobility may, for example, diffuse from anatomical structures in an aqueous or fixation medium, changing the element distribution during sample storage. Cryogenic approaches applied immediately after sampling, are hence favored, as they avoid fixation and embedding. Histological staining and anti-gen tagging of sections *prior* to elemental imaging is preferentially avoided, as the immersion of the tissue may displace the elements within the tissue. The support material can be chosen in function of the technique, *e.g.*, for XRF ultralene film and SiN₃ windows are used, and for LA-ICP-MS, high purity silicon wafers, Starfrost® adhesive slides and ITO slides are used.

1.3.2 Geological and archaeological samples

Epoxy-embedded geological samples are polished using SiC paper (P200-P4000), diamond abrasive suspensions (1 – 10 μm grain size) and colloidal silica suspension (40 nm grain size), acidic alumina suspension or CeO₂ suspension for final polishing (depending on the sample matrix) to expose the sample surface for analysis. Thin sections can also be produced when petrography will be conducted.

1.4 Bibliography

- (1) Van Malderen, S. J. M.; Managh, A. J.; Sharp, B. L.; Vanhaecke, F. J. *Anal. At. Spectrom.* **2016**, *31*, 423-439.
- (2) Van Malderen, S. J. M. *Trace element fingerprinting of stained glass (St. Jacobs Church, Antwerp) via laser ablation - ICP - mass spectrometry*, Master thesis. Ghent University, Ghent, Belgium, 2013.
- (3) Woodhead, J. D.; Hellstrom, J.; Hergt, J. M.; Greig, A.; Maas, R. *Geostandards and Geoanalytical Research* **2007**, *31*, 331-343.
- (4) Koenig, A. E.; Rogers, R. R.; Trueman, C. N. *Geology* **2009**, *37*, 511-514.
- (5) Gunther, D.; Frischknecht, R.; Heinrich, C. A.; Kahlert, H.-J. *J Anal Atom Spectrom* **1997**, *12*, 939-944.
- (6) Ulens, K.; Moens, L.; Dams, R.; Vanwinckel, S.; Vandeveldel, L. *J Anal Atom Spectrom* **1994**, *9*, 1243-1248.
- (7) Poitrasson, F.; Chenery, S.; Bland, D. J. *Earth and Planetary Science Letters* **1996**, *145*, 79-96.
- (8) Woodhead, J.; Hergt, J.; Shelley, M.; Eggins, S.; Kemp, R. *Chemical Geology* **2004**, *209*, 121-135.
- (9) Chernonozhkin, S. M.; Goderis, S.; Bauters, S.; Vekemans, B.; Vincze, L.; Claeys, P.; Vanhaecke, F. *J Anal Atom Spectrom* **2014**, *29*, 1001-1016.
- (10) Johnston, S.; Gehrels, G.; Valencia, V.; Ruiz, J. *Chemical Geology* **2009**, *259*, 218-229.
- (11) Cottle, J. M.; Kylander-Clark, A. R.; Vrijmoed, J. C. *Chemical Geology* **2012**, *332-333*, 136-147.
- (12) Gundlach-Graham, A.; Burger, M.; Allner, S.; Schwarz, G.; Wang, H. A.; Gyr, L.; Grolimund, D.; Hattendorf, B.; Gunther, D. *Anal Chem* **2015**, *87*, 8250-8258.
- (13) Jackson, S. E.; Pearson, N. J.; Griffin, W. L.; Belousova, E. A. *Chemical Geology* **2004**, *211*, 47-69.
- (14) Wang, H. A. O.; Grolimund, D.; Van Loon, L. R.; Barmettler, K.; Borca, C. N.; Aeschmann, B.; Guenther, D. *Anal Chem* **2011**, *83*, 6259-6266.
- (15) Resano, M.; Garcia-Ruiz, E.; Vanhaecke, F. *Mass Spectrom Rev* **2010**, *29*, 55-78.
- (16) van Elteren, J. T.; Izmer, A.; Šala, M.; Orsega, E. F.; Šelih, V. S.; Panighello, S.; Vanhaecke, F. *J Anal Atom Spectrom* **2013**, *28*, 994-1004.
- (17) Grun, R.; Aubert, M.; Joannes-Boyau, R.; Moncel, M. H. *Geochimica Et Cosmochimica Acta* **2008**, *72*, 5278-5290.
- (18) Sjästad, K.-E.; Andersen, T.; Simonsen, S. L. *Spectrochimica Acta Part B: Atomic Spectroscopy* **2013**, *89*, 84-92.
- (19) Abbegayle, J. D.; Pollock, E. M.; Land, D., Forensic Glass Analysis by LA-ICP-MS: Assessing the Feasibility of Correlating Windshield Composition and Supplier; United States Department of Justice 2010.
- (20) Deconinck, I.; Latkoczy, C.; Gunther, D.; Govaert, F.; Vanhaecke, F. *J Anal Atom Spectrom* **2006**, *21*, 279-287.
- (21) Berends-Montero, S.; Wiarda, W.; de Joode, P.; van der Peijl, G. *J Anal Atom Spectrom* **2006**, *21*, 1185.

- (22) Jackson, B.; Harper, S.; Smith, L.; Flinn, J. *Analytical and bioanalytical chemistry* **2006**, *384*, 951-957.
- (23) Hare, D. J.; Lee, J. K.; Beavis, A. D.; van Gramberg, A.; George, J.; Adlard, P. A.; Finkelstein, D. I.; Doble, P. A. *Anal Chem* **2012**, *84*, 3990-3997.
- (24) Izmer, A.; Gholap, D.; De Houwer, K.; Cuyckens, F.; Vanhaecke, F. *J Anal Atom Spectrom* **2012**, *27*, 413-418.
- (25) Giesen, C.; Wang, H. A.; Schapiro, D.; Zivanovic, N.; Jacobs, A.; Hattendorf, B.; Schuffler, P. J.; Grolimund, D.; Buhmann, J. M.; Brandt, S.; Varga, Z.; Wild, P. J.; Gunther, D.; Bodenmiller, B. *Nature methods* **2014**, *11*, 417-422.
- (26) Flórez, M. R.; Aramendía, M.; Resano, M.; Lapeña, A. C.; Balcaen, L.; Vanhaecke, F. *J Anal Atom Spectrom* **2013**, *28*, 1005-1015.
- (27) Lear, J.; Hare, D. J.; Fryer, F.; Adlard, P. A.; Finkelstein, D. I.; Doble, P. A. *Anal Chem* **2012**, *84*, 6707-6714.
- (28) Becker, J. S.; Zoriy, M. V.; Pickhardt, C.; Palomero-Gallagher, N.; Zilles, K. *Anal Chem* **2005**, *77*, 3208-3216.
- (29) Managh, A. J.; Hutchinson, R. W.; Riquelme, P.; Broichhausen, C.; Wege, A. K.; Ritter, U.; Ahrens, N.; Koehl, G. E.; Walter, L.; Florian, C.; Schlitt, H. J.; Reid, H. J.; Geissler, E. K.; Sharp, B. L.; Hutchinson, J. A. *Journal of immunology* **2014**, *193*, 2600-2608.
- (30) Urgast, D. S.; Feldmann, J. *J Anal Atom Spectrom* **2013**, *28*, 1367-1371.
- (31) Konz, I.; Fernandez, B.; Fernandez, M. L.; Pereiro, R.; Gonzalez-Iglesias, H.; Coca-Prados, M.; Sanz-Medel, A. *Analytical and bioanalytical chemistry* **2014**, *406*, 2343-2348.
- (32) Drescher, D.; Giesen, C.; Traub, H.; Panne, U.; Kneipp, J.; Jakubowski, N. *Anal Chem* **2012**, *84*, 9684-9688.
- (33) Wang, M.; Zheng, L. N.; Wang, B.; Chen, H. Q.; Zhao, Y. L.; Chai, Z. F.; Reid, H. J.; Sharp, B. L.; Feng, W. Y. *Anal Chem* **2014**, *86*, 10252-10256.
- (34) Aggarwal, S. K.; Jain, H. C. *Introduction to Mass Spectrometry*; Indian Society for Mass Spectrometry: Mumbai, 1997.
- (35) Gray, A. L. *Analyst* **1985**, *110*, 551-556.
- (36) Thomas, R. *Practical Guide to Icp-MS: A Tutorial for Beginners*; Marcel Dekker, 2004, p 324.
- (37) Turner, P. J.; Mills, D. J.; {Shr\"{o}der, E.; Lapitajs, G.; Jung, G.; Iacone, L. A.; D.A., H.; Montaser, A.; Wiley-VCH: New York, USA., 1998.
- (38) Resano, M.; McIntosh, K. S.; Vanhaecke, F. *J Anal Atom Spectrom* **2012**, *27*, 165-173.
- (39) Houk, R. S.; Fassel, V. A.; Flesch, G. D.; Svec, H. J.; Gray, A. L.; Taylor, C. E. *Anal Chem* **1980**, *52*, 2283-2289.
- (40) Houk, R. S.; Winge, R. K.; Chen, X. *J Anal Atom Spectrom* **1997**, *12*, 1139-1148.
- (41) Huang, M.; Hieftje, G. M. *Spectrochimica Acta*. **1989**, *44B*, 739-749.
- (42) Voronov, M.; Hoffmann, V.; Birus, D.; Engelhard, C.; Buscher, W. *J. Anal. At. Spectrom.* **2015**, *30*, 2089-2098.
- (43) Gray, A. L. *J Anal Atom Spectrom* **1989**, *4*, 371-373.

- (44) Kivel, N.; Potthast, H.-D.; Günther-Leopold, I.; Vanhaecke, F.; Günther, D. *Spectrochimica Acta Part B: Atomic Spectroscopy* **2014**, 93, 34-40.
- (45) Kivel, N. W. E.; Vanhaecke, F. p.; Günther, D. c.; Leopold-Günther, I. c. *Systematic study of instrumental mass discrimination in multi-collector inductively coupled plasma-mass spectrometry*. Ghent2015.
- (46) Vanhaecke, F.; Degryse, P. *Isotopic Analysis: Fundamentals and Applications Using ICP-MS*; Wiley, 2012.
- (47) Jarvis, K. E.; Gray, A. L.; Houk, R. S. *Inductively Coupled Plasma Mass Spectrometry*; Chapman and Hall, NY, 1991.
- (48) Makarov, A. *Anal Chem* **2000**, 72, 1156-1162.
- (49) Mirsaleh-Kohan, N.; Robertson, W. D.; Compton, R. N. *Mass Spectrom Rev* **2008**, 27, 237-285.
- (50) Dennis, E. A.; Ray, S. J.; Enke, C. G.; Gundlach-Graham, A. W.; Barinaga, C. J.; Koppenaal, D. W.; Hieftje, G. M. *Journal of the American Society for Mass Spectrometry* **2015**.
- (51) Burgoyne, T. W.; Hieftje, G. M. *Mass Spectrom Rev* **1996**, 15, 241-259.
- (52) Cagno, S. *Compositional analysis of historical glass*, Ph.D. thesis. University of Antwerp2012.
- (53) Gates, P. *Gas Chromatography Mass Spectrometry (GC/MS)* 2012.
- (54) Longerich, H. P.; Jackson, S. E.; Gunther, D. *J Anal Atom Spectrom* **1996**, 11, 899-904.
- (55) Jakubowski, N.; Prohaska, T.; Rottmann, L.; Vanhaecke, F. *J Anal Atom Spectrom* **2011**, 26, 693.
- (56) Myers, D. P.; Hieftje, G. M. *Microchemical Journal* **1993**, 48, 259-277.
- (57) Guilhaus, M. *Journal of Mass Spectrometry* **1995**, 30, 1519-1532.
- (58) Van Elteren, J. T.; Tennent, N. H.; Selih, V. S. *Anal Chim Acta* **2009**, 644, 1-9.
- (59) Dams, R. J.; Goossens, J.; Moens, L. *Microchim Acta* **1995**, 119, 277-286.
- (60) Todoli, J. L.; Mermet, J. M. *Liquid Sample Introduction in ICP Spectrometry: A Practical Guide*; Elsevier Science, 2011.
- (61) Einstein, A. *Physikalische Zeitschrift* **1917**, 18, 121.
- (62) Jackson, S. E. In *Mineralogical Association of Canada Short Course Series* Sylvester, P., Ed.; Mineralogical Association of Canada: Vancouver, 2008, pp 29-46.
- (63) Horn, I.; Guillong, M.; Gunther, D. *Appl. Surf. Sci.* **2001**, 182, 91-102.
- (64) Guillong, M. *Laser Ablation Inductively Coupled Plasma Mass Spectrometry: Laser ablation system developments and investigations on elemental fractionation*, Ph.D. thesis. ETH Zurich2004.
- (65) Telle, H. H.; Ure, A. G.; Donovan, R. J.; WILEY: Chichester, 2007.
- (66) Paetzel, R., *Comparison Excimer Laser - Solid State Laser*; Lambda Physik Goettingen, Germany 2002.
- (67) Gholap, D. *Development and Use of Approaches for Quantitative 2-D Elemental Mapping of Biological Samples via Laser*

Ablation ICP-Mass Spectrometry, Ph.D. thesis. Ghent University 2012.

(68) Bressler, C.; Lawrence, W. G.; Schwentner, N. *The Journal of Chemical Physics* **1996**, *105*, 10178-10188.

(69) Vince, L. *Advanced Spectroscopic Methods of Analysis, Course Master of Chemistry*; Ghent University, 2013.

(70) Guillon, M.; Horn, I.; Gunther, D. *J Anal Atom Spectrom* **2003**, *18*, 1224-1230.

(71) Gunther, D.; Heinrich, C. A. *J Anal Atom Spectrom* **1999**, *14*, 1369-1374.

(72) Bleiner, D.; Bogaerts, A. *Spectrochimica Acta Part B: Atomic Spectroscopy* **2006**, *61*, 421-432.

(73) Gutiérrez-González, A.; González-Gago, C.; Pisonero, J.; Tibbetts, N.; Menéndez, A.; Vélez, M.; Bordel, N. *J. Anal. At. Spectrom.* **2015**, *30*, 191-197.

(74) Vogel, A.; Venugopalan, V. *Chemical Reviews* **2003**, *103*, 577-644.

(75) Lorazo, P.; Lewis, L. J.; Meunier, M. *Physical Review Letters* **2003**, *91*, 225502.

(76) Paltauf, G.; Schmidtkloiber, H. *Lasers Surg. Med.* **1995**, *16*, 277-287.

(77) Oujja, M.; Rebollar, E.; Abrusci, C.; Amo, A. D.; Catalina, F.; Castillejo, M. *Journal of Physics: Conference Series* **2007**, *59*, 571-574.

(78) Gaspard, S.; Oujja, M.; Abrusci, C.; Catalina, F.; Lazare, S.; Desvergne, J. P.; Castillejo, M. *Journal of Photochemistry and Photobiology A: Chemistry* **2008**, *193*, 187-192.

(79) Niehaus, R.; Sperling, M.; Karst, U. *J Anal Atom Spectrom* **2015**, *30*, 2056-2065.

(80) Claverie, F.; Pécheyran, C.; Mounicou, S.; Ballihaut, G.; Fernandez, B.; Alexis, J.; Lobinski, R.; Donard, O. F. X. *Spectrochimica Acta Part B: Atomic Spectroscopy* **2009**, *64*, 649-658.

(81) Painter, L. R.; Hamm, R. N.; Arakawa, E. T.; Birkhoff, R. D. *Physical Review Letters* **1968**, *21*, 282-284.

(82) Li, Y.; Shrestha, B.; Vertes, A. *Anal Chem* **2007**, *79*, 523-532.

(83) Bogaerts, A.; Chen, Z.; Bleiner, D. *J Anal Atom Spectrom* **2006**, *21*, 384-395.

(84) Bogaerts, A.; Chen, Z. *Spectrochimica Acta Part B: Atomic Spectroscopy* **2005**, *60*, 1280-1307.

(85) Autrique, D.; Alexiades, V. *Journal of Applied Physics* **2014**, *115*, 166101.

(86) Tognoni, E.; Cristoforetti, G. *J Anal Atom Spectrom* **2014**, *29*, 1318-1338.

(87) Leung, A. P. K.; Chan, W. T.; Mao, X. L.; Russo, R. E. *Anal Chem* **1998**, *70*, 4709-4716.

(88) Garcia, C. C.; Lindner, H.; Niemax, K. *J Anal Atom Spectrom* **2009**, *24*, 14-26.

(89) Lindner, H.; Loper, K. H.; Hahn, D. W.; Niemax, K. *Spectrochimica Acta Part B: Atomic Spectroscopy* **2011**, *66*, 179-185.

(90) Root, R. G. In *Lasers-Induced Plasmas and Applications*, Radziemski, L. J.; Cremers, A., Eds.; Taylor & Francis: New York, 1989.

(91) Ma, Q.; Motto-Ros, V.; Laye, F.; Yu, J.; Lei, W.; Bai, X.; Zheng, L.; Zeng, H. *Journal of Applied Physics* **2012**, *111*, 053301.

- (92) Bleiner, D.; Bogaerts, A.; Belloni, F.; Nassisi, V. *Journal of Applied Physics* **2007**, *101*, 083301.
- (93) Autrique, D.; Chen, Z.; Alexiades, V.; Bogaerts, A.; Rethfeld, B. *AIP Conference Proceedings* **2012**, *1464*, 648-659.
- (94) Bäuerle, D. W. *Laser Processing and Chemistry*; Springer Berlin Heidelberg, 2011.
- (95) Bulgakova, N. M.; Bulgakov, A. V.; Bobrenok, O. F. *Phys. Rev. E* **2000**, *62*, 5624-5635.
- (96) Amoruso, S.; Wang, X.; Altucci, C.; de Lisio, C.; Armenante, M.; Bruzzese, R.; Spinelli, N.; Velotta, R. *Appl. Surf. Sci.* **2002**, *186*, 358-363.
- (97) Lorusso, A.; Nassisi, V.; Velardi, L.; Sicilano, M. V. *Journal of Physics: Conference Series* **2010**, *227*, 012037.
- (98) Bleiner, D.; Lippert, T. *Journal of Applied Physics* **2009**, *106*, 123301.
- (99) Gurevich, E. L.; Hergenroder, R. *J Anal Atom Spectrom* **2007**, *22*, 1043-1050.
- (100) LaHaye, N. L.; Harilal, S. S.; Diwakar, P. K.; Hassanein, A. *J. Anal. At. Spectrom.* **2014**, *29*, 2267-2274.
- (101) Russo, R. E.; Mao, X.; Gonzalez, J. J.; Zorba, V.; Yoo, J. *Anal Chem* **2013**, *85*, 6162-6177.
- (102) Bogaerts, A.; Chen, Z. Y.; Gijbels, R.; Vertes, A. *Spectrochim Acta B* **2003**, *58*, 1867-1893.
- (103) Bauerle, D. *Laser processing and chemistry*; Springer: Bern, 1996.
- (104) Harilal, S. S.; Brumfield, B. E.; Cannon, B. D.; Phillips, M. C. *Anal Chem* **2016**.
- (105) Zeng, X. Z.; Mao, X. L.; Mao, S. S.; Yoo, J. H.; Greif, R.; Russo, R. E. *Journal of Applied Physics* **2004**, *95*, 816-822.
- (106) Su, X.; Zhou, W.; Qian, H. *J. Anal. At. Spectrom.* **2014**, *29*, 2356-2361.
- (107) Eggins, S. M.; Kinsley, L. P. J.; Shelley, J. M. G. *Appl. Surf. Sci.* **1998**, *127-129*, 278-286.
- (108) Horn, I.; Gunther, D. *Appl. Surf. Sci.* **2003**, *207*, 144-157.
- (109) Gunther, D.; Heinrich, C. A. *J Anal Atom Spectrom* **1999**, *14*, 1363-1368.
- (110) Callies, G.; Schittenhelm, H.; Berger, P.; Hugel, H. *Appl. Surf. Sci.* **1998**, *127*, 134-141.
- (111) Russo, R. E.; Suen, T. W.; Bol'shakov, A. A.; Yoo, J.; Sorkhabi, O.; Mao, X.; Gonzalez, J.; Oropeza, D.; Zorba, V. *J Anal Atom Spectrom* **2011**, *26*, 1596-1603.
- (112) Russo, R. E.; Bol'shakov, A. A.; Mao, X.; McKay, C. P.; Perry, D. L.; Sorkhabi, O. *Spectrochimica Acta Part B: Atomic Spectroscopy* **2011**, *66*, 99-104.
- (113) Yoo, J. H.; Jeong, S. H.; Greif, R.; Russo, R. E. *Journal of Applied Physics* **2000**, *88*, 1638-1649.
- (114) Ho, J. R.; Grigoropoulos, C. P.; Humphrey, J. A. C. *Journal of Applied Physics* **1995**, *78*, 4696-4709.
- (115) Itina, T. E.; Hermann, J.; Delaporte, P.; Sentis, M. *Phys. Rev. E* **2002**, *66*.
- (116) Fann, W. S.; Storz, R.; Tom, H. W. K.; Bokor, J. *Physical Review Letters* **1992**, *68*, 2834-2837.

- (117) Tang, M.; Arevalo, R.; Goreva, Y.; McDonough, W. F. *J. Anal. At. Spectrom.* **2015**, *30*, 2316-2322.
- (118) Kuhn, H. R. *Laser Ablation ICP-MS: Fundamental investigations on aerosols generated by laser ablation at ambient pressure, Ph.D. thesis*; ETH Zurich, 2005.
- (119) Miclea, M.; Garcia, C. C.; Exius, I.; Lindner, H.; Niemax, K. *Spectrochimica Acta Part B: Atomic Spectroscopy* **2006**, *61*, 361-367.
- (120) Outridge, P. M.; Doherty, W.; Gregoire, D. C. *Spectrochim Acta B* **1997**, *52*, 2093-2102.
- (121) Koch, J.; Gunther, D. *Applied Spectroscopy* **2011**, *65*, 155A-162A.
- (122) Feldmann, J.; Kindness, A.; Ek, P. *J Anal Atom Spectrom* **2002**, *17*, 813-818.
- (123) Konz, I.; Fernandez, B.; Luisa Fernandez, M.; Pereiro, R.; Sanz-Medel, A. *Anal Chim Acta* **2014**, *809*, 88-96.
- (124) Kuhn, H. R.; Guillon, M.; Gunther, D. *Analytical and bioanalytical chemistry* **2004**, *378*, 1069-1074.
- (125) Aeschliman, D. B.; Bajic, S. J.; Baldwin, D. P.; Houk, R. S. *J Anal Atom Spectrom* **2003**, *18*, 1008-1014.
- (126) Vogt, C.; Latkoczy, C. *Laser Ablation ICP-MS*; Blackwell Publishing Ltd.: Hoboken, 2009, p 228-258.
- (127) Kros拉克ova, I.; Gunther, D. *J Anal Atom Spectrom* **2007**, *22*, 51-62.
- (128) Jackson, S. E. In *Mineralogical Association of Canada Short Course Series* Sylvester, P., Ed.; Mineralogical Association of Canada: Vancouver, Canada, 2008, pp 169-188.
- (129) Gunther, D.; Koch, J. In *Mineralogical Association of Canada Short Course Series* Sylvester, P., Ed.; Mineralogical Association of Canada: Vancouver, 2008, pp 19-34.
- (130) Fernandez, B.; Claverie, F.; Pecheyran, C.; Donard, O. F. X. *Trac-Trends Anal. Chem.* **2007**, *26*, 951-966.
- (131) Russo, R. E.; Mao, X. L.; Gonzalez, J. J.; Mao, S. S. *J Anal Atom Spectrom* **2002**, *17*, 1072-1075.
- (132) Shaheen, M. E.; Gagnon, J. E.; Fryer, B. J. *Spectrochimica Acta Part B: Atomic Spectroscopy* **2015**, *107*, 97-109.
- (133) Russo, R. E.; Mao, X. L.; Borisov, O. V.; Liu, H. C. *J Anal Atom Spectrom* **2000**, *15*, 1115-1120.
- (134) Kosler, J. In *Mineralogical Association of Canada Short Course Series* Sylvester, P., Ed.; Mineralogical Association of Canada: Vancouver, 2008, pp 79-92.
- (135) Fryer, B. J.; Jackson, S. E.; Longerich, H. P. *Can. Mineral.* **1995**, *33*, 303-312.
- (136) Kuhn, H.-R.; Gunther, D. *J Anal Atom Spectrom* **2004**, *19*, 1158-1164.
- (137) Mank, A. J. G.; Mason, P. R. D. *J Anal Atom Spectrom* **1999**, *14*, 1143-1153.
- (138) Horn, I.; Rudnick, R. L.; McDonough, W. F. *Chemical Geology* **2000**, *164*, 281-301.
- (139) Perkins, W. T.; Pearce, N. J. G.; Westgate, J. A. *Geostandard Newslett* **1997**, *21*, 175-190.
- (140) Bleiner, D. In *Mineralogical Association of Canada Short Course Series* Sylvester, P., Ed.; Mineralogical Association

of Canada: Vancouver, Canada, 2008, pp 35-52.

(141) Hirata, T.; Nesbitt, R. W. *Geochimica et Cosmochimica Acta* **1995**, 59, 2491-2500.

(142) Guillon, M.; Heinrich, C. A. *J Anal Atom Spectrom* **2007**, 22, 1488-1494.

(143) Pettke, T. In *Mineralogical Association of Canada Short Course Series* Sylvester, P., Ed.; Mineralogical Association of Canada: Vancouver, 2008, pp 189-218.

(144) Van Grieken, R.; Markowicz, A. *Handbook of X-Ray Spectrometry, Second Edition*; CRC Press, 2001.

(145) Haschke, M. *Laboratory Micro-X-Ray Fluorescence Spectroscopy: Instrumentation and Applications*; Springer International Publishing, 2014.

(146) Beckhoff, B.; Kanngieß, B.; Langhoff, N.; Wedell, R.; Wolff, H. *Handbook of Practical X-Ray Fluorescence Analysis*; Springer Berlin Heidelberg, 2007.

(147) Vergucht, E. W. E.; Vincze, L. p.; Vanhaecke, F. c.; Burghammer, M. c. U. *X-ray fluorescence imaging of biological samples on the (sub)micron scale using specialized sample environments*. Ghent University, Ghent, 2015.

(148) Garrevoet, J. U.; Vincze, L. p.; Vekemans, B. c. *Development of full-field and scanning X-ray fluorescence microspectroscopy*. Ghent University, Ghent, 2015.

(149) Cornea, A.; Conn, P. M. *Fluorescence Microscopy: Super-Resolution and other Novel Techniques*; Elsevier Science, 2014.

(150) Hell, S. W. *Science* **2007**, 316, 1153-1158.

(151) Huang, B.; Bates, M.; Zhuang, X. *Annu Rev Biochem* **2009**, 78, 993-1016.

(152) Schermelleh, L.; Heintzmann, R.; Leonhardt, H. *J Cell Biol* **2010**, 190, 165-175.

(153) Bendall, S. C.; Nolan, G. P.; Roederer, M.; Chattopadhyay, P. K. *Trends Immunol* **2012**, 33, 323-332.

Chapter 2 Aerosol transport systems

This chapter is based on a review paper titled 'Recent developments in the design of rapid response cells for Laser Ablation – Inductively Coupled Plasma – Mass Spectrometry and their impact on bioimaging applications', authored by Stijn J. M. Van Malderen, Amy J. Managh, Barry L. Sharp and Frank Vanhaecke, and a research article 'Development of a fast laser ablation-inductively coupled plasma-mass spectrometry cell for sub- μm scanning of layered materials', authored by Stijn J. M. Van Malderen, Johannes T. van Elteren, and Frank Vanhaecke.¹ S.V.M. is the first and principal author of both works.

Dispersion of the aerosol generated during transport of the aerosol can be reduced by optimizing the geometry of the inner volumes of the ablation cell and transport line through which the carrier gas and entrained particles flow. The assembly of a cell and transport line, designed to minimize the dispersion produced, is referred to hereinafter as a low-dispersion aerosol transport system (ATS). This chapter discusses, in detail, the development of low-dispersion ATSs for LA-ICP-MS. The reader is provided with an extensive description of the state-of-the-art and the design philosophy behind the engineering of these ATSs. The second part of this chapter describes the development and performance of an ATS comprising a tube-type ablation cell, in an analytical chamber equipped with a cryogenic module, and transport line with a co-axial mixing bulb, a device to mix in a make-up gas flow into the carrier gas stream.

2.1 Introduction

The figures of merit of the technique, relating to sample throughput, sensitivity, and spatial resolution, are largely dependent on the ability of the ablation setup to rapidly remove the aerosol from the ablation site to the ICP-MS instrument in a manner that minimizes the mass losses and the dispersion induced in the aerosol cloud. Compression of the aerosol cloud, introduced into the ICP and produced by a single laser shot, in a shorter time window effectively translates into a shorter, higher response peak. In an ideal situation, *i.e.* in the absence of particle losses and mass load effects, the integral of the signal peak remains constant, regardless of the dispersion induced. Given that detector dark noise is constant, and the relative contribution of Poisson process noise is reduced at higher count rates, higher transient responses provide better limits of detection. Current systems deployed in the field, with few exceptions, produce a signal peak in response to a single laser shot (sometimes referred to as washout time) of a duration (measure as peak width) in the region of multiple hundreds of millisecond to a second. Pulse repetition rates that exceed the level at which pulse response peaks are separated are often adopted, inducing an inevitable overlap of the pulse responses generated by sequential laser pulses. The extent of the negative effects thus exerted on the spatial resolution of the elemental map generated is governed by the washout time, *i.e.* the time required to flush the aerosol from the system, as well as by other experimental parameters, such as the ICP-MS dwell and settling time, the diameter of the laser beam and the speed at which this beam is traversing the sample surface. For example, the effective lateral resolution when scanning a surface at $20\ \mu\text{m s}^{-1}$ with a laser beam of $5\ \mu\text{m}$ in diameter, firing at 20 Hz, could amount to 20-40 μm . This shortcoming can be compensated for by operating at low sampling rates, effectively separating the pulse responses within one or more sequences of pulses², or by operating at high sampling rates and low scanning speeds, thereby mixing the dispersion of multiple overlapping signal peaks over a short scanning range.³ Both options lead to a decreased sample throughput and thus, increased costs. Sampling at high rates also consumes more sample material, which is often precious. Unless signal deconvolution is employed, the response from multiple ablation positions is hence convolved, and thus, the spatial response is nevertheless distorted in the scan direction.⁴ In a recent paper by van Elteren *et al.*, a novel experimental-modelling approach was presented, which allows to estimate the lateral resolution in line scan-based 2D imaging.⁵ When the responses of ablation positions are resolved in the time domain, the rate of information acquisition is limited to the reciprocal of the response duration. This feature produces a desire for low-dispersion systems for imaging applications. Recent developments have improved both the pulse response duration and transport efficiency. The sections below provide an overview of the latest developments in cell design, and related aspects, a section describing the experimental work performed, and the implications of the newfound capabilities for the applications of LA-ICP-MS within the biochemical, biological, and biomedical fields with a particular emphasis on high-resolution and 3D imaging.

For bulk analysis and isotope ratio experiments, signal damping, enacted through a signal smoothing devices or a collision gas in the collision cell, proves beneficial as it reduces the influence of LA-related sources of signal variability, improving precision.⁶ Signal smoothing devices, which (often unintentionally) act as a particle filter⁷, are preferred over the use of

gasses inside a collision/ reaction cell, as the former are able to buffer the influence of the matrix on the extent of mass discrimination. A design of a signal damping device, which allows to modulate the degree of smoothing during the experiment, was recently proposed by Pisonero *et al.*⁸

2.2 Rapid response ablation cells: the state-of-the-art

Over the past decades, a handful of research groups has invested in developing efficient ablation cell designs⁹⁻¹⁴ based on their understanding of the underlying physics and the fundamental studies and models describing them. It was identified early on that aerosol dispersion induced by the ablation cell is one of the important factors limiting the performance of LA-ICP-MS. The figure of merit preferred to characterize the aerosol dispersion is the pulse response duration. A condensed overview of compiled data on this metric for selected ablation cells is presented here below.

2.2.1 State-of-the-art figures of merit

In one early study, Leach and Hieftje¹³ explored the inverse relationship between the system volume and the peak width of pulse responses. The selection of the smallest cell and identification of the optimal He-Ar gas mixture composition yielded a transient signal of 85 ms at FWHM for ²³⁸U. Following the lead of Bogaerts *et al.*, computational fluid dynamics (CFD) modelling based on Reynolds-averaged or Favre-averaged Navier-Stokes models has taken a prominent role in the study and simulation of the aerosol and flow behaviour within the ablation cell and ICP¹⁵⁻¹⁸, *e.g.*, for visualizing the pressure gradients and kinetic energy (KE) of the flow in turbulent regions. The visualization of streamlines opens a pathway to improve design aspects of a virtual prototype of an ablation cell by an iterative *in silico* process, hence optimizing the FD behaviour *prior* to manufacturing. Lindner *et al.*¹¹, *e.g.*, reported on the FD behaviour of a non-contact, low-dispersion ‘High Efficiency Aerosol Dispersion’ (HEAD) cell, based on aerosol extraction *via* Venturi-driven pressure reduction using a realizable $k - \epsilon$ model. The simulation suggested that the aerosol dispersion of the last iteration of the design could be reduced to less than 10 ms.¹¹ The importance of a laminar flow regime, aerodynamically favourable outlets, and the relative position of the ablation site to the outlet have been demonstrated by Gurevich *et al.*⁹, who reported a chamber characterized by a signal peak with a FW0.1M of less than 100 ms. The proximity of the ablation site to the outlet was reported to be a critical factor in a cyclonic flux cell design by Monticelli *et al.*¹⁹, which delivers a transient peak down to 20 ms at FW0.1M, with a strong dependence on this distance. A more recent design by Wang *et al.*¹⁰ (Figure 10a) brought the dispersion down to a consistent 30 ms at the FW0.01M level. Gundlach-Graham *et al.*²⁰ reported that the latest iteration of the cell, which is based on the same working principle, has improved the dispersion to 9 ms at the FW0.01M level. An ablation cell reported by Van Malderen *et al.*²¹, developed in the context of this work and described in the next sections (Figure 10b), focuses on regions-of-interest smaller than 0.25 mm², and delivers transient peaks of 5 ms at the FW0.01M level. Douglas *et al.*²² also recently reported a low-dispersion interface, consisting of a two-volume ‘Sniffer’ cell (Figure 10c) and an integrated ‘Dual Concentric Injector’ (DCI), which produced signals of 5 ms at FW0.01M. The arrival of three new aerosol capture and transport interfaces characterized by a

pulse response of $< 10\text{ ms}$ at FW0.01M, demonstrates that considerable progress has been made within the past few years. Sensitivity improvements have been reported all-round, *e.g.*, the ‘sniffer’ cell was reported to yield an increase in absolute sensitivity (counts per mole) in the order of 5-10 fold compared to conventional setups. Low-dispersion cells are expected to find their way to all LA-ICP-MS and related applications, though their adoption may be hampered by the absence of affordable, fast, sensitive, simultaneous mass spectrometer systems.

2.2.2 Trends in instrumentation development

The following subsections present a general overview of the core concepts influencing the speed and efficiency of aerosol capture, transport, and detection, and their impact on ablation cell and transport conduit design.²³⁻²⁶ These developments and insight are stepping stones to further progress in ablation cell technology.

2.2.2.1 Cell design

The main strategy to minimize aerosol dispersion in the cell is confinement of the ejected particles, through gas flows, pressure, or cell walls, forming a controlled environment less than a few cm^3 in volume, and preventing further expansion of the ablation plume inside the cavity of the chamber, which would inevitably enlarge the initial dispersion of the aerosol. The residence time of particles in the cell is not governed exclusively by the cell volume and shape, it also depends on the local gas velocity, pressure, and flow regime, as well as the particle size distribution and initial dispersion and momentum of the aerosol in the cell.^{27,28} Confinement of the plume, either by gas flows or walls can simultaneously maintain a high local velocity of the carrier gas flow. In most designs this is dealt with by capturing the aerosol in a cup, *i.e.* a separate enclosure of small volume, or tube floating above the sample, whilst an XY(Z) stage or gantry is used to adjust the relative position of the fully-enclosed sample with respect to the aerosol capture component. Laser ablation designs can be subdivided based on the angle under which the carrier flow is extracting the aerosol plume. In the HEAD cell²⁹, the aerosol was extracted vertically using a He flow; an Ar auxiliary/sheath gas flow was added co-axially to the He flow just above the ablation site. CFD simulation suggested that the He carrier flow resides in a laminar flow regime and shows limited mixing with the Ar sheath flow. Major differences in relative speed or density of the core-annular laminar flow at fluid inlets or joints can limit intermixing of the flows.^{30,31} Autrique *et al.*^{15,32} explored the CFD behaviour of a cell designed for vertical extraction of the aerosol by a carrier gas, with an optional auxiliary flow, parallel to the sample, shielding the fused silica window and guiding the suspended aerosol into an outlet that is co-axial to the inlet of the auxiliary flow. Such design features are reflected in the non-contact ablation cell designed by Wang *et al.*¹⁰ (Figure 10a), in which the auxiliary flow inlet-outlet conduit is brought much closer to the sample surface, enabling a more efficient uptake of the particles in the carrier/sheath gas flow. Monticelli *et al.*¹⁹ designed a unique cell in which the plume is fully confined by a cyclonic gas flow. The drag/centrifugal force balance acting on the particles, results in a minimum curvature radius of the particle trajectories, estimated to be 0.1 mm under typical experimental conditions. Cell designs which introduce the aerosol directly into the transport line – sometimes referred to as a *tube cell design* – have been considered by Bleiner³³, Summerfield *et al.*³⁴ and Van Malderen *et al.* (Figure 10b) as a result of their envisaged

short washout times.^{21,33,34} The generated vapour cloud expands inside the transport line itself, and is constrained by the tube walls. The condensed aerosol is then carried with the carrier gas flow. A configuration reported by Douglas and Managh *et al.*²² (Figure 10c) captures the aerosol in a fluid-dynamic optimized capture cavity/cup, which uses walls, elevated pressure, and a combination of a co-axial and orthogonal flows to confine the plume expansion and transfer the aerosol into a small capillary.

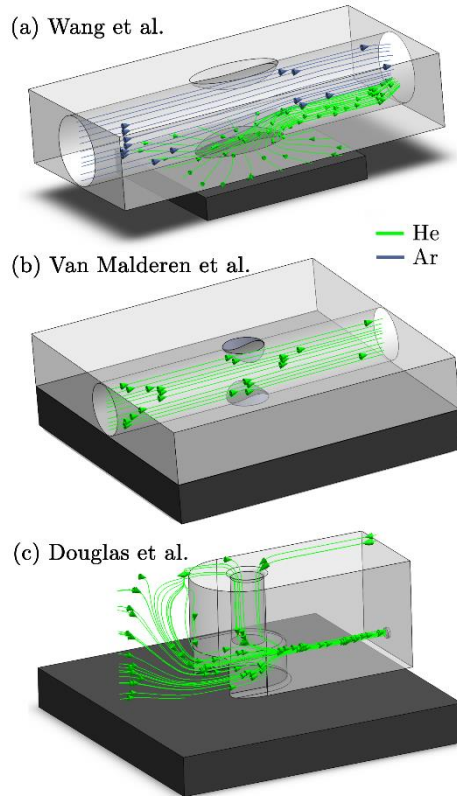


Figure 10 Overview of 3 of the third generation ablation cell designs. The dark gray block represents a $7.5 \times 7.5 \times 1 \text{ mm}$ sample. The scaling for each cell was performed separately, due to their size differences. The streamlines represent gas flows predicted by CFD.

Using a carrier flow parallel to the normal of the target surface (away from the surface) has been hypothesized to favor aerosol extraction, as the momentum of the carrier flow is opposite to the gravitational force and along the fastest ablation debris velocity component.^{35,36} Extraction using a flow with a momentum parallel to the surface, generally orthogonal to most particle trajectories, could potentially negate the dispersion of the aerosol plume along the normal of the target surface. The stopping power (mass density), shorter mean free path, lower ionization efficiency, and particle size-independent transport characteristics, favour Ar as a carrier gas over He. However, the high particle entrainment efficiency (limiting the surface condensate deposition), reduced plasma shielding (higher thermal diffusivity), higher breakdown

threshold at atmospheric pressures, and lower dynamic viscosity favour a He environment.^{28,37-41} These traits can be exploited to achieve narrow peak profiles most efficiently by conducting the ablation in He, with an option to utilize Ar as a sheath flow and make-up gas.¹³ A core concept of cell design is optimizing the design for flows in the laminar or laminar-turbulent transition regime, so as to avoid dispersion by turbulence, whilst enabling timely transport to limit the effect of diffusion on the aerosol dispersion. The initial dispersion of the aerosol, after thermalization –the process of particle-buffer gas interaction towards a thermal equilibrium–, is determined in part by the position, the velocity and angular distributions of velocity vectors of particles at ejection, *e.g.*, in He, particle ejection takes places at angles close to the normal.¹³ The evolution of the velocity component of the ejected particles on a *ps* – *μs* timescale depends on, among other factors, buffer gas properties, and the KE and development of the laser-induced shock wave (SW), which in turn is influenced by all the aforementioned parameters.^{35,42} Ar is the preferred buffer gas to shield walls from particle impact due to its ability to decelerate the contact front faster, compared to He, as a result of its higher collision frequency –Ar has a relatively larger collisional cross-section (dipole moment, polarizability), and mass.^{9,42} The stopping distance of the particles is also a function of the environment pressure.⁴² The stopping power (Chapter 1) is a function of time and space, as the collision frequency varies with the thermalized KE. When the stopping distance of particles falls short of the cell walls, the reflection of the SW – the SW density front edge outruns the contact front and bulk of ejected particles – may compress or disperse the aerosol cloud, as has been observed in laser-induced breakdown spectroscopy⁴³⁻⁴⁸. As such, the expansion of the condensing plume can also be curbed and restricted by walls, and the sample itself (*cf.* Mach reflection of the SW).^{49,50} Compression of the laser-induced plasma may create a hotter, denser plasma, resulting in an enhanced photon emission intensity.⁴³ Shadowgraphy has been used to study the SW and particle ejection phenomena in detail, and has, among many other aspects, confirmed that the blast wave follows a behaviour close to the Sedov-Taylor solution.⁵¹ In short, the initial dispersion is guided by the interplay of many physical processes, governed by environmental conditions, and laser beam and sample characteristics. The sample characteristics, aerosol particle size, and phase distribution are linked, as the condensational growth conditions in the supersaturated vapour shifts with the thermal conductivity of the sweep gas, and the spatial, size and phase distribution of condensation nuclei (*i.e.* ejected particles), which critically depend on the sample structure, composition, morphology and mechanical properties. This relationship can be compounded by the uptake of particles ejected by exfoliation and spallation, reablation of deposited material, and melt splashing/ droplet expulsion (by the recoil SW).^{37,52} When the pulse length exceeds the local thermal relaxation time (sub-*ps* range) of the sample material, zone heating arises. Extensive melting can impact the phase distribution of the ejecta, once again, changing the ablation cell washout characteristics. An additional flow in the ablation cell design, or a carrier flow along the normal of the sample can promote the uptake of these particles.¹⁰ Particle growth can also be achieved through aggregation (agglomeration) and coalescence of particles. The particle size distribution and particle structure should be highlighted as an important aspect, as the particle transport mechanics critically depend on the slip and drag coefficients of the particles, and therefore the aerosol dispersion will be affected. Furthermore, the degree of elemental fractionation is governed to a large extent by the

incomplete vaporization, atomization and ionization of mesoscopic particulates $> 200 - 500 \text{ nm}$ in size, in combination with non-stoichiometric sampling (differential partitioning results in a particle-size dependent elemental composition), which is natively linked to the laser unit, ICP-MS unit and target characteristics.⁵³⁻⁶⁰ A recent paper by Zhang *et al.*⁶¹ provides a comprehensive overview of elemental fractionation and matrix effects. A description of this phenomenon can also be found in Chapter 1. The particle size distribution can be acquired experimentally by, *e.g.*, optical laser scattering, differential mobility analysis or gravimetric determination of the yield in particle impactors.

Turbulence in aerosol transport. Once leaving the ablation cell, the aerosol is conducted to the ICP-MS instrument through flexible polymer tubing, which is typically a few mm in internal diameter and can be up to several m in length. This conduit has long been recognized as a potential source of material loss and a contributor to aerosol dispersion.⁶² Reynolds numbers $Re = v_{mean} D / \nu$ (with v_{mean} the mean fluid velocity, D the hydraulic diameter, and ν the kinematic viscosity) easily allow identification of the flow regime. Gas flows in the tubing are generally within the laminar flow regime ($Re < 2100$) under typical gas flow rates, and thus, follow a parabolic velocity profile⁴⁰ $v(r) = v_{max}(1 - r^2/R^2)$ with v the velocity at distance r of the center axis of a cylinder of radius R for subsonic velocities ($v_{max} < 0.2v_{sound}$). This Hagen-Poiseuille flow creates temporal axial dispersion through Taylor-Aris dispersion (Figure 11c) and diffusion. On the other hand, turbulent flows in a conduit are controlled by turbulent diffusion, rather than shear forces, which gives rise to erratic inter-layer mixing, and an average velocity flow profile uniform over the entire cross-section, with the exception of thin boundary layers near the conduit walls.³¹ Early experimental studies by Bleiner and Günther²⁷, and Leach and Hieftje¹³, demonstrated that dispersion increases with increasing transport volume for single shot LA-ICP-MS. This is a function of the tube diameter as well as its length, since the slower gas velocity in wider tubes allows for longer diffusion time. In a study by Summerfield *et al.*³⁴ a *tube cell design* was used to eliminate chamber effects and enable a focussed study of transport characteristics. Washout time was found to increase with increasing tubing length¹³, with the inclusion of valves, and in particular with the presence of bends. Sharp bends in the tubing will disrupt the flow dynamics because the outer radius flow experiences a higher velocity than inner radius, inducing swirling or rotation as a result of shear stress. Inertial deposition, as well as gravitational settling, in conduits of small radius has been shown to be particle-size dependent, inducing additional elemental fractionation.^{7,63,64} The flow path in early setups was intersected by a Y- or T-junction, for the addition of an Ar make-up gas. Computational modelling by Autrique *et al.*¹⁵ highlighted this junction as a major source of turbulence in the flow (Figure 11a).

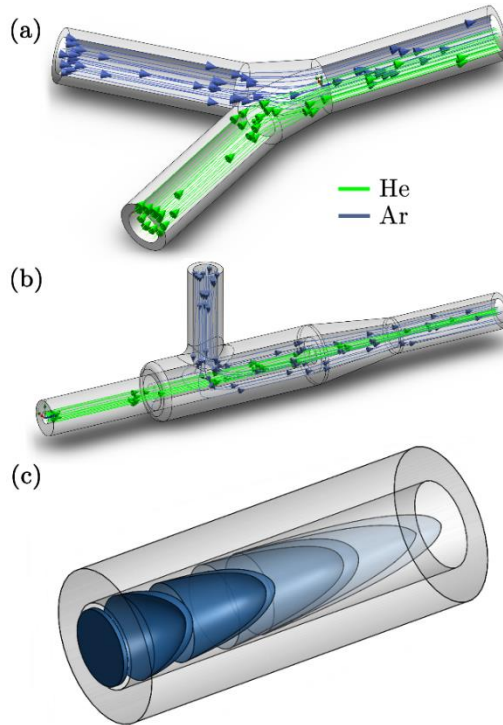


Figure 11 Schematic and CFD simulation to demonstrate processes that drive aerosol dispersion. The gas mixing processes in a Y- connector piece (a) and a coaxial mixing bulb (b) control downstream eddy formation and gas composition. The Taylor dispersion process acting upon an aerosol cloud injected uniformly across the cross-section, induced by the between-layer velocity differences, is displayed in (c)

In the CFD simulation displayed in Figure 11a, it can be observed that the introduction of a make-up gas in a Y-connection pushed the carrier gas towards the wall of the tubing, which induced surface friction and the formation of eddies near to the wall region. Furthermore, divergences in the tubing, for instance where the tubing connected onto the Y-junction, and later onto the torch, produced a clear turbulent flow pattern. Turbulence and eddy formation can be observed when the inner diameter of the conduit is changed or if dead volumes are present.⁴⁹ These fluid dynamic instabilities may trap smaller particles, increasing the width of the transient peak. Similar problems are present in GC and (HP)LC. The issue was addressed by coaxial mixing bulbs^{27,49,65} (Figure 11b), where the make-up gas was added on-axis to the carrier gas flow, through a concentric outer tube. The CFD simulations thus stimulated the deployment of a laminar flow gas connector in the field. Several groups have reported designs that avoid the use of a gas connector. These systems are exceptionally fast and all produce signals of 30 ms FW0.01M or considerably below.^{20,21} In the *tube cell designs*, ablation takes place through an opening in the transport tubing, with material directed orthogonally into the laminar carrier gas stream. In Van Malderen's cell, this tubing also passed through, and effectively became, the inner injector of the ICP torch. In this way, the ablation cell, transport conduit and ICP torch could be considered as an integrated device, and divergences in conduit diameter were completely eliminated. The DCI interface²² used an unbroken fused silica conduit, which passed

through the injector of the ICP torch, to transport the aerosol from the ablation cell directly into the plasma. The conduit could be extended up to 12 mm beyond the injector, past the turbulent region at the base of the plasma. This was thought to help keep material on axis with the orifices in the cones, which may have contributed to an improvement in absolute sensitivity, as well as speed. From the above studies, it appears that optimum transport characteristics can be achieved through the use of a short, straight and unbroken conduit, of narrow and constant diameter. Optimally, the conduit would be integrated into both the cell and the ICP torch. However, the practicality of some lab geometries may understandably restrict the implementation of these ideal conditions, particularly with regards to minimising tubing lengths and the avoidance of bends. It may be that optimum performance would be best achieved by better integration of LA with ICP-MS instrumentation.

2.2.2.2 *In-torch ablation*

The concept of ablating material within the ICP torch (in proximity to the injector outlet) was first reported by Liu and Horlick⁶⁶, in conjunction with optical emission spectrometry (OES), and was later adapted by Tanner and Günther for use with mass spectrometry (MS).⁶⁷⁻⁷⁰ In the MS arrangement, the laser beam was focussed through a small hole in the top of the torch box and onto the sample, which was mounted behind the injector on a small holder. The bulk of the signal occurred within the first 1 – 2 ms, with the remainder stretching out over ~30 ms. The arrangement has very limited practical applicability due to the restrictions on sample size and sample movement placed by the dimensions of the torch, and is limited to high melting point samples, due to the proximity of the target to the plasma. In-torch ablation is therefore mentioned in this work purely as a theoretical benchmark for the characterisation of new interfaces. It should be noted that in this configuration the aerosol particles still traverse the plasma, hence, the particles are transported over a distance of a few cm in atmospheric pressures before being extracted. As such, in practice, ablated particulates may become entrained in the turbulent flows at the base of the plasma within the *in-torch* design, thus methods that keep material aligned with the central channel of the plasma, or a sample configuration in closer proximity to the extraction site may eventually produce higher performance.¹⁶

2.2.2.3 *Ablation yield – transport efficiency*

The ultimate sensitivity of the technique is driven by the ablation yield, the overall efficiency of the entrainment of ejected particles and their transport from the ablation site to the mass analyzer, and the ionization, transmission and detection efficiencies. The laser interaction and particle formation processes, which affect the mobility of the aerosol, are profoundly influenced by the sample composition. In a study by O'Connor *et al.*⁷¹, the addition of a laser radiation absorbing compound (vanillic acid, pyrazinoic acid or nicotinic acid) to a sediment improved the ablation efficiency, even under soft ablation conditions. In MALDI-IMS, the addition of a laser radiation absorbing (and ionizing) matrix is part of the standard sample preparation procedure. Particle losses can occur through gravitational settling, non-stoichiometric particle entrainment of μm -sized particles, diffusional losses – disproportionately affecting nm-sized particles and gaseous phases –, aerosol condensation losses, carrier gas leaks, and inertial deposition on walls in the cell geometry obstructing the carrier flow.^{32,72} Selective particle losses in size-segregation

processes will change the particle size distribution, inducing elemental fractionation, as demonstrated by Koch *et al.*⁶² and Outridge *et al.*⁷³. The cell geometry has limited influence on the aerosol transport efficiency, under the conditions that no *dead volumes* of low local flow velocity in which particles can settle, are present, and particle deposition on the window and walls of the cell and tubing is negligible.^{32,74} Avoiding dead volumes within the ablation cell is readily achieved by adopting a fluid-dynamic optimized design – eliminating sharp angles and corners which may trap particles – and positioning the inlets such as to cover the entire volume to be flushed.^{27,28,75} Any trapped particles will be released slowly over time, resulting in broader response peaks or signal tailing, and/or higher background levels. An impact of debris on the wall may result in spattering, sputtering, adsorption or impingement of particles. Particle deposition on the cell walls – and the accompanied loss of material – can be mitigated by expanding the cell diameter¹³, increasing the volume of gas between the ablation site and cell walls to buffer the particle velocity, or by decreasing the initial dispersion of the aerosol in the cell by increasing the stopping power of the gas (or fluid), *e.g.*, by increasing the environmental pressure. A complete development of the ‘mushroom cloud’ plume⁷⁶ is not a necessary condition for achieving complete sample transport. Direct effects of the deposition processes (which are accompanied by non-stoichiometric particle losses) are a decline of the aerosol transport efficiency, and longer washout times as particles are detaching or being sputtered from the surface, with which they impacted, at a slower pace relative to the flush rate of the cell. Effects such as erosion may occur at high collision frequencies, as well as cross-contamination to subsequent ablation positions and samples. Transport efficiency in LA-ICP-MS using ns-lasers were reported in early studies^{27,72,77} to be $\geq 40\%$ for He as a carrier gas, as determined by optical particle counting (OPC) and chemical analysis of filtered particles. More recently, Garcia *et al.*³² reported efficiencies $> 80 - 90\%$ for fs lasers. Monticelli *et al.* reported a near to 100% recovery for the cyclonic design in combination with a fs laser unit.¹⁹ The efficiency of the particle transport process is difficult to determine with good accuracy.⁷ Back condensation of the vapour cloud on the target surface and losses in the impactor have not been taken into account in these studies. Recently, Niehaus *et al.*⁷⁸ reported on particle transport characteristics for particles generated by ablation of a gelatine section, a matrix that compares well to a biological matrix. A variation of the transport tube length was not found to increase the loss of particles. Based on OPC measurements, the same study reported, a positive correlation between the fluence and the portion of μm -sized particles in the particle size distribution, as well as between the fluence and ablation yield – this linear relationship quickly levels off at high fluence levels. The laser beam wavelength and energy density can have a profound influence on the ablation yield in biological matrices. The sample-specific characteristics, *e.g.*, the mass ratio of extracellular matrix (*e.g.*, collagen) to the total tissue, mediate the ablation threshold, attenuation length, scattering properties, and thermal conductivity of the target which impact the surface temperature profile, mechanical response, and ejected particle size and phase during ablation. Morphology of the sample, *e.g.*, the presence of porosities or fractures, and surface roughness/reflectivity will also influence the ablation yield. In the UV region, photochemical processes such as electron excitation (one- and multi-photon processes) can directly break chemical bonds, *e.g.*, covalent and ionic bonds and crosslinks. Thermal processes by vibrational excitation on the other hand will induce melting and evaporation at fluence levels

near or below the ablation threshold. At higher fluence levels, the rapid energy transfer can induce vaporization by phase explosion, with the ejection of μm -sized particles and spallation of fragments, as described in higher detail in the previous chapter (Section 1.1.3.2.3).⁷⁹

2.2.2.4 Mass spectrometers: suitability for LA

Whilst improving the washout time has several advantages, many of the current generation ICP-MS instruments were not designed to meet the challenges of fast transient analysis. A detailed analysis of common mass analysers and detectors used in the field of ICP-MS and their limitations for measuring short transient signals was previously published by Tanner *et al.*⁸⁰ Primary considerations include data acquisition and readout speed, minimization of dead time in the duty cycle, and maintenance of plasma stability on the millisecond time scale under highly variable mass load. The capability to detect multiple nuclides (pseudo-) simultaneously is important for isotope ratio determination studies, LA imaging, nanoparticle analysis with NPs consisting of ≥ 2 elements, and standardization approaches, but we will first consider the hardware specifications required for single isotope monitoring. The importance of high data acquisition speeds was recognized from the early *in-torch* experiments (as discussed above), where a quadrupole mass spectrometer was used to profile transient peaks of $\sim 4\text{ ms}$ FWHM.⁶⁷ In the original study, the time resolution of the mass spectrometer was limited to 0.5 ms (the minimum dwell time of the instrument), which recorded a log-normal peak shape, with 8 data points within the bulk of the peak. In a subsequent publication, the standard detection system was bypassed, and a digital oscilloscope recorded the signal from the analog detection stage of the mass spectrometer at $20\text{ }\mu\text{s}$ intervals.⁶⁹ The improved time resolution revealed a finer, bimodal peak structure, which comprised two overlapping Gaussian functions. Several other research groups have used plug-in devices to upgrade the data acquisition characteristics of commercial quadrupole⁸¹⁻⁸³ (Q), sector-field⁸⁴ (SF) and time-of-flight⁸⁵ (TOF) mass spectrometers. In recent years, ICP-MS instrument manufacturers have also begun to take note of the importance of time resolution, in reaction to the development of single particle analysis. This is reflected in recent product launches of ICP-quadrupole mass spectrometers by, *e.g.*, Perkin Elmer (NexION® 350, dwell time $10\text{ }\mu\text{s}$)⁸⁶, Agilent Technologies® (Agilent® 9700, $100\text{ }\mu\text{s}$ dwell time)⁸⁷, Thermo Scientific™ (iCAP Q™, $100\text{ }\mu\text{s}$ dwell time)⁸⁸ and AnalytikJena® (PlasmaQuant® MS, $50\text{ }\mu\text{s}$ dwell time)⁸⁹. Once acquisition speed has been improved, the existence of 'blind time' in the duty cycle, where no signal is measured, becomes apparent. Blind times of up to 0.9 ms have been reported for ICP-Q-MS⁹⁰ and $3 - 4\text{ ms}$ for electrostatic mode scanning in ICP-SF-MS instruments⁹¹. The reported losses predominantly result from the resetting of electronics after each acquisition segment, in contrast to dead time, *i.e.* time during which signal loss occurs as a result of electronic unawareness to ion detection whilst processing the previous pulse. The blind time may disproportionately affect fast transient signals compared to their slower counterparts. The extent of the data loss is dependent on the position of the peak within the duty cycle, which is variable and difficult to predict, but must be accounted for during data processing.⁹¹ Data losses and the effects of undersampling the transient signal are even more severe when simultaneous analysis of multiple elements/isotopes is required, especially as laser firing times are desynchronized from the dwell interval frequency. Quadrupole and single detector sector-field instruments are fundamentally restricted in their ability to perform

this type of analysis because they detect elements sequentially. In other words, whilst one isotope is measured, data for the other elements/isotopes is not acquired, limiting sensitivity and precision. Furthermore, the settling times, *i.e.*, the time required for the motion and stabilization of the ion beam whilst jumping to a new m/q ratio, can be substantial (1-500 ms), especially after a magnet jump in sequential SF instruments. Multi-collector ICP-MS enables simultaneous measurement of elements of similar mass with high sensitivity.⁹² Craig *et al.* recently demonstrated the use of multi-collector ICP-MS with the DCI/Sniffer interface to measure uranium isotope ratios in sub-micron particles.⁹³ However, the use of slow Faraday detectors in parallel with ion counters placed restrictions on the minimum time resolution that could be achieved. Furthermore, using the mixed detector array for transient analysis was reported to introduce a form of spectral skew, which was more pronounced for the signals acquired using the DCI/Sniffer interface compared to those from a much slower cell.⁹³ An alternative option is ICP-TOF-MS, which provides pseudo-simultaneous analysis (ions are sampled simultaneously but read-out sequentially) of a large part of the full mass range, with potentially fast data acquisition and readout. The feasibility of coupling an ICP to a TOF-MS was demonstrated as early as 1993⁹⁴, but these instruments are not as popular as ICP-Q-MS or ICP-SF-MS. ICP-TOF-MS has yet to reach the sensitivity of ICP-Q/SF-MS, however, improved S/N ratios provided by state-of-the-art LA cells, improved transmission efficiencies, and higher duty cycles may compensate for this limitation. In 2008, Tanner and Günther combined an ICP generator and interface from a quadrupole instrument with a commercial TOF-MS to measure Zn/Cu ratios in the context of *in-torch* LA.⁷⁰ The prototype system had five orders of magnitude poorer sensitivity compared to commercial ICP-Q-MS, but provided 30 μ s time resolution. Based on this work a commercial instrument, 'icpTOF', was developed by TOFWERK (Thun, Switzerland), which has been applied to other fast-transient applications.⁹⁵ The 'icpTOF' data processing hardware can output mass spectra with 41216 mass channels in the mass range ($m/z = 2-257$) and mass resolving power $R = M/\Delta M \approx 3000$ at frequencies of up to 667 Hz (1.5 ms/full elemental mass spectrum).⁹⁶ Another commercial ICP-TOF-MS instrument, which has been coupled to a low-dispersion ablation cell⁹⁷ is the 'CyTOF' instrument by Fluidigm (South San Francisco, CA, USA). Fluidigm's instruments provide a time resolution of 13 μ s and sensitivities approaching those of ICP-SF-MS, but at the expense of reduced mass resolving power $R \approx 900-1000$ and a restricted mass range ($m/z = 75-209$).⁹⁷ Quadrupoles or variants thereof are implemented in ICP-TOF-MS as a multi-notch mass filter to remove abundant plasma background ions and prevent detector saturation, or as a high-pass or low-pass filter to speed up data acquisition. GBC Scientific Equipment Pty Ltd (Melbourne, Victoria, Australia) offers the OptiMass 9500, a full range ($m/z = 1-260$) ICP-TOF-MS, with a spectral generation rate of 100 Hz and mass resolving power $R \approx 1500$ at mid mass range.⁹⁸ ICP – Mattauch-Herzog geometry SF – MS and distance-of-flight array detectors currently lack the S/N ratio to produce meaningful data at the time-resolution that would be required for pulse-to-pulse separation.^{96,99} The linear dynamic range of the detectors in MS spans between 6 and 10 orders of magnitude. This might be of concern as the temporal compression of the signal produces substantial increases in relative sensitivity [$\text{counts s}^{-1} \text{fmol}^{-1}$], even in the absence of increases in absolute sensitivity [counts fmol^{-1}], which can cause detector saturation at large beam waist sizes or high analyte concentrations. In summary, there is no 'ideal' ICP-MS

instrument type currently available that provides simultaneous multi-element detection across the full elemental mass range, with fast data readout, minimal blind time, wide linear dynamic detection range, high mass resolution, and high sensitivity. The increasing trend towards fast transient ICP-MS, not only for laser ablation imaging, but also for the single particle characterization promotes the adoption of low-dispersion cells.

Multiparametric analysis of biomarkers is an emerging area where the mass spectrometer used can play a deciding role. Biomarkers can be detected indirectly in cells or tissue sections through the application of metal-conjugated antibodies, which bind to their respective antigens on the cell surface. A range of metal-conjugated antibodies has been described in the literature^{100,101}, many of which are now commercially available¹⁰². By the use of multiple antibodies, each labeled with a different metal or even a specific nuclide of a metal, simultaneous detection of multiple proteins, phenotype and function are possible using LA-ICP-MS. In an early example of this, Hutchinson *et al.* used Eu- and Ni-coupled antibodies to image amyloid precursor protein and $\alpha\beta$ peptide in histological sections from a mouse model of Alzheimer's disease.¹⁰³ Other studies have imaged metal-conjugated antibodies in isolated cells¹⁰⁴, Western blot immunoassays¹⁰¹, protein microarrays¹⁰⁵, and sections of breast cancer tissue¹⁰⁶⁻¹⁰⁸. The advantages of using low-dispersion ablation cells for biomarker analysis were demonstrated by Wang and co-workers, as part of the first publication describing the performance of their tube cell¹⁰. The cell was coupled to a ICP-SF-MS instrument to image the distribution of ¹⁶⁵Ho-tagged anti-human epidermal growth factor 2 (HER2) antibody in breast cancer tissue. A very high lateral resolution, of $\sim 1 \times 1 \mu\text{m}^2$, enabled precise determination of HER2 on individual cell membranes, which was described as a crucial criterion for morphological assessment in cancer diagnostics. Importantly, superior sensitivity was observed for LA-ICP-MS using the tube cell compared to images of the same section analysed using micro-XRF with the same lateral resolution. Due to the limitations of ICP-SF-MS instruments for fast transient analysis (described above) only a single label was used in this experiment. However, in a later paper, the tube cell was coupled to a pseudo-simultaneous detecting ICP-TOF-MS unit, which enabled multiplexed analysis⁹⁷. Thirty-two proteins were simultaneously measured, which enabled identification of specific cell sub-populations within a 0.5 mm^2 area of breast cancer tissue and highlighted tumor heterogeneity. The $1 \times 1 \mu\text{m}$ resolution was sufficient to clearly distinguish the nuclei, plasma membranes and stromal compartments of individual cells on the basis of their protein expression. It is noted that the CyTOF equipment used by Giesen *et al.* has been targeted towards workers in the clinical field, with many of the resulting publications based around flow cytometry appearing in journals relevant to the clinical field.

2.2.3 Fundamental considerations

2.2.3.1 Peak profile shape

The shape of a signal peak arising from the response to a single shot is an important parameter in the performance of an LA-ICP-MS system and is therefore often used to benchmark these systems in terms of aerosol dispersion. Attempts to model the peak profile have supported our understanding of the aerosol entrainment/elution/transport processes, thus allowing the ablation cell design to be adapted in such a way that the limiting physical processes are

addressed. The single pulse response (SPR) can be constructed as a convolution of the aerosol particle release function and the setup transfer function (STF), which can be considered as the system response function. In 2001, Bleiner *et al.*^{27,40} reported on a theoretical model for the SPR in an ideal mixing system (Figure 12), by modeling the dispersion and diffusion in the system during particle transport.

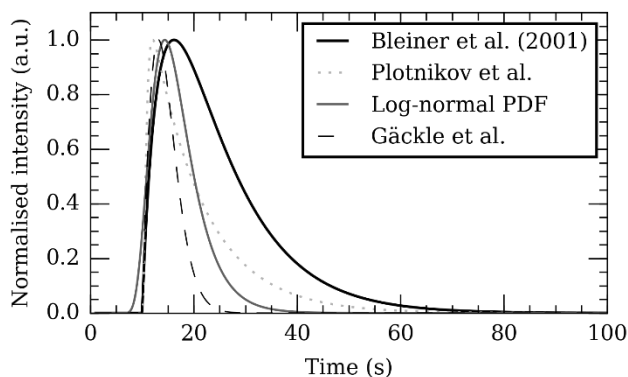


Figure 12 Theoretical peak profile shape models proposed in literature. The models were provided with matching initial parameters: $v_{g,c} = 10 \text{ ml s}^{-1}$, $V = 100 \text{ ml}$, $t_0 = 10 \text{ s}$. The log-normal probability density function (PDF) was added as a reference to its shape.

In a first approximation, a linear relationship can be established between the cell-induced dispersion and its volume.^{27,109} Accounting for a non-steady velocity profile in the transport line – assuming a laminar flow – an aerosol delivery function at time t was derived^{27,110}:

$$I(t) = I_0 \left(1 - \frac{t_0}{t}\right) \exp\left(-\frac{v_{g,c}(t - t_0)}{V_{cell}}\right) h(t - t_0) \quad \text{Equation 16}$$

With $v_{g,c}$ the carrier gas flow rate, I_0 an analyte-specific response factor proportional to the integrated response – and by extension the concentration of the analyte –, V_{cell} the volume of the cell, t_0 the minimum particle transit time through the system, and h a Heaviside step function $h(t - t_0) = \{0, t < t_0; 1, t \geq t_0\}$. The exponential decay of the signal has been observed widely, and appears in the factor relating to the rate of aerosol evacuation of the function.¹¹⁰⁻¹¹² Plotnikov *et al.*¹¹³ expanded upon this model, by introducing an additional exponential parameter:

$$I(t) = I_0 \left(1 - \exp\left(\frac{t - t_0}{k}\right)\right)^p \exp\left(-\frac{v_{g,c}(t - t_0)}{V_{cell}}\right) h(t - t_0) \quad \text{Equation 17}$$

With k a parameter introduced to describe the aerodynamic properties of the cell. The model (Figure 12) observes mass conservation, and is self-consistent in this aspect, and was provided a physical meaning by Bleiner *et al.*⁴⁰. An alternate model, building on Bleiner's model, was suggested by Gäckle *et al.*^{114,115}, in which the particle density at the margins of the cross-section of the conduit converges to the initial analyte density in the cell (under ideal mixing conditions). A total dispersion function was derived:

$$ID(t) = \left(1 - \frac{t_0}{t}\right) \exp\left(-\frac{v_{g,c}}{V_{cell}}\left(t - t_0 - t_0 \ln\left\{\frac{t}{t_0}\right\}\right)\right) h(t - t_0) \quad \text{Equation 18}$$

The model also attempts to account for the extraction yield by the interface by limiting the observed signal to the region of the cross-section around the center axis.¹¹⁴ Plotnikov *et al.*¹¹⁶ and Bleiner *et al.*⁴⁰ have argued that the model does not satisfy continuity, as the integrated area under the profile depends on transport parameters. Bleiner *et al.*⁴⁰ proposed a CFD model based on the model by Plotnikov *et al.* that accounts for the influence of gas characteristics and particle size distribution. The overall aerosol dispersion will depend on the particle size distribution, which is closely related to the ablation process itself, due to size-dependent segregation during transport.^{117,118} Despite efforts to derive all physical parameters relevant to the kernel, describing and predicting the SPR, current models remain incomplete as some processes have been ignored or disregarded, *e.g.*, ionization¹⁸, diffusion and turbulence in the plasma¹⁶, the geometry of the ablation damage, temporal changes in ablation yield linked to target composition variability, and the initial dispersion of the aerosol (a homogenous distribution of aerosol density within the cell has been assumed). Some of these effects can be accounted for in a straightforward manner by descriptive functions convolved with the I_0 profile, but other require an overhaul of the model. For the fastest cells^{22,119}, a Gaussian-like peak profile has been reported, in which the front dispersion has become comparable to the trailing dispersion. A fully symmetrical profile would be expected only if radial diffusion and/or pressure driven gas flow expansion were major contributors to dispersion and turbulence-, ablation-, and velocity gradient- induced dispersion were of minor influence. Empirically derived STF, *e.g.*, a linear combination of log-normal distributions¹¹⁹, can also model the peak profile. Multiple studies have reported a bimodal peak profile shape.^{9,22,69} It has been hypothesized that particle-size segregation in turbulent streamlines forms the basis of the phenomena. As noted by Russo *et al.*¹²⁰, the particle distribution created by fs-lasers trends towards smaller particles, and a narrower profile, which partly eliminates size-segregation based on differences in the relative velocity, originating from the link between particle mass, mean-free path length and hydrodynamic cross-section. Additional information on laser ablation models can be found in the literature.^{50,121} Deconvolution of the transient response in the time domain can improve the lateral or depth resolution by resolving the signal response for each laser shot, *i.e.* reversing the image blurring effects that result from pulse mixing. The deconvolution can be readily achieved through regularized or parameterized multivariate regression¹¹³, or a non-affine transformation¹¹⁰. There is, however, a trade-off between pulse response overlap and lateral resolution/accuracy/contrast ratio in the elemental image. It should be noted that a higher repetition rate will not necessarily increase the lateral resolution, as the S/N ratio of deconvolution algorithms aggravates with the overlap and number of parameters involved in the combined SPF. Within this approach, the peak profile model is used as a kernel function for the deconvolution. The signal response is modelled as a superimposition of SPR functions, *e.g.*, implemented as a convolution of the SPR with the Dirac δ function.¹¹⁰ Bleiner *et al.*¹¹⁰, *e.g.*, demonstrated data deconvolution through factorization. Plotnikov *et al.*¹¹³ proposed an algorithm to reconstruct the response peak for every pulse based on multivariate regression and regularization of the detector response, which was modelled as a superimposition of the SPR (fitted towards the experimental spectrum by the iterative Levenberg–Marquardt

algorithm). Deconvolution approaches allow pixel-by-pixel scanning method to be conducted at higher repetition rates and scanning speeds, without compromising on spatial resolution.

2.2.3.2 Ablation approaches

The evolution towards low-dispersion cell designs enabled single-shot analysis and created new opportunities for alternative scanning methods that improve imaging speed and resolution. Until recently, the approach to image biological samples was restricted to raster scanning, *i.e.* the laser is scanned across the sample surface in a rectilinear line pattern, at speeds comparable to the beam waist size, and fired continuously at a repetition rate that exceeds the width of a single pulse peak profile by a factor 2 or higher. The response, after clipping the temporal response in the areas when the laser is not firing, and restructuring the response for every line chronologically, can be projected into a 2D image for every nuclide. The time-resolved response is however decoupled or distorted from the spatial coordinates corresponding to the response, as the aerosol dispersion is the determining factor in the distortion of downstream sampling positions and in the trade-off between resolution and scanning speed. The offset between the ablation positions and the transient detector can be compensated for by cross-referencing the time traces from the laser and ICP-MS unit *via* software, however, this ultimately does not improve lateral resolution. A higher resolution can be obtained whilst scanning and firing slower, however, the resolution will never be better than the spot size. A 2D or 3D nuclide distribution map can also be derived by resolving the response of multiple ablation positions in the time domain.¹¹⁹ In other words, the aerosol is allowed to washout, with the integrated pulse response converted into the value of a single pixel, before an adjacent, non-overlapping location is sampled. This strategy generates spatially resolved pixel responses, which provides additional spatial resolution, but is only feasible when low-dispersion ablation cells are employed, due to the inherent time constraints associated with the finite washout after each pulse.

An early example of a 3D imaging approach in combination with resolved pixel acquisition *via* LA-ICP-MS was presented in a study by Peng *et al.*¹²² on the near-surface U and C accumulation in a basaltic clast sample. They proposed sampling in a pattern of overlaid rectangular grids of ablation points, in which the layers were sequentially ablated. The use of a standard ablation cell resulted in a measurement time of 4-7 h per layer. The quantification protocol was based on normalization of the summed concentration of 8 major elements to a known stable value of 51.8 ± 1.1 %wt, and forwarding the normalization factor to the signal intensity of all other elements. Van Elteren *et al.*² proposed a similar approach for 3D mapping of corroded glass: drilling a set of craters in a grid sequentially, whilst isolating every pulse response. Quantification was achieved by normalizing the sum of all oxides of all major and minor elements to 100%wt, an approach that was initially proposed for bulk analysis without internal standardization (IS)¹²³. Chirinos *et al.*¹²⁴ adopted an identical drilling pattern. When every pulse can be isolated and integrated, the peak area can be normalized by internal standardization. Alternatively, when a simultaneous full-elemental mass spectrum MS unit is used, individual channels can be normalized to a factor assumed to be proportional to total mass ablated, such as the sum of ion counts of populated channels, or the sum of all molar concentrations, as proposed by Leach *et al.*¹²⁵ Recently, this was demonstrated by Gundlach-Graham *et al.*²⁰ and

Marcel Burger *et al.*¹²⁶, in a study where the sum of the oxide forms of every detected element within their geological samples was utilized in the normalization of the results. The quantification of nuclide concentrations in multi-domain or multi-phase samples remains challenging for the 100% mass normalization procedure as the elemental sensitivities are ablation rate, and therefore, chemical-structure dependent. If a calibration standard is available for each domain, domain-boundaries would still prove challenging due to non-linear ablation effects. Although instability in the laser energy density is still present, the current generation of deep-UV ns- or fs- lasers has a laser energy density stability to within ~1%, along with optical auto-focusing during ablation, which helps to minimize focus drift).

Approaches based on scanning a 3D grid compare favourably to drilling the grid, as the steady-state fractionation in line scanning can be compensated for by tuning the ICP-MS unit, whilst fractionation during drilling is a transient phenomenon, and can be corrected for mathematically.¹²⁷ The effects of the crater aspect ratio on fractionation can be alleviated by alternative ablation approaches, *e.g.*, trepanning (drilling according to a helical pattern).¹²⁸ For biological targets, the difficulties of applying quantification approaches are compounded by the complex morphology. Unfortunately, the C signal, for use as an IS is compromised by fractionation effects.¹²⁹ Temporal and spatial changes in ablation rate impede 3D imaging based on drilling approaches in biological samples. 3D imaging for biological samples however can be conducted by analysing sequential sections (serial sectioning), obtained *via* (cryo)tome cutting of embedded or frozen organisms/organs/parts (Figure 13). The choice of ablation approach for bioimaging may also have to take into account the strategy towards internal standardization or variants thereof, as such strategies often require complete ablation through tissue sections, and in some cases, ablation through a spiked coating below or above the tissue. The 2D images are stitched into a 3D stack of 2D images, either by manual alignment, or by image registration (Figure 13d) based on marker points or selected elements such as P, which strongly outline the morphology of biological structures. A 3D volume can be reconstructed from the stack by stitching methods such as 3D Delaunay triangulation (Figure 13e). Clustering algorithms, *e.g.*, Fuzzy C-means clustering, K-means clustering¹³⁰, can then be used to isolate structures, *e.g.*, biological compartments, within the 3D volume. Alternatively, isosurface rendering can extract surfaces from the volume. It can be easily envisaged that isolation of pulse responses through low-dispersion ablation cells (Figure 13b), in combination with topographical or morphological information would allow a computation of a 3D model (Figure 13e) of the sample, in which the information and geometry for every ablated volume of every individual pulse is visualized as a single voxel, or a collection of voxels. Furthermore, analogous to software available in computer-aided manufacturing, the material removal process can be simulated, and arbitrary 3D and 2.5D ablation patterns can be adopted, *e.g.*, to selectively ablate parts of the sample volume by tracking the morphology within the sample in 3D.

In high-resolution LA-ICP-MS imaging, the laser beam waist size is intrinsically limited by: i. the analytical sensitivity and ii. the far-field diffraction limit. By virtue of their improved sensitivity, low-dispersion ablation cells allow for smaller ablation spots. They also facilitate applications such as the selective ablation of individual cells, *e.g.*, in combination with automated optical cell recognition software. The lateral resolution can be improved further by oversampling, *i.e.*

overlapping the ablation positions, and reconstructing the I_0 profile through deconvolution, reducing the impact of the blurring effect on lateral resolution. Based on his previous work, Plotnikov *et al.*¹¹⁶ pioneered deconvolution of the responses of overlapping ablation positions based on Fredholm integral equations of the first kind. Van Malderen *et al.*¹¹⁹ recently reported a deconvolution approach based on the iterative Richardson-Lucy algorithm to retrieve spatially resolved information on a level below the beam waist dimensions in 2D and 3D imaging (more information available on this subject in Chapter 3). Oversampling, whilst quantitatively removing the material at each ablation position, will improve the lateral distribution, as the response relates to the new edge of the tissue ablated, rather than the entire spot. The approach was reported by Drescher *et al.*³ for mapping of tissue sections. Analogous strategies can be encountered in other techniques, *e.g.*, MALDI-MS.¹³¹ In conclusion, low-dispersion cells, especially in combination with simultaneous multi-element detection open up new sampling and normalization approaches that were previously inaccessible as a result of throughput or sensitivity constraints.

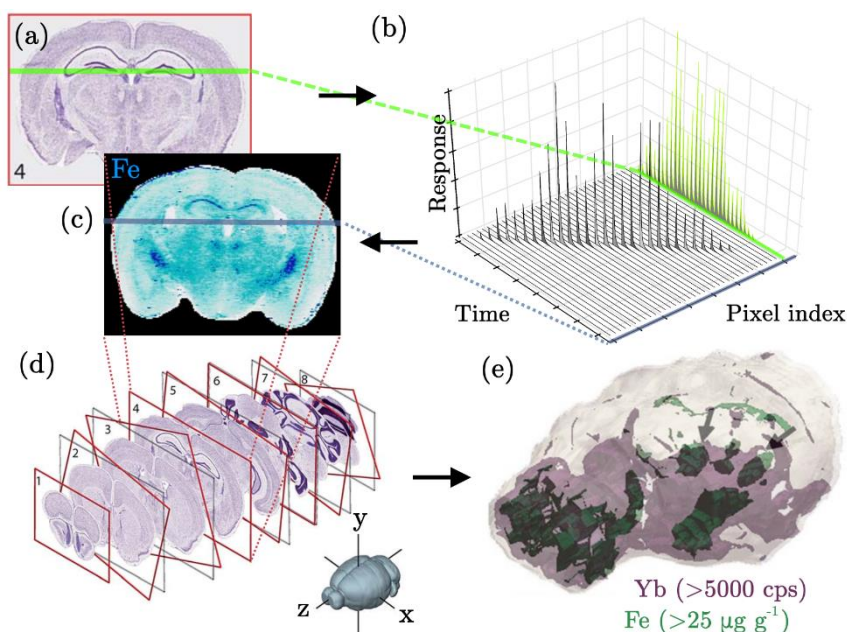


Figure 13 Schematic representation of the hypothetical combination of low-dispersion cells with single shot response isolation (b), producing spatially resolved images (c) of a tissue slice (a), and serial sectioning, in which a 3D volume (e) is reconstructed through image registration (d) of individual slices based on the P signal. Reformatted figure with components reprinted with permission of Paul *et al.*¹³²

2.3 Considerations for ablation cell design

One of the goals of this work was to improve the instrumentation for LA-ICP-MS to extend its application field by enhancing the lateral resolution and sample throughput attainable beyond

those available through state-of-the-art instrumentation and methods. To this end, the design of ablation cells and aerosol transport systems was investigated. Early on, the aerosol dispersion was identified as the main bottleneck for LA-ICP-MS figures of merit. The width of the washout profile of 1st generation (single-volume) ablation cells – often still in operation in many labs – can be 3 orders of magnitude worse as compared to state-of-the-art 3rd generation cells. When the transport lines are short and the internal volume of the ablation cell is reduced, the 1st generation designs achieve washout profiles of a width of 1-10s at the FW0.01M, hence, the profiles are already convolved at low repetition rates (Figure 14).

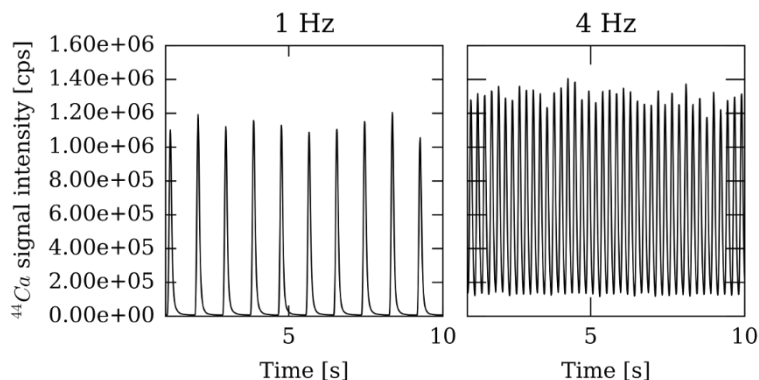


Figure 14 Performance and single-pulse convolution at low repetition rates for first generation (*i.e.* single volume) ablation cells (a NWR SuperCell™). Signal response for a line scan on NIST SRM 612 using a 100 μm spot size with an NWR 193-UP ablation system connected to a Thermo Fisher Scientific ICP-MS unit (10 ms dwell time).

Isolation of the aerosol in an internal cup, as is the case in 2nd generation ablation cells, reduces the dispersion to a few 100 ms. Clearly, academia and industry are poised to make the step towards 3rd generation cells, to save cost and to improve the value of the analytical information that can be extracted even further.

This work adopts a holistic approach to the aerosol transport system (ATS) in order to resolve the various issues bottlenecking the overall aerosol dispersion, as it is expected that each part of the ATS has a significant contribution to the overall dispersion. The strategy towards an improved ATS is based on an iterative approach consisting of: i) design of multiple ATS as CAD models, ii) CFD modelling of the particle and flow streams in the models, iii) improvement of the CAD model, based on input from the CFD results, iv) CFD modelling of the improved designs, v) manufacturing of the best prototype, vi) gathering of empirical data on the prototypes, and vii) using the feedback from the empirical data to improve the CAD model, and looping back to the start of step iv).

The initial requirements for the ATS are:

1. Safety features to prevent damage to the sample, system, and operator.
2. Compatibility with the laser ablation system in operation at Ghent University
3. Aerosol dispersion limited by the laws of physics, not the design of the ATS.

4. >99% aerosol transport efficiency of the current ATS.
5. Compatibility with all ICP-MS units in commercial production.
6. Low-profile design, allowing for objectives with a focal length < 10 mm, opening the path towards far-field sub- μm focusing using high NA objectives.
7. Cost-effective design with a feasible path towards commercialization of the technology.
8. Usability of the ATS on a day-to-day basis must be high (no continuous tuning required).
9. Flexibility in terms of sample size and nature.
10. The system must be modular to have enough flexibility for hardware upgrades, *e.g.*, cryogenic cooling stages.
11. Reduction of parts of the design.
12. Upgrade of the positioning stage.

Based on all information published in literature, design aspects which benefit aerosol dispersion were identified:

1. Smaller inner volumes of the ablation cell, in combination with carrier gas flow streams capable of flushing the entire cell effectively, *i.e.* elimination of dead zones in the flow field, reduce the residence time of particles in the cell and restrict the aerosol plume expansion zone, which limits the dispersion created within the cell. In order to minimize dispersion generated within the cell, the flow field should be homogenous and the stream lines should have similar path lengths (as not to induce different particle transit times for particles ejected from the sample surface under a different angle or with a different speed).
2. Eddy currents, turbulent vortices behind features in the flow field, occur when features are present which disturb the parabolic flow field. Eddy currents can also occur when the hydraulic cross-section of the transport volume increases, as turbulence can be induced through expansion of the flow into a low-pressure zone. Compression of the flow can also produce turbulence due to the sudden increase in flow velocity. The eddy currents will introduce dispersion, as particle transit velocities and path lengths will be different for each stream line in this turbulent zone, which means that the particles entrained in different parts of the carrier gas flow field will show different particle transit times. This segregation is also particle-size dependent, as the cross-sectional particle size distribution relates to the mean-free path length of the particles (smaller particles diffuse faster). The turbulence-inducing features may be present in the ablation cell, *e.g.*, a wall perpendicular to the particle trajectories, and in the transport line, *e.g.*, connectors, valves, and mixing pieces, and must be eliminated if possible.
3. In order to work as close as possible to the physical limits of the aerosol transport, we have to work near the transition zone between the laminar and turbulent flow regime (critical value $Re = 2320$). This region lies within the laminar flow regime, whilst operating at high fluid velocities, which is ideal for low particle transit times. For this reason, the fluid velocity in the CFD simulations will be optimized for $Re \sim 2000$. The Reynolds number for a flow within a solid pipe with a constant diameter D is:

$$R_{eD} = \frac{v_{mean}D}{\nu} = \frac{\rho v_{mean}D}{\mu} \quad \text{Equation 19}$$

With ν the kinematic viscosity, μ the dynamic viscosity, and ρ the fluid density. In order to maximize the mean fluid velocity v_{mean} for a constant $R_e = 2000$, the hydraulic diameter must be minimized and the kinematic viscosity (the ratio of dynamic viscosity to density) must be maximized. Smaller tube diameters are hence expected to be beneficial.

4. The distance between the ablation position and the ICP must be reduced to reduce the aerosol transit time. A straight path of the aerosol (the shortest line between two points) also reduces dispersion: particles following streamlines along the outside curvature of a bend tubing have a longer path length as compared to particles following stream lines in the inside curvature of the bent tubing. For curvatures $> 45^\circ$ and curvature radii < 100 mm, particles will also collide with or deposit onto the tubing walls (preferentially particles $> 1 \mu\text{m}$), resulting in larger variation in particle transit times as a result of erratic particle trajectories and the deposition-desorption equilibrium or particle loss.⁷
5. Some selected physical properties of the carrier gasses employed in LA-ICP-MS are detailed in Table 2. These properties are crucial to understanding which gas provides the most efficient particle capture and transport efficiency and the fastest heat dissipation of the laser plasma, and induces the lowest possible aerosol dispersion during aerosol transport.

Table 2 Inert gas properties under NIST standard conditions for normal temperature and pressure (1 atm, 293.15 K)

	Ar	He	N ₂
Density [kg m^{-3}]	1.6617	0.1664	1.1651
Dynamic Viscosity [$\text{kg m}^{-1}\text{s}^{-1}$]	2.2294E-5	1.96E-5	1.7550E-5
Kinematic Viscosity [$\text{m}^2 \text{s}^{-1}$]	1.3416E-5	1.178E-4	1.5064E-5
Heat capacity [$\text{J kg}^{-1}\text{K}$]	5.2162E+2	5.193E+3	1.0411E+3
Thermal Diffusivity [$\text{m}^2 \text{s}^{-1}$]	2.1117E-5	3.4112E-3	2.1002E-5
Mean free path [nm] at 273.15 K	68.33	192.66	59
Speed of sound [m s^{-1}]	323	972	353
First IP [kJ mol^{-1}]	1520	2372	1402

The diffusion flux can be estimated based on the elementary mean free path theory of diffusion and the kinetic theory as:

$$J = -D\delta n/\delta x \quad \text{Equation 20}$$

Where the diffusion coefficient D can be calculated as:

$$D = \frac{1}{3}lv_t = \frac{2}{3}\sqrt{\frac{k_B^3}{\pi^3 m_a}} \frac{T^{3/2}}{p_{ambient} d_a^2} \quad \text{Equation 21}$$

Where m_a is the atomic mass, d_a the atomic diameter, l the mean free path (Equation 22) and v_t the thermal speed (Equation 23).

$$l = \frac{k_B T}{\sqrt{2}\pi d_a^2 p_{ambient}} \quad \text{Equation 22}$$

$$v_t = \sqrt{\frac{8k_B T}{\pi m_a}} \quad \text{Equation 23}$$

From these equations, it can be seen that the diffusion flux is substantially larger for noble gasses with a smaller atomic diameter and mass; He hence diffuses faster into other gasses, and is able to diffuse more efficiently into the condensing particle cloud to entrain particles within and prevent them from depositing near the crater. Furthermore, as a result of the higher thermal diffusivity, He will dissipate the heat within the laser plasma much faster compared to the other carrier gasses (diffusivity and heat capacity are higher for He). On the other hand, heavier gasses will limit diffusion of the particles entrained within due to their shorter mean free length. The speed of sound relates to turbulence as it defines at which fluid-object velocity (Mach 1) the pressure-strain rate (inertial resistance to the compressional resistance experienced by an object moving through a fluid) becomes critical, and the laminar flow transitions into a conical shock wave behind the object as a result of shear stresses. Shear stresses also induce turbulence in a pipe flow; similar to the speed of sound, the mean fluid-wall velocity for He can be ~ 3 times higher compared to that for Ar for an identical critical Re (in a transitional regime). Gas mixtures have a more complex, intermediate behaviour.

Starting from the requirements and design considerations detailed above, the design concept was defined. The only cell design type which provides a homogenous fast flow field with minimal turbulence-inducing changes in the hydraulic diameter is one where the particle extraction is performed by the transport tubing itself. Confinement of the expanding particle cloud in a small volume ($<1 \mu\text{L}$) above the ablation site would also reduce the initial dispersion and prevent sample cross-contamination with condensates. When the incoming fluid field is homogenous and coaxial to the extraction flow field, the shear stress around the outlet walls is minimized, whilst the momentum of a coaxial flow will also help to capture and push the ejecta into the extraction tube with the fastest possible acceleration. Hence, a variation of the tube cell design, as described by Bleiner³³ was identified as the most promising design concept to start from. The cell described by Bleiner in 2002, achieves a pulse response profile with an FWHM of 0.34 s. The implementation of the design may not have been optimal, as the overall system was

limited by the aerosol dispersion generated in the connecting tubing, effectively bottlenecking the performance of the whole system. The cross-section of the inner volume through which particles travel varies significantly as a result of the presence of multiple connectors in the transport tubing, which is a potential major source of turbulence. Based on Equation 19, miniaturization of the hydraulic diameter allows to increase the mean fluid velocity and ambient pressures for a constant Re , hence, this was identified a promising strategy. Miniaturization is limited in the sense of the particle stopping distance, which relates to pressure, gas type, and fluid velocity. Although Ar remains a necessary make-up gas, He is used as the primary carrier gas to transport the aerosol towards the ICP, as this permits to attain the highest possible carrier fluid velocities in the transitional flow regime. It should be noted that the Taylor-Aris dispersion is more severe for He as compared to Ar, as the velocity difference between the core flow and the boundary flows is significantly higher for He.⁴⁰ Ar is added at the latest possible moment to limit carrier gas mixing *prior* to the analytical zone in the ICP. When Ar is added, the flow is laminar and parallel to the high speed He flow. When the velocity difference between two laminar flows is high enough, mixing is strongly reduced.

It is also important to consider the relative contribution of each part of the ATS to the overall dispersion in order to evaluate which bottlenecks have to be tackled first. For a HELEX two-volume ablation cell, the relative contribution of the aerosol dispersion to the overall dispersion of the connecting tubing and mixing bulb was found to be >95%, as the overall FW0.1M of the washout profile could be reduced from 500 ms down to 20 ms (based on the ²³⁸U signal for ablation of NIST SRM 612 using a 193 nm 5 ns lasing system) by employing a new aerosol transport system, named ARIS (aerosol rapid introduction system), developed in this work and described in section 2.7.1 below. The remaining contribution is split between the initial dispersion generated upon plume formation and melt expulsion (<1 ms), expansion of the particle cloud in the inner cell (~10-20 ms), and the entrainment of particles in turbulent streams in the plasma (<1 ms). From this, it can be seen that the transport line contributes the largest fraction to the aerosol dispersion, and thus, should be tackled first.

2.4 Transport line-induced dispersion

Valves, joints, and connectors which are present between the cell and the transport tubing, the tubing and the mixing component (which is used to introduce the make-up gas), and between the tubing and the injector inlet, are turbulence-inducing elements. The CleanShot® is a three-way pinch valve system, inserted into the transport tubing, that allows a vacuum to be drawn throughout the transport line, which removes air and moisture from the system after it has been exposed to the ambient environment. Air introduced into the ICP can destabilize the plasma; when the plasma gas flow, as a result of an unstable plasma fluid, is unable to maintain the thermal barrier the torch components may melt. Additional connectors and ductile tubing with a low Young's modulus (for closing the tubing by compression) are present within the CleanShot®.

Most valves and connectors can be eliminated from the transport line:

1. The transport lines can be made part of the ablation cell in such a way that a constant cross-section remains throughout the entire setup. As such, the flow does not perceive the presence of this connection, when the connection is tight,
2. The transport line can be introduced either directly through the injector, into the plasma, or a mixing bulb can introduce a coaxial flow of make-up gas behind the connection with the injector. Both concepts were explored.
3. A pressure gradient between the cell and the atmosphere is present as a result of the tubing. This pressure gradient can be used to temporally sustain a vacuum in the cell. The pressure drop over a tube with smooth walls in a laminar flow regime (for an ideal gas in the isothermal case) is determined by the Hagen-Poiseuille law for compressible fluids:

$$\Delta p = \frac{8\mu L v_{avg}}{R^2} = \frac{8\mu L \Phi}{\pi R^4} \quad \text{Equation 24}$$

Where L and R are the length and internal radius of the tube, respectively, μ the dynamic viscosity, and v_{avg} the mean fluid speed. Φ is the volumetric flow rate:

$$\Phi = \frac{\pi R^4}{16\eta L} \left(\frac{p_i^2 - p_0^2}{p_0} \right) \quad \text{Equation 25}$$

Where p_i and p_0 are the inlet and outlet pressure, respectively. For turbulent flows, the Darcy-Weisbach equation is used instead.

As a result of shear strain a velocity profile develops in laminar flows in pipes, with a velocity profile v as a function of the radius r and the distance of the profile relative to the inlet (ΔL):

$$v(r) = \frac{|\Delta p|}{4\eta \Delta L} (R^2 - r^2) = v_m (1 - r^2/R^2) \quad \text{Equation 26}$$

Where v_m is the maximum fluid velocity (present along the central axis in the tube). The average speed v_{avg} can be calculated based on the integration of the profile over the area:

$$v_{avg}^2 = \frac{v_m^2}{A} \int_0^R \left[1 - \frac{r^2}{R^2} \right]^2 2\pi r \, dr = \frac{v_m^2}{3} \quad \text{Equation 27}$$

Based on these equations, the following pressure drops can be predicted for a 0.5 L min^{-1} flow rate of He, with the outlet at atmospheric pressure and inlet pressure of 2 bar, at 293.15 K:

Table 3 Overview of predicted pressure drops in the transport tubing in realistic scenarios.

L [mm]	$2r$ [mm]	v_{avg} [$m\ s^{-1}$]	$ \Delta p $ [mbar]
500	0.5	42.4	692
500	0.75	18.9	109
500	1	10.6	33
500	2	2.7	2
750	0.75	18.8	167
750	1	10.6	51
750	2	2.7	3
1000	0.75	18.8	228
1000	1	10.6	68
1000	2	2.7	4
1500	0.75	18.8	358
1500	1	10.6	103
1500	2	2.7	6

In order to mitigate the intrusion of air through back pressure when drawing a vacuum in the cell, the pressure drop over the transport line must be larger than the pressure difference established between the inner cup of the two-volume cell and the atmosphere, which is approximately 200 mbar (~ 3 psi), for small flow rates. In a 900 mm long transport line, 0.75 mm in diameter, and at a $0.7\ L\ min^{-1}$ flow rate of He, a pressure gradient of 300 mbar is established, with a flow rate of $26.5\ m\ s^{-1}$ and R_e of 168, permitting the aerosol to be transferred in a fast laminar flow. When the rate of evacuation is high enough, *e.g.*, 1 full cycle / 20 s, the pressure gradient in the transport line limits the volume of air entering the tube to $< 0.1\ L$. However, when a vacuum of 800 mbar is maintained in the cell (constantly), a flow of $0.5\ L\ min^{-1}$ of air will be established, which will fill up the internal volume of the cell in $< 40\ s$. Fast evacuation/refilling processes are thus important to prevent air from occupying the cell. Furthermore, an overpressure of inert gas can be established *prior* to evacuation, to mitigate air from moving up through the transport line at each evacuation cycle, by flushing the line.

Based on these observations, two concepts were developed: i) a transport line incorporated into the cell itself and protruding through the injector, and ii) the ARIS system (Section 2.7.1), where an improved mixing bulb allows the introduction of make-up gas at the injector connection. Both concepts are explored in the next sections. All improved components were installed into a commercially available LA-system.

2.5 Background of CFD

Computational fluid dynamics simulation is a research field which calculates precise solutions to fluid movement. For the purposes of this work, basic simulations of the time-averaged motion for fluid flow based on Reynolds-averaged Navier-Stokes equations (RANS) are valid for studying the flow within the ablation cell and tubing (on the ms time scale) as the pressures,

velocities and temperatures lie within the Stokes' regime. The RANS equations are closed by eddy viscosity turbulence models (realizable k- ϵ , k- ω). The CFX/ FLUENT module in the ANSYS® multi-physics suite (ANSYS® Academic Research, Release 14.5){ANSYS Inc., #1297} was used to mesh the models, with a typical mesh density of > 1500 tetrahedrons mm^{-2} . The mesh resolution was increased around the fine features of the ablation cell. CFD calculations were performed in FLUENT, by entering all relevant boundary conditions and fluid properties. The iterative solver process will perform >100 iterations before a stable solution can be found. This process has to be conducted several times with different seed values to validate the solution. Furthermore, the solution was compared to the solution obtained in SolidWorks Flow Simulation 2014, another CFD program that calculates the flow field based on Favre-averaged Navier-Stokes equations (FANS), to give confidence into the solution. In most cases, the differences in the metrics of the solutions in both programs, were limited to $<10\%$. In a time-averaged solution, the instantaneous fluid velocity u is described as a superposition of the time-averaged component $\bar{u}(x_i, x_j)$ and the fluctuating component $u'(x_i, x_j)$, where x_i and x_j are two generic axes in the Cartesian coordinate system. The NS equations (Equation 30) are based on the conservation laws for continuity and momentum (Equation 28 and Equation 29, respectively) in Cartesian space (the Cauchy momentum equation)^{133,134}:

$$\frac{\delta \rho}{\delta t} + \frac{\delta}{\delta x_i}(\rho u_i) = 0 \quad \text{Equation 28}$$

$$\begin{aligned} \frac{\delta \rho u_i}{\delta t} + \frac{\delta}{\delta x_i}(\rho u_i u_j) + \frac{\delta p}{\delta x_i} &= \frac{\delta}{\delta x_j}(\tau_{ij} + \tau_{ij}^R) + s_i \frac{\delta \rho H}{\delta t} + \frac{\delta \rho u_i H}{\delta x_i} \\ &= \frac{\delta}{\delta x_i}(u_j(\tau_{ij} + \tau_{ij}^R) + q_i) + \frac{\delta P}{\delta t} - \tau_{ij}^R \frac{\delta u_i}{\delta x_j} + \rho \epsilon \\ &\quad + s_i u_i + Q_H \end{aligned} \quad \text{Equation 29}$$

$$\left(\frac{\delta}{\delta t} + u_j \frac{\delta}{\delta x_j} - v \frac{\delta^2}{\delta x_j \delta x_j} \right) u_i = - \frac{\delta w}{\delta x_i} + g_i = - \frac{1}{\rho} \frac{\delta \bar{\tau}^R}{\delta x_i} \quad \text{Equation 30}$$

where ρ is the fluid density, P is the pressure, τ is the viscous shear stress tensor, τ^R is the Reynolds-stress tensor (Equation 31), w the specific thermodynamic work ($\rho_0^{-1} \nabla p = \nabla w$), q is the diffusive heat flux, ϵ is the turbulent energy, and Q_H is a heat source/sink per unit volume.

Heat is here $H = h + \frac{u^2}{2}$, with h the thermal enthalpy. The Reynolds-stress tensor is:

$$\tau_{ij}^R = \mu_t \left(\frac{\delta u_i}{\delta x_j} + \frac{\delta u_j}{\delta x_i} + \frac{2}{3} \delta_{ij} \frac{\delta u_k}{\delta x_k} \right) - \frac{2}{3 \rho K \delta_{ij}} \quad \text{Equation 31}$$

where K is the turbulent energy:

$$\frac{\delta \rho K}{\delta t} + \frac{\delta}{\delta x_i}(\rho u_i K) = \frac{\delta}{\delta x_i} \left(\left(\mu + \frac{\mu_t}{\sigma_K} \right) \frac{\delta K}{\delta x_i} \right) + S_K \quad \text{Equation 32}$$

with S is a mass-distributed external force term (buoyancy term and force resulting from rotation of the coordinate system). By time-averaging the Navier-Stokes equation for an incompressible Newtonian fluid (Equation 30), The RANS equation can be derived:

$$\begin{aligned}
& \rho \left[\frac{\delta}{\delta x} (\overline{u^2}) + \frac{\delta}{\delta y} (\overline{uv}) + \frac{\delta}{\delta z} (\overline{uw}) \right] \\
&= -\frac{\delta \bar{p}}{\delta x} + \mu \left[\frac{\delta^2 \overline{u}}{\delta x^2} + \frac{\delta^2 \overline{u}}{\delta y^2} + \frac{\delta^2 \overline{u}}{\delta z^2} \right] \\
&\quad - \left[\frac{\delta}{\delta x} (\rho \overline{u'^2}) + \frac{\delta}{\delta y} (\rho \overline{u'v'}) + \frac{\delta}{\delta z} (\rho \overline{u'w'}) \right]
\end{aligned}
\tag{Equation 33}$$

where u , v and w are the velocity components of the x , y and z axis.

2.6 Development of new ablation cells

Based on the design concept outlined in Section 2.3, two tube cell types were explored: i) a low-profile, miniaturized half-open tube cell, in contact with the sample, and ii) a triple-inlet valve variation of the tube cell (Figure 15).

2.6.1 Triple-inlet cell

The idea behind the triple-inlet cell is that the He inlets are spread out and can compress the expanding particle plume in all directions, whilst shielding the window from high-speed ejecta. Multiple configurations with varying inner diameters (1.3-2 mm) and angles at which the inlets are positioned relative the central channel ($15^\circ - 45^\circ$) were manufactured and tested. The design (inlet angles, inner diameter) of the CAD models was optimized using CFD in CFX/Fluent in an attempt to minimize dead volume and maximize the local superficial gas velocity of He (Figure 16). The internal volume of the triple-inlet cell is estimated at a 41.87 μL , 25 μL of which contains aerosol particles. In total > 20 CAD models were evaluated (Figure 18). CFD simulations for this design were promising as a homogeneous laminar flow field was predicted inside the cell geometry, but the design has some drawbacks:

1. The force exerted by the sweep gas is spread out over the 3 inlet tubes, spreading out the kinetic energy contained within the flow directed towards the outlet. As compared with a tube cell, the momentum of the incoming fluid flow is not coaxial with the desired direction of transport.
2. Dead zones are present near the window, at the outlet side of the walls, as the vertical walls are not efficiently flushed.

3. As result of the height of the central channel (a cylindrical volume above the ablation site) into which the particle cloud expands, the incident angle of laser radiation is limited (Figure 17).

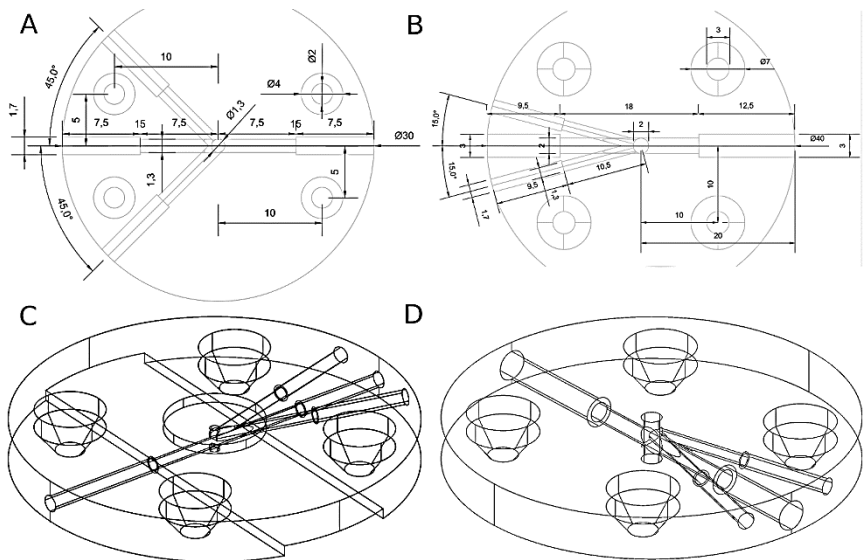


Figure 15 Three-inlet ablation cell CAD design. All dimensions in mm.

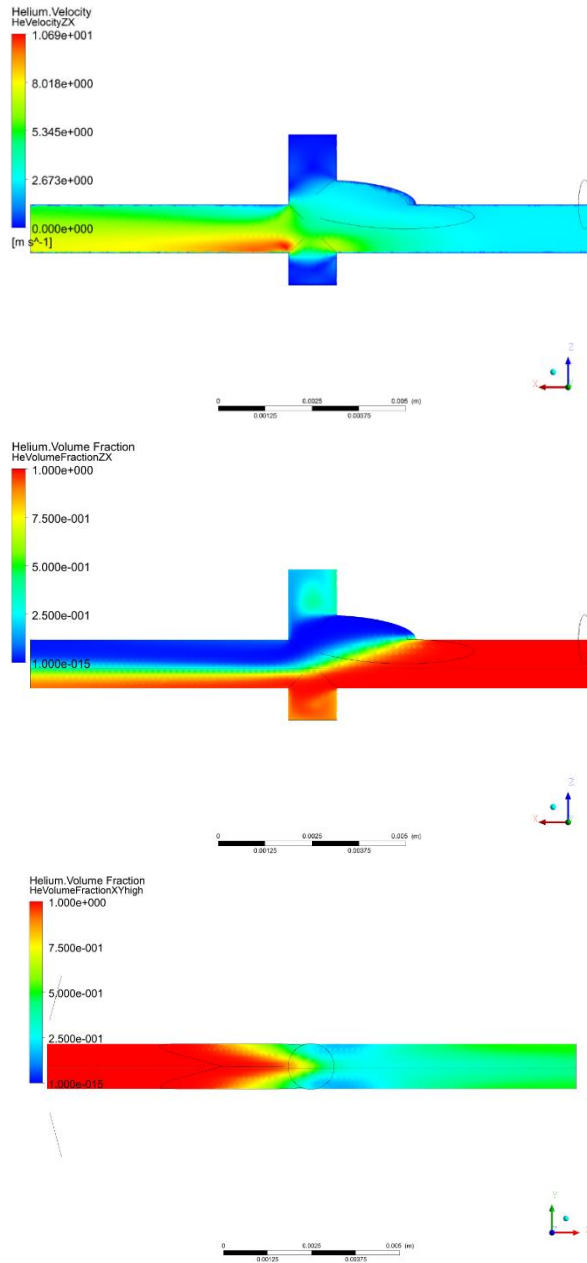


Figure 16 The top figure displays the simulated fluid velocity distribution plot in the axial cross-section of the triple-inlet cell. The other figures display the distribution of the local He fraction introduced in the center inlet in the axial plane, with a side view (mid) and top view in the mid-plane of the central channel (bottom)

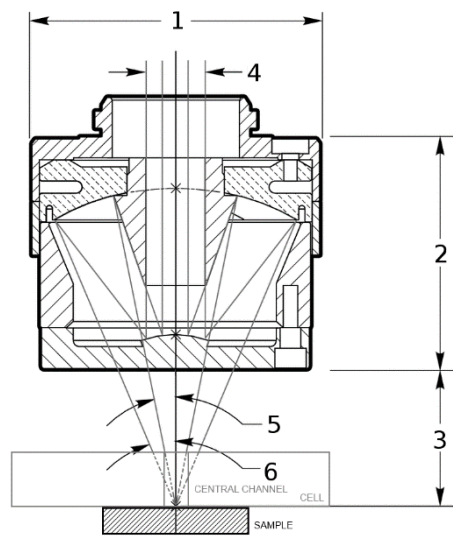


Figure 17 Cross-section of the triple-inlet cell and a Schwarzschild objective, with the light path drawn. Legend: 1) diameter of the objective, 2) height of the objective, 3) focal distance, 4) diameter of the laser beam, 5) smallest angle of incidence, and 6) largest angle of incidence.

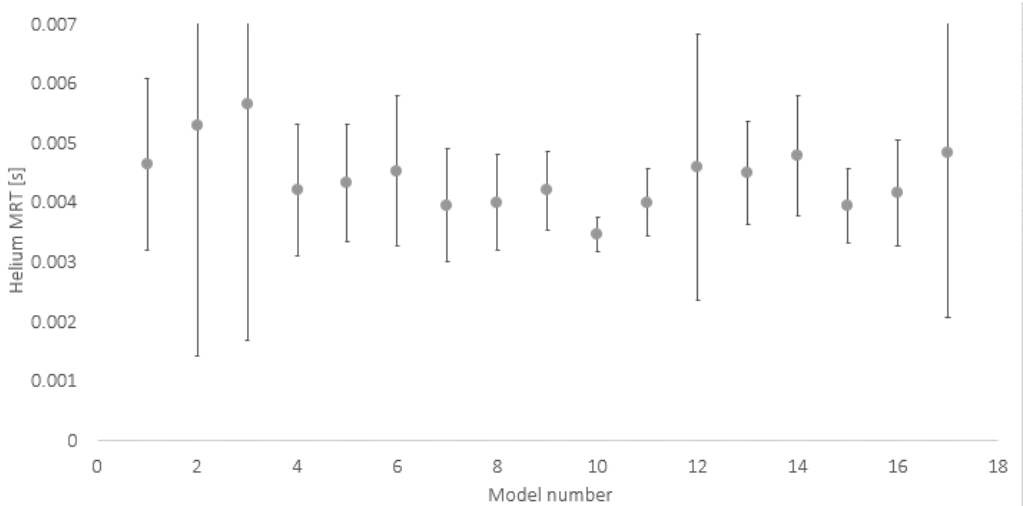


Figure 18 Mean residence time (MRT) of the He particle population (90 particles) flowing through the volume of 17 different designs behind the ablation site. Error bars represent the estimated standard deviation (within the population).

The sparse empirical data gathered on these designs indicates that the washout peak profile FW0.01M cannot be reduced to <50 ms. Simulations indicate that the spread on the residence time favors cell designs with narrow inlet angles (model 10 with a 15° inlet angle *versus* model 2 with a 45° inlet angle) The shortcomings described above are not present in the tube cell design, hence, this design was pursued further instead.

2.6.2 Tube cell

Based on the considerations discussed in the previous sections, it is clear that a correct implementation of the tube cell is crucial to realize the optimum performance. This comprises: i) incorporation of tubing with constant diameter into the cell housing, ii) lowering the profile to eliminate dead volume at the wall interfaces, and iii), the use of pure He to mitigate turbulence. A tube cell of this type was developed and manufactured. The performance of the tube cell, integrated into currently available commercial instrumentation was evaluated, and its potential for high spatial resolution scanning by LA-ICP-MS was demonstrated.

2.6.2.1 Particle-wall interaction

The lower window/wall-sample distance presents a potential danger of non-stoichiometric losses due to spattering, adsorption, and impingement of particles on the walls and windows. Furthermore, if this ejecta is sufficiently energetic, damage and particle loss onto/into cell walls as a result of spallation and corrosion of the window may occur. The yield/collision frequency and kinetic energy on impact are determined by: i) the laser-surface interaction, ii) the ablation site-wall distance and the geometry of the cell and transport assembly, and iii), background gas pressure. The particle expansion may, however, be potentially suppressed *via*: i) electric and magnetic fields, ii) the reflection of the bow SW, and iii) by momentum transfer of the carrier gas. An exact description of all physical processes related to mass ejection is beyond the scope of this work.

The tube cell was optimized to achieve a higher pressure (1.5-2 bar) in the environment of the cell, to increase the ability of the carrier fluid to contain ejected particles, as the density is directly proportional to the buffer capacity. Furthermore, gas velocities $> 20 \text{ m s}^{-1}$ can be attained, which is $> 10 \times$ the gas velocity found in 1st and 2nd generation ablation cells. The added gas velocity will transfer the plume faster towards the outlet, preventing the plume from fully expanding inside the cavity. The travel time for a single He atom travelling at 20 m s^{-1} to cover the distance from the ablation site to the outlet, 0.5 mm further, is 25 μs ; this is shorter than the time required for full plume expansion ($> 100 \mu\text{s}$), but it is longer than the characteristic time scale for gas buffer operation (in the order of 1 μs).^{36,76} Thus, the gas velocity only plays a minor role in the overall buffer capacity of the gas.

The SW is described by Taylor-Sedov equations (Chapter 1). Interaction of the SW and the walls is, however, more complex. In order to look at this phenomenon more in-depth, a 2D SW propagation simulation, based on Euler numerical processors, was performed to model the plasma shock reflection in a confined space (symmetrical cavity corresponding with a cross-section of the cell). ANSYS® AUTODYN{ANSYS Inc., #1298} is an analysis tool for modeling nonlinear dynamics, which is based on a large set of Jones-Wilkins and Lee equations of state. The SW propagation was simulated as a detonation of TNT from a point-source at the ablation position. The explosive energy of the TNT was modulated such that the detonation wave's initial velocity was $\sim 2000 \text{ m s}^{-1}$, which would concur with the observed SW initial expansion velocity in the first few 100 μm .^{51,135} Although a chemical explosion may not be able to model the intricate features of the laser-induced SW formation, the basic wave-front reflection physics are identical.

The progression of the pressure field is displayed below in Figure 19. In order to limit the effect of wall material deformation as a result of SW impact, the strength of the wall material (Figure 19.1) was set to infinity. The results are hence based on an inelastic reflection of the wavefront. As expected, the shockwave generates a low-pressure region (Figure 19.2) behind the shockwave, which expands into the cavity (Figure 19.3). This low-pressure region will expand as the SW travels up the walls (Figure 19.4, Figure 19.5). The high-pressure zone created at the top of the chamber will decelerate the incoming particles much more effectively than the low-pressure zone. As the particle wave is slower relative to the SW, they will arrive after this zone is created. This zone is thus expected to shield the window from incoming particles to some extent. Furthermore, the Mach reflection of the SW generates an inward, axial compression of the particle cloud. Ideally, the plume would collapse into the high-speed central axis of the fluid channel, though this simulation suggests the process is erratic. Spatially confined ablation is a topic which has been explored for LIBS. This research points towards significant effect of the spatial and magnetic confinements on plasma shape, resulting in emission enhancement as a result of higher plasma peak temperatures.^{43,44,47,48,136-139} It remains unclear how the particle cloud interacts with the Mach reflection, as more empirical data are required (obtained by *e.g.*, shadowgraphy). The occurrence of non-deterministic plasma breakdown in ns-lasers complicates this further.

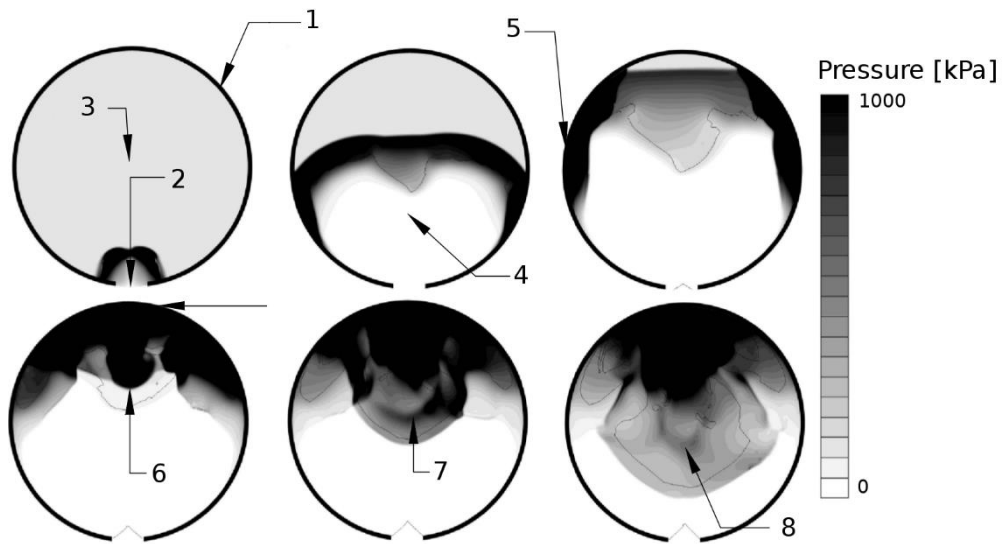


Figure 19 AUTODYN simulation of the shockwave propagation throughout a cross-section of the cell.

A half-open cell in contact with the surface was machined out of a 40 mm Ø PMMA (poly(methyl methacrylate)) cylinder (Figure 20). The incident laser beam enters through a 1 mm Ø aperture, which is sealed with a fused silica glass window.

2.6.2.2 Tube cell design

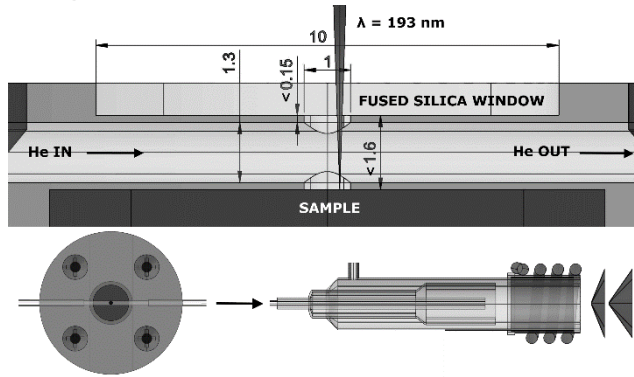


Figure 20. Technical drawing of the ablation cell and torch. All dimensions are provided in mm.

The aerosol formed upon ablation enters the central chamber through a cylindrical 1 mm \varnothing aperture at the bottom of the cell, perpendicular to the central chamber, a 1.3 mm \varnothing cylinder, in which the aerosol expands, and is transported by a high-velocity, compressed stream of He through PTFE (polytetrafluoroethylene) tubing (1.3 mm inner \varnothing , 372 mm in length), incorporated into the cell and the injector of the torch. The pressure of the background gas and the reflected plasma shockwave spatially confine the expanding plume.^{36,140} Particles, non-condensed clusters, and micro-droplets ejected and accelerated¹⁴¹ tangentially relative to the momentum of the He flow are likely to be trapped in this flow as momentum is transferred. The occurrence of plasma breakdown will alter the velocity vector along which particles are ejected. The expanding aerosol only fills part of the central chamber; it is, therefore, challenging to define a finite volume in which the aerosol expands. When regarding the ablation as a uniform hemispherical point source explosion, a model which is far too simple to accurately describe the dynamics of the ablation-induced expansion front, the aerosol can expand initially into a ~ 1.5 μL volume.

2.6.2.3 CFD simulation of the tube cell

The ablation cell and connecting transfer tubing were modeled in AutoCAD™ (Autodesk™), imported into CFX (ANSYS™), and meshed with a fine grid of > 1500 tetrahedrons mm^{-2} . Flow rates $\geq 1.7 \text{ L min}^{-1}$ He push the Reynolds number Re of this phase above 2000, out of the laminar flow regime and into the transitional zone ($1700 \leq Re \leq 2300$) as the velocity gradient between the wall and center flow becomes too large, inducing turbulence and the potential formation of vortices.^{11,17,28} As the gas flow rate is set near these levels, a statistical turbulence model, based on Reynolds Averaged Navier-Stokes (RANS) equations closed by eddy viscosity turbulence models (realizable k- ϵ , k- ω), was adopted. The bulk mass introduction rate at the He inlet was set to 4.516 mg s^{-1} (1.65 L min^{-1} , 293.15 K). The outlet was set to atmospheric pressure. He atoms reach an average velocity of $\sim 20.3 \text{ m s}^{-1}$ in the centre of the central chamber (Figure 21). The occurrence of turbulence in He is much less likely than in Ar or mixtures of these gases, as the inertia of He is lower compared to that of Ar (speed of sound in Ar > 3 times lower than in He).

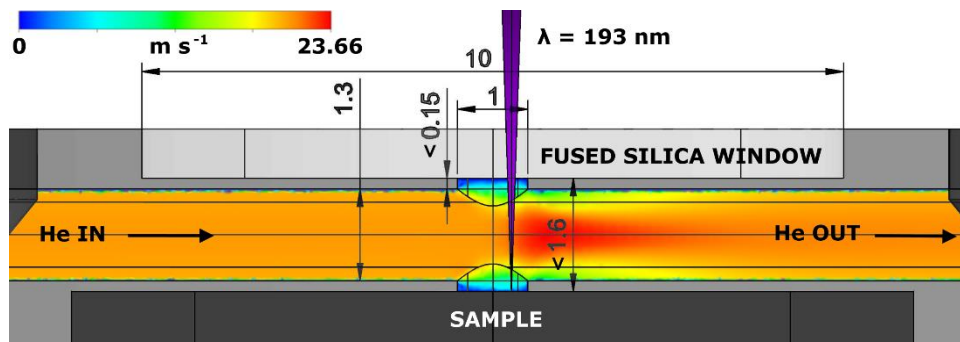


Figure 21 Velocity vector scale distribution of He atoms within the cell.

2.6.2.4 Experimental parameters for performance evaluation

The cell was mounted inside a purpose-built bracket (Figure 22) fixed onto the translation stage of an Analyte G2 (Teledyne Photon Machines, Bozeman, MT, USA) 193 nm ArF* excimer laser system (pulse duration < 5 ns, $\sim 1\%$ energy stability, 5.45 J cm^{-2} energy density) coupled to an Agilent 7900 quadrupole-based ICP-MS instrument (Agilent Technologies Inc., Tokyo, Japan), and evaluated by drilling NIST SRM 610 in sequences of 50 pulses under optimized conditions.

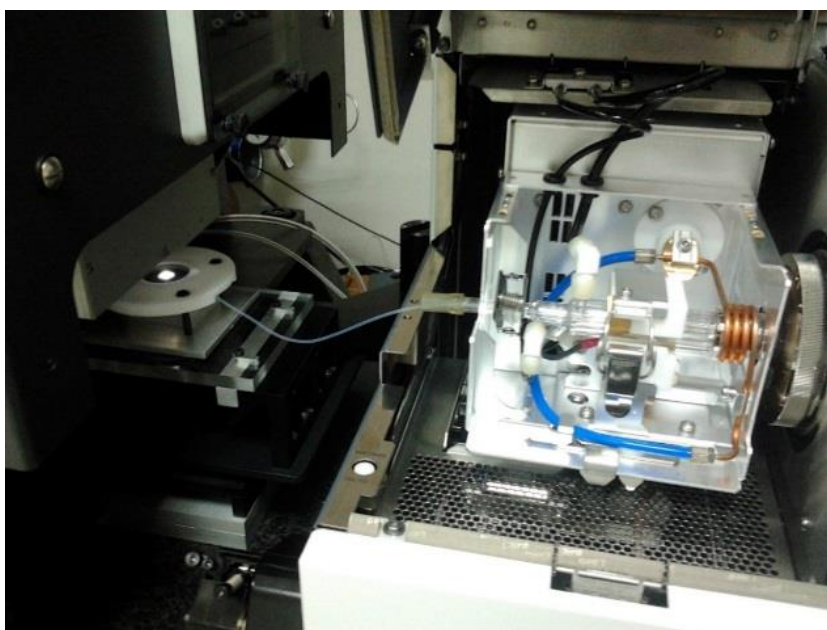


Figure 22 Practical implementation of the tube cell setup. The photograph shows the acrylic support mount structure, the PTFE connection tubing, and the bracket to hold the cell and window in place on top of the sample.

The ICP-MS unit was operated at an RF power of 1500 W, the flow rates tuned to 15 L min^{-1} for the Ar plasma gas, 0.2 L min^{-1} for the Ar auxiliary gas, and 1.65 L min^{-1} for the He carrier gas.

The objective of tuning the gas flow rates was to achieve a balance between drag and slipping effects on all particle sizes simultaneously, whilst keeping turbulence, radial and longitudinal diffusion, and plasma cooling at reasonable levels. The read time in the performance evaluation was set to 200 μ s. The dual mode discrete dynode detector employed is capable of recording the signal modulation of a single mass-to-charge (m/z) ratio down to 100 μ s intervals. Studies focusing on multiple nuclides can acquire the temporal resolution required by full-spectrum time- or mass-division inverse multiplexing *via* pseudo-parallel detection by time-of-flight (TOF) ICP-MS and simultaneous ion detection instruments of Mattauch-Herzog (MH) geometry.

2.6.2.5 Cell performance evaluation

In a configuration of the setup whereby the cell is located ~ 400 mm away from the plasma, the cell achieves aerosol washout for ^{27}Al (NIST SRM 612, 5 μ m square spot, 50 Hz, 5.45 J cm^{-2}) in $<4.7 \pm 0.4$ ms (sequence of 20 pulses; FW0.01M) under optimized conditions. More than 99% of the aerosol is removed in ~ 6 ms. Secondary processes can be observed at the base of each peak (below 3% of the maximum), preventing the signal to drop exponentially. Inherent limitations may be imposed on the dispersion of these secondary processes as they may originate from differential transport of fractal aggregates of mesoscopic particles (<100 nm) and larger particles formed by coalescence and aggregation.^{62,142,143} A potential supplemental source of dispersion is turbulence within the tubing and the plasma. For setups such as this, in which the cell is mounted externally, the total contribution of radial (gas flow rotational motion and diffusion) and co-axial mixing (Taylor-Aris dispersion) inside the transport tubing to the total aerosol dispersion increases with tube length. The physical limits for the transfer-induced dispersion of any setup consisting of an external ablation cell a considerable distance away from the plasma can be put into perspective by comparing it to the aerosol washout time of 1-3 ms for in-torch ablation⁶⁸⁻⁷⁰, in which the sample is located in very close proximity to the ICP. As the cell performs similarly to in-torch ablation with respect to the dispersion generated, we are advancing towards the physical limits of LA-ICP-MS in its current mode of operation. In Figure 23a, a sequence of 20 sequential pulses (NIST SRM 612, 5 μ m square spot, drilling at 50 Hz, 5.45 J cm^{-2}) is displayed (further zoomed in versions in Figure 23b and Figure 23c); the average peak area is $(3.4 \pm 0.6) \times 10^3$ counts ($1.7 \pm 0.04\%$ [m/m] Al, RSD on sequential pulses $\sim 5\%$); the average peak height is $(4.0 \pm 0.2) \times 10^6$ counts per second (RSD on sequential pulses $\sim 10\%$). The signal peak in Figure 23b drops down to the background level in ~ 15 ms. The limits of detection based on the abundance-normalized peak height sensitivities for ^{115}In , ^{140}Ce , ^{232}Th and ^{238}U , are ~ 0.25 ppm. The necessity for these fast cells becomes clear when considering that if the aerosol is transported towards the ICP in a much shorter timeframe, the sensitivity as well as sample throughput times are substantially improved, allowing for smaller beam diameters and their accompanying higher spatial resolution. In Figure 23d and Figure 23e, the spatiotemporal signal profile at high pulse repetition rates is shown; it is evident that pulse responses remain separated at repetition rates up to 200-300 Hz. Computational fluid dynamics simulations were used to replicate the conditions within the cell and connecting tubing (*vide supra*, Figure 21). The Reynolds number (Re) remains just below the turbulent flow regime ($Re \sim 1900$ for 1.650 L min^{-1} He). The average He residence time within the introduction system was 24.1 ± 0.4 ms. Preliminary experimental results of a cell and tubing approximately

30% smaller in diameter indicate that further miniaturization offers slightly better washout characteristics.

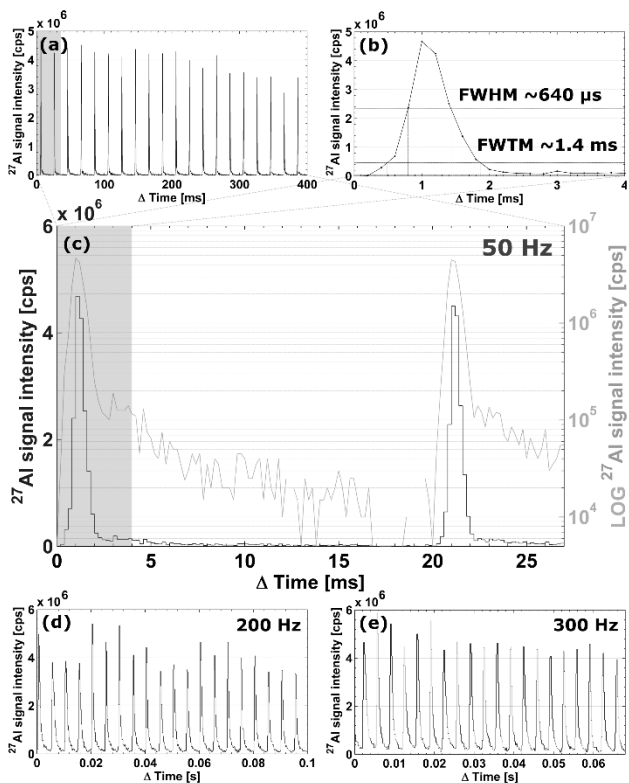


Figure 23. (a-c) Temporal signal intensity profiles for ^{27}Al when ablating NIST SRM 612 at 50 Hz (with various time axes). (d) Pulse repetition rate increased to 200 Hz. (e) Pulse repetition rate increased to 300 Hz. The peak profile has a FW0.01M of 4.7 ms, FW0.1M of 1.4 ms, and FWHM of 0.6 ms.

2.7 Development of a viable prototype

Though the tube cell performs well as compared to the state-of-the-art in terms of washout, repeatability, and transport efficiency, this setup is limited in more than one aspect: i) the sample area is limited to $\sim 10 \times 20 \text{ mm}^2$ in size, ii) the area which can be analysed is limited to $\sim 0.5 \times 0.5 \text{ mm}^2$; ablation in proximity of the walls changes the way in which the aerosol cloud expands, whilst a part of the beam will be cut off, resulting in a loss of fluence. The usefulness of an analytical technique (or setup of this technique) is not defined by the ensemble of metrics of the setup, but rather by the insights into the analytical problem that can be gained from the information that can be gathered by the setup in relation to the cost to produce the setup. This explains why microscopy is more broadly applied than NAA, and drives the direction of research and business, which work to improve analytical techniques (in all its aspects) to outperform competing analytical techniques. Technological challenges introduce inertia in this process, yet do not stop the evolution towards better techniques or the introduction of new techniques. From this perspective, it seems obvious that implementing the tube cell into a flexible and user-friendly setup, which overcomes the abovementioned shortcomings, would drastically increase the value of this setup. Commercialization of the setup is the next logical step towards broader acceptance of low-dispersion washout devices within the LA-ICP-MS application specialists.

2.7.1 ARIS

One of the first challenges was to minimize aerosol dispersion during transport through the transport line and mixing with the make-up gas. The mixing bulb currently supplied by Teledyne Photon Machines (Bozeman, MT, USA), abbreviated here as CMB consists of several m of 4 mm OD (outer ϕ), 2 mm ID (inner ϕ) PTFE tubing connected to a mixing bulb, which is connected to the injector inlet using another glass piece. The CleanShot® is placed either before or after the mixing bulb. In a first version, the two glass pieces were joined into a single new borosilicate piece (NMB) acting as a connector and mixing bulb simultaneously (Figure 24). The performance of the NMB, in combination with a 1.3 mm ID PTFE tubing was evaluated (Table 4) for 750 mm long tubing, which either had a moderate curvature ($\sim 300 \text{ mm}$ curvature radius), or no bend at all. The NMB outperforms the CMB (faster washout, higher repeatability), and is, in combination with a 1.3 mm ID tubing, unaffected by the moderate curvature radius of the tubing. For the 2 mm ID tubing, the larger ID produces more pronounced dispersion as a result of the bend, as the velocity gradient is larger across the cross-section of the tube, and the inner and outer streamlines in the bend have a larger difference in their path length.

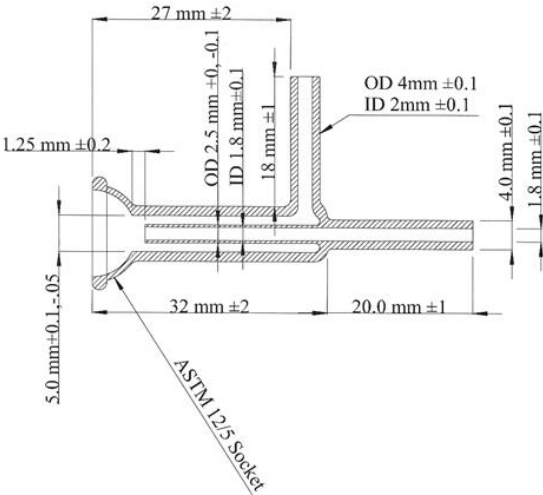


Figure 24 Schematic cross-section of the NMB.

Table 4 Peak statistics gathered from the ^{238}U signal response (2 ms dwell time) from 250 shots on NIST SRM 612 using a laser unit with a $20 \times 20 \mu\text{m}$ spot size operating at 5 Hz, with a fluence of 3.54 J cm^{-2} . The optimized carrier gas flow rate is 750 mL min^{-1} of He, and the make-up gas flow rate is 690 mL min^{-1} .

	Area [%]	RSD [%]	Max [%]	RSD [%]	FW0.1M [ms]	FW0.01M [ms]
CMB, 2 mm ID tube with large curvature	1.6×10^1	2.2×10^1	7.2×10^1	1.3×10^2		
CMB, 2 mm ID tube with no curvature	1.6×10^1	1.7×10^1	3.1×10^1	5.0×10^1		
CMB, 1.3mm ID tube with large curvature	1.7×10^1	1.6×10^1	5.7×10^1	1.0×10^2		
NMB, 1.3mm ID tube with large curvature	0.6×10^1	1.0×10^1	1.7×10^1	2.4×10^1		
NMB, 1.3 mm ID tube with no curvature	0.5×10^1	0.9×10^1	1.9×10^1	2.7×10^1		

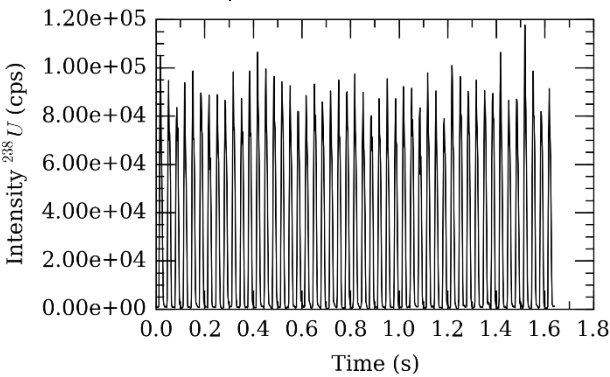


Figure 25 Raw pulse response of ^{238}U for the NMB with a 1.3 mm ID tubing, with the laser unit firing at a repetition rate of 30 Hz. At this frequency, the peaks are baseline separated at the 1 % level.

The production of the NMB is challenging and expensive: artifacts in the glass joints and the fragility of the inner capillary pose an issue. A second version of the NMB low-dispersion mixing bulb was manufactured in PEEK. Furthermore, the tubing material was also changed to PEEK due to its low surface friction coefficient, high chemical resilience, and high stiffness. Compared to PTFE tubing, PEEK tubing is less prone to twisting, which would deteriorate the peak profile. Flanged connectors were used to seal the tubing in place (VWR international, Radnor, PA, USA). Furthermore, 2 ICP-MS units were placed on hydraulic lifting tables (Figure 26), allowing the operator to align the ablation cell output and the injector inlet to the same height, reducing the distance between the ICP-MS and ablation cell, and eliminating the bend in the tubing as a result of height differences.



Figure 26 Photograph of the LA-ICP-MS instrumentation in the laboratory

A centering piece keeps the tubing on the center axis, allowing the make-up gas to form a concentric laminar flow around the carrier gas. The assembly is called the ARIS system. Technical drawings of the ARIS system are presented in the appendix (section A.2).

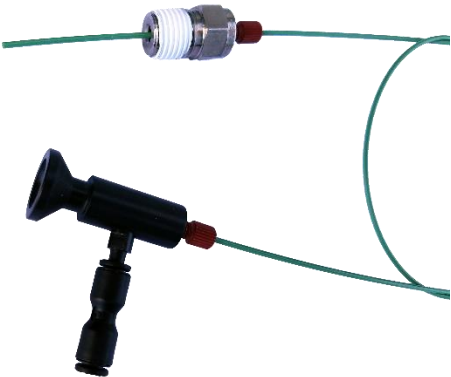


Figure 27 Photograph of a decoupled ARIS system.

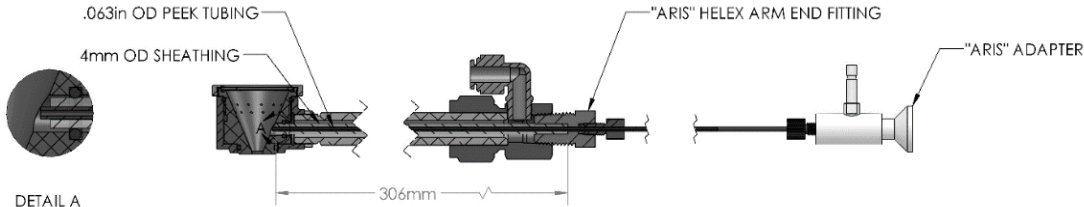


Figure 28 ARIS system, and its implementation together with the HELEX ablation cell.

The ARIS was launched on the commercial market in Q2-Q3 of 2016. It is supplied by Teledyne Photon Machines (Bozeman, MT, USA) for use with the HELEX 2 two-volume ablation cell. The ARIS performance exceeds that of the NMB (Figure 29) by a factor of 2, as a result of its optimized design.

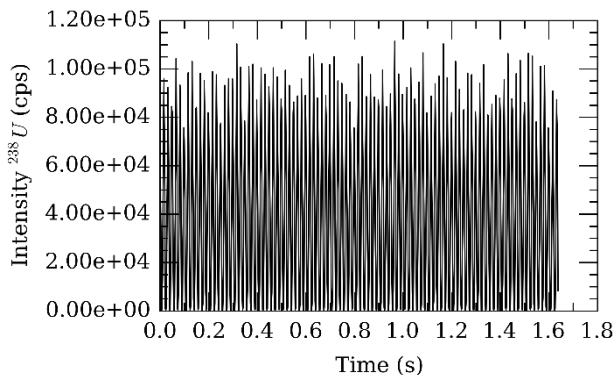


Figure 29 Raw pulse response of ^{238}U for the ARIS with a 0.75 mm ID tubing, with the laser firing at a repetition rate of 60 Hz. For this frequency, the peaks are baseline separated at FW0.01M.

2.7.2 ATS sample chamber

2.7.2.1 Design

The tube cell is in contact with the sample. This produces a number of issues: i) damage to the sample may occur when the material contacts the bottom of the cell, ii) the sample cannot be moved with respect to the cell, hence, only a small area of the sample can be imaged, and iii) it is difficult to position the cell over the desired area of interest. Hovering the cell above the sample would mitigate these problems. The shape and dimensions of the cell were altered to promote the performance of the cell. These improvements to the tube cell design are detailed in a patent application.¹⁴⁴ In order to prevent air from entering the tube cell, the sample and cell must be shielded from the atmosphere by means of an analytical air-tight chamber, as the carrier gas must be forced at a higher-than-atmospheric pressure into the outlet tubing. The ablation system must retain control of the sample position; hence a positioning stage must be present inside or outside the chamber. An analytical chamber in which the stages can reside was designed due to the intrinsic higher stage accuracy of a sample holder platform mechanically connect to a stage platform.

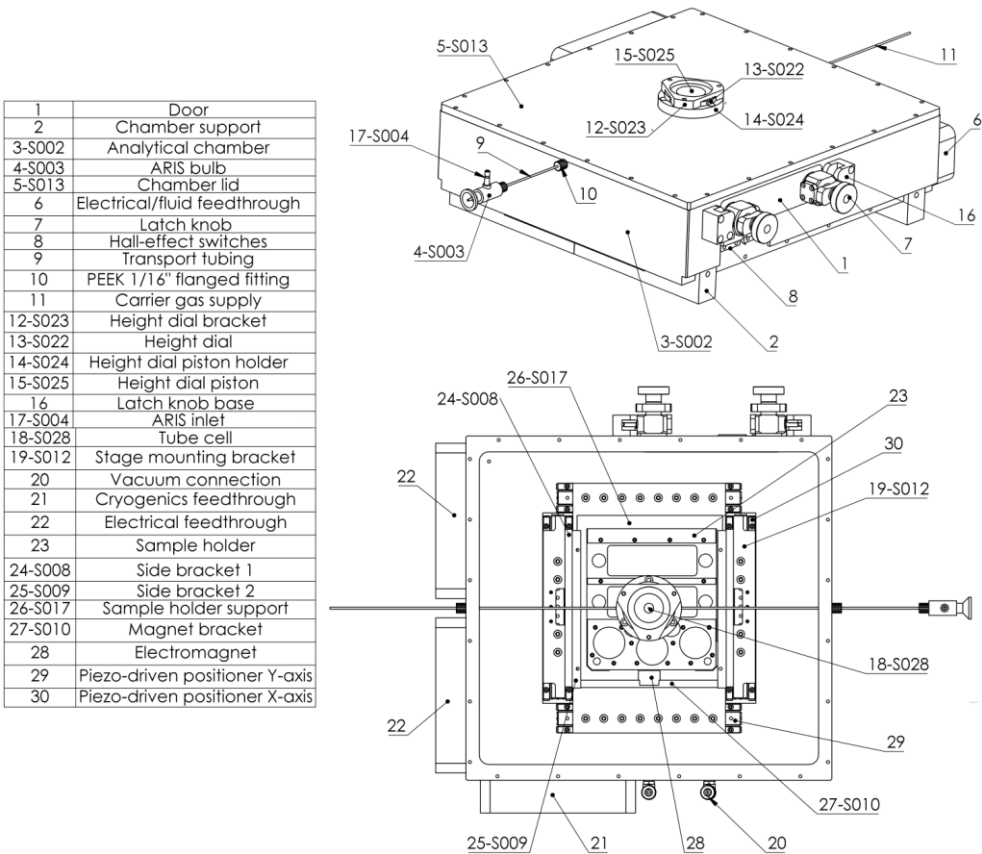


Figure 30 ATS sample chamber. Isometric and top views.

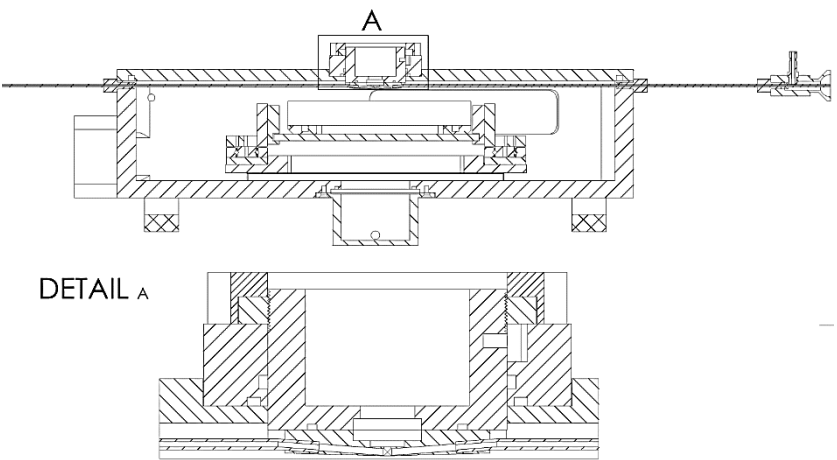


Figure 31 ATS sample chamber cross-section.

This system (Figure 30, Figure 31, and Figure 32) complies with many of the desired features described in Section 2.3. The chamber has external dimensions of $300 \times 280 \times 75 \text{ mm}^3$ and internal dimensions of $280 \times 260 \times 55 \text{ mm}^3$ and was machined from a solid block of 6061 Aluminium. The chamber (Figure 30.3-S002) houses an XY positioning system (Figure 30.29, Figure 30.30), which supports a platform (Figure 30.26) upon which a sample holder rests (Figure 30.23). The tube cell (Figure 30.18) can be lowered by a piston (Figure 30.15) which can be dialled (Figure 30.22) at a rate of $5 \mu\text{m}/\text{deg}$. This allows the operator to fine-tune the distance between the sample and the bottom aperture of the cell. Fine control on this distance is required, as it has a profound impact on the optimum gas settings and washout performance of the tube cell. Typically, this distance varies between 100-500 μm . The sample holder tray can be loaded with a sample holder ($110 \times 116 \times 21 \text{ mm}^3$) *via* the sample feedthrough door, located at the outward side of the chamber. An electromagnet holds the sample holder in place. The air and water vapour within the chamber can be removed, by means of an alternating evacuation/flushing sequence in approximately 25 minutes. The door of the chamber is sealed using two latch twist locks, and is interlocked by two hall-effect switches. Feedthrough flanges are present for the HV driving signal of the positioners. The stage consists of two SLC-24150 linear positioners (SMARACT GmbH, Oldenburg, Germany), which each have a range of 103 mm, step frequency of 18.5 kHz, and closed-loop bidirectional reproducibility of 150 nm. These stick-slip (ultrasonic) piezo motors have a minimum step width of 1 nm, and a maximum velocity of 20 mm s^{-1} . A piezo-stage controller is wired into the existing motion controller of the Analyte G2 ablation system. A polycarbonate lid allows the operator to view the sample in motion. Every port is sealed with an acrylonitrile butadiene rubber or ethylene propylene diene monomer rubber O-ring seal. A high-powered LED (325 lm) is mounted underneath the chamber, projecting transmitted light through the cell *via* a borosilicate window at the bottom of the chamber. Press-fit 6 mm connections allow the input and output of gasses. Additional feedthroughs are present for a high-current connector and cooling fluid, permitting a Peltier-type cooling system to be placed inside the chamber.

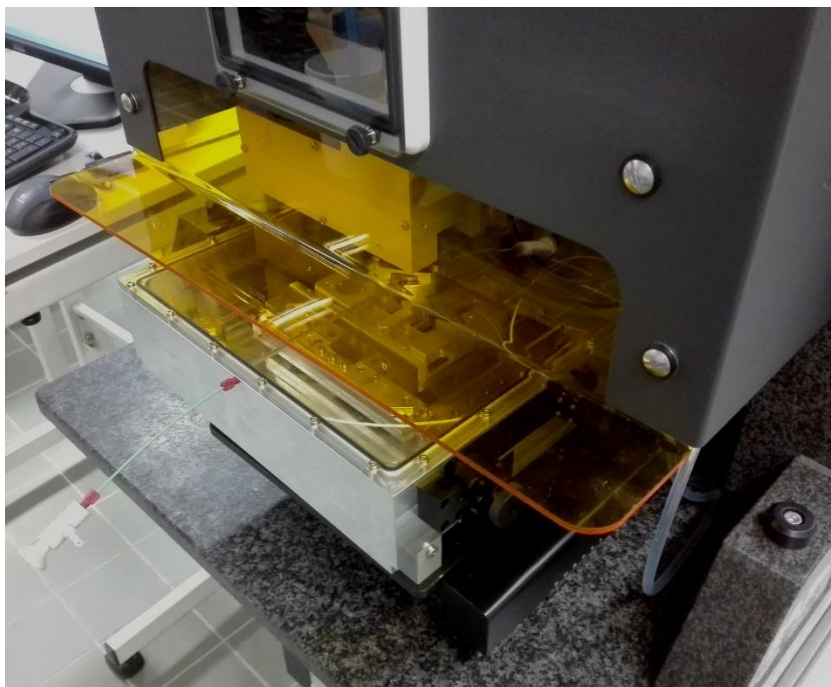


Figure 32 Photograph of the ATS sample chamber mounted into a Teledyne Photon Machines (Bozeman, MT, USA) Analyte G2 laser system.

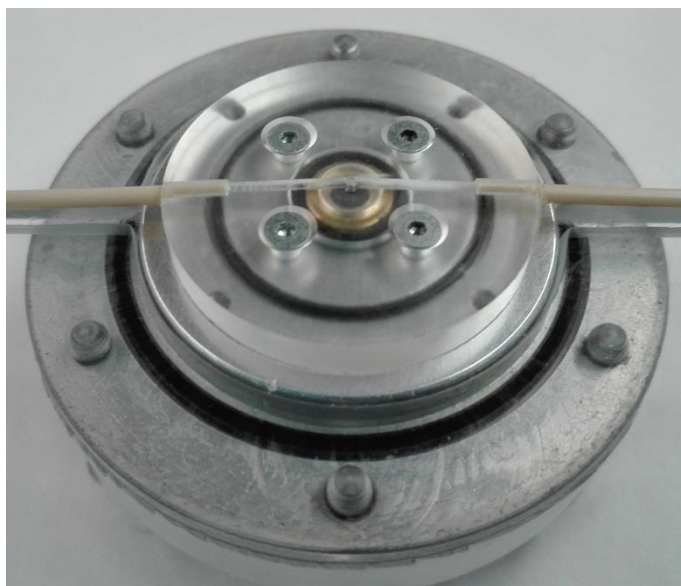


Figure 33 Photograph showing the bottom of the tube cell.

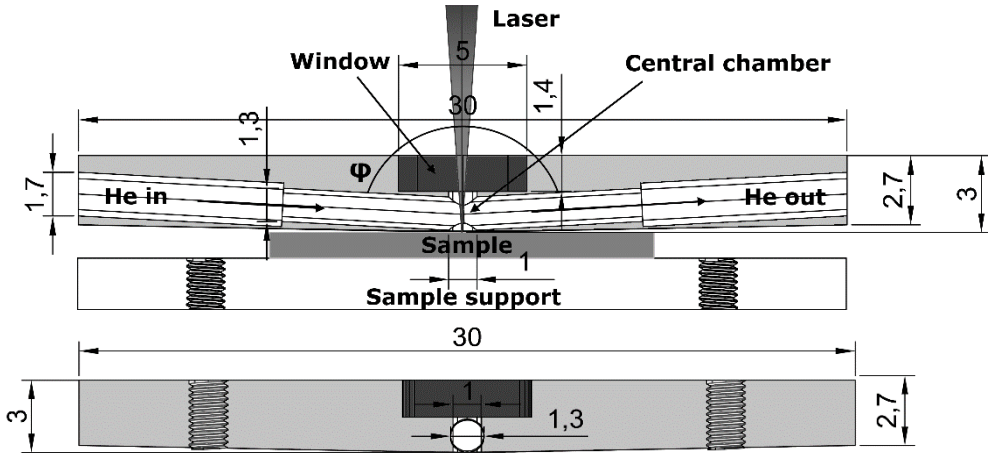


Figure 34 Sketch of the tube cell with optimized geometry.

2.7.2.2 Performance

The performance of the floating tube cell is similar to the performance that can be achieved with the stand-alone version of the tube cell, though further research is required to characterize and optimize its performance. Currently, the average pulse-response peak (over 1000 pulses) has a FW0.1M as low as 3.7 ± 0.5 ms (Figure 35). When operating the floating tube cell, the absolute pressure inside the cell reaches approximately 1.25×10^5 Pa.

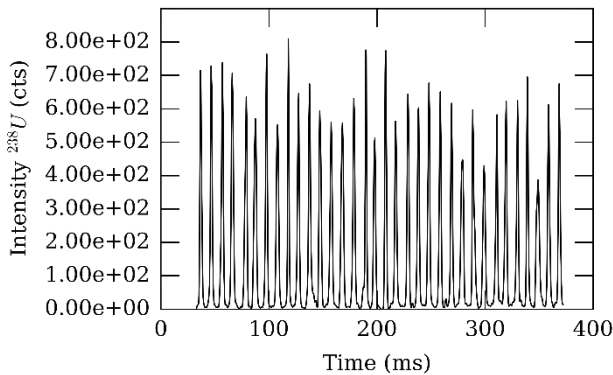


Figure 35 Raw pulse response of ^{238}U for the ATS sample chamber with tube cell and ARIS with a 1.0 mm ID tubing, with the laser unit firing at a repetition rate of 100 Hz. For this frequency, the peaks are baseline separated at FW0.01M.

2.8 Cryogenic low-profile stage

In the early 2000's, an interest towards the use of cryogenic conditions in the ablation cell was sparked due to the desire to readily analyze soft or wet samples *via* LA-ICP-MS. In an early work, Feldmann *et al.*¹⁴⁵ used a LN_2 flow, controlled *via* a solenoid valve on the dewar driven by a temperature controller. The results indicated that melting of the sample was no longer an issue. In literature, the benefits of cryogenic conditions for laser ablation-ICP-mass spectrometry

high-resolution imaging of biological tissues are described, *e.g.*, a reduced heat-affected zone and a reduction in melting at the crater surface, resulting in a more controlled crater size.^{145,146} Furthermore, biological samples can be frozen and cooled to sub-zero temperatures using thermoelectric cooling (TEC), to prevent migration and diffusion of species in a liquid environment, and sample degradation. Although the benefits of cryogenic conditions in LA-ICP-MS are described, no detailed study has been conducted relating to the underlying mechanisms of the observations. Additionally, freezing the sample increases the ablation threshold and prevents the liquid content of the cellular material from leaking from its membrane container.¹⁴⁷ Ablation in cryogenic conditions may also have benefits for fluid inclusion analysis.^{148,149} Frozen samples, such as ice cores, require cryogenic cooling to be kept stable during analysis.¹⁵⁰⁻¹⁵²

In this work, a low-profile cryogenic stage was designed, which sets itself apart from previous works by i) the way it can be incorporated in the analytical chamber: the TEC unit can be mounted on the positioning stage, inside the ablation chamber of a low-dispersion tube cell and ii) by its features: the temperature can be registered and a feedback loop provides a more accurate temperature control than most commercially available packages. Although there have been attempts to optimize the cryo-cooled ablation cell geometry for faster washout¹⁵³, the performance of these cells still lacks behind the 3rd generation ablation cells. A TEC unit (Figure 36, Figure 39), comprising a stack of 2 70W Peltier elements $40 \times 40 \times 40 \text{ mm}^3$ in size, a water-cooling circuit, and a temperature feedback-control system, was built and developed in-house.

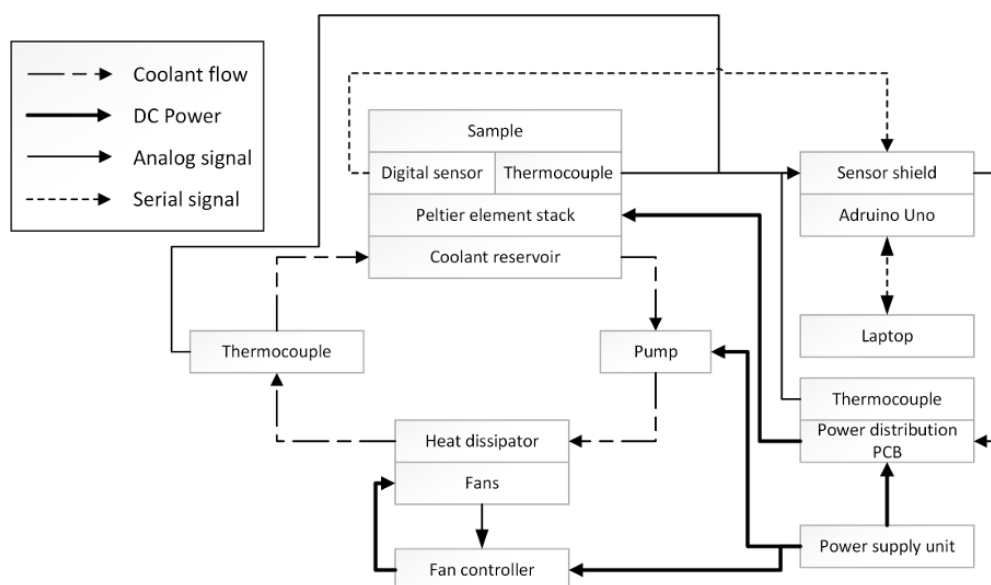


Figure 36 Schematic representation of the entire cryogenic system.

The elements are powered by a dedicated 450W (active power factor correction) 12 V DC low ripple power supply, controlled using N-channel logic level MOSFET *via* pulse width modulation (PWM). Two printed circuit boards (PCBs) were produced: a shield for a microcontroller,

containing a temperature sensor array, and a stand-alone PCB dedicated to power management *via* MOSFETS. The PCBs were designed and assembled in-house. The PWM signal is produced by a microcontroller (Arduino Uno, Italy), which can be interfaced to a laptop using a USB connection. Using this connection, a custom temperature program, scripted in the ARDUINO/C language, using a proportional-integral-derivative (PID) controller-type feedback loop, was transferred. Furthermore, the serial data are forwarded to a Python 2.7 script, which allows to monitor and plot the temperature data on-line. The entire cooling assembly is meant to be encapsulated in the dry helium environment of the ablation chamber to prevent condensation of water vapor onto the electronic components. The Peltier element themselves generate heat as a result of the thermoelectric effect which displaces heat. The elements were cooled using a closed-loop liquid cooling system (Alphacool International GmbH, Braunschweig, Germany), mounted externally in a separate housing. The elements were placed on a 2 mm thick Cu platform, which is part of a low-profile, high-performance cooling stage. The $56 \times 56 \text{ mm}^2$ Cu platform contains 0.5 mm channels, specifically machined to increase the surface contact area from $3 \times 10^3 \text{ mm}^2$ to 10^4 mm^2 . The connection is sealed by an NBR ring, and the threads for two 6 mm external diameter fluid feedthroughs were machined into the aluminum 6061 block. The block is fastened onto an exchangeable base plate with a pattern of fasteners specific to the translation stage, allowing the setup to be mounted onto any type of imaging setup. The sample mount is held down by a 3D printed ABS bracket, which has a hollow internal honeycomb structure to maximize thermal isolation. The coolant (a water-based fluid) is pumped towards a heat dissipater, which is itself cooled by air using six 120 mm fans. An extensive temperature control program was elaborated, which allows individual Peltier elements to be controlled. Independent thermocouples on the coolant pump and a fan speed controller are tied into the scripting, as a safety measure, and to detect thermal anomalies in the water cooling system. The sample temperature is monitored to a resolution of 0.06°C *via* up to 3 independent digital temperature sensors of the DS1820 type (B+B Thermo-Technik GmbH, Germany; range: $[-55^\circ\text{C}, +125^\circ\text{C}]$), which can interface to the micro-controller using the Dallas Temperature Library. The TEC unit is designed to cool samples down to 253 K (-20.15°C) (Figure 37). The system is capable of cooling down to $\sim 235 \text{ K}$ (-38.17°C) (Figure 38). The sensor signal, cooling fluid and power are run through a vacuum feedthrough into the ablation cell. The PID control-loop cools the system down to -25.0°C in a controlled way in approximately 8 minutes. The coolant temperature was measured at the outlet of the heat dissipater.

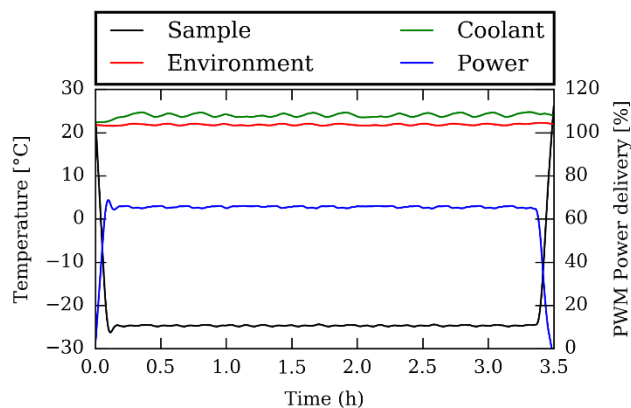


Figure 37 Transient profile of the temperature monitor status for a set point at -25.0°C . A run time of 3h would correspond with the time required to map a large sample area.

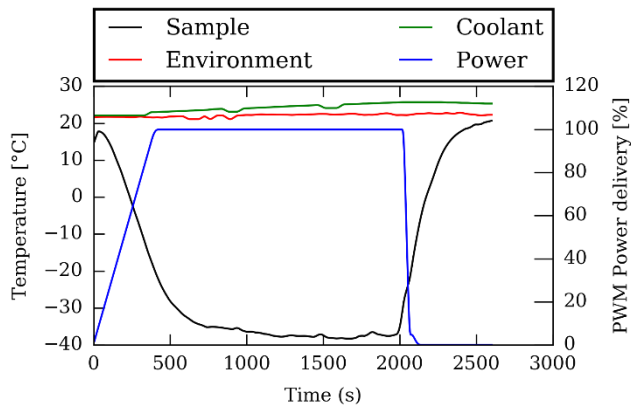


Figure 38 Transient profile of the temperature monitor status for a power delivery of 100%. At this level, the power-efficiency of the Peltier elements is significantly lower.

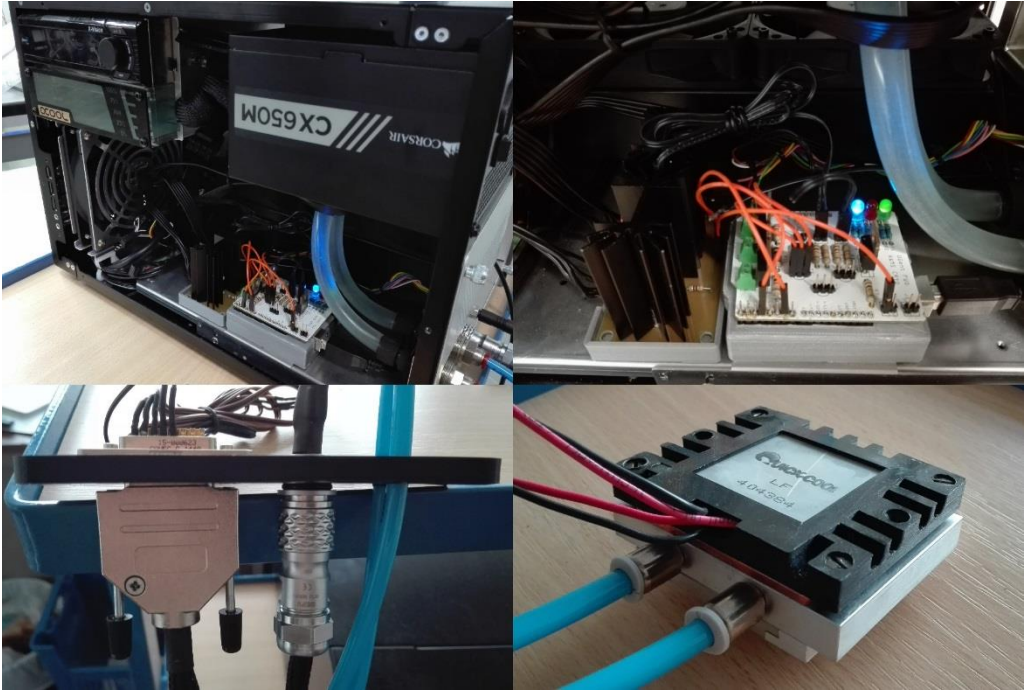


Figure 39 Compilation of photographs of different parts of the cryogenic cooling unit.

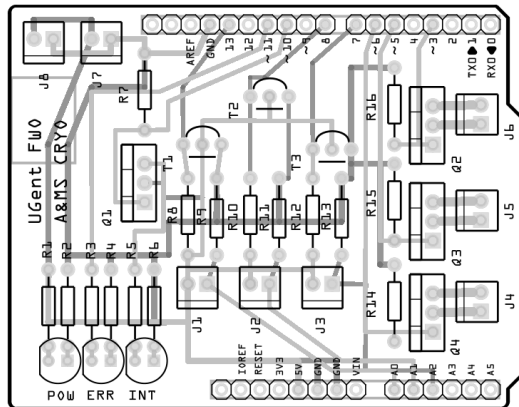


Figure 40 Temperature control shield for the Arduino Uno microcontroller. Light gray lanes are at the top Cu layer level of the PCB; dark gray lanes are in the bottom Cu layer level of the PCB.

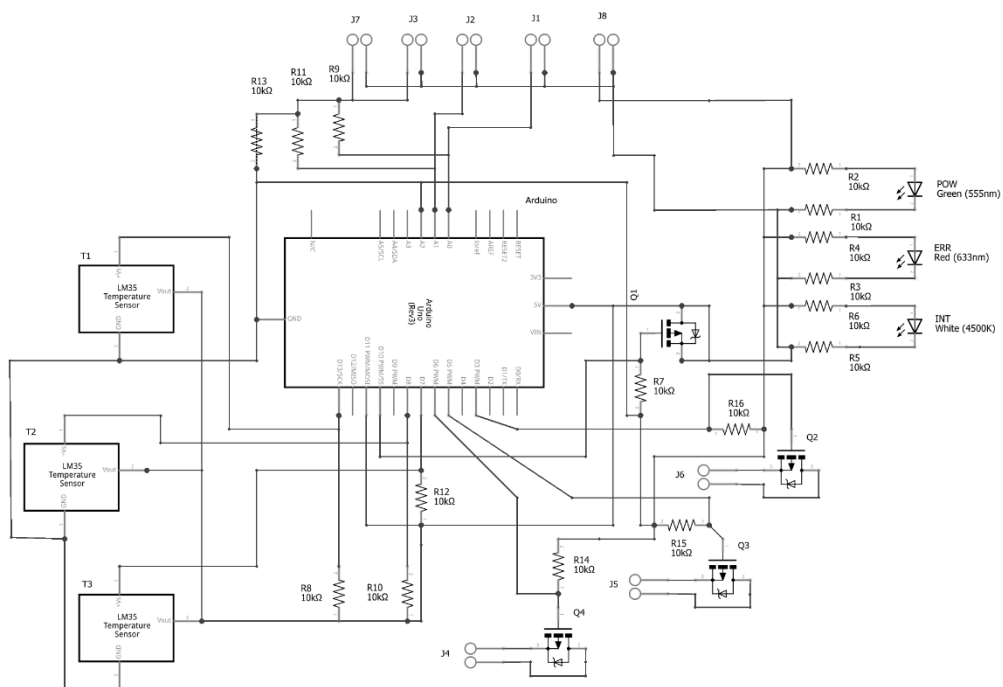


Figure 41 Electronic scheme of the temperature control shield.

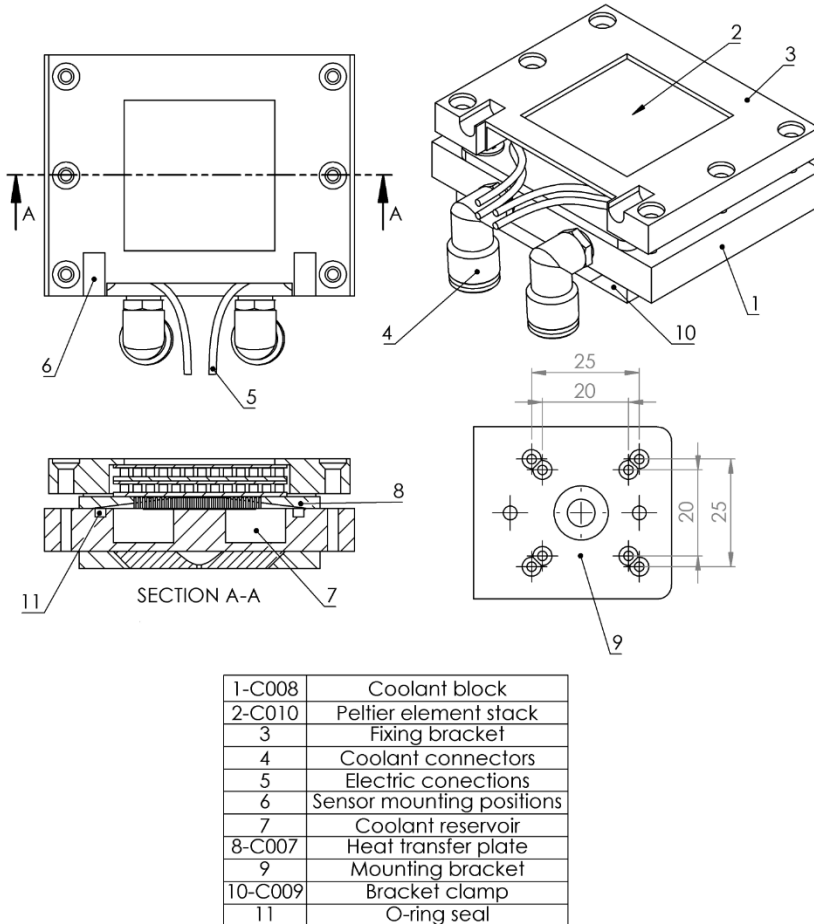


Figure 42 Annotated CAD rendering of the TEC block. Technical drawings for each part of the TEC unit can be found in the appendix (section A.2).

2.9 Conclusions

In this chapter, the development of an aerosol transport system was described. A low-dispersion mixing bulb, which enables the isolation of single pulse response peaks at frequencies of up to 60 Hz, was developed, tested and commercialized. Based on theoretical considerations, the tubing length and diameter were optimized to allow for evacuation of the HELEX system, whilst ensuring a high mean carrier fluid velocity. A newly developed low-dispersion ablation tube cell permits separation of individual signal peaks generated at pulse repetition rates up to 200-300 Hz. This allows for fast and sensitive line scanning with high lateral resolution, circumventing issues related to peak broadening due to impaired aerosol washout as generally encountered in ablation cells in use for continuous laser ablation. Despite its simplicity, the tube cell constitutes an ideal geometry in which to capture the aerosol plume. CFD indicates the formation of multiple zones of different fluid velocity when multiple inlets are

introducing carrier gas in the central aperture. The current dimensions of the cell are at their limit: a significantly smaller cell would result in highly energetic particles impacting the window, low visibility through the central aperture, mechanical failure, and/or the Reynolds number would exceed a critical value for turbulence. The LA-induced shockwave reflects on the walls of a tube cell and builds up a high-density gas buffer zone near the window, which has a momentum towards the surface. An analytical chamber was built, in which the tube cell hovers above the sample. The chamber can house large samples, up to $100 \times 100 \times 15 \text{ mm}^3$ in size. The performance for this configuration is similar to the performance obtained for the stand-alone tube cell. A cryogenic stage was developed to cool samples down to -25°C . This extends the capabilities of the cell significantly for specific geological and biological applications.

2.10 Bibliography

- (1) Van Malderen, S. J. M.; Managh, A. J.; Sharp, B. L.; Vanhaecke, F. *J. Anal. At. Spectrom.* **2016**, *31*, 423-439.
- (2) van Elteren, J. T.; Izmer, A.; Šala, M.; Orsega, E. F.; Šelih, V. S.; Panighello, S.; Vanhaecke, F. *J Anal Atom Spectrom* **2013**, *28*, 994-1004.
- (3) Drescher, D.; Giesen, C.; Traub, H.; Panne, U.; Kneipp, J.; Jakubowski, N. *Anal Chem* **2012**, *84*, 9684-9688.
- (4) van Elteren, J. T.; Vanhaecke, F. *J. Anal. At. Spectrom.* **2016**, *31*, 1998-2004.
- (5) van Elteren, J. T.; Izmer, A.; Selih, V. S.; Vanhaecke, F. *Anal Chem* **2016**, *88*, 7413-7420.
- (6) Takafumi, H., Vanhaecke, F.; Degryse, P., Eds.; Wiley-VCH, 2012.
- (7) Kuhn, H. R. *Laser Ablation ICP-MS: Fundamental investigations on aerosols generated by laser ablation at ambient pressure, Ph.D. thesis*; ETH Zurich, 2005.
- (8) Pisonero, J.; González-Gago, C.; Iglesias, M.; Cuervo, R.; Blanco, D.; Stoll, H.; Bordel, N. In *European Workshop on Laser ablation 2016*; Ljubljana, Slovenia, 2016.
- (9) Gurevich, E. L.; Hergenroder, R. *J Anal Atom Spectrom* **2007**, *22*, 1043-1050.
- (10) Wang, H. A.; Grolimund, D.; Giesen, C.; Borca, C. N.; Shaw-Stewart, J. R.; Bodenmiller, B.; Gunther, D. *Anal Chem* **2013**, *85*, 10107-10116.
- (11) Lindner, H.; Autrique, D.; Pisonero, J.; Gunther, D.; Bogaerts, A. *J Anal Atom Spectrom* **2010**, *25*, 295-304.
- (12) Asogan, D.; Sharp, B. L.; O' Connor, C. J. P.; Green, D. A.; Hutchinson, R. W. *J Anal Atom Spectrom* **2009**, *24*, 917-923.
- (13) Leach, A. M.; Hieftje, G. M. *Applied Spectroscopy* **2002**, *56*, 62-69.
- (14) Müller, W.; Shelley, M.; Miller, P.; Broude, S. *J Anal Atom Spectrom* **2009**, *24*, 209.
- (15) Autrique, D.; Bogaerts, A.; Lindner, H.; Garcia, C. C.; Niemax, K. *Spectrochimica Acta Part B: Atomic Spectroscopy* **2008**, *63*, 257-270.
- (16) Lindner, H.; Bogaerts, A. *Spectrochimica Acta Part B: Atomic Spectroscopy* **2011**, *66*, 421-431.

- (17) Asogan, D.; Sharp, B. L.; O'Connor, C. J. P.; Green, D. A.; Wilkins, J. *J Anal Atom Spectrom* **2011**, 26, 631-634.
- (18) Aghaei, M.; Bogaerts, A. *J Anal Atom Spectrom* **2016**, 31, 631-641.
- (19) Monticelli, D.; Gurevich, E. L.; Hergenroder, R. *J Anal Atom Spectrom* **2009**, 24, 328-335.
- (20) Gundlach-Graham, A.; Burger, M.; Allner, S.; Schwarz, G.; Wang, H. A.; Gyr, L.; Grolimund, D.; Hattendorf, B.; Gunther, D. *Anal Chem* **2015**, 87, 8250-8258.
- (21) Van Malderen, S. J. M.; van Elteren, J. T.; Vanhaecke, F. *J. Anal. At. Spectrom.* **2014**, 30, 119-125.
- (22) Douglas, D. N.; Managh, A. J.; Reid, H. J.; Sharp, B. L. *Anal Chem* **2015**, 87, 11285-11294.
- (23) Hirata, T. *Analytical Sciences* **2007**, 23, 1195-1201.
- (24) Wu, B.; Becker, J. S. *International Journal of Mass Spectrometry* **2012**, 323, 34-40.
- (25) Monk, S. M.; Lev, S. M. *J Anal Atom Spectrom* **2013**, 28, 274-279.
- (26) Becker, J. S.; Matusch, A.; Wu, B. *Anal Chim Acta* **2014**, 835, 1-18.
- (27) Bleiner, D.; Gunther, D. *J Anal Atom Spectrom* **2001**, 16, 449-456.
- (28) Bleiner, D.; Bogaerts, A. *Spectrochimica Acta Part B: Atomic Spectroscopy* **2007**, 62, 155-168.
- (29) Pisonero, J.; Fliegel, D.; Gunther, D. *J Anal Atom Spectrom* **2006**, 21, 922-931.
- (30) Kouris, C.; Tsamopoulos, J. *Chemical Engineering Science* **2000**, 55, 5509-5530.
- (31) Grigoriev, R.; Schuster, H. G. *Transport and Mixing in Laminar Flows: From Microfluidics to Oceanic Currents*; Wiley-VCH: Weinheim, Germany, 2012.
- (32) Garcia, C. C.; Lindner, H.; Niemax, K. *Spectrochimica Acta Part B: Atomic Spectroscopy* **2007**, 62, 13-19.
- (33) Bleiner, D. *Optimization of a Laser Ablation Inductively Coupled Plasma Mass Spectrometry System for the Detection of Short Transient Signals*, Ph.D. thesis. ETH Zurich 2002.
- (34) Summerfield, L. In *Winter Conference on Plasma Spectrochemistry: Winter Conference on Plasma Spectrochemistry*, Tucson, Arizona, USA, 2012.
- (35) Gusarov, A. V.; Smurov, I. *J. Phys. D- Appl. Phys.* **2001**, 34, 1147-1156.
- (36) Bleiner, D.; Lippert, T. *Journal of Applied Physics* **2009**, 106, 123301.
- (37) Eggins, S. M.; Kinsley, L. P. J.; Shelley, J. M. G. *Appl. Surf. Sci.* **1998**, 127-129, 278-286.
- (38) Leung, A. P. K.; Chan, W. T.; Mao, X. L.; Russo, R. E. *Anal Chem* **1998**, 70, 4709-4716.
- (39) Leung, A. P. K.; Chan, W. T.; Mao, X. L.; Russo, R. E. *Anal Chem* **1998**, 70, 4709-4716.
- (40) Bleiner, D.; Bogaerts, A. *J Anal Atom Spectrom* **2006**, 21, 1161-1174.
- (41) Garcia, C. C.; Lindner, H.; Niemax, K. *J Anal Atom Spectrom* **2009**, 24, 14-26.

- (42) Amoruso, S.; Schou, J.; Lunney, J. G. *Applied Physics A* **2008**, 92, 907-911.
- (43) Popov, A. M.; Colao, F.; Fantoni, R. *J Anal Atom Spectrom* **2009**, 24, 602-604.
- (44) Popov, A. M.; Colao, F.; Fantoni, R. *J Anal Atom Spectrom* **2010**, 25, 837-848.
- (45) Guo, L. B.; Hu, W.; Zhang, B. Y.; He, X. N.; Li, C. M.; Zhou, Y. S.; Cai, Z. X.; Zeng, X. Y.; Lu, Y. F. *Optics express* **2011**, 19, 14067-14075.
- (46) Wang, Z.; Hou, Z.; Lui, S.-l.; Jiang, D.; Liu, J.; Li, Z. *Optics express* **2012**, 20, A1011-A1018.
- (47) Choi, S. J.; Lee, K.-j.; Yoh, J. J. *Spectrochimica Acta Part B: Atomic Spectroscopy* **2014**, 97, 113-117.
- (48) Li, C. M.; Guo, L. B.; He, X. N.; Hao, Z. Q.; Li, X. Y.; Shen, M.; Zeng, X. Y.; Lu, Y. F. *J Anal Atom Spectrom* **2014**, 29, 638-643.
- (49) Lindner, H.; Autrique, D.; Garcia, C. C.; Niemax, K.; Bogaerts, A. *Anal Chem* **2009**, 81, 4241-4248.
- (50) Tognoni, E.; Cristoforetti, G. *J Anal Atom Spectrom* **2014**, 29, 1318-1338.
- (51) Zeng, X.; Mao, X.; Mao, S. S.; Wen, S.-B.; Greif, R.; Russo, R. E. *Applied Physics Letters* **2006**, 88, 061502.
- (52) Bleiner, D.; Bogaerts, A. *Spectrochimica Acta Part B: Atomic Spectroscopy* **2006**, 61, 421-432.
- (53) Russo, R. E.; Mao, X. L.; Borisov, O. V.; Liu, H. C. *J Anal Atom Spectrom* **2000**, 15, 1115-1120.
- (54) Guillong, M.; Gunther, D. *J Anal Atom Spectrom* **2002**, 17, 831-837.
- (55) Aeschliman, D. B.; Bajic, S. J.; Baldwin, D. P.; Houk, R. S. *Anal Chem* **2004**, 76, 3119-3125.
- (56) Krosiakova, I.; Gunther, D. *J Anal Atom Spectrom* **2007**, 22, 51-62.
- (57) Saetveit, N. J.; Bajic, S. J.; Baldwin, D. P.; Houk, R. S. *J Anal Atom Spectrom* **2008**, 23, 54-61.
- (58) Gaboardi, M.; Humayun, M. *J Anal Atom Spectrom* **2009**, 24, 1188-1197.
- (59) Mikova, J.; Kosler, J.; Longerich, H. P.; Wiedenbeck, M.; Hanchar, J. M. *J Anal Atom Spectrom* **2009**, 24, 1244-1252.
- (60) Ohata, M.; Tabersky, D.; Glaus, R.; Koch, J.; Hattendorf, B.; Gunther, D. *J Anal Atom Spectrom* **2014**, 29, 1345-1353.
- (61) Zhang, S.; He, M.; Yin, Z.; Zhu, E.; Hang, W.; Huang, B. *J. Anal. At. Spectrom.* **2016**.
- (62) Koch, J.; Feldmann, I.; Jakubowski, N.; Niemax, K. *Spectrochimica Acta Part B: Atomic Spectroscopy* **2002**, 57, 975-985.
- (63) Kuhn, H.-R.; Gunther, D. *J Anal Atom Spectrom* **2004**, 19, 1158-1164.
- (64) Kuhn, H. R.; Guillong, M.; Gunther, D. *Analytical and bioanalytical chemistry* **2004**, 378, 1069-1074.
- (65) Halicz, L.; Gunther, D. *J Anal Atom Spectrom* **2004**, 19, 1539-1545.
- (66) Liu, X. R.; Horlick, G. *Spectrochimica Acta Part B: Atomic Spectroscopy* **1995**, 50, 537-548.
- (67) Tanner, M.; Gunther, D. *J Anal Atom Spectrom* **2005**, 20, 987-989.
- (68) Tanner, M.; Gunther, D. *J Anal Atom Spectrom* **2006**, 21, 941-947.

- (69) Tanner, M.; Gunther, D. *J Anal Atom Spectrom* **2007**, 22, 1189-1192.
- (70) Tanner, M.; Gunther, D. *Analytical and bioanalytical chemistry* **2008**, 391, 1211-1220.
- (71) O'Connor, C.; Landon, M. R.; Sharp, B. L. *J Anal Atom Spectrom* **2007**, 22, 273-282.
- (72) Jeong, S. H.; Borisov, O. V.; Yoo, J. H.; Mao, X. L.; Russo, R. E. *Anal Chem* **1999**, 71, 5123-5130.
- (73) Outridge, P. M.; Doherty, W.; Gregoire, D. C. *Spectrochim Acta B* **1997**, 52, 2093-2102.
- (74) Günther, D.; Hattendorf, B. *TrAC Trends in Analytical Chemistry* **2005**, 24, 255-265.
- (75) Bleiner, D.; Altorfer, H. *J Anal Atom Spectrom* **2005**, 20, 754-756.
- (76) Koch, J.; Schlamp, S.; Rösigen, T.; Fliegel, D.; Günther, D. *Spectrochimica Acta Part B: Atomic Spectroscopy* **2007**, 62, 20-29.
- (77) Horn, I.; Gunther, D. *Appl. Surf. Sci.* **2003**, 207, 144-157.
- (78) Niehaus, R.; Sperling, M.; Karst, U. *J Anal Atom Spectrom* **2015**, 30, 2056-2065.
- (79) Vogel, A.; Venugopalan, V. *Chemical Reviews* **2003**, 103, 577-644.
- (80) Tanner, M.; Gunther, D. *Anal Chim Acta* **2009**, 633, 19-28.
- (81) Hobbs, S. E.; Olesik, J. W. *Anal Chem* **1992**, 64, 274-283.
- (82) Nomizu, T.; Hayashi, H.; Hoshino, N.; Tanaka, T.; Kawaguchi, H.; Kitagawa, K.; Kaneco, S. *J Anal Atom Spectrom* **2002**, 17, 592-595.
- (83) Streng, I.; Engelhard, C. *J. Anal. At. Spectrom.* **2015**.
- (84) Managh, A. J. *Single cell tracking of therapeutic cells using laser ablation - inductively coupled plasma - mass spectrometry, Ph.D. thesis*; Loughborough University, 2014.
- (85) Willie, S.; Mester, Z.; Sturgeon, R. E. *J Anal Atom Spectrom* **2005**, 20, 1358-1364.
- (86) Perkin Elmer. NexION® 350 ICP-MS [06/09/2015]. Available from: http://www.perkinelmer.co.uk/CMSResources/Images/44-157289BRO_NexION350ICPMSBrochure.pdf.
- (87) Agilent Technologies. Agilent 7900 ICP-MS [06/09/2015]. Available from: <https://www.agilent.com/cs/library/brochures/5991-3719EN.pdf>.
- (88) Thermo Scientific. iCAP Q ICP-MS [06/09/2015]. Available from: <http://www.thermoscientific.com/content/dam/tfs/ATG/CMD/cmd-documents/bro/spec/ea/icp-ms/PS-43096-ICP-MS-iCAP-Q-PS43096-EN.pdf>.
- (89) Analytik Jena. PlasmaQuant® MS [06/09/2015]. Available from: https://www.analytik-jena.de/fileadmin/content/pdf_analytical_instrumentation/ICP/ICP-MS/Br_PlasmaQuant_MS_en.pdf.
- (90) Degueldre, C.; Favarger, P. Y. *Talanta* **2004**, 62, 1051-1054.
- (91) Ramkorun-Schmidt, B.; Pergantis, S. A.; Esteban-Fernandez, D.; Jakubowski, N.;

Gunther, D. *Anal Chem* **2015**, *87*, 8687-8694.

(92) Walder, A. J.; Freedman, P. A. *J Anal Atom Spectrom* **1992**, *7*, 571-575.

(93) Craig, G. *Improving the utility of LA-ICP-MS for isotope ratio analyses of single particles with application to uranium oxide*, Ph.D. thesis. Loughborough University 2015.

(94) Myers, D. P.; Hieftje, G. M. *Microchemical Journal* **1993**, *48*, 259-277.

(95) Borovinskaya, O.; Hattendorf, B.; Tanner, M.; Gschwind, S.; Günther, D. *J. Anal. At. Spectrom.* **2013**, *28*, 226-233.

(96) Gundlach-Graham, A.; Dennis, E. A.; Ray, S. J.; Enke, C. G.; Barinaga, C. J.; Koppenaal, D. W.; Hieftje, G. M. *J. Anal. At. Spectrom.* **2015**, *30*, 139-147.

(97) Giesen, C.; Wang, H. A.; Schapiro, D.; Zivanovic, N.; Jacobs, A.; Hattendorf, B.; Schuffler, P. J.; Grolimund, D.; Buhmann, J. M.; Brandt, S.; Varga, Z.; Wild, P. J.; Gunther, D.; Bodenmiller, B. *Nature methods* **2014**, *11*, 417-422.

(98) GBC Scientific Equipment Pty Ltd. OptiMass 9500 ICP-TOFMS [06/09/2015]. Available from: http://www.gbcsoci.com/products/icp_tof/optimass.asp.

(99) Felton, J. A.; Schilling, G. D.; Ray, S. J.; Sperline, R. P.; Denton, M. B.; Barinaga, C. J.; Koppenaal, D. W.; Hieftje, G. M. *J. Anal. At. Spectrom.* **2011**, *26*, 300-304.

(100) Lou, X.; Zhang, G.; Herrera, I.; Kinach, R.; Ornatsky, O.; Baranov, V.; Nitz, M.; Winnik, M. A. *Angewandte Chemie* **2007**, *46*, 6111-6114.

(101) Waentig, L.; Jakubowski, N.; Hardt, S.; Scheler, C.; Roos, P. H.; Linscheid, M. W. *J Anal Atom Spectrom* **2012**, *27*, 1311-1320.

(102) Fluidigm. Maxpar® reagents [29/08/2015]. Available from: <http://maxpar.fluidigm.com/product-catalog-metal.php>.

(103) Hutchinson, R. W.; Cox, A. G.; McLeod, C. W.; Marshall, P. S.; Harper, A.; Dawson, E. L.; Howlett, D. R. *Analytical biochemistry* **2005**, *346*, 225-233.

(104) Managh, A. J.; Hutchinson, R. W.; Riquelme, P.; Broichhausen, C.; Wege, A. K.; Ritter, U.; Ahrens, N.; Koehl, G. E.; Walter, L.; Florian, C.; Schlitt, H. J.; Reid, H. J.; Geissler, E. K.; Sharp, B. L.; Hutchinson, J. A. *Journal of immunology* **2014**, *193*, 2600-2608.

(105) Waentig, L.; Techritz, S.; Jakubowski, N.; Roos, P. H. *Analyst* **2013**, *138*, 6309-6315.

(106) Seuma, J.; Bunch, J.; Cox, A.; McLeod, C.; Bell, J.; Murray, C. *Proteomics* **2008**, *8*, 3775-3784.

(107) Giesen, C.; Waentig, L.; Mairinger, T.; Drescher, D.; Kneipp, J.; Roos, P. H.; Panne, U.; Jakubowski, N. *J Anal Atom Spectrom* **2011**, *26*, 2160-2165.

(108) Giesen, C.; Mairinger, T.; Khoury, L.; Waentig, L.; Jakubowski, N.; Panne, U. *Anal Chem* **2011**, *83*, 8177-8183.

(109) Moenke-Blankenburg, L.; Gackle, M.; Gunther, D.; Kammel, J. *Processes of laser ablation and vapor transport to the ICP*; Royal Soc Chemistry: Cambridge, United Kingdom, 1990; Vol. 85, p 1-17.

- (110) Bleiner, D.; Belloni, F.; Doria, D.; Lorusso, A.; Nassisi, V. *J Anal Atom Spectrom* **2005**, *20*, 1337-1343.
- (111) Triglav, J.; van Elteren, J. T.; Selih, V. *S. Anal Chem* **2010**, *82*, 8153-8160.
- (112) Wang, H. A. O.; Grolimund, D.; Van Loon, L. R.; Barmettler, K.; Borca, C. N.; Aeschmann, B.; Guenther, D. *Anal Chem* **2011**, *83*, 6259-6266.
- (113) Plotnikov, A.; Vogt, C.; Wetzig, K. *J Anal Atom Spectrom* **2002**, *17*, 1114-1120.
- (114) Gäckle, M.; Merten, D. *Spectrochimica Acta Part B: Atomic Spectroscopy* **2004**, *59*, 1893-1905.
- (115) Gäckle, M.; Merten, D. *Spectrochimica Acta Part B: Atomic Spectroscopy* **2005**, *60*, 1517-1530.
- (116) Plotnikov, A.; Vogt, C.; Wetzig, K.; Kyriakopoulos, A. *Spectrochimica Acta Part B: Atomic Spectroscopy* **2008**, *63*, 474-483.
- (117) Guillion, M.; Horn, I.; Gunther, D. *J Anal Atom Spectrom* **2003**, *18*, 1224-1230.
- (118) Claverie, F.; Pécheyran, C.; Mounicou, S.; Ballihaut, G.; Fernandez, B.; Alexis, J.; Lobinski, R.; Donard, O. F. X. *Spectrochimica Acta Part B: Atomic Spectroscopy* **2009**, *64*, 649-658.
- (119) Van Malderen, S. J. M.; van Elteren, J. T.; Vanhaecke, F. *Anal Chem* **2015**, *87*, 6125-6132.
- (120) Russo, R. E.; Mao, X. L.; Gonzalez, J. J.; Mao, S. S. *J Anal Atom Spectrom* **2002**, *17*, 1072-1075.
- (121) Bleiner, D. In *Mineralogical Association of Canada Short Course Series* Sylvester, P., Ed.; Mineralogical Association of Canada: Vancouver, Canada, 2008, pp 35-52.
- (122) Peng, S.; Hu, Q. H.; Ewing, R. P.; Liu, C. X.; Zachara, J. M. *Environmental Science & Technology* **2012**, *46*, 2025-2032.
- (123) Gratuze, B. *J Archaeol Sci* **1999**, *26*, 869-881.
- (124) Chirinos, J. R.; Oropeza, D. D.; Gonzalez, J. J.; Hou, H.; Morey, M.; Zorba, V.; Russo, R. E. *J Anal Atom Spectrom* **2014**, *29*, 1292-1298.
- (125) Leach, A. M.; Hieftje, G. M. *J Anal Atom Spectrom* **2000**, *15*, 1121-1124.
- (126) Burger, M.; Gundlach-Graham, A.; Allner, S.; Schwarz, G.; Wang, H. A.; Gyr, L.; Burgener, S.; Hattendorf, B.; Grolimund, D.; Gunther, D. *Anal Chem* **2015**, *87*, 8259-8267.
- (127) Jackson, S. E. In *Mineralogical Association of Canada Short Course Series* Sylvester, P., Ed.; Mineralogical Association of Canada: Vancouver, Canada, 2008, pp 169-188.
- (128) Russo, R. E.; Mao, X.; Gonzalez, J. J.; Zorba, V.; Yoo, J. *Anal Chem* **2013**, *85*, 6162-6177.
- (129) Frick, D. A.; Günther, D. *J Anal Atom Spectrom* **2012**, *27*, 1294.
- (130) Oros-Peusquens, A. M.; Matusch, A.; Becker, J. S.; Shah, N. J. *International Journal of Mass Spectrometry* **2011**, *307*, 245-252.
- (131) Jurchen, J. C.; Rubakhin, S. S.; Sweedler, J. V. *Journal of the American Society for Mass Spectrometry* **2005**, *16*, 1654-1659.

- (132) Paul, B.; Hare, D. J.; Bishop, D. P.; Paton, C.; Nguyen, V. T.; Cole, N.; Niedwiecki, M. M.; Andreozzi, E.; Vais, A.; Billings, J. L.; Bray, L.; Bush, A. I.; McColl, G.; Roberts, B. R.; Adlard, P. A.; Finkelstein, D. I.; Hellstrom, J.; Hergt, J. M.; Woodhead, J. D.; Doble, P. A. *Chem. Sci.* **2015**, 6, 5383-5393.
- (133) Tropea, C.; Yarin, A. L.; Foss, J. F. *Springer Handbook of Experimental Fluid Mechanics*; Springer, 2007.
- (134) Johnson, R. W. *The Handbook of Fluid Dynamics*; Springer Berlin Heidelberg, 1998.
- (135) LaHaye, N. L.; Harilal, S. S.; Diwakar, P. K.; Hassanein, A. J. *Anal. At. Spectrom.* **2014**, 29, 2267-2274.
- (136) Li, X.; Wang, Z.; Mao, X.; Russo, R. E. *J. Anal. At. Spectrom.* **2014**.
- (137) Banerjee, S. P.; Chen, Z.; Fedosejevs, R. *Journal of Applied Physics* **2013**, 113, 183101.
- (138) Hou, Z.; Wang, Z.; Liu, J.; Ni, W.; Li, Z. *Optics express* **2014**, 22, 12909-12914.
- (139) Guo, L. B.; Hao, Z. Q.; Shen, M.; Xiong, W.; He, X. N.; Xie, Z. Q.; Gao, M.; Li, X. Y.; Zeng, X. Y.; Lu, Y. F. *Optics express* **2013**, 21, 18188-18195.
- (140) Bogaerts, A.; Chen, Z. Y.; Gijbels, R.; Vertes, A. *Spectrochim Acta B* **2003**, 58, 1867-1893.
- (141) Lorusso, A.; Nassisi, V.; Velardi, L.; Sicilano, M. V. *Journal of Physics: Conference Series* **2010**, 227, 012037.
- (142) Hergenroder, R. *J Anal Atom Spectrom* **2006**, 21, 1016-1026.
- (143) Koch, J.; Waelle, M.; Dietiker, R.; Gunther, D. *Anal Chem* **2008**, 80, 915-921.
- (144) EPO, PCT/EP2015/07 1525 (EP14185463.8), 2015.
- (145) Feldmann, J.; Kindness, A.; Ek, P. *J Anal Atom Spectrom* **2002**, 17, 813-818.
- (146) Zoriy, M. V.; Kayser, A.; Izmer, A.; Pickhardt, C.; Becker, J. S. *International Journal of Mass Spectrometry* **2005**, 242, 297-302.
- (147) Becker, J. S.; Zoriy, M. V.; Pickhardt, C.; Palomero-Gallagher, N.; Zilles, K. *Anal Chem* **2005**, 77, 3208-3216.
- (148) Albrecht, M.; Derrey, I. T.; Horn, I.; Schuth, S.; Weyer, S. *J. Anal. At. Spectrom.* **2014**, 29, 1034-1041.
- (149) Aerts, M.; Hack, A. C.; Reusser, E.; Ulmer, P. *American Mineralogist* **2010**, 95, 1523-1526.
- (150) Reinhardt, H.; Kriews, M.; Miller, H.; Schrems, O.; Ludke, C.; Hoffmann, E.; Skole, J. *Fresenius J. Anal. Chem.* **2001**, 370, 629-636.
- (151) Reinhardt, H.; Kriews, M.; Miller, H.; Ludke, C.; Hoffmann, E.; Skole, J. *Analytical and bioanalytical chemistry* **2003**, 375, 1265-1275.
- (152) Müller, W.; Shelley, J. M. G.; Rasmussen, S. O. *J Anal Atom Spectrom* **2011**, 26, 2391.
- (153) Konz, I.; Fernandez, B.; Luisa Fernandez, M.; Pereiro, R.; Sanz-Medel, A. *Anal Chim Acta* **2014**, 809, 88-96.

Chapter 3 Image deconvolution

*This chapter consists of sections that were published in two research papers. The first paper, entitled 'Development of a fast laser ablation–inductively coupled plasma–mass spectrometry cell for sub- μm scanning of layered materials', was authored by Stijn J. M. Van Malderen, Johannes T. van Elteren, and Frank Vanhaecke.¹ The second paper, entitled 'Sub- μm imaging by laser ablation–inductively coupled plasma–mass spectrometry via signal and image deconvolution approaches', was authored by Stijn J. M. Van Malderen, Johannes T. van Elteren, and Frank Vanhaecke and was published in *Analytical Chemistry* (2015).² Both papers have S.V.M. as the first and principal author.*

In this chapter, image and signal processing algorithms which can be applied to improve the quality of the LA-ICP-MS nuclide distribution images and correct distortion effects are discussed.

3.1 Introduction

Lateral resolution in LA-ICP-MS imaging procedures is governed by the laser beam waist size projected onto the sample, in combination with the degree of overlap of the asymmetric pulse response peaks, bi-directional stage velocity, precision, and repeatability, sampling approach and conditions, and mass analyzer dwell and settling timings (the last two only apply to scanning mass analyzers). Recently, a number of studies^{3,4} have demonstrated the use of beam waist of $\sim 1\ \mu\text{m}$ for LA-ICP-MS imaging. The far-UV laser beam waist can be focused to sub- μm dimensions using near-field (NF) laser ablation,⁵ high numerical aperture objectives⁶, or Fresnel zone plates. Craters of several 100 nm can also be created by ablating the surface with a fs-lasers operating at an energy near the ablation threshold (due to non-linear absorption effects).⁷ However, the conflicting demand for higher spatial resolution – in some instances a

resolution below the far-field diffraction limit of UV lasers – and higher sensitivity of the setup, and challenges associated with the practical implementation of these focusing techniques or extreme UV/X-ray lasers⁸ have impeded the deployment of smaller beam waists. Numerous analytical applications would benefit from higher lateral resolution, as nuclide distributions at the nm-level within μm -sized features could reveal essential information on, *e.g.*, trace element transport processes in geological samples^{9–11}, biomarker distributions on subcellular levels¹² and surface layer phenomena in solid samples. None of the strategies for sub- μm focusing proposed have, up to this point, to the best of the author’s knowledge, been demonstrated to be a viable option for sub- μm scanning using LA-ICP-MS. Commercially available LA-systems use far-field optics to achieve beam waist diameters ranging from 1–200 μm ; this directly limits the lateral spatial resolution. The decrease in the amount of material ablated is concomitant with a loss in sensitivity, hence, at the sub- μm level of lateral resolution, only the major elements can be monitored using current ICP-MS instrumentation. It may be noteworthy that the thickness of sub-nm metal layers can be determined by LA-ICP-MS through an absolute determination of the number of atoms of the layer. This implies a full consumption of the irradiated parts of the layer using a large spot in a drilling approach.¹³

LA-ICP-MS can extract information on a scale smaller than the beam waist or diffraction limit by oversampling the region of interest (ROI), *i.e.* by overlapping ablation positions by spacing them apart by a distance less than the laser beam waist diameter. Drescher *et al.*¹⁴ reported an approach based on oversampling, which, if the pulse(s) fired at each ablation position are capable of quantitatively removing the material, and the concentrations of the targeted nuclides in the substrate are negligible relative to the concentrations in the sample, ameliorates the lateral resolution in the nuclide distribution image, as only a part of the laser beam covers the sample at each shot. As a result of these prerequisites, this approach is fit for 2D mapping of soft, sliceable samples that are no thicker than a few 10 μm (the depth which can be removed by a sequence of pulses). A similar strategy has been reported earlier for MALDI-MS.¹⁵ If the pulse(s) fired is (are) unable to ablate through the sample, the laser resamples the sample surface, in a part of the ablated area of the previous ablation positions, confounding the response across ablation positions and in depth, resulting in an image convolved in the spatial domain. This problem raises the necessity for deconvolution approaches for destructive probes. Plotnikov *et al.*¹⁶ proposed reconstructing a 1D nuclide concentration profile *via* direct deconvolution of the transient signal, indirectly limiting the approach to a resolution larger than the beam waist size. The strategy described by Plotnikov *et al.*¹⁶ for the deconvolution of continuous scan data composed of overlapping signal peaks is based on the regularization of a system of linear equations and on Fredholm integral equations of the first kind. This approach enhanced edge resolution whilst scanning in a single direction considerably, however, did not demonstrate lateral resolution below the beam width.

In the first part of this chapter, a novel post-acquisition methodology is demonstrated for the deconvolution of overlapping ablation positions in scanning mode by an iterative Richardson-Lucy algorithm. This enables correction of the distortion in the scan profile upon traversing layers with dimensions below the physical size of the laser beam, analogous to super-resolution microscopy. By overlapping the ablation positions of a 1 μm diameter laser beam, a lateral

resolution in the order of $0.3 \pm 0.1 \mu\text{m}$ was demonstrated for scanning of μm -sized layers in high capacitance multi-layer ceramic capacitors. The deconvolution of a single scan, with a 1D kernel function is designed to resolve the response of overlapping ablation positions in a single direction; 2D deconvolution on the other hand, extends this principle by deconvolving an image in which the ablation positions overlap in 2 directions, with a 2D kernel function. Multiple layers can be subsequently ablated via LA, permitting 2D deconvolution to be performed in every layer, thus permitting a 3D image to be formed. In the second part of this chapter, (pre- and post-) acquisition procedures are introduced to reconstruct the 2D or 3D nuclide distribution *via* image deconvolution from the temporally resolved response of overlapping ablation positions. A lateral resolution better than the laser beam waist can be achieved in scenarios of sensitivity-limited or far field-limited laser beam waists in laser spectrochemistry, without the limitation of requiring complete ablation at each ablation position. Furthermore, the approaches to signal deconvolution of the pulse response peaks reported in literature¹⁴ were improved upon by considering peak-to-peak interval variation and tailored peak fitting functions.

3.2 Deconvolution of spatially overlapping positions in one dimension

3.2.1 Theoretical background

The scanning and numerical deconvolution methodologies are aimed at spatially resolving the elemental response within every overlapping zone between overlapping ablation positions. The target zone is oversampled by scanning the sample – *i.e.* by lateral translation of the sample stage – at a scanning speed dx equal to $\frac{2rf}{\Delta_x}$ with f the pulse repetition rate of the laser, r the radius of the laser spot, and Δ_x the desired number of pulses overlapping in the \vec{x} direction. Hence, ablation positions are projected at an interspacing of $\frac{2r}{\Delta_x}$, producing artificially convolved data, analogous to the approach of Plotnikov *et al.*¹³ in this aspect. A simulation of a $1 \mu\text{m}$ laser beam spot traversing three closely-spaced layers with $\Delta_x = 5$ and the corresponding detector signal response are shown in Figure 43a and Figure 43b, respectively. In Figure 43c, it can be seen how each individual layer contributes cumulatively to the total integrated signal peak area at each ablation position. This superimposed response is deconvolved to obtain the spatiotemporal response at a virtual lateral resolution of $\frac{2r}{\Delta_x}$. The isotropic kernel for deconvolution, the theoretical LSF (Figure 43d), was derived from the ablation damage inflicted, modeled as an inverted two-dimensional Gaussian distribution of the space-invariant intensity profile (Figure 43f) of the beam from a laser operated in the fundamental transverse mode. When considering a beam of $1 \mu\text{m}$ diameter (as determined by the two points at $1/e^2$ of the maximum intensity), a two-dimensional Gaussian model reflects crater damage more accurately than a binary cylinder would.

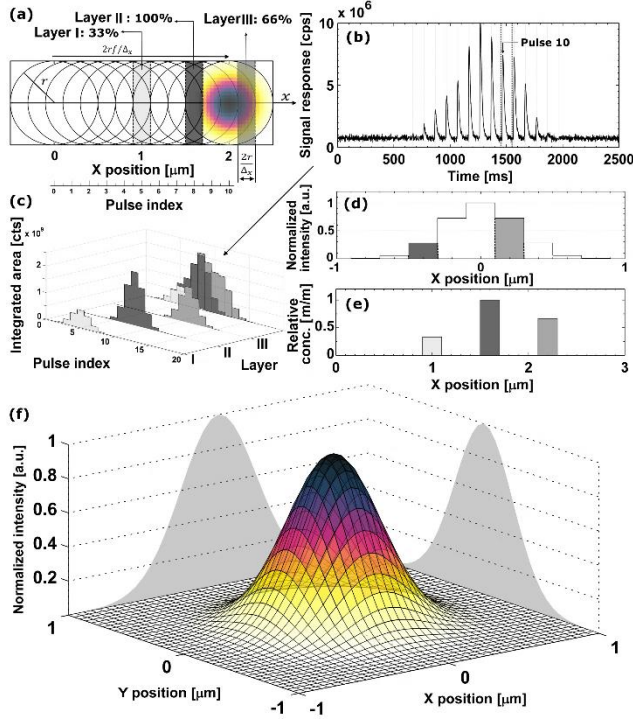


Figure 43 (a) Schematic of a line scan over three layers (indicated by different shades of gray), containing the nuclide of interest in different concentrations. (b) Simulation of the signal response for the experiment in (a). (c) Integrated peak areas of the response, as well as the individual contribution of each layer to the cumulative signal. (d) LSF after virtual down sampling with $\Delta_x = 5$. The layer locations relative to the ablation position of pulse 10 are indicated by their grayscale. (e) The result of the deconvolution of the integrated peak areas based on the LSF. (f) Simulated two-dimensional normalized Gaussian beam intensity distribution profile. The time-averaged intensity distribution of irradiance is:

$$I(r, z) = \frac{|E(r, z)|^2}{2\eta} = I_0 \left(\frac{w_0}{w_z} \right)^2 e^{-\frac{2r^2}{w_z^2}} \quad \text{Equation 34}$$

where $E(r, z)$ is the amplitude of the complex electric field, η the characteristic impedance of the medium, w_0 the radius of the beam at its narrowest point at which the field intensity drops to e^{-2} of the centre intensity, w_z the radius at which the field amplitude drops to e^{-1} of the axial value, z the axial distance for the beam's narrowest point, and r the radial distance from the centre axis of the beam. Based on Equation 34, the fluence on a sample located outside of the focal point can be calculated. Despite the presence of beam homogenizer optics, round, flat-top beam profiles cannot be obtained due to the fundamental limitations of a UV laser beam at these beam dimensions, as diffraction effects will distort the uniformity of the beam profile.¹⁵ A Gaussian beam profile is the default net system spread function of the lateral energy distribution as it is the result of multiple convolutions of all component spread functions.

The theoretical LSF of the system is extracted from the convolution of the two-dimensional Gaussian model with a binary line, perpendicular to the direction of travel, \vec{x} . In essence, the model is downsampled virtually in the direction of travel to the dimensions and step size associated with the setup, whilst being projected onto the yz plane. Conventional non-iterative deconvolution approaches, *e.g.*, Fourier deconvolution in combination with Wiener filtering, are not well suited to handle the deconvolution in LA-ICP-MS due to the formation of artifacts in the spatial frequency domain as a result of typical S/N levels. Deconvolution approaches in confocal imaging *via* 3D fluorescence microscopy include Tikhonov-Miller inverse filtering¹⁷, Wavelet denoising¹⁸, Carrington¹⁹ and Richardson-Lucy^{20,21} (RL) with Total Variation (TV) regularization.^{22,23} In this work, the RLTV algorithm was preferred to process the data, as it computes a maximum likelihood estimation robust to Poisson noise, which dominates the noise statistics in ICP-MS at low count rates²⁴, whilst counteracting noise amplification by regularization constraints based on TV.^{23,25} The regularizing constraint performs smoothing of oscillations while preserving feature edges and provides stable convergence onto a solution. The RL algorithm is a broadly accepted multiplicative gradient-based iterative deconvolution algorithm in confocal optical microscopy for noisy image restoration, derived from a Bayesian-based maximum likelihood approach ($p(o|i) = p(i|o)p(o)/p(i)$ with i the raw image of nuclide distribution o). RL maximizes the maximum likelihood probability $p(i|o)$:

$$p(i|o) = \prod_x \left(\frac{[(h \otimes o)(x)]^{i(x)} e^{-(h \otimes o)(x)}}{i(x)!} \right) \quad \text{Equation 35}$$

where $i = \wp(h \otimes o)$, \wp being a Poisson process and h the impulse function. This is a general image formation model from the LSF and the spread of the detector noise. From this equation and assuming that at convergence, the ratio $\frac{o_{k+1}(x)}{o_k(x)} = 1$, the estimate $o_k(x)$ at iteration k can be derived²²:

$$o_{k+1}(x) = o_k(x) \left[h(-x) \otimes \frac{i(x)}{(h \otimes o_k)(x)} \right] \quad \text{Equation 36}$$

Regularization constraint algorithms, *e.g.*, Tikhonov-Miller, maximum entropy, and total variation (TV) regularization are often applied to combat noise amplification in the iterative process of RL. TV regularization minimizes $-\log p(i|0) + \lambda \text{div} \left(\frac{\nabla o}{|\nabla o|} \right)$, with λ the regularization parameter. The estimate $o_k(x)$ becomes^{22,24}:

$$o_{k+1}(x) = \frac{o_k(x)}{1 - \lambda \text{div} \left(\frac{\nabla o_k(x)}{|\nabla o_k(x)|} \right)} \left(\left[\frac{i(x)}{(o_k \otimes h)(x)} \right] \otimes h(-x) \right) \quad \text{Equation 37}$$

For all runs, a positive constraint on the images of iterations was enabled to further stabilize the RLTV algorithm. The DeconvolutionLab software package by Vonesch *et al.*²⁶ implements the RLTV algorithm and was used for our purposes for the deconvolution of the integrated areas associated with overlapping ablation positions within the Java-based ImageJ image processing software. The algorithm retrieves the original concentration distribution within the set of layers (Figure 43e). A positive constraint on the values at each iteration was enabled to further stabilize the RLTV algorithm. The strategy proposed is not limited to the minimum beam waist size of a diffraction-limited, highly collimated, TEM00 (transverse electromagnetic) mode (X)UV laser beam, as it is not based on focusing the beam to dimensions beyond the physical diffraction barrier, but on the statistical likelihood of the presence of a nuclide within the targeted zone and its detection. At a certain level, the statistics of this strategy will break down; however, this level can be further decreased by improving the sensitivity of ICP-MS instrumentation and optimizing the design of the introduction system assembly. It could be argued that decreasing the beam waist size would be a superior option for achieving higher lateral resolutions, as no deconvolution would be required, and scanning time would remain identical. The methodological strategy proposed should however still operate when more advanced focusing techniques are deployed in the field, and beam radii decrease. The beam radius achievable for an ideal Gaussian beam is determined by the constant beam parameter product (BBP, Equation 38).

$$BBP = w_0 \theta / M^2 = \lambda / \pi \quad \text{Equation 38}$$

Where θ is the divergence, w_0 the half-angle radius of the beam waist, and M^2 the beam quality factor. The beam is diffraction limited when the radial beam divergence is close to the minimum possible value, *i.e.* when $M^2 \sim 1$. The minimum theoretical spot size diameter achievable for the ablation cell employed, together with a 193 nm ArF* laser, using refractive lenses, is ca. 265 nm (as determined by the two points at $1/e^2$ of the maximum intensity, and based on the paraxial approximation). Since excimer lasers are characterized by poor spatial and temporal coherence, and the beam quality degrades at higher divergence angles, this theoretical beam waist w_0 and the dimensions of the PSF model are underestimated.²⁷ Apart from fundamental focusing limits in the far field, the minimum spot size is typically restricted by the sensitivity of the setup for the nuclides targeted. The main advantage of the methodology proposed is that the sampling takes place at a relatively large spot size, thus, a higher S/N ratio can be upheld than when sampling directly at the level of the desired lateral resolution. Rectangular slits can be used in this procedure to increase S/N ratios even further. The deconvolution protocol operates at its highest spatial resolution when employed in a setup equipped with a low-dispersion ablation chamber.

3.2.2 Experimental section

For proof-of-concept purposes of the deconvolution approach, the LA-ICP-MS setup was used for mapping of a high capacitance Multi-Layer Ceramic Capacitor, abbreviated as MLCC (10 μF $\pm 10\%$, rated at 25V), of X5R architecture (class II), 0805 case style, manufactured by AVX (Kyocera, Japan). This capacitor is characterized by a highly regular, layered architecture of alternating planar Ni electrodes and dielectric BaTiO₃ layers. The granular structure of the

BaTiO₃ layer gives rise to a coarse transition between the electrodes and BaTiO₃ layers within the MLCC.

3.2.2.1 Sample preparation MLCC

The capacitor was embedded into an epoxy resin (bisphenol A diglycidyl ether), cleaved transversally at the electrode end connections with a diamond saw, and polished mechanically with SiC paper (P1200 to P4000) and colloidal silica suspension (0.04 μm grain size). The Ni layer interspacing (Figure 44) is determined by the capacitance, number of electrodes and electrode area set forth by the manufacturer.

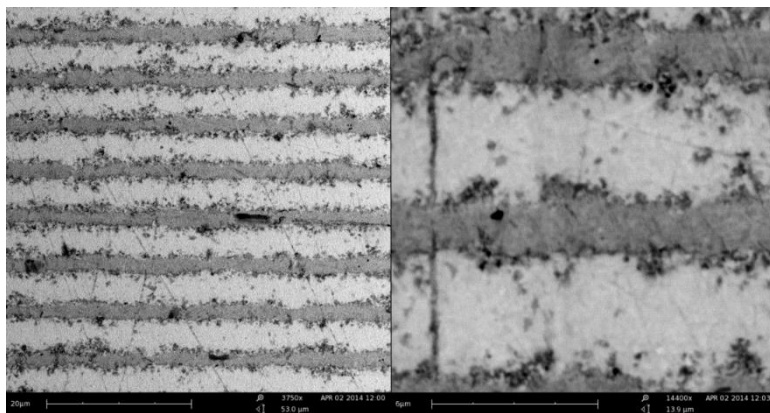


Figure 44 Scanning electron microscopy images (5kV accelerating voltage, BSE, Phenom, Phenom-World, Eindhoven, Netherlands) of the polished MLCC surface.

3.2.2.2 Scanning

An Analyte G2 (Photon Machines Inc., Bozeman, Montana, USA) 193 nm ArF* excimer laser system (pulse duration <5 ns, ~1% energy stability, 5.45 J cm^{-2} energy density), equipped with the tube cell described in Chapter 2, was coupled to an Agilent 7900 quadrupole-based ICP-MS instrument (Agilent Technologies Inc., Tokyo, Japan). The ICP-MS unit was operated at an RF power of 1500 W, the flow rates tuned to 15 L min^{-1} for the Ar plasma gas, 0.2 L min^{-1} for the Ar auxiliary gas, and 1.65 L min^{-1} for the He carrier gas. A laser beam of 1 μm in diameter (the mask uses a circular aperture), set to a pulse repetition rate of 25 Hz, was scanned over 47 electrode end connections, traversing 250 μm perpendicular to the direction of the electrodes at $2.5 \mu\text{m s}^{-1}$ ($\Delta x = 10$). The theoretical virtual lateral resolution that can be achieved, given the amount of overlap between ablation positions, is 100 nm. The response for ^{138}Ba was monitored at a dwell time of 500 μs . The setup was operated at a low scanning speed to eliminate potential inaccuracy associated with rapid acceleration and high speeds of the positioning stage.

3.2.2.3 Data treatment

The integration of individual pulse responses resulting in a discrete number of counts, as opposed to the use of continuous scan data, contributes to the spatial resolution obtained as it limits intermixing of the aerosol from a pulse with the aerosol generated by preceding pulses at different ablation positions. Thus, the overlap of peak profiles is preferably avoided. Temporal

displacements in peak positions are generated by small firing frequency shifts in the solid state pulse power module and flow fluctuations in the mass flow controllers. To correct for this gradual peak position drift, which becomes apparent at high frequencies, integration intervals were based on the peak maxima detected. In regions where no peaks were present, integration intervals were inter- and extrapolated *via* the base frequency of the laser. The integration intervals of major elements could be propagated to minor and trace elements. The data reduction process was automated in MATLAB® 8.1. The integrated areas were stored in a multi-dimensional array containing the response for each nuclide recorded and the spatial coordinates of the ablation location in a user-defined Cartesian coordinate system, associated with each peak.

3.2.3 Results and discussion

The deconvolution procedure implies the assumption that homogeneity exists on a depth scale (optical slice thickness) of Δ_x times the ablation depth per pulse, which varies depending on the coupling efficiency and density of the material ablated, the wavelength of the laser, fluence, and the pulse duration, between a few 10 to a few 100 nm.^{11,13,28,29} This assumption is often valid for layered structures, crystallographic domains as well as μm -sized volumes containing liquids. Failure to comply with this premise will result in a deterioration of spatial resolution. The spatial resolution may be compounded further by beam energy inhomogeneity variation, astigmatism, non-linear signal response, spatially variant fluid dynamic effects, temporal aberrations in the definition of the beam profile, non-flat sample topography, re-ablation of deposited material, sample vibration and local thermal effects, such as melting at the target zone (zone heating), which provokes a rearrangement of particles within the crater walls, and topographical change. Melting effects at the crater walls and elemental fractionation are preferably reduced by operating at fluence levels just above the ablation threshold or by using a ps or fs laser system. The majority of concerns remaining can be addressed by polishing the sample surface and by upgrading to a higher quality laser and a high resolution stabilized positioning stage. Some samples, such as thin sections of biological samples obtained by (cryo-)microtoming may not even require deconvolution of the scan data if single pulses are capable of quantitatively removing the material from the targeted ablation zone and the concentrations of the nuclide of interest in the substrate are negligible relative to the concentrations in the sample.¹⁴ Sequential pulses remove material from the new non-overlapping edge of the ablation position and substrate material from the zone overlapping to the preceding pulses. The sensitivity may, however, suffer in this procedure as only small segments of the sample surface, depending on the amount of overlap dictated by the beam diameter, the repetition rate, and the scanning speed, are ablated. In any case, the sampling frequency has to be high enough to enable spatial resolutions at which the targeted features can be distinguished. Failure to do so will result in spatial aliasing effects due to undersampling. Hence, the critical sampling distance determined by the Nyquist rate has to be respected if possible. Too much overlap between successive pulses could also negatively influence the quality of the deconvolved data, as the modulation transfer function (MTF) and the data in Fourier transform space are very sensitive to noise; the artefacts in the spatial frequency domain produced by high S/N ratios in LA-ICP-MS result in severe defects in the deconvolved data. Overlaying of ablation positions introduces

defocusing effects as well, thus, the evolution of the ablation rate and crater radius could be taken into account. This factor is, however, of minimal importance due to the good correlation between crater depth and a limited (<20) number of pulses.¹¹ Residual variation within the integrated area may originate from laser fluence instability (typically <1%), plasma shielding by inverse Bremsstrahlung and photoionization, changing transport properties (temporal variation in the particle size distribution), target zone lateral inhomogeneity on a μm scale, and instability and stochastic noise within the ICP-MS unit.

As can be observed from the scanning electron microscopy (SEM) and optical images of the MLCC in Figure 45a and Figure 45b, the dielectric layer thickness is ca. 3.5-4.5 μm , while the Ni electrodes are ca. 1.7-2.5 μm thick. The raw signal modulation upon scanning perpendicular to the electrodes (Figure 45c), and the resulting integrated areas (Figure 45d) show an aliasing effect due to the layered pattern. This effect becomes more pronounced after deconvolution (RLTV, 5 iterations, $\lambda = 0.01$), as the concentration gradient between the electrodes and the dielectric material is reflected more accurately due to an increase in lateral resolution (Figure 45b and Figure 45d). The width of the negative space at half of the maximum response ($1.7 \pm 0.4 \mu\text{m}$), as well as the normalized average concentrations gradient ($\sim 0.6 \mu\text{m}^{-1}$), has increased $\sim 100\%$ relative to the traditional approach of scanning using non-overlapping pulses ($\sim 1 \mu\text{m}^{-1}$ and $\sim 0.25 \mu\text{m}^{-1}$, respectively). A sharp concentration gradient in the transition zone between the electrode and dielectric material would be in accordance with the SEM and optical images, which indicate a well-defined pattern.

3.2.3.1 Estimating the lateral resolution

The MLCC can be considered as a square-wave grating with an object contrast ~ 1 , hence, an estimate of the lateral resolution can be computed. The dip-to-noise ratio resolution criterion by Senoner *et al.*³⁰ was adapted for sequences of n peaks:

$$D_{\text{avg}} / \sigma_{\text{NR}} = \frac{\sum_n I_{\text{max}} / n - \sum_{n-1} I_{\text{min}} / (n-1)}{(4/S_{\text{pp}})^{1/2} \sigma_{\text{N}}} \geq 4 \quad \text{Equation 39}$$

With D_{avg} the average dip, I_{max} and I_{min} , the median of 5 integrated peak areas centered around the maximum of the peak, and the minimum in between peaks, respectively, σ_{NR} the standard deviation of the reduced noise (noise ratio σ_{N} calculated for the electrode end connection region) and S_{pp} the number of sampling points per period of the grating. Figure 46a displays a selected sequence of 8 peaks, a general linear combination of 8 Gaussians (LCG), fitted to the curve *via* the Levenberg–Marquardt algorithm, and a square wave corresponding to the MLCC pattern. The computation of the dip-to-noise ratio as a function of the interspace in between the layers (Figure 46b) was based on simulating the response for a varying interspacing of the square-wave grating by virtually stacking resolved peak profiles as shown in Figure 46c. The original dip-to-noise ratio of 28.2 was interpolated towards the limit of resolution in accordance with the criterion and was estimated to be $0.3 \pm 0.1 \mu\text{m}$. The effective lateral resolution obtained in the scans was hence estimated to be $0.3 \pm 0.1 \mu\text{m}$. This lateral resolution exceeds the virtual lateral resolution of $0.1 \mu\text{m}$ and is concurrent with the estimate for the limit of resolution for the LCG as defined by the Rayleigh criterion.³⁰ Considering the coarse transition

between the electrodes and BaTiO₃ layers, the effective limit of resolution is expected to be better than the limit of resolution calculated.

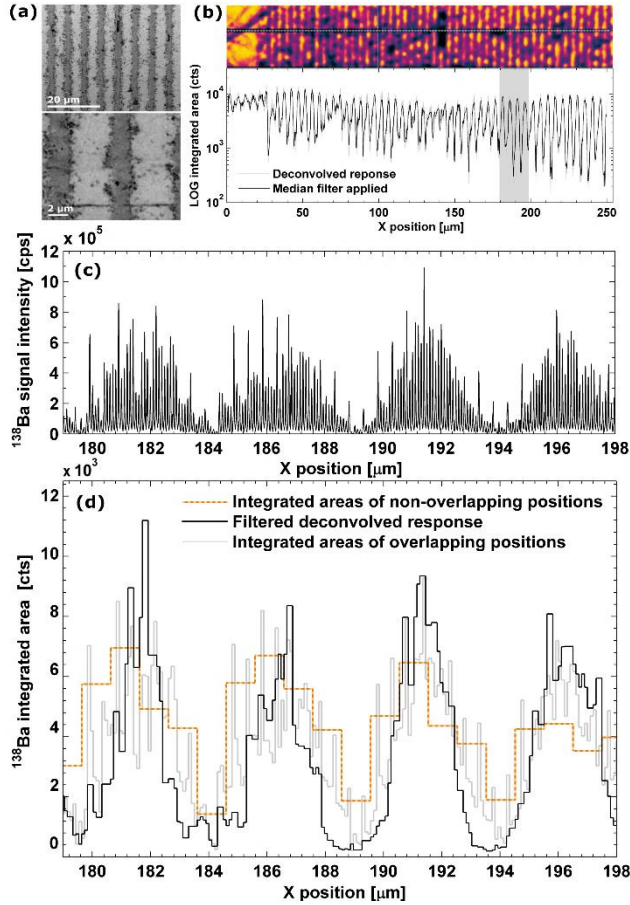


Figure 45 Profile scan of the MLCC and the deconvolved signal. (a) SEM (5 kV accelerating voltage, BSE, Phenom, Phenom-World, Eindhoven, Netherlands) images of the polished MLCC surface. (b) grayscale image of the target zone and aligned deconvolved response. (c) Temporal signal intensity profiles for ¹³⁸Ba within a selected target zone. (d) Detail of the spatiotemporal change of pulse response areas in a selected target zone; the deconvolved response from the procedure proposed here, and the response from the edge-to-edge scanning procedure ($\Delta_x = 1$, non-overlapping pulses, no deconvolution) are displayed.

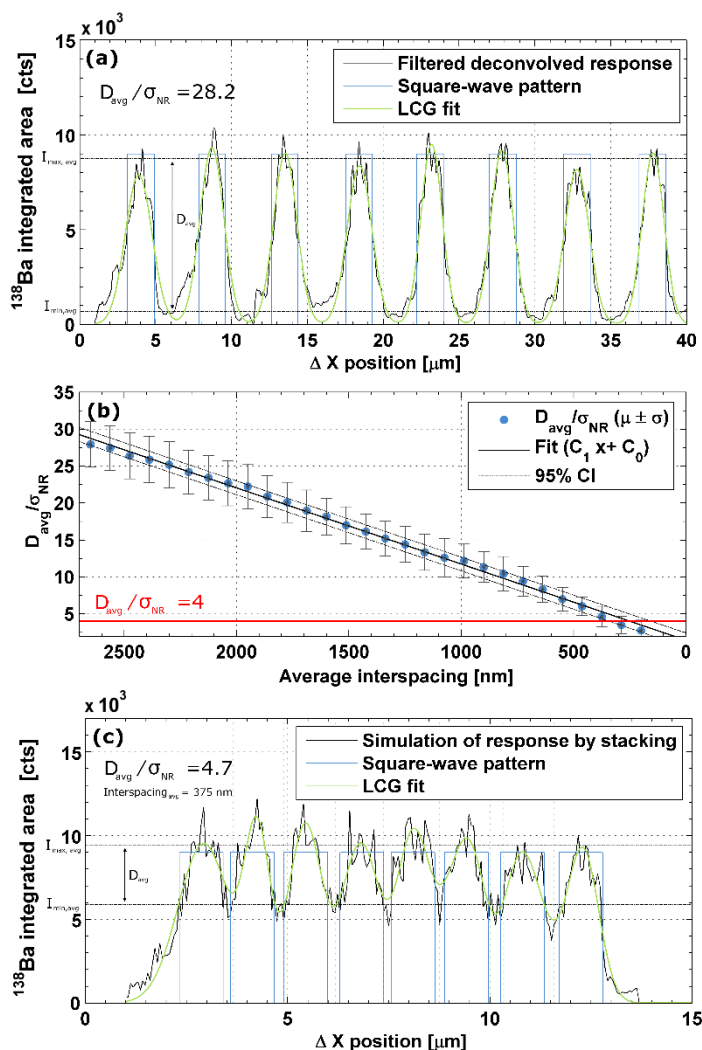


Figure 46 Simulation of the MLCC interspacing to determine the lateral resolution. (a) Detailed spatiotemporal change of the filtered deconvolved integrated peak areas in a selected sequence of 8 peaks ([204 μm , 244 μm] of the MLCC scan). (b) Dip-to-noise ratio as a function of the interspace in between the layers. (c) Simulation of the response for a closely spaced layered MLCC structure, based on stacking the response of resolved layers in (a).

3.2.3.2 Temporal deconvolution

The use of low-dispersion cells is favored over post-acquisition signal deconvolution of overlapping pulse response peaks as the former elevates S/N ratios and avoids dispersion artifacts. Both tactics can, however, be combined in a quadrupole-based ICP-MS setup due to recent progress in the read times of dual mode discrete dynode detectors. Fast read times can also be achieved in time-of-flight and sector-field ICP-MS. Spectral deconvolution schemes have

already been developed and adopted in LA-ICP-MS in parallel to the adoption of the methodology in other fields of study, such as chromatography.^{28,31,32} The scheme deployed in the field of LA-ICP-MS is based on a numerical correction of a peak area, based on a fixed relative contribution of the residuals from preceding peaks, assuming exponential signal decay.³¹ We propose a model in which a superimposition of single shot pulse functions (SPFs) is fitted to the ensemble of all or a part of the pulse response peaks in the experimental response $I(t)$, while allowing for a variable correction based on the specific amount of overlap, at an individual peak-to-peak level, as the amount of overlap will vary with the laser frequency timings and jittering, gas flow rate fluctuations, and the detector timing. Stage-priority lasing – a lasing approach in which the laser trigger circuit is tied into the XY translation stage driver – can also introduce additional discrepancies in the pulse repetition rate. Detectors capable of fast sampling and short rise times are essential; the elevated number of data points detailing each peak profile ensures an accurate fit of the dispersion model to the experimental spectrum. The dispersion of the aerosol originating from a single shot can be modeled as a setup transfer function (STF) of the aerosol dispersion function model (ADF), previously reported to provide an accurate fit (Equation 40).^{32,33}

$$\text{STF}(t) = I_0 e^{-k_{\text{flush},1}(t-t_0)} (1 - e^{-k_{\text{flush},2}(t-t_0)}) h(t - t_0) \quad \text{Equation 40}$$

with I_0 a factor proportional to nuclide concentration and sensitivity, t_0 the transfer time for the aerosol to reach the detector, t the time, $k_{\text{flush},1}$ and $k_{\text{flush},2}$ the flush rates, which depend on the cell geometry, and h the Heaviside step function. The SPF (Equation 41) is a convolution of an STF with a Gaussian function and is a model for the laser pulse delivery function, which lasts approximately 5 ns. The peak superimposition was implemented as the convolution (Equation 43) of a sequence of Kronecker delta functions (Equation 42) with the SPF.

$$\text{SPF}(t) = \int_0^t \frac{1}{\sigma_{\text{pulse}} \sqrt{2\pi}} e^{-\frac{\tau^2}{2\sigma_{\text{pulse}}^2}} * \text{STF}(t - \tau) d\tau \quad \text{Equation 41}$$

$$\delta_{\text{stack}}(t) = \sum_{n=1}^{N_{\text{pulses}}} \delta_{n/f-t+t_{\text{shift},n}} \quad \text{Equation 42}$$

$$I(t) = \int_0^t \text{SPF}(t) * \delta_{\text{stack}}(t - \tau) d\tau \quad \text{Equation 43}$$

An unconstrained nonlinear Nelder-Mead simplex optimization scheme³² for parameters $k_{\text{flush},1}$, $k_{\text{flush},2}$ and $t_{\text{shift},n}$ based on multivariate mean least squares regression was used as a fitting method. Similarly, other iterative constrained and unconstrained schemes can also be

used to converge on the values of these parameters, with case-specific rates of convergence. The flush rates $k_{\text{flush},1}$ and $k_{\text{flush},2}$ were global variables for all pulses of one nuclide as the behavior of aerosol dispersion should remain stable for the duration of a single line scan. As mentioned above, relatively small shifts at high firing frequency f may result in gradual peak position drift over time; the algorithm was designed to counter this drift by resynchronizing the model to the experimental data by optimizing the peak positions on a peak-by-peak basis by simulated annealing. Alternatively, other constrained peak position optimization schemes, *e.g.*, differential evolution, may be applied. Seed values for the peak position drift $t_{\text{shift},n}$ for each peak were estimated by calculating the residual time displacement in the interval with length $1/f$, between the peak maximum of the pulse n – retrieved through a peak maxima detection algorithm – and the peak maximum of the preceding pulse $n - 1$ of a nuclide of a major or minor element, relative to the base frequency of the laser firing circuit. The peak position drift data can be propagated toward all other (trace) element nuclides. Peak positions of missing peaks were derived by interpolating or extrapolating the detected peak positions with the base frequency of the laser firing circuit, derived from detected peak positions or provided by the operator. Detrimental effects of temporal distortions in the dispersion profiles and high-frequency noise on the accuracy could be suppressed by integrating the area under of each isolated peak, rather than experimental data directly. The response for each nuclide and the spatial coordinates of the ablation position in a user-defined coordinate system, associated with each individual pulse, were stored in a 5-dimensional (5D) array within an HDF5 file. The signal deconvolution algorithm was implemented for 5D data in Python 2.7 (in conjunction with the Numpy library). In the case of narrow dispersion profiles, the forward dispersion of the asymmetrical STF is underestimated in Equation 40 due to an approximation in the model from which the equation is derived, resulting in a significant bias between the SPF and the experimental pulse response. A linear combination of Gaussian functions (LCG, Equation 44) or linear combination of log-normal distributions (LCLN, Equation 45) provides a better multi-parameter model for approximating the aerosol delivery function; for the experimental representative single shot dispersion profile illustrated below (Figure 47), the relative integrated residual area is $\sim 0.1 \pm 0.1\%$ for an SPF based on a three-term LGC model, and $\sim 1 \pm 0.5\%$ for an SPF based on a single-term LCLN model.

$$\text{STF}(t) = I_0 \sum a_i e^{-\frac{1}{2} \left(\frac{t-t_i}{\sigma_i} \right)^2} \quad \text{Equation 44}$$

$$\text{STF}(t) = I_0 \sum a_i e^{-\frac{1}{2} \left(\frac{\ln t-t_i}{\sigma_i} \right)^2} \quad \text{Equation 45}$$

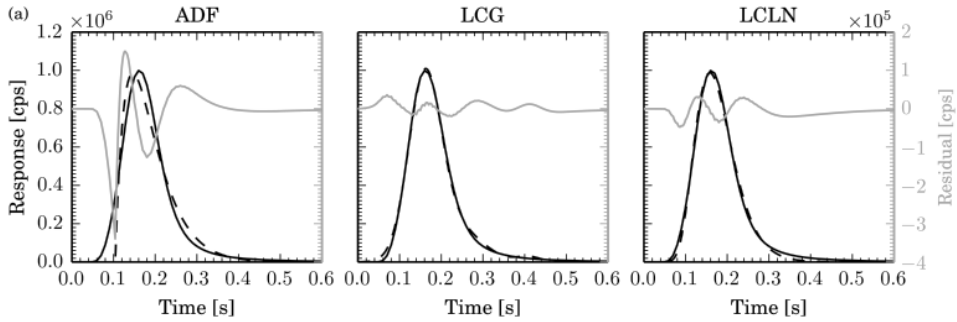


Figure 47 The primary axis (left) displays three SPF models (dashed line) fitted to a single pulse response (solid black line). The secondary axis displays the residual area (solid gray line) after fitting.

In comparison, the relative integrated residual area for an SPF based on Equation 1 is $\sim 5 \pm 2\%$. Advantageously, the single-term LCLN and LGC fitting algorithms demand less computational resources to estimate the STF parameters, allowing for rapid online data reduction given sufficient allocated processing power, memory, and bandwidth. If a surplus of temporal resolution is available, signal deconvolution can isolate overlapping pulse response profiles at pulse repetition rates $2 - 3 \times$ higher than the pulse repetition rate at which peaks are natively separated at the 1% of the maximum peak intensity level. The fitting errors will however propagate and amplify throughout the signal deconvolution, markedly in the situation of strong pulse response overlap at higher laser repetition rates. Furthermore, the (residual) noise that can't be corrected for by the model, adversely affects the limit of detection, which results in a decrease in the contrast ratio. Conversely, the strong overlap of pulse responses also results in more stable plasma conditions, as the relative aerosol load fluctuates less in time. Spectral

deconvolution of the mass-to-charge ratio spectra, with the purpose of increasing mass resolution, can be applied independently from signal deconvolution of the transient signal.

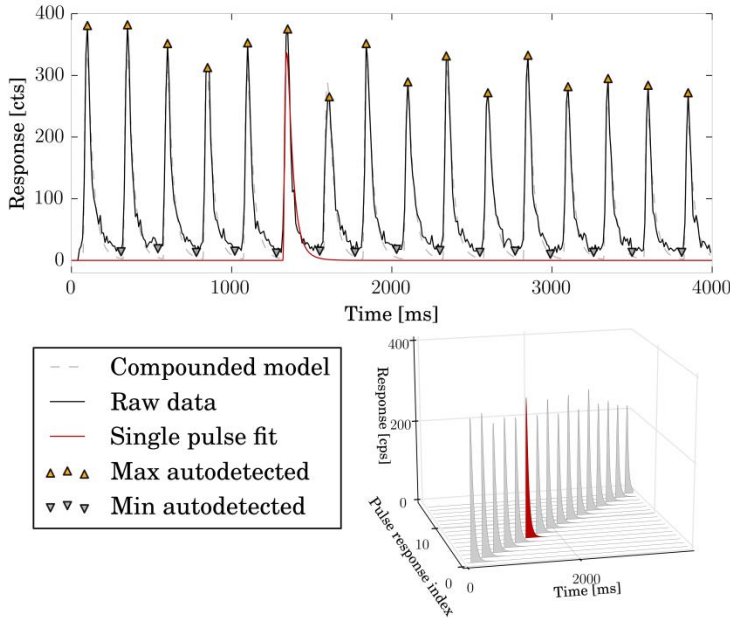


Figure 48 An LCG-based model is fitted toward a ^{44}Ca pulse response from scanning a $100\ \mu\text{m}$ diameter beam at $10\ \mu\text{m s}^{-1}$ over the surface of a micro-scale homogenous industrial glass inside a cell characterized by a slow washout at a 4 Hz pulse repetition rate for a total of 250 pulses (16 shown), generating moderate response overlap. The deconvolved single pulse profiles are shown in the secondary axis; the gray areas define the integrated area stored in the multi-dimensional pixel corresponding to that pulse.

3.3 Deconvolution of 2D and 3D images

2D and 3D image deconvolution strategies have been adopted to readily resolve data from overlapping positions of non-destructive probes in a number of fields, including (confocal) 3D microscopy, astronomical imaging, electron microscopy, and X-ray-based imaging, *e.g.*, for depth profile reconstruction in confocal $\mu\text{-XRF}$.³⁴ The 2D image deconvolution approach proposed in this work is presented schematically in Figure 49 which serves to guide the reader; the concepts of the methodology will be explained step-by-step. Summed up briefly, a target (Figure 49a) is oversampled, such that after signal deconvolution of pulse response peaks (Figure 49b), this approach produces a nuclide distribution image in which the ablation positions are artificially convolved (Figure 49c). Non-blind image deconvolution reconstructs the nuclide distribution image or volume, employing a point spread function (PSF, Figure 49f), derived from a theoretical model of the laser beam energy distribution (Figure 49d) or topographical scans of single shot craters (Figure 49e), as a deconvolution kernel function. The lateral resolution of deconvolved images (Figure 49g) can be improved enormously, relative to

images produced based on adjacent ablation positions (Figure 49h), the scanning approach currently adopted in practically all studies requiring high lateral resolution.

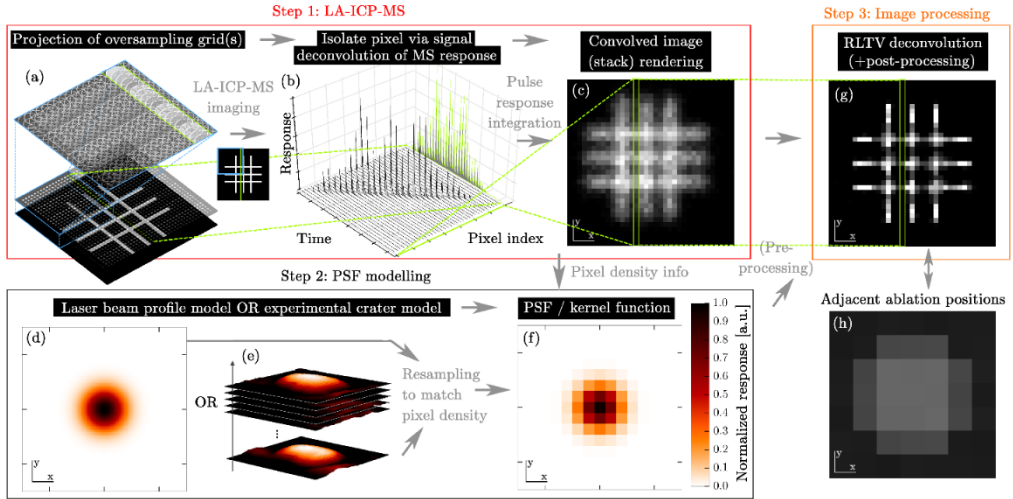


Figure 49 Schematic of the workflow *via in silico* simulation. The green highlight follows a row of pixels. (a) Oversampling layer projected onto a resolution test target (grayscale corresponds to nuclide distribution). (b) 3D line plot showing the individual contribution of pulse responses. (c) Nuclide distribution; each pixel represents an integrated pulse response. (d) Theoretical laser beam profile. (e) A stack of AFM maps of single pulse craters. (f) Point spread function. (g) Deconvolved image. (h) Image of the test target based on adjacently placed ablation positions. For comparison purposes.

3.3.1 Theoretical section

3.3.1.1 Deconvolution approaches

Recently, a methodology for the deconvolution of overlapping single shot ablation positions in a 1D scan was demonstrated in a paper by Van Malderen *et al.*¹ In order to extend this oversampling methodology to two spatial dimensions, the approach to compose the convolved image by oversampling the target zone must be expanded. In a first approach (1), the ablation pattern for 2D imaging was constructed by projecting a virtual 2D $[x_{\max}, y_{\max}]$ grid of parallel lines onto the target surface, each line projected at a distance of $2r/\Delta_y$ (the step size in the y -axis direction) below the preceding line position, with r the radius of the laser spot, and Δ_y the desired number of ablation craters overlapping in the y -direction, such that two consecutive lines share $(100 - 100/\Delta_y)\%$ of their ablation area. The grid was scanned at a scanning speed dx equal to $2rf/\Delta_x$ with f the firing frequency of the laser, and Δ_x the desired number of ablation craters overlapping in the x -axis. On any given pixel location within the bulk of the layer, up to $\Delta_x\Delta_y$ ablation positions overlap (Figure 49a). The LA-ICP-MS image of the oversampled target, in which each pixel corresponds to an integrated pulse area, isolated *via* signal deconvolution and associated to a sampling position in the oversampling layer (Figure 49c), is a convolution of the nuclide distribution and the impulse response of the LA-system. Richardson-Lucy²¹ (RL)

with Total Variation (TV) regularization, an iterative Bayesian-based deconvolution algorithm for image restoration, was selected (see previous sections) as a means of reconstructing the nuclide distribution, as it computes a robust estimate while considering the Poisson counting statistics of low S/N signals in ICP-MS^{22,23}. Other iterative deconvolution schemes, such as Tikhonov-Miller and split-gradient deconvolution, can offer similar results. The RL algorithm derives from a maximum likelihood approach, while optionally, regularization constraints enable stable convergence throughout multiple iterations.^{23,25} The algorithm can be readily expanded to two ($x = [X, Y]$) or three dimensions ($x = [X, Y, Z]$).²³ The DeconvolutionLab software package from Vonesch *et al.*²⁶ implements the algorithm and was used for 2D image stack reconstruction by 2D deconvolution within the Java-based ImageJ image processing software (National Institutes of Health, Bethesda, USA). The regularization parameter λ and the number of iterations were optimized. Edge effects resulting from the deconvolution of undersampled boundary regions can be avoided by sampling a larger region $[x_{\min} - 2r: x_{\max} + 2r, y_{\min} - 2r: y_{\max} + 2r]$ around the ROI $[x_{\min}: x_{\max}, y_{\min}: y_{\max}]$. After deconvolution, the ROI is rescaled to the integrated number of counts within the ROI *prior* to deconvolution. Image refinement (smoothing, binning, normalization and spatial denoising) and segmentation by clustering or multivariate methods for colocalization of chemical species into distinct regions can be performed after deconvolution. The utility of the approach is demonstrated in a proof-of-principle mapping of the cross-section of a 75 μm diameter Ag sheath surrounding a 5 μm diameter Pt/Rh (90:10) wire (Figure 50). The deconvolution has resolved the 5 μm Pt/Rh wire from the Ag sheath. Note that the surface area of the wire is smaller than the beam waist area. The embedded wire was mounted in a HelEx 2 ablation cell of an Analyte G2 193 nm excimer laser ablation unit Teledyne Photon Machines (Bozeman, MT, USA) coupled to an Element XR sector-field mass spectrometer (Thermo Fisher Scientific). A single nuclide was recorded in every run at a dwell time of 5 ms. The 0.5 L min^{-1} He carrier flow was mixed with a 0.85 L min^{-1} make-up Ar flow before entering the injector. RF power was optimized to 1200 W. Separate maps for ^{107}Ag (waist size, 5 μm square; repetition rate 1 Hz; 50 \times 125 ablation positions) and ^{195}Pt (waist size, 5 $\mu\text{m} \times 5 \mu\text{m}$; repetition rate, 1 Hz) were recorded (Figure 50).

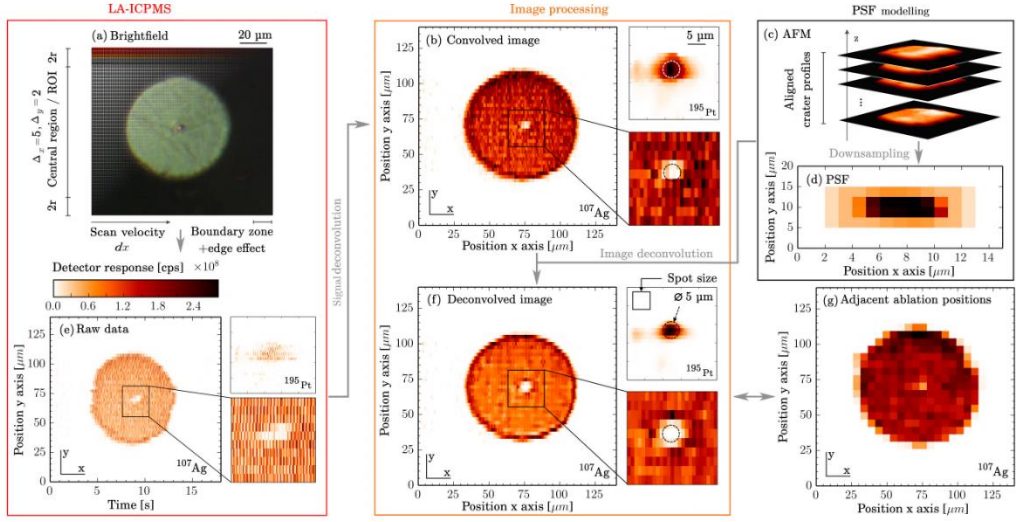


Figure 50 Example of the 2D image deconvolution approach for imaging a cross-section of a 75 μm diameter Ag sheath surrounding a 5 μm diameter Pt/Rh (90:10) alloy thermocouple wire (Goodfellow corp., Coraopolis, USA), embedded in epoxy resin and polished mechanically with SiC paper (P1200 to P4000), oil-based diamond suspension (1 μm grain size) and colloidal silica suspension (0.04 μm grain size). (a) Brightfield microscopy image of the ROI. The virtual oversampling grid is displayed as an overlay (50 \times 125 ablation positions). (b) Image of the integrated pulse areas of ^{107}Ag (pixel size, 1.0 \times 2.5 μm) and ^{195}Pt (independent run at higher resolution after repolishing; pixel size, 0.5 \times 1.0 μm) after signal deconvolution. (c) Image stack of craters profiles, created by a single 6.8 J cm^{-2} 5 μm \times 5 μm square *flat-top* laser beam shot, after registration and isolation from the background. (d) Point spread function as a resampled image of the z-projected crater profile. (e) Raw data acquired by LA-ICP-MS imaging of the ROI using a square laser beam (waist size, 5 μm \times 5 μm). (f) Deconvolved ^{107}Ag and ^{195}Pt distribution image (λ , 0.01; 10 iterations). (g) ^{107}Ag distribution image for a sampling approach based on adjacently positioned ablation positions (5 μm ablation position interspacing in x and y-axis); for comparison purposes.

3.3.1.2 Point spread function (PSF)

The PSF in the deconvolution, the impulse response function of the system to an infinitesimally small feature, accounts for the spatial variation in sampling efficiency between equidimensional areas of the ablation damage zone of a single shot. Astigmatism and non-uniform beam profiles, caused by imperfections in the optical components for beam homogenization, alignment errors, and aberrations in the focusing system, alter the laser beam energy distribution and shape projected through the mask. An experimentally derived PSF can reflect the laser-sample surface interaction, by considering the sample volume removed by a representative individual ablation event through characterization of ablation craters by, *e.g.*, optical profilometry or atomic force microscopy (AFM). Non-linear ablation mechanisms and coupling efficiency, characteristic to

the laser properties and thermal diffusivity, surface reflectivity, optical absorption coefficient, and melting temperature of the target, impact spatial delocalization of the deposited energy and extraction of the mass by ablation, vaporization and evaporation, and by extension, the sampling efficiency. The distortion introduced through melting, splashing, and droplet expulsion decouples the shape of the crater with the volume effectively removed and transferred into an aerosol, as a substantial part of the melt solidifies, after laser and fluid dynamic driven mobilization, on the crater surface. The crater morphology in metallic surfaces hence may not correctly translate into a PSF, as a direct translation of ablation damage volume to sampling efficiency is unlikely. The crater model can be constructed from the normalized average of inverted 3D topography maps, or from the convolution of 2 line spread functions (LSF) as derived from 2 inverted perpendicular 1D depth profile scans of the cross-section of a crater in a material of high coupling efficiency, under the assumption that the PSF is space-invariant. The crater models in this work were acquired experimentally by AFM (Figure 51); single shots were fired on the surface of a polished $10 \times 10 \times 10$ mm float glass block, sequentially in grids of 8×8 ($1 \mu\text{m}$ circular spot; interspacing, $5 \mu\text{m}$), 4×4 ($3 \mu\text{m}$ round spot; interspacing, $9 \mu\text{m}$) and 2×2 ($5 \mu\text{m}$ square spot; interspacing, $20 \mu\text{m}$) ablation positions. Non-contact (NC) AFM imaging was performed in $45 \times 45 \mu\text{m}$ scan areas using an XE-70 AFM unit (Park Systems Inc., Santa Clara, USA) with an Al-coated tip (z-corrected). Maps from each crater were aligned in a virtual stack of images (Figure 49e) using image registration³⁶ *via* scale-invariant feature transform (SIFT, locked to rigid translation). The feature representing the crater within the z-projected inverted background-corrected image stack was isolated on a threshold of 5% of the maximum intensity. An anisotropic PSF is generated by virtually resampling the model of the crater to a pixel size corresponding to the pixel density (pixel size, $2r/\Delta_x, 2r/\Delta_y$) associated with the sampling layer (Figure 49c). Alternatively, theoretically derived PSFs can be constructed based on known laser beam profile properties and modeling of the crater wall geometry. Median pre-filtering with a window of 2×2 pixels can be applied to $o_0(x)$, the initial estimate of the solutions, having only a limited effect on the edge resolution, whilst decreasing Gaussian noise within high-intensity regions. The relevant PSF for larger craters created by round flat-top beam profiles from homogenized systems can be modeled by the convolution of the image of a point source and a binary cylindrical model (Equation 47).

$$f_{\text{gauss}}(x, y) = \frac{1}{2\pi\sigma_x\sigma_y} e^{-\frac{1}{2}\left[\left(\frac{x-x_c}{\sigma_x}\right)^2 + \left(\frac{y-y_c}{\sigma_y}\right)^2\right]} \quad \text{Equation 46}$$

$$f_{\text{cylinder}}(x, y) = \begin{cases} 1 & \text{for } \sqrt{(x-x_c)^2 + (y-y_c)^2} \leq r \\ 0 & \text{for } \sqrt{(x-x_c)^2 + (y-y_c)^2} > r \end{cases} \quad \text{Equation 47}$$

An isotropic PSF based on a 2D Gaussian or Super-Gaussian model could be adopted to approximate the net system spread function of the lateral energy distribution in non-homogenized beams. The PSF for larger craters created by circular flat-top beam profiles from homogenized systems can be modeled theoretically by the convolution of the image of a point source and a binary cylindrical model. These PSF can be resampled similarly to the PSF derived

from experimental data. Alternatively, the PSF can also be constructed directly by oversampling a feature of dimensions smaller than the step size.

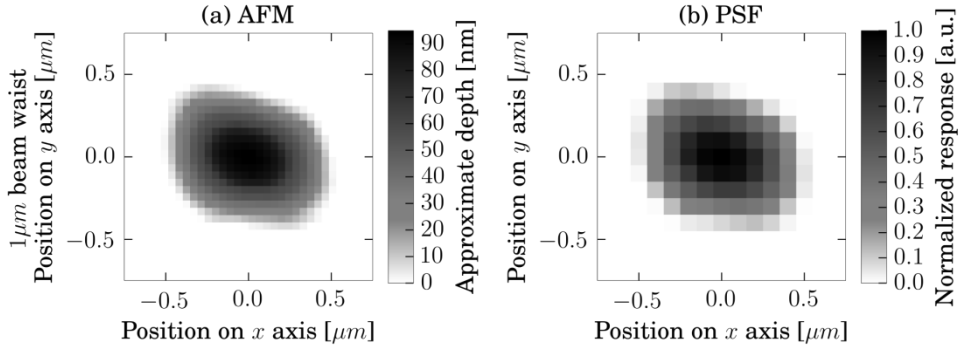


Figure 51 (a) 2D z-projected averaged inverted background-corrected AFM image of the crater region of a 1 μm (diameter at e^{-2} of the maximum intensity) Gaussian beam in float glass. (b) PSF of a 1 μm Gaussian beam obtained by resampling the AFM-derived images for $\Delta_x, \Delta_y = 10$ (3D image reconstruction pixel size, 100 nm \times 100 nm). Asymmetry is observed within the AFM images and PSF.

3.3.1.3 3D imaging

3D volumes can be generated by stacking 2D layers of sampling grids onto each other, followed by 2D image stack reconstruction *via* deconvolution of individual layers. The sampling methodology towards creating the 3D convolved image (hyper) stack contains specific topographical requirements – a flat surface after ablation, as the 2D deconvolution procedure operates on a plane. The ablation damage inflicted in the 2D imaging procedure leaves the central zone surrounded by inclined crater walls. Direct resampling of the identical region ablates these crater walls at an elevated z position relative to the central zone, resulting in artifacts in the boundary zone of $2r$ thickness. Independently, the deconvolution introduces edge effects in the resolved image, induced by undersampling in the boundary zone around the ROI. The initial ROI of dimensions $[x_{\min}:x_{\max}, y_{\min}:y_{\max}]$ must hence be enlarged to $[x_{\min} - 4r: x_{\max} + 4r, y_{\min} - 4r: y_{\max} + 4r]$. If a flat central region $[x_{\min} + 2r: x_{\max} + 2r, y_{\min} + 2r: y_{\max} + 2r]$ is observed after the first ablation level, the progressive superimposed crater damage of the 3D imaging procedure should render flat surfaces in the $[x_{\min} + 2r: x_{\max} + 2r, y_{\min} + 2r: y_{\max} + 2r]$ target zone at deeper levels/layers if no significant position-dependent ablation rate differences are present, and allow for a correct deconvolution within the $[x_{\min}: x_{\max}, y_{\min}: y_{\max}]$ ROI. Based on a numerical simulation of the crater damage in Python 2.7 (Figure 52), it was concluded that this approach is invalid for cylindrically shaped beam profiles as the superimposition of the layers resulted in systematic, coarse artifact structures in the ROI. To combat the persisting nature of these artifacts, the ablation positions can be shifted transversely by $(r/\Delta_x, r/\Delta_y)$, alternately in subsequent layers. This strategy partially mitigates the surface artifact formation, as is evident from an improvement in the root mean square roughness within the central zone of the simulation model by a factor of ~ 2 (Figure 53).

Gaussian- and square-shaped beam profiles are characterized by a distinct advantage over flat-top circular beams in this respect, as the superimposed damage from overlapping positions creates a quasi-flat central zone, negating the need for any positional shift between layers. The artifact formation effect by flat-top circular beam profiles aggravates with increasing amounts of overlap and progressively deteriorates the depth resolution with the number of layers ablated. Conversely, a decrease of the ablation spot interspacing for Gaussian shaped beam profiles ameliorates the surface roughness in the central zone; the ablation damage pile-up of the different layers is, therefore, less critical towards the depth resolution. Furthermore, Gaussian beam profiles offer a better spatial resolution after deconvolution, as a larger target volume is removed near the center of the ablation position, thus resulting in a sharper PSF. However, the penetration depth or waist diameter of the Gaussian beam may need to be increased in order to attain an equivalent sensitivity level/amount of material volume removed relative to flat-top cylindrical and square beams. The PSF can be adjusted for each layer to take into account the changes associated with defocusing effects, or the laser can be refocused onto the surface after ablation of each layer.

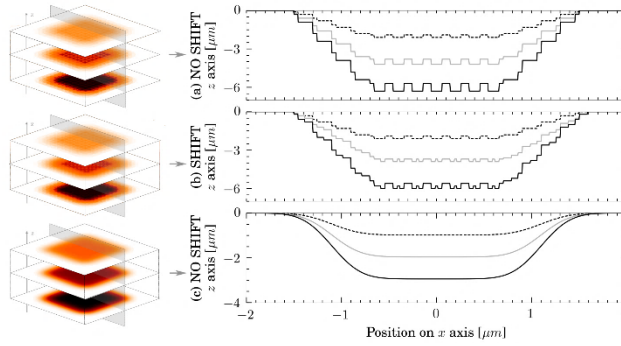


Figure 52 Cross-section of a 4D simulation of superimposed laser ablation damage for overlapping ablation positions, assuming flat-top circular ($1\text{ }\mu\text{m}$ diameter, $\Delta_x, \Delta_y = 5, 100\text{ nm}$ ablation depth per pulse) and Gaussian beam profiles ($1\text{ }\mu\text{m}$ diameter at e^{-2} of the maximum intensity, $\Delta_x, \Delta_y = 5, 100\text{ nm}$ ablation depth per pulse at the maximum). The target zone was subjected to ablation; 3 sequential 2D layers were superimposed. (a) The laser ablation patterns for a flat-top circular beam profile in which all 3 scans were aligned to a single reference position. (b) The laser ablation pattern for a flat-top circular beam profile in which layer 2 was shifted transversely according to vector $(r/\Delta_x, r/\Delta_y)$. (c) The laser ablation patterns for a Gaussian beam profile in which all 3 scans were aligned to a single reference position.

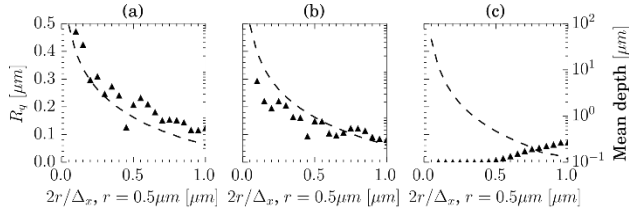


Figure 53 The root mean square surface roughness (triangles) and mean depth (dashed line) for the central zone of layer 3 of the ablation damage simulation script, as a function of the ablation position interspacing. The model indices (a-c) correspond to the model indices in Figure 52. The central zone from which the surface roughness data were extracted features a 4 fold larger ablation area than displayed in Figure 52.

Figure 51 demonstrates the resampling process of the PSF for an experimental model of a $1 \mu\text{m}$ diameter laser beam waist. Figure 52 and Figure 53 relate to the simulation in Figure 54.

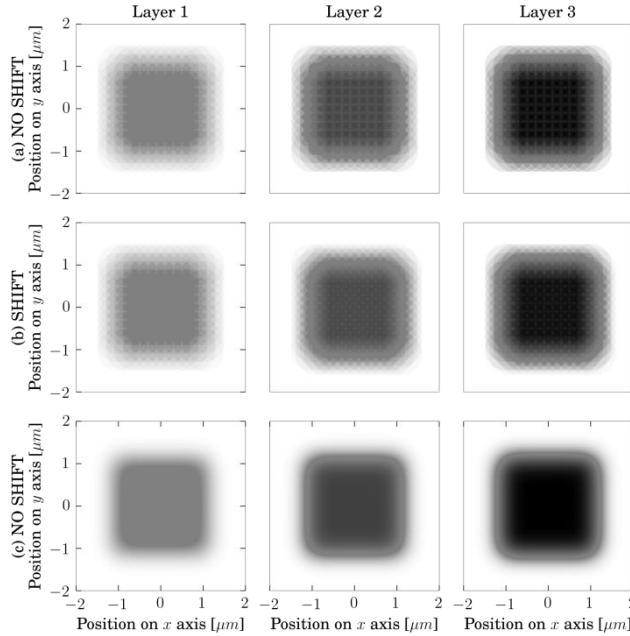


Figure 54 Graphical representation of the 4D simulation of superimposed laser ablation damage for overlapping ablation positions, assuming a flat-top circular ($1\ \mu\text{m}$ diameter, $\Delta_x, \Delta_y = 5, 100\ \text{nm}$ ablation depth per pulse) and Gaussian beam profiles ($1\ \mu\text{m}$ diameter at e^{-2} of the maximum intensity, $\Delta_x, \Delta_y = 5, 100\ \text{nm}$ ablation depth per pulse at the maximum). The target zone was subjected to ablation; 3 sequential 2D layers were superimposed. (a) The laser ablation patterns by a flat-top circular beam profile in which all 3 scans were aligned to a single reference point. (b) The laser ablation pattern by a flat-top circular beam profile in layer 2 was shifted transversely according to vector $(\frac{r}{\Delta_x}, \frac{r}{\Delta_y})$. (c) The laser ablation patterns by a Gaussian beam profile in which all 3 scans were aligned to a single reference point.

3.3.1.4 Other considerations

In theory, it would be possible to improve the depth resolution in LA-ICP-MS using deconvolution. However, the implementation of the sampling grid would not be straightforward. Assuming a lateral homogeneity between the sampling positions and a known, fixed ablation rate, one can oversample the depth by drilling the positions, which must all have a different, well-characterized, initial surface height differences (smaller than the ablation depth of a single pulse). The initial surface may be micro-machined by ablation with a beam of modulated energy density. Deconvolution of the compiled data set of all ablation positions with the appropriate LSF would, theoretically, result in a higher depth resolution (better than the ablation depth). The deconvolution result can be affected by the translation stage positioning repeatability, which is compounded by backlash, instability, cross-coupling, hysteresis, nonorthogonality and static friction. The laser fluence, wavelength, focus position, pulse length, beam waist and repetition rate guide the coupling efficiency to the target material, thus

directing the volume ablated by a single laser pulse – directly affecting the spatial resolution of the deconvolved image –, and the melt- and heat-affected zone.³³

3.3.1.5 Deconvolution of the transient signal

The integration of isolated, indexed pulse response peaks in the transient mass analyzer response is preferred over continuous sampling in a line scan, as the former establishes a direct correlation between the nuclide concentration and the spatial coordinates of the ablated region. The latter procedure will approach the lateral resolution of the former for low lateral translation speeds and high repetition rates; however, artifacts will always bias the response for downstream sampling positions. In an attempt to correct for the contribution of the peak tail towards sequential pulse responses, a spectral deconvolution algorithm, resolving the pulse response peaks in the time domain, was deployed. The purpose-built algorithm fits a model simulating the superimposed pulse responses towards the experimental response by multivariate mean least square regression. The pulse response profile was implemented as a convolution of a single shot pulse function (SPF) and laser pulse delivery function. The SPF shape was pre-optimized manually and refined further by an unconstrained non-linear Nelder-Mead simplex optimization scheme. A linear combination of log-normal distributions was found to be an accurate and computationally efficient model for the SPF. Furthermore, the SPF positions were optimized on a peak-by-peak basis *via* simulated annealing; the seed positions were provided by a peak maxima detection algorithm.

3.3.2 Experimental section

The deconvolution approach was applied in the examination of the 3D distribution of ^{55}Mn in a corrosion growth ring inside an archaeological glass. The tube cell assembly described in Chapter 2 was mounted inside an Analyte G2 Teledyne Photon Machines (Bozeman, MT, USA) 193 nm ArF* excimer laser ablation system (pulse duration < 5 ns, 1% energy stability mode, 6.8 J cm^{-2}), coupled to an Agilent 7900 ICP-(Q)MS instrument (Agilent Technologies, Santa Clara, USA). The pulse response profile, which is a critical component in the severity of response peak overlap, is an expression of the cumulative aerosol dispersion induced by the fluid dynamics inside the ablation cell, transport tubing, and ICP-MS unit.^{4,35-40} Low-dispersion cells, as deployed in this work, are hence preferred, considering the pivotal impact of aerosol dispersion on the overall spatial resolution, throughput, and sensitivity. RF power (1500W), plasma gas (Ar, 17 l min^{-1}), carrier gas (He, 1.65 l min^{-1}), and make-up gas flow (Ar, 0.2 l min^{-1}) rates were optimized, as well as data acquisition settings (detector dwell time, 500 μs ; single nuclide mode). The performance of the ICP-MS instruments was verified and optimized (gas flow rates, torch position, and electrostatic lenses) daily for LA-ICP-MS. The criteria for acceptable performance while ablating NIST SRM612 (mode, scanning; energy density, 3.5 J/cm^2 ; repetition rate, 20 Hz; spot size and shape, 20 μm diameter circular; scanning speed, $20 \mu\text{m s}^{-1}$) include: maximum sensitivity (^{238}U), oxide ratios ($^{238}\text{U}^{16}\text{O}^+ / ^{238}\text{U}^+ < 1.5\%$), and fractionation ($^{232}\text{Th} / ^{238}\text{U} \approx 1$). Before LA, a multi-element $1 \mu\text{g/l}$ solution is nebulized in a cyclonic spray chamber to verify the performance of the ICP-MS.

3.3.2.1 Corroded glass

Glass is weathered by a plethora of complex degradation phenomena (*e.g.*, dealcalinization by radial leaching, hydrolysis, selective dissolution). The glass piece analyzed displays spatiotemporal corrosion growth rings (Figure 55) which have a profound effect on the micro- and macro-morphology and crystal structure over a considerable depth ($> 100\ \mu\text{m}$) and area (mm^2).⁴¹ These corrosion patterns show visual resemblance to Liesegang rings. Nuclide distribution patterns may provide an insight into their formation mechanism, which has been hypothesized to be a diffusion-controlled process⁴², resulting in a spatial separation of the ions based on their mobility. The Mn distribution (bulk MnO concentration, $0.69 \pm 0.02\ [\text{w/w}\%]$)¹⁰ is of interest due to the precipitation of Mn within the cracks and capillaries of the surface,⁴³ formed by progressive ion migration and subsequent degradation of the remaining network formers, which is expected to yield a complex 3D Mn distribution, permitting the approach to demonstrate its merits. The ^{55}Mn distribution may also be representative of other network modifiers (*e.g.*, Co, Ni, and Pb). 4 layers of grids of 840×41 ablation positions were ablated in the ROI (Figure 21), generating 5.6×10^6 datapoints. The laser was operated at 30 Hz (every pulse response was isolated in the time domain) and scanned a beam of $3\ \mu\text{m}$ in diameter, and characterized by a near-Gaussian intensity distribution profile, over the surface at $15\ \mu\text{m s}^{-1}$ ($\Delta_y, 2; \Delta_x, 6$). The PSF was obtained *via* AFM of craters that were created using a single shot of a beam of $3\ \mu\text{m}$ in diameter under conditions identical to those used in the experiments. The data were processed *via* the 3D deconvolution approach (1) of the central zone (4×37 line scans); generating a volume with a voxel size of $1.5 \times 0.5 \times \sim 1.2\ \mu\text{m}$.

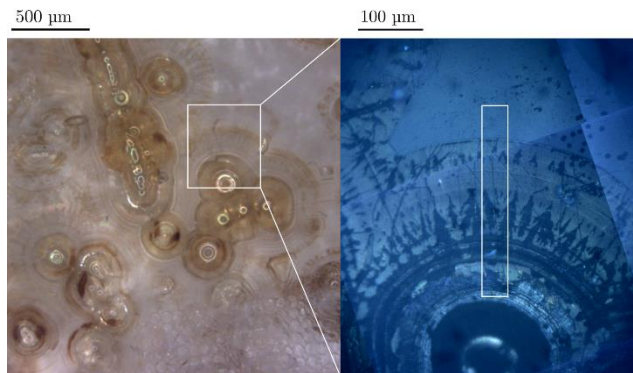


Figure 55 Brightfield images of the ROI (right figure inset, rectangle; dimensions, $55.5\ \mu\text{m} \times 430\ \mu\text{m}$).

3.3.3 Results and discussion

3.3.3.1 Image deconvolution

Overlapping the ablation spots represents a trade-off between axial (depth) resolution and lateral resolution, due to the inability of LA to resample an ablated volume – the destructive nature of LA inhibits direct 3D deconvolution. The deconvolution procedure implies the

assumption that axial homogeneity exists on a depth scale of $\Delta_x \Delta_y$ times the ablation rate per pulse, in a concept analogous to an optical slice thickness. Whether or not this prerequisite is fulfilled will depend on the degree of depth heterogeneity on a level below the beam waist diameter. Depth resolutions in LA-ICP-MS vary between a few 10 to a few 100 nm, whilst operating within typical parameter settings.^{14,26} Hence, the amount of overlapping ablation positions ($\Delta_x \Delta_y$) within the range $[x_k: x_k + 2r/\Delta_x, y_j: y_j + 2r/\Delta_y]$ of the grid can be chosen in such a way that the superimposed ablation damage aspect ratio of deconvolved voxels approaches (1:1:1). If the nuclide distribution image voxels are not equidimensional, the required aspect ratio can be obtained by altering the dimensions of the voxels/polyhedrons correspondingly, thereby avoiding geometric distortions that misrepresent the nuclide distribution. Apart from approach (1) (*vide supra*), alternative scanning patterns for 2D oversampling can be conceived; (2) Δ_x grids $\{n_l | l \in \mathbb{N}^0 \wedge l < \Delta_x\}$ of line scans (scanning speed, $2rf$; line vertical interspacing, $2r/\Delta_y$), shifted horizontally over a distance of $2rl/\Delta_x$ relative to a reference position, (3) Δ_y grids $\{n_m | m \in \mathbb{N}^0 \wedge m < \Delta_y\}$ of line scans (scanning speed, $2rf/\Delta_x$; line vertical interspacing, $2r$), shifted vertically over a distance of $2rm/\Delta_y$ relative to a reference position, (4) $\Delta_x \Delta_y$ grids $\{n_{l,m} | l \in \mathbb{N}^0 \wedge l < \Delta_x, m \in \mathbb{N}^0 \wedge m < \Delta_y\}$ of line scans (scanning speed, $2rf$; line vertical interspacing, $2r$), can be overlaid at an interspacing of one of the permutations of $(\{2rl/\Delta_x | l \in \mathbb{N}^0 \wedge l < \Delta_x\}, \{2rm/\Delta_y | m \in \mathbb{N}^0 \wedge m < \Delta_y\})$. The compiled data from these alternative scanning approaches can be interlaced to construct a convolved image o_i analogous to approach (1), *i.e.* grid positions are resampled into the convolved layer, *e.g.*, in approach (4):

$$o_i \left(x_k + \frac{2rl}{\Delta_x}, y_j + \frac{2rm}{\Delta_y} \right) = n_{l,m}(x_k, y_j) \quad \text{Equation 48}$$

for $k, j \in \begin{bmatrix} x_{\min}, y_{\min} & \cdots & x_{\max}, y_{\min} \\ \vdots & \ddots & \vdots \\ x_{\min}, y_{\max} & \cdots & x_{\max}, y_{\max} \end{bmatrix}$ and grid $n_{l,m} \in \{n_{l,m} | l \in \mathbb{N}^0 \wedge l < \Delta_x, m \in \mathbb{N}^0 \wedge m < \Delta_y\}$

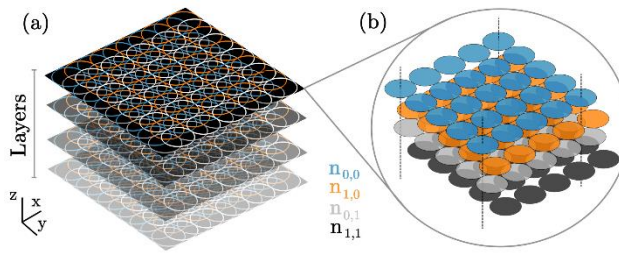


Figure 56 Schematic of the oversampling approach (4). (a) A stack of 2D sampling layers for 3D imaging. (b) Stack of $n_{l,m}$ shifted grids of adjacent ablation positions inside the top layer.

The last approach (4) (Figure 56) permits, besides the reconstruction of a deconvolved image of high lateral resolution as in approach (1), construction of a 3D image stack of low lateral, high depth resolution from all grids $n_{l,m}$, suitable for evaluating whether or not the sample is in agreement with the assumption of sample homogeneity within a depth of $\Delta_x \Delta_y$ times the probe

depth. As this procedure performs scanning based on adjacent ablation positions, prolonged exposure of a single target area to repetitive pulses of the laser beam is avoided, reducing the likelihood of particle-induced plasma breakdown and local thermal effects at the target zone. For 3D sampling *via* approach (4), the $n_{l,m}$ grids inside each layer can be regarded as a low-lateral high-depth resolution volume inside each layer. The grid data can hence be regarded as an additional spatial dimension, resulting in a 5D volume – 4 spatial dimensions and a dimension containing the nuclides. The grids can be deconvolved themselves, to correct for residual overlap and beam aberrations. The bilateral reproducibility of the stage is however of critical importance in approaches (2-4), and it must exceed the virtual resolution by far – calling for piezo nanopositioning technology –, to achieve an accurately reconstructed image. Note that any number of grids of overlapping ablation positions can be interlaced provided an adequate structure in the relative position of the grids. It is imperative to the functioning of the deconvolution protocol to minimize sources of non-deterministic variability in the experimental conditions. These sources include stage vibration, laser fluence drift, beam wander, laser timing jitter and thermal mass flow controller stability. The aforementioned signal deconvolution procedure addresses the variability within the sources that create temporal aberrations. Particle deposition near ablation craters is preferably minimized, as reablation of these particles of non-stoichiometric composition (preferential depletion or enrichment of nuclides) induces elemental fractionation, which will bias quantification. Internal/external standardization or bracketing-based procedures to correct for the progressive decline in laser beam energy density, temporospatial variation in ablation rate, and drift in transport, ionization, and detection efficiency have to be applied before any image deconvolution is performed on the data. The efficiency of the deconvolution procedure and gains in the lateral resolution are expected to decline as the width of the beam waist projected onto the sample decreases, and trace elements are targeted, as the relative overall signal to noise ratio decreases. One of the main benefits of the approach is that the sensitivity associated with the spot size is maintained when imaging at a lateral resolution below the spot size. This becomes especially important in scenarios where the spot size is limited by the sensitivity available. The resolution achievable is inherently limited by a number of stochastic sources, the Poisson statistics of the signal-to-noise ratio being a dominant factor. The response also becomes decoupled from the concentration gradient when the ablation spots are too closely positioned.

3.3.3.2 Results.

The first two depth layers ($< 3\mu\text{m}$) demonstrate the presence of a superficial aggregation of ^{55}Mn across the entire cross-section, in a band pattern of varying width (Figure 57). The band pattern shows correspondence to the yellow/brown discoloration observed by optical microscopy.^{43,44} A secondary high-frequency stratified pattern of lamellae $1 - 5\mu\text{m}$ in width, extending radially from the pit center are made visible through the enhanced lateral resolution. Notably, a similar pattern of shallow ($0 - 5\mu\text{m}$ depth) trenches was observed in the surface topography; hence, the ^{55}Mn pattern may indicate an aggregation of Mn as a result of the morphology. The Mn deposition at the surface can be induced by an external source present in the environment, *e.g.*, the soil in which the glass resided for centuries, and/or by an internal

source, *e.g.*, the Mn(II/III) that has leached from the corroded surface and migrated in a diffusion-controlled flux to the surface, may have been deposited onto the surface as insoluble MnO₂-containing components, formed in an oxidative environment.^{44,45} In deeper layers ($\sim 3 - 6 \mu\text{m}$ in depth), a radial Mn depletion in the outer and center rings of the cross-section relative to the bulk Mn composition, and an aggregation of Mn near the central crater (depletion relative to the bulk) is observed (in accordance with previous observations *via* LA-ICP-MS¹¹), suggesting an internal Mn source.⁴⁴ Additional real-world applications of the oversampling and deconvolution approach are provided in Section 3.3.4.

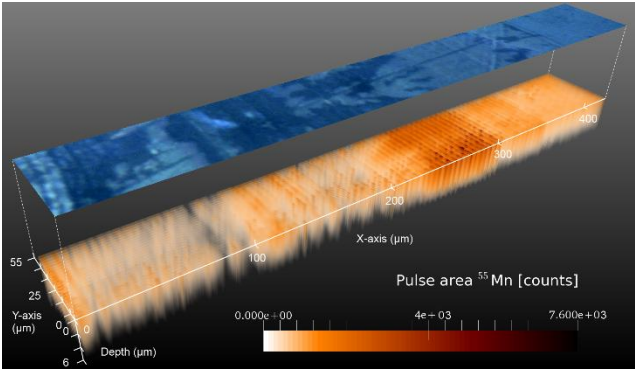


Figure 57 Volume rendering of the ⁵⁵Mn radial 3D distributions ($430 \times 55.5 \times 6 \mu\text{m}$; $\lambda, 0.01$; number of iterations, 4) in corrosion growth rings. The brightfield image of the ROI is projected onto the volume. The z axis was upscaled by a factor of $10 \times$ for clarity.

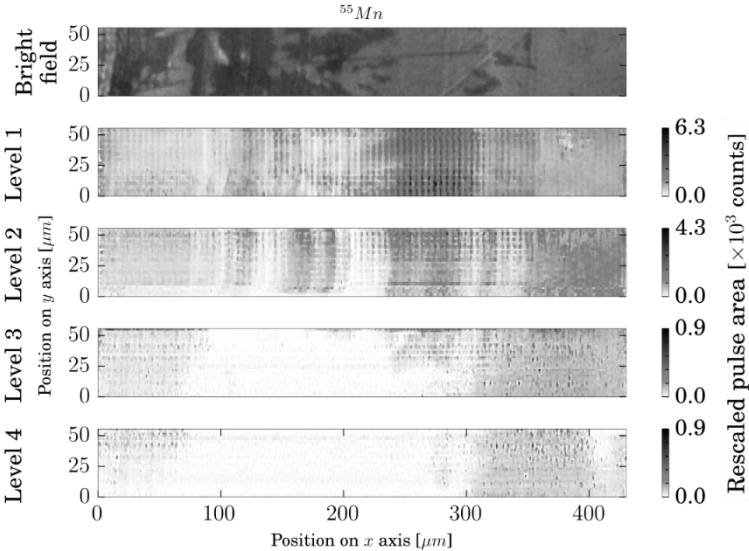


Figure 58 The corroded glass volume data before deconvolution.

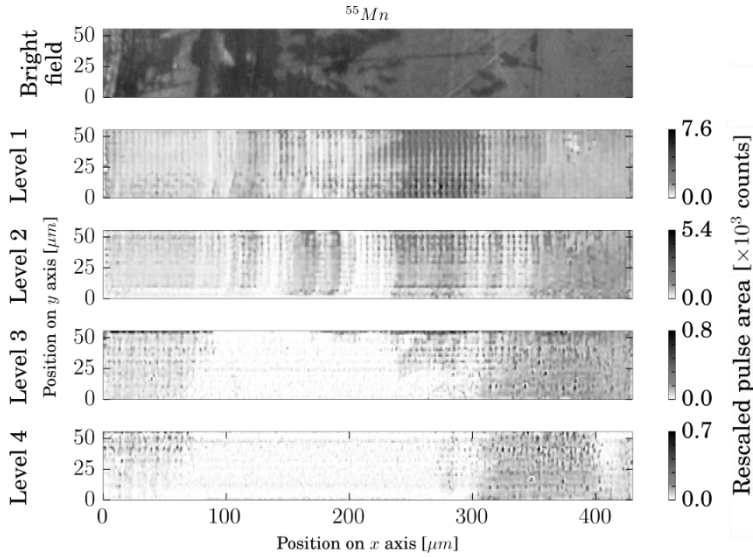


Figure 59 The corroded glass volume data after deconvolution.

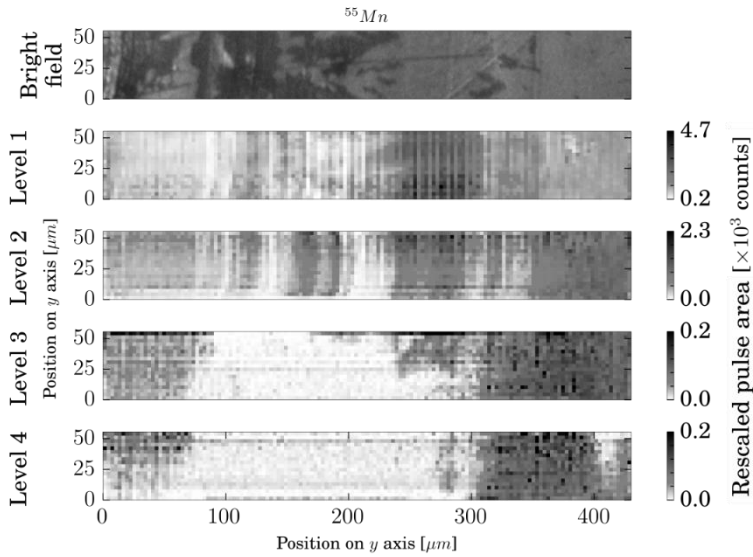


Figure 60 The corroded glass volume data resampled to simulate an imaging approach in which the ablation positions are placed adjacently. For evaluation purposes.

The integrated pulse area for the corroded glass volume before deconvolution is 7.4104×10^6 counts; after deconvolution, the integrated pulse area decreases to 7.3884×10^6 counts, a relative difference of 0.3 %. The integrated pulse area after deconvolution was rescaled to match the area before deconvolution.

3.3.4 2D mapping applications

The deconvolution approach was tested on multiple other samples to confirm its validity.

3.3.4.1 Multilayer Ceramic Capacitors.

Sub- μm sampling and numerical 2D deconvolution are demonstrated in the analysis of a high capacitance Multi-Layer Ceramic Capacitor (MLCC, $10\ \mu\text{F} \pm 10\%$, rated at 25 V), of X5R architecture (class II), 0805 case style, manufactured by AVX (Kyocera, Japan). The same operational parameters were used as in the analysis of the corroded glass. A grid of 22 lateral line scans, positioned at $1\ \mu\text{m}$ intervals in the y-axis direction, was projected onto the sample (Figure S-5), slanted relative to the direction of the electrodes at an angle of $\sim 15^\circ$. The lines were scanned using a Gaussian beam (mask set to the $1\ \mu\text{m}$ aperture), a pulse repetition rate of 25 Hz and a translation speed of $5\ \mu\text{m s}^{-1}$ ($\Delta_x, 5; \Delta_y, 1$).

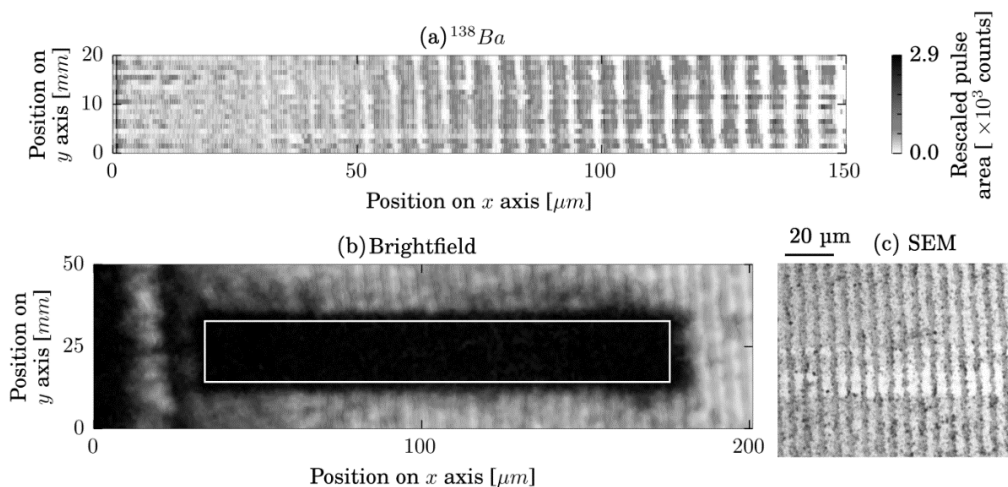


Figure 61 (a) ^{138}Ba distribution in MLCC (20×750 ablation positions; $\lambda, 0.01$; number of iterations, 4). (b) Brightfield image of the ROI after ablation (white rectangular outline denotes ROI). (c) Scanning electron microscopy (SEM) image (BSE, 5kV accelerating voltage, Phenom, Phenom-World, Eindhoven, Netherlands) of the polished MLCC surface.

This well-structured layered sample permits evaluation of the limitations of the approach. The MLCC was embedded into an epoxy resin (bisphenol A diglycidyl ether), cleaved transversally at the electrode end connections with a diamond saw, and polished mechanically with SiC paper (P1200 to P4000), oil-based diamond suspension ($1\ \mu\text{m}$ grain size) and colloidal silica suspension ($0.04\ \mu\text{m}$ grain size). The planar Ni electrodes were estimated to be on average $2\ \mu\text{m}$ in width; the mean thickness of the dielectric layer of BaTiO_3 was estimated to be $\sim 3\text{--}4\ \mu\text{m}$, based on SEM images (5 kV accelerating voltage, BSE, Phenom, Phenom-World, Eindhoven, Netherlands). The pixel size in the deconvolved ^{138}Ba image of $0.2\ \mu\text{m} \times 1\ \mu\text{m}$ suffices to

visualize the layered pattern of BaTiO₃ and Ni planar electrodes in the MLCC. Spatial aliasing effects when oversampling the pattern in the ablation zone in the absence of the deconvolution step will interfere severely with the elemental image. Although the beam size (1 μm in diameter at e^{-2} of the maximum intensity) is of the same order as the ablation position interspacing in the y-axis, the deconvolution contributes to the image quality in the y direction by correcting the asymmetry in the beam profile (by utilizing a PSF derived from the atomic force microscopy data) and the overlap of the edges of the laser spot with the edges of neighbouring craters. Asymmetry in the image can be observed as a result of the inclination between the orientation of planar electrodes and the sampling grid.

3.3.4.2 Sb Patterns in Murano Glass Decorations.

The deconvolution approach may also be useful on a μm -level; a decorative Murano Sb-containing glass pattern (Figure 62c) was ablated with a square laser beam of $65 \times 65 \mu\text{m}$. *A priori*, the glass surface was polished mechanically. A grid of 90×125 ablation spots, at an interspacing of 13 μm ($\Delta_x, 5$; $\Delta_y, 5$) was projected on the glass surface. The PSF employed was a binary cube, as the flat-top laser beam profile generates craters with a flat central zone and crater walls that are inclined at a steep angle. When considering the deconvolved image (pixel size $13 \times 13 \mu\text{m}$) in Figure 62a, relative to the procedure of discrete, adjacent ablation positions (Figure 62b), an enhancement of lateral resolution by deconvolution can be observed in the same order (~ 5) as the number of overlapping spots in the line scans. The additional level of detail in the ^{121}Sb distribution image demonstrates a structural correspondence with the microscopy images (under the assumption of correlation between the pattern location and the presence of ^{121}Sb , which may be present in the form of an opacifier).

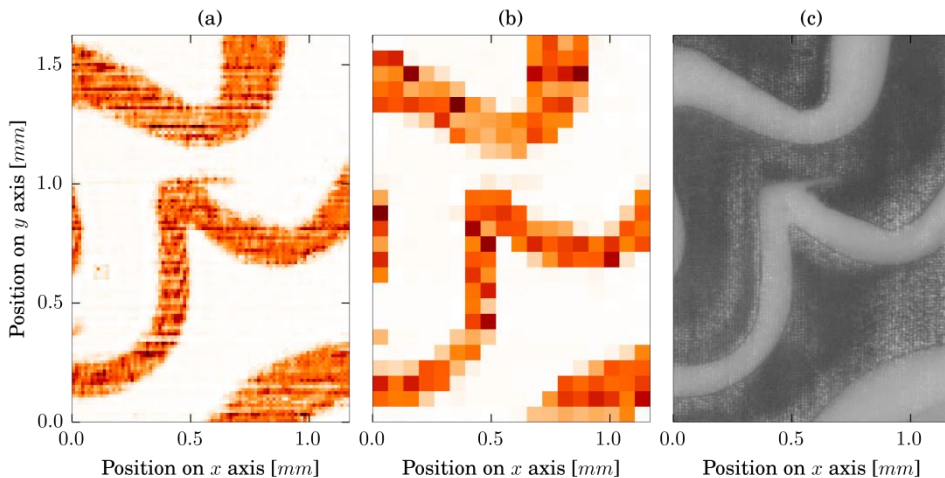


Figure 62 (a) Scanned area: $1.170 \times 1.625 \text{ mm}$; (b) Adjacent ablation positions approach result (for ^{121}Sb), constructed by sampling from (a) at every fifth data point in x- and y-axis (subsampling). (c) Brightfield microscopy image after ablation. Close observation reveals the square ablation damage pattern.

3.4 Conclusion

In this chapter, a sampling methodology and post-acquisition deconvolution procedure was proposed to enhance the lateral resolution of LA-ICP-MS imaging. The approach for deconvolving an artificially convolved image, created by oversampling, is a tool that proves to be beneficial in the aspect of lateral resolution, in the μm range, as well as in the sub- μm range, in scenarios where the laser beam waist size is far-field- or sensitivity-limited. When correctly implemented, the spatial resolving power of the methodology surpasses that of any other in LA-ICP-MS, as a lateral resolution below the beam dimensions can be obtained. The RLTV algorithm was demonstrated to spatially resolve the response of overlapping ablation spots at lateral resolutions down to $0.3 \pm 0.1 \mu\text{m}$ and thus below the laser beam diameter used ($1 \mu\text{m}$). This brings the technique closer to competing with nanoprobe and super-resolution imaging techniques for trace nuclide levels. There are two main limiting factors in the approach: (i) the level of axial homogeneity over the depth of the accumulated ablation damage inside each sampling layer, which will affect the accuracy of the deconvolution solution, and (ii) the sensitivity, which may limit the use of small laser beam waist sizes. Due diligence should be observed when constructing the sampling layers from which the convolved image is derived. Apart from overlapping line scans ablated at high repetition rates, it is also possible to interlace multiple overlaid sampling grids of spatially distinct ablation positions with a relative positional shift into a single high resolution convolved image. Through superimposition of the 2D sampling layers, 3D nuclide distributions at the minor or trace level can be reconstructed. Gaussian-type laser beam intensity profiles are particularly well-suited in the context of this approach as a result of their sharp PSFs and flat central zone in the superimposed ablation damage crater of the sampling grid. The PSF can be derived directly from topographical information gathered by surface characterization techniques, providing a meaningful correction for the beam shape and its aberrations. The deconvolution approach may be found useful even in scenarios where ablation positions are bordering each other, as it can correct for any overlap between the edges of the ablation craters, enabling the reconstruction of a more accurate representation of the nuclide distribution. In conclusion, the methodology may prove indispensable as an approach to correctly translate the ablated volume to representative voxels, and provides a pathway to push the lateral resolution of laser spectrochemistry 3D images below the laser beam waist size and far-field diffraction limits. Signal deconvolution of the pulse response peaks was also shown to enable higher repetition rates whilst permitting single pulse isolation, thus ensuring that the spatial information associated with each pulse remains accessible. These findings open up new fields of application for LA-ICP-MS and for other methods based on laser plasma spectrochemistry.

3.5 Bibliography

- (1) Van Malderen, S. J. M.; van Elteren, J. T.; Vanhaecke, F. *J. Anal. At. Spectrom.* **2014**, *30*, 119-125.
- (2) Van Malderen, S. J. M.; van Elteren, J. T.; Vanhaecke, F. *Anal. Chem.* **2015**, *87*, 6125-6132.
- (3) Giesen, C.; Wang, H. A.; Schapiro, D.; Zivanovic, N.; Jacobs, A.; Hattendorf, B.; Schuffler, P. J.; Grolimund, D.; Buhmann, J. M.; Brandt, S.; Varga, Z.; Wild, P. J.; Gunther, D.; Bodenmiller, B. *Nature methods* **2014**, *11*, 417-422.
- (4) Wang, H. A.; Grolimund, D.; Giesen, C.; Borca, C. N.; Shaw-Stewart, J. R.; Bodenmiller, B.; Gunther, D. *Anal. Chem.* **2013**, *85*, 10107-10116.
- (5) Zoriy, M. V.; Kayser, M.; Becker, J. S. *International Journal of Mass Spectrometry* **2008**, *273*, 151-155.
- (6) Russo, R. E.; Suen, T. W.; Bol'shakov, A. A.; Yoo, J.; Sorkhabi, O.; Mao, X.; Gonzalez, J.; Oropeza, D.; Zorba, V. *J. Anal. At. Spectrom.* **2011**, *26*, 1596-1603.
- (7) Fernández-Pradas, J. M.; Florian, C.; Caballero-Lucas, F.; Morenza, J. L.; Serra, P. *Appl. Surf. Sci.* **2013**, *278*, 185-189.
- (8) Vaschenko, G.; Etxarri, A. G.; Menoni, C. S.; Rocca, J. J.; Hemberg, O.; Bloom, S.; Chao, W.; Anderson, E. H.; Attwood, D. T.; Lu, Y.; Parkinson, B. *Opt. Lett.* **2006**, *31*, 3615-3617.
- (9) Woodhead, J.; Hergt, J.; Shelley, M.; Eggins, S.; Kemp, R. *Chemical Geology* **2004**, *209*, 121-135.
- (10) Chernonozhkin, S. M.; Goderis, S.; Bauters, S.; Vekemans, B.; Vincze, L.; Claeys, P.; Vanhaecke, F. *J. Anal. At. Spectrom.* **2014**, *29*, 1001-1016.
- (11) van Elteren, J. T.; Izmer, A.; Šala, M.; Orsega, E. F.; Šelih, V. S.; Panighello, S.; Vanhaecke, F. *J. Anal. At. Spectrom.* **2013**, *28*, 994-1004.
- (12) Managh, A. J.; Edwards, S. L.; Bushell, A.; Wood, K. J.; Geissler, E. K.; Hutchinson, J. A.; Hutchinson, R. W.; Reid, H. J.; Sharp, B. L. *Anal. Chem.* **2013**, *85*, 10627-10634.
- (13) Hattendorf, B.; Pisonero, J.; Gunther, D.; Bordel, N. *Anal. Chem.* **2012**, *84*, 8771-8776.
- (14) Drescher, D.; Giesen, C.; Traub, H.; Panne, U.; Kneipp, J.; Jakubowski, N. *Anal. Chem.* **2012**, *84*, 9684-9688.
- (15) Jurchen, J. C.; Rubakhin, S. S.; Sweedler, J. V. *Journal of the American Society for Mass Spectrometry* **2005**, *16*, 1654-1659.
- (16) Plotnikov, A.; Vogt, C.; Wetzig, K.; Kyriakopoulos, A. *Spectrochimica Acta Part B: Atomic Spectroscopy* **2008**, *63*, 474-483.
- (17) Van Kempen, G. M. P.; Van Vliet, L. J.; Verveer, P. J.; Van Der Voort, H. T. M. *Journal of microscopy* **1997**, *185*, 354-365.
- (18) de Monvel, J. B.; Le Calvez, S.; Ulfendahl, M. *Biophys. J.* **2001**, *80*, 2455-2470.
- (19) Carrington, W. A.; Lynch, R. M.; Moore, E. D. W.; Isenberg, G.; Fogarty, K. E.; Fredric, F. S. *Science* **1995**, *268*, 1483-1487.
- (20) Richards, W. H. *Journal of the Optical Society of America* **1972**, *62*, 55-59.
- (21) Lucy, L. B. *Astron. J.* **1974**, *79*, 745-754.

- (22) Verveer, P. J.; Gemkow, M. J.; Jovin, T. M. *Journal of microscopy* **1999**, *193*, 50-61.
- (23) Dey, N.; Blanc-Feraud, L.; Zimmer, C.; Roux, P.; Kam, Z.; Olivo-Marin, J. C.; Zerubia, J. *Microscopy research and technique* **2006**, *69*, 260-266.
- (24) Tanner, M. *J Anal Atom Spectrom* **2010**, *25*, 405.
- (25) Laasmaa, M.; Vendelin, M.; Peterson, P. *Journal of microscopy* **2011**, *243*, 124-140.
- (26) Vonesch, C.; Unser, M. *IEEE transactions on image processing : a publication of the IEEE Signal Processing Society* **2008**, *17*, 539-549.
- (27) Voelkel, R.; Weible, K. J.; Duparre, A.; Geyl, R., Eds.; SPIE Conference proceedings: 'Laser beam homogenizing: limitations and constraints', *SPIE Conference proceedings*, 2008, 71020J, p 71020J.
- (28) Bleiner, D.; Belloni, F.; Doria, D.; Lorusso, A.; Nassisi, V. *J Anal Atom Spectrom* **2005**, *20*, 1337-1343.
- (29) Diwakar, P. K.; Gonzalez, J. J.; Harilal, S. S.; Russo, R. E.; Hassanein, A. *J Anal Atom Spectrom* **2014**, *29*, 339-346.
- (30) Senoner, M.; Wirth, T.; Unger, W. E. S. *J Anal Atom Spectrom* **2010**, *25*, 1440.
- (31) Wang, H. A. O.; Grolimund, D.; Van Loon, L. R.; Barmettler, K.; Borca, C. N.; Aeschmann, B.; Guenther, D. *Anal Chem* **2011**, *83*, 6259-6266.
- (32) Plotnikov, A.; Vogt, C.; Wetzig, K. *J Anal Atom Spectrom* **2002**, *17*, 1114-1120.
- (33) Bleiner, D.; Bogaerts, A. *J Anal Atom Spectrom* **2006**, *21*, 1161-1174.
- (34) Wrobel, P.; Czyzycki, M. *Talanta* **2013**, *113*, 62-67.
- (35) Gurevich, E. L.; Hergenroder, R. *J Anal Atom Spectrom* **2007**, *22*, 1043-1050.
- (36) Lindner, H.; Autrique, D.; Pisonero, J.; Gunther, D.; Bogaerts, A. *J Anal Atom Spectrom* **2010**, *25*, 295-304.
- (37) Asogan, D.; Sharp, B. L.; O' Connor, C. J. P.; Green, D. A.; Hutchinson, R. W. *J Anal Atom Spectrom* **2009**, *24*, 917-923.
- (38) Tabersky, D.; Nishiguchi, K.; Utani, K.; Ohata, M.; Dietiker, R.; Fricker, M. B.; de Maddalena, I. M.; Koch, J.; Günther, D. *J Anal Atom Spectrom* **2013**, *28*, 831-842.
- (39) Bleiner, D.; Gunther, D. *J Anal Atom Spectrom* **2001**, *16*, 449-456.
- (40) Wen, S.-B.; Mao, X.; Greif, R.; Russo, R. E. *Journal of Applied Physics* **2007**, *101*, 023115.
- (41) Dal Bianco, B.; Bertoncello, R. *J Non-Cryst Solids* **2008**, *354*, 773-779.
- (42) Geisler, T.; Janssen, A.; Scheiter, D.; Stephan, T.; Berndt, J.; Putnis, A. *J Non-Cryst Solids* **2010**, *356*, 1458-1465.
- (43) Watkinson, D.; Weber, L.; Anheuser, K. *Archaeometry* **2005**, *47*, 69-82.
- (44) Schalm, O.; Proost, K.; De Vis, K.; Cagno, S.; Janssens, K.; Mees, F.; Jacobs, P.; Caen, J. *Archaeometry* **2011**, *53*, 103-122.
- (45) Nuyts, G.; Cagno, S.; Hellemans, K.; Veronesi, G.; Cotte, M.; Janssens, K. *Procedia Chemistry* **2013**, *8*, 239-247.

Chapter 4 Software development

This chapter describes the software developed in the context of this work. In the first part of this chapter, the architecture of the software is described. In the second part of this chapter, selected algorithms, central to the operation of the software library are discussed. The third part of this chapter presents the graphical user interface associated with this software library.

4.1 Introduction

Data processing poses a significant challenge in the analytical sciences. In recent years, the volume of data in mass spectrometry imaging (MSI) methods has been steadily increasing, as well as the time required by the user to process MSI data, as a result of advances in lateral resolution and the emergence of multiplexed, complex data sets. Efforts within the community have given rise to numerous data reduction GUIs. Still to this day, results are sometimes processed in spreadsheet software, *e.g.*, in LAMTRACE or LamTools, despite the availability of dedicated tools for data reduction of LA-ICP-MS data. Even in numerical computing environments, such as MATLAB, manual image processing can be cumbersome and labor-intensive.¹ For bulk processing, SILLS, a GUI based on MATLAB is also available at no charge. LA-ICP-MS image generation platforms such as IMAGENA² and GLITTER (IDL-based) have significant limitations in terms of image processing due to their age; they only cover the special case of unidirectional scanning along a set of parallel lines and are thus limited in their applicability. Iolite^{3,4}, on the other hand, is a well-developed, recently commercialized data reduction platform based on IgorPro™, Iolite has been maintained to a good extent and is continuously being extended, *e.g.*, for 3D imaging using the BioLite plugin. There is also a library⁵ in R 'LAICPMS' available on CRAN. Other software, designed for organic mass spectrometry can also be useful for browsing through raw data and calibration, *e.g.*, BioMap, MSiReader, DataCubeExplorer, omniSpect, MALDIVision. msiQuant. As for the output,

sequential mass analyzers still supply their data in human readable formats (HRF), such as ASCII comma-separated files. For organic mass spectrometry, a common data format, imzML, was developed under the Computis project, a European FP6 project.⁶ Another standard format, mzML was developed by the HUPO Proteomics Standards Initiative. ImzML and mzML consist of a hierarchical set of raw binary files in folders, annotated by XML files. This information is accessible through an IPython notebook in OpenMSI's web API.⁷ Although these software packages do a fine job for their specific application, analytical data is expected to become of such complexity, that these programs and formats will be limited in their applicability. There is a general evolution towards 3D data and multimodal approaches, in which multiple techniques are incorporated into a single data format. Furthermore, as data volumes become much larger, keeping all data in RAM becomes problematic. To this end, a data format for LA-ICP-MS imaging, based on a NeXus application definition for HDF5, is proposed. NeXus is a common hierarchical data format mostly used for large data storage in neutron, x-ray, and muon science, held to high standing by the international community of scientists representing major research facilities which are involved with the analysis and visualization of neutron, x-ray, and muon data. NeXus is a set of definitions for how an HDF5 file should be structured; HDF5 is a standardized hierarchical and highly optimized binary data format.

This chapter presents an introduction to HDIP (hyper-dimensional image processing), a python 3.4 library designed to be a platform for processing imaging data such as transient mass spectrometry data, with a specific emphasis on laser ablation-inductively coupled plasma-mass spectrometry imaging. This python library is based around the HDF5 file-type for full metadata retention and consists largely of unsupervised methods. Python was the preferred language to interface with HDF5 files, over *e.g.*, MATLAB, due to it being a cross-platform, open-source, high-level object-oriented language which can be easily extended due to its broad language compatibility. The library provides support towards Paraview (Kitware Inc., New York, USA), an open-source data analysis and visualization application based on VTK. The library is designed towards flexibility and supports large datasets both in storage, processing, and rendering through distributed and parallel out-of-core computation. It is also envisaged that the structure of the HDF5 files produced by the software will largely mirror the structure of HDF5 files produced by the icpTOF, an ICP-TOF-MS unit produced by TOFWERK AG, as the current implementation of this unit in combination with a LA system, is perceived to be the LA-ICP-MS system evolved furthest at the time of writing. This would enable the user to read the raw data of the icpTOF in the native format, without conversion.

4.2 Goals

The objective of the HDIP library is to be a fast, flexible and extensible platform for large, complex, image processing. The library will process numerical data with up to 32 dimensions (limited by HDF5). Every algorithm is designed to handle multi-dimensional data, with an arbitrary organization of the dimensions. The dimensions relevant to the algorithm can either be specified as a parameter, or be retrieved by a label attached to the dimensions. The data to be processed can be significantly larger than the RAM, which is limited, on most workstations, to 16-64 GB (at the time of writing). Distributed solutions exist, yet these large-scale facilities

are not always available. The algorithms of the library only load a chunk of the data in memory, corresponding to the slice that is required. For some operations, however, the algorithm requires continuous access to the entire dataset, in which case the data is cached entirely into RAM.

4.3 Description of the architecture

HDIP focusses on data reduction rather than image rendering or image acquisition. To help the laser operator interact more easily with the library, a graphical user interface (GUI) was developed. This GUI was designed in the Qt 4.8.5 toolkit employing PySide 1.2.2 bindings, to allow for fast interaction with the software. Many of the 1D and 2D plotting occurs with the Qt framework through the PyQtGraph library, allowing for fast, OpenGL-based (*i.e.* vector-based) hardware accelerated rendering. Vispy, a fast OpenGL-based data visualization library generates the 3D rendering scenes. Vispy allows low-level access to OpenGL/GLSL objects, *e.g.*, textures, framebuffers (FBO), vertexbuffers (VBO) and shaders, through an object-oriented OpenGL API called 'gloo'.

4.3.1 Library structure

The library is build up from 5 packages comprising 61 modules, which contain a total of 558 functions or classes. In order to display the links between these structures, an undirected graph of the hierarchy was constructed with Graphviz, a graph visualization software package, which uses a scalable multilevel force-directed algorithm to organize the levels. The 'dot' code describing the structure was generated using a Python script. From Figure 63 it is clear that the *computation* and *gui* packets have the most complex organization. The structure at the function/class level (Figure 64) cannot be easily visualized in 2D due to its complexity. The library is organized as such that it can operate independently of the GUI package. Packages other than the GUI package do not call any function in the GUI package, whilst the GUI package imports the library as a whole. This is made so the library can be compiled without the Qt framework.

When a page would contain an average of 45 lines of code, a printout of the HDIP library would be >2000 pages long. The amount of code is a measure of code complexity. A utility was used to count the lines of code (Code snippet 1).

Code snippet 1 Output of CLOC utility for counting lines of code

Language	files	blank	comment	code
Python	262	6820	16240	35035
C	16	1310	5541	15216
Qt	14	0	0	10654
XML	34	83	720	3486
HTML	1	13	1	2110
Cython	3	7	57	205
C/C++ Header	5	0	0	7
SUM:	335	8233	22559	66713

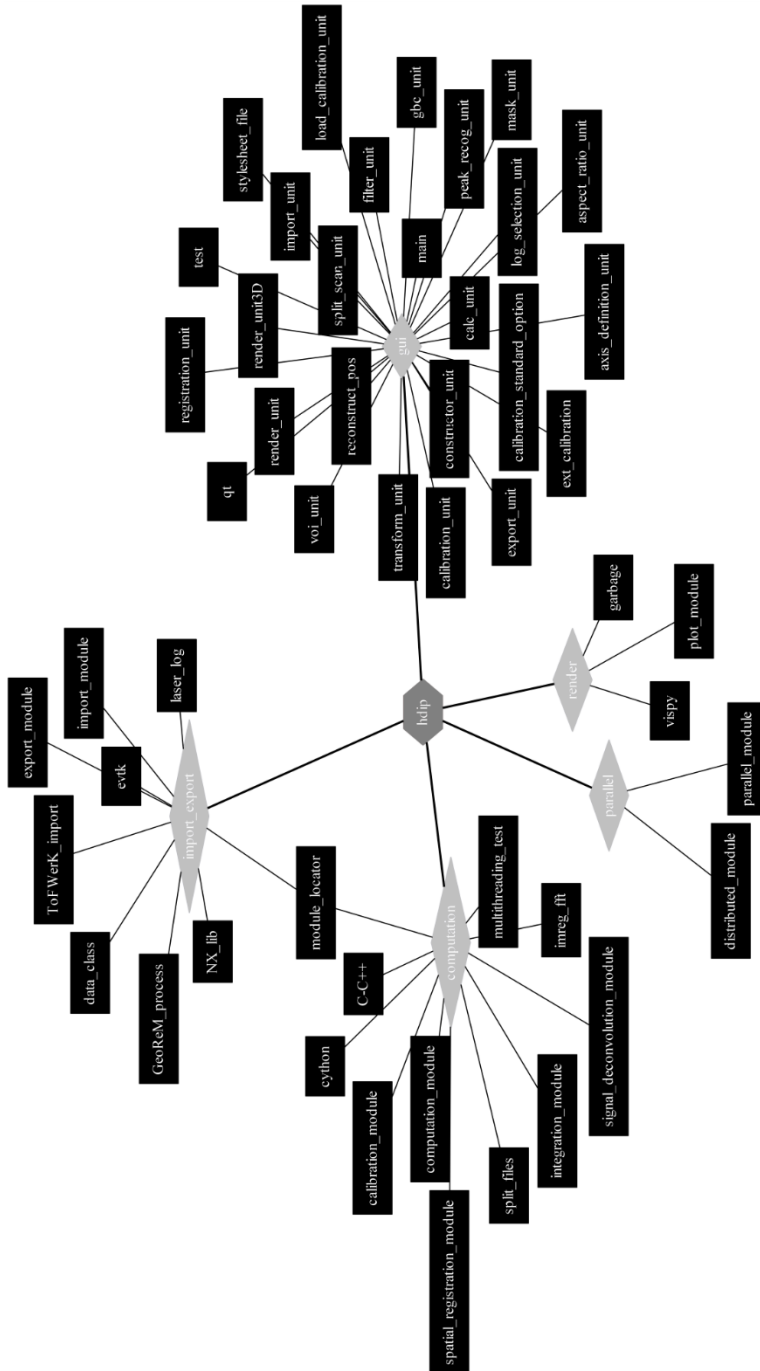


Figure 63 Undirected organizational graph of the library structure down to the module level with annotations in every module.

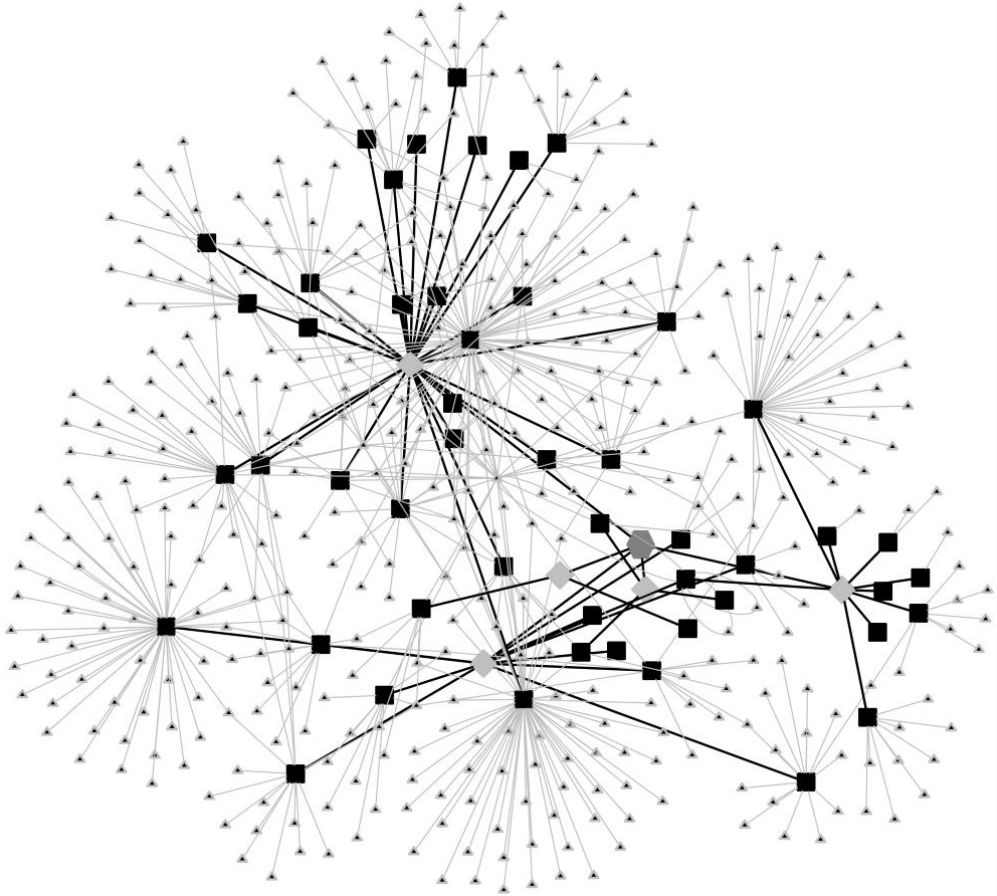


Figure 64 Undirected organizational graph of the library structure down to the function level. An identical color scheme was used as in Figure 63.

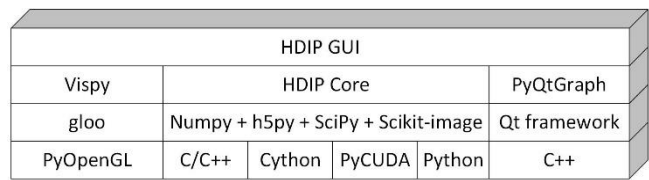
4.3.2 Dependencies

The library has a number of top-level dependencies: (parts of) these packages/libraries are imported into the library to be utilized as functions or API. These packages are of course also relying on their own dependencies. The library relies most heavily on the Numpy, Scipy (mainly ndimage), and Scikit-image packages. The module can be compiled for the Windows and Linux platform. The development platform is Linux Red Hat 7.0.

Table 5 Dependencies HDIP

Dependency	Description	License
Anaconda 4.2.0 with Python 3.4 environment	Distribution of Python containing 110 packages	BSD
PyEVTk 1.0.0	Package for exporting VTK binary files	Custom (free usage under all conditions with disclaimer)
PyQtGraph 0.9.10	GUI/visualization library	MIT open-source license
Vispy	Visualization library	BSD 3-Clause License
PyOpenGL	Binding to OpenGL	BSD

Figure 65 Dependency stack



4.3.3 Documentation

Most functions/classes in the HDIP core have an extensive docstring – a header at the start of each function explaining the functionality and parameter specifications. The docstring is build up in a fixed way (Code snippet 2, Code snippet 3). This scheme matches the one of the numpy library. The HDIP GUI is not documented to such an extent.

Code snippet 2 Conventions within a docstring

```
'''
    This part describes the general function of the function or class.

    Parameters
    -----
    parameter: dtype
        explains what the parameter is and how it is used in the algorithm

    Returns
    -----
    Return variable: dtype

    Notes
    -----
    Additional information regarding the algorithm

    Examples
    -----
    This is the part where a doctest is placed, i.e a small test to see if the\
    function is properly working
'''
```

Code snippet 3 Example of a docstring

```
def fw(y,x=0,h=0.5):
    """
        This function looks for the full width of the largest peak in the vector.

        Parameters
        -----
        y: vector, array-like
            vector containing the peak
        x: vector,array-like, optional
            vector corresponding to the y dimension; time, mass,...
        h: float, optional
            defines at which fraction (<1.0) of the height the maximum of the peak\
            the width must be determined

        Returns
        -----
        out: float
            the width of the peak at a fraction of the height

        Notes
        ----
        Only a single peak is expected. This function can fail when the signal is very\
        noisy.

        Examples
        -----
        >> fw(y=np.array([1,1,2,3,2,1,1]),x=np.array([1,2,3,4,5,6,7]), h=0.5)
        3.0
        """
    if h>1 or h<0:
        print('No correct height criterium.')
        return None
    if x.shape!=y.shape:
        x=np.arange(len(y))
    %% normalization
    h=h*np.max(y)
    if y.max()>np.abs(y.min()):
        c=np.argmax(y)
    else:
        c=np.argmin(y)
    i=1
    %% finding the lead index
    while np.sign(y[i]-h)==np.sign(y[i-1]-h):
        i+=1
        if i==y.shape[0]:
            return None
    interp=(h-y[i-1])/(y[i]-y[i-1])
    l=x[i-1]+interp*(x[i]-x[i-1])
    i=c
    while np.sign(y[i]-h)==np.sign(y[i-1]-h) and i<=len(y)-2:
        i=i+1
    if not i==len(y):
        interp=(h-y[i-1])/(y[i]-y[i-1])
        r=x[i-1]+interp*(x[i]-x[i-1])
        return r-l
    else:
        return None
```


4.4 Data import

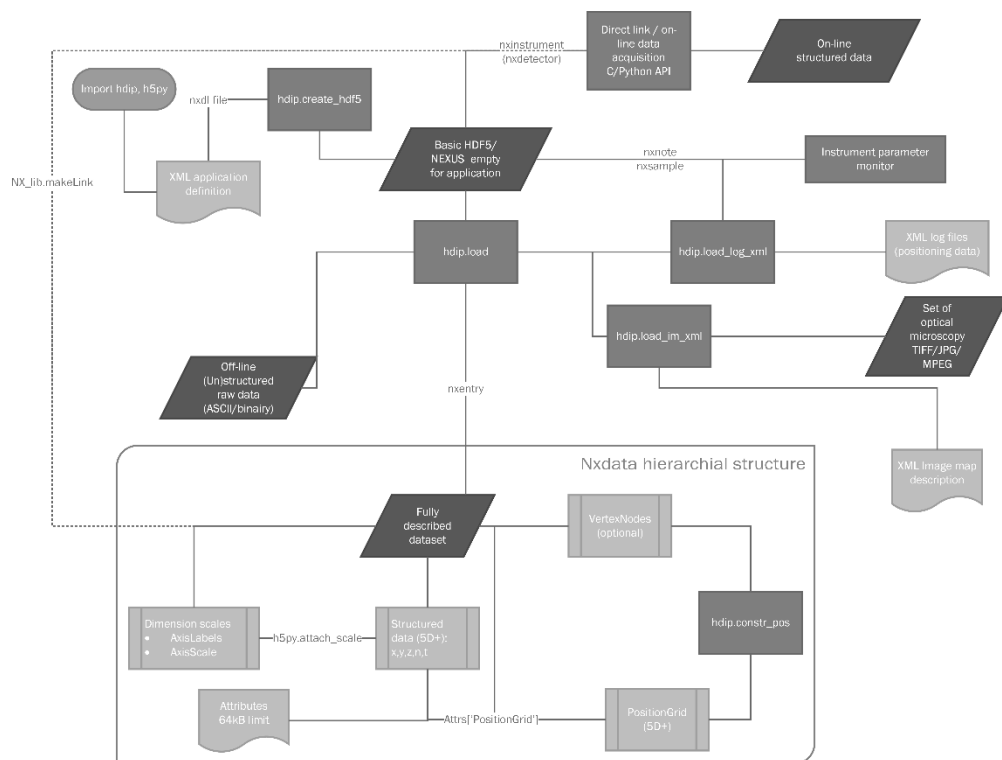
LA data in various data formats, as produced by ubiquitous ICP-MS data acquisition software, can be imported into an HDF dataset. Optionally, metadata such as laser log files, topographical data, and other analytical data can be attached to the dataset (Figure 66). There are 2 ways in which metadata is added: i) as an attribute of the dataset, and ii) as a dimension scale attached to the dataset. Attributes (Code snippet 4) are attached to the dataset as a dictionary: small sets of data (<64kB of any data type) are assigned to keys, which can be retrieved on the fly. The attributes can also reference other datasets; in this case, only the reference id is stored, not the entire dataset. This is, for example, the case for the `PositionGrid`, an array describing the spatial coordinates of each voxel individually. Other modalities, *e.g.*, optical microscopy images, can also be attached in this manner. There are two main paradigms in programming: object-oriented programming (OOP) and procedural (sometimes called functional) programming. The HDIP architecture embraces both paradigms: computations are carried out in a procedural way, but the HDF datasets can be seen as persistent objects, with a very complex subset of methods and properties. The `h5py` library is an API to some of the built-in methods of HDF.

Code snippet 4 Example of attributes

```
(('AspectRatio', array([ 1.3174269,  2.4872449,  1.          ])))
('Name', '1819_spheroid-1')
(['Events:Pass1.Event0'].ChangeGas', '1')
(['GasControl:Online'].FlowController2.RampTime', '70')
(['Events:Pass0.Event0'].GasMode', '1')
(['GasControl:Evacuate'].FlowController0.End', '0.2')
(['Events:Pass0.Event4'].SetTrig', '0')
('Dosage', 10.0)
('Laser.RepRate', 50.0)
('DIM_TYPE', array([b'spatial', b'spatial', b'spatial', b'spectral', b'spectral'],
                    dtype='|S8'))
('DIMENSION_LIST', array([array([<HDF5 object reference>, <HDF5 object reference>],
                                dtype=object),
                           array([], dtype=object), array([], dtype=object),
                           array([<HDF5 object reference>], dtype=object),
                           array([], dtype=object)], dtype=object))
('DIMENSION_LABELS', array([b'spatial_x', b'spatial_y', b'spatial_z', b'spectral_x',
                             b'spectral_y'], dtype=object))
('DIM_AXIS', array([b'x', b'y', b'z', b'x', b'y'],
                    dtype='|S1'))
('Thresholds', array([[ 715.49          , 1442.44803347],
                       [ 39972.76977712, 18579.72168765]]))
('Bounds', <HDF5 object reference>)
```

The `'DIM_TYPE'` item of the attribute set designates the type of data of each dimension. The library accepts spatial, temporal and spectral dimensions. The `'DIM_AXIS'` argument, on the other hand, describes the coordinate system attached to each dimension. The library accepts any coordinate system, though a Cartesian system is most commonly used, as it can be visualized by the GUI and is accepted by spatial filters.

Figure 66 Workflow of loading LA-ICP-MS data into HDF5



Dimension scales, on the other hand, are (1D) datasets attached to a single dimension. For mass spectrometry signals, this includes the time log, position log, and the mass calibration. These dimension scales length often matches the size of the dimension they are attached to, though this is not a requirement. A special type of dimension scale is a ‘channel header’, this compound dataset can annotate spectral channels with a label, *e.g.*, the name of the nuclide. The `hdip.load` functions are responsible for loading the data and metadata. A small part of the code of the function `hdip.load_ASCII`, responsible for loading a single human-readable file in a generic way, is displayed in Code snippet 5. This is the most basic action performed by the `hdip.load_ASCII` function. The organization of the data to be imported is inferred from the hierarchical directory structure in which the data files are placed. As such, the 2D, 3D, and 4D data spread over >100 files can be imported directly into a single array. For images, the filenames or time of writing indicate the order in which they are recorded and at which position they should be placed in the image.

Code snippet 5 First part of `hdip.load ASCII`.

```
def
load_ASCII(source_path_str,dgroup,node='',mode=0,order=True,log='',log_select=0,header_1
ist=[],delim_str=None,header_int=0,footer_int=0,export_type=None,export_path=None,units=
b'counts',progressbar='',_axis_rank=(0,3),_axis_dimension=(0),_dimension_units=(b's'),_f
ile_format='*.csv',_source=''):
    import hdip
```

```

import sys
from hdip.import_export import NX_lib
import h5py

attrs={}
if not os.path.exists(source_path_str):
    print('Import failed. The path {} does not exist'.format(source_path_str))
    sys.exit()
    return None
if log:
    if not os.path.exists(log):
        print('Import failed. The log path {} does not exist'.format(log))
        sys.exit()
        return None
    attrs,ablation_data,vertex_grid = hdip.load_log_xml(log)
    if mode ==1 or mode == 'icpTOF' or mode == 'icpTOF_FullSpectra' or mode==
'icpTOF_PeakData':
        if isinstance(source_path_str,str):
            path_list= [source_path_str]
        elif isinstance(source_path_str,list):
            path_list = source_path_str
    if node:
        attrs['Name'] = node
    else:
        node = os.path.split(source_path_str)[-1]
        attrs['Name']= node

    if (not isinstance(path_list,list)) and (not isinstance(path_list,str)):
        print('Import failed. The argument provided ({} ) is not a list or a
string.'.format(path_list[0]))
        return None
    if mode==1:
        for k in range(len(path_list)):
            if os.path.isfile(path_list[k]):
                if not os.path.exists(path_list[k]):
                    print('Import failed. The path {} does not
exist'.format(path_list[0]))
                    sys.exit()
                    return None
            if not delim_str:
                delim_str = get_delim(path_list[0])
            if not header_int:
                header_int=get_header_int(path_list[0])
            if not footer_int:
                footer_int=get_footer_int(path_list[0])
            if header_list==[]:
                main_path = hdip.import_export.module_locator.module_path()
                header_list
get_header_1D(path_list[0],delim_str,get_header_row_index(path_list[0],main_path,delim_s
tr))

temp_array=np.genfromtxt(path_list[0],delimiter=delim_str,skip_header=header_int,skip_fo
oter=footer_int)
        if len(temp_array.shape)==2:
            # standardizing the output with other multi-dimensional arrays
            array_out
hdip.init_write(shape=(np.shape(temp_array) [0],1,1,np.shape(temp_array) [1],1),
node=name)

            array_out[:,0,0,:,0] = temp_array
            if len(_axis_rank)>1:

```

```

            if                               isinstance(_axis_rank[0],int)                and
isinstance(_axis_rank[1],int):
            array_out=np.swapaxes(array_out,0,_axis_rank[0])
            array_out=np.swapaxes(array_out,3,_axis_rank[1])
        elif len(temp_array.shape)==1:
            array_out = np.zeros(shape=(np.shape(temp_array)[0],1,1,1,1))
            array_out[:,0,0,0,0] = temp_array
            if isinstance(_axis_rank,int):
                array_out=np.swapaxes(array_out,0,_axis_rank)

```

A new HDF5 file is created by the `hdip.create_hdf5` function, which constructs an HDF5 file according to a NeXus application definition, retrieved as an XML file (35 different definitions available).

Code snippet 6 First part of `hdip.create_hdf5`.

```

def create_hdf5(path,nxdl='NX1aICP-MS.nxdl',dset=np.array([]),title=''):
    import xml.etree.ElementTree as ET
    from hdip.import_export import NX_lib
    from hdip.import_export import module_locator
    import datetime
    timestamp = "T".join( str( datetime.datetime.now() ).split())
    f = NX_lib.makeFile(path, file_time=timestamp,\
                        HDF5_version='1.8.13',\
                        NeXus_version='3.0.0',\
                        file_name = os.path.split(path)[1],\
                        initial_format = 'HDF5')

    main_path = module_locator.module_path()
    nxdl_path = os.path.join(main_path,'NXDL')
    nxdl = os.path.join(nxdl_path,nxdl+'.xml')

    def parse_and_get_ns(file):
        events = "start", "start-ns"
        root = None
        ns = {}
        for event, elem in ET.iterparse(file, events):
            if event == "start-ns":
                if elem[0] in ns and ns[elem[0]] != elem[1]:
                    raise KeyError("Duplicate prefix with different URI found.")
                ns[elem[0]] = "{%s}" % elem[1]
            elif event == "start":
                if root is None:
                    root = elem
        return ET.ElementTree(root), ns

    def create_groups(parent,root,ns):
        for child_group in root.findall(ns['']+ 'group'):
            if child_group.get('name'):
                new_group = NX_lib.makeGroup(parent, child_group.get('name'),
child_group.get('type'))
            else:
                new_group = NX_lib.makeGroup(parent, child_group.get('type')[2:],
child_group.get('type'))
            create_groups(new_group,child_group,ns)
        for child_field in root.findall(ns['']+ 'field'):
            new_dset = parent.create_dataset(child_field.get('name'),())
            for attr in ['type','units']:

```

```

        if child_field.get(attr):
            new_dset.attrs[attr]=child_field.get(attr)
    if os.path.exists(nxdl):
        tree, ns = parse_and_get_ns(nxdl)
        root = tree.getroot()
        create_groups(f,root,ns)
    else:
        print('nxdl file was not found, creating a standard hdf5 file')
    f.close()
    print('hdf5 file {} initialized.'.format(path))

```

The definition of the application definition for LA-ICP-MS is displayed below (Code snippet 7).

Code snippet 7 NeXus application definition proposal for LA-ICP-MS.

```

<?xml version="1.0" encoding="UTF-8"?>
<?xml-stylesheet type="text/xsl" href="nxdlformat.xsl" ?>
<definition name="NXlaICP-MS" extends="NXobject" type="group"
  category="application"
  xmlns="http://definition.nexusformat.org/nxdl/3.1"
  xmlns:xsi="http://www.w3.org/2001/XMLSchema-instance"
  xsi:schemaLocation="http://definition.nexusformat.org/nxdl/3.1 ../nxdl.xsd"
  version="1.0b"
>
<doc>
  Instrument definition for a laser ablation-inductively coupled plasma mass
  spectrometer hyphenated instrument. Suited for sector, quadrupole, DOF and TOF mass
  analyzers using single of multiple (pseudo-)simultaneous detectors
</doc>
<group type="NXentry" name="entry">
  <field name="title"/>
  <field name="start_time" type="NX_DATE_TIME"/>
  <field name="definition">
    <doc> Unofficial NeXus NXDL schema</doc>
    <enumeration>
      <item value="NXlaICP-MS"/>
    </enumeration>
  </field>
  <group type="NXinstrument">
    <group type="NXlaser">
      <field name="wavelength" type="NX_FLOAT" units="NX_WAVELENGTH"/>
      <field name="name"/>
      <field name="probe">
        <enumeration>
          <item value="photon"/>
        </enumeration>
      </field>
      <field name="spot size"/>
    </group>
    <group type="NXicp">
      <field name="RF power" type="NX_FLOAT" units="NX_POWER"/>
      <field name="expansion chamber pressure" type="NX_FLOAT"
units="NX_PRESSURE"/>
      <field name="analysis chamber pressure" type="NX_FLOAT"
units="NX_PRESSURE"/>
      <field name="RF frequency" type="NX_FLOAT" units="NX_FREQUENCY"/>
    </group>
  </group>

```

```

        <group type="NXdetector">
            <field name="data" type="NX_FLOAT" signal="1">
                <dimensions rank="1">
                    <dim index="1" value="ndet" />
                </dimensions>
            </field>
        </group>
    </group>
    <group type="NXsample">
        <field name="name">
            <doc>Descriptive name of sample</doc>
        </field>
    </group>
    <group type="NXnote">
        <field name="name">
            <doc>Descriptive notes on the sample</doc>
        </field>
    </group>
    <group type="NXlog">
        <field name="name">
            <doc>Logfiles of both the laser and MS</doc>
        </field>
    </group>
    <group type="NXmonitor">
        <field name="mode">
            <doc>
                Count to a preset value based on either clock time (timer)
                or received monitor counts (monitor).
            </doc>
            <enumeration>
                <item value="monitor"/>
                <item value="timer"/>
            </enumeration>
        </field>
        <field name="preset" type="NX_FLOAT">
            <doc>preset value for time or monitor</doc>
        </field>
        <field name="integral" type="NX_FLOAT" units="NX_ANY">
            <doc>Total integral monitor counts</doc>
        </field>
    </group>
    <group type="NXdata">
        <link name="data" target="/NXentry/NXinstrument/NXdetector/data">
            <doc>Link to data in /NXentry/NXinstrument/NXdetector</doc>
        </link>
    </group>
</group>
</definition>

```

4.5 Data processing

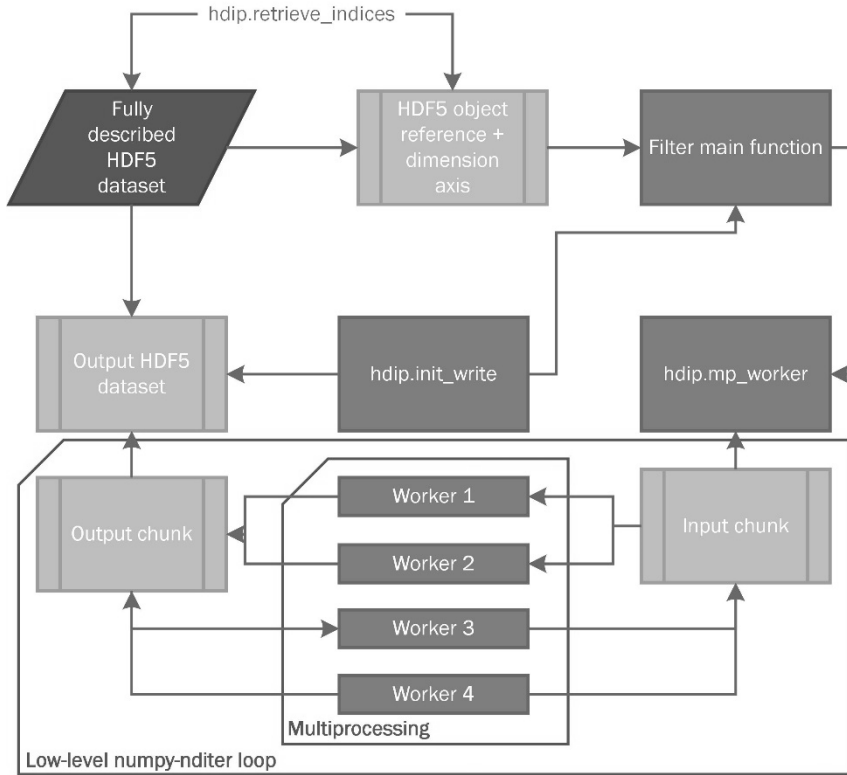
The library contains many different algorithms for N-dimensional image processing. Many of these functions are parallelized through the parallel module. A few very intensive filter functions are implemented in C/C++ and are pre-compiled, to achieve faster calculations. The bytecode was pre-compiled using the CMake compiler for Windows (.c) and the GNU Compiler Collection (GCC) for Linux (.so). Cython can also be used to pre-compile Python code, though it

does require static typing of all variables. Algorithms can be parallelized in a very generic way using the `hdip.mp_worker` function.

4.6 Workflow

The `hdip.mp_worker` function (Figure 67, Code snippet 8) will chunk the dataset during processing: slices of the dataset relevant to the scope of the function will be extracted and handed down to one or more worker functions. As a result of this, the datasets larger than the RAM can be processed. These worker functions contain the core algorithms. As both the HDF5 datasets following the NeXus specification and default numpy arrays are written in C-order, the `hdip.mp_worker` chunks the data in contiguous parts following C-order style indexing. This means the last index is the fastest iterator (as opposed to Fortran-style indexing). Some functions require buffering of more than one dimension, *e.g.*, 3D filter algorithms, hence, the chunking algorithm also works on tuples of axes to be buffered. When the data within the slice is not contiguous, the data must be read intermittently across a larger space on the secondary storage and transposed on-the-fly, resulting in increased time for IO operations. Faster IO and compression is possible for data with a chunked storage layout, in which the dataset is divided up into regularly-sized pieces which are stored haphazardly on disk and indexed using a B-tree, though such layout is not practical given the generic nature of the imaging data. It is possible to perform data refactoring to speed up IO operations, *e.g.*, when repetitive read-write cycles are required, so that the dimensions relevant to the algorithm are placed as the last indices. Data layout in the secondary storage remains important, despite recent gains in IO speed due to the availability of flash memory (SDDs). Implicit indexing of the relevant dimensions, *i.e.* retrieving a specific axis using the `and` properties, is widely used in the GUI and relies upon the `hdip.retrieve_indices` function. The pool of workers typically contains a number of workers equal to the number of available threads -1, as a node is reserved for the main process (and GUI). The multiprocessing approach used here overcomes the global interpreter lock (GIL) and is thread-safe.

Figure 67 Multiprocessing workflow using a pool of workers.

Code snippet 8 The `hdip.mp_worker` function

```
def mp_worker(func, *args, **kwargs):
    """
    multiprocessing working unit for parallel out-of-memory computation to run a\
    function on an N-dimensional array, with a given operational dimension range

    Parameters
    -----
    func: function
        function to which the arguments should be applied
    *args: dummy variables
        arguments should not be present
    **kwargs: named variables
        input for the function

    Returns
    -----
    out: array, N-dimensional

    Notes
    -----
    none

    Examples
    -----

```



```

DOCTEST ABSENT
"""
import h5py
if 'dset' in kwargs.keys():
    if isinstance(kwargs['dset'], h5py.Dataset) or
isinstance(kwargs['dset'], np.ndarray):
        dset=kwargs['dset']
        # del kwargs['dset']
    if 'out' in kwargs.keys():
        if isinstance(kwargs['out'], h5py.Dataset) or
isinstance(kwargs['out'], np.ndarray):
            out=kwargs['out']
        else:
            out=np.zeros(shape=dset.shape)
    else:
        out=np.zeros(shape=dset.shape)

if '_axis' in kwargs.keys():
    _axis=kwargs['_axis']
    if not isinstance(_axis, tuple):
        _axis=(_axis,)
else:
    _axis=(kwargs['dset'].shape[-1])

rank = len(dset.shape)
## option 1: the result can be broadcasted into the same shape
if dset.shape==out.shape:
    pool = Pool(processes=cpu_count()-1)
    ## if only one axis, buffer axis
    if rank==1:
        it=np.nditer([dset,out], flags=['external_loop','buffered'],\
            op_flags=['readonly'], ['readwrite','allocate',
'no_broadcast']], order='C', buffersize=dset.shape[0]/cpu_count()-1)
        for x,y in it:
            kwargs['dset']=x
            y[...]=pool.apply_async(func, args = (*args,**kwargs)).get()
            if isinstance(out, np.ndarray):
                return y
    ## chunk an axis not in _axis for read/write operations; but iterate over the
slice provided in _axis in the function
    elif isinstance(_axis, tuple) or isinstance(_axis, int):
        ## find the axis not in _axis
        chunk_ax = -1
        for ax in range(rank):
            if ax not in _axis:
                chunk_ax = ax
                break
        if chunk_ax== -1:
            if 'quiet' in kwargs:
                if not kwargs['quiet']:
                    print('WARNING: cannot find axis to chunk; importing entire array
in memory and performing function once')
            kwargs['dset']=dset
            if 'progressbar' in kwargs:
                kwargs['progressbar'].setValue(0)
            out[...]=func(*args,**kwargs)
            if 'progressbar' in kwargs:
                kwargs['progressbar'].setValue(100)
        if chunk_ax!= -1:

```

```

        chunk = np.nditer(np.zeros(shape=(dset.shape[chunk_ax])),
flags=['multi_index'],order='C')
        ## recalculate the _axis selection to match the chunk: _axis2 is the index
of the axes selected in the chunk_dset
        _axis2=[]
        for i,_ax in enumerate(_axis):
            if _ax<chunk_ax:
                _axis2.append(_ax)
            else:
                _axis2.append(_ax-1)

        while not chunk.finished:
            ## chunk index provides the slice of the chunk
            chunk_index=[]
            if chunk_ax>0:
                chunk_index+= [slice(None)]*ax
            chunk_index+=list(chunk.multi_index)
            if 'progressbar' in kwargs:

kwargs['progressbar'].setValue(chunk_index[chunk_ax]/dset.shape[chunk_ax]*100)
            chunk_index+= [slice(None)]*(rank-ax-1)
            ## generate the buffersize and swap axis to align for iteration
            ## permute axis to get the desired _axis in the last indices (in
the correct order):
            chunk_dset = dset[tuple(chunk_index)]
            ## place the first indices of _axis as the last axis in the chunk
            permutation=np.delete(np.arange(rank-1),_axis2).tolist()+_axis2
            chunk_dset=np.transpose(chunk_dset,axes=permutation)
            ## calculate reverse permutation for end result
            permutation_r=[0]*len(permutation)
            for i,n in enumerate(permutation):
                permutation_r[n]=i
            _buff=np.prod(chunk_dset.shape[-len(_axis):])
            chunk_out=np.zeros(shape=chunk_dset.shape)
            it=np.nditer([chunk_dset,chunk_out],
flags=['external_loop','buffered'],\
            op_flags=[['readonly'],['readwrite'],'allocate',
'no_broadcast'],order='C',buffersize=_buff)
            for x,y in it:
                ## call to python or numba functions
                kwargs['dset']= np.reshape(x,chunk_dset.shape[-len(_axis):])
                y[...] =np.reshape(pool.apply_async(func, args =
(*args,**kwargs)).get(),_buff)
                if isinstance(out, np.ndarray) or isinstance(out, h5py.Dataset):

out[tuple(chunk_index)]=np.transpose(it.operands[1],axes=permutation_r)
                chunk.iternext()

        ## option 2: broadcasting into a array of different size happens using a slower non-
buffered single threaded loop
        else:
            ## isolate the axes to be buffered, in the chunk
            it_axis= [k for k in range(len(dset.shape)) if k not in _axis]
            it_size = [dset.shape[k] for k in it_axis]
            _buffer = np.nditer(np.zeros(shape=tuple(it_size)),
flags=['multi_index'],order='C')
            while not _buffer.finished:
                axis_buff = list(_buffer.multi_index)
                if 'progressbar' in kwargs:
                    kwargs['progressbar'].setValue(np.prod(axis_buff)/np.prod(it_size)*100)
                for ax in _axis:

```

```

        axis_buff.insert(ax, slice(None))
        kwargs['dset'] = dset[tuple(axis_buff)]
        out[tuple(axis_buff)] = func(*args, **kwargs)
        _buffer.iternext()
    if 'progressbar' in kwargs:
        kwargs['progressbar'].setValue(100)
    if isinstance(out, np.ndarray):
        return out

```

4.6.1 Filtering and transformations

The HDIP library offers multiple 1D and 2D filtering options (Code snippet 9). These filters can be applied to an arbitrary number of dimensions, with the axes in any order. Finite impulse response (FIR) filters are implemented as a convolution of the signal along the selected axis with a window function (flat, hanning, hamming, bartlett, blackman, Gaussian), while other filters (median, Savitzky-Golay) have a dedicated filtering algorithm. Fast Fourier Transform (FFT) filters (Wiener, Kalman) are implemented in a separate module for frequency-domain filters. Many of these filters try to reduce the stochastic noise levels and improve the contrast ratios of the image.

Code snippet 9 The `hdip.filt` function.

```

def filt(dset, axis=(),
        window=5, filter_choice='hamming', overwrite=False, progressbar='', dgroup='', node=''):
    """
    Filtering script that applies filters to the data.

    Parameters
    -----
    dset: N-D array
        data
    axis: int
        specifies the axis upon which the filter is acting
    window: int or tuple
        the window of the filter; must match the mode in length
    filter_choice: string
        specifies the exact filter that will be used
    overwrite: boolean
        enables/disables overwriting of the original dataset
    dgroup: HDF5 group
        group in which the filtered data will be put
    node: string
        name of the new node to be created within dgroup

    Returns
    -----
    out: HDF5 dataset
        contains the filtered data (5D)

    Notes
    -----
    none

    Examples
    -----
    """

```

```

        if filter_choice not in filter_list():
            raise ValueError('Filter not available, choose a different filter')
    import hdip
    import h5py
    if isinstance(dset, h5py.Dataset):
        if not overwrite:
            out_dset=        init_write(dset_template=dset,        dgroup=dgroup,
node=node, _defaultSuffix='_filtered', copy_template=True)
        else:
            if isinstance(dset, h5py.Dataset):
                dset_value=dset.value
                out_dset=dset
    else:
        dset_value=dset
        out_dset=np.zeros(shape=dset_value.shape)
        from hdip.parallel.parallel_module import mp_worker
        return mp_worker(filt_worker, dset=dset, _axis=axis, out=out_dset,
window_len=window, filter=filter_choice)

```

Sometimes the data needs to be transformed; datasets can be cropped, expanded, scaled, rotated and flipped using the `hdip.transform_dset` function (Code snippet 10). As can be seen in the code, this is a top-level function which redirects the work to subroutines responsible for the transformation.

Code snippet 10 The `hdip.transform_dset` function.

```

def transform_dset(dset, boundaries_l, dim_type_l, dim_axis_l, mode='Scale',
progressbar='', _file='', dgroup='', node=''):
    '''
        This function crops/flips/expands/scales a N-dimensional dataset

        Parameters
        -----
        dest: hdf-type dataset
            N-dimensional dataset
        boundaries_l: tuple or tuple of tuples
            a tuple containing the set of indices to which to constrain the dataset.
            Each dimension targeted requires a 2-element tuple containing the first and last index.
        dim_type_l: list of strings
            list containing the dimension type ('spatial', 'temporal' or 'spectral')
            of each axis targeted
        dim_axis_l: list of strings
            list containing the dimension designation ('x', 'y' or 'z') of each axis
            (in order)
        mode: string, optional
            specifies how the data is transformed: Scale, Expand/Crop, or Flip
        dgroup: hdf5 group, optional
            the parent in which the output will be stored
        dnode: hdf5 node, optional
            the dataset in which the output will be stored

        Returns
        -----
        out: writes a dataset cropped in its dimensions.

        Notes
        ----
        none

        Examples
    '''

```

```

None
'''
if mode=='Scale' or mode=='Expand/Crop':
    _shape_edit=[]
    if isinstance(boundaries_l[0], tuple):
        for i,k in enumerate(boundaries_l):
            if isinstance(k, tuple):
                if len(k)==2:
                    _shape_edit.append((retrieve_indices(dset,
                        [dim_type_l[i]], [dim_axis_l[i]])[0],\
                        k[0],k[1]))
                else:
                    print('Error: boundaries require 2
elements')
                    return None
            else:
                print('Error: boundaries must be tuple of
tuples')
                return None
        elif len(boundaries_l)==2:
            _shape_edit.append((retrieve_indices(dset, dim_type_l,\
dim_axis_l)[0],boundaries_l[0],boundaries_l[1]))
        else:
            print('Error: boundaries require tuple of 2 elements')
            return None
        if mode=='Scale':
            scale_worker(dset, _shape_edit, _file=_file, dgroup=dgroup,
node=node, _axis = retrieve_indices(dset,dim_type_l,dim_axis_l), progressbar=progressbar)
        elif mode=='Expand/Crop':
            crop_worker(dset, _shape_edit, _file=_file, dgroup=dgroup,
node=node)
        elif mode=='Flip':
            ax_l = []
            for i in range(len(dim_type_l)):
                ax_l.append(retrieve_indices(dset,[dim_type_l[i]], [dim_axis_l[i]]))

            from hdip.parallel.parallel_module import mp_worker
            def flip_worker(dset, _axis=(), progressbar='', out=[]):
                return dset[::-1]
            for ax in ax_l:
                if progressbar:
                    mp_worker(flip_worker, dset=dset, _axis=ax ,
progressbar=progressbar, out=dset)
                else:
                    mp_worker(flip_worker, dset=dset, _axis=ax , out=dset)

```

4.6.2 Image segmentation

Voxels or pixels within the image data can be selected for different purposes.

1. Part of the voxels can be masked, so the values of the masked voxels are ignored when the data is queried or rendered. In this case, a binary mask dataset (typically sharing a parent group with the primary dataset) is attached to the primary dataset, by referencing the mask in the 'mask' attribute. This masking operation can, for example,

be based on a threshold of the signal height. When creating a mask, a 'Bounds' dataset is also added to delineate the outer boundaries of the unmasked data.

2. The data can be segmented into multiple volumes-of-interest (VoIs). The library allows for these volumes to be inspected individually. The VoIs are implemented in exactly the same way as the mask, with this difference that the VoIs are not attached.

The shape of the VoIs and Masks must match the shape of the primary dataset, as this permits masking in the spatial, spectral and temporal domain (simultaneously).

4.6.3 Peaks recognition and characterization

Algorithms for peak integration were implemented, with a strong focus on automation and flexibility. The peak integration is based on automatic peak detection by a continuous wavelet-based algorithm of a filtered function. The algorithm has a number of input parameters, *e.g.*, thresholds, expected frequency, interval length, etc. which are adjustable by the user and refine the peak intervals. The single requirement of the algorithm is the presence of a first signal peak at the first laser shot (on any mass channel), and an additional adjacent peak. In areas where no signal is present, the integration intervals are interpolated and extrapolated on the basis of the base interval (set as a parameter or derived from the detected frequency).

4.7 Export / interoperability

Although some advanced rendering features are present in the GUI, the focus of the HDIP library does not lie upon data rendering. Users are hence expected to export the data to dedicated visualization platforms such as Avizo, VGStudio Max, ParaView, VisIt, etc. Many functions are hence present to export the data. The data can be exported as raw, uncompressed image data (*e.g.*, 32/16bit TIF files), ASCII data, binary data, publication-quality plots, or as VTK point clouds.

4.8 GUI

Interactive user interfaces provide direct, low-barrier access to the routines in software libraries and can be used to expedite the workflow and preview or inspect the data at a glance. As the N-dimensional data is stored and processed in the HDF5 format, a GUI was required to read these files. HDF5 readers are available, examples include Nexpy (Python), HDFview (Java), and others. Although these readers prove useful due to their generic nature, their applicability for imaging is limited. These readers have limited or slow render engines (limited to 2D) and are not easily extended with custom algorithms. This is why a GUI for HDIP was developed. The GUI was built using the Qt 5.0 framework *via* PySide, a library which 'pythonizes' Qt. Fully scripted and command line data processing remain possible of course. The GUI itself is a superobject, which keeps track of hundreds of parameters and methods. Every function within the GUI is linked to the Main Class.

4.8.1 Main interface

When the GUI is started using the `hdip.GUI()` function, the main window is shown. The window can be broken down into 4 parts (Figure 69): i. the pipeline, ii. the interactive render window, iii. the toolbox for rendering, and iv. the properties/actions window. This way the GUI is not overloaded and presented as a clean software interface. The actions in the properties/actions window are revealed, once a method or setting is chosen in the 'Edit' file menu or on the icon toolbar (Figure 68).

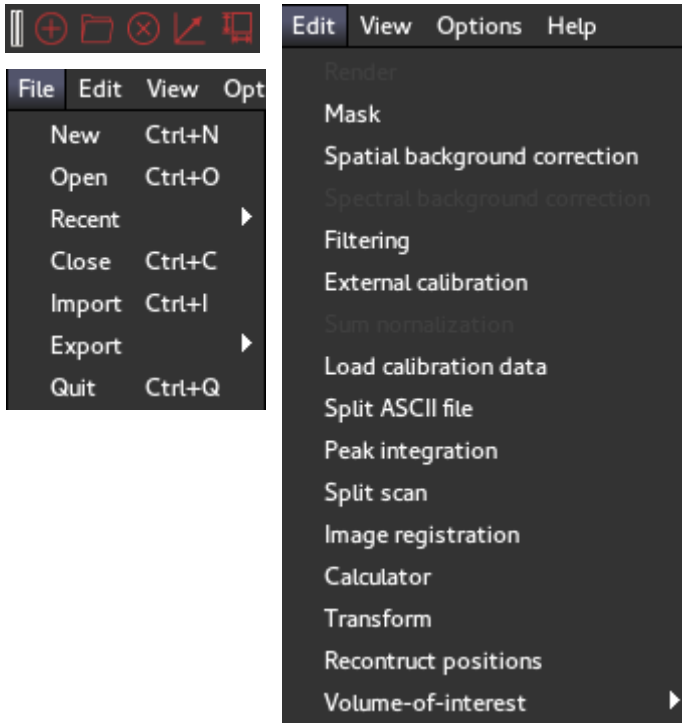


Figure 68 Icon toolbar and file/edit menus.

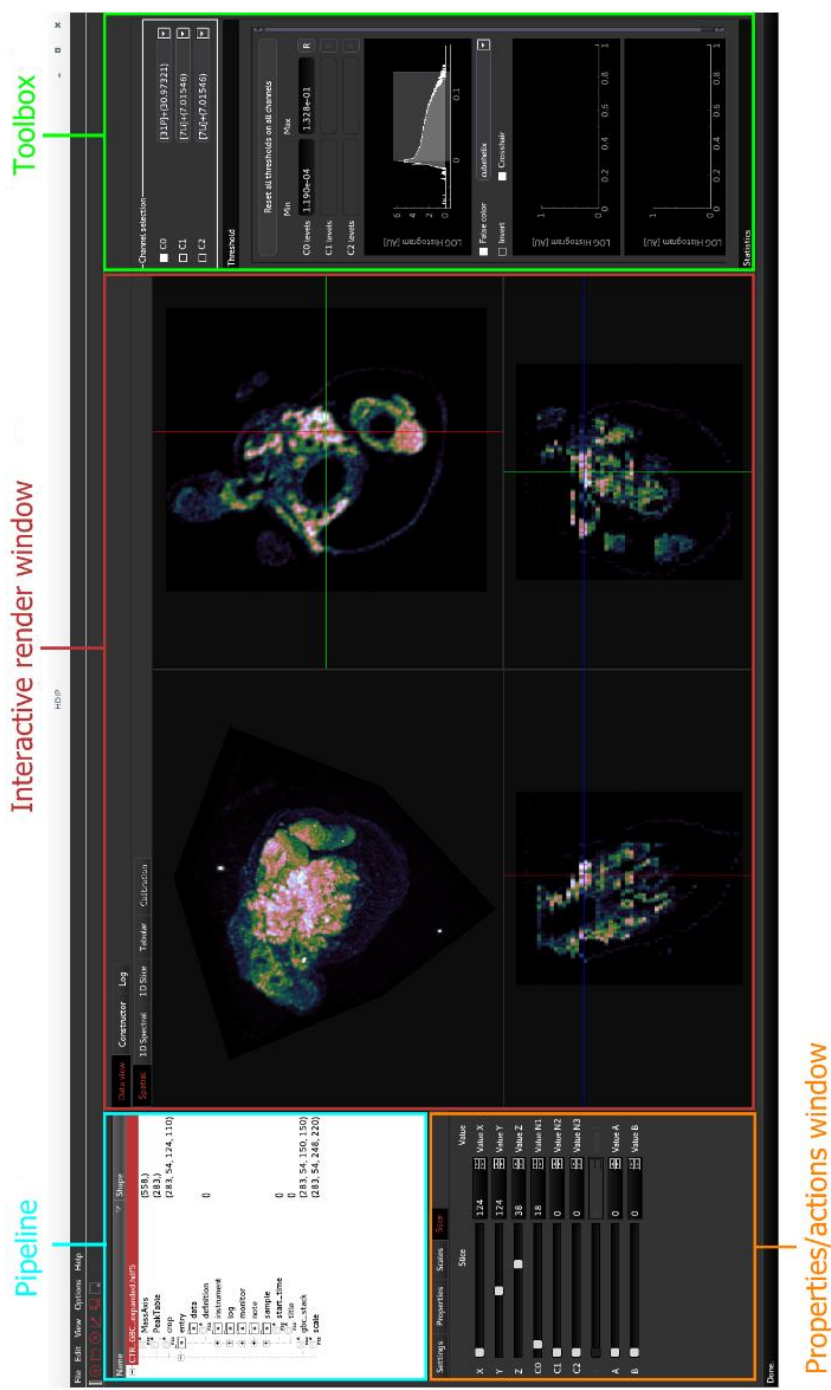


Figure 69 Screenshot of the GUI main interface on a Linux system at a resolution of 1080x1920 pixels.

The file and edit drop-down menus provide access to all main functions, which will be discussed briefly in the next paragraphs. Many of the functions require user input, therefore, these functions produce a context menu in the 'Settings' pane of the Properties/actions window. A collection of these context menus is provided in Figure 70. Each action has an 'OK', 'Apply' and/or 'Cancel' button; the 'Apply' button executes the function but does not sweep away the context menu, in contrast to the 'OK' button.

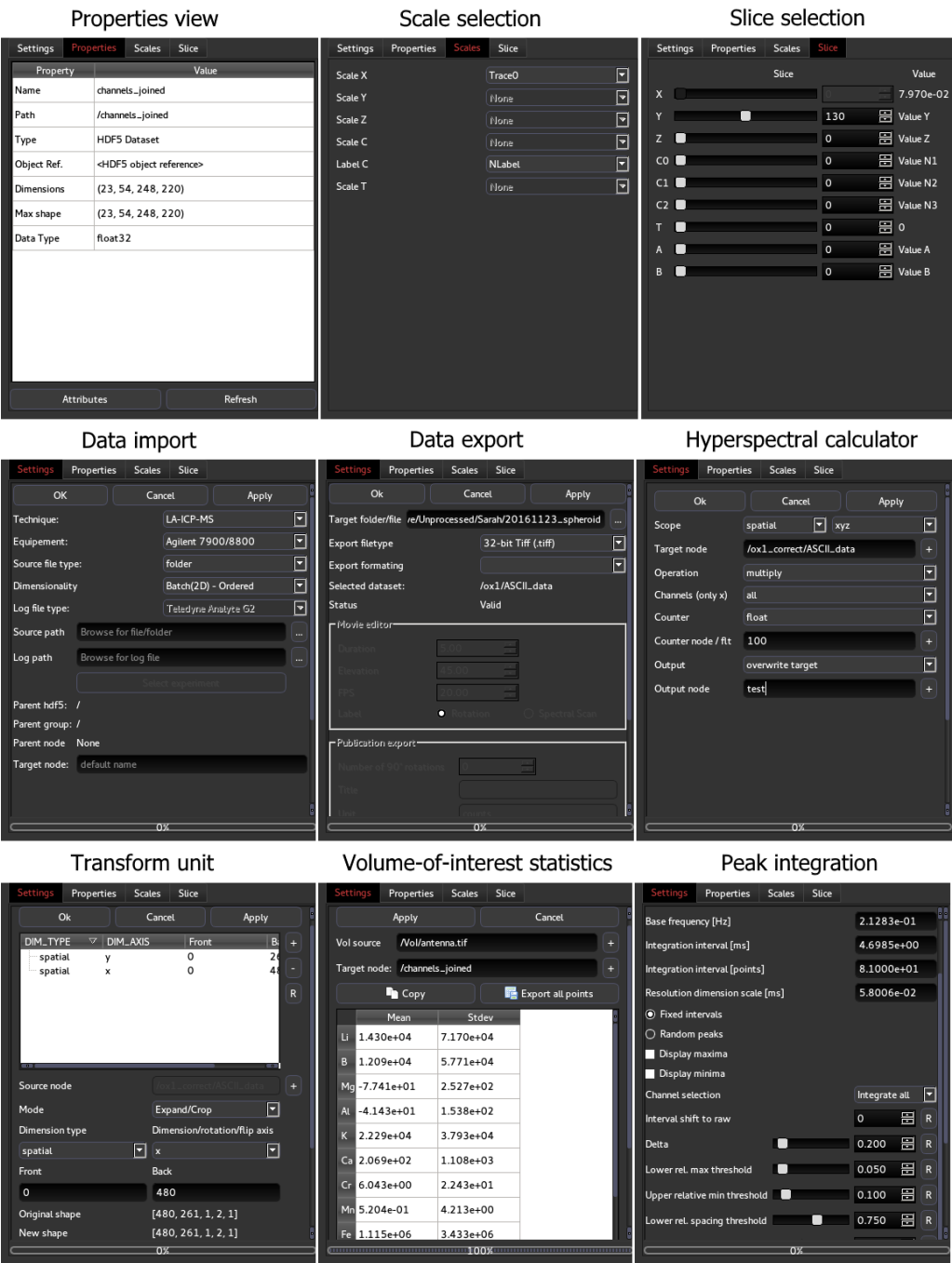


Figure 70 Mosaic of possible context menus in the Properties/actions window.

4.8.2 Defining datasets

The type and relevant coordinate system of each axis of an imported dataset must be defined in order to render and manipulate the data correctly. This can be performed implicitly by the import algorithm, or manually by a menu (Figure 71). Within this menu, each axis can also be given a label for reference. The changes are saved as persistent attributes: they are saved as metadata attached to the primary dataset. (*vide supra*). Thresholds on the data for the render engine, set on each mass channel, are also persistent. It is important to realize that each axis must be assigned to a unique type and coordinate system, or be left unassigned.

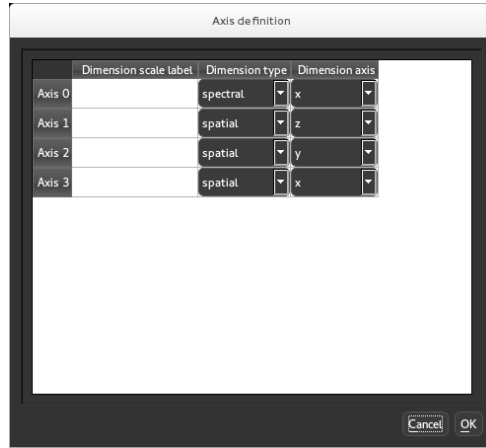


Figure 71 Axis definition stand-alone menu.

Once the axes are defined, metadata in the form of dimension scales can be attached to each axis. Within the metadata, the spatial position of the data relative to the instrument's absolute coordinate system are included. For rectilinear arrays, the metadata includes outline positions in the spatial domain: these are the XYZ coordinates of the box enclosing the data. Furthermore, the aspect ratios and pixel dimensions are calculated. This information is pulled from the log files (of the laser in this case). The information can be edited manually through a stand-alone menu (Figure 72).

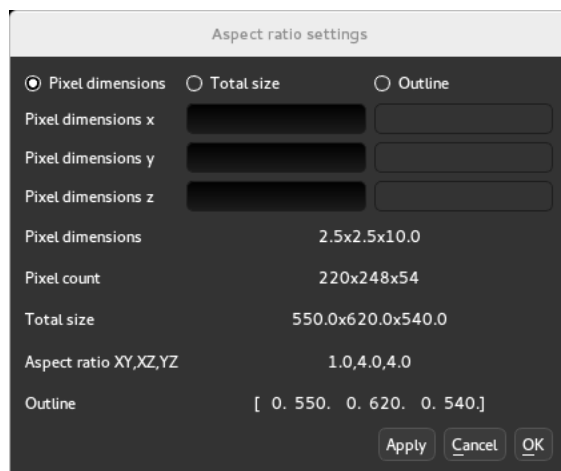


Figure 72 Spatial position settings stand-alone menu.

4.8.3 Importing/exporting data

The File >> Import (Ctrl+I) menu reveals the import unit in the properties/action window. Once the data type, data location and name for the new node are known, the import process can start (context menu Figure 70). A variety of data types is accepted: ASCII data, TIFF files, binary data, binary TIFF files (for masking and Vol operations), and some XML files. One of the XML files that can be imported is a .imagemap file, which describes the position and file path of microscopy images recorded on the laser system. The import algorithm will import each microscopy image described along with its positional metadata. Exporting data is straightforward: the dataset to be exported must be selected and running the export function (File >> Export >> Dataset) will export the data in the desired format.

4.8.4 Pipeline

The pipeline displays the HDF file structure (Figure 73). An HDF5 file contains 2 different types of objects: datasets and groups. A dataset is a rectangular array containing data. The data is typically of the same data type (*e.g.*, 64bit floating point numbers), but can also consist of mixed data types in so-called compound type-datasets. A group object can be seen as a folder object (analogous to a file directory system), which clusters datasets into a hierarchical substructure. The selected dataset in the B-tree will be displayed in the interactive render window. When an HDF5 group is selected, the GUI will determine whether the group has an attribute with the key 'signal'. This key contains a reference to the dataset that was last edited within the group. The GUI will then display this data in the interactive render window. Datasets have an attribute with key 'DTYPE'; its value, 'signal', 'mask' or 'reference', will determine how the data is displayed in the render window. Typically, all datasets related to a single mapping experiment are part of a group (the name of the group reflects the name of the sample).

Name	Shape
prosperpine.hdf5	
29062016_Proserpine	
ASCII_data	(25, 249, 1, 17, 1)
ASCII_data_calibrated	(25, 249, 1, 17, 1)
NLabel	(17,)
PositionGrid	(25, 249, 1, 3, 1)
Trace0	(25,)
VertexNodes	(2, 499, 1, 3, 1)
mask	(25, 249, 1, 17, 1)
mean_out	(249, 1, 17, 1)
std_out	(249, 1, 17, 1)
trim	(2, 249, 1, 17, 1)
29062016_Proserpine2	
29062016_Proserpine3	
BHVO-2G	
BIR-1G	
GSD-1G	
GSE-1G	
MACS3	
NIST610	
NIST612	
entry	
data	
definition	0
instrument	

Figure 73 Pipeline of HDIP GUI displaying an HDF5 file containing 11 groups.

4.8.5 Segmentation

A mask, which is a binary array of Boolean values of matching dimensions of the dataset, can be applied to any dataset. A mask can be generated in many different ways: i) a mask can be generated based on a threshold on one of the (mass) channels, ii) a mask can be imported as an image file, and iii) a mask can be automatically applied based on the signal derivative. Data for LA-ICP-MS typically contains a signal rise (when ablation starts) and fall (when ablation stops). For bulk analysis, the periods when the laser is not firing must be ignored (Figure 74). A mask can be applied in this case to remove such regions from the calculations for sensitivity, signal stability, average response, etc., without a loss of access to the original, raw data. Simultaneously, a 'Trim' dataset is created, which contains where the mask boundaries are in the spatial x-axis dimension. The overall workflow aims to preserve the integrity of the raw data, whilst minimizing data redundancy. No distinction is made between imaging and bulk sampling experiments. It is also possible, using the 'split scan' function, to splice a single transient signal into multiple slices based on a signal threshold. This function is useful for creating either a 2D or 3D image from 1D transient signals.

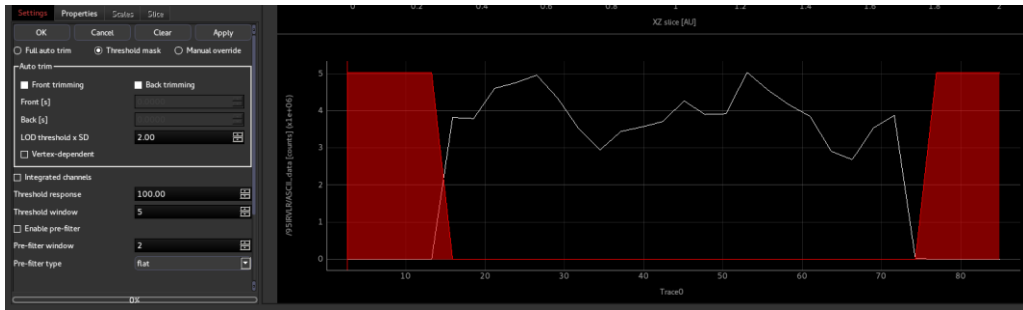


Figure 74 Screenshot of the mask selection window with a preview plot active. The regions highlighted in red are masked.

4.8.6 Registration

3D imaging of soft materials is often based on serial sectioning: the sample is sectioned, and each section is numbered and analyzed, after which a 3D volume is constructed by stacking individual sections. The relative orientation of each section in the stack is different; when a section cut by a microtome is picked up by the microscope slide, or by a droplet of water, its orientation is unique. Sections within a stack can be oriented relative to each other based on the presence of similar features in adjacent sections. An interface (Figure 75) was built to (automatically) align the sections *via* discrete Fourier transform rigid registration. Furthermore, sections can be registered relative to other sections in other datasets. This can, for example, be used to register LA-ICP-MS images relative to micro-Computed Tomography images or optical microscopy images. An option to manually transform (rotations and translations) the sections is also present. It is also possible to flip the section in any direction; the section's orientation may have changed during its transfer to the microscope slide, this may need to be correct for.

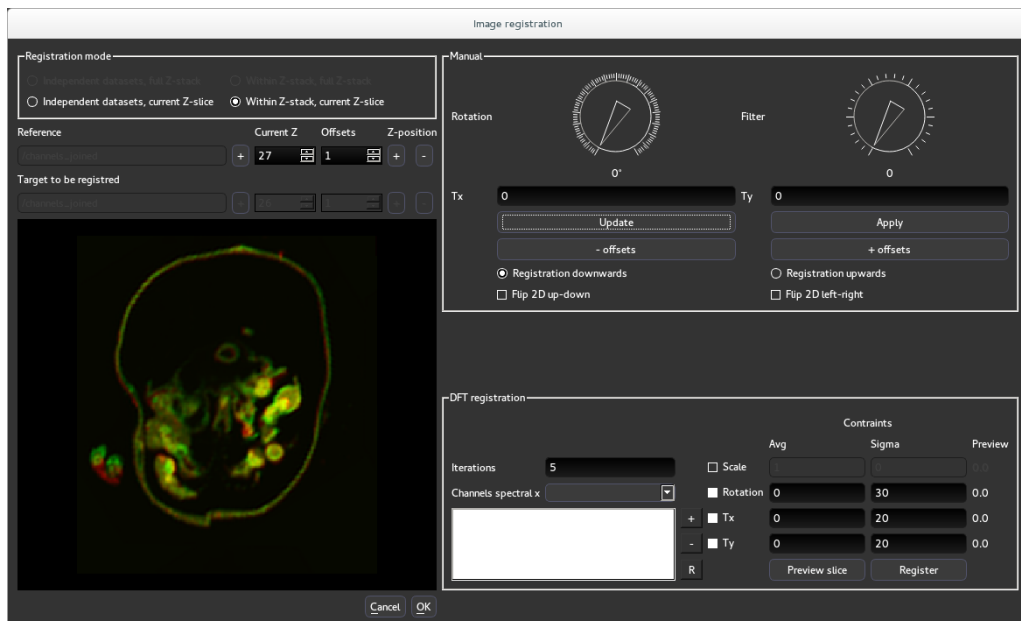


Figure 75 Dedicated interface for registration.

4.8.7 Calibration

Once a dataset of a calibrant is masked, its average mass channel intensity can be used to calculate a dataset containing the sensitivity values (Edit >> Load calibration data). The HDIP GUI can calculate sensitivities from the dataset if it is present in its database. The database currently available contains all entries in the GeoReM database of preferred values for elemental contents. Additional reference materials can be added manually.

One or more of these ‘reference’ datasets can be used to construct calibration curves for all elements entered into the database. A dedicated interface (Figure 76) was developed to provide the user a straightforward workflow for calibration. Each replicate of the calibrant can be assigned a weighting factor. Outliers can be removed by setting the weighting factor to zero. The currently selected replicates are highlighted in orange.

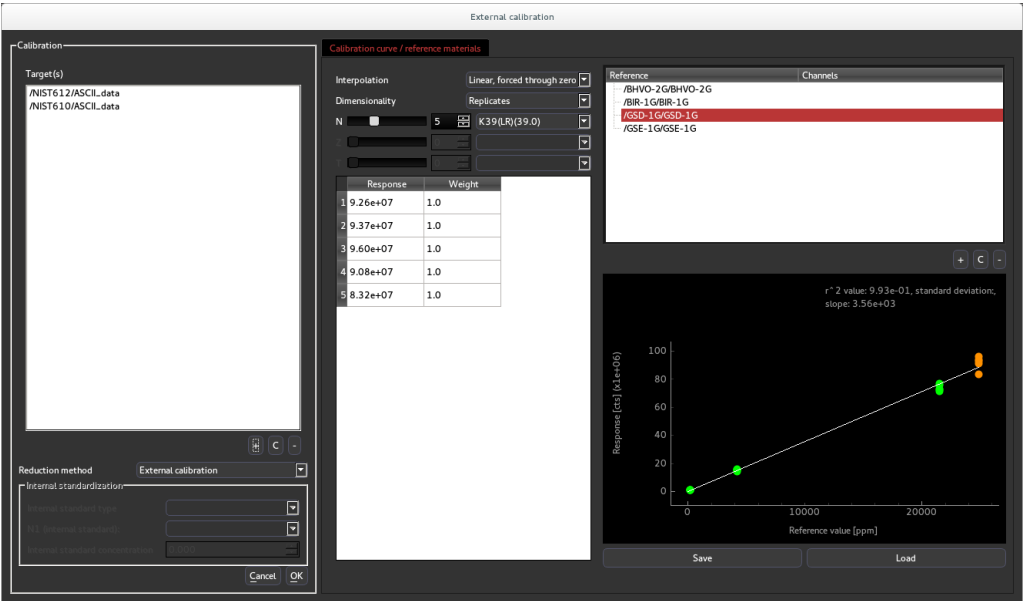


Figure 76 Interface for creating calibration curves and performing calibrations.

4.8.8 Filtering

A number of filters (1,2 and 3D dimensional) can be applied to the data. The user can choose to overwrite the original dataset, which brings about an irreversible change of the data, or the user can choose to write the data to a new dataset. A preview of the filtered signal is available. When the 1D slice viewer is active within the interactive render window, the preview plot is shown as an overlay (Figure 77). When the 3D spatial viewer is active, the 2D image slice frames show the dataset after it has been filtered.

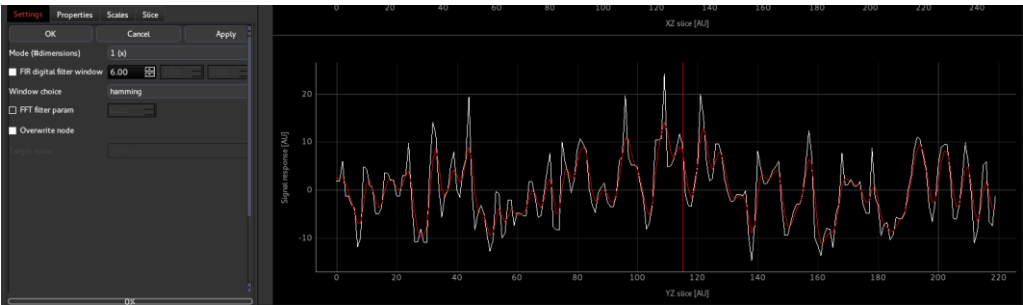


Figure 77 Screenshot of the context menu for signal filtering and a 1D preview plot active.

4.8.9 Rendering

There are currently 4 different viewers to visualize the data. The most prominent one is '3D spatial' viewer. This viewer (Figure 78) shows a 3D volume (with scaling based on the metadata) of the spatial dimensions, and slices of the data parallel to the XY, XZ, and YZ planes. Up to 3 channels of the spectral dimension can be visualized simultaneously. A drop-down menu

in the right-hand top corner allows the user to select channels based on the 'channel header' dimension scale attached to the spectral axis. A histogram of the voxel values is shown in the toolbox below the channel selection options. Within this histogram, a range can be selected in which the voxels are displayed: when the value of the voxel falls below the range, it is not rendered, when the value is greater than the range, it is displayed as a voxel with an opaque color (corresponding to the maximum of the color scale).

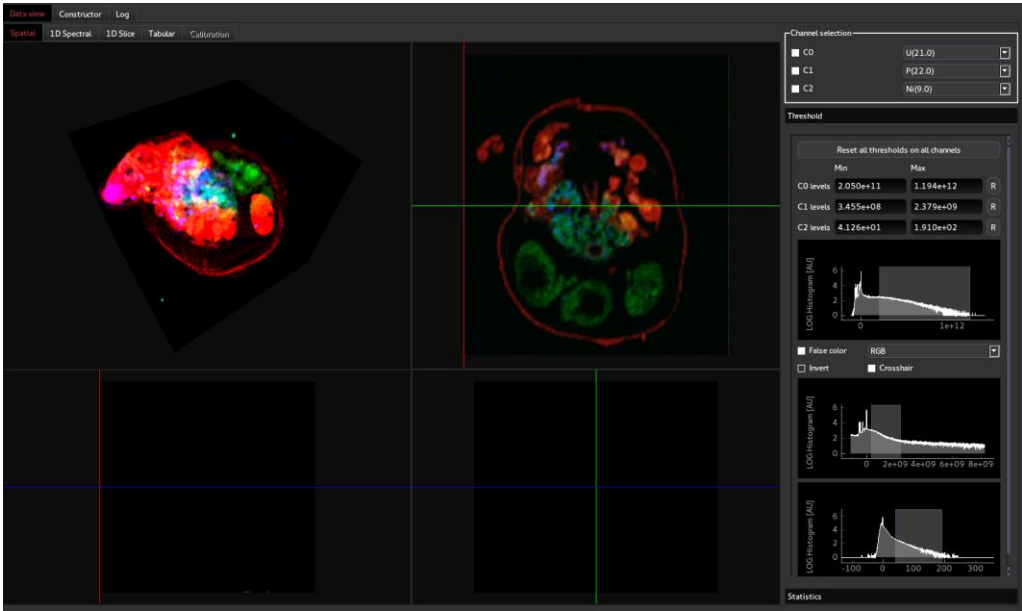


Figure 78 Screenshot of a 3D spatial viewer with the RGB mode active (3 channels visible).

The raw data can be seen in a spreadsheet through the tabular viewer (Figure 79). Within this viewer, 2 axes can be selected implicitly using their type and coordinate system. The user can choose to average or integrate all other dimensions or show only the currently selected slice. The table column and row headers are produced from the information in the 'channel header'.

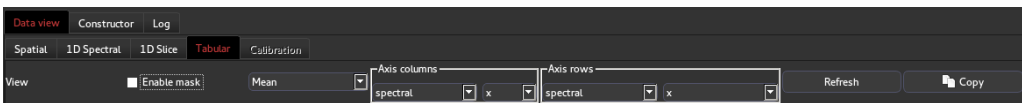


Figure 79 Tabular viewer.

One of the spectral or temporal dimensions can be visualized in the spectral viewer (Figure 80). Displaying contiguous data written in C-order (with the last axes as the spatial dimensions) may drastically slow down the performance of the GUI, as the entire dataset must be queried to produce this information. Labels are again assigned based on the 'channel header'.

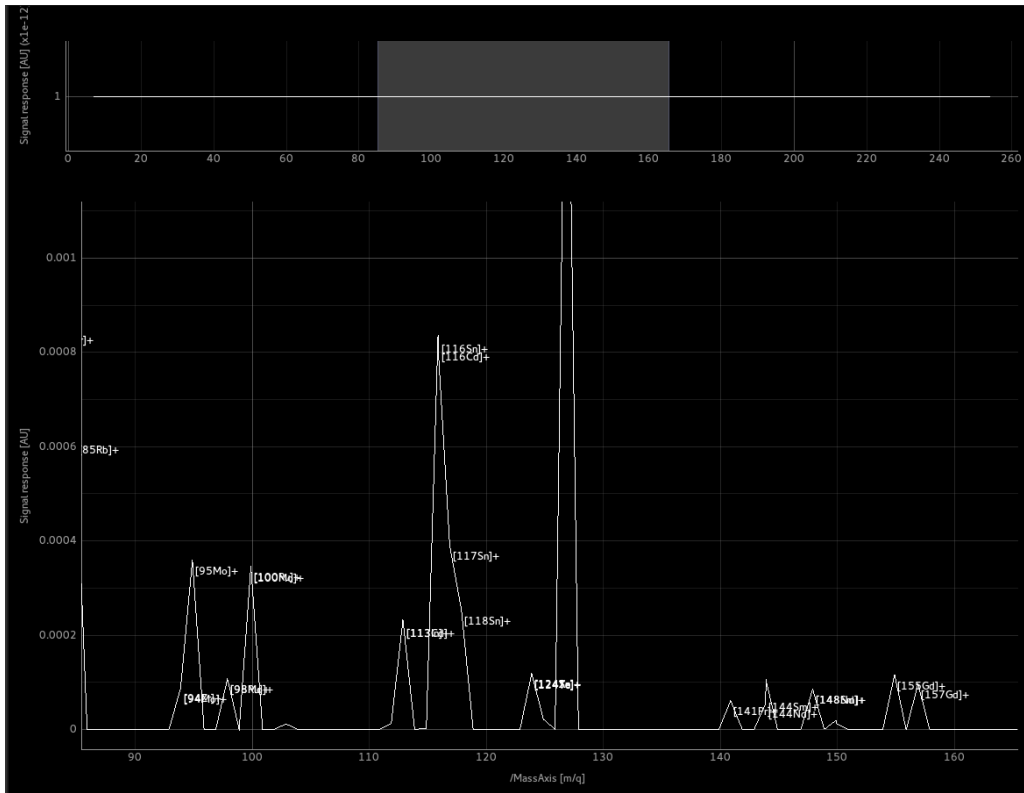


Figure 80 Spectral viewer.

4.9 Conclusions and outlook

This chapter describes a software library and accompanying GUI, designed to process image data. The library is designed for processing a large volume of data in a versatile way and is well-suited for processing LA-ICP-MS data. The level of flexibility in the software, enabling the analysis of multi-dimensional data in a straightforward way, is not yet available on any other platform for LA-ICP-MS data processing. The largely automated approach allows for a fast workflow for most standard imaging applications. A large array of signal processing algorithms is implemented in the software to manipulate the image. The GUI currently focuses on processing data present in a Cartesian coordinate system but could be extended to other coordinate systems. Although the software has many possible applications, LA-ICP-MS processing will remain its primary focus for now. As functionality expands, dedicated data processing options will also be added for other techniques. Data integrity, implicit indexing, and n-dimensional filters will remain the core parts of the HDIP library. One of the main challenges that still remains is rendering multiple datasets with millions of voxels in 3D space without compromising rendering performance. Further work is required to optimize the processing speed. The Blaze (Dask) library is currently being implemented for distributed computing. Numba pre-compilation is also ongoing to speed up the CPU bottlenecked algorithms.

4.10 Bibliography

(1) de S. Pessôa, G.; Capelo-Martínez, J. L.; Fdez-Riverola, F.; López-Fernández, H.; Glez-Peña, D.; Reboiro-Jato, M.; Arruda, M. A. Z. *J. Anal. At. Spectrom.* **2016**.

(2) Osterholt, T.; Salber, D.; Matusch, A.; Becker, J. S.; Palm, C. *International Journal of Mass Spectrometry* **2011**, 307, 232-239.

(3) Paul, B.; Paton, C.; Norris, A.; Woodhead, J.; Hellstrom, J.; Hergt, J.; Greig, A. *J Anal Atom Spectrom* **2012**, 27, 700.

(4) Paton, C.; Hellstrom, J.; Paul, B.; Woodhead, J.; Hergt, J. *J Anal Atom Spectrom* **2011**, 26, 2508-2518.

(5) Rittner, M.; Müller, W. *Computers & Geosciences* **2012**, 42, 152-161.

(6) Römpp, A.; Schramm, T.; Hester, A.; Klinkert, I.; Both, J.-P.; Heeren, R. M. A.; Stöckli, M.; Spengler, B. In *Data Mining in Proteomics: From Standards to Applications*, Hamacher, M.; Eisenacher, M.; Stephan, C., Eds.; Humana Press: Totowa, NJ, 2011, pp 205-224.

(7) Fischer, C. R.; Ruebel, O.; Bowen, B. P. *Arch Biochem Biophys* **2016**, 589, 18-26.

Chapter 5 Microarray standards for single cell analysis and imaging

This chapter is based on a research paper, 'Quantitative Determination and Subcellular Imaging of Cu in Single Cells via Laser Ablation-ICP-Mass Spectrometry Using High-Density Microarray Gelatin Standards', authored by Stijn J. M. Van Malderen, Eva Vergucht, Maarten De Rijcke, Colin Janssen, Laszlo Vincze, and Frank Vanhaecke. S.V.M. was the first and principal author of this work.

The usage of LA-ICP-MS for bioimaging is fairly well established and has been thoroughly reviewed by various authors.¹⁻³ Typical applications include mapping endogenous metal distributions in organs⁴ and determining the tissue penetration depth of administered drug complexes⁵⁻⁷. A common theme throughout these applications is the requirement for a high spatial resolution to differentiate regions and structures of interest. This necessitates rapid washout, high repetition rates, and fast scanning speeds if imaging is to be completed within an acceptable timeframe. Low-dispersion cells, such as described in Chapter 2, are essential tools here. Small-scale structural features, for instance, cortical fibers in ocular tissue, are obscured if larger spot sizes are used⁸, whilst some emerging applications specifically demand lateral resolution on the level of cell structures. The increasing development and use of cellular therapies have produced a requirement for strategies to monitor their persistence *in vivo* and their delivery to target organs. Managh *et al.* demonstrated that therapeutic cells can be individually tracked in recipients using a combination of elemental labeling and LA-ICP-MS detection.⁹ Cells were labeled with a Gd-based MRI contrast agent, *prior* to infusion into a mouse model, and the Gd label was detected within extracted cell samples at 10 days post-infusion. Two subsequent publications have reported imaging of administered cells within tissue sections, using gold nanoparticles¹⁰ and Tm-based contrast agent labels¹¹, respectively. The LA-

ICP-MS approach offered several advantages over other detection methods for cell tracking; namely high sensitivity, the ability to selectively target and/or identify individual cells and compounds, and the capability to detect cells at periods when the labels would no longer be detectable by other techniques.

This chapter describes the development and characterization of a high-density microarray calibration standard, manufactured in-house, and designed to overcome the limitations in precision, accuracy, and throughput of current calibration approach for the quantification of elemental concentrations on the cellular level using laser ablation-inductively coupled plasma-mass spectrometry (LA-ICP-MS). As a case study, the accumulation of Cu in the model organism *Scrippsiella trochoidea* resulting from transition metal exposure (ranging from 0.5 to 100 µg/L) was evaluated. After the Cu exposure, cells of this photosynthetic dinoflagellate were treated with a critical point drying protocol, transferred to a carbon stub and sputter-coated with a Au layer for scanning electron microscopy (SEM) analysis. In subsequent LA-ICP-MS analysis, approximately 100 cells of each population were individually ablated. This approach permitted to evaluate the mean concentration of Cu in the cell population across different exposure levels and also allowed to examine the cellular distribution of Cu within the populations. In a cross-validation exercise, subcellular LA-ICP-MS imaging was demonstrated to corroborate synchrotron radiation confocal X-ray fluorescence (SR-XRF) microimaging of single cells investigated under in vivo conditions.

5.1 Introduction

Insights into the subcellular behavior of (transition) metals could enhance our understanding of the complex biotic and abiotic factors that play a role in the proliferation of single cell organisms. In this study, the marine microalgae *Scrippsiella trochoidea* (Von Stein) Loeblich III was selected as a model organism to monitor the exposure effects of toxic concentration levels of Cu on dinoflagellates.^{12,13} It is generally assumed that this type of harmful microalgae or their cysts can be used as indicators of water quality and pollution¹⁴, yet the links between heavy metal concentrations and the survival rate of these organisms are not well understood. Therefore, a correct quantification of transition metals is crucial to obtain accurate insights. Elemental analysis through ICP-MS analysis is attractive in this context due to its low limits of detection, high selectivity for targeted nuclides, the capability of providing quantitative information on multiple nuclides, and the availability of specialty sample introduction systems.

Microwave digestion approaches can, for example, provide information on the bulk concentration of a cell population, yet requires a substantial number of cells and introduces a risk of contamination during the sample preparation. A characterization of the spread of the elemental concentrations across an entire population is also of interest as the behavior of individual cells is expected to vary across a population, resulting in the need for introducing single cells into an ICP-MS. Mueller *et al.*¹⁵ recently provided an overview of a number of methods for injecting single cells into the ICP, including the use of a piezo-electric micro-droplet generator to generate single droplets into which single cells can be suspended. In a recent study by Shigeta *et al.*, Cu was detected in single selenized yeast cells at the attogram level.¹⁶ Mass cytometry¹⁷⁻¹⁹ also allows single cells to be introduced individually into the plasma,

unfortunately, calibration methods are not yet well established, as the technique focusses more on the multi-parametric assays of single cells labeled using multiple single-isotope lanthanide tags. Laser ablation (LA) is a versatile introduction system and microprobe for ICP-MS, fit-for-purpose for single cell analysis, as it features high spatial resolution, and large flexibility in terms of the physical size, format, and type of a sample. The capabilities of LA-ICP-MS have been promoted further by the recent development of low-dispersion laser ablation cells.²⁰⁻²⁴ Yet, the accuracy of single-cell analysis *via* LA-ICP-MS largely depends on matrix-induced elemental fractionation effects and, by extension, the availability of matrix-matched calibration standards. It remains, therefore, challenging to directly evaluate the methodological accuracy due to the lack of suitable and certified reference material (CRM) for this specific type of application. Alternative approaches to determine the measurement uncertainty *via* on-line isotope dilution, have been described.²⁵

Tissue-type section standards can be readily prepared using well-described, broadly-deployed, in-house procedures.^{26,27} This approach, however, is unsuitable for single-cell analysis because the assumption that the volume can be directly derived from the quantitative removal of the irradiated material may underestimate the mass removed. In particular, the ablation may release material outside of the irradiated zone, due to phase explosion-induced spallation of mesoscopic fragments, and evaporation of the melt. For large spots, it could be argued that the mass removal *via* secondary mechanisms is negligible relative to the irradiated mass, however, as the beam size decreases, the beam profile degrades, and it becomes increasingly difficult to precisely define the volume removed without a posteriori surface characterization. In addition, an accurate estimation of the tissue section thickness may be challenging in some cases.

In droplet-based approaches, centrosymmetric inhomogeneities or residues can be observed in droplets, either freely dried²⁸ or deposited on a pre-cut disk of filter paper²⁹, as a result of the 'coffee stain effect'. The latter involves an outward radial flow towards the droplet perimeter, induced by a higher relative rate of evaporation at the contact line, as was described by Deegan *et al.*^{30,31}. On a macro scale, this problem can be overcome by ablating the entire droplet. This strategy, however, is time-consuming due to the dimensions of each dried droplet but can be facilitated by drying the droplets on a hydrophobic (polymeric) surface, ultimately resulting in a reduced surface area as they evaporate, or by only sampling a representative part, *e.g.*, a cross-section, of the droplet.³²⁻³⁵ The continuous surface evaporation also jeopardizes the accuracy of gravimetric approaches, whilst volumetric approaches on a macro scale are inherently less accurate due to the multitude of environmental factors, *e.g.*, pressure, temperature, and fluid-dynamic effects (*e.g.*, capillary action) which interfere with accurate micropipetting. One reported strategy to address this problem was proposed in a study by Zhai *et al.*, where a MicroFab JetLab microdispensing unit was used to create a rectangular grid of gold standard solutions droplets for calibrating the response for a peptide-Au cluster in human erythroleukemia cells.³⁶ This micropipetting system, based on a piezoelectrically actuated ink-jet dispenser, is capable of dispensing droplets with less than 1% mass variation under controlled conditions, though switching between different standards in a single inkjet head system requires extensive flushing of the system. This specialized instrumentation was used in a similar approach by Wang *et al.* to determine the number of Au nanoparticles (NPs) in single

cells in situ.³⁷ Rhodamine B 2% (wt) was added into the standard solution of dispensed droplets in an attempt to match the droplet matrix to the cellular matrix and to visualize them. Gelatin can be considered a matrix-matched standard to the dinoflagellate matrix, as its properties partially resemble the properties of the fibrous protein collagen, its precursor and the most abundant protein in extracellular biological tissue, furthermore, the protein-rich composition of gelatin matches well the protein-rich (40-55% of the dry weight) cellular material.^{38,39} Gelatin has been deployed in the past as a matrix for standards in LA-ICP-MS tissue section imaging.^{5,31,39-41} The ionization efficiencies and particle transport properties are similar for gelatin and for biological material.³⁹ Self-aliquoting microarray plates – analogous to nanotiter plates, which are extensively deployed in microbiological assays – designed to distribute samples into *pL* volumes for matrix-assisted laser desorption/ionization mass spectrometry (MALDI) were coined by Urban *et al.* as Micro arrays for Mass Spectrometry (MAMS).⁴²⁻⁴⁴ In the current study, high-density microarray plates are evaluated as microcontainers for holding spiked gelatin as matrix-matched LA-ICP-MS single-cell standards. The microarrays themselves are manufactured using the analytical laser ablation system, *i.e.* serving as a micromachining platform.

Although LA-ICP-MS imaging at subcellular lateral resolution is still in its infancy, several studies have reported promising results. Enhanced S/N ratios may also be beneficial when sub-cellular imaging is required. Giesen *et al.* imaged iodinated fibroblast cells using a 4 μm spot size, which is around one tenth of the size of a fibroblast cell nucleus.⁴⁵ The iodine stain preferentially accumulated within the nucleus, which enabled differentiation of the nucleus and cytoplasmic regions on the basis of the ¹²⁷I signal. However, iodine suffers from a high instrumental background, so an alternative approach for staining cells using Tm containing maleimide-DOTA complex has since been proposed¹⁵. Besides histology, sub-cellular resolution is also important in the emerging field of nano-toxicology. With the increasing use of nanomaterials for therapeutic applications, there is a requirement to quantify their accumulation within cells³⁷ and to determine their cellular localization pattern following uptake. In 2012, Drescher and co-workers performed sub-cellular imaging of individual fibroblast cells using a 4 μm spot size⁴⁶. Au and Ag nanoparticle accumulation was localized to the perinuclear region of the cells. Subsequent studies have also reported the cellular distribution of smaller, 14 nm sized Au nanoparticles⁴⁷ and silica nanoparticles containing an inner Au or Ag core.⁴⁸ However, all of the aforementioned studies imaged fibroblast cells, which at $\geq 50 \mu\text{m}$ in diameter can be considered fairly large in size. Thus, the application would benefit from improved spatial resolution if the distribution of nanoparticles within smaller cells is to be studied. In pioneering studies by Wang *et al.*⁴⁹ and Giesen *et al.*²³, a 1 μm beam was used to image the lanthanide tags for human epidermal growth factor receptor 2 and 32 proteins in a human breast tissue section.

This work reports on direct high-resolution LA-ICP-MS imaging of Cu exposed *S. trochoidea* cells, supporting the quantitative analysis, and ultimately demonstrating the potential of LA-ICP-MS of being a powerful tool for labelless bio-imaging at the single-cell level. Moreover, the subcellular transition metal distributions revealed allowed to cross-validate the conclusions drawn by Vergucht *et al.* based on in vivo synchrotron radiation (SR)-XRF microimaging.^{12,13}

This type of comparative study is pivotal in the context of validation of LA-ICP-MS for imaging at the subcellular level.

5.2 Experimental section

This section expands upon the culturing conditions, the sample preparation approach, the fabrication of the microarray gelatin standards and the experimental parameters.

5.2.1 Exposure.

S. trochoidea cells were isolated and cultured from North Sea phytoplankton samples. 19 populations (C0-C18) were cultured in L1 medium spiked with increasing Cu levels (from a $1 \text{ mg} \cdot \text{L}^{-1}$ Cu stock solution; $\text{CuCl}_2 \cdot 2\text{H}_2\text{O}$, Sigma-Aldrich, St. Louis, MO, USA), resulting in concentrations varying between $0 - 650 \text{ } \mu\text{g L}^{-1}$. The populations were visually assessed and retrieved after 96 hours of exposure. As observed, 7 populations (Cu level $\geq 150 \text{ } \mu\text{g L}^{-1}$) were found to suffer from structural cell degradation (blebbing, shrinkage, fragmentation) and were therefore not considered for analysis.

5.2.2 Sample preparation.

After fixation (protein cross-linking) in a 4% formaldehyde solution, the cells were dehydrated using an alcohol series (25%, 50%, 75%, 90%, 95%, 100%, 10 minutes residence time in every solution), and critical point dried. For control purposes, the cells from each population were subsequently transferred from a polycarbonate membrane to a carbon stub and some of the cells were sputtered with a gold coating (JFC-1200, JEOL, Tokyo, Japan) for Scanning Electron Microscope-based imaging (SEM) analysis (Figure 81), which permitted to verify the identity of the algae species and the intactness of the morphology of the cells after fixation. The carbon stub, which provides structural support for mapping, was then mounted inside the laser ablation cell.

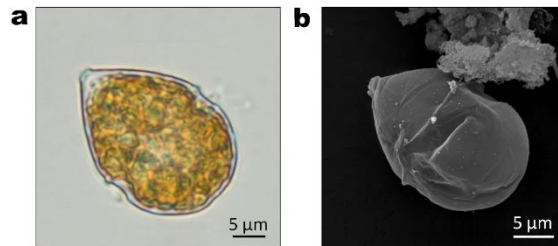


Figure 81 *S. trochoidea* microalgae. (a) Brightfield microscope image of a vegetative *S. trochoidea* cell. (b) SEM image (JSM 5600LV, JEOL, Tokyo, Japan, accelerating voltage of 14 kV) obtained after sample preparation of a motile cell. Reproduced from Vergucht *et al.*¹³ with permission of the International Union of Crystallography.

5.2.3 Preparation microarray standards.

A rectilinear, structured grid of 44×28 cylindrical craters, $110 \text{ } \mu\text{m}$ in diameter, spaced $185 \text{ } \mu\text{m}$ apart was manufactured by laser machining (Analyte G2, Teledyne Photon Machines, Bozeman, MT, USA) into a borosilicate cover glass slide (VWR, Radnor, PA, USA) (Figure 82a, b). 250 shots (energy density, 3.37 J cm^{-2} ; pulse length, 5 ns ; pulse repetition rate, 25 Hz) were fired by the laser unit on each ablation position of the grid. A 1 L min^{-1} Ar was used to flush away ablation

debris. After structuring, the microarray was etched for 60 s with 10% trace metal grade HF acidic solution (Seastar Chemicals Inc., Sidney, Canada) and rinsed with Milli-Q water ($18.2\text{ M}\Omega\text{ cm}$, Millipore, Billerica, MA, USA) to remove residual surface debris of glass particles deposited around the craters. A gelatine solution ($10\%\text{ }^W/W$, VWR BDH Prolabo, Radnor, PA, USA) was prepared gravimetrically and spiked with $10, 20, 50$ or $200\text{ }\mu\text{g} \cdot \text{g}^{-1}$ of Cu (from a $1\text{ mg} \cdot \text{L}^{-1}$ stock solution in $2\%\text{ HNO}_3$, Chem-Lab NV, Zedelgem, Belgium) and $50\text{ }\mu\text{g} \cdot \text{g}^{-1}$ of In (from a $1\text{ mg} \cdot \text{L}^{-1}$ stock solution in $2\%\text{ HNO}_3$, Inorganic Ventures, Christiansburg, VA, USA) as an internal standard for sensitivity drift correction. The solution was heated to 50°C allowing the gelatin to liquefy and homogenize. A droplet ($\sim 30^\circ\text{C}$, $\sim 1\text{ }\mu\text{l}$ in volume) was dispensed onto the center of the microarray and the surface was carefully closed with an etched cover glass. The droplet volume is approximately 5 times the integrated volume of the microarray. Pressure ($> 20\text{ N cm}^{-2}$) was applied onto the assembly, forcing the gelatin into the craters and any redundant gelatin away from the surface. The gelatin was allowed to cool to room temperature ($\sim 20^\circ\text{C}$), and the cover glass was carefully removed in a sliding motion, leaving the craters filled. In case of incomplete crater filling, ring-like patterns can be observed inside the wells, resulting from the outward directed liquid flow during surface evaporation, as described by Rieger *et al.*⁵⁰

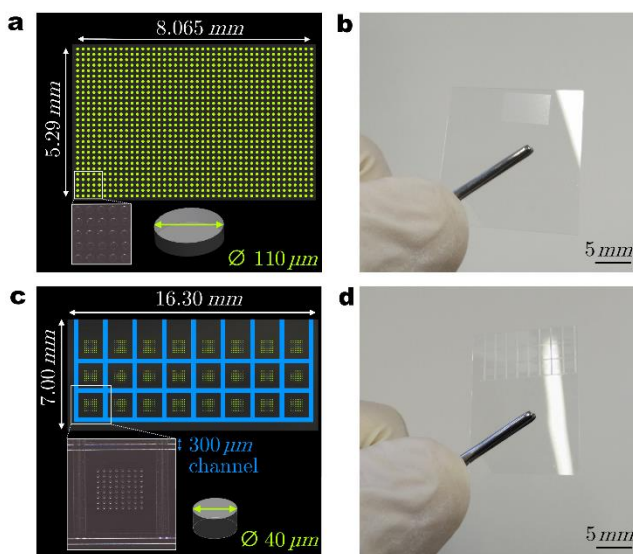


Figure 82 Microarray layouts and photographs. (a) The layout of a chip with a rectilinear grid. The inset is a darkfield microscopy image (EZ4 HD, Leica, Wetzlar, Germany). (b) Photograph of the microarray. (c) The layout of a microarray 24-sample chip containing 8×3 rectilinear grids of 8×8 microwells separated by $300\text{ }\mu\text{m}$ evacuation channels. The inset is a darkfield microscopy image. (d) Photograph of the multi-sample chip.

Many standards can be placed in close proximity on a single microarray chip if evacuation channels are put in place, compartmentalizing individual microarrays and preventing between-standard cross-contamination (Figure 82c,d). The substrate surface may also be coated with an (ultra)hydrophobic coating to promote self-patterning properties of the array through surface tension.⁵¹ The mass of Cu in each crater can be calculated based on the volume of the well and a

volumetric mass density of the gelatin solution ($\rho_{gelatin} = 1.04 \pm 0.01 \text{ g/ml}$ at 25°C , determined gravimetrically based on 5 batches of 50 ml): $m_{Cu,crater} = m_{Cu,spiked} \rho_{gelatin} V_{crater} / m_{solution,gelatin}$. In order to accurately estimate the average volume of each crater, a grid of these pits was analyzed using optical profilometry (Veeco NT9080, Plainview, NY, USA). A total of 6 zones ($622 \times 466 \mu\text{m}^2$), each containing 6-9 craters were measured (Figure 83). The craters in each of these zones were isolated using a thresholding algorithm. The mean ablation rate was estimated at $105 \pm 3 \text{ nm}$ per shot. Microwells created by 250 shots are estimated to be $26.25 \pm 0.5 \mu\text{m}$ in depth and $\sim 0.186 \text{ nl}$ in volume.

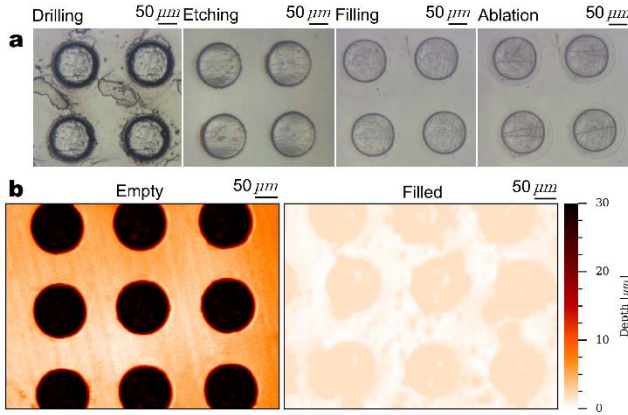


Figure 83 (a) Microscopic images of 4 microwells after each manufacturing/analysis step. (b) Surface topography of surface after structuring (left) and filling (right) as determined by optical profilometry.

5.2.4 Calibration and sampling strategy.

Selective ablation of the gelatin within the crater can be achieved by selecting an energy density below the ablation threshold of glass, and above the ablation threshold of gelatin and the cells. Quantitative removal of gelatin is enabled at a 0.7 J cm^{-2} energy density (well above the ablation threshold³⁹), whilst only a marginal amount of glass is removed (as observed in the ^{29}Si signal). Hence, matrix-matching is maintained, and the Cu background from the glass remains negligible. At least 70 individual cells, $> 30 \mu\text{m}$ removed from neighboring cells, of each Cu exposure level were manually selected for analysis and pinpointed with a single stationary ablation position, at which the laser beam was masked and focused to cover an area larger than the cell. The integrated pulse response areas of individual cells were then averaged across the sampled set of cells within the population to obtain bulk information. For 2 out of 12 (indices C8, C11) populations, the amount of non-aggregated cells retrieved on the carbon stub was insufficient, preventing sampling a representative part of the population and therefore these results were discarded. A bracketing approach was adopted: a calibration sequence was performed before and after each population. Each sequence encompasses 1 run for every standard ($10, 20, 50$ and $200 \mu\text{g} \cdot \text{g}^{-1} \text{ Cu}$), 60 s in duration, and comprising quantitative ablation of 20 replicate microwells, and integration of the response on each well. The beam size was enlarged to encompass the microwells; the beam sizes are not required to be matched, as the approach is based on determination of the absolute sensitivity, rather than a relative one.

The relatively large microwells, as compared the cell volume, exhibit low detection limits (3 fg for ^{65}Cu) and can be manufactured and characterized precisely. Within-sequence normalization based on the ^{115}In pulse response area was performed to compensate for sensitivity drift related to the ablation position and small differences in crater volume between different runs. The slope of the linear fit to the calibration curve of the average integrated pulse response was used to calculate an absolute average sensitivity of 9.14 cts/fg.† Relative concentrations can be calculated based on the cell volume, estimated to be $\sim 2.36 \times 10^3 \mu\text{m}^3$ (surface area, $8.7 \times 10^2 \mu\text{m}^2$; cross-section, $\sim 2.36 \times 10^2 \mu\text{m}^2$), as the shape of an average cell can roughly be considered to be an ellipsoid with characteristic outer dimensions ($L \times W \times D$, $\sim 15 \times \sim 15 \times \sim 20 \mu\text{m}^3$). The ICP-MS instrument was tuned daily by ablating NIST SRM612 for maximum signal intensity across the 7-238 m/z range, an oxide ratio ($^{238}\text{U}^{16}\text{O}^+ / ^{238}\text{U}^+$) below 1.0% and $^{232}\text{Th}^+ / ^{238}\text{U}^+ \approx 1$. The operational parameters are summarized in Table 1. The sensitivity drift for Cu in the gelatin standards in the 8-hour run (not including 2 hour warmup and tuning) was $\sim 4.8\%$ RSD (between-replicate sequence RSD $\sim 5\%$).

Table 6 Instrument settings and data acquisition parameters for all ablation approaches (unless mentioned otherwise).

Ablation target	Algae cells	Gelatin standard	Algae imaging
Teledyne Photon Machines Analyte G2 low-dispersion laser ablation system			
Energy density [$J \cdot cm^{-2}$]	0.74	0.74	1.31
Repetition rate [Hz]	200	200	30
Scan mode	Drilling	Drilling	Line scanning
Scan speed [$\mu m \cdot s^{-1}$]			10
Shot number / position	25	25	
Beam waist diameter [μm]	40	130	2
He carrier gas flow rate [$L \cdot min^{-1}$]	0.450	0.450	0.550
Thermo XSeries 2 ICP-MS unit			
RF power [W]	1300	1300	1300
Sampling depth [mm]	9.1	9.1	9.1
Ar plasma gas flow rate [$L \cdot min^{-1}$]	13.0	13.0	13.0
Ar auxiliary gas flow rate [$L \cdot min^{-1}$]	0.70	0.70	0.70
Ar make-up gas flow rate [$L \cdot min^{-1}$]	0.79	0.79	0.79
Acquisition parameters			
Nuclides monitored	^{31}P , ^{65}Cu , ^{115}In , ^{197}Au	^{31}P , ^{65}Cu , ^{115}In , ^{197}Au	^{65}Cu , ^{197}Au
Duty cycle time [ms]	28	28	59
Respective dwell time [ms]	1, 5, 1, 1	1, 5, 1, 1	40, 2

Visualizing the intracellular Cu distribution is useful to support any hypothesis concerning the transition metal metabolism of the microalgae model organism. Moreover, these results could be used to validate the conclusions of Vergucht *et al.*¹² who performed in vivo subcellular SR confocal XRF microimaging on this model organism using optical tweezers technology. To compare both studies in terms of resulting intracellular elemental distribution, a sample

preparation procedure was required *prior* to LA-ICP-MS analysis. If not, piercing of the cell membrane upon laser beam irradiation would allow the cytoplasm to spill out and potentially displace the enclosed cell organelles. To prevent this from occurring, cryogenic or impregnation/embedding techniques could be applied. The critical point drying protocol employed here preserves the external morphology of the sample, and prevents the above-mentioned cell collapse upon ablation. Selected cells were centered in a $50 \times 50 \mu\text{m}^2$ ablation grid (pixel size, $0.6 \times 2 \mu\text{m}^2$; *scanning mode, adjacent line scans*). All data were processed (background correction and trimming) using an in-house written Python 3.4 / HDF5 library. Table 1 documents the instrumental settings during image acquisition. The energy density was increased for mapping to boost sensitivity, however, could not be increased further due to a risk of the laser shockwave displacing the sample, and of breakdown of the structural integrity of the cell. The non-directional sputter process does not yield a fully uniform coating due to the surface topography, hence, the Au signal cannot be used to correct drift in the sensitivity of the ICP-MS. The Au coating and carbon stub do not interfere with the imaging analysis, as no significant amount of Cu could be detected outside the cell. For *in vivo* SR-XRF imaging analysis, optical tweezer (OT) technology was applied for non-contact sample manipulation in an aqueous environment, resulting in the unique possibility to analyse organisms in their natural, hydrated state. The microalgae were lifted using an IR laser (0.2-0.3 W power), positioned into the X-ray beam and raster-scanned while capturing the fluorescent signal under confocal detection geometry ($3 \times 2 \mu\text{m}^2$ X-ray beam size; $2 \mu\text{m}$ step size; 0.5 s/point dwell time; 2×10^{10} photons/s incident intensity, 12.9 keV excitation energy).

5.2.5 Safety considerations.

Normal lab precautions (double heavy nitrile gloves, full face shield, lab coat, chemical splash apron, well-ventilated fume hood) should be taken in the formaldehyde (toxic, carcinogenic, combustible), ethanol (toxic, combustible) and etching (HF, toxic, highly corrosive) procedure. The LA-ICP-MS and critical point drying procedures use compressed gasses. The use of a class 1 ablation device is highly advised.

5.3 Results and discussion

5.3.1 Microarray gelatine standards.

The linear model fitted towards the calibration curve based on 4 standards was found to show a good fit ($r^2 = 0.9985$) within the range of $5 - 200 \mu\text{g} \cdot \text{g}^{-1}$ Cu. A calibration curve can be constructed in minutes. The ability to readily create matrix-matched gelatin standards contained within an area smaller than the beam focus area would be highly desirable for single-cell analysis, as it allows the laser to rapidly probe a highly defined sample volume, without the need to raster a large area to achieve a stable signal for a standard inhomogeneous on the microscale. CRMs available in the high-density multi-sample microarray chip format could prove useful, as the space required in the sample chamber to house standards is reduced and a single chip could be used for hundreds of analysis runs, provided that the stability of the CRM is maintained. Obviously, the microarray plate is also suitable as a platform to house many (replicate) samples, for example, in the LA-ICP-MS analysis of body fluids in a clinical environment, *e.g.*, in combination with a micro assay on the same plate. Alternatively, these

microarray platforms can be used for single cell isolation, *e.g.*, based on gravitational settling.^{52,53} The overall mass introduced within the plasma, *i.e.* the mass load, can be controlled by the size of the microwells, ensuring the ionization conditions for sample and standard to be similar. The manufacturing process of the microarray chips could be sped up by utilizing an inexpensive masking (lithography or etching), injection moulding or drilling strategies, which are very common in nanofluidics.⁵³ A glass substrate for microarray manufacturing was preferred over silicon wafers as the high transmission efficiency at 193 nm, and relative high ablation threshold of glass allow for selective ablation of gelatin, ensuring that the aerosol created remains matrix-matched towards the sample. Fused silica glass may also be a suitable substrate, as it has an even higher transmission efficiency. The use of polymeric or crystalline substrates can prove beneficial when lower blank levels for the targeted element(s) are required, however, the matrix-matching component of this approach is likely to be lost. Our findings suggest the microarray technology could be further miniaturized to microwells of a diameter of 20 μm .

5.3.2 Cu exposure effects on the population.

Copper is an essential trace element for all aquatic algae. As a result, free Cu ions are readily and rapidly taken up by phytoplankton.⁵⁴ However, like most reactive nutrient metals, Cu exhibits toxic effects at high concentrations.⁵⁵ It is hence not surprising that the overall net effect of the exposure of *S. trochoidea* to a Cu-rich environment, is a dose-dependent accumulation of the Cu from the environment into the cell. As can be observed in Figure 84c, the accumulation holds at a lethal intracellular concentration of $\sim 310 \mu\text{g} \cdot \text{g}^{-1}$, at an exposure of $\sim 50 \mu\text{g} \cdot \text{L}^{-1}$. As observed by Vergucht *et al.*, a similar Cu accumulation behaviour is displayed by *S. trochoidea* cells investigated under *in vivo* conditions using optical tweezers-based sample manipulation. In good agreement with the LA-ICP-MS findings, a strong initial increase of algal Cu concentration is observed, followed by a plateau phase upon increasing the concentration of Cu in the culture medium. A semi-quantitative evaluation was made by relying on a NIST SRM 1577c (Bovine liver) pressed pellet measured under the exact same experimental conditions. This 2D-dimensional approach can be further extended by assuming an algae density close to $1 \text{ g} \cdot \text{cm}^{-3}$ and an average cell thickness of 20 μm . For an areal concentration c_i of approximately $2.0 \text{ fg}/\mu\text{m}^2$, a corresponding weight fraction ω_i of 100 ppm is derived ($c_i = \omega_i \times d \times \rho$), which is in the same concentration range as determined *via* LA-ICP-MS analysis. Similarly, the cellular burden for Cu δ_{Cu} can be derived by taking into account the cell cross-sectional area A , estimated to be $314 \mu\text{m}^2$ (20 μm^2 diameter section): $\delta_{\text{Cu}} = c_i \times A$ (Figure 84c).

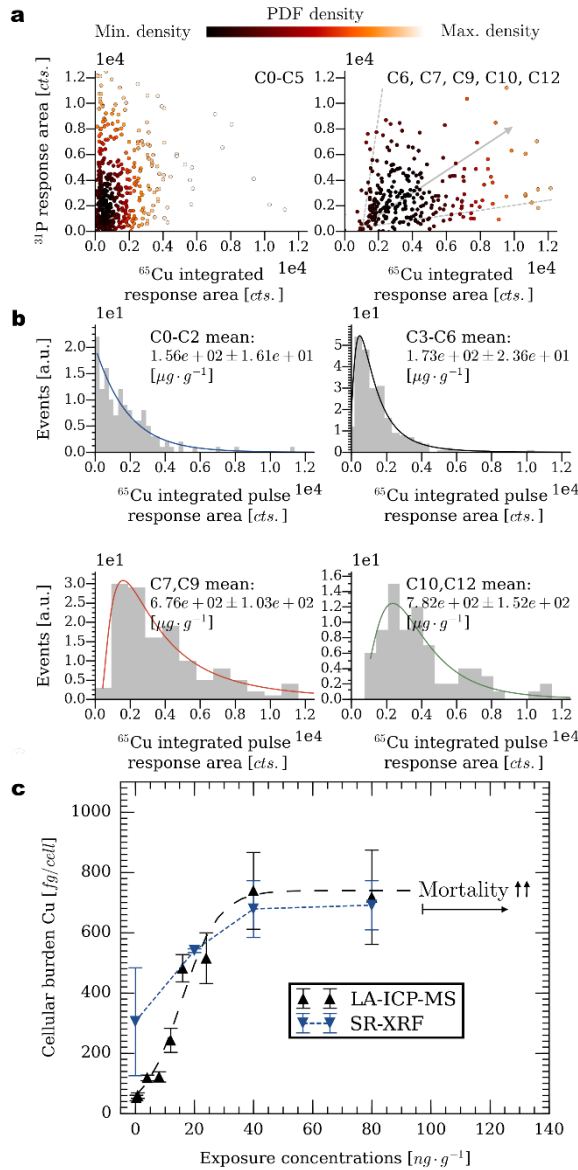


Figure 84 (a) ^{31}P - ^{65}Cu distribution for 2 sets of exposure ranges; at high exposure levels, a positive correlation can be observed. The linear color scale correlates the density of the data points (as determined by a kernel-density estimate of the probability density function using Gaussian kernels) and is scaled to the range of minimum to maximum density. (b) Probability density function for the ^{65}Cu response for 4 sets of exposure ranges. A log-normal distribution was fitted to the data. (c) Intracellular Cu concentration as a function of the exposure concentration. Black triangle: LA-ICP-MS population averages. Error bars represent the 1 s.d. precision on the population average. A sigmoidal curve was fitted to illustrate the trend. Blue triangle: SR-XRF population averages. Error bars represent the 1 s.d. precision on the population average.

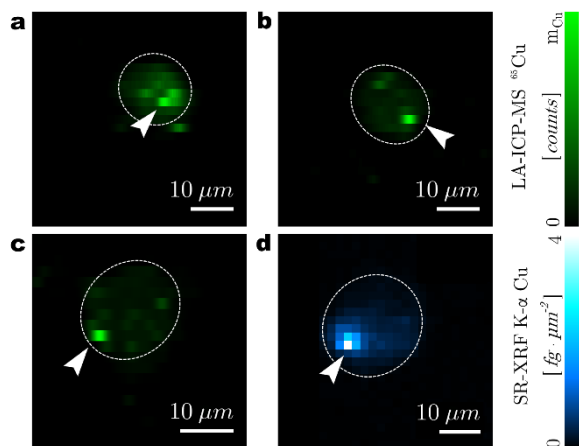


Figure 85 Side-by-side comparison of the Cu distribution in *S. trochoidea* analyzed by LA-ICP-MS and SR-XRF. (a, b, c) LA-ICP-MS images of single algae cells for increasing uptake ($a \rightarrow c$), at an exposure level of $15 \text{ ng} \cdot \text{g}^{-1}$. A large spread in the uptake is present at this exposure level. Arrows highlight the accumulation centers, the cell contours are highlighted. Green color scale scaled between the minimum and maximum intensity of Cu (m_{Cu} , $a = 71 \text{ cts.}$, m_{Cu} , $b = 381 \text{ cts.}$, m_{Cu} , $c = 1089 \text{ cts.}$). (d) SR-XRF image, blue color scale scaled between the minimum and the maximum areal concentration.

5.3.3 Microimaging.

A set of 3 cells exposed to $20 \mu\text{g} \cdot \text{g}^{-1}$ Cu was imaged *via* LA-ICP-MS. The uptake of Cu varies widely within a population. The biological variation was revealed in the quantitative experiment of this study (Figure 84a,b), and is reflected in these images. The cell in Figure 85a displays a lower uptake of Cu, in contrast to the other cells (Figure 85b,c). At high Cu uptake, an accumulation center is clearly observed (highlight Figure 85b, c), which may reflect preferential storage of Cu (*e.g.*, bound into metalloproteins or to chaperone proteins) in an important organelle (*e.g.*, Golgi apparatus, secretory vesicles). A similar accumulation center is visible in the SR-XRF microimaging results (Figure 85d), which supports the hypothesis that preferential accumulation of Cu in an organelle, heavily involved in Cu storage or secretion, of this dinoflagellate is, taking place.^{12,13} Furthermore, as the results of both techniques are similar, it is plausible that LA-ICP-MS imaging can produce the *in vivo* intracellular elemental distribution using a matching beam size, albeit at worse signal-to-noise ratio compared to SR-XRF, as can be observed in the figure. The trend in Figure 85 suggests that the accumulating organelle stores more Cu when the bulk concentration of Cu in the cell increases, whilst the cytoplasmic concentrations of Cu increase at a slower rate.

5.4 Conclusions

The proposed microarrays for multiple matrix-matched standards or samples are an attractive alternative for microdispensed droplet arrays as the microarrays, which can contain replicates at densities of $> 1000 \text{ wells} \cdot \text{cm}^{-2}$, can be produced in a fast, cheap, accurate, and precise way. Furthermore, production of these micromachined wells was feasible owing to the versatility of the analytical laser as a sample introduction system and micromachining platform, albeit at different operating parameters. Since all necessary instrumentation is already readily available

in the vast majority of LA-ICP-MS labs, further investment into a microdroplet dispenser or micropipetting system is not required. The features of these microarrays could be especially attractive in high-throughput single cell analysis, array spotting, and tissue micro-assay mapping. These microarrays could eventually be combined with micropipetting (*e.g.*, array spotting) techniques to produce standards directly inside each microwell. Using this proposed type of calibration standard, Cu ppm-level concentrations were evaluated at the single-cell level. A dose-dependent accumulation of Cu was found to occur in *S. trochoidea* upon exposure to the spiked medium. Here, for the first time (to the best of the authors' knowledge), intracellular LA-ICP-MS imaging results were cross-evaluated with the *in vivo* intracellular elemental distributions as obtained by SR-XRF elemental analysis. An accumulation center was observed in the cells using both techniques, ultimately demonstrating the potential of LA-ICP-MS for bio-imaging at the subcellular level, and corroborating conclusions drawn from the SR-XRF elemental analysis.

5.5 Supporting Information

5.5.1 Cell culture conditions

In the summer of 2013, the phytoplankton population of the Belgian Part of the North Sea was sampled aboard the RV Simon Stevin. At multiple sites, the water column was sampled with 5 L Niskin bottles at depths ranging from the bottom to the surface layer. For each sampling site, these water samples were pooled and filtered over a 10 μm phytoplankton net. The resulting concentrate was then screened for dinoflagellates under an inverse microscope. Individual cells were handpicked, washed and placed in L1 medium (32 PSU, pH 8), which was prepared with autoclaved Instant Oceantm artificial seawater (Belcopet, Belgium), according to Guillard and Hargraves.⁵⁶ Ever since, this algae was cultivated at 20°C with a light-dark cycle of 12 hours (300 – 600 $\mu\text{mol} \cdot \text{m}^{-2} \cdot \text{s}^{-1}$). To monitor sustainable growth, frequent cell counts were performed with a Sedgewick Rafter counting chamber (SPI supplies, West Chester, USA) and $\pm 80\%$ of the culture medium was replaced every 2 weeks.

5.5.2 Microwell preparation

An alternative method to dispense the gelatin in the microarray consists of dispensing the gelatin on the surface and removing the gelatin, after allowing it to solidify, with a new razor blade in a sliding motion, removing the surface-residing gelatin. The surface outside the wells was then cleared of residuals of the gelatin by a cotton swab with 1% HNO₃. The total mass dispensed into all craters $m_{\text{Cu},\text{total}}$ was measured using an MP3 microbalance (Sartorius Stedim Biotech GmbH, Göttingen, Germany). As the number of craters n is known, the calculation of the absolute Cu sensitivity $s_{\text{Cu},\text{abs}}$ based on the Cu contents within a single crater $m_{\text{Cu},\text{crater}}$ is straightforward: $s_{\text{Cu},\text{abs}} = {}^{65}\text{Cu}/m_{\text{Cu},\text{crater}} = {}^{65}\text{Cu}/(m_{\text{Cu},\text{total}}/n)$. The approach finally applied and reported in the paper was found to be more reproducible and accurate compared to this alternative approach, as surface evaporation will alter the weight during weighing in the alternative approach. A gravimetric calculation based on the alternative method estimates the crater volume at $200 \pm 30 \text{ nl}$ based on 2500 craters; this gravimetric estimate is skewed as a result of the evaporation effects and residual gelatin on the surface. The information in the figures below is described in their captions.

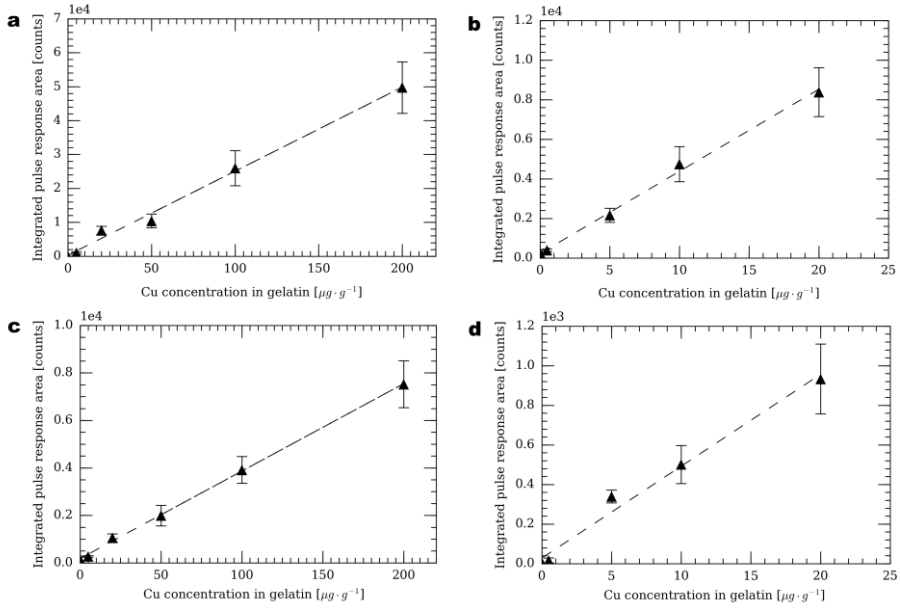


Figure 86 Calibration curves of the microarray standard based on the mean response of 3 sequences (20 microwells per sequence) for every 1 out of 8 standards. The error bars represent the between-sequence standard deviation (1. s.d.). (a) Calibration curve acquired from 110 μm \emptyset microwells. (b) Detail of the graph (a) at the lower end of the concentration scale. (c) Calibration curve acquired from 40 μm \emptyset microwells. (d) Detail of the graph (c) at the lower end of the concentration scale. All calibration curves have an $r^2 \geq 0.995$.

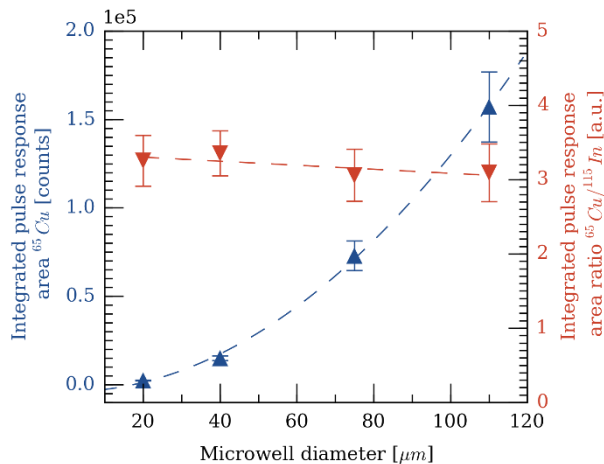


Figure 87 Pulse area and pulse area ratio as a function of microwell diameter (20 – 110 μm , 1 run of 60 microwells each for every well size, ^{65}Cu dwell time increased to 15 ms). Gelatin concentration: $200 \mu\text{g} \cdot \text{g}^{-1} \text{Cu}$, $50 \mu\text{g} \cdot \text{g}^{-1} \text{In}$. The error bars represent within-run precision (1 s.d.). (left) The mean background-corrected ^{65}Cu pulse response area as a function of the microwell diameter follows a quadratic function curve. (right) The $^{65}\text{Cu} / ^{115}\text{In}$ ratio, indicative of the stability of the sensitivity, increases towards microwell of a smaller diameter.

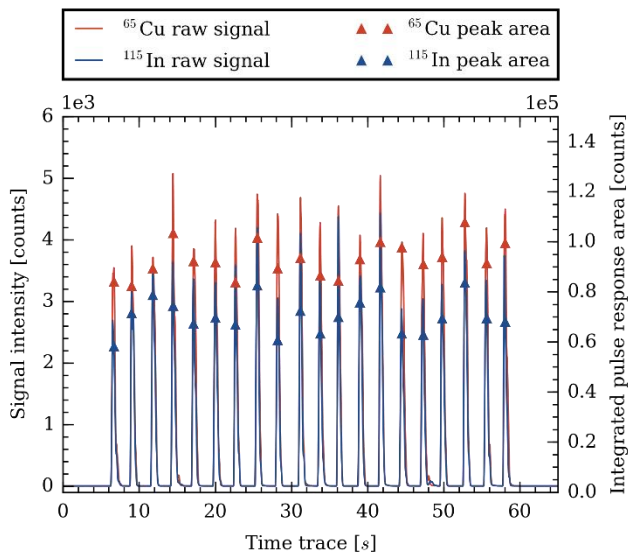


Figure 88 Raw transient signal example (left) of ^{65}Cu and ^{115}In and the integrated peak area (right) for each of the 20 wells.

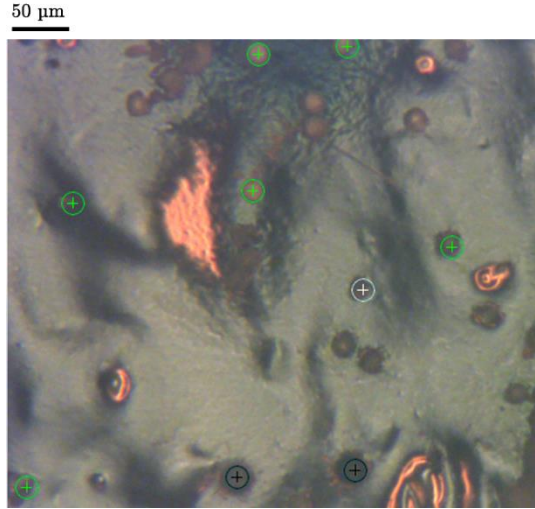


Figure 89 Individual algae cells were selected in the viewport of the laser control software Chromium, based on the relative proximity to other cells and ablated sequentially. The dimensions of the circles are indicative of the spot size (diameter, $40\ \mu\text{m}$). The black ablation positions have been ablated, the white position is the current focus position, and the green positions are yet to be ablated. The carbon stub glue is reflecting the light from the brightfield microscope, as can be seen in the bright regions.

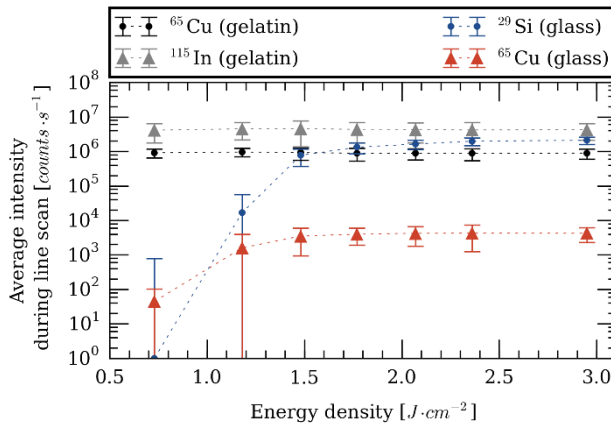


Figure 90 Background-corrected response of the system at different energy densities of the laser radiation. The error bars indicate the within-run precision (1 s.d.). The gelatin was spiked with Cu ($200\ \mu\text{g}\cdot\text{g}^{-1}$) and In ($50\ \mu\text{g}\cdot\text{g}^{-1}$). The beam waist diameter was $130\ \mu\text{m}$.

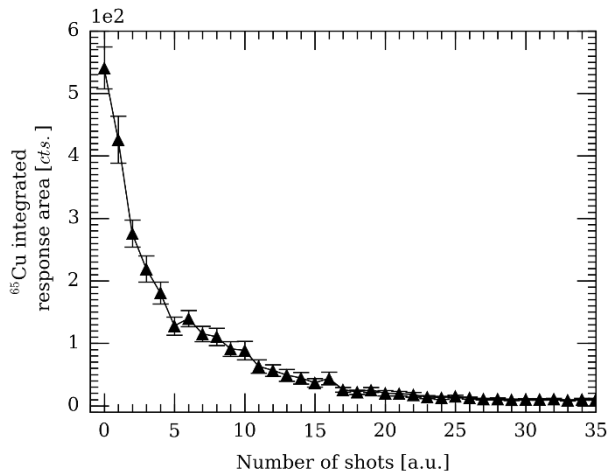


Figure 91 Response area decline for consecutive single-shot ablations of a single well. The error bars indicate the precision (1 s.d.) on the average of 25 replicate measurements. The gelatin is removed quantitatively from the well after 25 shots.

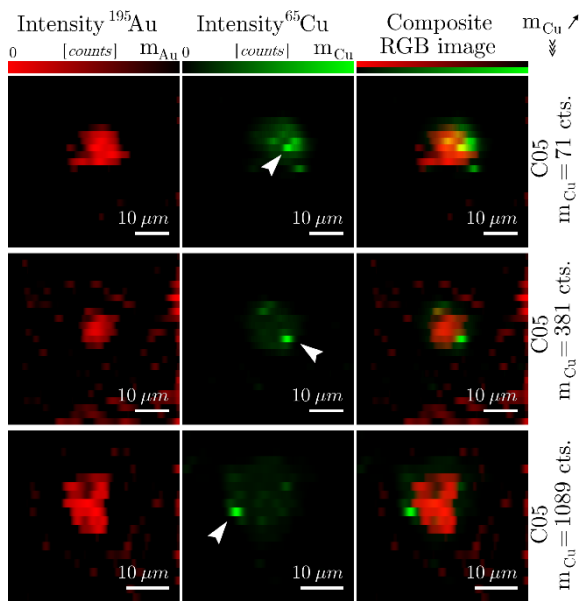


Figure 92 Supplementary imaging results, displaying composite images of the Au and Cu signal.

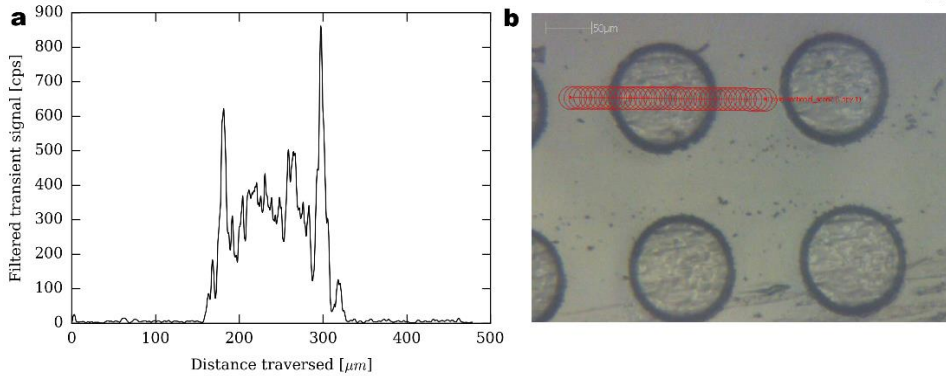


Figure 93 transient response for a line profile over the microwell. (b) Scan placement of the profile. The 30 μm \varnothing laser traversed the scan at a speed of 10 $\mu\text{m/s}$.

5.5.3 Surface hydrophobicity

Surface modification of the substrate surface, *e.g.*, with a (ultra)hydrophobic coating, *prior* to well manufacturing can promote the self-aliquoting properties of the microarray, facilitating the array filling process and improving reproducibility; a PTFE coating, 0.1-1 μm in thickness, applied *via* spin coating (10000 RPM, Spin150, Polos) increases the contact angle for gelatin from $\sim 43^\circ$ to $>70^\circ$. The coating can be removed in the first laser shot, exposing the glass substrate underneath, hence, the wettability of the wells is maintained, whilst hydrophobicity of the substrate surface increases. The cover glass used to close the microarrays can be coated as well.

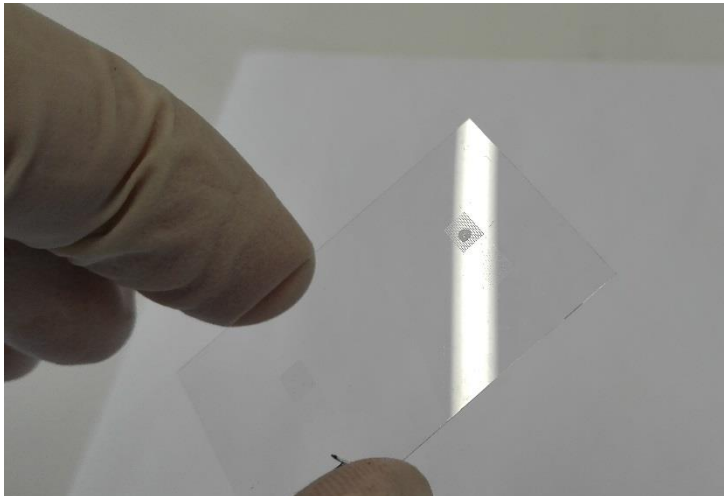


Figure 94 Droplet placement onto microarray

5.5.4 Choice of the standard medium

The use of standards sectioned on a cryomicrotome implicitly assumes that both the density of the standard and sample follow similar expansion behavior (for cutting), which is rarely valid,

except when the standard is produced based on the exact same tissue-type as the sample. Compared to cryosectioned gelatin standards, the gelatin microarray standards are not frozen in their preparation, thus, the thermal expansion properties of gelatin are less critical. Gelatin may not be an ideal standard for each biological tissue type, however, a similar argument can be made for sectioned standards of spiked homogenized tissue, as multiple tissue types are often present in a single section, which would require the use of a separate standard for each tissue type and biological substructure. In the case of single cell analysis, the use of cell lysate as a matrix for calibration standards (using standard addition) could prove beneficial.

5.6 Bibliography

- (1) Becker, J. S.; Matusch, A.; Wu, B. *Anal Chim Acta* **2014**, *835*, 1-18.
- (2) Pozebon, D.; Scheffler, G. L.; Dressler, V. L.; Nunes, M. A. G. *J Anal Atom Spectrom* **2014**, *29*, 2204-2228.
- (3) Hare, D. J.; New, E. J.; de Jonge, M. D.; McColl, G. *Chem Soc Rev* **2015**, *44*, 5941-5958.
- (4) Matusch, A.; Depboylu, C.; Palm, C.; Wu, B.; Hoglinger, G. U.; Schafer, M. K.; Becker, J. S. *Journal of the American Society for Mass Spectrometry* **2010**, *21*, 161-171.
- (5) Gholap, D.; Verhulst, J.; Ceelen, W.; Vanhaecke, F. *Analytical and bioanalytical chemistry* **2012**, *402*, 2121-2129.
- (6) Egger, A. E.; Theiner, S.; Kornauth, C.; Heffeter, P.; Berger, W.; Keppler, B. K.; Hartinger, C. G. *Metallomics* **2014**, *6*, 1616-1625.
- (7) Egger, A. E.; Kornauth, C.; Haslik, W.; Hann, S.; Theiner, S.; Bayer, G.; Hartinger, C. G.; Keppler, B. K.; Pluschnigh, U.; Mader, R. M. *Metallomics* **2015**, *7*, 508-515.
- (8) Konz, I.; Fernandez, B.; Fernandez, M. L.; Pereiro, R.; Gonzalez-Iglesias, H.; Coca-Prados, M.; Sanz-Medel, A. *Analytical and bioanalytical chemistry* **2014**, *406*, 2343-2348.
- (9) Managh, A. J.; Edwards, S. L.; Bushell, A.; Wood, K. J.; Geissler, E. K.; Hutchinson, J. A.; Hutchinson, R. W.; Reid, H. J.; Sharp, B. L. *Anal Chem* **2013**, *85*, 10627-10634.
- (10) Managh, A. J.; Hutchinson, R. W.; Riquelme, P.; Broichhausen, C.; Wege, A. K.; Ritter, U.; Ahrens, N.; Koehl, G. E.; Walter, L.; Florian, C.; Schlitt, H. J.; Reid, H. J.; Geissler, E. K.; Sharp, B. L.; Hutchinson, J. A. *Journal of immunology* **2014**, *193*, 2600-2608.
- (11) Reifschneider, O.; Wentker, K. S.; Strobel, K.; Schmidt, R.; Masthoff, M.; Sperling, M.; Faber, C.; Karst, U. *Anal Chem* **2015**, *87*, 4225-4230.
- (12) Vergucht, E.; Brans, T.; Beunis, F.; Garrevoet, J.; De Rijcke, M.; Bauters, S.; Deruytter, D.; Vandegheuchte, M.; Van Nieuwenhove, I.; Janssen, C.; Burghammer, M.; Vincze, L. *Scientific Reports* **2015**, *5*, 9049.
- (13) Vergucht, E.; Brans, T.; Beunis, F.; Garrevoet, J.; Bauters, S.; De Rijcke, M.; Deruytter, D.; Janssen, C.; Riekkel, C.; Burghammer, M.; Vincze, L. *J Synchrotron Radiat* **2015**, *22*, 1096-1105.
- (14) Dale, B. *Science of the Total Environment* **2001**, *264*, 235-240.
- (15) Mueller, L.; Traub, H.; Jakubowski, N.; Drescher, D.; Baranov, V. I.; Kneipp, J. *Analytical and bioanalytical chemistry* **2014**, *406*, 6963-6977.
- (16) Shigeta, K.; Koellensperger, G.; Rampler, E.; Traub, H.; Rottmann, L.; Panne, U.; Okino, A.; Jakubowski, N. *J Anal Atom Spectrom* **2013**, *28*, 637.
- (17) Bendall, S. C.; Simonds, E. F.; Qiu, P.; Amir el, A. D.; Krutzik, P. O.; Finck, R.; Bruggner, R. V.; Melamed, R.; Trejo, A.; Ornatsky, O. I.; Balderas, R. S.; Plevritis, S. K.; Sachs, K.; Pe'er, D.; Tanner, S. D.; Nolan, G. P. *Science* **2011**, *332*, 687-696.
- (18) Ornatsky, O. I.; Kinach, R.; Bandura, D. R.; Lou, X.; Tanner, S. D.; Baranov, V. I.; Nitz, M.; Winnik, M. A. *J Anal At Spectrom* **2008**, *23*, 463-469.

- (19) Bandura, D. R.; Baranov, V. I.; Ornatsky, O. I.; Antonov, A.; Kinach, R.; Lou, X.; Pavlov, S.; Vorobiev, S.; Dick, J. E.; Tanner, S. D. *Anal Chem* **2009**, *81*, 6813-6822.
- (20) Van Malderen, S. J. M.; van Elteren, J. T.; Vanhaecke, F. *Anal Chem* **2015**, *87*, 6125-6132.
- (21) Van Malderen, S. J. M.; van Elteren, J. T.; Vanhaecke, F. *J. Anal. At. Spectrom.* **2014**, *30*, 119-125.
- (22) Van Malderen, S. J. M.; Managh, A. J.; Sharp, B. L.; Vanhaecke, F. *J. Anal. At. Spectrom.* **2016**, *31*, 423-439.
- (23) Giesen, C.; Wang, H. A.; Schapiro, D.; Zivanovic, N.; Jacobs, A.; Hattendorf, B.; Schuffler, P. J.; Grolimund, D.; Buhmann, J. M.; Brandt, S.; Varga, Z.; Wild, P. J.; Gunther, D.; Bodenmiller, B. *Nature methods* **2014**, *11*, 417-422.
- (24) Douglas, D. N.; Managh, A. J.; Reid, H. J.; Sharp, B. L. *Anal Chem* **2015**, *87*, 11285-11294.
- (25) Douglas, D. N.; O'Reilly, J.; O'Connor, C.; Sharp, B. L.; Goenaga-Infante, H. *J Anal Atom Spectrom* **2016**, *31*, 270-279.
- (26) Konz, I.; Fernandez, B.; Fernandez, M. L.; Pereiro, R.; Sanz-Medel, A. *Analytical and bioanalytical chemistry* **2012**, *403*, 2113-2125.
- (27) Hare, D. J.; Lear, J.; Bishop, D.; Beavis, A.; Doble, P. A. *Analytical Methods* **2013**, *5*, 1915.
- (28) Kumtabtim, U.; Siripinyanond, A.; Auray-Blais, C.; Ntwari, A.; Becker, J. S. *International Journal of Mass Spectrometry* **2011**, *307*, 174-181.
- (29) Nischkauer, W.; Vanhaecke, F.; Bernacchi, S.; Herwig, C.; Limbeck, A. *Spectrochimica acta. Part B: Atomic spectroscopy* **2014**, *101*, 123-129.
- (30) Deegan, R. D.; Bakajin, O.; Dupont, T. F.; Huber, G.; Nagel, S. R.; Witten, T. A. *Nature* **1997**, *389*, 827-829.
- (31) Limbeck, A.; Galler, P.; Bonta, M.; Bauer, G.; Nischkauer, W.; Vanhaecke, F. *Analytical and bioanalytical chemistry* **2015**, *407*, 6593-6617.
- (32) Yang, L.; Sturgeon, R. E.; Mester, Z. *Anal Chem* **2005**, *77*, 2971-2977.
- (33) Grinberg, P.; Yang, L.; Mester, Z.; Willie, S.; Sturgeon, R. E. *J Anal Atom Spectrom* **2006**, *21*, 1202-1208.
- (34) Do, T.-M.; Hsieh, H.-F.; Chang, W.-C.; Chang, E. E.; Wang, C.-F. *Spectrochimica Acta Part B: Atomic Spectroscopy* **2011**, *66*, 610-618.
- (35) Hsieh, H. F.; Chang, W. S.; Hsieh, Y. K.; Wang, C. F. *Anal Chim Acta* **2011**, *699*, 6-10.
- (36) Zhai, J.; Wang, Y.; Xu, C.; Zheng, L.; Wang, M.; Feng, W.; Gao, L.; Zhao, L.; Liu, R.; Gao, F.; Zhao, Y.; Chai, Z.; Gao, X. *Anal Chem* **2015**, *87*, 2546-2549.
- (37) Wang, M.; Zheng, L. N.; Wang, B.; Chen, H. Q.; Zhao, Y. L.; Chai, Z. F.; Reid, H. J.; Sharp, B. L.; Feng, W. Y. *Anal Chem* **2014**, *86*, 10252-10256.
- (38) Raymont, J. E. G. *Phytoplankton: Plankton and Productivity in The Oceans*; Elsevier Science, 2013.
- (39) Niehaus, R.; Sperling, M.; Karst, U. *J Anal Atom Spectrom* **2015**, *30*, 2056-2065.

- (40) Birka, M.; Wentker, K. S.; Lusmoller, E.; Arheilger, B.; Wehe, C. A.; Sperling, M.; Stadler, R.; Karst, U. *Anal Chem* **2015**, *87*, 3321-3328.
- (41) Steingrobe, T.; Niehoff, A.-C.; Franze, B.; Lenhard, D.; Pietsch, H.; Engelhard, C.; Karst, U.; Buscher, W. J. *Anal. At. Spectrom.* **2015**, *30*, 2120-2124.
- (42) Urban, P. L.; Jefimovs, K.; Amantonico, A.; Fagerer, S. R.; Schmid, T.; Madler, S.; Puigmarti-Luis, J.; Goedecke, N.; Zenobi, R. *Lab on a Chip* **2010**, *10*, 3206-3209.
- (43) Pabst, M.; Fagerer, S. R.; Kohling, R.; Kuster, S. K.; Steinhoff, R.; Badertscher, M.; Wahl, F.; Dittrich, P. S.; Jefimovs, K.; Zenobi, R. *Anal Chem* **2013**, *85*, 9771-9776.
- (44) Kuster, S. K.; Fagerer, S. R.; Verboket, P. E.; Eyer, K.; Jefimovs, K.; Zenobi, R.; Dittrich, P. S. *Anal Chem* **2013**, *85*, 1285-1289.
- (45) Giesen, C.; Waentig, L.; Mairinger, T.; Drescher, D.; Kneipp, J.; Roos, P. H.; Panne, U.; Jakubowski, N. *J Anal Atom Spectrom* **2011**, *26*, 2160-2165.
- (46) Drescher, D.; Giesen, C.; Traub, H.; Panne, U.; Kneipp, J.; Jakubowski, N. *Anal Chem* **2012**, *84*, 9684-9688.
- (47) Büchner, T.; Drescher, D.; Traub, H.; Schrader, P.; Bachmann, S.; Jakubowski, N.; Kneipp, J. *Analytical and bioanalytical chemistry* **2014**, *406*, 7003-7014.
- (48) Drescher, D.; Zeise, I.; Traub, H.; Guttmann, P.; Seifert, S.; Büchner, T.; Jakubowski, N.; Schneider, G.; Kneipp, J. *Advanced Functional Materials* **2014**, *24*, 3765-3775.
- (49) Wang, H. A.; Grolimund, D.; Giesen, C.; Borca, C. N.; Shaw-Stewart, J. R.; Bodenmiller, B.; Gunther, D. *Anal Chem* **2013**, *85*, 10107-10116.
- (50) Rieger, B.; van den Doel, L. R.; van Vliet, L. J. *Physical review. E, Statistical, nonlinear, and soft matter physics* **2003**, *68*, 036312.
- (51) Xu, K.; Wang, X.; Ford, R. M.; Landers, J. P. *Anal Chem* **2016**, *88*, 2652-2658.
- (52) Lindstrom, S.; Andersson-Svahn, H. *Biochim Biophys Acta* **2011**, *1810*, 308-316.
- (53) Kim, S.-H.; Lee, G. H.; Park, J. Y. *Biomedical Engineering Letters* **2013**, *3*, 131-137.
- (54) Granéli, E.; Turner, J. T. *Ecology of Harmful Algae*; Springer, Berlin: New York, 2007.
- (55) Brand, L. E.; Sunda, W. G.; Guillard, R. R. L. *J Exp Mar Biol Ecol* **1986**, *96*, 225-250.
- (56) Guillard, R. R. L.; Hargraves, P. E. *Phycologia* **1993**, *32*, 234-236.

Chapter 6 3D imaging

This chapter is based on a research paper, 'Imaging the 3D trace metal and metalloid distribution in mature wheat and rye grains via laser ablation-ICP-mass spectrometry and micro-X-ray fluorescence spectrometry', authored by Stijn J. M. Van Malderen, Brecht Laforce, Thibaut Van Acker, Laszlo Vincze, and Frank Vanhaecke. S.V.M. was the first and principal author of this work.

The usage of LA-ICP-MS for 3D elemental imaging is a relatively recent concept, but with the development of faster LA technology, it is one that is gaining momentum. Two new approaches to performing 3D imaging with low-dispersion cells have already been reported this year^{1,2}, both of which used non-biological targets.

6.1 Introduction

6.1.1 LA-ICP-MS 3D imaging

At the time of writing, there is relatively little literature covering 3D imaging of biological samples. Despite this, a 3D imaging approach would be highly beneficial in this area, as tissue inhomogeneity may result in an uncharacteristic representation of small-scale features within individual 2D sections. 3D imaging could also prove useful to isolate hotspots in larger volumes such as organs, which might be missed when analyzing a single cross-section. Additionally, small organisms could be fully ablated, to determine the distribution of targeted compounds in each body compartment. Specific 3D imaging approaches tuned towards biological samples have been developed. In 2010, Hare *et al.* used a serial sectioning and imaging approach to create a 3D representation of Mn, Fe, Cu, and Zn distribution within a mouse brain³. Twelve sections from a single animal, each of 30 μm thickness, were consecutively ablated. Integrated Spectral Imaging Data Analysis Software (ISIDAS), an in-house Python-based program, was

used to compile the individual data files and align 2D images of each slice using image registration⁴ to create a 3D representation of the mouse brain. The same research group later applied a similar approach to create a 3D atlas of trace metals in the mouse brain⁵. A total of 46 sections were taken at 150 μm intervals. Each slice was 30 μm thick and covered a $\sim 10\text{ mm}^2$ area, with imaging of each slice performed using a 80 μm spot size and 160 $\mu\text{m s}^{-1}$ scan speed. It is clear that such an approach requires a lengthy time commitment, which would be a limiting factor for some users. The above studies were reported to take 36 and 158 hours for the ablation of 12 and 46 sections, respectively. Improvements in acquisition speed (Chapter 2), and the concurrent development of software (Chapter 4) to handle new data formats, may lead to the growing use of 3D LA-ICP-MS imaging and higher spatial resolution⁶ in the future, in parallel to a similar ongoing evolution towards 3D imaging MS.^{5,7} 3D imaging has also been explored in the field of LIBS, most notably for imaging nanoparticles in kidney tissue in a recent paper by Busser *et al.*⁸ 3D imaging with femtosecond laser ionization time-of-flight mass spectrometry (fs-LI-TOFMS) on a Nantan meteorite sample was also recently demonstrated by He *et al.*, albeit at a mediocre voxel size of $50 \times 50 \times 9\text{ }\mu\text{m}^3$.⁹ In this chapter, a procedure to image the 3D trace metal and metalloid distribution in mature wheat and rye grains *via* laser ablation-ICP-mass spectrometry and micro-X-ray fluorescence spectrometry is presented.

6.1.2 3D trace metal and metalloid distribution in mature wheat and rye grains

Micronutrients, (trace) metals and metalloids, which perform important functional roles in the metabolism of plant life with regard to growth and development, are kept in homeostasis. Cu and Zn are examples of such micronutrients – Cu is the metal ion cofactor of plastocyanin, and Zn is contained within hundreds of active sites of enzymes (*e.g.*, carbonic anhydrases) as cofactor and within transcription cofactors – while other trace metals and metalloids, *e.g.*, Pb, Hg, As, are considered contaminants with no essential metabolic role.¹⁰ Human exposure to high levels of toxic trace metals and metalloids (further abbreviated as TMs) in the environment *via* dietary, respiratory and cutaneous absorption pathways, resulting in an increased metal and metalloid uptake *via* these exposure routes, may induce neurotoxic (Pb, Hg), carcinogenic/genotoxic (Cr, As), and acute toxic effects (As), as metals and metalloids can *bioaccumulate*, interfere with protein folding processes, and cause oxidative damage.^{11,12} This study focuses on the distribution of selected essential and non-essential trace metals and metalloids commonly present or introduced into the environment, some of which exhibit a relatively high toxicity towards animal life across wheat and rye grains. Harmful doses of these TMs can be present within such grains, which act as a sink (storage location) for TMs in the plant, well before phytotoxic phenomena become apparent. Knowledge of the TM distribution allows the identification of the TM sinks inside the grain's compartments, which has direct implications regarding the dietary bioavailability of metals, apart from other factors, such as their concentration and speciation.¹³ It is important to understand and identify the pathways through which the TMs are taken up, transported, and accumulated in nutritional parts of the plants, as well as the bottlenecks and barriers inhibiting translocation of TMs between tissue types (Figure 1).

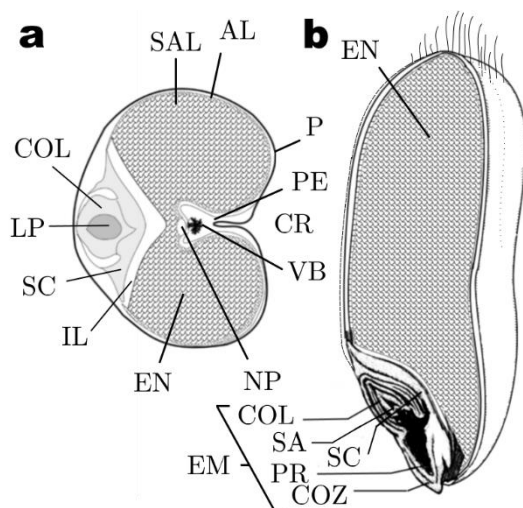


Figure 95 Schematic view of a wheat grain. Annotations: embryo (EM), scutellum (SC), endosperm (EN), crease (CR), aleurone layer (AL), sub-aleurone layer (SAL), nucellar projection (NP), leaf primordia (LP), pericarp (PE), testa (P), coleorhizae (COZ), primary root (PR), coleoptile (COL), shoot apex (SA), intermediary layer at the scutellum-endosperm interface (IL) and vascular bundle (VB).

Insights into these pathways and bottlenecks allow one to comprehend how TM compartmentalization in specific tissue types is established and can be regulated to reduce human exposure to TMs. The distribution patterns of macronutrients (P, Ca, Mg, K, C, S) and abundant micronutrients (Mo, Na, Cu, Zn, Mn, B, Cl, Fe) in wheat grain (embryos) have been extensively assessed *via* LA-ICP-MS in an earlier study by Wu *et al.* (2013), whom reported that Mg, P, Cu, and Fe were enriched in the scutellum relative to the endosperm. Furthermore, the macronutrient distribution has been visualized *via* synchrotron radiation X-ray fluorescence spectrometry (SR-XRF), nano-secondary ion mass spectrometry (Nano-SIMS) and micro-proton-induced X-ray emission spectrometry (μ -PIXE), in earlier studies.¹⁴⁻¹⁹ Remobilized metal ions are transported in the rachis *via* xylem vessels and unloaded symplastically into phloem tissue and towards the crease vascular bundle (VB) *via* plasmodesmata, from where they are distributed through the chalaza and the nucellar projection (NP) into the apoplastic space.²⁰⁻²² NP cells are the cellular sites of nutrient efflux (into the apoplasm) and endosperm transfer cells (ETCs) take up these nutrients into the filial tissue.²² Both cell types are characterized by a transfer cell morphology.²³ Cuticle formation within the cell walls of integuments surrounding the starchy endosperm prevents nutrient transfer towards the starchy endosperm from occurring in other areas. However, the VB phloem strands, which split off at the base of the grain may also provide nutrients directly to the pericarp on the dorsal side (and possibly on the ventral side) and the embryo.^{22,24} TMs supplied at high levels, under laboratory conditions or in severe cases of plant exposure to environmental contamination, may saturate metal transport pathways, and accumulate at bottlenecking sites.^{25,26} Many studies operate under these high exposure / high uptake conditions, as detection of TMs at lower levels is challenging for all but a few analytical techniques. It can be envisaged that these conditions potentially alter the

normal TM source-sink transport dynamics.²⁷ It would thus be insightful to know the distribution of TMs at exposure levels typically encountered in the environment.

LA-ICP-MS, a hyphenated elemental microprobe, with a high detection power and wide linear dynamic range, is widely deployed for 2D bioimaging.²⁸⁻³⁰ 3D imaging *via* LA-ICP-MS is however still in its infancy, with only a handful of examples scattered across the literature as a result of the time-consuming and complex nature of the data processing and representation. Ablation strategies for 3D imaging, either based on drilling/trepanning a virtual rectilinear grid or based on sequentially ablating multiple overlaid layers, are relatively straightforward, though they are plagued by a number of potential issues: i. the occurrence of ablation yield losses becomes more significant as the depth increases as a result of changes in energy density produced by drift of the irradiated material surface away from the focal plane, ii. the particle extraction and entrainment efficiency drops as the crater aspect (width/depth) ratio decreases, iii. elemental fractionation induced by reablation of deposited and (re)condensed ablation-generated particles and reheating of the crater walls (by the laser beam) iv. the fluctuation of ablation yield across the probed area as an indirect result of the presence of multiple matrix types, the proximity to crater walls, or changes in reflectivity, thermal conductivity and other properties in the sampled area.³¹⁻³⁴ As each depth layer probed must be fully consumed before the laser can probe the layer below and the typical ablation rates are <1 μm per shot, phenomena that take place over a depth larger than a few tens of μm cannot be readily visualized due to practical constraints in experimental time and cost, and the exacerbation of the aforementioned issues.¹

² These problems can be overcome for soft biological samples by serial sectioning: 3D images can be built by sectioning the sample with a microtome at different, often equally spaced depths. Each slice of the Z-stack is mapped individually by scanning grids of parallel profiles on the transverse section and the multi-channel slices are subsequently aligned in order to reconstruct a volume that correctly reflects the elemental distribution along the Z-axis. In a pioneering study by Paul *et al.* (2015), C57BL/6 mouse brains were mapped in 3D by serial sectioning and subsequent volume reconstruction based on image registration.^{4,5} Unfortunately, such strategies are not readily applicable to all sample types, as many materials, *e.g.*, crystalline material, are too brittle or hard to section with a microtome.

The aim of this study was to quantify the concentrations of a selected set of TMs in sub-regions throughout *Secale cereale* L. (rye) and *Triticum aestivum* L. (common wheat) grains and reveal their distribution *via* elemental imaging techniques in 3D. In the present study, a serial sectioning strategy, based on polishing the epoxy-embedded sample, is presented as an alternative to serial sectioning by microtomy.

6.2 Experimental section

6.2.1 Sample preparation for LA-ICP-MS

Seeds of each grain type, grown in Belgium and purchased from a local farmers' market, were rinsed with ultrapure water (resistivity $\geq 18.2 \text{ M}\Omega \text{ cm}$), provided by a Milli-Q Element water purification system (Millipore, France), and dried to avoid external contamination. The two seeds were embedded in a two-component epoxy resin (bisphenol A diglycidyl ether, Struers, Ballerup, Denmark), in a vertical orientation, with the embryo oriented towards the bottom.

After curing the resin for 24 h, the resin was cleaved transversally using an oscillating diamond saw and polished mechanically with SiC paper (P500 to P4000) until a transverse section just below the epidermis and brush was exposed at the surface. In order to reconstruct a 3D volume containing nuclide distribution information, which reflects the actual *in situ* 3D nuclide distribution, the 2D distribution was mapped at ≥ 20 different cross-sections along the central axis of the grain. The cross-section mappings were performed at a regular spacing, with an interval between images of 350 μm on the central axis. The cross-sections were exposed by mechanical polishing with SiC paper. The surface of the exposed epoxy-embedded grain was polished for ~ 150 s using P500 grade paper at 400 RPM and ~ 10 N of pressure (LaboPol-5 with LaboForce-1, Struers, Detroit, MI, USA), removing a ~ 300 μm thick layer of material. The remaining 50 μm was removed using a P1200 grade paper disc at 200 RPM for a 2-5 minutes. The thickness of the removed layer was monitored after every 30 s of polishing, by measuring the change in thickness of the resin block with a micrometer (Mitutoyo, Kawasaki, Japan) with 0.01 mm graduations. The surface underwent a finishing polishing action with P2000 and P4000 grade paper. The sequential images thus acquired are stacked up into a single volume.

For quantification purposes, a standard addition method was applied based on spiked matrix-matched solid standards in the form of pressed pellets, a type of standards which is commonly used for this type of application.³⁵ Approximately 700 mg of seeds from each grain type was crushed with an agate mortar and pestle. A pellet press ($6 \cdot 10^4$ N, 12T Spectropress, Chemplex, Palm City, FL, USA) was used to obtain 200 mg, 12.7 mm \varnothing pellets of each grain type. From a 1 g mixture of the residual 500 mg powder from each grain type, 4 powder fractions, 200 mg in weight, were taken and spiked with multi-element solutions (in 0.24 M subboiled HNO_3), prepared from standard solutions (1 g L^{-1} stock solutions in 0.31 M HNO_3 , Inorganic Ventures, Christiansburg, VA, USA). The 4 powder fractions, spiked with Cu, Mn, Zn (1, 10, 50 and 100 $\mu\text{g g}^{-1}$), As, Cd, Cr, Cu, Ni, Pb (0.1, 1, 5 and 10 $\mu\text{g g}^{-1}$), Hg (0.1, 0.25, 0.5, 1 $\mu\text{g g}^{-1}$) and Ir (5 $\mu\text{g g}^{-1}$, internal standard), were dried at 60 $^\circ\text{C}$ for 2 h, and pressed into individual 12.7 mm \varnothing pellets. The pellets were stored in a desiccator under N_2 .

6.2.2 Sample preparation for PN-ICP-MS

In order to validate the pellet standards and the ability of 3D LA-ICP-MS to estimate bulk TM concentrations, crushed powder fractions of each grain type, as well as the corresponding dried pellets and spiked pellets, were taken into solution through acid digestion. After appropriate dilution, these digests were subsequently measured by solution-based pneumatic nebulization (PN) ICP-MS, using a quadrupole-based Agilent 7900 ICP-MS unit (Agilent Technologies Inc., Santa Clara, CA, USA). From the powder mixture (*vide supra*) and pressed pellet of each grain type, 200 mg was digested in Teflon beakers (Savillex) using a mixture of 4 mL of 16 M HNO_3 (pro analysis grade, BDH Prolabo, VWR, Radnor, PA, USA) and 2 mL of 9.8 M H_2O_2 (ultra-trace analysis grade, Sigma-Aldrich, St. Louis, MO, USA). The container was loosely capped and kept on a hot plate at 90 $^\circ\text{C}$ for 0.5 h, after which the digest container was closed and kept for another 24 h at 110 $^\circ\text{C}$. The acidic solution was subsequently evaporated to dryness (may take up to 12 h). The residues were redissolved in 2 mL of 1.6 M HNO_3 and thereafter diluted to 10 mL (15 mL ultra-trace element tubes, VWR, Radnor, PA, USA), vortexed, sonicated (15 min, Branson 5510EDTH, Emerson Industrial Automation, St. Louis, MO, USA), and centrifuged (4400 rpm, 5

min, Centrifuge 5702, Eppendorf, Hamburg, Germany), after which 5 mL of clear supernatant was micropipetted and 500 μL of a 100 $\mu\text{g L}^{-1}$ Ir solution (obtained from a 1 g L^{-1} Ir stock solution in 0.31 M HNO_3 , Inorganic Ventures, Christiansburg, VA, USA) was added as an internal standard, correcting for possible matrix effects, signal drift and instrument instability. The solution was further diluted to 10 mL for PN-ICP-MS analysis. A set of multi-element calibration standards containing Cr, As, Cd, Pb (0.1, 1, 5, and 10 $\mu\text{g L}^{-1}$), Mn, Ni, Cu, Zn (1, 10, 50, and 100 $\mu\text{g L}^{-1}$), and Hg (0.1, 0.25, 0.5, and 1.0 $\mu\text{g L}^{-1}$) was prepared (all solutions contain 0.16 M HNO_3 and 5 $\mu\text{g L}^{-1}$ Ir), and measured together with the samples using solution-based PN-ICP-MS, providing linear calibration curves ($R^2 \geq 0.99925$) for all elements.

6.2.3 LA-ICP-MS imaging

The LA-ICP-MS setup consisted of an Analyte G2 Excimer 193 nm ArF* laser ablation system (Teledyne Photon Machines, Bozeman, MT, USA) connected to a quadrupole-based Agilent 7900 ICP-MS unit (Agilent Technologies Inc., Santa Clara, CA, USA). The LA-system is equipped with the ARIS³⁶ a low-dispersion mixing bulb developed at Ghent University and commercialized by Teledyne Photon Machines (Bozeman, MT, USA), which improves the overall throughput and sensitivity of the LA-system. The settings of the LA-ICP-MS setup were tuned at the start of each experiment (after 1-2 h of warm-up) whilst ablating NIST SRM 612 glass certified reference material (National Institute for Standards and Technology, Gaithersburg, MD, USA) to achieve high sensitivity for $^7\text{Li}^+$, $^{89}\text{Y}^+$, $^{115}\text{In}^+$, $^{238}\text{U}^+$ whilst maintaining low oxide levels ($^{238}\text{U}^{16}\text{O}^+ / ^{238}\text{U}^+ < 1.5\%$), low elemental fractionation ($^{238}\text{U}^+ / ^{232}\text{Th}^+ \approx 1$), and low background levels ($^{32}\text{S}^+$, $^{31}\text{P}^+$). The final operating parameters are described in Table 7. The sensitivity, elemental fractionation, and oxide and background levels were monitored closely on a daily basis. No significant drift of these metrics was observed during the course of the experiments.

Table 7 Operational parameters for LA-ICP-MS imaging.

Teledyne Photon Machines (Bozeman, MT, USA) Analyte G2 laser ablation system with ARIS		Agilent 7900 ICP-MS	
Energy density [$J\ cm^{-2}$]	3.00	RF power [W]	1500
Repetition rate [Hz]	150	Sampling depth [mm]	9.1
Scan mode	Line scanning	Ar plasma gas flow rate [$L\ min^{-1}$]	15.0
Scan speed [$\mu m\ s^{-1}$]	200	Ar auxiliary gas flow rate [$L\ min^{-1}$]	0.90
Number of shots per position	15	Ar make-up gas flow rate [$L\ min^{-1}$]	1.07
Beam waist diameter [μm]	20	Acquisition parameters	
Mask shape	Square	Nuclides monitored	^{31}P , ^{32}S , ^{52}Cr , ^{55}Mn , ^{60}Ni , ^{65}Cu , ^{66}Zn , ^{75}As , ^{111}Cd , ^{193}Ir , ^{202}Hg and ^{208}Pb
He carrier gas flow rate [$L\ min^{-1}$]	0.450	Respective dwell times [ms]	2, 2, 10, 2, 5, 1, 1, 10, 5, 5, 2, 5

All pellets and the epoxy block with the grains were mounted in the ablation chamber of the LA-system. Before and after mapping each cross-section, 15 evenly distributed scan profiles, 6 mm in length, were acquired on each of the spiked pellets. The sensitivity was calculated based on the slope of a linear interpolation of the response; linear calibration curves ($R^2 \geq 0.99$) were established for all target nuclides, with the exception of Cr and Ni, which were heterogeneously distributed across the pellets.

Rectilinear grids of 100-300 parallel line scans, ~ 0.5 -3 mm in length, were projected on each cross-section, enclosing the exposed kernel surface. The detector signal was monitored continuously for the duration of the mapping (300-4800 s), with no pause in-between scans. The signal for each scan was isolated using a thresholding algorithm written in Python 3.4, which can detect signal drops in-between scans, based on the signal at m/z 52, which is observed at a relatively high intensity when sampling the epoxy as a response to the increase in the $^{40}Ar^{12}C^+$ signal intensity, and is characterized by a relatively low gas blank signal. The collection of scans was combined into an image slice using in-house developed software which takes into account the relative position of each scan based on the laser log file. A total of 20-24 layers were mapped for each seed, resulting into Z-stacks of 20-24 image slices. All images were

expanded to match the dimensions of the largest slice. A background correction based on the gas blank and calibration of the data based on the standard addition approach using the spiked pellets was performed for each slice individually to correct for potential drift in instrumental sensitivity. The relative alignment of the slices was performed using image registration (Euclidian transform) in OpenCV, based on the algorithm by Evangelidis *et al.*³⁷ The total time required to run the experiment, including the polishing steps and excluding data processing time, is approximately 120 h.

6.2.4 Supporting CT and XRF imaging

Longitudinal sections of the grains were imaged using μ -XRF to independently validate our findings regarding the major element distribution. The XRF spectrometer employed is an EDAX EagleIII, using a 50 W rhodium X-ray tube equipped with polycapillary optics, focusing the X-rays into a 60 μm spot, and an 80 mm^2 liquid nitrogen cooled Si(Li) detector. The step size was 60 μm with a 10 s live time per point for all mappings. The measurements were performed under mild vacuum conditions. The XRF spectra were evaluated using AXIL, an iterative least-squares fitting procedure^{38,39}, resulting in elemental distribution images for each detectable element.^{38,39} Three-dimensional imaging of the morphology present in the grain samples was performed using X-ray Computed tomography (μ -CT). A tungsten anode tube (X-ray WorX, Hanover, Germany) is used to generate the conical X-ray beam illuminating the sample which is mounted on a rotation stage. An XYZ air-bearing motor stage (LAB, Leuven, Belgium) allows positioning and magnification of the sample while aligning the sample and rotation axis is performed by an XY piezo motor system (SmarAct, Oldenburg, Germany). Detection of the X-rays is performed with a CCD camera (Photonic Science, Millham, UK). The voxel size of this setup can be tuned by changing the source-object distance and can be as small as 0.5 μm for small samples. During this study, a voxel size of $10 \times 10 \times 10 \mu\text{m}^3$ was employed. A total of 1000 projections were recorded, with a 1 s dwell time.

6.3 Results and discussion

6.3.1 3D imaging

In the study of Wu *et al.*, a 25 μm \emptyset spot was scanned at 40 $\mu\text{m s}^{-1}$, whilst in the current experiment, the ARIS low-dispersion system was used, enabling an improved methodology; a smaller spot size (20 μm \emptyset) could traverse the sample 5 times faster, without introducing distortions indicative of response overlap or impaired aerosol washout effects. By compressing the aerosol into a shorter time frame, in combination with an ICP-MS instrument approximately 1 order of magnitude more sensitive, TM patterns – previously difficult to detect – were revealed. This evolution in instrumentation was highlighted in two recent reviews on this topic.^{31,40} Individual image slices, for *T. aestivum* through the root primordia and for *S. cereale* are shown in Figure 96 and Figure 97, respectively. The colormap in the images was scaled up to the maximum response value, tabulated in Table 8 and Table 9, for Figure 96 and Figure 97, respectively.

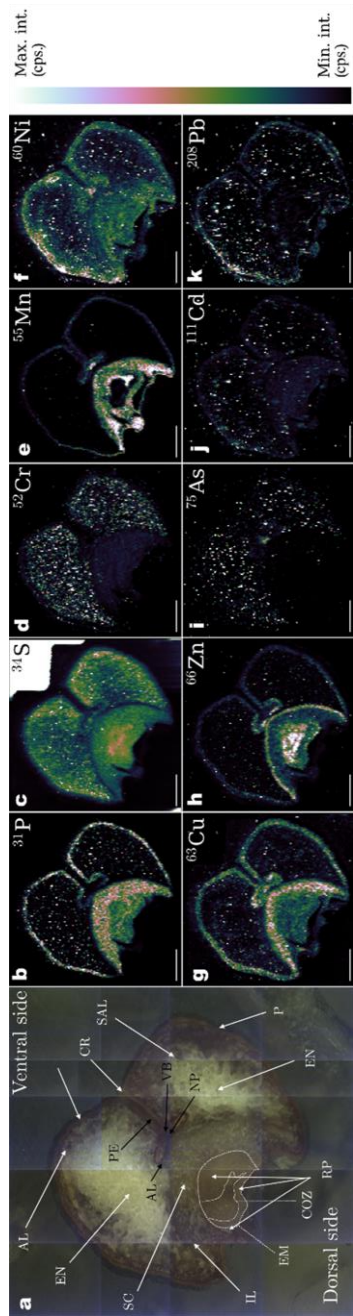


Figure 96 LA-ICP-MS mappings of slice 19 of *Triticum aestivum* L. at the level of the root primordia. (a) brightfield microscopy image of the grain. (b-k) Individual elemental distributions as acquired by LA-ICP-MS. The image colormap is scaled between 0 and the maximum intensity of the nuclide (Table 2). The scale bar in the lower left corner of each map is 500 μm in length.

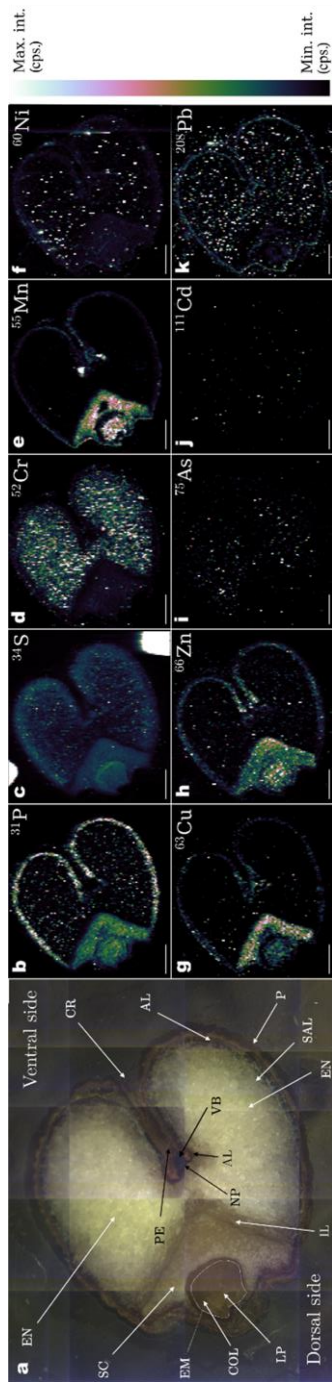


Figure 97 LA-ICP-MS mapping of slice 16 of *Secale cereale* L. at the level of the leaf primordia (a) brightfield microscopy image of the grain. (b-k) Individual elemental distributions as acquired by LA-ICP-MS. The images are scaled between 0 and the maximum intensity of the nuclide (Table 3). The scale bar in the lower left corner of every map is 500 μm in length.

Table 8 Maximum response level for slice 19 of *Triticum aestivum* L. (Figure 96).

	<i>Maximum response [cps]</i>	<i>Equivalent concentration [$\mu\text{g g}^{-1}$]</i>	<i>element</i>
^{31}P	4.9×10^5		
^{34}S	6.5×10^3		
^{52}Cr	1.4×10^4	1.1	
^{55}Mn	1.6×10^5	2.6×10^3	
^{60}Ni	2.9×10^2	0.9×10^1	
^{63}Cu	2.2×10^3	4.8×10^1	
^{66}Zn	1.4×10^4	3.0×10^3	
^{75}As	1.2×10^2	2.2	
^{111}Cd	2.0×10^2	9.7	
^{208}Pb	6.9×10^2	2.7	

Table 9 Maximum response level for slice 16 of *Secale cereale* L. (Figure 97).

	<i>Maximum response [cps]</i>	<i>Equivalent concentration [$\mu\text{g g}^{-1}$]</i>	<i>element</i>
^{31}P	6.7×10^5		
^{34}S	2.0×10^4		
^{52}Cr	1.8×10^4	1.4	
^{55}Mn	2.2×10^5	3.5×10^3	
^{60}Ni	4.8×10^2	1.6×10^1	
^{63}Cu	6.0×10^3	1.3×10^2	
^{66}Zn	2.7×10^4	6.0×10^3	
^{75}As	1.4×10^3	2.6×10^1	
^{111}Cd	1.9×10^3	9.5×10^1	
^{208}Pb	9.2×10^2	3.5	

For *S. cereale* and *T. aestivum*, 24 and 20 slices, spaced $350\ \mu\text{m}$ apart, were registered, respectively. As visible in Figure 98, rotations and translations are applied in the registration process to correctly match the morphological features between subsequent slices, permitting the reconstruction of the entire seed. Registration is an essential process in correctly representing the 3D metal distribution within the seed; misalignment of the images would confound the compartmentalization of the metal distribution into individual seed structures. Polishing of the epoxy block to reveal individual layers is a cumbersome and time-consuming strategy, though it does enable an increase of the probe depth of LA-ICP-MS beyond the maximum laser drilling depth, for solid samples which cannot be readily sectioned, which include many geological samples and mineralized tissues such as teeth and shells. Hence, we expect this serial polishing methodology to be applied in the future for these types of samples. For soft tissue or soft materials however, microtome sectioning still remains preferable due to its ease-of-use. For the serial polishing approach, matrix-dependent ablation rates will, in contrast to the approach based on microtome sectioning, still bias quantification, as a quantitative removal of material in a layer is not possible – an issue which also affects the drilling approach for 3D imaging. The ablation rates on the sample and matrix-matched pellets will be similar, which will alleviate the bias.

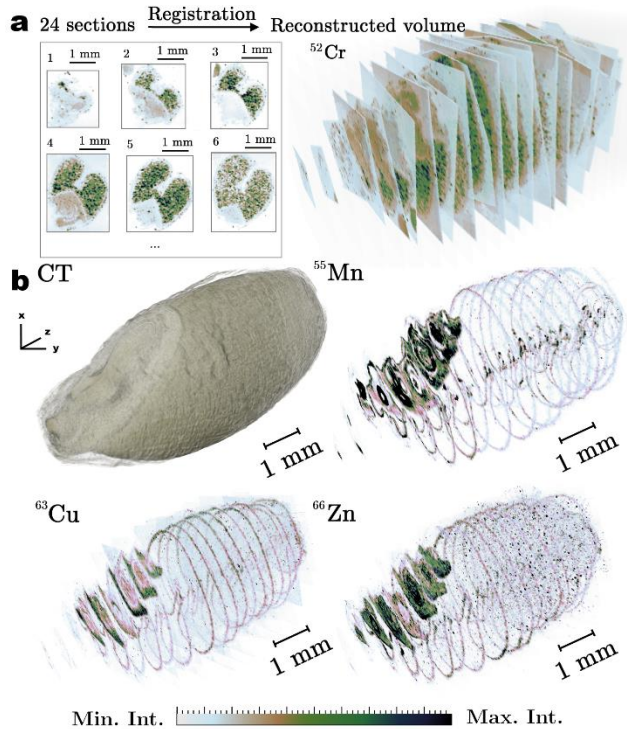


Figure 98 a) Schematic illustration of the feature-based registration process, showing the transition from a set of 2D images towards a stack of aligned 2D images of the Cr distribution in *S. cereale*. b) 3D distribution of selected micronutrients in *T. aestivum* L. and a micro-CT image of the grain.

It is possible to take advantage of the sectioning approach to reduce the area that needs to be ablated; the area ablated was the smallest possible rectangle enclosing the sample, *i.e.* no time was dedicated to the ablation of epoxy for the sake of removing it to access the layer below it, resulting in a significant reduction of the area ablated, and measurement time. However, this approach does result in images of different dimensions. Stacking the multi-dimensional images into a 3D volume, however, requires each image to be of the same size. The image dimensions were hence expanded post-acquisition to match the dimensions of the largest image, by placing this image in the center of a larger array filled with zero values, with dimensions matching the larger image. As a background correction was performed, the response for the resin blends is zero on average. This allows the image to blend in well with the array and dissolves the boundaries of the image. A background correction for the signal of the resin is required: if this feature is not eliminated, it would interfere with the registration of the images.

Regions of interest corresponding to structural layers and zones within the bran and embryo, *e.g.*, the aleurone layer and seed coat, can be distinguished based on their concentration differences for major elements. The elemental distribution in data slices perpendicular to the cross-sectional mapping provides information on the distribution along the crease. Little variation in the elemental distribution was observed along this axis in the endosperm, though

As was observed to be accumulated in *T. aestivum* away from the embryo, at the dorsal side. The 3D image provides a better insight in the embryonal structures; coleorrhizae, coleoptile, leaf primordia, mesocotyl and shoot apex can be distinguished in separate slices. It is evident that connective tissues have a shared TM distribution across slices, *e.g.*, Mn is present in the outer regions of the root and leaf primordia in each slice of the embryo. A montage of all cross-section is provided as a multimedia file in the electronic supplementary information. A single 2D image would be unable to reflect the TM distribution across the embryo and crease simultaneously. An image mapped on the surface of a length-wise section, would not visualize the nucellar projection and vascular bundle, whilst a cross-section in the width of the embryo only captures either root or leaf primordia, dependent on the height at which the section is taken.

6.3.2 Metal distribution in seeds

The absolute elemental concentrations for anatomical features of the wheat and rye grain were calculated by extracting the concentrations of the elements attached to pixels belonging to these features (see the electronic supplementary information). Below, the TM distribution patterns are discussed in their biological context for each TM individually; the distribution of macro- and micronutrients (P, S, Mn, Cu, and Zn), is discussed in the electronic supplementary information.

6.3.2.1 Cadmium

Cd exhibits high phytotoxicity and bioavailability and has the potential to induce mitochondrial damage; the toxicity of Cd is affected by the Zn/Cd ratio as they share transporter proteins (ZIP-IRT1 and P_{1B}-ATPases) in important root uptake pathways.^{41,42} Cd²⁺ may also compete with transmembrane carriers of Ca²⁺, Fe²⁺, Mg²⁺ and Cu²⁺. Its low concentration of $\leq 50 \text{ ng g}^{-1}$, challenges the detection of this element in the seeds for both LA-ICP-MS and SR-XRF. A higher accumulation of Cd can be observed in the scutellum, embryo and aleurone layer (Figure 99a). The areas match well to the areas where Zn accumulates (Figure 99b), suggesting that Cd and Zn are colocalized to some extent in wheat and rye grains. The pattern of Cd accumulation is however obscured by very high, local levels of Cd in the endosperm and resin, which challenges detection of this pattern. In the endosperm however, Cd is more prevalent relative to Zn, which supports the existence of within-seed controlled processes for the transfer of Zn from maternal tissues towards the endosperm.

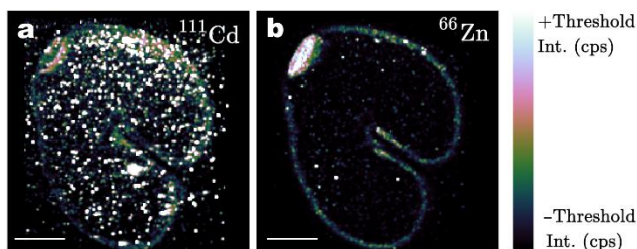


Figure 99 LA-ICP-MS mapping of slice 16 of *Secale cereale* L. for ^{111}Cd (a) and ^{66}Zn (b). The scale of the colormap for the ^{111}Cd image (a) was thresholded to a range of $[0 \text{ cps} - 60 \text{ cps} (3 \mu\text{g g}^{-1} \text{ Cd})]$ to visualize the correlation of this element with Zn, for which the response in the range of $[0 - 6.0 \times 10^3 \mu\text{g g}^{-1} \text{ Zn}]$ is displayed in (b).

6.3.2.2 Chromium

Cr is located primarily in the starchy endosperm; a closer observation reveals a very heterogeneous distribution, which could be characteristic for storage vacuoles, which locally concentrate Cr. Transmembrane exchange of nutrients at symplasmic disjunctions at the filial-maternal interface does not seem to be limiting Cr transport towards the endosperm storage sink.

6.3.2.3 Nickel

Whilst Ni is distributed fairly homogeneously across the filial and maternal tissues, a slightly higher background is present in the embryo and aleurone layer. Ni is involved in embryo and endosperm development, polyphenolic oxidation and dehydrogenase activities. Ni^{2+} is also present in urase, a metalloenzyme involved with urea hydrolysis and suggested to have a protective role against phytopathogens.⁴³⁻⁴⁷ For Ni and Pb, a lower but uniform distribution is detected in the bran layers, resulting in comparable levels within the endosperm.^{26,48}

6.3.2.4 Lead

Pb has accumulated in the seed coat and, at significantly lower levels, in the embryo and scutellum. Hence, gradient-driven transport of these metals, *i.e.* osmotic pressure, is not the main driver of transport. The limited biofunctionality of Pb – Pb is not readily incorporated into proteins –, and affinity of Pb for chelates or ligands, such as nicotinamine and phytic acid, may hamper transport of Pb across symplastic and apoplastic spaces, which would explain the distribution observed. In the z-axis, Pb has migrated away from the embryonal tissue; a gradient is observed towards the opposite side of the grain.

6.3.2.5 Arsenic

On the macro scale, the distribution of As is fairly homogeneous over the endosperm. However, on a micro scale, small hot spots dotted across the endosperm were observed. It is clear that the mechanisms of TM transport differ strongly from those of the essential metals, as their distribution is opposite to each other. In a study by Carey *et al.* (2011), the As distribution in rice grains was mapped. H and high concentrations of organic As in the region of the ovular vascular trace (VB) were detected.⁴⁹ The high mobility of As as dimethyl arsenic acid enables leaf-grain transport.⁴⁹ In another study on brown rice grains, Sb, As, Cu, Fe, Mn, and Zn were reported to accumulate in the bran layers. The speciation of As in bran and endosperm was linked to As(III)-thiol complexes (*e.g.*, As-phytochelatin, As-metalllothionein) and dimethyl arsenic acid in rice grains, which is likely to be similar to the speciation in wheat grains as a result of the abundance of S-containing proteins in the starchy endosperm.^{25,50,51} Previously, it was observed that As tends to accumulate in proximity to the pericarp and aleurone layer in (brown) rice grains and is potentially colocalized with Cu, Fe, Mn, Sb and Zn, which is in contrast to our findings in wheat.^{25,26,48} Nano-SIMS analysis revealed As to be concentrated in the sub-aleurone endosperm cells in association with the protein matrix of rice grains.¹⁷ As was also detected near the ovular vascular trace and nucellar projection using SR-XRF at levels approximately 2-fold higher (As:S ratio) than the endosperm level; Nano-SIMS revealed the As to be distributed as micrometer-sized hotspots.¹⁷ In wheat grains, the storage mechanism

appears to be different, and storage of As takes place in the starchy endosperm. No significant amount of As was detected in the maternal tissues.

6.3.2.6 Antimony

Sb transport is not well-characterized.^{52,53} Sb coordinates with oxygen in an octahedral arrangement ($\text{Sb}(\text{OH})_6$), which may result in competition of Cd and Zn for octahedral binding sites.^{26,54} However, no significant Sb was detected across the grains, which is, considering a bulk concentration $\leq 50 \text{ ng g}^{-1}$, likely considering typical LOD levels.

6.3.2.7 Cross-elemental patterns for TMs

The results show that Cr, Cd, Pb, and As are transported towards the endosperm, suggesting the existence of, possibly non-specific, metabolic transport routes through the symplastic space, different from the nutrient transport routes used by Zn, Fe, Mn and Cu. Transmembrane transport enables nutrient uptake into the filial tissue from the maternal tissue between apoplasmically isolated compartments. Although the sink capacity for micronutrients is limited in the endosperm, the sink capacity for TMs in the endosperm is relatively high. As the embryo is removed upon milling, essential metals are lost, whilst remaining TMs become dietary available. When TMs are supplied at high levels, these transport routes and storage sinks may change as a result of saturation of the transport routes towards the endosperm. An example of this is As, which, when supplied at high levels, accumulates in the husk and bran, whilst As was mainly detected in the endosperm in this study.^{17,49,54} Remarkably, trace elements such as As, Hg, Cr and Cd do not show any accumulation in maternal tissues. Unloading of these TMs from the VB into the endosperm appears to be efficient, though transport towards the bran layers occurs at a slower rate than for other metals. Biofortification strategies focusing on increasing the micronutrient content in the endosperm by promoting translocation processes from embryonal tissue towards the endosperm could hence be designed to operate independently from TM transport processes. Inhibition of the non-specific transport routes, on the other hand, would mitigate accumulation of the TMs into the endosperm, but will likely simultaneously disturb crucial metabolic processes relying on the pathways. Antagonistic and synergistic effects, *e.g.*, Cu was reported to affect Zn phytotoxicity, should be considered when designing these strategies, as well as the speciation of the TM, *e.g.*, arsenate will be taken up at different rates than the more mobile arsenite.^{25,49,55} Although significant efforts have been made towards biofortification strategies, more research is required to prevent TM accumulation in the endosperm.

6.3.3 Bulk concentrations

The bulk elemental contents obtained *via* acidic digestion are listed in Table 10.

Table 10 Elemental concentrations of essential and non-essential trace metals/metalloids determined by solution-based PN-ICP-MS after acidic digestion of wheat and rye grains. Results are presented as the mean \pm standard deviation of 3 replicates.

	<i>S. cereale</i> L. [$\mu\text{g g}^{-1}$ DW]		<i>T. aestivum</i> L. [$\mu\text{g g}^{-1}$ DW]	
	Powder mixture	Pellet	Powder mixture	Pellet
Cr	0.267 \pm 0.003	0.602 \pm 0.005	0.366 \pm 0.005	0.733 \pm 0.008
Mn	22.09 \pm 0.14	19.89 \pm 0.08	19.22 \pm 0.18	19.93 \pm 0.19
Ni	0.194 \pm 0.0005	0.152 \pm 0.002	0.268 \pm 0.004	0.327 \pm 0.002
Cu	4.628 \pm 0.023	4.838 \pm 0.030	2.339 \pm 0.020	2.193 \pm 0.020
Zn	32.36 \pm 0.42	33.11 \pm 0.13	19.27 \pm 0.13	20.10 \pm 0.14
As	0.034 \pm 0.0002	0.0258 \pm 0.004	0.036 \pm 0.002	0.049 \pm 0.005
Cd	0.019 \pm 0.0005	0.016 \pm 0.0006	0.052 \pm 0.0009	0.063 \pm 0.001

Concentrations of micronutrients (Cu, Mn, Ni, and Zn) are within the expected ranges.^{12,16,19} Cr is a non-essential metal contaminant in plant life with a potential to induce oxidative damage as Cr(VI).⁵⁶ Though Cr has no specific uptake mechanism –Cr(III) is passively taken up and Cr(VI) is taken up by metabolically driven processes–, its relatively high abundance in the environment induces within-grain Cr concentrations an order of magnitude higher than the levels of other TMs, such as As, Cd and Pb.⁵⁷ The levels of these TMs are lower than reported previously.^{12,16} Cr(VI) has been reported to hinder seed germination in *T. aestivum*.⁵⁶ The level of Cr in the pellet and powder mixture is substantially different in view of the overall accuracy of the sample preparation method, potentially as a result of contamination during pellet preparation. This difference was corrected for by using a correction for Cr in the calibration of the LA analysis. No contamination issues were detected for other elements.

6.3.4 Longitudinal section via XRF

XRF images (Figure 100) give an additional insight into the distribution of major elements not included in the LA-ICP-MS duty cycle in *S. cereale* and *T. aestivum*. Ca and K are concentrated in the aleurone layer or bran, embryo, and scutellum, phloem strand/crease, and generally at the ventral side of the grain base. Fe on the other hand is predominantly found in the scutellum. The grains were mounted into an aperture of a stainless steel plate, hence, the Fe background reflects this. Zn is found in the embryo and scutellum at comparable levels. Mn has been accumulated in the scutellum, mesocotyl, and crease VB – corroborating the distribution observed via 3D LA-ICP-MS. These results compare well to the distribution reported by Neal *et al.* (2013).⁵⁸

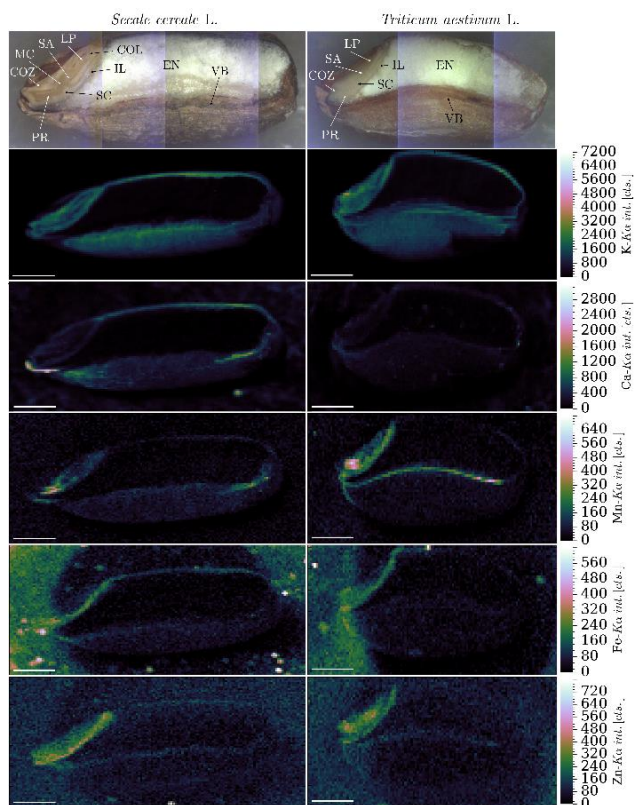


Figure 100 XRF $K\alpha$ intensity maps in the longitudinal direction of the *S. cereale* and *T. aestivum* grains. The scale bar in the lower left corner is 1 mm in length.

6.3.5 Micro-CT

The μ -CT rendering, published as a multimedia file in the electronic supplementary information, provides a more detailed insight into the morphology of the grains. In Figure 98, the leaf and root primordia can clearly be distinguished from other structures, though it remains difficult to identify individual cell layers. The outer surface shape of the μ -CT volume does match well with the surface contours of the reconstructed 3D LA-ICP-MS volume, which indicates that the reconstruction accurately reflects the grain morphology.

6.3.6 Contamination risks associated with a polishing approach

It was originally feared that the starchy endosperm, a soft, porous tissue, might be prone to the uptake of contaminant particles, possibly leading to higher levels of TMs in this tissue type. In contrast to sectioning approaches which are based on microtomy, the approach presented is based on polishing of the sample, which introduces an increased risk of metal cross-contamination between tissues and between the tissue and its environment. In order to confirm the endogenous presence of trace levels of non-essential nutrients in the endosperm, one *S. cereale* grain was split lengthwise through the crease using a razor blade, and a longitudinal section was imaged using LA-ICP-MS, using identical instrumental parameters as before. The

distribution of all elements was in good agreement with the results obtained for the cross-sections, which suggests the influence of cross-tissue contamination was negligible.

6.4 Conclusions

Advances in instrumental performance in combination with the serial polishing methodology developed, have permitted the reconstruction of the 3D trace metal and metalloid distribution in seed samples. For the first time to the best of the authors' knowledge, toxic trace metal/metalloid distribution patterns along the transverse sections of wheat and rye grains exposed to natural background concentrations were visualized and quantified per structural compartment. Strong accumulation of Mn and Zn in the aleurone layer was observed, along with the possible identification of a non-specific metal transport barrier to filial tissue. Trace metals and metalloids concentrated in the endosperm such as As, Cd, Cr, and Pb have a tendency to show up in concentrated micron-sized zones; other metals are far less abundantly present in the endosperm. Further improvements in the throughput of LA-ICP-MS, will allow to reduce the interspacing between sections, which is desirable, as this would enable a more accurate registration of the individual slices, permitting the reconstruction to more accurately reflect the elemental distribution along this axis.

6.5 Supporting information

6.5.1 Discussion on macro- and micronutrients

The paragraphs below discuss the distribution of every macro- and micronutrient as acquired using LA-ICP-MS analysis.

6.5.1.1 *Phosphorus*

In both *S. cereale* and *T. aestivum*, P is particularly prevalent in the aleurone layer, which is not surprising given its function as compartment for P storage (for germination) under the form of proteins, phytic acid, and phospholipids.⁵⁸⁻⁶⁰ P is distributed evenly across the scutellum and embryo, and present at lower levels in the starchy endosperm.

6.5.1.2 *Sulfur*

S is one of the main plant nutrients and is found throughout the seed protein sinks in its role as a constituent of the amino acids methionine and cysteine, and in the form of glucosinolates, glutathiones, and phytochelatins. The primary pathway towards S assimilation is based on the production of cysteine.⁶¹ S is located fairly uniformly across the seed, with the relative concentration slightly higher in the embryo and sub-aleurone layer, in accordance with previous studies.^{14,19}

6.5.1.3 *Copper*

Cu mainly accumulated in the scutellum and nucellar projection and at lower concentrations in the embryo and seed coat, whilst Mn, As, Cd, Cr, Ni and Pb show overall higher levels in the starchy endosperm and lower doses in the scutellum and embryo. Cu has an essential role as a reducing or oxidizing agent in photosynthesis, mitochondrial respiration, carbon and nitrogen metabolism and oxidative stress protection. The complexation of Cu to small chaperone proteins and thiolate complexes allow Cu to accumulate.⁶² Some biochemical reactions can be

catalyzed using enzymes with Cu or Fe metal cofactors, *e.g.*, Cu/Zn-superoxide dismutase (Cu/Zn-SOD) and Fe-superoxide dismutase; the distribution of Cu, Zn, and Fe is remarkably similar, yet it is unclear why Cu accumulates more in the scutellum relative to the embryo.⁶³

6.5.1.4 Manganese

Manganese is a cofactor in dozens of enzymes, as well as an activator; Mn thus represents a crucial function in the proteome.⁶² In both grains, Mn is predominantly present in the outer perimeter of the primary and lateral roots (coleoptile/coleorhiza), scutellum, VB and the seed coat, as noted previously in literature.¹⁴ In barley grains, the embryo contains high levels of Mn, Zn, and Cu, while Fe and Mg concentrations were highest in the aleurone-containing fractions.⁶⁴ In Figure 96e and Figure 97e, elevated levels of Mn in the crease pericarp surrounding the VB can be observed. Similar observations were made by Neal *et al.* (2013) in mature wheat grains and by Lombi *et al.* (2011) in barley grains.^{58,64} Manganese-activated enzymes play a role in the nitrogen metabolism, gibberellic acid biosynthesis, RNA polymerase activation, and fatty acid biosynthesis.⁶²

6.5.1.5 Zinc

Zn, a fairly mobile nutrient, is predominantly present in the embryo, intermediary layer at the scutellum-endosperm interface, with lower levels in the inner pericarp, aleurone layer, scutellum and trace levels in the endosperm.⁶⁵ The general pattern of TM sinks is similar in both grains, though significant differences exist as to the relative concentrations in these sinks between the genotypes. Wang *et al.* (2011) identified a transport barrier between the rachis and grains of *T. aestivum* by evaluating the bulk concentration at different development stages.⁶⁶ The presence of Zn in the aleurone layer is expected; EXAFS has shown Zn (and Fe) to be complexed with phytates and coordinated tetrahedrally by four O atoms and approximately 1.5 P atoms.⁵⁸ Zn-phytate complexes are stored in globoid crystals, which are protein storage vacuoles located in the aleurone layer and scutellum.^{67,68} Furthermore, Zn is omnipresent in large numbers of Zn-finger containing proteins and transcription factors, oxidoreductases, β -carbonic anhydrase, and hydrolytic enzymes, such as metalloproteases.^{69,70} Persson *et al.* (2009) suggested that the speciation of Zn in seeds correlates with the presence of proteins with the S-containing amino acids methionine and cysteine, whilst Fe (and P) are mainly associated with phytic acid.⁵⁹ Pongrac *et al.* (2013) exposed *T. aestivum* to Zn-enriched soil during grain filling, and as a result, Ca, Fe and Zn bulk concentrations increased significantly, whilst Na, P, Mg, Mn, Cu, Cd, K, and Mo bulk concentrations decreased, supporting the hypothesis that Zn is competing to some extent with other metals (*e.g.*, Cd, Na) for phytic acid.¹⁶

6.5.1.6 Cross-elemental patterns for macro- and micronutrients

Given the accumulation of Mn, Cu, and Zn in the VB and NP regions, transport towards the filial tissue may be limited because of (i) the low sink capacity of the endosperm or (ii) the lack of sufficient transmembrane transporters. Sites of nutrient transfer, such as the crease VB and nucellar projection, can be distinguished. The gradient of Cu and Zn is similar, with accumulation towards the endosperm; the presence of some proteins, such as the Cu/Zn-SOD would explain this colocalization. The colocalization can also point towards shared transport pathways – Cu and Zn share transporters of the P1B-type ATPase family – and storage systems

(phytic acid), though the relative scutellum/embryo level ratio is significantly higher for Cu.⁷⁰ In the intermediary layer at the scutellum-endosperm interface, Zn is present at a higher level in *T. aestivum* compared to the level of Zn in this layer in *S. cereale*, which indicates that the transport and storage pathways of the genotypes are not identical in this zone. In *S. cereale*, accumulation of Mn, Cu, P in the aleurone layer is accompanied by low concentrations in the endosperm. In the bran layers, P, Cu, Zn, and Ni were located in the aleurone cells, whilst Mn and Pb were predominantly present in the seed coat. These elements appear to have a non-generic complexation mechanism, as the accumulation in the seed coat is exceptional. Gene expression of the micronutrient transporters, chelation agents, and storage structures, *e.g.*, the globoid crystals, are higher in the aleurone layer and embryo, resulting in accumulation of Fe and P into these sinks. Large concentration differences between the seed coat and epidermis suggest the presence of transport barriers, *e.g.*, the cuticular layer, between endosperm and epidermis.²²

6.5.2 Segmentation

Table 11 Abbreviation list for Regions-of-interest (ROIs)

Abbreviation	Definition of the ROI
P+PE	Testa (seed coat), pigment strand and pericarp (inner and outer)
SC	Scutellum
COL	Coleoptile
EN	Starchy endosperm
EM	Embryo
LP	Leaf primordia
IL	Intermediary layer at the scutellum-endosperm interface
AL	Aleurone layer
RP	Lateral root primordia
COZ	Coleorhizae

Figure 101 Pixel assignment to the ROIs for (a) *Secale cereale* L. and (b) *Triticum aestivum* L.

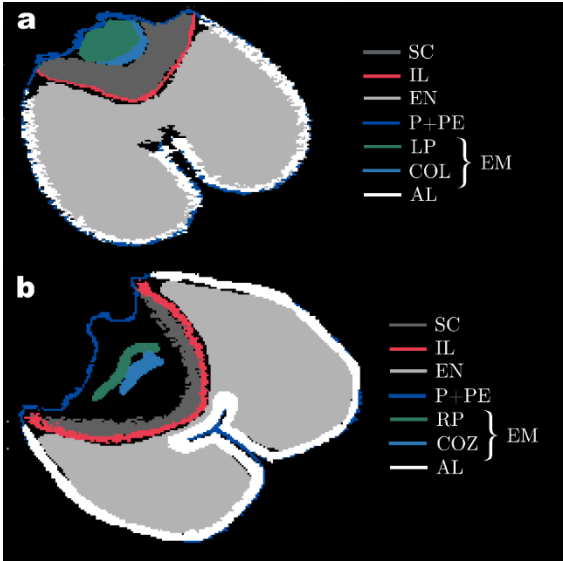


Figure 102 RGB composites of metals and metalloids in *S. cereale* at the level of the root primordia (slice 19). The scale bar is 500 μm in length.

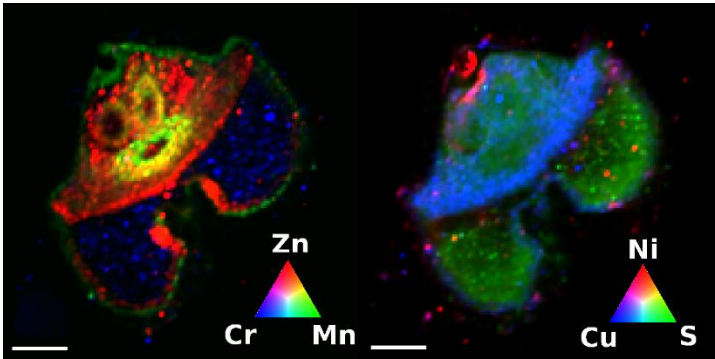


Table 12 Average concentration of heavy metals in $\mu g\ g^{-1}$ in Secale Cereale L. at slice 16, which contains the leaf primordia. The ROIs correspond with those indicated in Fig. S1. The precision is specified as 1 standard deviation (s). The list of abbreviations can be found in Table S-1.

Element	Cr	s	Mn	s	Ni	S	Cu	s	Zn	s	As	s	Cd	s	Pb	s	# Pixels
P+PE	2.1E-01	2.2E-03	4.7E+02	1.0E+01	1.4E+00	1.0E-01	2.3E+01	4.7E-01	7.5E+02	2.3E+01	2.7E-01	1.7E-02	5.4E-01	6.6E-02	6.3E-01	1.5E-02	1013
SC	2.3E-01	1.3E-03	1.2E+03	1.9E+01	1.1E+00	2.3E-02	5.5E+01	7.1E-01	1.9E+03	1.2E+02	3.2E-01	2.8E-02	1.1E+00	1.9E-01	3.1E-01	1.2E-02	1532
COL	5.2E-01	2.3E-01	2.1E+02	1.2E+01	1.3E+00	4.1E-02	2.0E+01	7.3E-01	1.7E+03	1.0E+02	3.3E-01	3.8E-02	5.6E-01	1.6E-01	2.1E-01	2.6E-02	157
EN	4.9E-01	1.7E-02	6.1E+01	3.0E+00	1.5E+00	8.0E-02	8.9E+00	1.2E-01	3.0E+02	7.1E+00	7.6E-01	2.9E-02	9.6E-01	3.6E-02	4.6E-01	1.3E-02	10250
EM	2.3E-01	1.5E-03	1.4E+03	4.6E+01	1.9E+00	3.9E-01	3.2E+01	5.3E-01	2.1E+03	6.1E+01	3.5E-01	5.2E-02	5.8E-01	5.6E-02	3.4E-01	1.2E-02	598
LP	2.3E-01	1.6E-03	1.4E+03	4.4E+01	1.3E+00	5.9E-02	3.3E+01	5.4E-01	2.1E+03	6.2E+01	3.7E-01	5.4E-02	6.7E-01	7.7E-02	3.4E-01	1.1E-02	587
IL	2.2E-01	3.7E-03	9.8E+01	6.2E+00	1.0E+00	1.5E-01	1.6E+01	5.9E-01	1.3E+03	7.0E+01	4.2E-01	6.0E-02	5.1E-01	9.4E-02	3.4E-01	5.1E-02	220
AL	2.4E-01	2.7E-03	2.3E+02	5.8E+00	1.5E+00	8.9E-02	2.4E+01	3.4E-01	1.2E+03	2.2E+01	3.5E-01	3.1E-02	5.5E-01	3.7E-02	4.5E-01	1.6E-02	1479

Table 13 Average concentration of heavy metals in Triticum aestivum L. in $\mu g\ g^{-1}$ at slice 19, which contains the root primordia. The ROIs correspond with those indicated in Fig. S1. The precision is specified as 1 standard deviation (s). The list of abbreviations can be found in Table S-1.

Element	Cr	s	Mn	s	Ni	s	Cu	s	Zn	s	As	s	Cd	s	Pb	s	# Pixels in ROI
P+PE	1.8E-01	2.7E-03	4.4E+02	1.3E+01	2.9E+00	7.5E-02	1.2E+01	2.1E-01	2.6E+02	8.3E+00	1.9E-01	3.2E-02	9.0E-01	6.0E-02	5.7E-01	2.0E-02	958
SC	2.3E-01	1.0E-03	1.1E+03	1.8E+01	2.6E+00	5.5E-02	2.6E+01	2.4E-01	6.6E+02	1.0E+01	9.3E-02	3.4E-03	1.2E+00	1.2E-01	3.2E-01	1.9E-02	1094
RP	2.2E-01	1.2E-03	1.1E+03	2.8E+01	2.7E+00	3.8E-02	1.1E+01	1.8E-01	1.1E+03	4.3E+01	5.8E-02	2.4E-03	1.1E+00	2.4E-02	2.1E-01	7.8E-03	253
COZ	2.3E-01	1.4E-03	2.4E+02	2.2E+01	2.9E+00	1.4E-01	1.2E+01	2.3E-01	2.5E+03	1.3E+02	4.8E-02	2.5E-03	1.2E+00	2.5E-02	2.2E-01	7.5E-03	198
IL	2.0E-01	1.3E-03	5.0E+02	2.3E+01	2.1E+00	3.3E-02	1.7E+01	3.0E-01	1.3E+03	2.4E+01	9.1E-02	9.2E-03	9.4E-01	1.8E-02	2.4E-01	6.5E-03	603
EM	2.2E-01	8.9E-04	7.3E+02	2.1E+01	2.6E+00	3.1E-02	1.1E+01	1.1E-01	1.4E+03	3.0E+01	6.7E-02	1.6E-03	1.1E+00	1.8E-02	2.4E-01	9.5E-03	1415
EN	3.2E-01	1.0E-02	2.3E+01	9.5E-01	2.1E+00	5.6E-02	5.1E+00	7.5E-02	1.4E+02	4.1E+00	3.1E-01	1.6E-02	8.1E-01	4.0E-02	3.4E-01	1.0E-02	8989
AL	2.0E-01	1.5E-03	2.5E+02	5.7E+00	3.3E+00	5.0E-02	1.5E+01	1.5E-01	4.5E+02	2.1E+01	1.8E-01	1.5E-02	1.2E+00	5.7E-02	5.8E-01	1.9E-02	2310

6.6 Bibliography

- (1) Burger, M.; Gundlach-Graham, A.; Allner, S.; Schwarz, G.; Wang, H. A.; Gyr, L.; Burgener, S.; Hattendorf, B.; Grolimund, D.; Gunther, D. *Anal Chem* **2015**, *87*, 8259-8267.
- (2) Van Malderen, S. J. M.; van Elteren, J. T.; Vanhaecke, F. *Anal Chem* **2015**, *87*, 6125-6132.
- (3) Hare, D. J.; George, J. L.; Grimm, R.; Wilkins, S.; Adlard, P. A.; Cherny, R. A.; Bush, A. I.; Finkelstein, D. I.; Doble, P. *Metallomics* **2010**, *2*, 745-753.
- (4) Paul, B.; Hare, D. J.; Bishop, D. P.; Paton, C.; Nguyen, V. T.; Cole, N.; Niedwiecki, M. M.; Andreozzi, E.; Vais, A.; Billings, J. L.; Bray, L.; Bush, A. I.; McColl, G.; Roberts, B. R.; Adlard, P. A.; Finkelstein, D. I.; Hellstrom, J.; Hergt, J. M.; Woodhead, J. D.; Doble, P. A. *Chem. Sci.* **2015**, *6*, 5383-5393.
- (5) Hare, D. J.; Lee, J. K.; Beavis, A. D.; van Gramberg, A.; George, J.; Adlard, P. A.; Finkelstein, D. I.; Doble, P. A. *Anal Chem* **2012**, *84*, 3990-3997.
- (6) Kuznetsov, I.; Filevich, J.; Dong, F.; Woolston, M.; Chao, W.; Anderson, E. H.; Bernstein, E. R.; Crick, D. C.; Rocca, J. J.; Menoni, C. S. *Nature communications* **2015**, *6*, 6944.
- (7) Palmer, A. D.; Alexandrov, T. *Anal Chem* **2015**, *87*, 4055-4062.
- (8) Gimenez, Y.; Busser, B.; Trichard, F.; Kulesza, A.; Laurent, J. M.; Zaun, V.; Lux, F.; Benoit, J. M.; Panczer, G.; Dugourd, P.; Tillement, O.; Pelascini, F.; Sancey, L.; Motto-Ros, V. *Sci Rep* **2016**, *6*, 29936.
- (9) He, M.; Meng, Y.; Yan, S.; Hang, W.; Zhou, W.; Huang, B. *Anal Chem* **2016**.
- (10) Coleman, J. E. *Current opinion in Chemical Biology* **1998**, *2*, 222-234.
- (11) Banfalvi, G. *Cellular Effects of Heavy Metals*; Springer Netherlands, 2011.
- (12) Huang, M.; Zhou, S.; Sun, B.; Zhao, Q. *Science of the Total Environment* **2008**, *405*, 54-61.
- (13) White, P. J.; Broadley, M. R. *New Phytologist* **2009**, *182*, 49-84.
- (14) Mazzolini, A. P.; Pallaghy, C. K.; Legge, G. J. F. *New Phytologist* **1985**, *100*, 483-509.
- (15) Singh, S. P.; Vogel-Mikus, K.; Arcon, I.; Vavpetic, P.; Jeromel, L.; Pelicon, P.; Kumar, J.; Tuli, R. *Journal of Experimental Botany* **2013**, *64*, 3249-3260.
- (16) Pongrac, P.; Kreft, I.; Vogel-Mikus, K.; Regvar, M.; Germ, M.; Vavpetic, P.; Grlj, N.; Jeromel, L.; Eichert, D.; Budic, B.; Pelicon, P. *Journal of the Royal Society Interface* **2013**, *10*, 296-304.
- (17) Moore, K. L.; Schroder, M.; Lombi, E.; Zhao, F. J.; McGrath, S. P.; Hawkesford, M. J.; Shewry, P. R.; Grovenor, C. R. *New Phytologist* **2010**, *185*, 434-445.
- (18) Moore, K. L.; Zhao, F.-J.; Gritsch, C. S.; Tosi, P.; Hawkesford, M. J.; McGrath, S. P.; Shewry, P. R.; Grovenor, C. R. M. *Journal of Cereal Science* **2012**, *55*, 183-187.
- (19) Wu, B.; Andersch, F.; Weschke, W.; Weber, H.; Becker, J. S. *Metallomics* **2013**, *5*, 1276-1284.
- (20) Hell, R.; Stephan, U. W. *Planta* **2003**, *216*, 541-551.
- (21) Tanaka, K.; Fujimaki, S.; Fujiwara, T.; Yoneyama, T.; Hayashi, H. *Soil Science and Plant Nutrition* **2007**, *53*, 72-77.

- (22) Patrick, J. W.; Offler, C. E. *Journal of Experimental Botany* **2001**, *52*, 551-564.
- (23) Wang, H. L.; Offler, C. E.; Patrick, J. W. *Protoplasma* **1994**, *182*, 39-52.
- (24) Pearson, J. N.; Rengel, Z.; Jenner, C. F.; Graham, R. D. *Physiologia Plantarum* **1995**, *95*, 449-455.
- (25) Lombi, E.; Scheckel, K. G.; Pallon, J.; Carey, A. M.; Zhu, Y. G.; Meharg, A. A. *New Phytologist* **2009**, *184*, 193-201.
- (26) Basnet, P.; Amarasiriwardena, D.; Wu, F.; Fu, Z.; Zhang, T. *Environmental Pollution* **2014**, *195*, 148-156.
- (27) Zhao, F. J.; Moore, K. L.; Lombi, E.; Zhu, Y. G. *Trends Plant Sci* **2014**, *19*, 183-192.
- (28) Pozebon, D.; Scheffler, G. L.; Dressler, V. L.; Nunes, M. A. G. *J Anal Atom Spectrom* **2014**, *29*, 2204-2228.
- (29) Wu, B.; Becker, J. S. *Metallomics* **2012**, *4*, 403-416.
- (30) Zhu, Y.; Hioki, A.; Itoh, A.; Umemura, T.; Haraguchi, H.; Chiba, K. *Analytical Sciences* **2012**, *28*, 1121-1124.
- (31) Van Malderen, S. J. M.; Managh, A. J.; Sharp, B. L.; Vanhaecke, F. *J. Anal. At. Spectrom.* **2016**, *31*, 423-439.
- (32) van Elteren, J. T.; Izmer, A.; Šala, M.; Orsega, E. F.; Šelih, V. S.; Panighello, S.; Vanhaecke, F. *J Anal Atom Spectrom* **2013**, *28*, 994-1004.
- (33) Peng, S.; Hu, Q. H.; Ewing, R. P.; Liu, C. X.; Zachara, J. M. *Environmental Science & Technology* **2012**, *46*, 2025-2032.
- (34) Chirinos, J. R.; Oropeza, D. D.; Gonzalez, J. J.; Hou, H.; Morey, M.; Zorba, V.; Russo, R. E. *J Anal Atom Spectrom* **2014**, *29*, 1292-1298.
- (35) Koelmel, J.; Leland, T.; Wang, H.; Amarasiriwardena, D.; Xing, B. *Environmental Pollution* **2013**, *174*, 222-228.
- (36) Teledyne CETAC Technologies Inc. Aerosol Rapid Introduction System [15/07/2016]. Available from: <http://www.teledynecetac.com/product/laser-ablation/aris>.
- (37) Evangelidis, G. D.; Psarakis, E. Z. *Ieee T Pattern Anal* **2008**, *30*, 1858-1865.
- (38) Vekemans, B.; Janssens, K.; Vincze, L.; Adams, F.; Van Espen, P. *X-Ray Spectrom* **1994**, *23*, 278-285.
- (39) Vekemans, B.; Janssens, K.; Vincze, L.; Adams, F.; Van Espen, P. *Spectrochimica Acta Part B: Atomic Spectroscopy* **1995**, *50*, 149-169.
- (40) Gundlach-Graham, A.; Gunther, D. *Analytical and bioanalytical chemistry* **2016**, *408*, 2687-2695.
- (41) Gallego, S. M.; Pena, L. B.; Barcia, R. A.; Azpilicueta, C. E.; Iannone, M. F.; Rosales, E. P.; Zawoznik, M. S.; Groppa, M. D.; Benavides, M. P. *Environmental and Experimental Botany* **2012**, *83*, 33-46.
- (42) Chen, F.; Wu, F.; Dong, J.; Vincze, E.; Zhang, G.; Wang, F.; Huang, Y.; Wei, K. *Planta* **2007**, *227*, 223-232.
- (43) Gerendas, J.; Sattelmacher, B. *Plant and Soil* **1997**, *190*, 153-162.
- (44) Sirko, A.; Brodzik, R. *Acta Biochim Pol* **2000**, *47*, 1189-1195.

- (45) Seregin, I. V.; Kozhevnikova, A. D. *Russian Journal of Plant Physiology* **2006**, 53, 257-277.
- (46) Pandolfini, T.; Gabbrielli, R.; Comparini, C. *Plant, Cell & Environment* **1992**, 15, 719-725.
- (47) Follmer, C. *Phytochemistry* **2008**, 69, 18-28.
- (48) Meharg, A. A.; Lombi, E.; Williams, P. N.; Scheckel, K. G.; Feldmann, J.; Raab, A.; Zhu, Y.; Islam, R. *Environmental Science and Technology* **2008**, 42, 1051-1057.
- (49) Carey, A. M.; Norton, G. J.; Deacon, C.; Scheckel, K. G.; Lombi, E.; Punshon, T.; Guerinot, M. L.; Lanzirotti, A.; Newville, M.; Choi, Y.; Price, A. H.; Meharg, A. A. *New Phytologist* **2011**, 192, 87-98.
- (50) Raab, A.; Schat, H.; Meharg, A. A.; Feldmann, J. *New Phytologist* **2005**, 168, 551-558.
- (51) Raab, A.; Feldmann, J.; Meharg, A. A. *Plant Physiol* **2004**, 134, 1113-1122.
- (52) Tschan, M.; Robinson, B. H.; Schulin, R. *Environmental Chemistry* **2009**, 6, 106-115.
- (53) Clemens, S. *Biochimie* **2006**, 88, 1707-1719.
- (54) Wilson, S. C.; Lockwood, P. V.; Ashley, P. M.; Tighe, M. *Environmental Pollution* **2010**, 158, 1169-1181.
- (55) Luo, Y.; Rimmer, D. L. *Environmental Pollution* **1995**, 88, 79-83.
- (56) Singh, H. P.; Mahajan, P.; Kaur, S.; Batish, D. R.; Kohli, R. K. *Environmental Chemistry Letters* **2013**, 11, 229-254.
- (57) Pradas-del-Real, A. E.; García-Gonzalo, P.; Alarcón, R.; González-Rodríguez, A.; Lobo, M. C.; Pérez-Sanz, A. *Spanish Journal of Agricultural Research* **2013**, 11, 685-694.
- (58) Neal, A. L.; Geraki, K.; Borg, S.; Quinn, P.; Mosselmans, J. F.; Brinch-Pedersen, H.; Shewry, P. R. *Journal of Biological Inorganic Chemistry* **2013**, 18, 557-570.
- (59) Persson, D. P.; Hansen, T. H.; Laursen, K. H.; Schjoerring, J. K.; Husted, S. *Metallomics* **2009**, 1, 418-426.
- (60) Ozturk, L.; Yazici, M. A.; Yucel, C.; Torun, A.; Cekic, C.; Bagci, A.; Ozkan, H.; Braun, H.-J.; Sayers, Z.; Cakmak, I. *Physiologia Plantarum* **2006**, 128, 144-152.
- (61) Ravilious, G. E.; Jez, J. M. *Natural Product Reports* **2012**, 29, 1138-1152.
- (62) Hansch, R.; Mendel, R. R. *Current Opinion in Plant Biology* **2009**, 12, 259-266.
- (63) Pilon, M.; Abdel-Ghany, S. E.; Cohu, C. M.; Gogolin, K. A.; Ye, H. *Current Opinion in Plant Biology* **2006**, 9, 256-263.
- (64) Lombi, E.; Smith, E.; Hansen, T. H.; Paterson, D.; de Jonge, M. D.; Howard, D. L.; Persson, D. P.; Husted, S.; Ryan, C.; Schjoerring, J. K. *Journal of Experimental Botany* **2011**, 62, 273-282.
- (65) Stomph, T. J.; Choi, E. Y.; Stangoulis, J. C. *Annals of Botany* **2011**, 107, 927-937.
- (66) Wang, Y. X.; Specht, A.; Horst, W. J. *New Phytologist* **2011**, 189, 428-437.
- (67) Bohn, L.; Meyer, A. S.; Rasmussen, S. K. *Journal of Zhejiang University Science B* **2008**, 9, 165-191.
- (68) Palmgren, M. G.; Clemens, S.; Williams, L. E.; Kramer, U.; Borg, S.; Schjoerring, J. K.; Sanders, D. *Trends in Plant Science* **2008**, 13, 464-473.

(69) Krämer, U.; Clemens, S. In *Molecular Biology of Metal Homeostasis and Detoxification: From Microbes to Man*, Tamas, M. J.; Martinoia, E., Eds.; Springer Berlin Heidelberg: Berlin, Heidelberg, 2006, pp 215-271.

(70) Yruela, I. *Metallomics* **2013**, 5, 1090-1109.

Chapter 7 Multimodal registration

This chapter is based on a manuscript, 'Three-dimensional reconstruction of the tissue-specific multi-elemental distribution within Ceriodaphnia dubia via multimodal registration using laser ablation ICP-mass spectrometry and X-ray spectroscopic techniques', authored by Stijn J. M. Van Malderen, Björn de Samber, Brecht Laforce, Thibaut Van Acker, Charlotte Nys, Maarten De Rijcke, Riet de Rycke, Michiel De Bruyne, Karel De Schamphelaere, Olga Borovinskaya, Laszlo Vincze, and Frank Vanhaecke. S.V.M. was the first and principal author of this work.

Multimodal registration is a process in which spatial positions of pixels or voxels of different sets of image data from multiple modalities are transformed in one coordinate system based on the relative position of similar features or intensity distributions in the images.

7.1 Introduction

Multimodal (co-)registration approaches have, for example, been utilized in neuroimaging via imaging mass spectrometry (IMS) for the automated alignment of the molecular ion images relative to i) anatomic brain atlases, e.g., the Allen Brain Atlas, or ii) relative to histochemical microscopy information.¹⁻⁵ The registration of multiple modalities allows one to generate a multi-channel image in which correlations between modalities can be clearly demonstrated.⁶ In serial 3D IMS, 3D molecular ion distributions are reconstructed from serially imaged sections. In the reconstruction, molecular ion images of adjacent sections are stacked and aligned through registration to reflect the true 3D morphology in the sample. A similar approach has been proposed for laser ablation-inductively coupled plasma-mass spectrometry (LA-ICPMS), an elemental probe characterized by limits of detection at the sub- $\mu\text{g g}^{-1}$ level, a lateral resolution down to 1 μm and relatively simple mass spectra that permit one to immediately

draw qualitative and even semi-quantitative conclusions.^{7,8} Multimodal registration can also be applied in serial 3D IMS; the registration of matrix-assisted laser desorption/ionization (MALDI) IMS images to positron emission tomography (PET), computed tomography (CT), single-photon emission CT (SPECT) or (functional) magnetic resonance imaging (MRI) images has been proposed for 3D medical imaging.^{6,9-11} These macroscale multimodal registration approaches, which often operate based on edge-detection algorithms, have however not yet been demonstrated to work for elemental imaging of objects $< 1 \text{ mm}^3$ in volume. Non-destructive high-resolution 3D imaging techniques such as CT and MRI are typically used to describe the internal morphology of a sample, as light microscopy techniques encounter difficulties in providing an accurate description of internal structures of the sample even when its outer surface is transparent due to the presence of distortions and non-described features outside of the field of vision. High-performance laser ablation-inductively coupled plasma-time-of-flight mass spectrometry (LA-ICP-TOF-MS) setups offer high sample throughput and lateral resolutions in the order of a few μm .^{12,13} In this work, we describe and demonstrate a multimodal registration methodology to obtain the 3D elemental distribution of a small crustacean *Ceriodaphnia dubia* *via* alignment of a set of 2D element distribution images using a 3D micro-absorption CT dataset. This methodology, relying on serial sectioning, can be applied to other (molecular and elemental) 3D imaging methods. Typically, quantification in LA-ICPMS *via* external calibration is based on the signal of a single nuclide in the spectrum. Within the mass spectra provided by the LA-ICP-TOF-MS set-up, however, a signal for each isotope of an element is available. As there is a small variance in the natural isotopic composition of the elements, the signals of these isotopes can be considered as redundant information. In this work, multiple calibrated mass channels within the LA-ICP-TOF-MS mass spectrum, belonging to the isotopes of a single element, were integrated to produce more robust elemental imaging data. Segmentation of the 3D LA-ICPMS dataset was demonstrated as, in contrast to MALDI-IMS where segmentation has been established in the form of atlas-based correlation-based querying, few examples are available for LA-ICPMS.^{14,15}

C. dubia was chosen as a study object in the context of this study for the following reasons: (i) the organism's overall size allows the entire organism to be imaged within a reasonable time span of approx. 24 h for the highest lateral resolutions available on state-of-the-art instrumentation, (ii) *C. dubia* is a well-documented water flea genus which is frequently deployed to evaluate acute and chronic effects of metal exposure, which makes its 3D metal distributions of high interest to the field of aquatic toxicology, (iii) there are several highly intricate anatomical features in this organism, making it ideal for verifying the limits of multimodal imaging, (iv) the a priori estimated concentrations of elements of interest in *C. dubia* are at the $\mu\text{g g}^{-1}$ level, near the limits of detection and of quantification of the elemental probes utilized in this work, (v) *C. dubia* is easily cultured, due to its short reproductive cycle based on parthenogenesis, and (vi) the organism is small in size and is mainly composed of lighter elements, allowing even relatively low-energy X-ray fluorescence lines to escape. The position of *C. dubia* in the food chain forms a link between primary producers (planktonic flagellates, protococcal algae, and diatoms) and higher order vertebrates. Metal and metalloids assimilate through the ion regulatory channels of both the gill tissue (respiratory uptake) and the

alimentary channel (dietary uptake). Biotic ligand models have been developed for many metals, and the primary metal uptake routes, transport mechanisms, and assimilation efficiencies have been studied as a function of environmental conditions for individual metals in related species such as *Daphnia magna*.¹⁶⁻¹⁸ However, the effect of interactions between, e.g., Cu, Ni and Zn on the overall uptake efficiency, chronic toxicity, and tissue-specific distribution are still under active investigation; a chronic metal mixture bioavailability model has been proposed.¹⁹

7.2 Experimental section part 1 / Materials and Methods

7.2.1 Sample preparation

A monoclonal stock culture of 25 specimens of juvenile *Ceriodaphnia dubia* (*C. dubia*), 72 h old, was provided by the Environmental Toxicology Unit, Ghent University, Belgium (Supporting information). Juveniles (<24 h old) were exposed to a mixture containing 9.4 $\mu\text{g L}^{-1}$ of dissolved Cu, 3.9 $\mu\text{g L}^{-1}$ of dissolved Ni and 25.2 $\mu\text{g L}^{-1}$ of dissolved Zn (realistic values for European stream water, as recorded in the FOREGS repository).²⁰ Each specimen was isolated and transferred into a separate well of a well plate using a Pasteur pipette (Figure 103, step A). Each specimen underwent a 1 h primary fixation using a formaldehyde (4%, EM-grade) and glutaraldehyde (2.5%, EM-grade) fixative solution in 0.1 M Na cacodylate buffer in a vacuum chamber and was subsequently left rotating for 3 h at room temperature. This fixative solution was renewed and the specimens were left rotating overnight at 4 °C. After washing, the sample was dehydrated through a graded ethanol series towards 100% dried ethanol, including a bulk staining with 1% uranyl acetate ($\text{UO}_2(\text{CH}_3\text{COO})_2 \cdot 2\text{H}_2\text{O}$) at the 50% ethanol step followed by embedding in Spurr's resin (Figure 103, step B). For $\mu\text{-CT}$ analysis (Figure 103, step C), the resin block was trimmed to a cuboid shape with a cross-section of approx. $600 \times 800 \mu\text{m}^2$, outlining the sample exterior. The excess of resin was removed in order to minimize X-ray scatter, resulting in an improved signal-to-noise ratio for the reconstructed $\mu\text{-CT}$ image. For LA-ICPMS analysis (Figure 103, step D), the resin containing the specimen was sectioned dorsoventrally to 120 adjacent sections of 5 μm thickness each, using a Leica™ ultramicrotome (Wetzlar, Germany). Each section was picked up in a water droplet, deposited on a Starfrost® microscope slide and numbered, resulting in a total amount of 118 sections. For maintaining a reasonable total measuring time, only every odd numbered section was submitted to LA-ICPMS analysis, resulting in 59 2D LA-ICPMS datasets in total. For measuring *C. dubia* *via* SR-based 3D confocal $\mu\text{-XRF}$ and laboratory $\mu\text{-CT}$, an HMDS drying procedure for SEM imaging on daphnids as described by Laforsch et al. was adapted and used (Supporting information).²¹⁻²³

7.2.2 LA-ICP-MS

LA-ICP-TOF-MS is characterized by limits of detection at the sub- $\mu\text{g g}^{-1}$ level, a lateral resolution down to 1-10 μm and relatively simple mass spectra. The LA-ICPMS setup comprises an Analyte G2 Excimer 193 nm ArF* excimer laser ablation system Teledyne Photon Machines (Bozeman, MT, USA) coupled to an icpTOF (TOFWERK AG, Thun, Switzerland) TOF-based ICPMS instrument with a mass resolution of 4,000 and sampling rate of 33 kHz. Sequences of 10 mass spectra were extracted for each individual laser shot. The rastering parameters are chosen such that overlap of the laser craters is negligible, resulting in 'square pixels'. LA craters

were characterized using non-contact atomic force microscopy and scanning electron microscopy (BSE). Although the voxel size is $5 \times 5 \times 5 \mu\text{m}^3$, the slices have interspaces of $5 \mu\text{m}$, as a result of skipping the even-numbered sections. The biological material was removed quantitatively using a single shot. The LA system's HelEx II two-volume ablation cell is equipped with the ARIS²⁴, a low-dispersion mixing bulb developed at Ghent University and commercialized by Teledyne Photon Machines (Bozeman, MT, USA), which improves the overall throughput and sensitivity of the LA system. This low-dispersion LA-ICP-TOF-MS setup for single-shot quantitative imaging provides performance characteristics well beyond those currently available in conventional LA-ICPMS imaging setups. The low-dispersion aerosol transport in the ARIS component eliminates the effects of pulse-to-pulse mixing at laser-pulse repetition rates up to 20 Hz for biological material and up to 50 Hz for glass and glass-like materials. Recently, the benefits of low-dispersion LA-ICP-TOF-MS were demonstrated for imaging geological samples in a study by Burger and Gundlach-Graham et al.^{25,26}

The LA (Table 14) and ICPMS settings (Supporting information) were optimized at the start of each experiment (after 2 h of warm-up) while ablating NIST SRM 612 (Trace elements in glass, National Institute of Standards and Technology, Gaithersburg, MD, USA) to achieve high sensitivities for $^{24}\text{Mg}^+$, $^{89}\text{Y}^+$, $^{115}\text{In}^+$, $^{238}\text{U}^+$ whilst maintaining low oxide levels ($^{238}\text{U}^{16}\text{O}^+ / ^{238}\text{U}^+ < 1.5\%$), low elemental fractionation ($^{238}\text{U}^+ / ^{232}\text{Th}^+ \approx 1$), and low background levels (evaluated via the signal intensities for $^{16}\text{O}_2^+$, $^{15}\text{N}^{16}\text{O}^+$).

Table 14 LA settings

Teledyne Photon Machines (Bozeman, MT, USA) Analyte G2 laser ablation system with ARIS		
Imaging mode	3D	High-resolution
Energy density [J cm^{-2}]	3.5	4
Repetition rate [Hz]	20	20
Scan mode	Fixed dosage scanning	
Image XY dimensions [$\mu\text{m} \times \mu\text{m}$]	600 \times 600	
Scan speed [$\mu\text{m s}^{-1}$]	100	40
Number of shots per position	1	1
Beam waist diameter [μm]	5	2
Mask shape	⊠	⊗
He carrier gas flow rate [L min^{-1}]	0.450	

7.2.3 High-resolution X-Ray Computed Tomography

The μ -CT scanner at the ‘University Ghent Computed Tomography’ center (UGCT, Ghent University, Belgium) is equipped with an open-type microfocus X-ray tube with a high-resolution transmission target. Voltages can be set between 20 and 100 kV, the filament current can be set from 50 to 1000 μA with the restriction that the tube power should not exceed 80 W

(max. target power is 3 W). For our experiment, a voxel size of about $1\text{ }\mu\text{m}^3$ could be achieved by optimizing the sample-source distance. A Photonic Science VHR CCD sensor (Photonic Science™, Millham, UK) equipped with a GdOS:Tb scintillator was used to detect the transmitted X-rays. The CCD detector contains 4008×2672 pixels of $9 \times 9\text{ }\mu\text{m}^2$ with a 20 MHz read-out. A total of 635 projections (0.57° steps) were recorded.

7.2.4 Synchrotron radiation based 3D confocal μ -XRF

The experiments were performed at the former beamline L of the DORISIII synchrotron at the Deutsches Elektronensynchrotron (DESY) in Hamburg, Germany. A W/Ni multilayer monochromator enabled high-intensity monochromatic excitation at 15 keV. A polycapillary optic (XOS, East Greenbush, NY, USA) with 15 μm focus size and 30% transmission at 17 keV, 4.8 mm working distance and a 3000-fold intensity gain was used to focus the monochromatic radiation. A second polycapillary optic at the detector side was aligned in a confocal geometry. A depth scan through a thin Au foil delivered an acceptance for the confocal volume of approximately 18 μm full-width-half-maximum (FWHM) at the Au-L α fluorescent line.

7.2.5 Safety considerations

Normal lab precautions (double heavy nitrile gloves, full face shield, lab coat, chemical splash apron, well-ventilated fume hood) should be taken in the formaldehyde/glutaraldehyde (toxic, carcinogenic, combustible), and ethanol (toxic, combustible) steps. Standard safety procedures for lasers, ionizing radiation, and compressed gasses apply.

7.3 Experimental section part 2 / Data processing

7.3.1 Data pre-processing and reconstruction of the LA-ICP-MS dataset

Data pre-processing and reconstruction of the 3D LA-ICP-TOF-MS dataset. The LA-ICP-TOF-MS data were processed using in-house developed software based on Python 3.4. The data pre-processing (Figure 103, step E) comprises the following steps: (i) drift correction of the mass peak position in the spectra over time in the mass calibration, (ii) reading the dimensions of the ablated zone from the laser log file, (iii) rescaling the data based on this information, (iv) performing a background (signal for the gas blank) correction for each individual image and each nuclide monitored, (v) sensitivity drift correction in each image, and (vi) writing the data into a predefined data volume (stack) in the correct order. The result of the pre-processing is a stack of multiplexed (i.e. multi-nuclide) 2D elemental images, which have a random orientation relative to each other (Figure 103). In the following step, the images in the stack are aligned through registration.

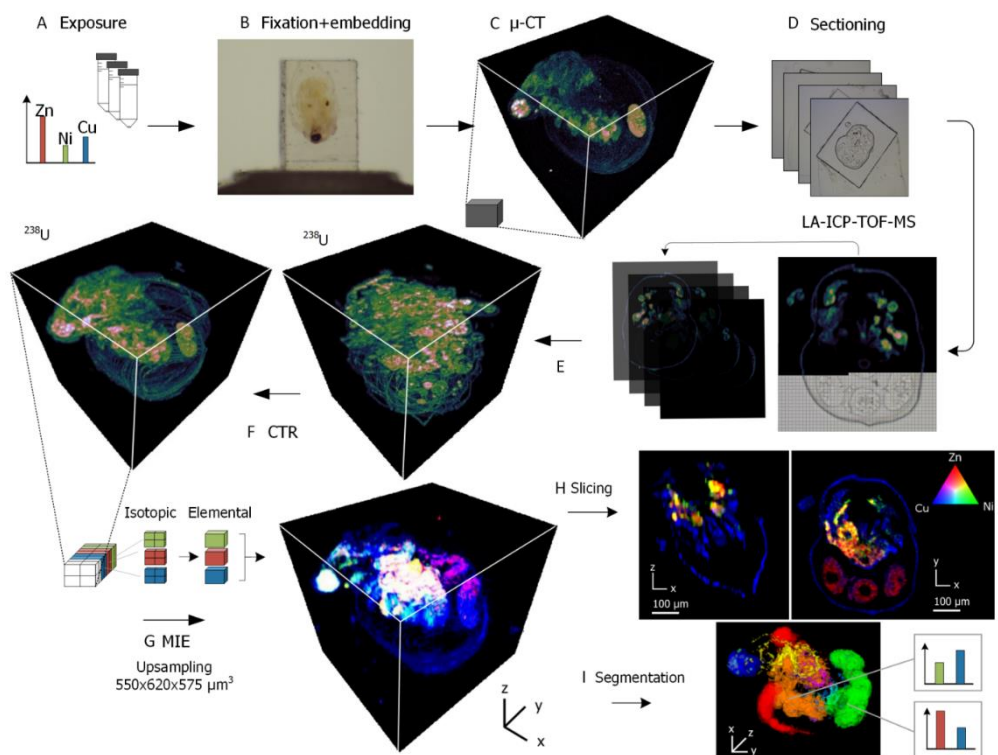


Figure 103 Schematic workflow of the experimental and data processing workflow. (A) Initial exposure of *C. dubia* to a mixture of Cu, Ni, and Zn, (B) fixation and embedding in resin, (C) μ -CT experiment, (D) sectioning, (E) LA-ICP-TOF-MS imaging and data preprocessing, (F) alignment of the 2D LA-ICP-TOF-MS dataset based on the μ -CT dataset, (G) multi-isotope extraction (MIE) for improving image quality, (H) sagittal and dorsoventral cross-sections in *C. dubia* and composite figures of the Zn, Cu and Ni elemental distribution, and (I) segmentation to obtain quantitative data on different tissues.

3D LA-ICPMS data registration approaches reported in literature are based on the sequential registration of neighboring slices (sequential slice registration – SSR), and operate under the assumption that shared features are present in neighboring slices and that the relative positions of these features can be extrapolated along the Z-axis. Two approaches for image reconstruction were compared in this study: i. SSR registration of each Z-slice relative to adjacent Z-slices and ii. CSR (correlative slice registration) registration of a Z-slice in the LA-ICPMS data volume relative to the corresponding slice in the CT data volume. The CSR approach requires (i) the modalities to be linked in the spatial domain through an affine transformation and (ii) the presence of shared distinguishable features across all modalities. A coordinate transformation is typically defined in terms of the 6 degrees of freedom (dof), i.e. the 3 translational and 3 rotational degrees of freedom which a mounted sample has, and a scaling parameter. By sectioning the sample on-axis with its rotational axis, 2 rotational degrees of freedom were eliminated. This alignment of the multi-modal data in the vertical-axis is crucial: it allows each

image slice of the LA-ICPMS to be correlated directly to a corresponding image slice in the CT volume. Furthermore, by cropping the CT data to the upper and lower bounds of the organism, the on-axis translational degree of freedom was eliminated. The coordinate transformation is hence limited to a one-dimensional rotation, and a two-dimensional translation, vastly reducing the alignment procedure and computation power required for multimodal registration. Since each rotational transformation is accompanied by a loss in image resolution; the number of transformations is preferably limited. In order to counteract this loss, the cropped 4D LA-ICPMS dataset of $282 \times 59 \times 124 \times 110$ data points underwent upsampling to $282 \times 59 \times 248 \times 220$ data points prior to registration, while the CT image was downsampled to $395 \times 248 \times 220$ data points such that the XY dimensions of the voxels match those in the LA-ICPMS dataset ($2.5 \times 2.5 \mu\text{m}^2$). It is not possible to accurately derive X-ray absorption - a pseudo-quantized local material density correlating with electron density - based on a partially known elemental distribution in the case of polychromatic CT, as insufficient information is available to characterize all photoionization and scattering effects. Multimodal registration based on a limited collection of endogenous elements within the tissue is hence very difficult due to the absence of a correlation between the distribution of these elements and the electron density. A uranyl acetate stain, which deeply penetrates the sample, was applied upon the *C. dubia* specimen (Materials and Methods section). The ^{238}U contained within the stain was detected with high accuracy and sensitivity in LA-ICPMS imaging as a result of the low background levels and absence of spectral interferences at the heavy end of the mass spectrum. Due to the large total absorption cross-section for U (expressed in $\text{cm}^2 \text{g}^{-1}$), the uranyl acetate stain also provided enhanced tissue contrast in the absorption μ -CT dataset. Tissue staining with a U-containing agent was therefore ideally suited to register the CT and LA-ICP-TOF-MS datasets *via* CSR, as the approach circumvents the difficulties associated with establishing a direct element-to-tissue correlation. The data were registered in SSR and CSR in two steps: (i) a rough registration based on feature extraction and discrete Fourier transformations, and (ii) fine registration, using an iterative closest point (ICP) algorithm, with sub-pixel precision.^{27,28}

7.3.2 Multi-isotope extraction (MIE) of mass spectra

An algorithm was developed to pool the information from multiple calibrated mass channels in the mass spectrum corresponding to the isotopes of a single element to produce elemental images with an improved signal-to-noise ratio. A total of 46 nuclides of 20 elements (Mg, Al, P, K, Ca, Cr, Mn, Fe, Ni, Cu, Zn, Ga, Sr, Ag, Cd, In, Ba, Tl, Pb, and U) were selected from the data based on known spectral interferences from isobaric, polyatomic and doubly charged ions or from the low abundance sensitivity (spectral overlap by peak tailing). The mass channels c_{m,k_E} around mass m in the mass range $[m_-; m_+]$ related to the response for isotope k_E of element E were integrated. The background signal b_{m,k_E} was subtracted and the response was calibrated by dividing the response by the sensitivity for the nuclide s_{k_E} . The sensitivity was determined through external calibration; four droplets of gelatin, spiked with a multi-element solution, were spotted on a cover glass slide and ablated quantitatively, permitting a drift-corrected multi-point calibration curve ($r^2 \geq 0.99$) to be constructed by interpolation (Supporting information). Due to the way a TOF analyzer acquires the signals, the isotopes of an element are sampled at different points in time. For count rates higher than a few counts per acquisition, the

uncertainty on the signal intensity can be estimated as the square root of the number of counts registered (following the ordinary Poisson distribution in the Poisson–Gauss approximation). Thus, the lower count rates in the mass channels corresponding to the isotopes of low abundance are influenced by Poisson process noise to a relatively higher extent.²⁹ For flickering sources like the ICP, doubly stochastic Poisson distributions apply and excess variance may have to be taken into account.^{29,30} The influence of frequency-independent white noise was reduced by compiling the calibrated responses of n selected isotopes of a specific element E into a single local elemental concentration V_E using a linear combination (LC). Within the LC a weight factor is introduced based on the natural abundance of an isotope a_{k_E} normalized to the cumulative natural abundances for all selected isotopes, and theoretical Poisson process noise:

$$V_E = \sum_1^n \left[\frac{a_{k_E} \sqrt{\sum_{m-}^{m+} c_{m,k_E}}}{\sum_1^n a_{k_E} \sqrt{\sum_{m-}^{m+} c_{m,k_E}}} \left(\sum_{m-}^{m+} [c_{m,k_E} - b_{m,k_E}] \right) / s_{k_E} \right] \quad \text{Equation 49}$$

Note that the cumulative natural abundance does not amount to 100% when not all isotope(s) of the element are selected. This calculation was performed in 2.8×10^6 voxels, for 20 elements, taking into account 46 nuclides. After MIE, the speckle/shot noise levels were suppressed further through a median filter with a window of $2 \times 2 \times 2$ voxels, which is an edge-preserving spatial denoising approach.

7.4 Results and discussion

7.4.1 MIE

Multiple sets of integrated mass channels, each representing an isotope of an element, were combined to reduce the noise levels. This can be seen as a form of competitive fusion, as it exploits data already available in the mass spectrum in a straightforward way. The standard deviation of the signal in the resin, representative of the background noise, relative to the average response within *C. dubia*, was compared for individual integrated mass channels (isotopes) and the extracted elemental data (Figure 104A-C). The signal-to-noise ratio has improved – albeit slightly – relative to most data available from individual mass channels (Figure 104D). The data are also more robust: if one isotope skews the result, the skew will be mediated by other isotopes. Information on individual nuclides is lost in the MIE process.

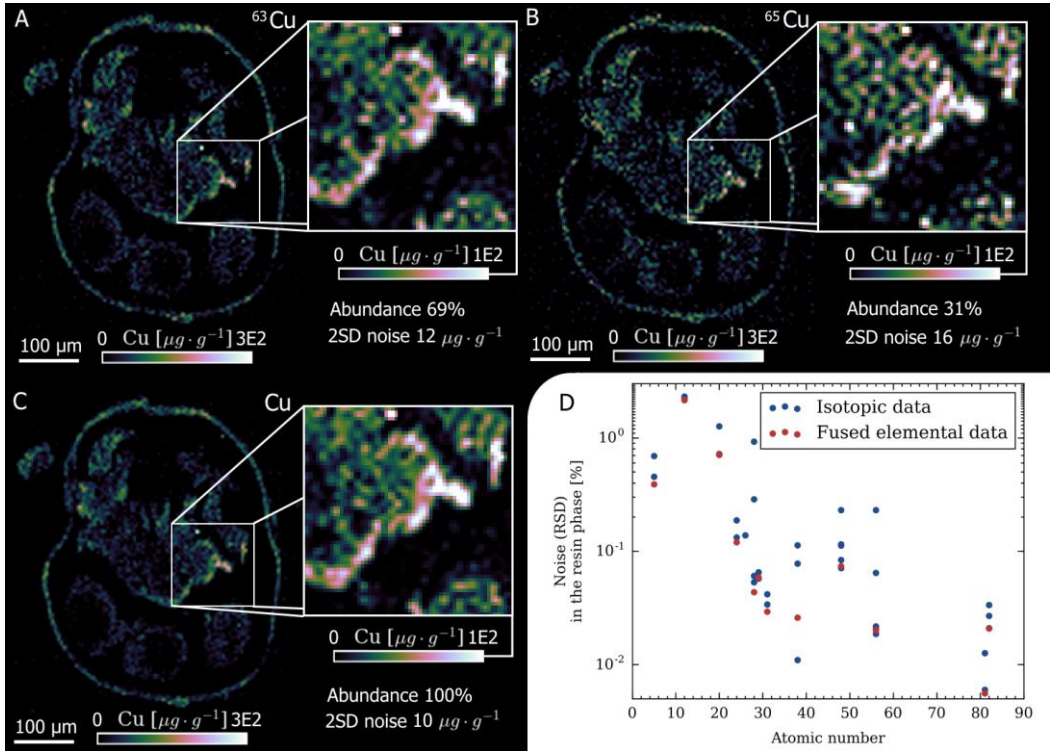


Figure 104 A-C) Fusion (MIE) of two integrated mass channels of the Cu isotopes, ^{63}Cu (A) and ^{65}Cu (B) in a single data slice (C) in the XY plane. D) Effect of the multi-isotope extraction on elemental data noise levels (for elements for which a calibration curve is available) in the resin phase.

7.4.2 SSR vs. CSR

CSR has shown two distinct advantages over SSR; (i) each slice is correlated to their matching slice in CSR (which provides a better correlation with the morphology), and (ii) CSR will correctly reflect the sample orientation, as can be seen in Figure 105. Fast changes in the morphology will impede registration between adjacent slices as not all small features, such as the apical spine of the chitinous carapace are present in both slices. When the plane in which the sample is sliced, is not perpendicular to a symmetry plane of the sample (e.g., in the axial direction), SSR will force features to be aligned along the vertical axis. The information about the curvature of the sample object along its boundary orthogonal to the cutting plane is lost in the cutting process.⁶ This known problem is exposed in this experiment: the central axis of the sample is located in a plane, tilted relative to the cutting plane. As a result, the SSR fails to mimic the orientation of the sample (Figure 105A). With multimodal registration *via* CSR, however, the orientation during CT imaging is mirrored, and a correct reconstruction is obtained, even without the use of artificial fiducial markers included within the embedding medium. Supersampling the image prior to CSR reduces the aliasing effect induced as a result of the

rotational transformation, though in any case, the number of transformations is preferably limited, as each transformation increases uncertainty.

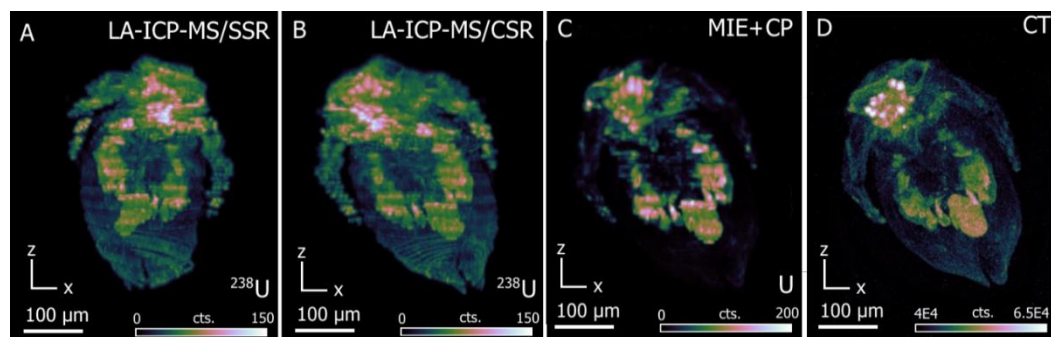


Figure 105 Comparison of the registration algorithms SSR and CSR and MIE/CP. (A) Frontal view of the ^{238}U 3D profile, with the volume registered using the SSR algorithm. (B) Frontal view of the ^{238}U 3D profile, with the volume registered using the CSR algorithm. (C) View of the data after MIE and cross-modality projection (Supporting information). (D) CT absorption image of the embedded sample, thresholded to visualize its features.

7.4.3 Combined synchrotron radiation based confocal μ -XRF and absorption μ -CT.

Using a dynamic scanning routine, SR-based confocal μ -XRF analysis provided 29 dorsoventral 2D elemental distributions with $30\text{ }\mu\text{m}$ distance in height within a chemically fixed and air-dried *C. dubia* without any need of sectioning. A single plane consisted of 35×34 pixels with $20\text{ }\mu\text{m}$ step size and a measuring time of 2 s per point, resulting in a total analysis time of approximately 24 h. The 34,510 XRF point spectra were fitted with the AXIL software and processed with the IDL programming-data visualization software (Harris corp., Florida, US). In order to generate elemental isosurfaces, thresholds were set in such a manner that optimal distinction could be made between the tissue and surrounding air (Figure 106). Mn could be clearly correlated to the region of hepatopancreas, gut, and eggs, whereas Fe and Zn were also clearly present within the osmoregulatory tissue. In comparing the data obtained *via* LA-ICPMS and SR-XRF we find the following similarities: presence of Mn in the digestive tract and Zn in the gill and eggs. Both techniques are also complementary in terms of sensitivity: Whereas the Ca-rich signature of the exoskeleton and the Mn distribution are clearly visible in confocal μ -XRF, these cannot be distinguished clearly from the background signal for Ca and Mn in LA-ICPMS. LA-TOF-ICPMS on the other hand shows higher sensitivity for heavier elements such as Pb (Supporting information). The absolute sensitivity for SR-XRF and LA-ICP-TOF-MS is on par within a mass range [50 amu -100 amu]. Animations of the 3D confocal micro-XRF elemental isosurfaces were produced. (Supporting information)

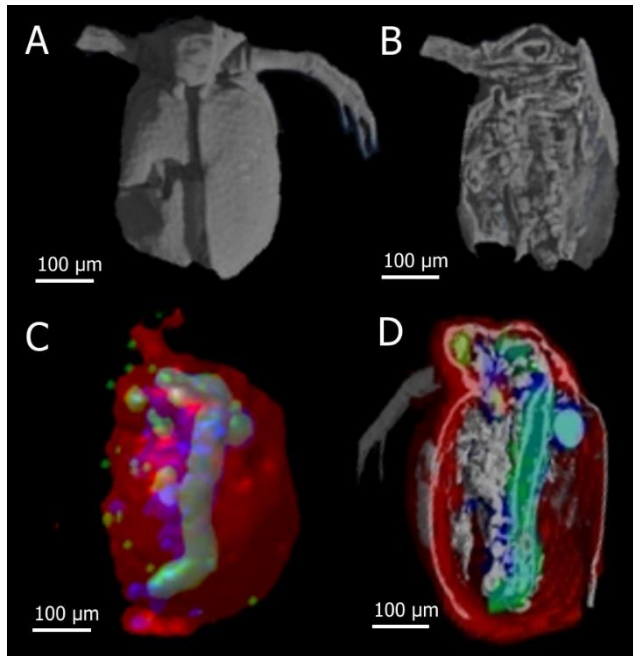


Figure 106 (A-B) μ -CT 3D renderings of *C. dubia* (C-D) RGB Ca/Mn/Zn isosurfaces with absorption μ -CT.

7.4.4 3D segmentation & quantification

In order to extract the element concentrations from each major anatomical structure, voxels associated with these structures were isolated and grouped in so-called volumes-of-interest (VoIs). Each anatomical structure was extracted from each slice based on a spatial clustering approach in which a zone of connected pixels above a manual threshold is extracted within a confined region of a composite of the ^{238}U and ^{31}P images, as shown in Figure 107. A pixel can be connected *via* any of its 8 neighboring pixels. At least one of these two nuclides is present in each anatomical feature. The average relative concentrations (the data were calibrated in the MIE procedure) of Cu, Ni, and Zn were calculated for 9 VoIs, representing 9 anatomical compartments, in the non-fused data (Figure 108, Supporting information). Metal toxicity is determined by the bioavailability of individual metal ions and their competition with other cations.

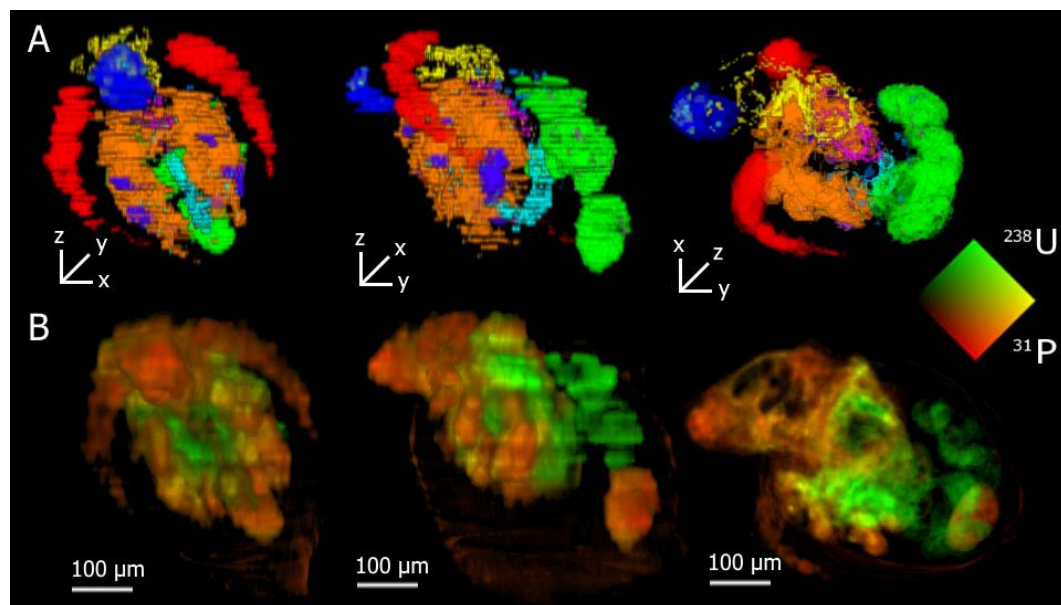


Figure 107 Segmentation of the volume into Voxels which correlate with biological structures based on a ^{238}U - ^{31}P composite. (A) Views (on all sides) of the cloud of voxels designated to multiple Voxels *via* a color coding, (B) Views of a ^{238}U - ^{31}P composite image of the sample.

The interactive effects of metal mixtures are highly dependent on the pH of the medium.³¹ Previously, Ni, Cu, and Zn have been shown to act antagonistically on reproductive toxicity.^{19,31-33} However, it remains yet unclear if the interactions observed can be linked with uptake or distribution patterns. Interactions between, Cu, Ni, and Zn cannot be directly derived from a single sample, yet the metal-specific storage sinks can be identified. In this experiment, trophic transfers of metal accumulation, i.e. incorporation of metals through the food source (*Pseudokirchneriella subcapitata* algae), were not considered and cannot be excluded entirely. Figure 103 and Figure 108 show that Cu, Ni and Zn are distributed in a different way across the anatomy; although environmental exposure to Cu, Ni, and Zn induces metal concentration changes in the different tissues, metals generally already show different distribution across the anatomy. In several studies by Nys et al., the toxicity of binary and ternary combinations of Ni, Zn, Cu, and Pb on *C. dubia* reproduction could be best predicted based on the independent action theory, which may indicate that different mechanisms of toxicity are present.^{19,33} The distribution among different tissues may explain the occurrence of independent toxicity mechanisms. *C. dubia* is expected to be more sensitive to metal exposure than *D. magna*.³⁴⁻³⁶ Chronic exposure to Zn may cause hypocalcemia, i.e. inhibition of Ca uptake³⁷. For Zn and Ni, the respiratory uptake (gills) is expected to be the dominating uptake and excretion route due to the low assimilation efficiency from food in *D. magna*.¹⁷ Similar to previous observations on *D. magna*, Zn was distributed between the eggs, gut and gill tissue in the *C. dubia* specimen in this work.^{21,38,39} The applicability of the 3D imaging and segmentation approach for mechanistic studies, which require a substantial number of specimens to be analyzed, is currently still

limited by time constraints, though the potential to perform such experiments in the future is present.

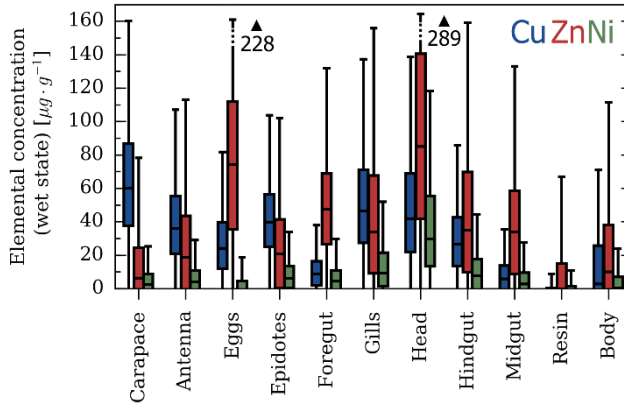


Figure 108 Boxplot of the spread in elemental concentrations of Cu, Ni and Zn in the VoIs within *C. dubia* exposed to elevated Ni, Cu, and Zn concentrations.

7.5 Conclusions

This work reports on multimodal registration of LA-ICP-TOF-MS and μ -CT absorption data. A correlative μ -CT-guided slice registration approach, abbreviated as CSR, permits the accurate reconstruction of the 3D elemental distribution data, as acquired by LA-ICP-TOF-MS through serial sectioning, within specimens with a high level of depth inhomogeneity and tilted orientation relative to the cutting plane. The merits of CSR are highlighted by comparing the image registered by CSR and the image registered by a rigid registration approach based on adjacent sections, relative to the μ -CT data. Noise levels in the LA-ICPMS volume could be reduced by pooling the information contained within mass channels associated with multiple isotopes of a single element. Additionally, synchrotron radiation based μ -XRF merged with absorption μ -CT datasets provided complementary information on the 3D trace level elemental distributions within these millimeter-sized model organisms. The exposure of *C. dubia* to dissolved Cu, Ni, and Zn has introduced a distinct distribution of those metals throughout the organism, which could be described in detail and quantified in individual anatomical structures by segmenting the data in volumes-of-interest. A full 3D profile of the elemental and morphological information of *C. dubia* obtained by merging data from all three analysis techniques contributed to a better and representative assignment of the elemental distribution to specific tissues within the organism. Quantification of tissue-specific concentrations could permit mechanistic pathways, linked to metal mixture toxicity, to be unraveled.

7.6 Supporting information

7.6.1 Exposure conditions

C. dubia originated from an in-house laboratory culture, which is maintained and acclimated to the test medium as described in Nys et al. (2016).⁴⁰ Twenty juveniles (<24 h old) were exposed to a mixture containing 25.2 µg of dissolved Zn/L, 3.9 µg of dissolved Ni/L, and 9.4 µg of dissolved Cu/L (ICP-OES; ICAP 7200 DUA; Thermo Fisher Scientific Inc., reference material TM 28-4; method limit of detection: 2.0 µg Cu/L, 1.0 µg Ni/L and 0.5 µg Zn/L; limit of quantification: 5.0 µg Cu/L, 3.0 µg Ni/L and 2.0 µg Zn/L) in two test units (10 juveniles each) with 200 mL medium (Table S-1) during 72 h. During the exposure period, daphnids were fed daily with *Pseudokirchneriella subcapitata* algae (2.105 cells/mL) and YUT-mixture (Yeast-Urtica-Trout Chow mixture in a concentration of 12 mg dried mixture/L).⁴¹

Table 15 Overview of the main physicochemical parameters measured in the exposure medium. Measured ± standard deviations are given.

	Measured values
pH ^a	7.2±0.1
Ca (mg/L) ^b	42±1
Mg (mg/L) ^b	7.4±0.4
K (mg/L) ^b	14±1
Na (mg/L) ^b	12±0
Cl (mg/L) ^c	32±0
SO ₄ (mg/L) ^c	116±4
DOC (mg/L) ^d	11±1
DIC (mg/L) ^d	3.9±0.2

^aThe pH was measured with a glass electrode (Hanna Instruments).

^bCa, Mg, Na, K were measured using ICP-OES (Reference Material Cranberry 05 [Environment Canada]).

^cCl and SO₄ were measured colorimetrically (Aquamate, Thermo Electron Corporation; Chloride: Merck, Spectroquant 1.14897.001; Sulfate: Merck, Spectroquant 1.14548.001).

^dDOC and Dissolved Inorganic Carbon (filtered through 0.45 µM Acrodisc, PALL Life Science) were measured for randomly selected treatments with a Total Organic Carbon analyzer (L-CPH, Shimadzu; Limit of Quantification 1.5 mg DOC/L; Method Detection Limit 0.5 mg DOC/L).

7.6.2 Analytical standards and sample preparation

7.6.2.1 *Preparation of analytical standards for LA-ICP-MS*

Gelatin solutions (10% w/w, VWR BDH Prolabo, Radnor, PA, USA) spiked with 0, 0.98, 10.8, 54.4 or 108 µg/g Ag, Al, B, Ba, Bi, Ca, Cd, Cr3, Cu, Fe, Ga, In, K, Li, Mg, Mn, Na, Ni, Pb, Sr, and Tl (from a 1 mg/l multi-element solution IV-stock-4, 5% HNO₃ (v/v), Inorganic Ventures, Christiansburg, VA, USA) and 51 µg/g In (from a 1 mg/l solution, 2% HNO₃, Inorganic Ventures, Christiansburg, VA, USA), were prepared gravimetrically in 1.5 mL microcentrifuge Eppendorf tubes. The solutions were placed in a laboratory water bath (MP-5, Julabo GmbH, Seelbach, Germany) at 50 °C and vortexed (VWR International, Belgium) periodically to homogenize the solution. 4 droplets of spiked gelatin spotted on a cover glass slide (VWR International, Belgium), varying between 170 and 425 µg in weight (Sartorius M3P microbalance, Sartorius, Germany), were ablated quantitatively, permitting a drift-corrected multi-point calibration curve ($r^2 \geq 0.99$) to be constructed by interpolation. Each set of integrated mass channels (for each nuclide) was background-corrected using a second-degree smoothing spline interpolation of the gas background between two 10 s gas blank acquisition intervals at the start and end of each run.

7.6.2.2 *Preparation of analytical standards for SR µ-XRF*

A weighed amount of NIST SRM1577b powder was pressed into a self-supporting pellet with known areal concentration

7.6.2.3 *Sample preparation for SR µ-XRF*

dubia samples were dehydrated through a graded acetone series. Subsequently, the specimens were immersed in 1-1.5 mL HMDS (1,1,1,3,3,3-hexamethyldisilazane) in 20 mL vials. After 30 minutes, approximately 90% of the HMDS was removed and the vials were immediately transferred to a desiccator. The bottom of the desiccator was covered by silica gel beads and the desiccator itself was evacuated to avoid water contamination, which would cause shrinkage in the specimens. The remaining HMDS was allowed to evaporate overnight under anhydrous conditions. After drying, the samples were inspected using an optical (reflection) microscope and then glued onto the tip of a polymer support capillary. Note that metal leaching of free metal ions cannot be excluded, however, in the context of this work, imaging of bound metals was envisaged.

7.6.3 High-resolution dorsoventral section.

A dorsoventral section was imaged at higher lateral resolution (2 µm) prior to 3D imaging to produce a detailed description of the elemental distribution in 2D (Figure 109) and assess whether 3D imaging was feasible. In the image, all major and minor anatomical features of the daphnia were identified, including the fine details of the thoracic limbs – which constitute the filtering apparatus. Although it is possible to achieve fine-grained high-resolution images using LA-ICPMS, there is a significant trade-off in terms of the limit of detection (LOD) and of throughput; compared to a 5 µm spot, the LOD for a 2 µm spot is degraded 8-fold and the total time required for mapping this section is $> 6 \times$ longer. This particular specimen contains young daphnids in the brood chamber. Cu can be detected in the ovary, thoracic limbs and, carapace.

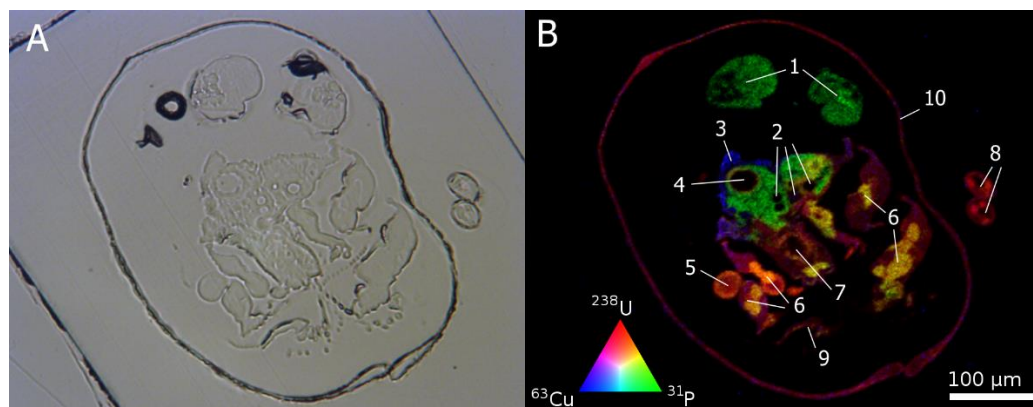


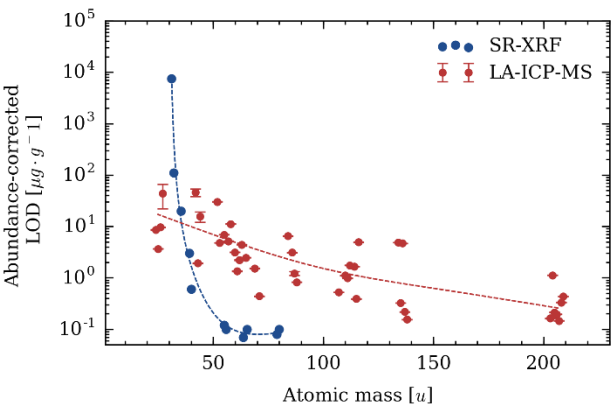
Figure 109 (A) High-resolution brightfield microscopy image and (B) corresponding LA-ICP-MS nuclide distribution image of a single dorsoventral cross-section for selected mass channels. Legend: 1, eggs; 2, Maxillary gland; 3, Ovarium; 4, midgut; 5, epipodites/ exopodite; 6, thoracic limbs; 7, hindgut; 8, antenna; 9, part of the filter screens which collect food particles; 10, carapace.

7.6.4 Limits of detection (LOD)

Access to the full-mass spectrum through TOF-MS enabled the integration of all stable isotopes of every individual element with an abundance $> 0.1\%$. Nuclides suspected to suffer from spectral interferences (both polyatomic and isobaric) were ignored. As each mass channel is sampled at a different time, most of the stochastic dark noise can be canceled out when rejecting single detection events. The mass resolution R of 3200 permits to distinguish most molecular spectral interferences from the targeted nuclides, *e.g.*, $^{32}\text{S}^+$ (mass 31.97207 u) can be differentiated from $^{16}\text{O}_2^+$ (mass 31.98983 u), though some interferences, such as the isobaric overlap of $^{40}\text{Ar}^+$ and $^{40}\text{Ca}^+$ remain unresolvable as a result of the relative peak height and mass proximity. The LOD for LA-ICP-TOF-MS was calculated using the IUPAC gold book definition with $k=3$ for the beam size used in the imaging experiment [$5 \times 5 \mu\text{m}$]. The instrumental background variation was determined by calculating the standard deviation of the mean based on 20 signal segments whilst not firing the laser. The duration of a single data buffer, corresponds to the time dedicated to capture a single pulse response (which is later integrated to establish a value for the corresponding voxel). In order to reference these results relative to similar elemental imaging techniques, the LOD of the synchrotron radiation XRF setup, were included in Figure 110. The LODs for the SR-XRF setup were calculated based on a 1 s measurement time and a $\sim 20 \times 20 \times 30 \mu\text{m}^3$ probed volume. A point measurement in confocal mode was performed just below the surface of a pressed pellet of NIST SRM1577B 'Bovine liver'. Note that Figure 110 shows an LOD for two techniques with a probed volume, different by a factor of almost two orders of magnitude. The absolute sensitivity for SR-XRF and LA-ICP-TOF-

MS is hence on par for a mass range [50 amu -100 amu]. Furthermore, the acquisition speed of LA-ICP-TOF-MS is 20 × faster.

Figure 110 Graphical representation of the abundance-corrected LOD of SR-XRF (over the mass range [31 amu – 80 amu]), and LA-ICP-TOF-MS (over the mass range [24 amu -205 amu]) for biological material. Note that the probed volumes, and acquisition speed of SR-XRF and LA-ICP-TOF-MS are different. Error bars indicate the ± 2SD uncertainty on the calibration curve slopes.



7.6.5 3D segmentation tabulated results

Table 16 Quantitative information for Cu and Ni for individual compartments based on 3D segmentation.*

Vol	Color	# Voxels	$Cu_{mean,w}$ [$\mu g\ g^{-1}$]	S_{mean} [$\mu g\ g^{-1}$]	Relativ e mass [%]	$Ni_{mean,wet}$ [$\mu g\ g^{-1}$]	S_{mean} [$\mu g\ g^{-1}$]	Relativ e mass [%]
Foregut	Yellow	3,683	1.1 $\times 10^1$	4.2 $\times 10^{-1}$	0.2	6.0 $\times 10^0$	1.5 $\times 10^{-1}$	0.5
Midgut	Magenta	5,819	8.9 $\times 10^0$	2.9 $\times 10^{-1}$	8.9	4.8 $\times 10^0$	1.3 $\times 10^{-1}$	0.6
Hindgut	Cyan	2,185	3.1 $\times 10^1$	5.2 $\times 10^{-1}$	0.4	1.0 $\times 10^1$	2.8 $\times 10^{-1}$	0.5
Antenna	Red	17,085	4.6 $\times 10^1$	2.6 $\times 10^{-1}$	4.5	6.2×10^0	8.3 $\times 10^{-2}$	2.2
Head	Blue	4,890	7.2 $\times 10^1$	8.2 $\times 10^{-1}$	2.0	5.6 $\times 10^1$	7.4 $\times 10^{-1}$	5.7
Brood sac	Green	40,571	3.2 $\times 10^1$	1.6 $\times 10^{-1}$	7.5	9.9 $\times 10^{-1}$	3.9 $\times 10^{-2}$	0.8
Gills	Orange	45,843	5.7 $\times 10^1$	2.2 $\times 10^{-1}$	15	6.0 $\times 10^0$	1.5 $\times 10^{-1}$	15
Epidotes	Purple	4,566	4.4 $\times 10^1$	4.1 $\times 10^{-1}$	1.1	8.6 $\times 10^0$	1.7 $\times 10^{-1}$	0.8

Carapace	(not displayed)	66,250	6.7×10^1	2.9×10^{-1}	25	4.4×10^0	0.3×10^{-1}	6
Whole body	(not displayed)	1.0×10^6	1.7×10^1	3.9×10^{-2}	100	4.7×10^0	1.7×10^{-2}	100

*Studies disagree on the evolution of the bioconcentration factor (BCF, the ratio of metal concentrations in the organism and equilibrated medium) as a function of exposure metal concentrations, although there are indications that there is an inverse relationship as a result of active regulation. BCFs are hence not good predictors of chronic toxicity. The metal elimination rate constant is independent of the metal concentration in ingested food; the BCF is likewise expected to be constant.

Table 17 Quantitative information for Zn for individual compartments based on 3D segmentation.

Vol	Color	# Voxels	$Zn_{mean,wet}$ [$\mu g\ g^{-1}$]	S_{mean} [$\mu g\ g^{-1}$]	Relative mass [%]
Foregut	Yellow	3,683	4.8×10^1	5.3×10^{-1}	0.7
Midgut	Magenta	5,819	3.4×10^0	4.8×10^{-1}	0.8
Hindgut	Cyan	2,185	4.4×10^1	1.1×10^0	0.4
Antenna	Red	17,085	2.2×10^1	2.7×10^{-1}	1.6
Head	Blue	4,890	9.4×10^1	9.7×10^{-1}	2.0
Brood sac	Green	40,571	7.5×10^1	2.6×10^{-1}	13
Gills	Orange	45,843	5.2×10^1	4.8×10^{-1}	10
Epidotes	Purple	4,566	2.2×10^1	4.7×10^{-1}	0.4
Carapace	(not displayed)	66,250	2.3×10^1	8.8×10^{-2}	2.3
Whole body	(not displayed)	1.0×10^6	1.7×10^1	3.9×10^{-2}	100

7.6.6 Cross-modality projection (CP) of CT info onto LA-ICP-MS data

CT visualizes the local attenuation coefficient which correlates with local electron density (representative for mass density). It is essentially non-destructive and offers a spatial resolution down to $\sim 1\ \mu m$, but lacks elemental specificity. 2D LA-ICP-TOF-MS, on the other

hand, reveals the elemental distribution, but requires invasive microtomy. When a strong relationship exists between imaging modalities, an image of high spatial resolution from one modality can, to some extent, be used to predict the spatial distribution within an image of low spatial resolution from another modality in a process known as upsampling or sharpening in data fusion.^{42,43} Morphological features are often closely related to elemental and molecular distribution patterns as a result of the strong link between the presence and function of anatomical features and the local chemical composition. From the μ -CT image, zones of high local electron density, which acts as a proxy for tissue density, can be isolated using a threshold to set a level which differentiates tissue from resin. This information on the tissue structure of *C. dubia* can be taken advantage of to sharpen elemental images acquired by LA-ICP-TOF-MS, when a strong correlation exists between the element and tissue distribution. Heterogeneity of the data types and the diversity in the resolution of the data are typically challenging aspects in this approach. In this case, the LA-ICPMS data registered *via* CSR contain $59 \times 248 \times 220$ voxels; these data were interpolated in the axial (Z-) direction to match its size to the CT data size ($395 \times 248 \times 220$ voxels). To estimate the predictive power of the tissue distribution for elemental distributions and find out which structural features are cross-modality supported, the strength of element-to-tissue correlations was determined in a limited kernel volume V_p ($15 \times 15 \times 15$ voxels). The strength of the cross-modality relationship in V_p is reflected by $\sigma_{e,N}$, the Pearson correlation coefficient of the electron and nuclide density. In volumes V_p , where the correlation is statistically significant ($p < 0.05$), high confidence exists in cross-modality projection, and the LA-ICPMS voxels in V_p for which the corresponding voxels of the CT image indicate that no tissue is present, are hidden. For low confidence cross-modality prediction, the elemental distribution remains in place, preserving features which are not apparent in the CT image. As the seed position of the kernel V_p affects the result, the algorithm is always run a second time, with the kernel seed position shifted by 2 voxels, and the reconstructions are averaged. The kernel V_p in which the correlation is evaluated is limited, as the strength of cross-modality relationships may be very location-specific: one of the features in the CT image may be reflected strongly by the local nuclide density, whilst other features in the nuclide distribution may be absent in the CT image: Zn for example has a strong presence in the V_p s containing the brood sacs, which are not all visible in the CT image. Other features visible in the CT image, such as the carapace, may not appear in the nuclide distribution image. Based on the μ -CT data and the predictive power of element-to-tissue correlations (recorded through different modalities), an enhanced representation of the nuclide distribution was produced. The image after CP highlights fine details of *C. dubia*, whilst eliminating noise outside of it. Although CP can be seen as an artificial improvement – and should be treated as such, its primary objective is to enhance the correlation of the elemental images towards the morphology of the sample as recorded by CT. In view of this, segmentation and other quantitative calculations are still performed on the data *prior* to CP, yet after MIE.

7.6.7 Experimental parameters of the ICP-MS system during imaging

Table 18 Operational parameters of the TOFWERK AG icpTOF

TOFWERK AG icpTOF	
RF power [<i>W</i>]	1550
Sampling depth [<i>mm</i>]	2.6
Ar plasma gas flow rate [<i>L min⁻¹</i>]	13.9
Ar auxiliary gas flow rate [<i>L min⁻¹</i>]	0.78
Ar make-up gas flow rate [<i>L min⁻¹</i>]	0.86
Acquisition parameters	
Mass range monitored [<i>u</i>]	3.4 – 278.8
Extraction events / buffer	10
Buffer integration time [<i>ms</i>]	50

7.7 Bibliography

- (1) Skraskova, K.; Khmelinskii, A.; Abdelmoula, W. M.; De Munter, S.; Baes, M.; McDonnell, L.; Dijkstra, J.; Heeren, R. M. *Journal of the American Society for Mass Spectrometry* **2015**, *26*, 948-957.
- (2) Verbeeck, N.; Yang, J.; De Moor, B.; Caprioli, R. M.; Waelkens, E.; Van de Plas, R. *Anal Chem* **2014**, *86*, 8974-8982.
- (3) Abdelmoula, W. M.; Skraskova, K.; Balluff, B.; Carreira, R. J.; Tolner, E. A.; Lelieveldt, B. P.; van der Maaten, L.; Morreau, H.; van den Maagdenberg, A. M.; Heeren, R. M.; McDonnell, L. A.; Dijkstra, J. *Anal Chem* **2014**, *86*, 9204-9211.
- (4) Seeley, E. H.; Caprioli, R. M. *Proc Natl Acad Sci U S A* **2008**, *105*, 18126-18131.
- (5) Lanekoff, I.; Thomas, M.; Carson, J. P.; Smith, J. N.; Timchalk, C.; Laskin, J. *Anal Chem* **2013**, *85*, 882-889.
- (6) Thiele, H.; Heldmann, S.; Trede, D.; Strehlow, J.; Wirtz, S.; Dreher, W.; Berger, J.; Oetjen, J.; Kobarg, J. H.; Fischer, B.; Maass, P. *Biochim Biophys Acta* **2014**, *1844*, 117-137.
- (7) Hare, D. J.; Lee, J. K.; Beavis, A. D.; van Gramberg, A.; George, J.; Adlard, P. A.; Finkelstein, D. I.; Doble, P. A. *Anal Chem* **2012**, *84*, 3990-3997.
- (8) Paul, B.; Hare, D. J.; Bishop, D. P.; Paton, C.; Nguyen, V. T.; Cole, N.; Niedwiecki, M. M.; Andreozzi, E.; Vais, A.; Billings, J. L.; Bray, L.; Bush, A. I.; McColl, G.; Roberts, B. R.; Adlard, P. A.; Finkelstein, D. I.; Hellstrom, J.; Hergt, J. M.; Woodhead, J. D.; Doble, P. A. *Chem. Sci.* **2015**, *6*, 5383-5393.
- (9) Maes, F.; Collignon, A.; Vandermeulen, D.; Marchal, G.; Suetens, P. *Proceedings of the Ieee Workshop on Mathematical Methods in Biomedical Image Analysis* **1996**, 14-22.
- (10) Pluim, J. P.; Maintz, J. B.; Viergever, M. A. *IEEE Trans Med Imaging* **2003**, *22*, 986-1004.
- (11) Seeley, E. H.; Wilson, K. J.; Yankeelov, T. E.; Johnson, R. W.; Gore, J. C.; Caprioli, R. M.; Matrisian, L. M.; Sterling, J. A. *Bone* **2014**, *61*, 208-216.
- (12) Gundlach-Graham, A.; Gunther, D. *Analytical and bioanalytical chemistry* **2016**, *408*, 2687-2695.
- (13) Van Malderen, S. J. M.; Managh, A. J.; Sharp, B. L.; Vanhaecke, F. *J. Anal. At. Spectrom.* **2016**, *31*, 423-439.
- (14) Trede, D.; Schiffler, S.; Becker, M.; Wirtz, S.; Steinhorst, K.; Strehlow, J.; Aichler, M.; Kobarg, J. H.; Oetjen, J.; Dyatlov, A.; Heldmann, S.; Walch, A.; Thiele, H.; Maass, P.; Alexandrov, T. *Anal Chem* **2012**, *84*, 6079-6087.
- (15) Oetjen, J.; Aichler, M.; Trede, D.; Strehlow, J.; Berger, J.; Heldmann, S.; Becker, M.; Gottschalk, M.; Kobarg, J. H.; Wirtz, S.; Schiffler, S.; Thiele, H.; Walch, A.; Maass, P.; Alexandrov, T. *Journal of proteomics* **2013**, *90*, 52-60.
- (16) Guan, R.; Wang, W. *Environmental Toxicology* **2004**, *23*, 2689-2698.
- (17) Yu, R. Q.; Wang, W. X. *Limnol Oceanogr* **2002**, *47*, 495-504.

- (18) Taylor, G.; Baird, D. J.; Soares, A. M. V. *M. Environmental Toxicology and Chemistry* **1998**, *17*, 412-419.
- (19) Nys, C.; Janssen, C. R.; De Schamphelaere, K. A. *Environ Pollut* **2017**, *220*, 1271-1281.
- (20) Salminen, R.; tutkimuskeskus, G. *Geochemical Atlas of Europe: Background information, methodology and maps*; Geological Survey of Finland, 2005.
- (21) De Samber, B.; Evens, R.; De Schamphelaere, K.; Silversmit, G.; Masschaele, B.; Schoonjans, T.; Vekemans, B.; Janssen, C. R.; Van Hoorebeke, L.; Szalóki, I.; Vanhaecke, F.; Falkenberg, G.; Vincze, L. *J Anal Atom Spectrom* **2008**, *23*, 829.
- (22) De Samber, B.; Silversmit, G.; De Schamphelaere, K.; Evens, R.; Schoonjans, T.; Vekemans, B.; Janssen, C.; Masschaele, B.; Van Hoorebeke, L.; Szaloki, I.; Vanhaecke, F.; Rickers, K.; Falkenberg, G.; Vincze, L. *Journal of Analytical Atomic Spectrometry* **2010**, *25*, 544-553.
- (23) Laforsch, C.; Tollrian, R. *Archiv Fur Hydrobiologie* **2000**, *149*, 587-596.
- (24) Teledyne CETAC Technologies Inc. Aerosol Rapid Introduction System [15/07/2016]. Available from: <http://www.teledynecetac.com/product/laser-ablation/aris>.
- (25) Gundlach-Graham, A.; Burger, M.; Allner, S.; Schwarz, G.; Wang, H. A.; Gyr, L.; Grolimund, D.; Hattendorf, B.; Gunther, D. *Anal Chem* **2015**, *87*, 8250-8258.
- (26) Burger, M.; Gundlach-Graham, A.; Allner, S.; Schwarz, G.; Wang, H. A.; Gyr, L.; Burgener, S.; Hattendorf, B.; Grolimund, D.; Gunther, D. *Anal Chem* **2015**, *87*, 8259-8267.
- (27) Gelfand, N.; Ikemoto, L.; Rusinkiewicz, S.; Levoy, M. In *3-D Digital Imaging and Modeling, 2003. 3DIM 2003. Proceedings. Fourth International Conference on*, 2003, pp 260-267.
- (28) Gruen, A.; Akca, D. *ISPRS Journal of Photogrammetry and Remote Sensing* **2005**, *59*, 151-174.
- (29) Ulianov, A.; Muntener, O.; Schaltegger, U.; Bussy, F. *J Anal Atom Spectrom* **2016**, *31*, 597-630.
- (30) Ulianov, A.; Muntener, O.; Schaltegger, U. *J Anal Atom Spectrom* **2015**, *30*, 1297-1321.
- (31) Nagai, T.; De Schamphelaere, K. A. *Environ Toxicol Chem* **2016**, *35*, 2765-2773.
- (32) Nys, C.; Asselman, J.; Hochmuth, J. D.; Janssen, C. R.; Blust, R.; Smolders, E.; De Schamphelaere, K. A. *Environ Toxicol Chem* **2015**, *34*, 1091-1102.
- (33) Nys, C.; Van Regenmortel, T.; Janssen, C. R.; Blust, R.; Smolders, E.; De Schamphelaere, K. A. *Environ Toxicol Chem* **2016**.
- (34) Deleebeeck, N. M.; De Schamphelaere, K. A.; Heijerick, D. G.; Bossuyt, B. T.; Janssen, C. R. *Ecotoxicol Environ Saf* **2008**, *70*, 67-78.
- (35) Balcaen, L. I.; De Schamphelaere, K. A.; Janssen, C. R.; Moens, L.; Vanhaecke, F. *Analytical and bioanalytical chemistry* **2008**, *390*, 555-569.
- (36) De Schamphelaere, K. A.; Canli, M.; Van Lierde, V.; Forrez, I.; Vanhaecke, F.; Janssen, C. R. *Aquat Toxicol* **2004**, *70*, 233-244.

(37) Muyssen, B. T.; De Schamphelaere, K. A.; Janssen, C. R. *Aquat Toxicol* **2006**, *77*, 393-401.

(38) Gholap, D.; Izmer, A.; De Samber, B.; van Elteren, J. T.; Selih, V. S.; Evens, R.; De Schamphelaere, K.; Janssen, C.; Balcaen, L.; Lindemann, I.; Vincze, L.; Vanhaecke, F. *Anal Chim Acta* **2010**, *664*, 19-26.

(39) De Samber, B.; Silversmit, G.; Evens, R.; De Schamphelaere, K.; Janssen, C.; Masschaele, B.; Van Hoorebeke, L.; Balcaen, L.; Vanhaecke, F.; Falkenberg, G.; Vincze, L. *Analytical and bioanalytical chemistry* **2007**, *390*, 267-271.

(40) Nys, C.; Janssen, C. R.; Blust, R.; Smolders, E.; De Schamphelaere, K. A. *Environ Toxicol Chem* **2016**, *35*, 1796-1805.

(41) Environmental Protection Agency, U.; USA government: Washington, DC., 2002, p 56.

(42) Van de Plas, R.; Yang, J.; Spraggins, J.; Caprioli, R. M. *Nature methods* **2015**, *12*, 366-372.

(43) Blum, R. S.; Liu, Z. *Multi-sensor Image Fusion and Its Applications*; CRC Press, 2005.

Chapter 8 Conclusions and outlook

In the past few years, research efforts directed towards the optimization of the design of low-dispersion ablation cells were intensified, which has led to the emergence of new applications of LA-ICP-MS. Still, further development of low-dispersion ablation cells characterized by a high transport efficiency is highly desirable. The optimum design criteria for low-dispersion ablation cells that were identified in this work can be summarized as: i) a small volume, confined by solid walls or gas flows, in which the plume can expand, ii) efficient uptake by utilizing the momentum and the characteristics of He, iii) fluid-dynamic-optimized design to transfer the aerosol by laminar flows to the transport conduit without creating advection/turbulence as a result of dead volume, and iv) minimization of tubing lengths, bends and divergences in the conduit diameter. Miniaturization of the low-dispersion ablation cell and connecting tubing enabled a 99% washout of the aerosol in ~6 ms, enabling separated pulse responses at frequencies up to 200 Hz. The low-dispersion cryogenically cooled ablation cell assembly developed in this work permits fast and sensitive line scanning with high lateral resolution, partly mitigating issues related to peak broadening due to impaired aerosol washout as generally encountered in ablation cells in use for continuous laser ablation. The performance characteristics of low-dispersion cells are advantageous for imaging applications spanning a variety of fields, as these share a common requirement for high speed, high sensitivity, and high spatial resolution. Applications such as 3D imaging, single-cell analysis, and sub-cellular imaging, previously impossible or extremely time-consuming, are enabled by the low-dispersion technology. Recent demonstrations of these kinds of applications reported in the literature include, the analysis of corroded glass¹, a multi-layer ceramic capacitor², Opalinus clay rock³, a Seymchan pallasite meteorite⁴, individual uranium particles⁵, fluid inclusions in quartz⁶, cytometry on breast tumor tissue⁷ and individual cells⁸. In this work, a novel method involving oversampling, *i.e.* overlapping ablation positions on the sample surface as such that a position is sampled more than once, was developed to boost the lateral resolution obtained by

a laser ablation methodology. When oversampling, an artificially convolved image is produced. This work demonstrated that the distortion introduced by oversampling can be corrected for by using a post-acquisition iterative deconvolution procedure, permitting an image with a resolution below the beam waist size to be reconstructed. The Richardson-Lucy deconvolution algorithm, in combination with regularization using total variation, was found to successfully resolve the noisy LA-ICP-MS response of overlapping ablation spots. The point-spread-function of the beam could be derived directly from topographical information on the ablation craters. Lateral resolutions down to $0.3 \pm 0.1 \mu\text{m}$, a resolution below the laser beam diameter of $1 \mu\text{m}$, were demonstrated for 1D scanning of multi-layer ceramic capacitors. There were two limiting factors in the approach: (i) the level of axial homogeneity over the depth of the accumulated ablation damage inside each sampling layer, which affected the accuracy of the deconvolution solution, and (ii) the sensitivity of the ICP-MS unit, which may limit the use of small laser beam waist sizes. Through superimposition of 2D sampling layers, 3D nuclide distributions at the minor or trace level were reconstructed. This methodology is applicable in scenarios where the laser beam waist size is far-field- or sensitivity-limited and permits LA-ICP-MS to compete with nanoprobe and super-resolution imaging techniques for trace nuclide patterns. Other signal processing algorithms can increase the throughput of LA-ICP-MS: signal deconvolution of the transient signal can be applied to obtain isolated individual pulse response peaks at higher laser repetition rates than would be possible in a scenario of baseline separated peaks. When individual pulse response peaks can be integrated, the intensity within the mass spectrum and the spatial information associated with each laser shot are accessible, which enables the best possible lateral resolution to be obtained. Signal processing within LA-ICP-MS remains challenging due to the lack of flexible and powerful software focused on (3D) imaging, with algorithms tailored to LA-ICP-MS and geared towards accepting information from other modalities. In order to address this shortcoming, a software library for processing large volumes of LA-ICP-MS data in a versatile way was developed. The architecture of the software is based on HDF5 files and is capable of dealing with complex, arbitrarily structured arrays in many coordinate systems in highly automated ways. The library contains a large array of signal processing algorithms, made accessible to the user through a graphical user interface (GUI). The library core algorithms can operate independently of the GUI, allowing for fully scripted, automated data processing, with or without the supervision of the operator.

As mentioned above, low-dispersion aerosol transport systems are crucial to the continued advancement of single cell-analysis and sub-cellular imaging. In order to enable the accurate determination of element concentrations within single cells, a highly controlled volume of a matrix-matched calibration standard must be introduced. Conventional sectioned tissue standards may be ill-suited for this application, as i) it is challenging to accurately determine the volume ablated without surface characterization techniques, ii) tissue and spike homogeneity may be an issue in the production of these standards, and iii) placement of the conventional standards in the cell may be inconvenient, due to their typical dimensions. An approach based on dispensing standards on a substrate as a droplet *via* a micropipetting system has been proposed by Zhai *et al.*⁹ An alternative to this work, high-density self-aliquoting microarray plates – nanotiter plates designed to distribute samples in *pL* volume

microcontainers, was proposed and evaluated for holding spiked gelatin standards.¹⁰⁻¹² The proposed microarrays can contain multiple matrix-matched standards or samples and were found to be an attractive alternative for microdispensed droplet arrays, as the microarrays can contain replicates at densities of $> 1000 \text{ wells} \cdot \text{cm}^{-2}$, while they can (also) be produced in a fast, cheap, accurate, and precise way. The micro-array format was demonstrated successfully in the quantification of ppm-level concentrations of Cu at the single-cell level. A dose-dependent accumulation of Cu was observed in *Scrippsiella trochoidea* upon exposure to spiked medium. The sensitivity observed in LA-ICP-MS with the low-dispersion ablation cell was demonstrated to be high enough to permit intracellular imaging. A set of single cells were submitted to 2D imaging using a $2 \mu\text{m}$ spot size. An accumulation center, only a few μm in size, was observed in the cells, demonstrating the applicability of LA-ICP-MS for bio-imaging at the subcellular level, and corroborating observations from SR-XRF elemental *in vivo* analysis.

3D imaging using LA-ICP-MS is still in its infancy, as several difficulties of the approach still have to be overcome. The most significant challenges are the extended experimental time required and the associated cost of 3D imaging, which both can be reduced by increasing the number of spatially resolved pixels acquired per second; the significantly higher throughput of low-dispersion cells lowers the cost and time barriers to 3D LA-ICP-MS imaging significantly. 3D imaging of soft (biological) material entails sectioning the sample using a microtome, analysis of the serial sections in 2D, followed by reconstruction of a 3D image using computational methods. Data produced from serial sections need to be aligned (*alias* registered) to reconstruct the original spatial relations between the sample material captured within the sections. A common strategy in MALDI and DESI-imaging is to align the data indirectly by registering the optical tissue images coupled to the data based on similar features in the optical images, rather than registration of the IMS images themselves. As the features can vary between tissue sections, and information on the curvature of a sample is lost, artificial fiducial markers can be included within the embedding medium that are identifiable and provide the basis for alignment. However, tissue shrinkage during drying and alignment or shift of the marker during sectioning may still create artifacts. This work reports on a new approach for the multimodal registration of serial sections imaged using LA-ICP-TOF-MS, relative to the corresponding slice in the $\mu\text{-CT}$ image of the same sample, based on shared distinguishable features across the modalities, which were artificially introduced through a heavy mass element stain. This correlative multimodal approach permits the accurate reconstruction of the 3D elemental distribution data, within specimens with a high level of depth inhomogeneity and tilted orientation relative to the sectioning plane. A strategy is presented to link the modalities in the spatial domain through a set of rigid transformations *prior* to registration. Furthermore, an approach was reported in which data of a full-spectrum analysis was pooled to reduce the noise levels in the LA-ICP-TOF-MS images: the information contained within mass channels associated with isotopes of a single element can be integrated to extract elemental data. In a demonstration of these new approaches, *Ceriodaphnia dubia*, a small water flea, was 3D imaged. A specimen, $\sim 500 \mu\text{m}$ in size, was exposed to dissolved Cu, Zn, and Ni, which introduced a distinct distribution of those metals throughout the organism. From the 3D data, the elemental concentration in individual anatomical structures could be quantified *via* image segmentation.

Additionally, synchrotron radiation based μ -XRF merged with absorption μ -CT datasets provided complementary information on the 3D trace level elemental distributions within these model organisms. For 3D imaging in solid samples, the laser can be used to drill the sample away, layer by layer. This strategy is however restricted in the depth that can be probed within the sample, due to constraints in the aspect ratio of the craters. A serial polishing methodology developed in this work, has permitted the reconstruction of the 3D trace metal and metalloid distribution in seed samples. This approach is applicable to solid and brittle samples which cannot be readily sectioned. Toxic trace metal/metalloid distribution patterns along the transverse sections of wheat and rye grains exposed to natural background concentrations were visualized and quantified per structural compartment.

In conclusion, within the context of this work, an improved aerosol transport system, and advanced sampling strategies for applications that benefit greatly from low-dispersion systems have been developed, such that the goal of this work, an optimization and extension of 2D and 3D-imaging using LA-ICP-MS has been achieved.

8.1 Outlook

It is becoming clear that fast (pseudo-) simultaneous mass analyzers and detection systems have the potential to displace quadrupole and sector-field mass analyzers for LA-ICP-MS mapping, as sequential mass monitoring restricts the sampling speed. (Quasi-)simultaneous detection of the full elemental mass spectrum, or a large part thereof, enables a more detailed look at the co-spatial distribution of elements, and calibration based on 100%wt normalization for every laser shot. An ICP-MS instrument capable of handling highly transient mass loads, whilst offering simultaneous multi-element detection across the full mass range, a wide linear dynamic range, fast data readout, minimal blind time, high mass resolution and high sensitivity, would make a good match to low-dispersion laser ablation systems.

2D imaging of biological tissue samples is becoming an accepted approach in biomedical research and, in some cases, has been suggested as a clinical diagnostic aid. The sample preparation, calibration, ablation, and image processing protocols enabling this analysis are meanwhile fairly well established. In order to better establish LA-ICP-MS for the analysis of biological samples by application-oriented users, who often desire a 'sample in – press a button – results out' instrument, further efforts are required, notably in instrument and software development. A major limitation in cell tracking studies is the speed of analysis, which compares unfavorably to other elemental imaging techniques within the biological and clinical fields, *e.g.*, fluorescence microscopy. If the technology is to be proposed as a clinical or diagnostic aid, high throughput and sensitivity become paramount. If low-dispersion laser systems incorporated automated optical cell recognition software, then a more clinically acceptable analysis rate of $> 100 \text{ cells s}^{-1}$ could be achieved. As the target audience widens and the complexity of experimental designs increases, requiring more replicates to be analyzed in a set time span, new approaches to increase throughput are necessary. It should be noted that a 6-10-fold increase in absolute sensitivity is established when using the low-dispersion interface, compared to conventional technology. This indicates that tracking cells with LA-ICP-MS could be feasible over a greater number of divisions. Sensitivity will grow in relative importance as new

applications emerge requiring targeted nuclide analysis at sub- μm lateral resolution. The features of the microarray standards proposed in this work, and droplet arrays could be attractive in high-throughput single-cell analysis, array spotting, and tissue micro-assay mapping. The microarrays could eventually be combined with micropipetting (*e.g.*, array spotting) techniques to produce standards directly inside each microwell. Further improvements in the throughput of LA-ICP-MS will also allow the interspacing between sections in 3D imaging to be reduced, which is desirable, as this would enable a more accurate registration of the individual slices, permitting the reconstruction to more accurately reflect the elemental distribution along this axis. Only a handful of researchers is looking at the 3D imaging and single-cell analysis, both of which currently are niche applications, but show potential.

The newly developed low-dispersion cells are well suited to these applications, as has already been demonstrated by specialized research groups. The key concepts highlighted in this work, provide strong indicators for the further development of ablation cells. The level of aerosol dispersion is pushing ever closer towards the aerosol dispersion of 1 – 2 ms achieved in in-torch ablation¹³⁻¹⁶. As the environment within an ablation cell can be isolated and controlled to a large extent, we may encounter cells in the future achieving even lower aerosol dispersion. The ablation cell is placed in ever closer proximity to the ICP; it is anticipated that as a result of this, one of the main bottlenecks will become the turbulence within the ICP itself. A new or optimized ionization source may have to be proposed, as the residence time in the ion cloud should be minimized or the turbulence somehow controlled. The plume expansion process into the atmosphere also creates a delay (in the order of a few 100 ms) and dispersion of the aerosol cloud and which will have to be addressed by plume confinement through magnetic or pressure fields (*e.g.*, shockwave reflection). The internal geometry of the volume in which the plume expands hence may become crucial. The low-dispersion cells enables a sensitivity at which nano-scale (*i.e.* with $< 1\mu\text{m}$ resolution) LA-ICP-MS becomes feasible. It seems likely this will be exploited *via* far- and near-field focusing at some point. It also seems likely that challenging analytical applications will rely increasingly on multiple modalities. Synergy between modalities – in particular for 3D imaging and single-cell imaging – may be exploited by data fusion. As LA remains a destructive technique (in these cases), complementary, non-destructive techniques, such as confocal fluorescence, wide-field or multi-photon (super-resolution) microscopy, μ -Raman spectroscopy, SPECT, PET, fMRI, SEM, CT, and μ - or nano-X-ray spectroscopy, will be highly applicable towards multi-modal analysis. Other techniques, such as IMS, TEM, SIMS, FIB, and PIXE, will not always enable analysis on the same sample, but may provide complementary information nonetheless, *e.g.*, through analysis of adjacent sections.

8.2 Bibliography

- (1) Van Malderen, S. J. M.; van Elteren, J. T.; Vanhaecke, F. *Anal Chem* **2015**, *87*, 6125-6132.
- (2) Van Malderen, S. J. M.; van Elteren, J. T.; Vanhaecke, F. *J. Anal. At. Spectrom.* **2014**, *30*, 119-125.
- (3) Burger, M.; Gundlach-Graham, A.; Allner, S.; Schwarz, G.; Wang, H. A.; Gyr, L.; Burgener, S.; Hattendorf, B.; Grolimund, D.; Gunther, D. *Anal Chem* **2015**, *87*, 8259-8267.
- (4) Gundlach-Graham, A.; Burger, M.; Allner, S.; Schwarz, G.; Wang, H. A.; Gyr, L.; Grolimund, D.; Hattendorf, B.; Gunther, D. *Anal Chem* **2015**, *87*, 8250-8258.
- (5) Craig, G. *Improving the utility of LA-ICP-MS for isotope ratio analyses of single particles with application to uranium oxide*, Ph.D. thesis. Loughborough University 2015.
- (6) Harlaux, M.; Borovinskaya, O.; Frick, D. A.; Tabersky, D.; Gschwind, S.; Richard, A.; Günther, D.; Mercadier, J. *J. Anal. At. Spectrom.* **2015**, *30*, 1945-1969.
- (7) Giesen, C.; Wang, H. A.; Schapiro, D.; Zivanovic, N.; Jacobs, A.; Hattendorf, B.; Schuffler, P. J.; Grolimund, D.; Buhmann, J. M.; Brandt, S.; Varga, Z.; Wild, P. J.; Gunther, D.; Bodenmiller, B. *Nature methods* **2014**, *11*, 417-422.
- (8) Douglas, D. N.; Managh, A. J.; Reid, H. J.; Sharp, B. L. *Anal Chem* **2015**, *87*, 11285-11294.
- (9) Zhai, J.; Wang, Y.; Xu, C.; Zheng, L.; Wang, M.; Feng, W.; Gao, L.; Zhao, L.; Liu, R.; Gao, F.; Zhao, Y.; Chai, Z.; Gao, X. *Anal Chem* **2015**, *87*, 2546-2549.
- (10) Urban, P. L.; Jefimovs, K.; Amantonico, A.; Fagerer, S. R.; Schmid, T.; Madler, S.; Puigmarti-Luis, J.; Goedecke, N.; Zenobi, R. *Lab on a Chip* **2010**, *10*, 3206-3209.
- (11) Pabst, M.; Fagerer, S. R.; Kohling, R.; Kuster, S. K.; Steinhoff, R.; Badertscher, M.; Wahl, F.; Dittrich, P. S.; Jefimovs, K.; Zenobi, R. *Anal Chem* **2013**, *85*, 9771-9776.
- (12) Kuster, S. K.; Fagerer, S. R.; Verboket, P. E.; Eyer, K.; Jefimovs, K.; Zenobi, R.; Dittrich, P. S. *Anal Chem* **2013**, *85*, 1285-1289.
- (13) Liu, X. R.; Horlick, G. *Spectrochimica Acta Part B: Atomic Spectroscopy* **1995**, *50*, 537-548.
- (14) Tanner, M.; Gunther, D. *J Anal Atom Spectrom* **2006**, *21*, 941-947.
- (15) Tanner, M.; Gunther, D. *J Anal Atom Spectrom* **2007**, *22*, 1189-1192.
- (16) Tanner, M.; Gunther, D. *Analytical and bioanalytical chemistry* **2008**, *391*, 1211-1220.

Chapter 9 Samenvatting

Laser ablatie-inductief gekoppeld plasma-massaspectrometrie (LA-ICP-MS) is naast X-straal fluorescentie spectroscopie (XRF) en secundaire ionen massaspectrometrie uitgegroeid tot één van de belangrijke methoden voor de beeldvorming van de verdeling van elementen in het voorbije decennia. Dit doctoraat had als doel om deze analytische techniek op verscheidene punten te verbeteren waaronder: de analysesnelheid, de gevoeligheid, ruimtelijke resolutie en de toegang tot de derde ruimtelijke dimensie. Dit werkstuk heeft meerdere wegen bewandeld om deze doelen te bereiken: i) het ontwerp van de ablatiekamer en de transportleidingen werden verbeterd om een kleinere dispersie van het getransporteerde aerosol te bewerkstelligen, ii) algoritmes voor de deconvolutie en filtering van het signaal werden ontwikkeld om de ruimtelijke resolutie te verbeteren, en iii) strategieën voor beeldvorming van stalen in drie dimensies werden verder ontwikkeld. Daarnaast werden de meetgegevens samengesmolten met gegevens verzameld door complementaire beeldvormingstechnieken.

De laterale resolutie van LA-ICP-MS ($\sim 1 - > 50 \mu m$) is minder goed in vergelijking met deze bereikbaar met technieken zoals X-straal fluorescentie spectroscopie (aan een synchrotron) en nano-secondaire ionen massaspectrometrie (SIMS), dewelke resoluties van minder dan 100 nm kunnen bereiken. De detectielimieten van LA-ICP-MS zijn in de meeste gevallen echter beter ($\mu g/g - ng/g$). De kwantificering van LA-ICP-MS gegevens is ook eenvoudiger en betrouwbaarder. Een groot deel van de gevestigde en nieuwe onderzoeksvelden, zoals *metallomics*, zirkonium geochronologie, diagnostische analyse van biologische weefsels, en beeldvorming van de spoorelementpatronen, zouden baat hebben bij een verbetering van de ruimtelijke resolutie van LA-ICP-MS beeldvorming, gezien het belang van de ruimtelijke verdeling van nucliden op de micrometer en sub-micrometer schaal, en de beperkte beschikbaarheid van technieken zoals SIMS. De mogelijkheden van LA-ICP-MS met betrekking

tot de analysesnelheid, de gevoeligheid en ruimtelijke resolutie, hangen voor een groot deel af van het vermogen van de opstelling om het aerosol te transporteren van de locatie waar ablatie plaats vindt naar het ICP-MS instrument, zonder daarbij massa te verliezen of dispersie binnen de aerosolwolk te introduceren. Als de aerosolwolk, dewelke in het ICP wordt gebracht en geproduceerd wordt door een laser schot, wordt samengedrukt, zal de signaalpiek (ten gevolge van de detectie van het aerosol) hoger en korter in duur zijn. In een ideale situatie, met andere woorden in de afwezigheid van het verlies van deeltjes tijdens het transport en effecten verbonden met de belasting van het plasma, zal het oppervlak onder de signaalpiek constant blijven ongeacht de dispersie binnen de aerosolwolk. De dispersie binnen het aerosol vindt zijn oorzaak in de beweging van de stroming van het draaggas tijdens het transport en opname van het aerosol in het draaggas. Een aantal ablatiekamers werd ontworpen en uitgetest, onder andere door middel van numerieke simulaties van de gasstromen. De kamers werden geïnstalleerd in een commercieel beschikbare LA-ICP-MS opstelling. De nieuwe ablatiekamers brachten belangrijke verbeteringen teweeg in de prestatie van de opstelling: de gevoeligheid en doorvoersnelheid werd met 2 tot 3 grootteordes verbeterd ten opzichte van de conventionele (voorgaande) opstellingen. Het eerste prototype van de nieuwe ablatiekamers was een variatie op de lage-dispersie *tube cell*. Deze kamer en daarbij horende transportleidingen zijn in staat om 99% van de aerosolwolk ontstaan vanuit één enkel laser shot in een tijd van ongeveer 6 ms uit het systeem te laten vloeien, wat toelaat om de individuele signaalpieken te zien bij een laser schot frequentie tot 200 Hz. De *tube cell* werd geïntegreerd binnen een grotere buitenkamer, waardoor het mogelijk werd om grotere stalen ($100 \times 100 \times 20 \text{ mm}^3$) te analyseren. Bovendien laat deze buitenkamer toe om het staal cryogeen te koelen, een snellere staaldoorvoer te bewerkstelligen, en de stalen accurater te positioneren, zonder daarbij toegevingen inzake prestaties te moeten doen. Nieuwe methodes voor signaalverwerking en laserbemonstering werden ontwikkeld om de prestaties van de techniek nog verder op te krikken. Een post-acquisitie methode werd ontwikkeld om een deconvolutie uit te voeren op het massaspectrometrie signaal afkomstig van een scan waarin de belichte posities telkens overlappen. Door dezelfde positie meerdere keren te ableren met een laserstraal met een diameter van 1 μm , kan de laterale resolutie na signaalverwerking verhoogd worden tot op sub- μm niveau. De signaalverwerking die toegepast werd maakt gebruik van het Richardson-Lucy algoritme, dewelke de distorsie van zo'n scan kan corrigeren. Gebruikmakend van deze nieuwe methodologie kon in een beeld van keramische condensatoren een laterale resolutie van 0.3 μm aangetoond worden. De strategie werd daarna uitgebreid tot meerdere dimensies, door binnen een rechthoekig veld de belichte posities te laten overlappen in meerdere richtingen, en zodoende twee-dimensionele beeldvorming met een resolutie kleiner dan de breedte van de laser straal mogelijk te maken. Door deze velden te overlappen, konden drie-dimensionele beelden gemaakt worden. Dit werd gedemonstreerd door een beeld te maken van de verdeling van spoorelementen in gecorrodeerd glas. De zogenaamde punt spreiding functie (PSF) kon bepaald worden aan de hand van topografische beelden van ablatiekraters, verkregen *via atomic force microscopy*. Deze experimenteel bepaalde PSF laat toe om de vorm van de ablatiekraters, aberraties van de straal, en de interactie van de laser straal met het oppervlak, in rekening te brengen tijdens de deconvolutie, en zodoende de accuratesse van de reconstructie te verbeteren. Deconvolutie kon ook nog voor andere doeleinden gebruikt

worden: door een deconvolutie uit te voeren op het massaspectrometrie signaal konden de signalen afkomstig van individuele laser shots geïsoleerd worden, zelfs indien deze deels overlappen in de tijd.

Een nieuw type kalibratie-standaard, gebaseerd op hoge-dichtheid microplaten werd ontwikkeld om aan tekortkomingen in de precisie, accuratesse en doorvoersnelheid binnen huidige kalibratiemethoden voor elementanalyse op cellulair niveau tegemoet te komen. Om dit nieuwe type standaard te testen, werd het kopergehalte in cellen van het genus *Scrippsiella trochoidea* bepaald, nadat deze werden blootgesteld aan media die van 0.5 tot 100 µg/L koper bevatten. Na de blootstelling werden deze cellen behandeld in een kritisch-punt-droogapparaat, waarna deze overgebracht werden op een koolstof-film en gecoat werden met een laagje goud zodoende dat deze werden in beeld gebracht konden worden met een rasterelektronenmicroscoop (SEM). In de daaropvolgende LA-ICP-MS analyse werden ongeveer 100 cellen van elke blootstellingsgraad één voor één gebeeld. Deze aanpak liet toe om de gemiddelde concentratie aan Cu te bepalen bij elke blootstellingsgraad, alsook de spreiding op deze waarde binnen de populatie van cellen. Daarnaast werden beelden gemaakt door LA-ICP-MS van individuele cellen met een resolutie van enkele µm. De kenmerken van de cellen geanalyseerd door LA-ICP-MS beeldvorming zijn gelijklopend aan de kenmerken in beelden opgenomen van analoge blootgestelde cellen onder *in vivo* omstandigheden door synchrotron XRF (SR-XRF) microscopie. De beeldvorming van elementverdelingen op sub-cellulair niveau werd mogelijk doordat die gebruik maakte van een verbeterde opstelling van de transportleidingen, die de gevoeligheid van de opstelling verhoogde.

De hoeveelheid informatie die LA-ICP-MS voortbrengt kan vergroot worden door beeldvorming van de stalen in 3D. Verder kan deze informatie gecombineerd worden met complementaire informatie van andere technieken. Dit doctoraat heeft onderzocht hoe de synergie tussen verschillende beeldvormingstechnieken, zoals LA-ICP-MS en micro-computertomografie (µ-CT), kan geëxploiteerd worden. De verweving van spectrale en ruimtelijke informatie van deze technieken heeft hier als doel om de 3D visualisatie van objecten te verbeteren, en extra, verborgen informatie te onthullen. Een kleine zoetwater crustaenia, *Ceriodaphnia dubia*, werd bestudeerd. Deze watervlo werd gefixeerd, gekleurd met uranyl acetaat, en ingebed, om vervolgens geanalyseerd te worden door µ-CT. Het diertje werd daarna in coupes gesneden met behulp van een microtroom, waarna deze coupes werden geanalyseerd door middel van LA-ICP-MS. Om de resultaten (beelden) in de verschillende coupes met grote precisie te oriënteren in de verticale richting, werden in dit doctoraat de coupes georiënteerd (*alias* geregistreerd) op basis van de overeenkomstige deelfiguren in de computertomografie beelden. Er werd aangetoond dat deze manier van werken superieur is ten opzichte van de gevestigde methoden. De data binnen het massaspectrum werd daarna gecombineerd om het ruisniveau binnen de beelden te onderdrukken. Het gereconstrueerde beeld werd daarna vergeleken met de elementverdeling binnen een *Ceriodaphnia dubia* gevisualiseerd door synchrotron-XRF. Daarnaast werd in dit werk ook een nieuwe manier voorgesteld om stalen, die moeilijk te snijden zijn met een microtroom, toch in beeld te brengen in 3D. Met de aanpak die werd voorgesteld en die gebaseerd is op polijsten, kunnen 3D beelden worden gemaakt op een niveau die dieper liggen dan de kraters die men kan boren met de laser.

De praktische uitwerking van de signaalverwerking (registratie, deconvolutie en data verweving) werd mogelijk gemaakt door de ontwikkeling van een computerprogramma. Een python pakket werd ontwikkeld voor de signaalverwerking van massaspectrometrie-signalen en andere types van beeldvorming, met een nadruk op de verwerking van LA-ICP-MS data. Het python pakket is gebaseerd op het HDF-bestandsformaat, dat toelaat om alle meta-data op te slaan en de data te verwerken zonder supervisie. Het pakket laat toe om de data te exporteren naar Paraview, een *open-source* softwarepakket ontwikkeld voor de visualisatie van data. Het python pakket is zo ontwikkeld zodat zeer flexibel kan omgegaan worden met grote datasets (zowel voor opslag, verwerking en weergave). Het pakket laat toe om resultaten in parallel te verwerken. Een grafische gebruikersomgeving laat toe snel en efficiënt de data te verwerken.

Chapter A Appendix

A.1 Publications and Activities

A.1.1 Peer-reviewed A-1 type publications

- A1.1– Article Development of a fast laser ablation-inductively coupled plasma-mass spectrometry cell for sub-um scanning of layered materials, Stijn J. M. Van Malderen *et al.*, J. Anal. At. Spectrom. (IF 2013: 3.396), 2015, **30**, 119
- A1.1– Article Submicrometer Imaging by Laser Ablation-Inductively Coupled Plasma Mass Spectrometry *via* Signal and Image Deconvolution Approaches, Stijn J. M. Van Malderen *et al.*, Anal. Chem.(IF 2013: 5.825), 2015, **87**, 6125-6132
- A1.1– Article Laser ablation-tandem ICP-mass spectrometry (LA-ICP- MS/MS) for direct Sr isotopic analysis of solid samples with high Rb/Sr ratios, Eduardo Bolea-Fernandez *et al.*, J. Anal. At. Spectrom. (IF 2015: 3.379), 2016, **31**, 464-472
- A1.1– Review Recent developments in the design of rapid response cells for laser ablation-inductively coupled plasma-mass spectrometry and their impact on bioimaging applications, Stijn J. M. Van Malderen *et al.*, J. Anal. At. Spectrom. (IF 2015: 3.379), 2016, **31**, 423-439
- A1.1– Article Quantitative Determination and Subcellular Imaging of Cu in Single Cells *via* Laser Ablation-ICP-Mass Spectrometry Using High-Density Microarray Gelatin Standards, Stijn J. M. Van Malderen *et al.*, Anal. Chem. (IF 2015: 5.886), 2016 , **88**, 5783-5789
- A1.1– Article Nanoscopic tumor tissue distribution of platinum after intraperitoneal administration in a xenograft model of ovarian cancer, Charlotte Carrier *et al.*, J. Pharma. Biomed. Anal. (IF 2015: 3.169), 2016, **131**, 256-262

- A1.1– Article High-Resolution Laser Ablation-Inductively Coupled Plasma-Mass Spectrometry Imaging of Cisplatin-Induced Nephrotoxic Side Effects, Thibaut Van Acker *et al.*, Anal. Chem. Acta (IF 2015: 4.712), 2016, **945**, 23-30
- A1.1– Article Imaging the 3D trace metal and metalloid distribution in mature wheat and rye grains *via* laser ablation-ICP-mass spectrometry and micro-X-ray fluorescence spectrometry, Stijn J.M. Van Malderen *et al.*, J. Anal. At. Spectrom. (IF 2013: 3.396), 2017, **32**, 289-298
- A1.1– Article A comparison of laser ablation-inductively coupled plasma-mass spectrometry and high-resolution continuum source graphite furnace molecular absorption spectrometry for the direct determination of bromine in polymers, Jefferson S. de Gois *et al.* (IF 2013: 3.396), **132**, 50-55
- A1.1– Article Three-dimensional reconstruction of the tissue-specific multi-elemental distribution within *Ceriodaphnia dubia* *via* multimodal registration using laser ablation ICP-mass spectrometry and X-ray spectroscopic techniques. Stijn J. M. Van Malderen *et al.*, Anal. Chem. (IF 2013: 5.825), 2017, **89**, 4161-4168
- A1.1– Article Hybrid imaging labels; providing the link between mass spectrometry-based molecular pathology and theranostics, Tessa Buckle *et al.*, Theranostics (IF 2015: 8.854), **7**, 624-633

A-1 type publications submitted to peer review

- Article – Quantitative laser ablation ICP-MS and μ XRF element mapping of zoned olivines of main group pallasites, Stepan M. Chernonozhkin *et al.*
- Article – Assessment of ns-LA-MC-ICP-MS for Pb and Sr isotopic analysis of archaeological glass – mass bias correction strategies and Corning glass standards, Alicia Van Ham-Meert *et al.*
- Article – Tropical seasonality in the Late Campanian: Multiproxy evidence from shells of three associated bivalve species, Niels de Winter *et al.*

A.1.2 Conferences and meeting abstracts

- C4 – Conference Abstract Low-dispersion LA-ICP-MS cells: high-resolution tissue imaging and single cell analysis, Stijn J. M. Van Malderen *et al.*, Winter Conference on Plasma Spectrochemistry. Tucson, AZ, USA, 2016.
- C4 – Conference Abstract Combination of a fast ablation cell and deconvolution approaches for high resolution LA-ICP-MS scanning of layered materials, Stijn J. M. Van Malderen *et al.*, European Winter Conference on Plasma Spectrochemistry. Münster, Germany, 2015
- C4– Conference Abstract Fast High Resolution 2D and 3D Laser Ablation–Inductively Coupled Plasma–Mass Spectrometry Imaging *via* Deconvolution approaches and Ablation Cell Design, Stijn J. M. Van Malderen *et al.*, National Meeting of the Society for Applied Spectroscopy (SciX). Providence, RI, USA, 2015.
- C4– Conference Abstract High resolution LA-ICP-MS imaging in three dimensional tumor spheroids, Sarah Theiner *et al.*, European Winter Conference on Plasma Spectrochemistry, Vienna, Austria, 2017

- C4 – Conference Abstract Reconstruction of the 3D full elemental profile of *Ceriodaphnia dubia* using multimodal registration approaches Stijn J. M. Van Malderen *et al.*, European Winter Conference on Plasma Spectrochemistry, Vienna, Austria, 2017
- C4 – Conference Abstract High-resolution 3D and (sub-)cellular level LA-ICP-MS imaging approaches: accumulation of toxic metals in biological material, Stijn J. M. Van Malderen *et al.*, European workshop on Laser Ablation, Ljubljana, Slovenia, 2016
- C4 – Conference Abstract Distribution of platinum after clinical (H)IPEC using LA-ICP-MS, Charlotte Carlier *et al.*, SSO Annual Cancer Symposium. Boston, MA, USA, 2016
- Performance evaluation of a novel high efficiency, low-dispersion aerosol transport system for laser ablation ICP-MS, Simon Jackson *et al.*, Goldschmidt, Yokohama, Japan, 2016.
- C4 – Conference Abstract Assessment of ns-LA-MC-ICP-MS for Pb and Sr isotopic analysis of archaeological glass– mass bias correction strategies and Corning glass standards, Alicia Van Ham-Meert *et al.*, Joint European stable isotopes user group meeting, Ghent, Belgium, 2016.
- C4 – Conference Abstract Stable isotope ratios and trace elements in modern mammal tooth enamel, Niels de Winter *et al.*, Annual Meeting of the European Association of Archaeologists. Vilnius, Lithuania, 2016.
- C4 – Conference Abstract High-Resolution Laser Ablation-Inductively Coupled Plasma-Mass Spectrometry Imaging of Cisplatin-Induced Nephrotoxic Side Effects, Thibaut Van Acker *et al.*, European workshop on Laser Ablation, Ljubljana, Slovenia, 2016.
- C4 – Conference Abstract Growth rates and geochemical proxies in Late Campanian bivalves – New insights from micro-X-ray Fluorescence mapping and numerical growth modelling, Niels de Winter *et al.*, European Geosciences Union General Assembly 2017, Vienna, 2017.
- C4 – Conference Abstract High resolution, fast and more informative LA imaging with the icpTOF, Olga Borovinskaya *et al.*, European workshop on Laser Ablation, Ljubljana, Slovenia, 2016.
- C4 – Conference Abstract Low-dispersion LA aerosol transport systems and CT-based registration approaches: advanced 3D and high-resolution imaging. Stijn J. M. Van Malderen *et al.*, North American Workshop on Laser Ablation, Austin, USA, 2017.
- C4 – Conference Abstract High-resolution LA-ICP-MS imaging of lanthanide-based (hybrid) labels with low-dispersion aerosol transport systems. Stijn J. M. Van Malderen *et al.*, Metallomics, Vienna, Austria, 2017.
- C4 – Advances in 3D and High-Resolution LA-ICP-MS Imaging, Stijn J. M. Van Malderen *et al.*, National Meeting of the Society for Applied Spectroscopy (SciX). Reno, USA, 2017.

A.1.3 Patents

- C3– Patent Laser ablation probe, EPO Patent application, inventors: S. J. M. Van Malderen and F. Vanhaecke, PCT/EP2015/07 1525 (based on EP14185463.8), 2015

A.1.4 Product on the commercial market

- ARIS An add-on for LA-ICP-MS units to improve their performance was developed by the fellow and tested at Ghent University, in cooperation with Teledyne Photon Machines (Bozeman, MT, USA), a wholly owned subsidiary of Teledyne CETAC Technologies. The product (<http://www.teledynecetac.com/product/laser-ablation/aris>) is now commercially available worldwide.

A.1.5 Products in development

REDACTED – UNDER NDA

A.1.6 Attended SR-XRF beamtimes

- ESRF, France, 2016.04, XRF, data acquisition on micrometeorite

A.1.7 Research trips

- National institute of Chemistry, Slovenia, 2013.10, laser ablation, training and knowledge transfer
- Ametek, Germany, 2013.11, ICP-MS, training
- National institute of Chemistry, Slovenia, 2014.02, laser ablation, scientific cooperation
- National institute of Chemistry, Slovenia, 2014.04, laser ablation, scientific cooperation
- TOFWERK, Switzerland, 2016.07, LA-ICP-MS, data acquisition

A.1.8 Teaching activities

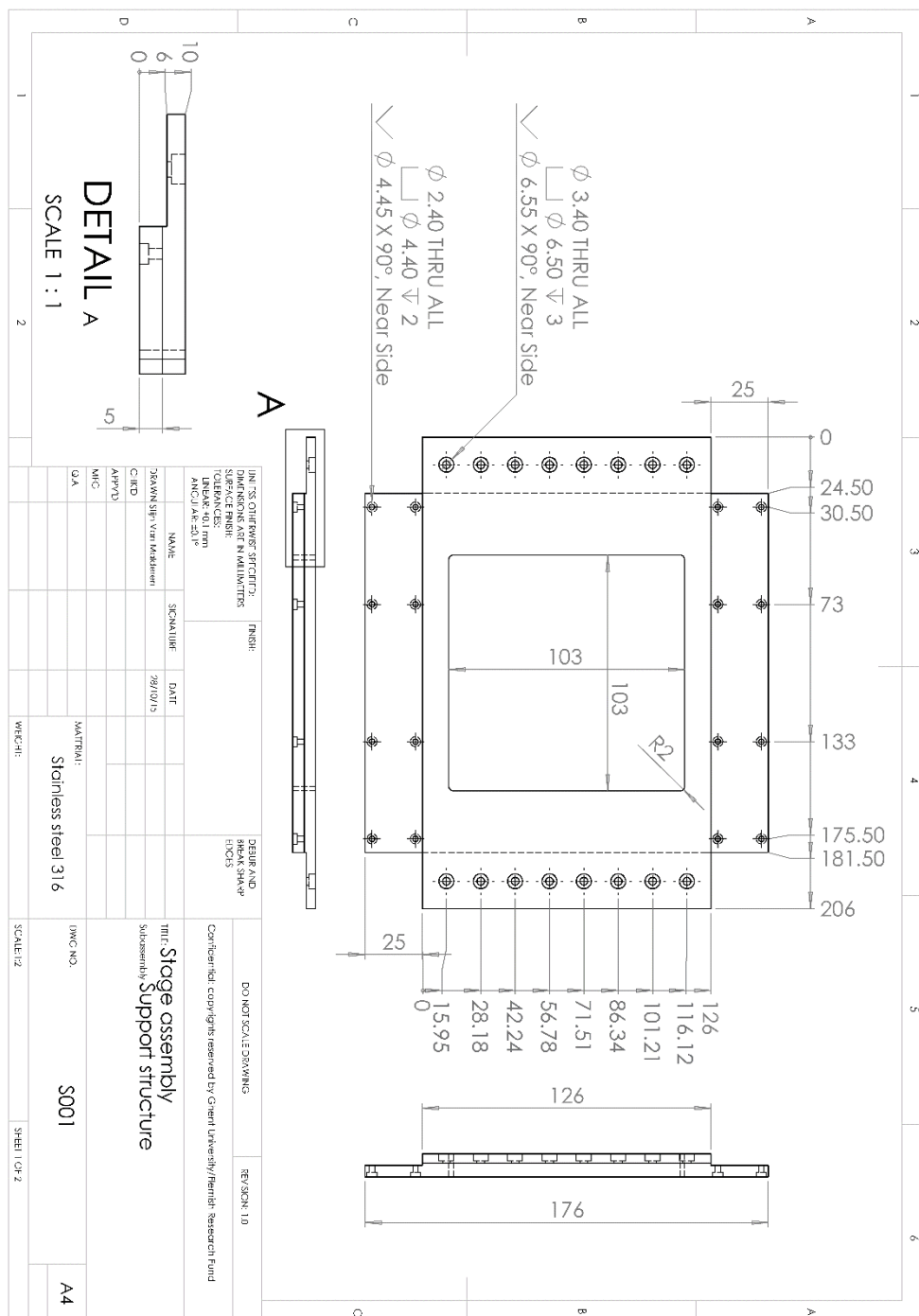
- 4 year of practical guidance of the practical sessions of Atomic Spectroscopy (one semester)
- Workshop lecture and practical session organizer EWLA 2016

A.2 Technical drawings

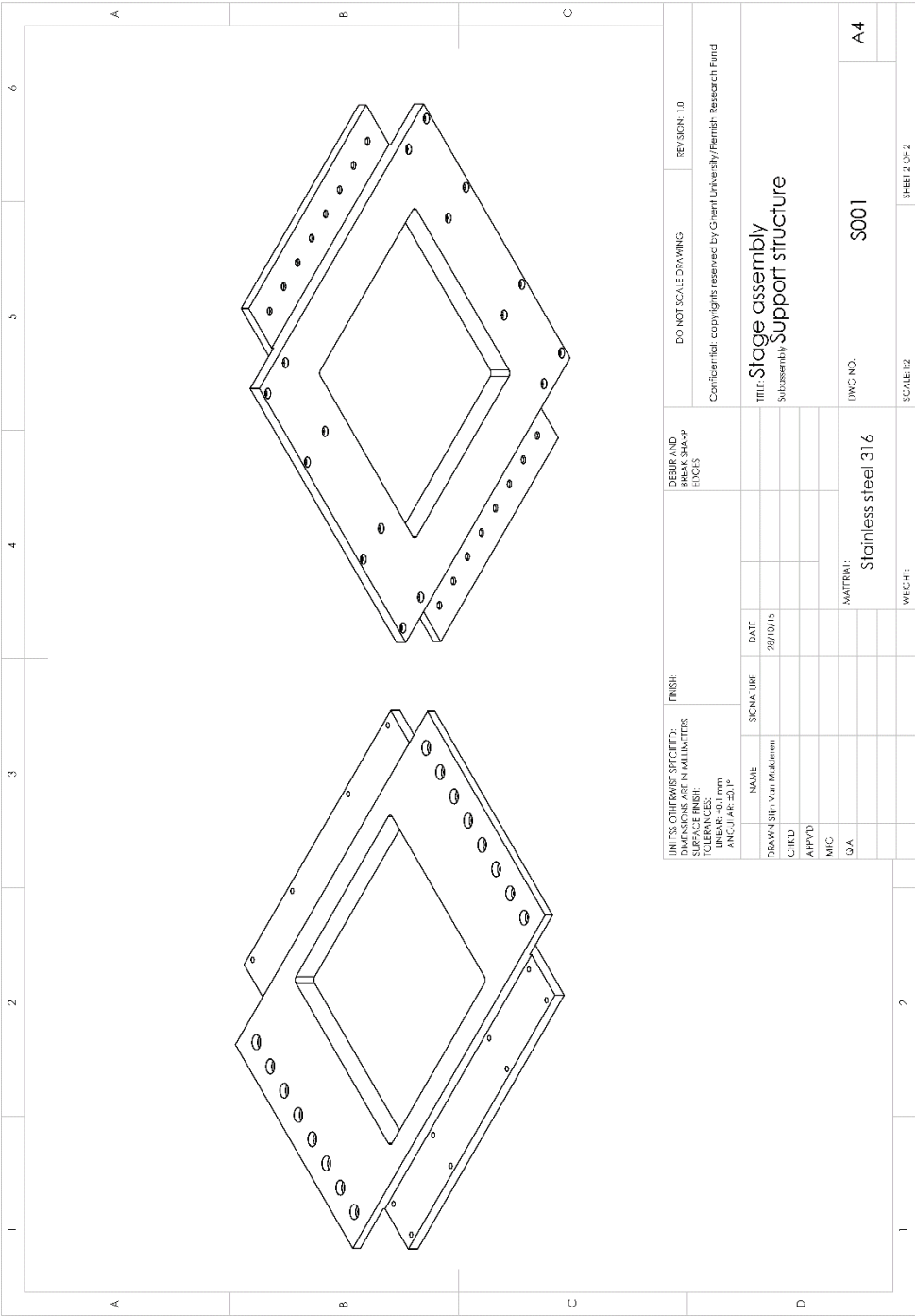
A.2.1 List of CAD drawings

CAD drawing 1 S001 Stage support structure, part 1	270
CAD drawing 2 S001 Stage support structure, part 2	271
CAD drawing 3 S002 Main analytical chamber, part 1.....	272
CAD drawing 4 S002 Main analytical chamber, part 2.....	273
CAD drawing 5 S002 Main analytical chamber, part 3.....	274
CAD drawing 6 S002 Main analytical chamber, part 4.....	275
CAD drawing 7 S007 Z-stage bracket-horizontal	276
CAD drawing 8 S008 Horizontal bracket 1.....	277
CAD drawing 9 S009 Horizontal bracket 2.....	278
CAD drawing 10 S010 Magnet bracket.....	279
CAD drawing 11 S012 Y stage bracket smaract	280
CAD drawing 12 S013 Analytical chamber lid, part 1	281
CAD drawing 13 S013 Analytical chamber lid, part 2	282
CAD drawing 14 S013 Analytical chamber lid, part 3	283
CAD drawing 15 S017 Sample holder window.....	284
CAD drawing 16 S018 Transmission light/window holder	285
CAD drawing 17 S020 Fluid feedthrough flange	286
CAD drawing 18 S021 Electronics feedthrough flange.....	287
CAD drawing 19 S022 Height dial	288
CAD drawing 20 S023 Top bracket.....	289
CAD drawing 21 S024 Outer bracket.....	290
CAD drawing 22 S025 Cell holder piston, part 1	291
CAD drawing 23 S025 Cell holder piston, part 2	292
CAD drawing 24 S028 Tube cell, part 1	293
CAD drawing 25 S028 Tube cell, part 2	294
CAD drawing 26 S028 Tube cell, part 3	295
CAD drawing 27 S029 Sample holder drawer front.....	296
CAD drawing 28 C004 Sample platform.....	297
CAD drawing 29 C007 Heat transfer plate	298
CAD drawing 30 C008 Cooling liquid reservoir	299
CAD drawing 31 C009 Mount plate holder.....	300
CAD drawing 32 C010 Stage mount plate.....	301
CAD drawing 33 C011 Peltier element holder.....	302

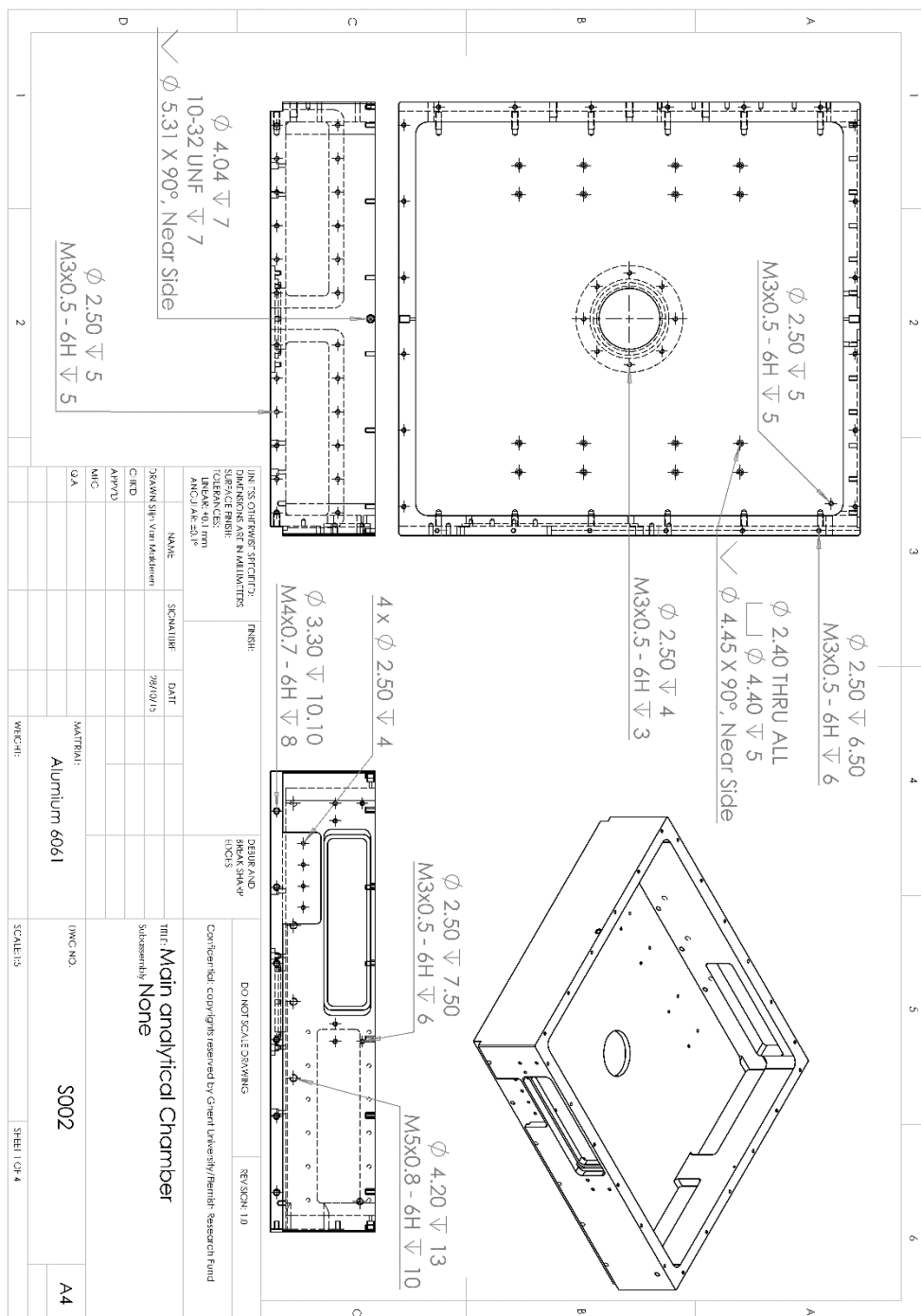
A.2.2 Cad Drawings

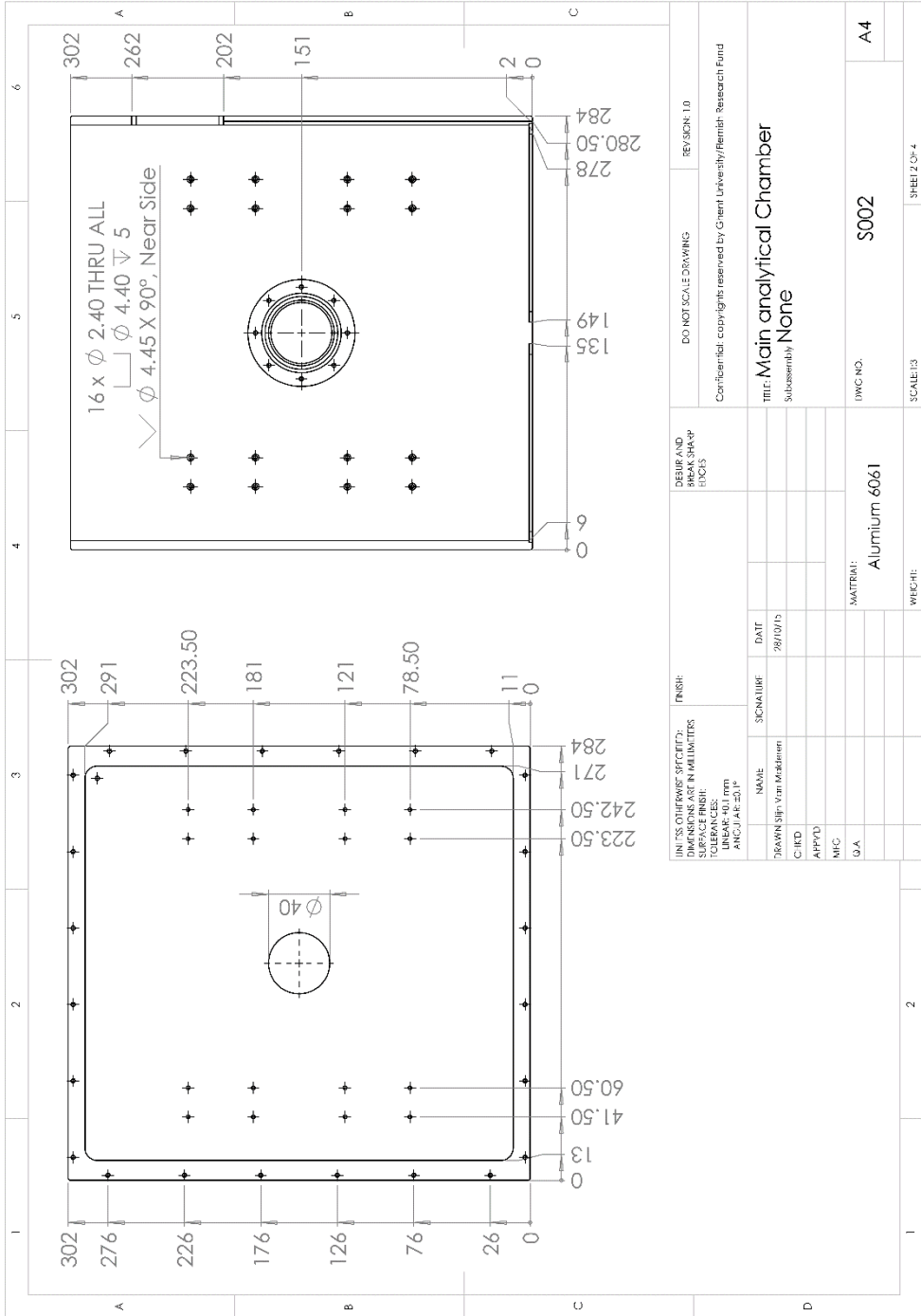


CAD drawing 1 S001 Stage support structure, part 1

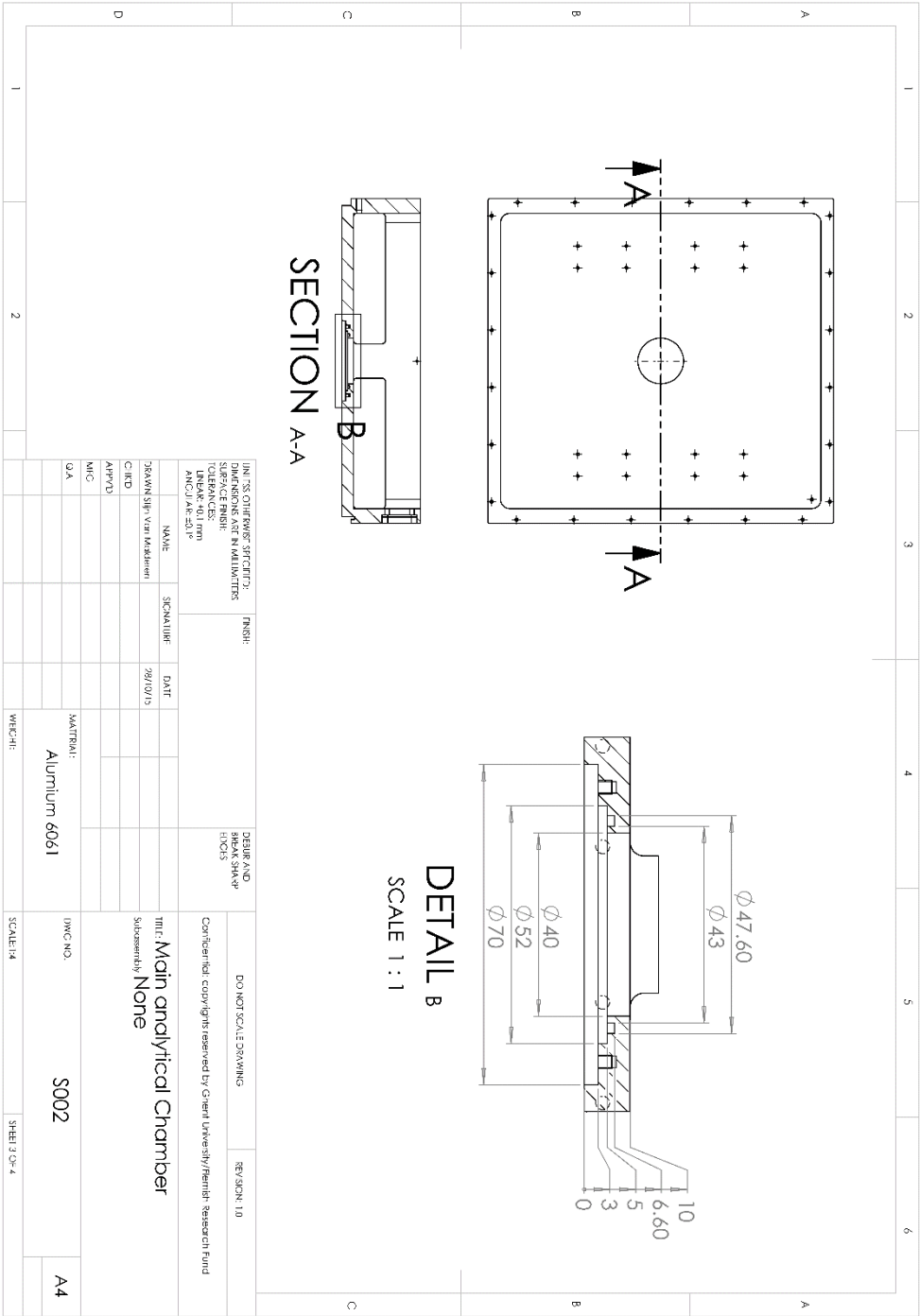


CAD drawing 2 S001 Stage support structure, part 2

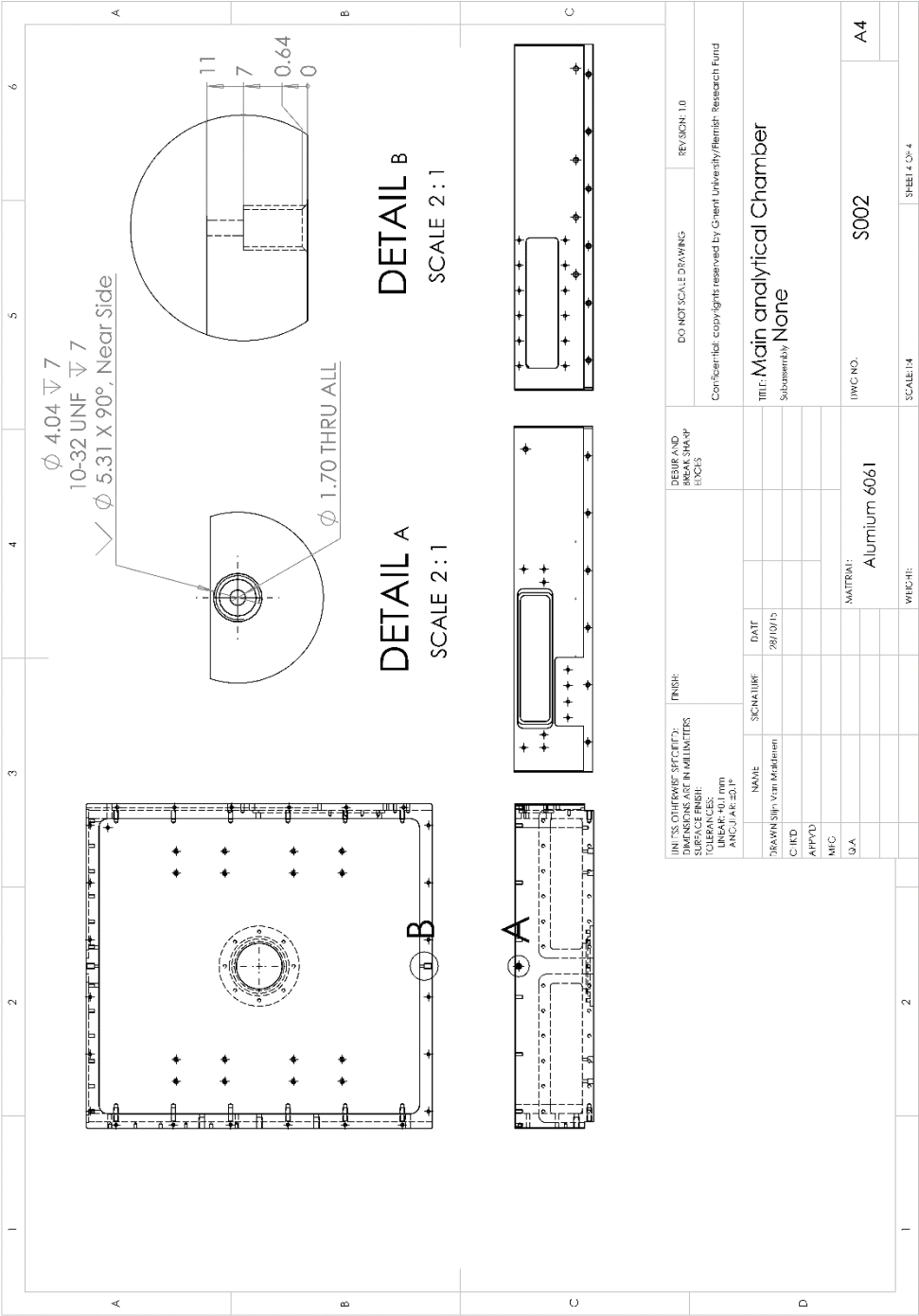


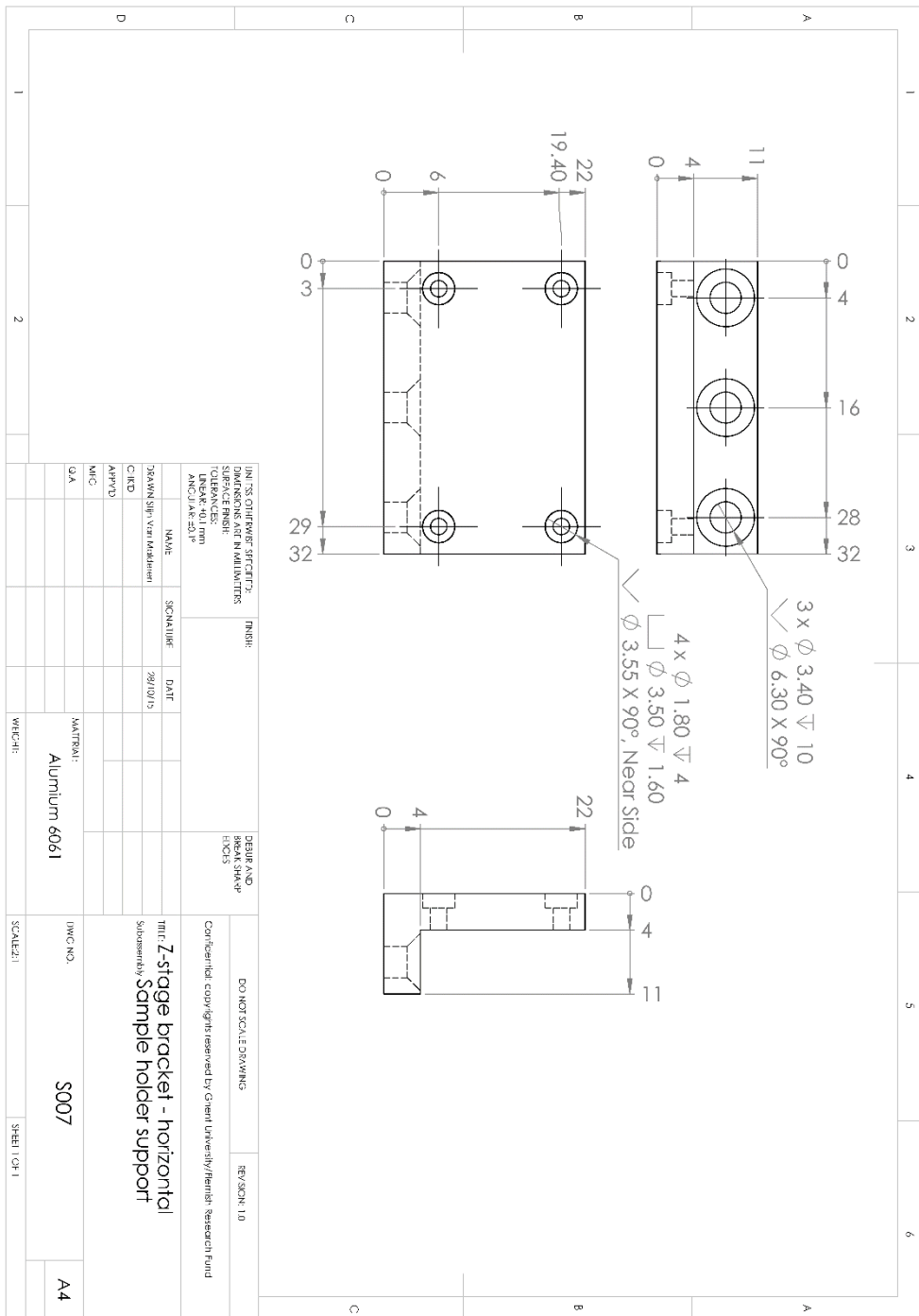


CAD drawing 4 S002 Main analytical chamber, part 2

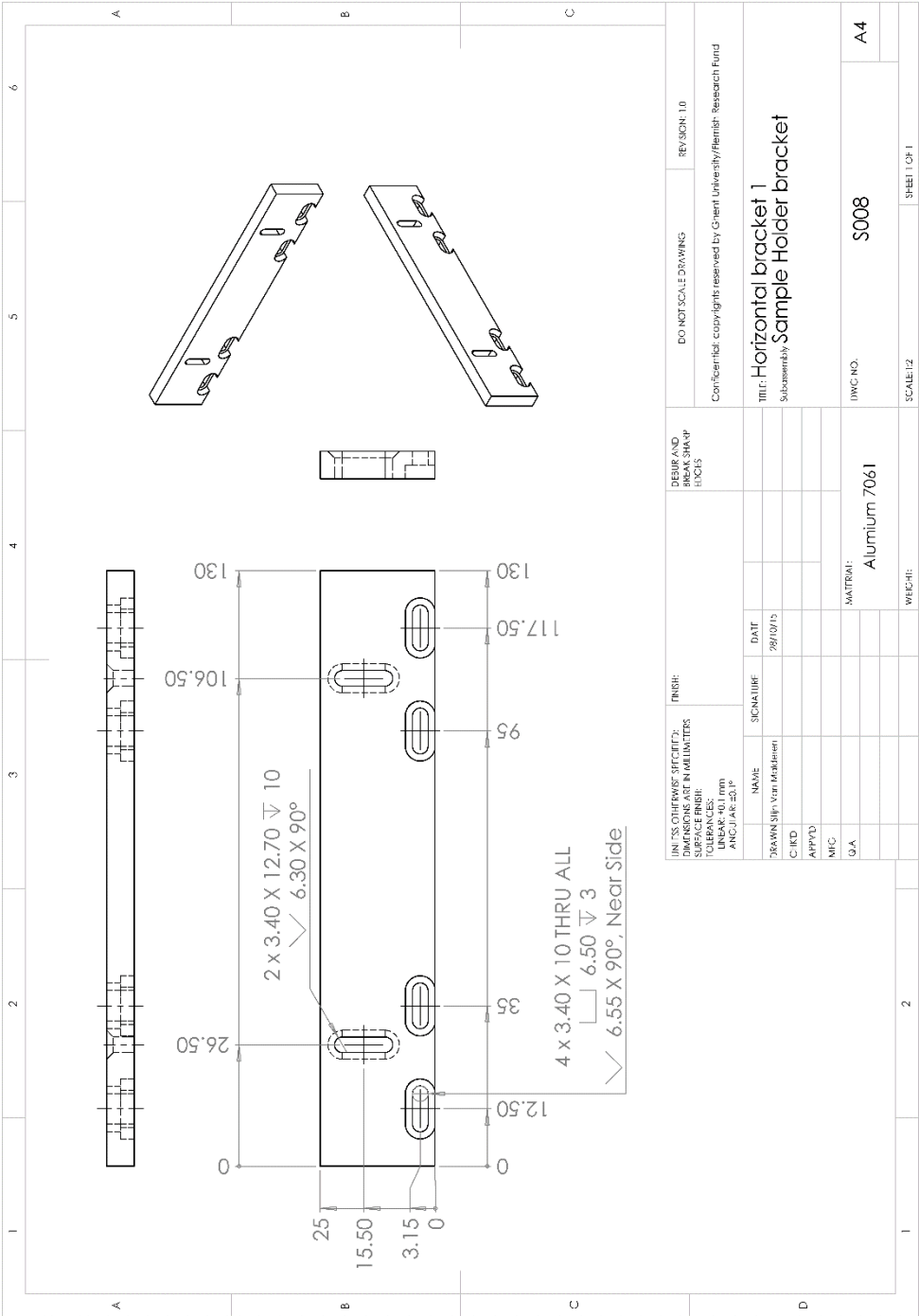


CAD drawing 5 S002 Main analytical chamber, part 3

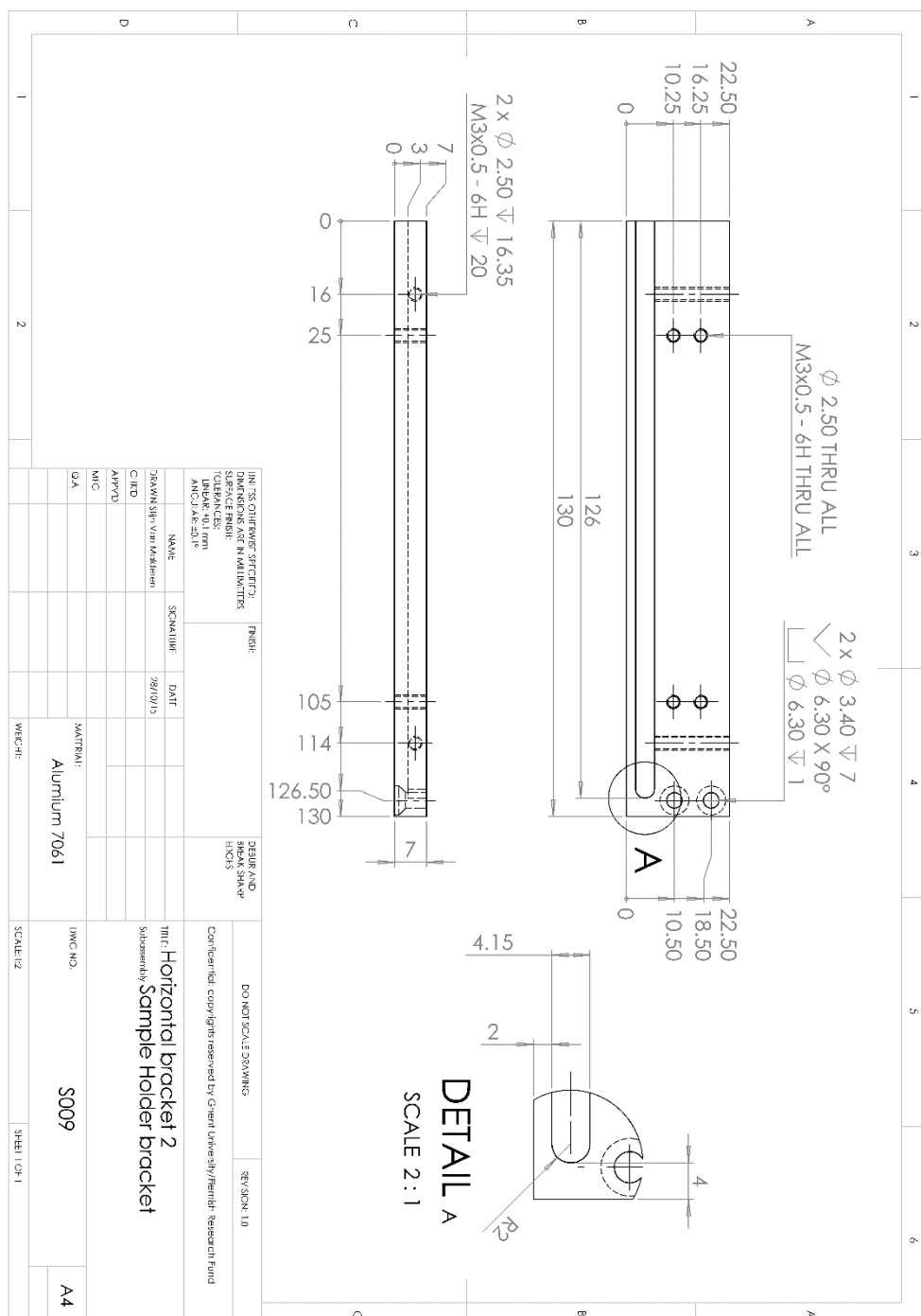


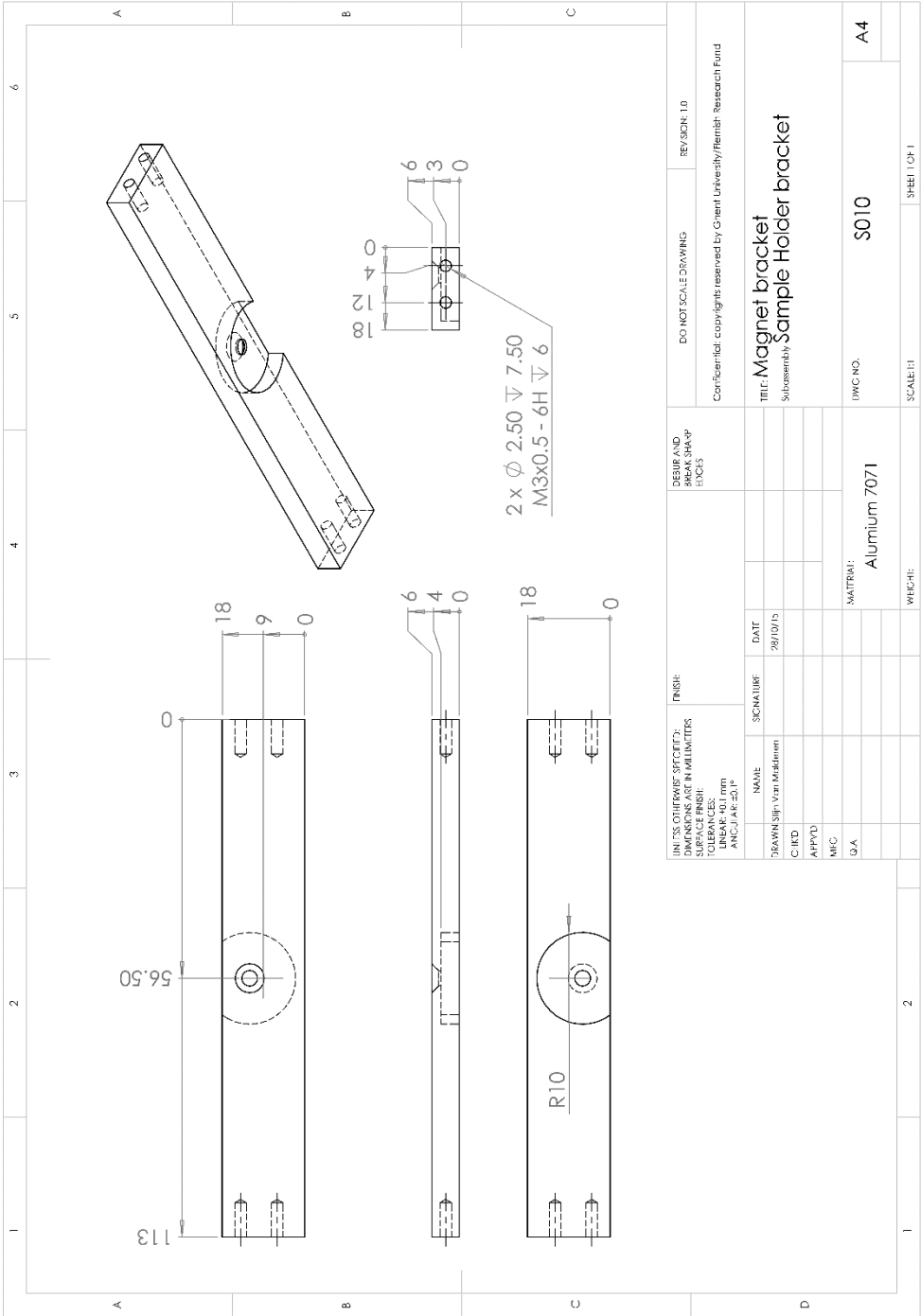


CAD drawing 7 S007 Z-stage bracket-horizontal

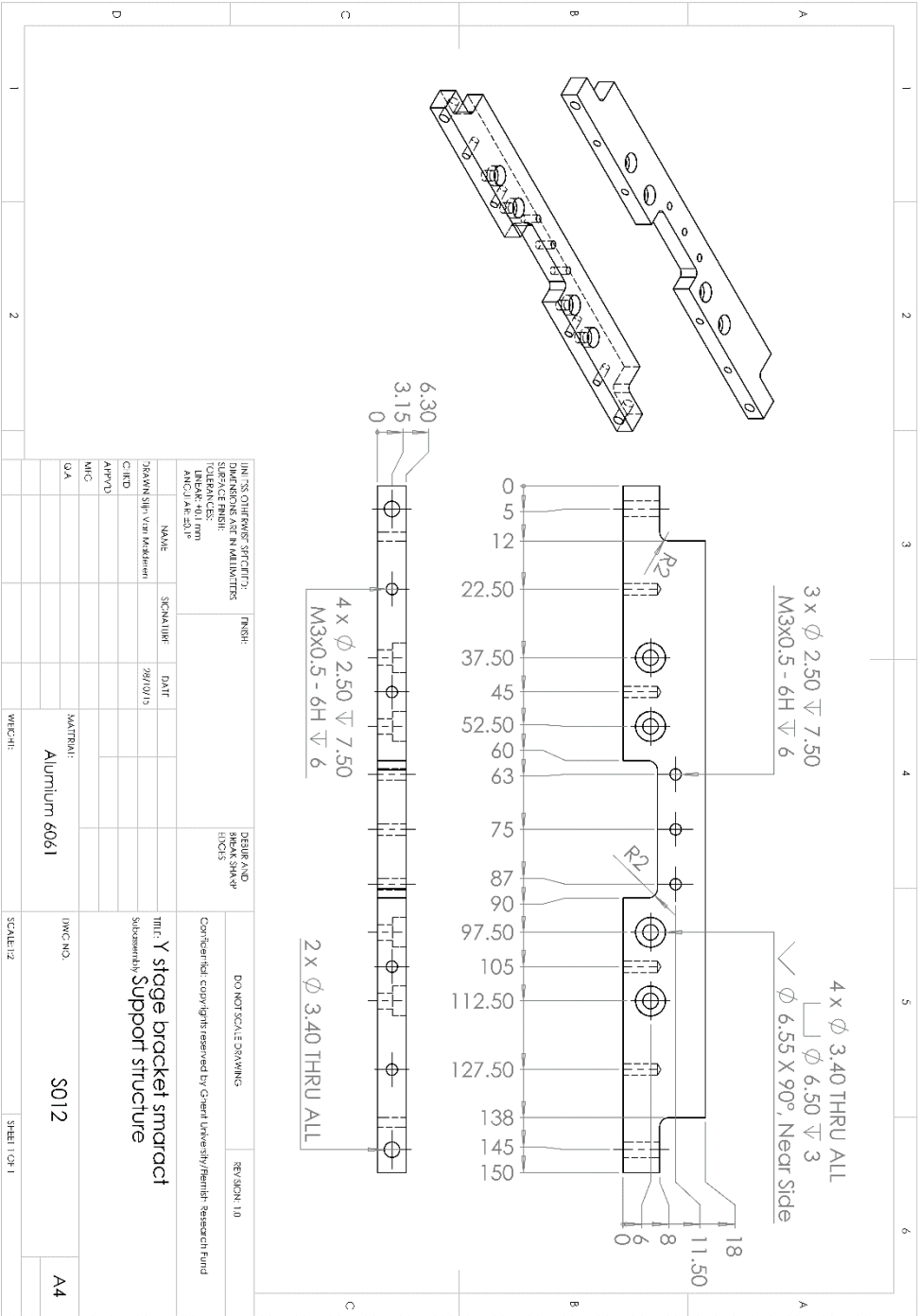


CAD drawing 8 S008 Horizontal bracket 1

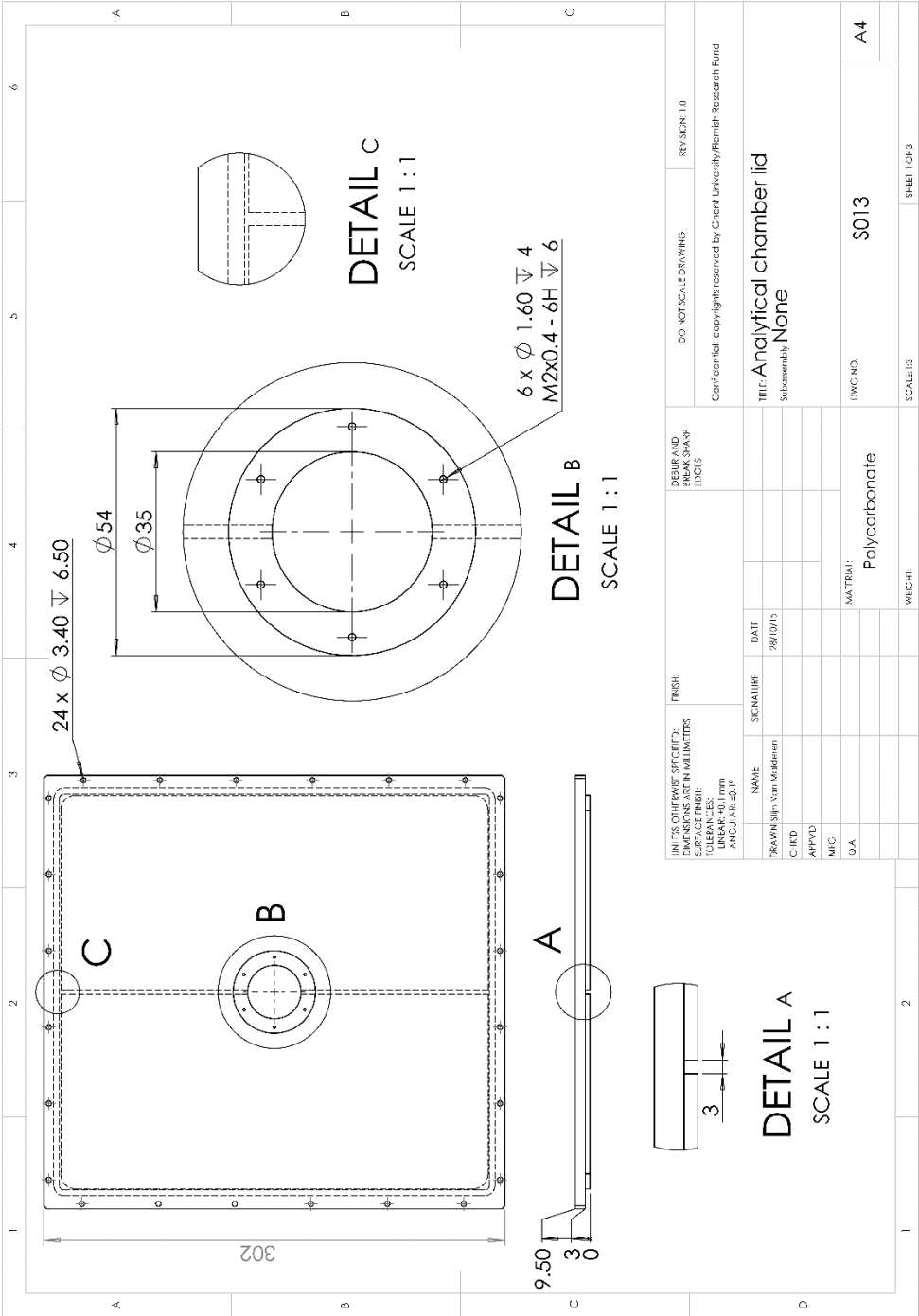




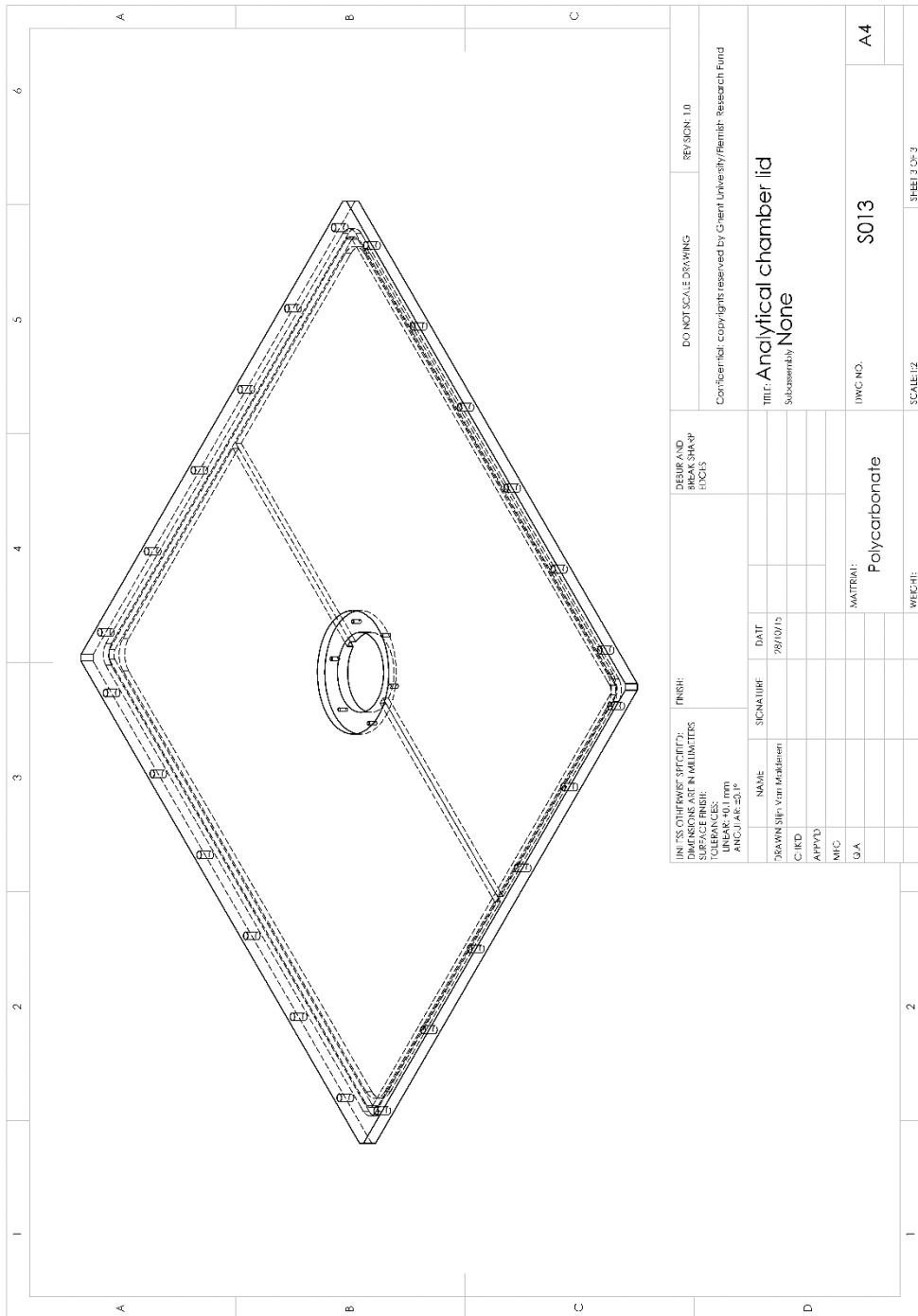
CAD drawing 10 S010 Magnet bracket



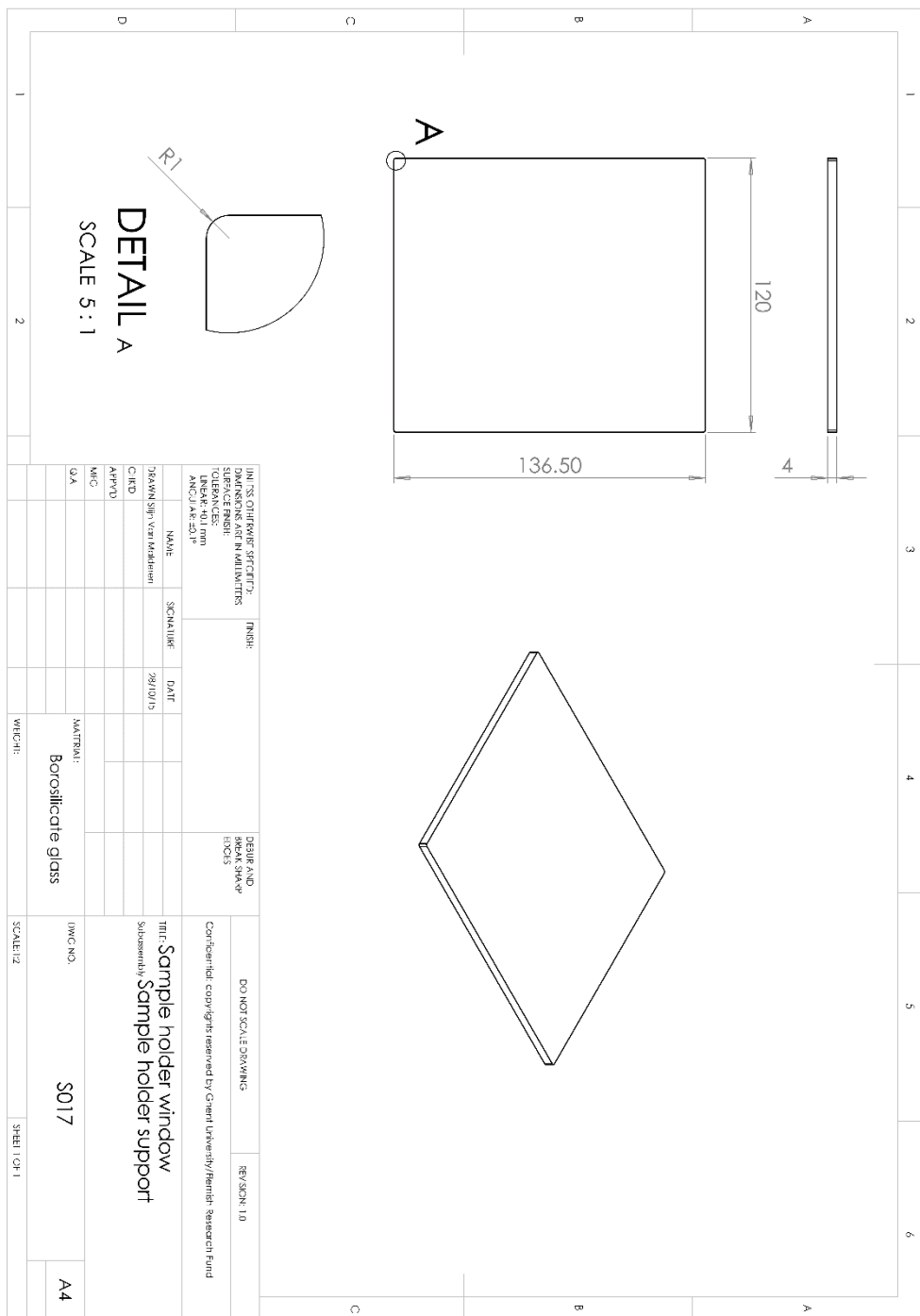
CAD drawing 11 S012 Y stage bracket smaract



CAD drawing 12 S013 Analytical chamber lid, part 1

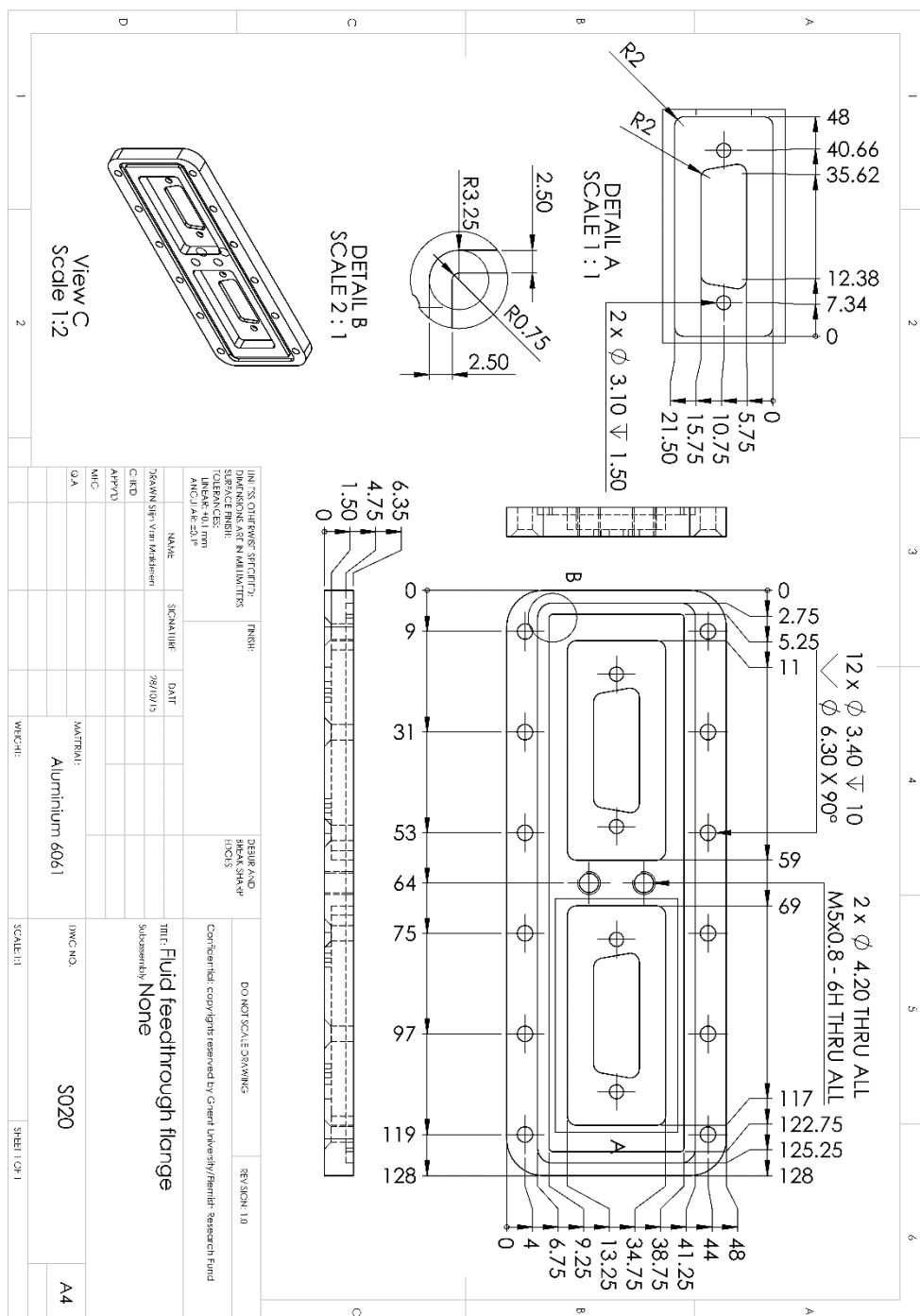


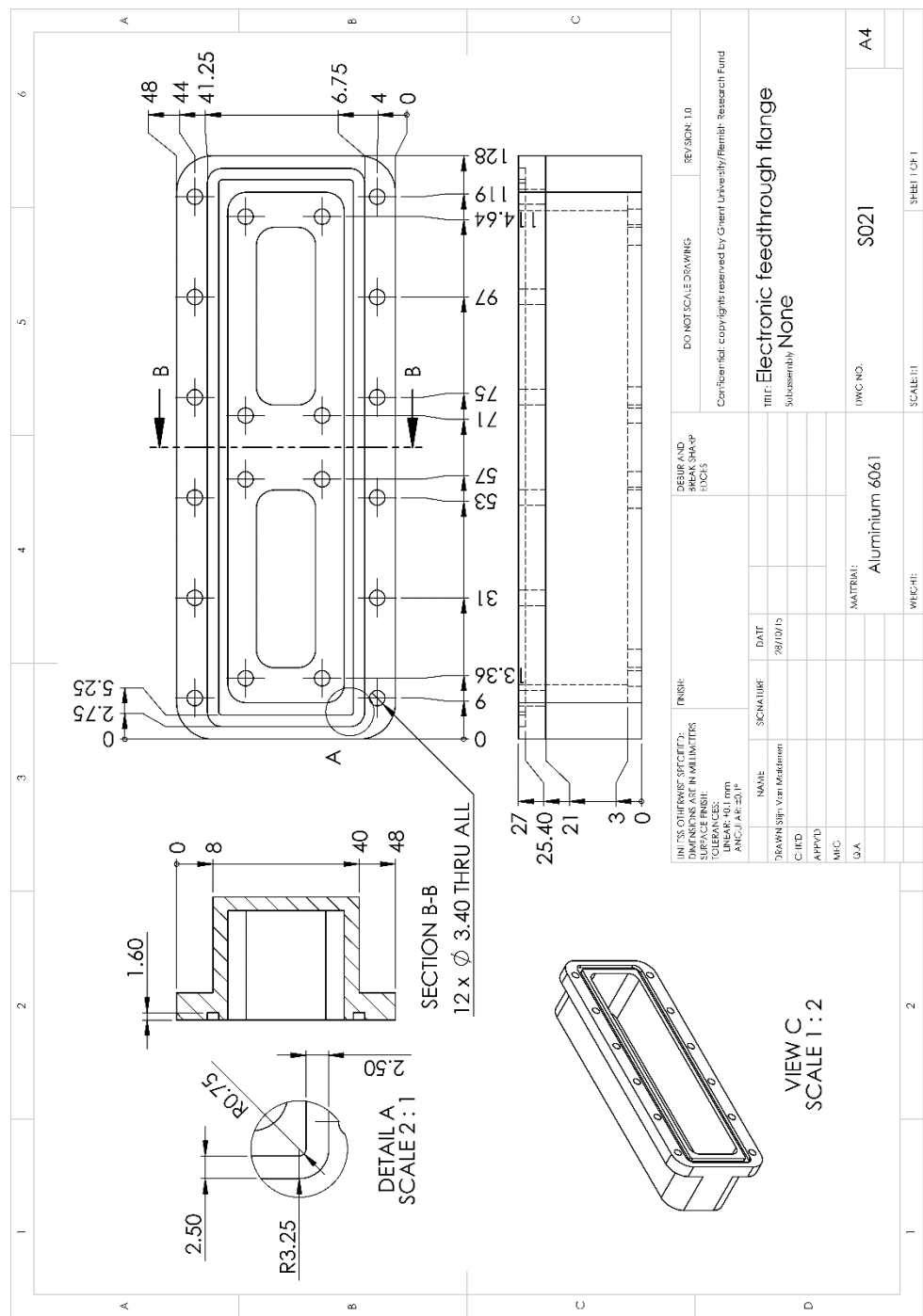
CAD drawing 14 S013 Analytical chamber lid, part 3

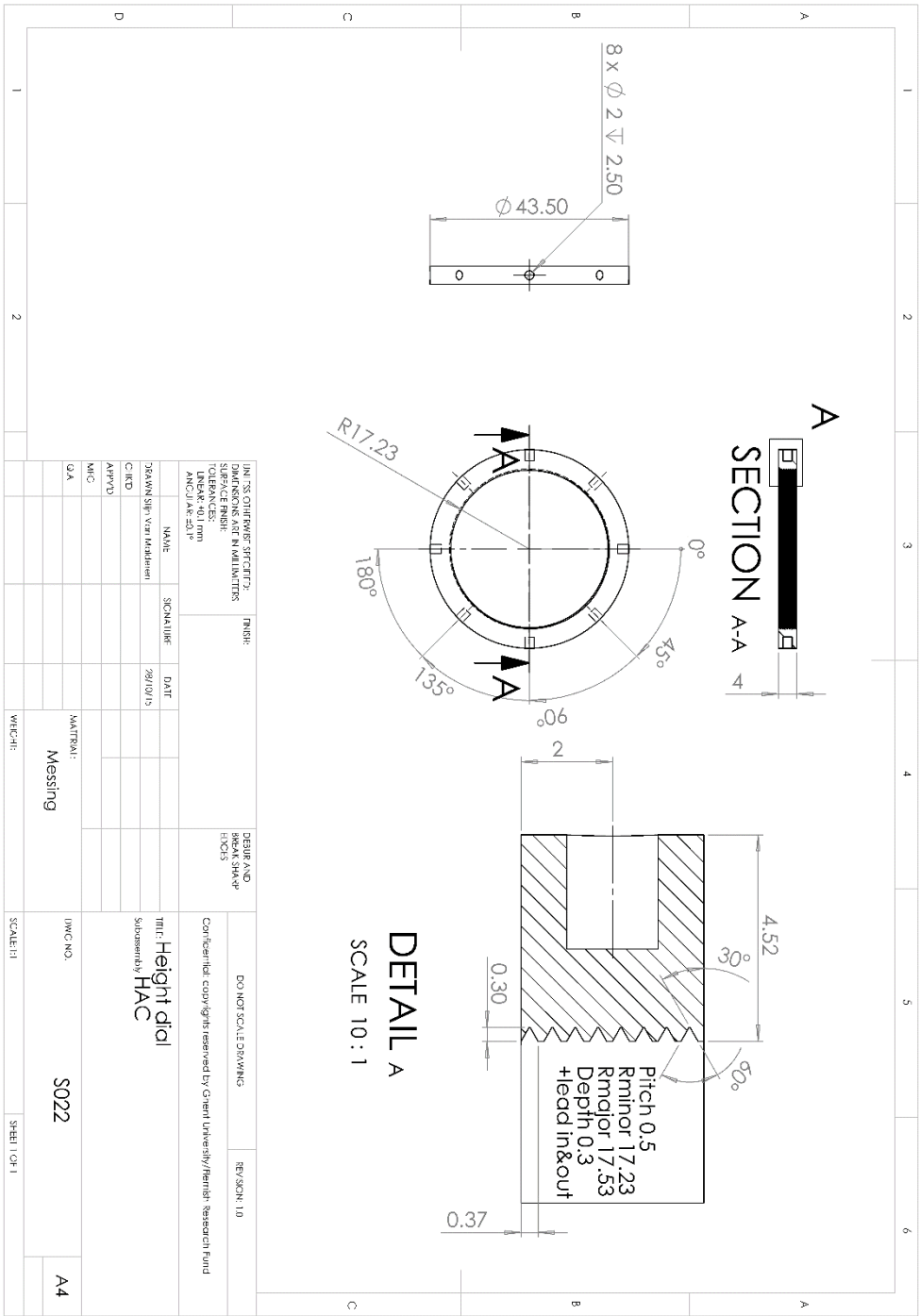


CAD drawing 15 S017 Sample holder window

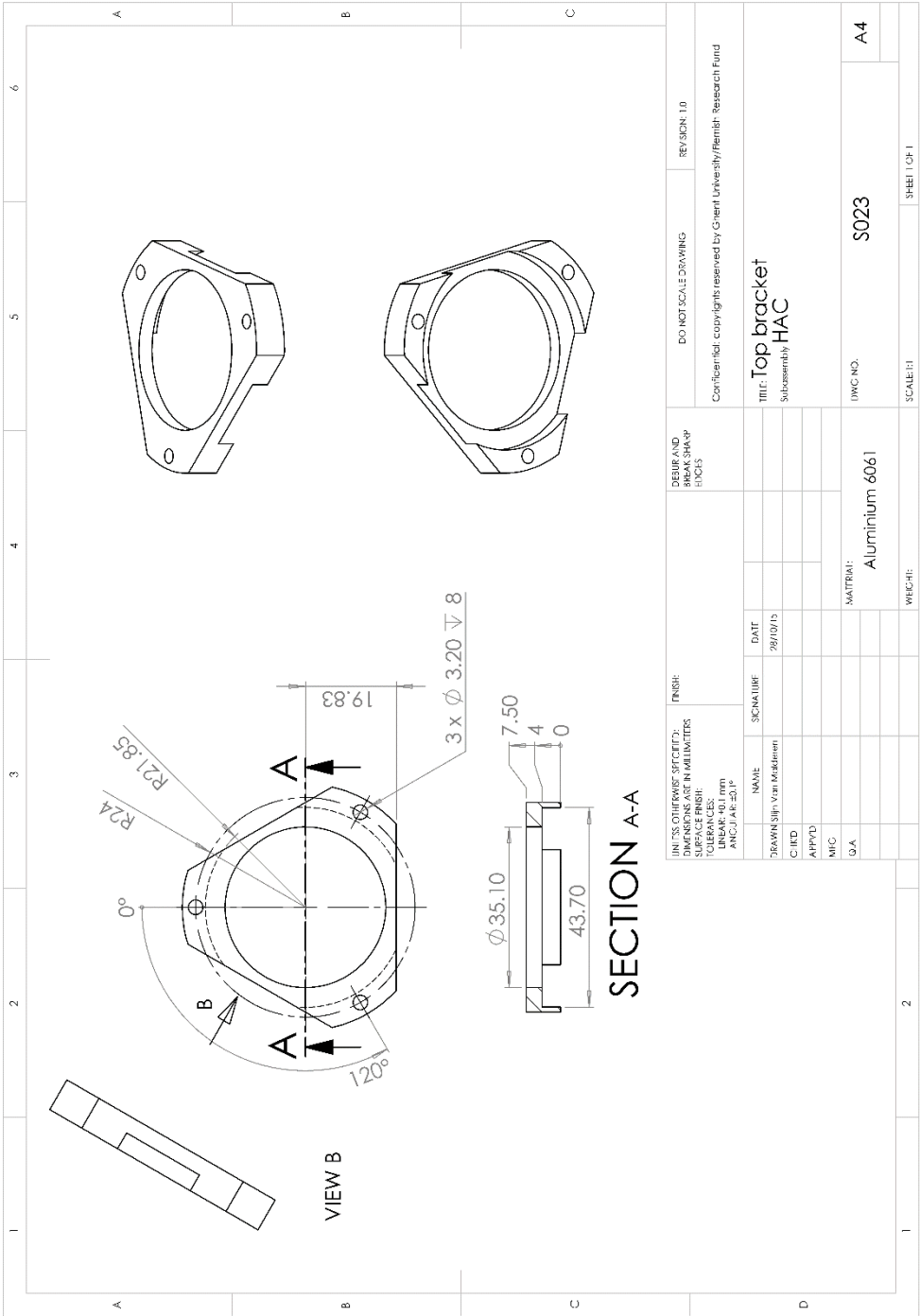
CAD drawing 17 S020 Fluid feedthrough flange



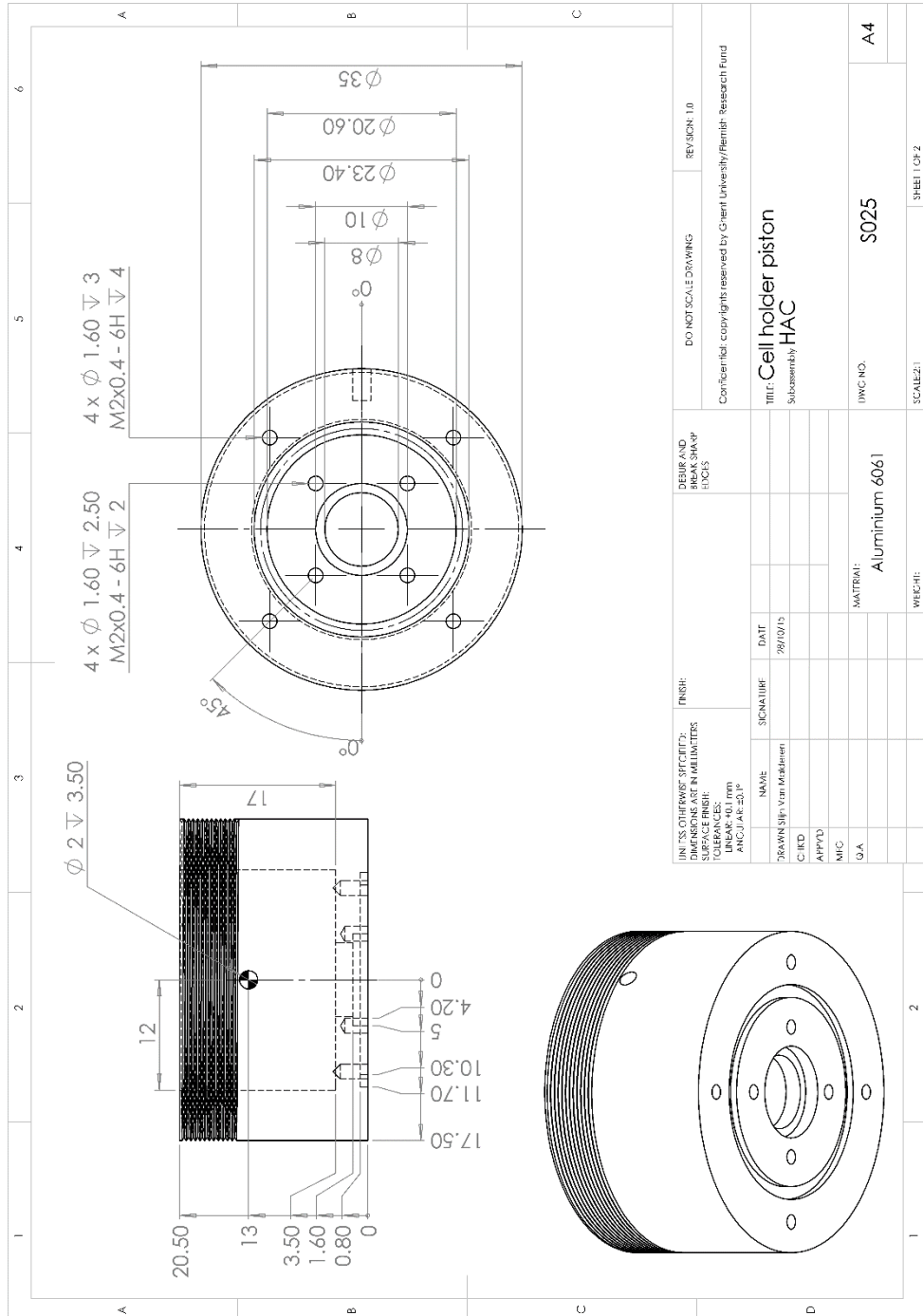




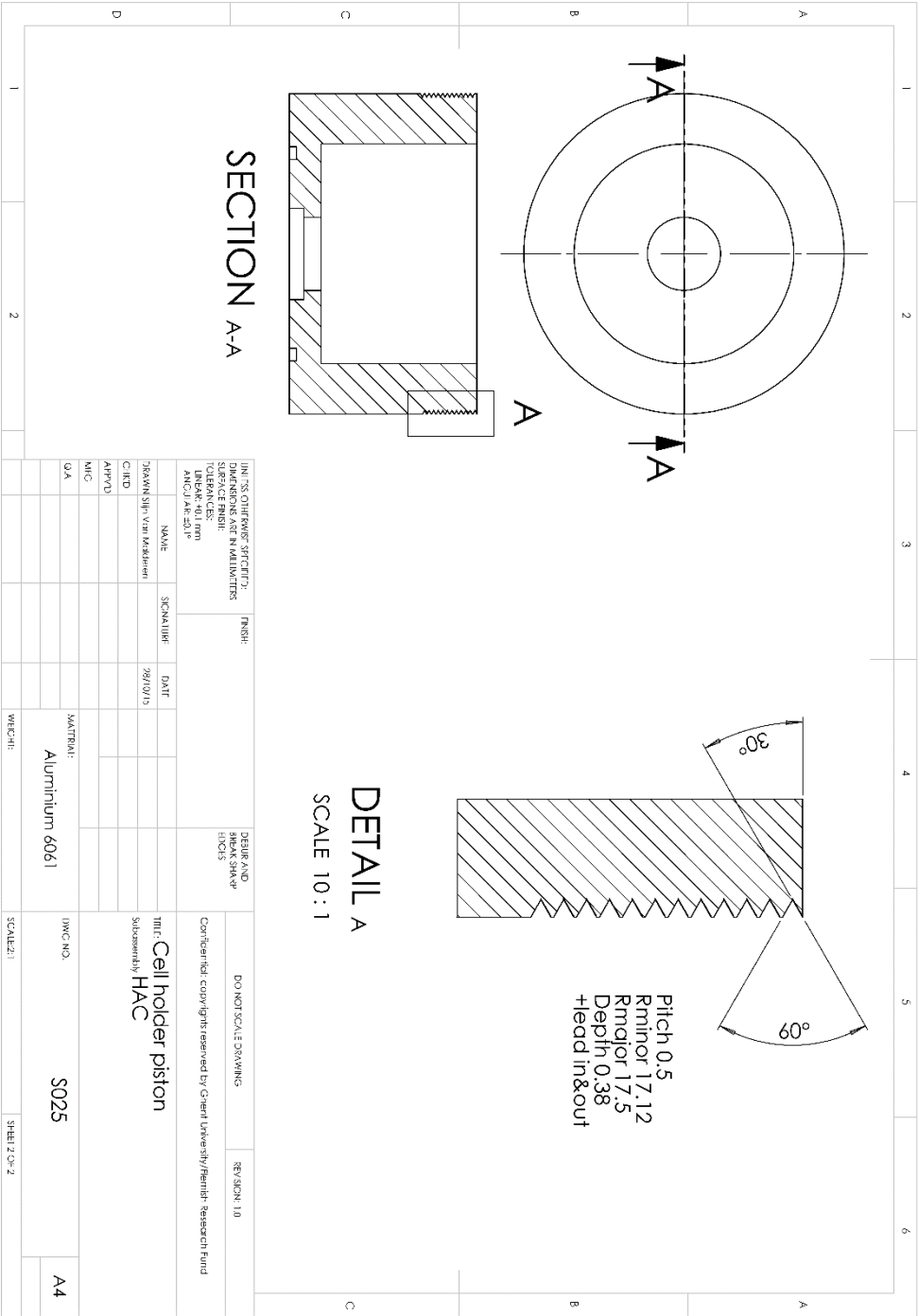
CAD drawing 19 S022 Height dial



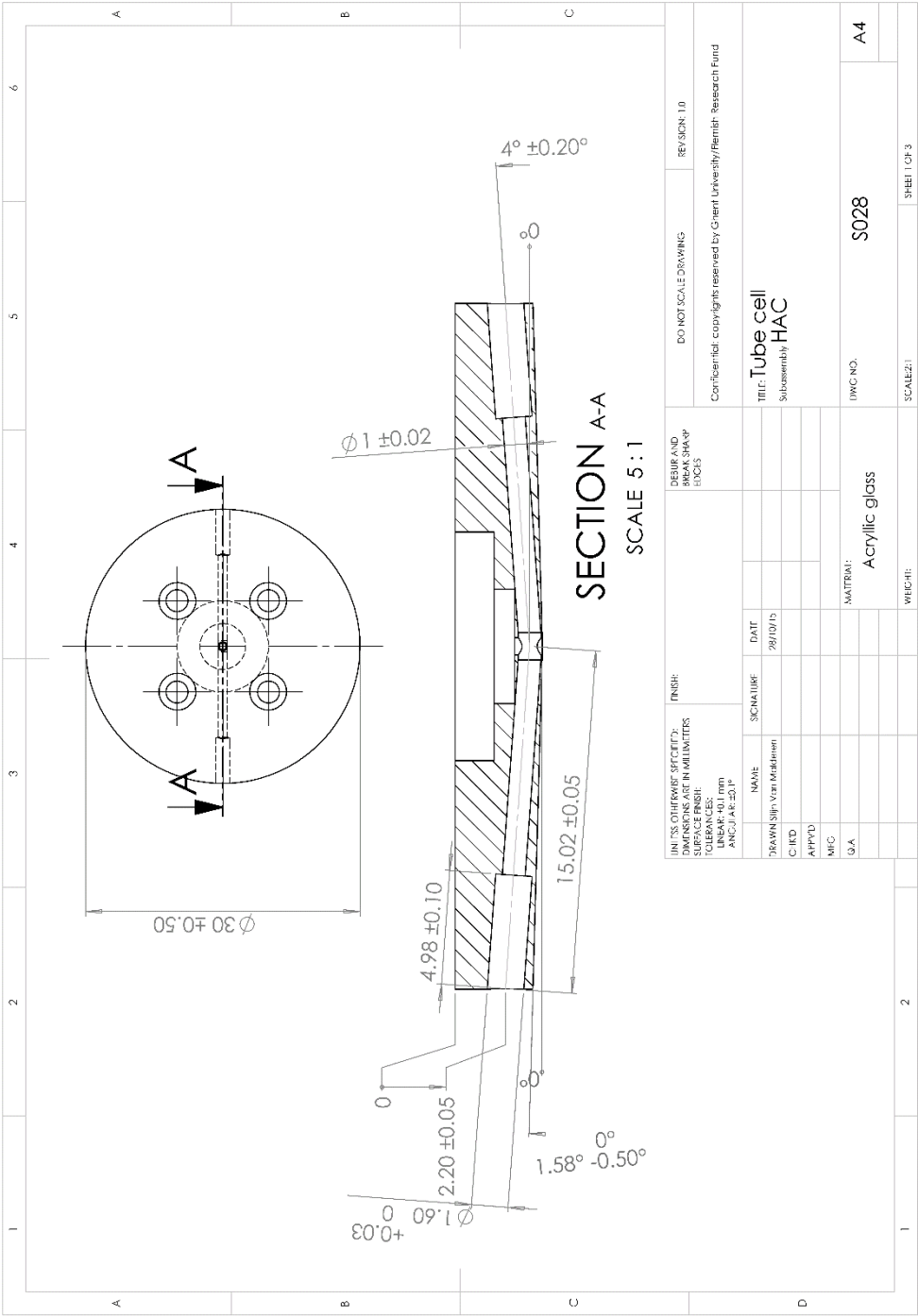
CAD drawing 20 S023 Top bracket



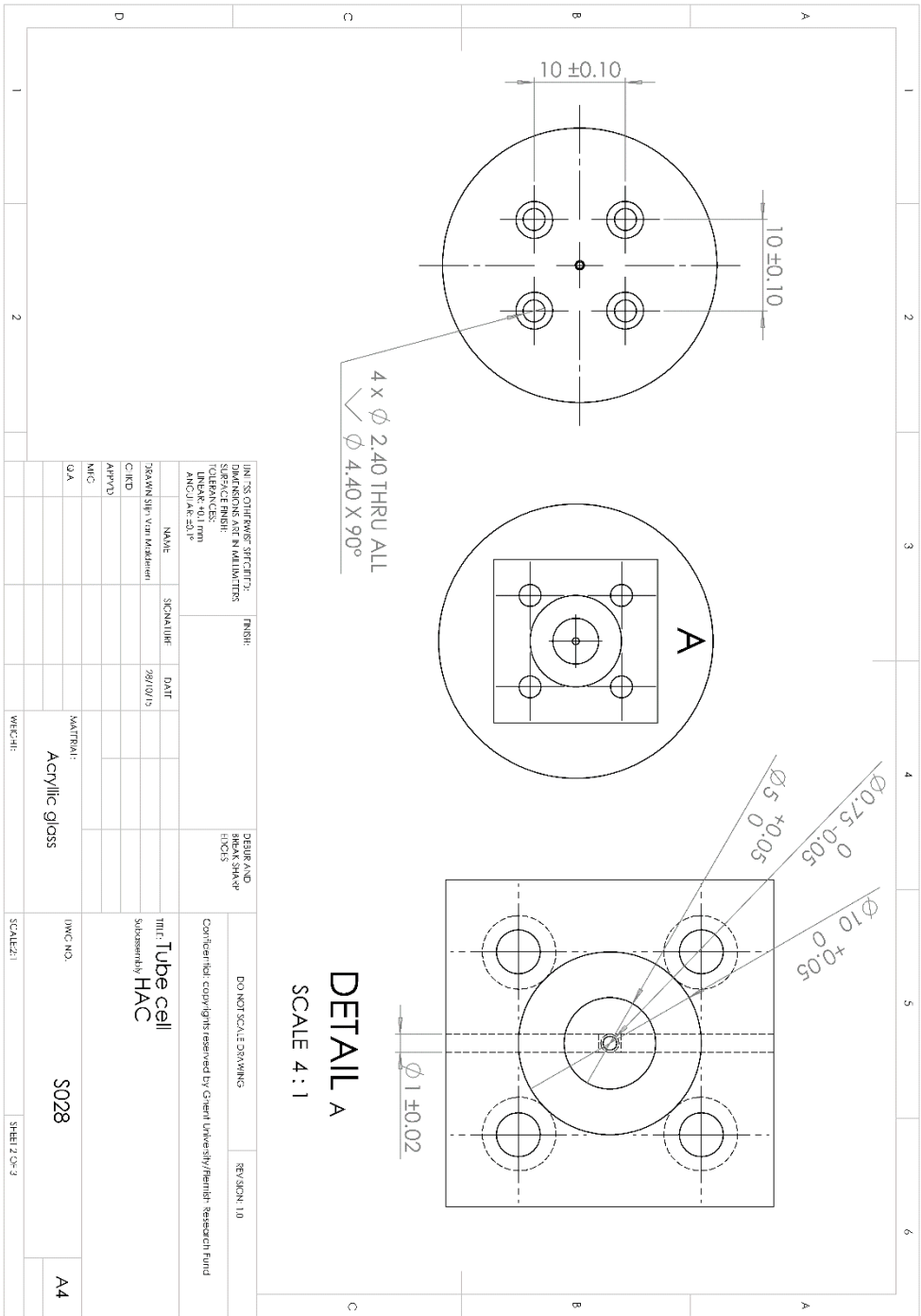
CAD drawing 22 S025 Cell holder piston, part 1



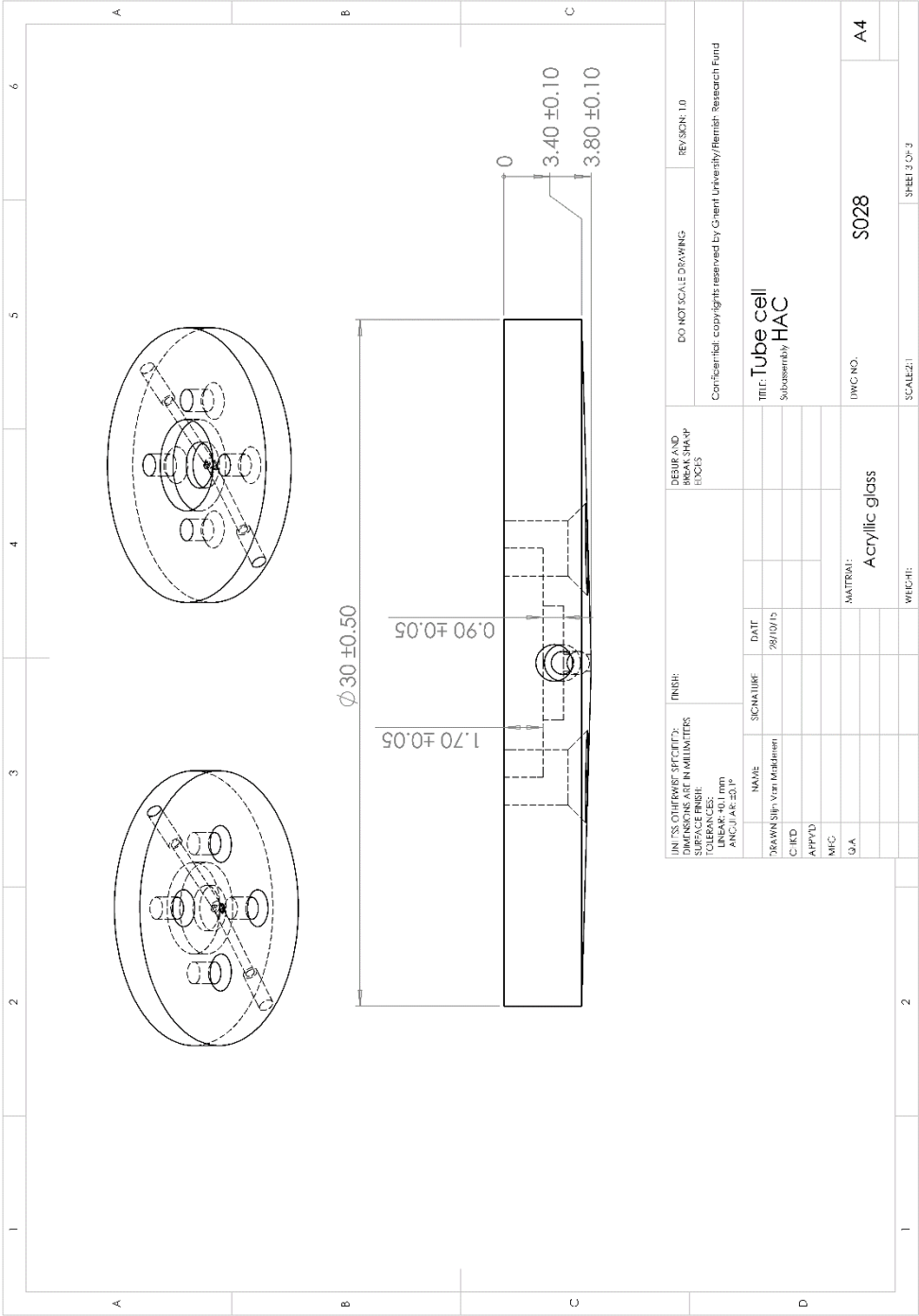
CAD drawing 23 S025 Cell holder piston, part 2



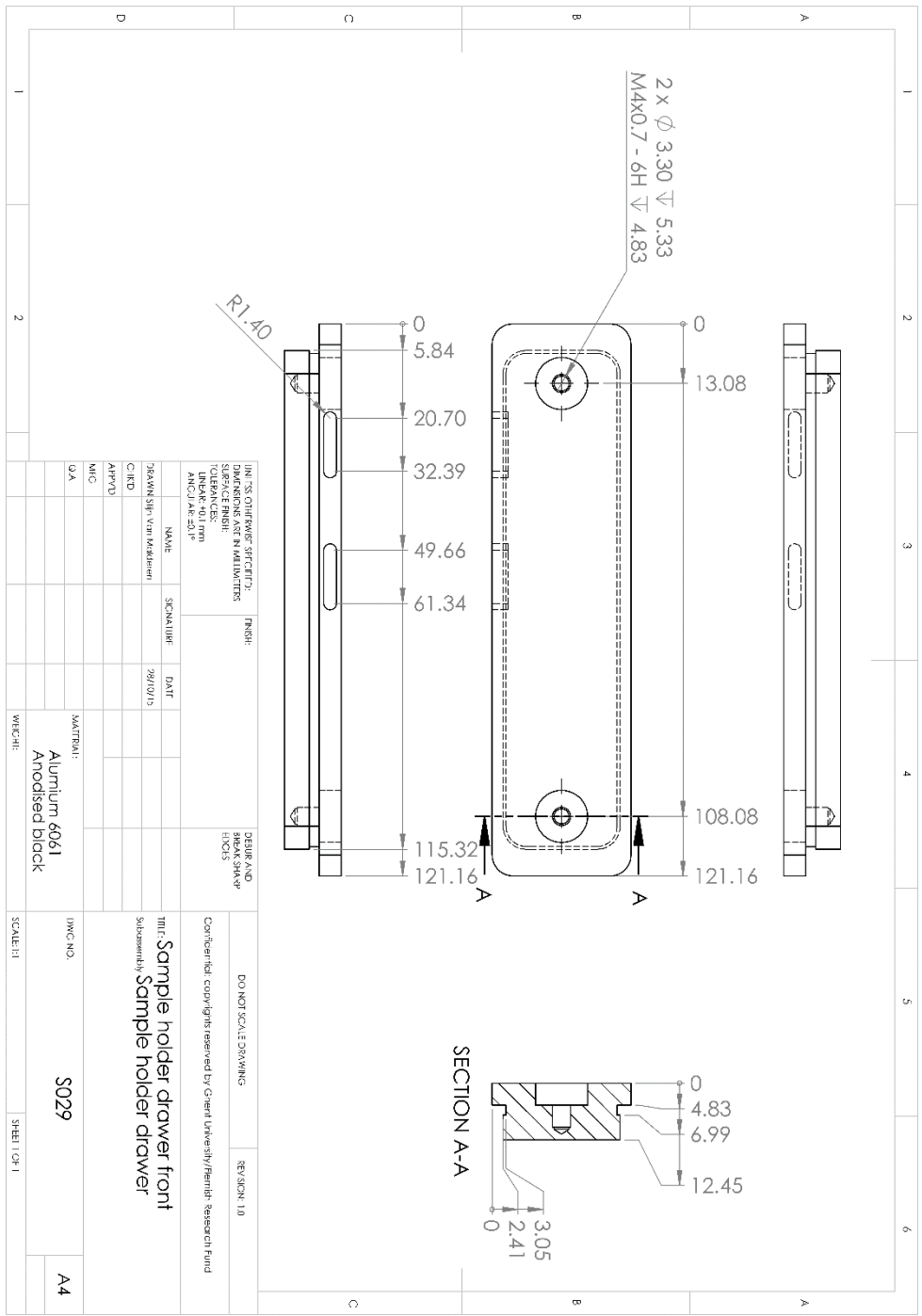
CAD drawing 24 S028 Tube cell, part 1



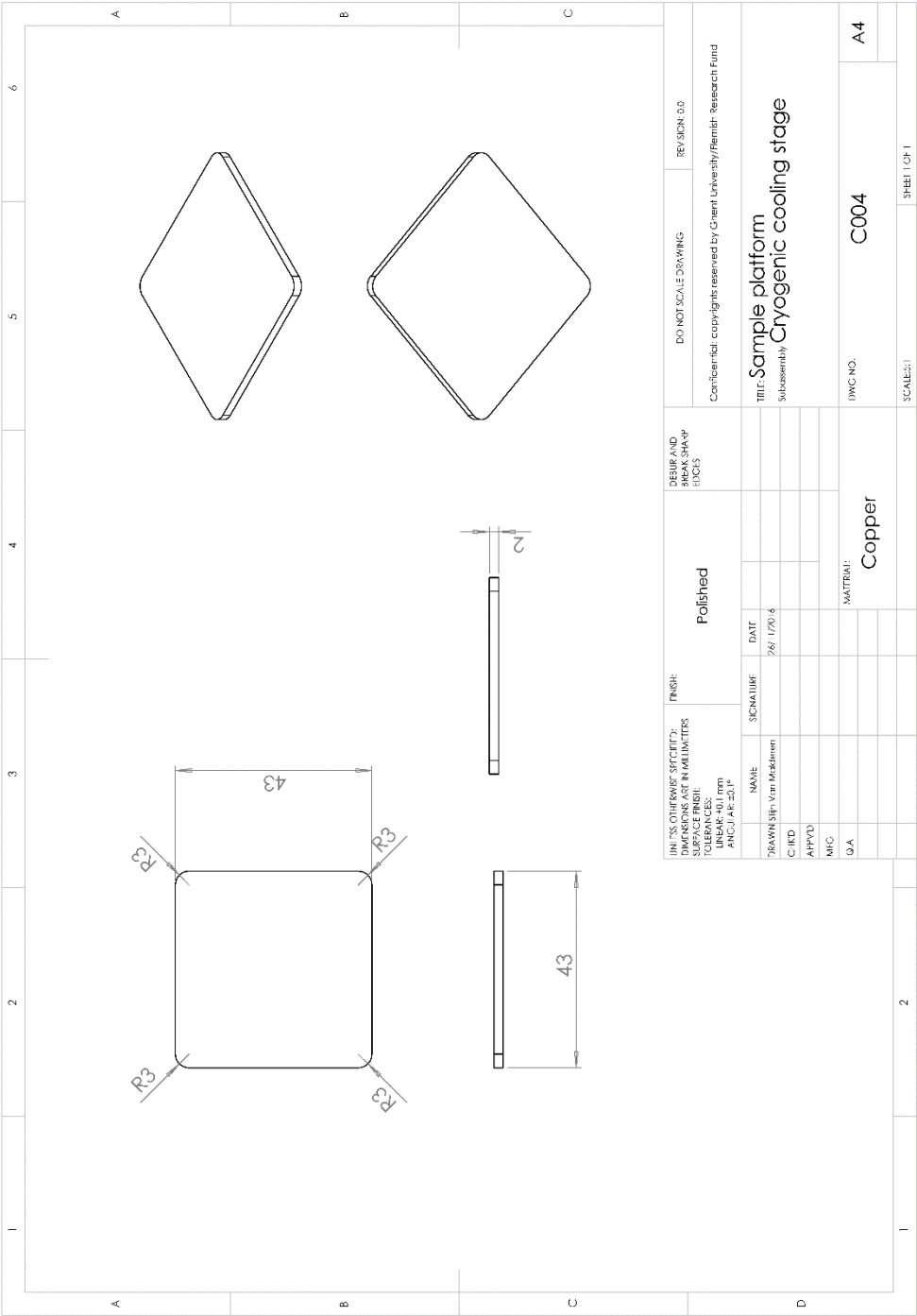
CAD drawing 25 S028 Tube cell, part 2



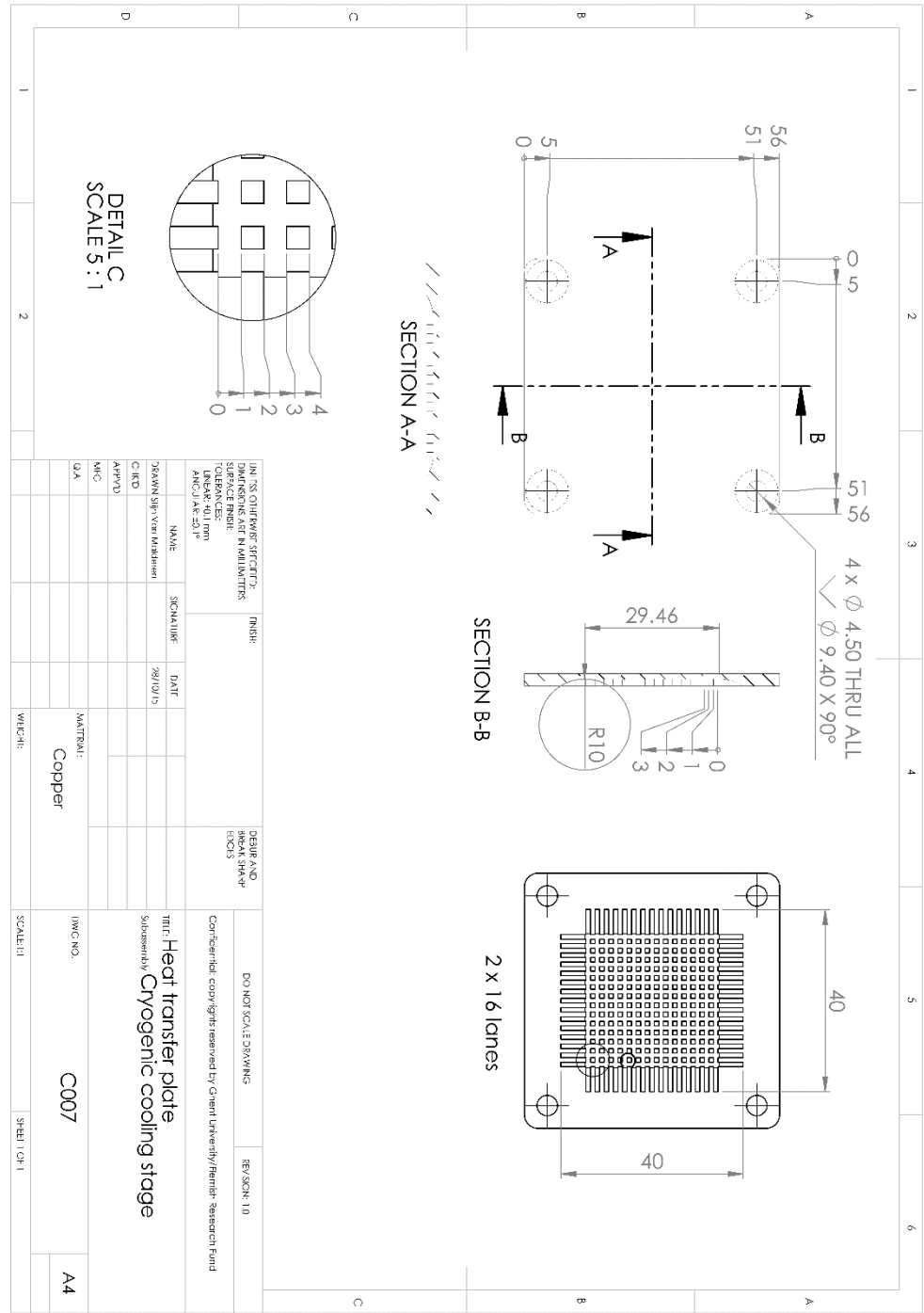
CAD drawing 26 S028 Tube cell, part 3



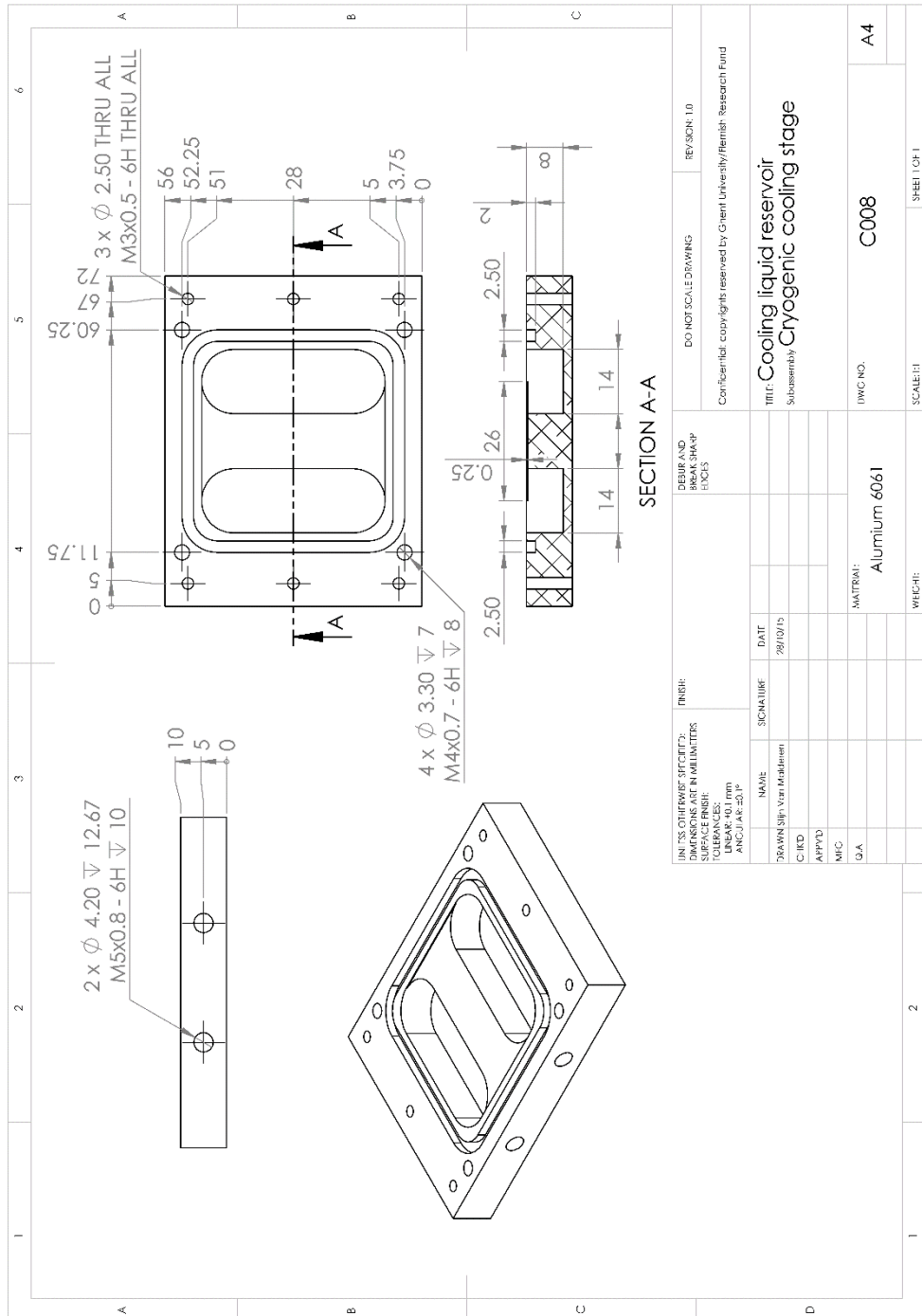
CAD drawing 27 S029 Sample holder drawer front



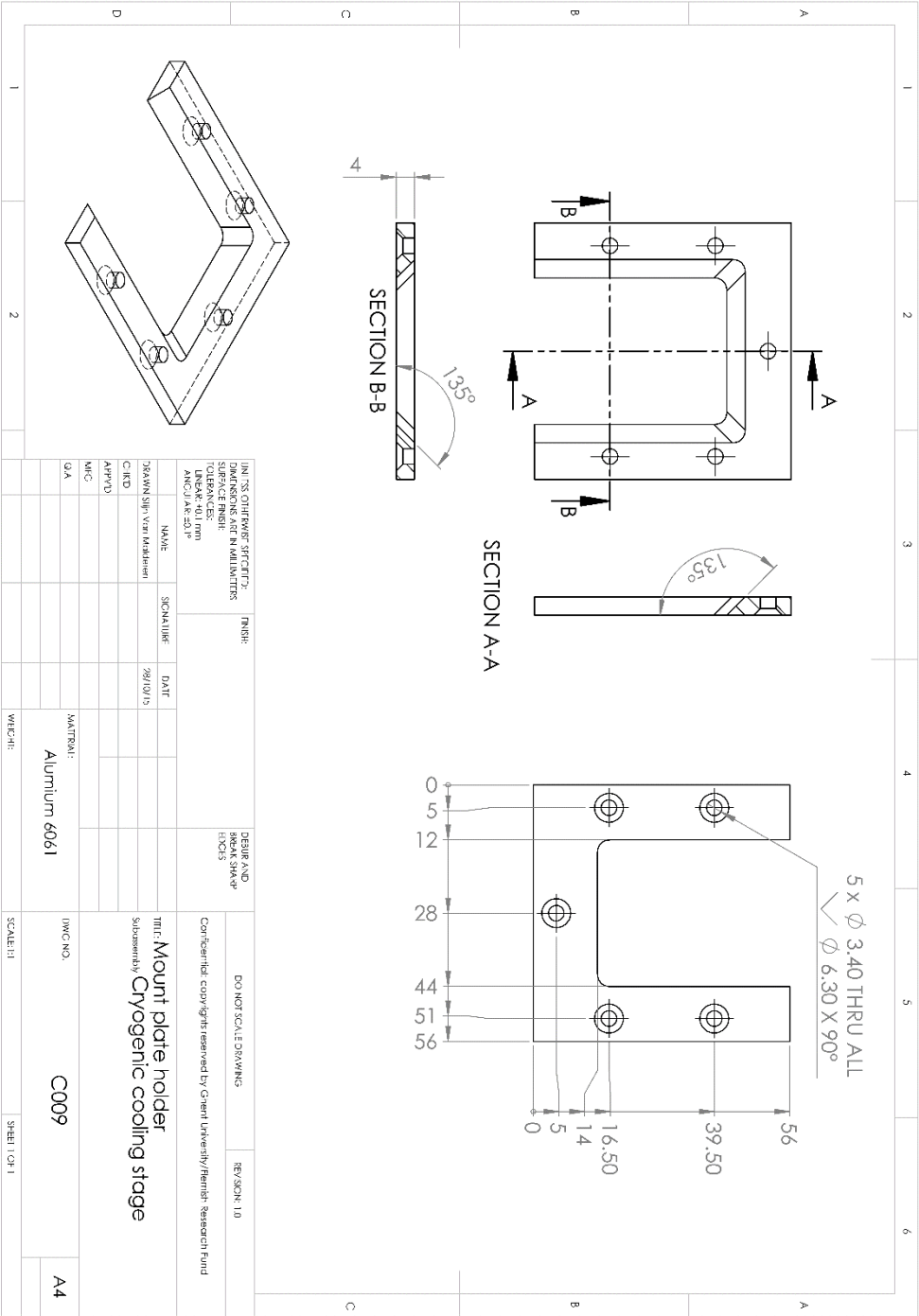
CAD drawing 28 C004 Sample platform



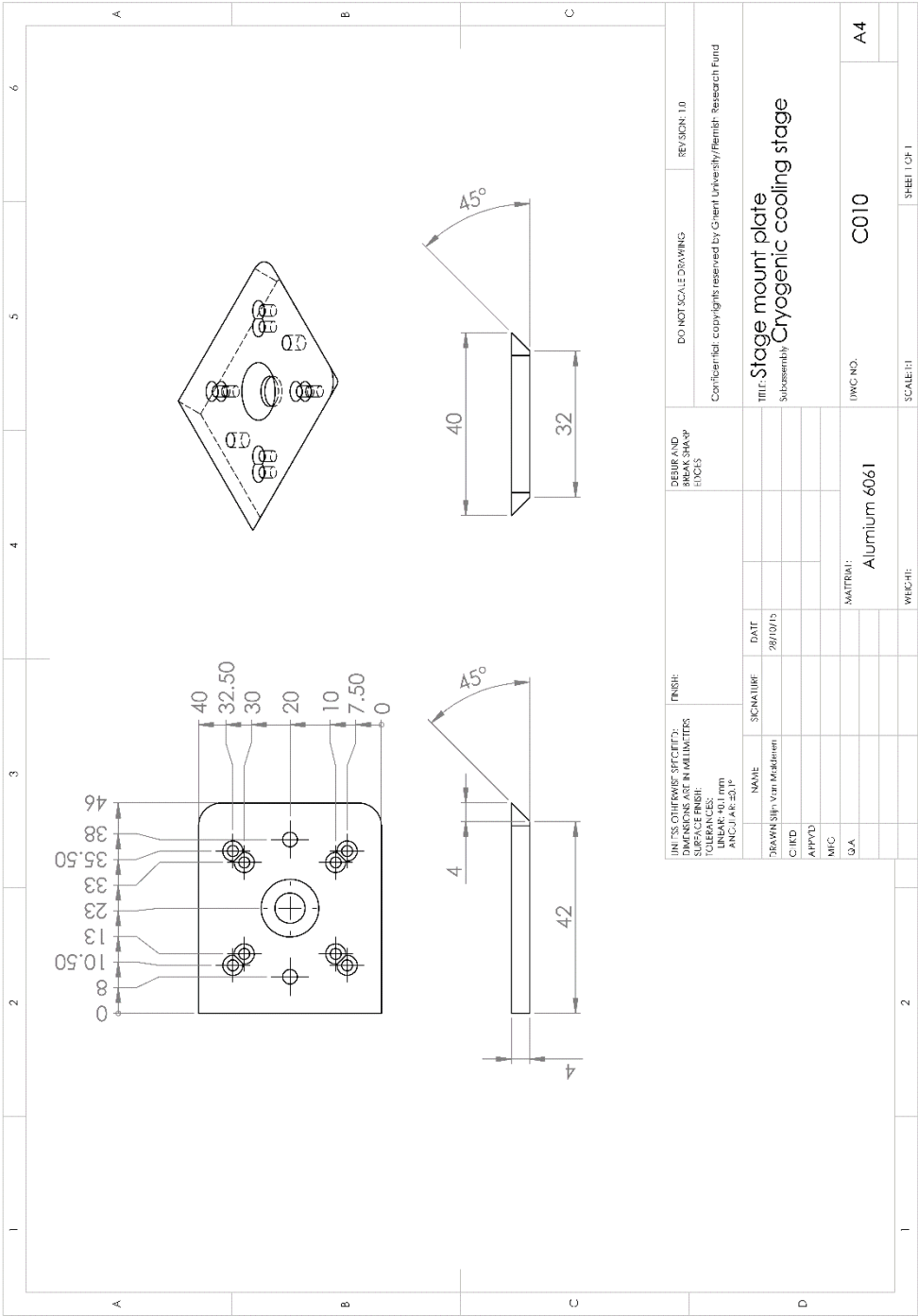
CAD drawing 29 C007 Heat transfer plate



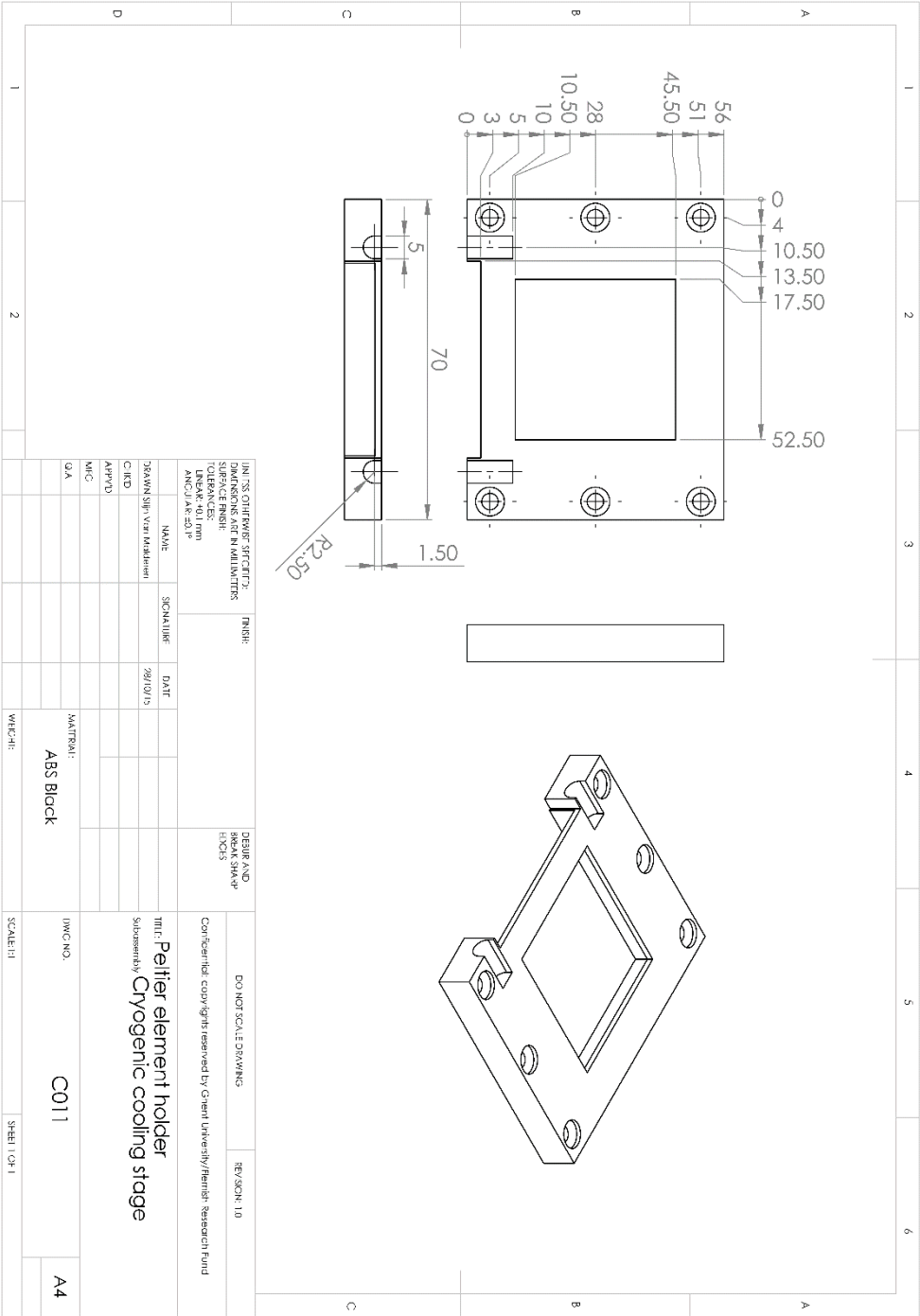
CAD drawing 30 C008 Cooling liquid reservoir



CAD drawing 31 C009 Mount plate holder



CAD drawing 32 C010 Stage mount plate



CAD drawing 33 C011 Peltier element holde

